

Cover Page



Universiteit Leiden



The following handle holds various files of this Leiden University dissertation:  
<http://hdl.handle.net/1887/79191>

**Author:** Hoff, M.L.R. van 't

**Title:** Chemistry in embedded disks: setting the stage for planet formation

**Issue Date:** 2019-10-08

# **Chemistry in embedded disks:**

*Setting the stage for planet formation*



# **Chemistry in embedded disks:**

*Setting the stage for planet formation*

Proefschrift

ter verkrijging van  
de graad van Doctor aan de Universiteit Leiden,  
op gezag van Rector Magnificus prof.mr. C.J.J.M. Stolker,  
volgens besluit van het College voor Promoties  
te verdedigen op dinsdag 8 oktober 2019  
klokke 15:00 uur  
door

Merel Lydia Roselinda van 't Hoff

geboren te Groningen, Nederland  
in 1988

## Promotiecommissie

Promotor: Prof. dr. E. F. van Dishoeck

Co-promotor: Dr. J.J. Tobin National Radio Astronomy  
Observatory

Overige leden: Prof. dr. H.J.A. Röttgering

Prof. dr. I. Snellen

Prof. dr. M.R. Hogerheijde UL, UvA

Prof. dr. Y. Aikawa University of Tokyo

Prof. dr. J.P. Williams University of Hawaii

Prof. dr. K.I. Öberg Harvard-Smithsonian Center  
for Astrophysics

ISBN: 978-94-028-1678-5

Cover design by author

**Believe those who seek the truth,  
doubt those who find it.**

André Gide  
*Ainsi soit-il, ou les jeux sont faits*  
(1952)



# Table of Contents

<b>1</b>	<b>Introduction</b>	<b>3</b>
1.1	Formation of low-mass stars and planetary systems . . . . .	4
1.1.1	Protostar formation . . . . .	6
1.1.2	Disk formation . . . . .	6
1.1.3	Planet formation . . . . .	7
1.2	Chemistry during star and planet formation . . . . .	10
1.2.1	Dark cloud and dense core chemistry . . . . .	10
1.2.2	Hot core chemistry . . . . .	12
1.2.3	Protoplanetary disk chemistry . . . . .	13
1.2.4	Chemical composition of comets . . . . .	18
1.3	Chemistry as a thermometer . . . . .	18
1.3.1	Molecular line observations . . . . .	21
1.3.2	Radiative transfer . . . . .	21
1.4	Studies of embedded disks . . . . .	22
1.4.1	Identification of protostars . . . . .	22
1.4.2	Embedded disk studies before ALMA . . . . .	23
1.4.3	Embedded disk studies with ALMA . . . . .	25
1.4.4	Modeling of embedded-disk temperature and composition . . . . .	26
1.5	This thesis . . . . .	27
1.5.1	Overview of chapters . . . . .	28
1.5.2	General conclusions and outlook . . . . .	30
<b>PART I - The <math>\lesssim 20\text{--}25</math> K regime: freeze out of CO</b>		<b>32</b>
<b>2</b>	<b>Robustness of <math>\text{N}_2\text{H}^+</math> as tracer of the CO snowline</b>	<b>37</b>
2.1	Introduction . . . . .	40
2.2	Protoplanetary disk model . . . . .	41
2.2.1	Physical model . . . . .	41
2.2.2	Chemical model . . . . .	43
2.2.3	Line radiative transfer . . . . .	46
2.3	Results . . . . .	47
2.3.1	Distribution and emission of $\text{N}_2\text{H}^+$ . . . . .	47
2.3.2	Influence of CO and $\text{N}_2$ abundances . . . . .	50
2.3.3	Importance of the $\text{N}_2\text{H}^+$ surface layer . . . . .	50
2.3.4	Influence of CO and $\text{N}_2$ binding energies . . . . .	54
2.3.5	Influence of the cosmic ray ionization rate . . . . .	54



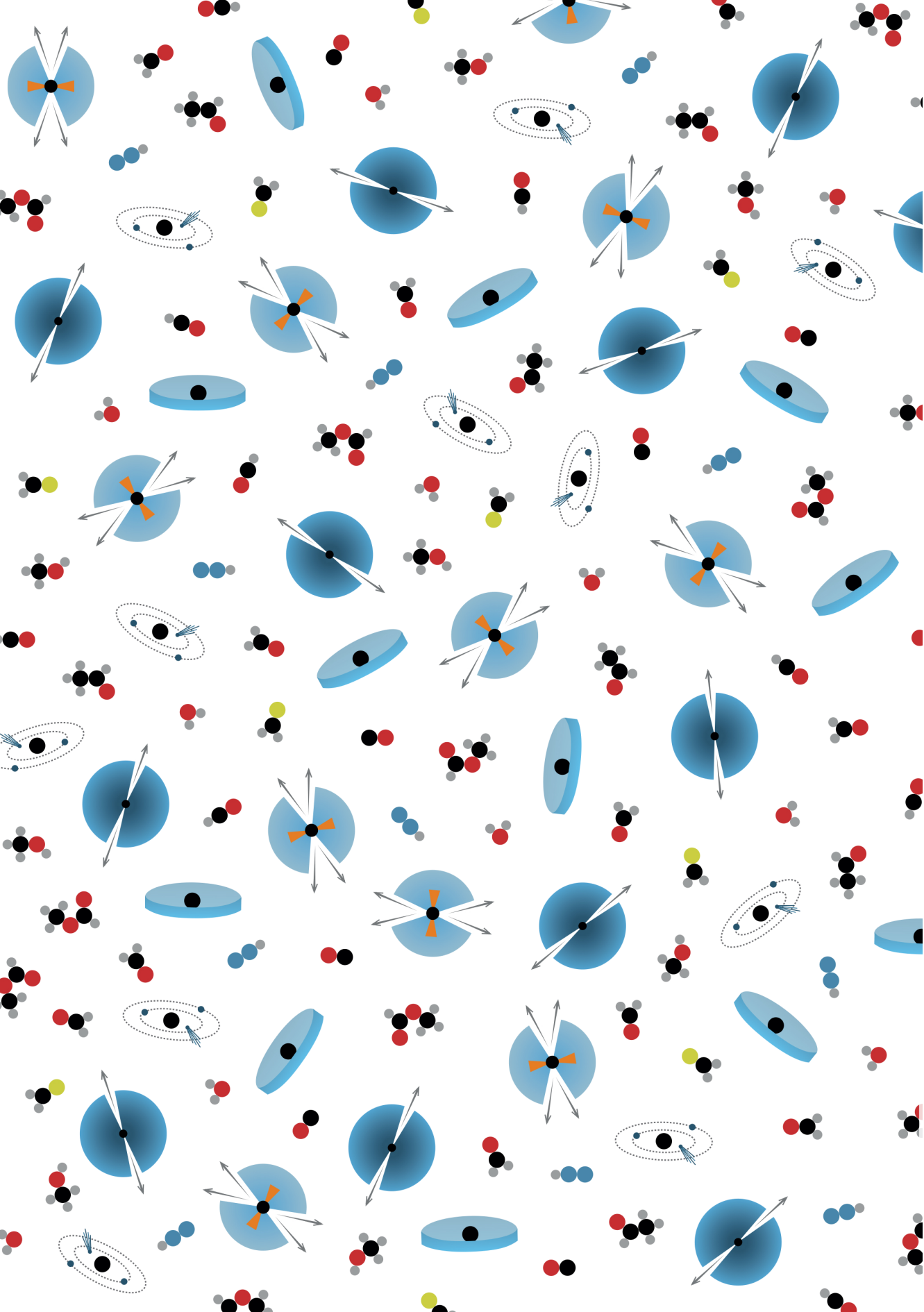
2.3.6	Influence of grain settling . . . . .	55
2.3.7	Constraints provided by multiple $N_2H^+$ transitions . . . . .	56
2.3.8	Outer edge of $N_2H^+$ emission . . . . .	57
2.4	Discussion . . . . .	58
2.5	Conclusions . . . . .	61
Appendices . . . . .		63
2.A	Chemical model . . . . .	63
2.A.1	Freeze-out and desorption balance . . . . .	63
2.A.2	Simple chemical network . . . . .	64
2.A.3	Photodesorption . . . . .	65
2.B	$N_2H^+$ $J=4-3$ peak integrated intensity . . . . .	66
2.C	$N_2H^+$ line ratios . . . . .	67
2.D	Photodesorption . . . . .	68
<b>3</b>	<b>Unveiling the physical conditions of the youngest disks</b>	
	<i>A warm embedded disk in L1527</i>	71
3.1	Introduction . . . . .	74
3.2	Observations . . . . .	76
3.3	Results . . . . .	78
3.4	Analysis . . . . .	79
3.4.1	$^{13}CO$ optical depth . . . . .	80
3.4.2	Gas temperature . . . . .	81
3.4.3	Disentangling disk and envelope emission . . . . .	85
3.5	Modeling of the line emission . . . . .	89
3.5.1	$^{13}CO$ and $C^{18}O$ . . . . .	89
3.5.2	CO abundance . . . . .	95
3.5.3	$N_2D^+$ . . . . .	96
3.6	Discussion . . . . .	98
3.6.1	Dust opacity . . . . .	99
3.6.2	Comparison with other observations . . . . .	100
3.6.3	Implications of a warm disk in the embedded phase . . . . .	102
3.7	Conclusions . . . . .	103
Appendices . . . . .		105
3.A	$^{13}CO/C^{18}O$ line ratio . . . . .	105
3.B	Brightness temperature . . . . .	105
3.C	Physical model for disk and envelope . . . . .	108
3.D	Free fall velocity . . . . .	111
<b>4</b>	<b>Temperature structure of embedded disks</b>	
	<i>Young disks in Taurus are warm</i>	115
4.1	Introduction . . . . .	118
4.2	Observations . . . . .	120
4.3	Results . . . . .	120
4.3.1	$C^{17}O$ and $H_2CO$ morphology . . . . .	120
4.3.2	$C^{17}O$ and $H_2CO$ column densities . . . . .	124
4.3.3	HDO and $CH_3OH$ upper limits . . . . .	126
4.4	Analysis . . . . .	127
4.4.1	Temperature structure in the edge-on disks . . . . .	127
4.4.2	Temperature structure in less-inclined disks . . . . .	133

4.5	Discussion . . . . .	134
4.5.1	Temperature structure of young disks . . . . .	134
4.5.2	Decrease in H <sub>2</sub> CO in the inner disk . . . . .	135
4.6	Conclusions . . . . .	136
	Appendices . . . . .	138
4.A	C <sup>17</sup> O and H <sub>2</sub> CO Observations . . . . .	138
4.B	Schematics of the disk models . . . . .	141
<b>PART II - The <math>\gtrsim 100</math> K regime: thermal desorption of H<sub>2</sub>O and COMs</b>		<b>141</b>
<b>5</b>	<b>Imaging the water snowline in protostellar envelopes with H<sup>13</sup>CO<sup>+</sup></b>	
	<i>The case of NGC1333 IRAS2A</i>	147
5.1	Introduction . . . . .	150
5.2	Observations . . . . .	152
5.3	Results . . . . .	156
5.4	Analysis and discussion . . . . .	157
5.4.1	Parametrized abundance profile for H <sup>13</sup> CO <sup>+</sup> . . . . .	157
5.4.2	Comparison with a full chemical model . . . . .	159
5.4.3	Tracing the CO snowline: signs of an accretion burst? . . . . .	162
5.4.4	Attenuation of the cosmic ray ionization rate . . . . .	164
5.4.5	Physical structure . . . . .	165
5.5	Summary and outlook . . . . .	165
	Appendices . . . . .	166
5.A	Initial abundances in the GRAINOBLE model . . . . .	166
5.B	Effect of an attenuated cosmic ray ionization rate . . . . .	167
<b>6</b>	<b>Imaging the water snowline in protostellar envelopes with H<sup>13</sup>CO<sup>+</sup></b>	
	<i>A small survey of protostars in Perseus</i>	171
6.1	Introduction . . . . .	174
6.2	Observations . . . . .	176
6.3	Results . . . . .	178
6.3.1	Line detections . . . . .	178
6.3.2	H <sup>13</sup> CO <sup>+</sup> emission morphology . . . . .	180
6.3.3	H <sup>13</sup> CO <sup>+</sup> and the water snowline . . . . .	180
6.4	Discussion and Conclusions . . . . .	181
	Appendices . . . . .	183
6.A	H <sup>13</sup> CO <sup>+</sup> channelmaps . . . . .	183
6.B	H <sup>13</sup> CO <sup>+</sup> moment one maps . . . . .	188
<b>7</b>	<b>Methanol and its relation to the water snowline</b>	
	<i>The disk around the young outbursting star V883 Ori</i>	191
7.1	Introduction . . . . .	194
7.2	Observations . . . . .	196
7.3	Results . . . . .	196
7.3.1	Detection of warm methanol in the disk . . . . .	196
7.3.2	Column density and excitation temperature . . . . .	199
7.3.3	Methanol outer radius . . . . .	200
7.4	Discussion . . . . .	201
7.4.1	Location of the water snowline . . . . .	201

---

7.4.2	Ice composition of planet forming material . . . . .	202
<b>8</b>	<b>Temperature profiles of young disk-like structures</b>	
	<i>The case of IRAS 16293A</i> . . . . .	205
8.1	Introduction . . . . .	208
8.2	Observations . . . . .	210
8.3	Results . . . . .	214
	8.3.1 Kinematics . . . . .	214
	8.3.2 Peak fluxes . . . . .	216
	8.3.3 Temperature . . . . .	217
8.4	Discussion . . . . .	222
8.5	Conclusions . . . . .	223
	Appendices . . . . .	225
	8.A Formaldehyde and thioformaldehyde lines . . . . .	225
	8.B Position-velocity diagrams . . . . .	227
	8.C Peak fluxes . . . . .	230
	8.D RADEX results for H <sub>2</sub> CS . . . . .	231
	8.E Radial temperature profiles . . . . .	234
	<b>Bibliography</b> . . . . .	237
	<b>Nederlandse samenvatting</b> . . . . .	260
	<b>List of publications</b> . . . . .	261
	<b>Curriculum Vitae</b> . . . . .	263
	<b>Acknowledgements</b> . . . . .	265







# 1. Introduction

For centuries, people have gazed at the stars and planets, and wondered about our place in the cosmos. Where do we come from? And, are we alone? With the discovery of more than 3000 planets around other stars in the last few decades<sup>1</sup>, the potential of life in other solar systems has become reality. These planetary systems display a large diversity in size, and the number and types of planets, but our own Solar System seems atypical (see e.g., Raymond et al. 2019), immediately raising the question whether the occurrence of life is uncommon as well. One way to try and answer these questions is by examining the properties of the discovered planets, for example, their atmospheric composition, and comparing that to what we think are the requirements for life. Another way is to study the material around newborn stars that will eventually make up planets. On the one hand, comparing the composition of planetary building blocks to the composition of Solar System comets, which are remnants of the young Solar System, can tell whether the initial conditions for the formation of the Solar System are unique or very common. On the other hand, using this information in planet formation models can predict the likelihood of forming an Earth-like planet under given conditions. Moreover, studying the chemical complexity at these early stages can tell us whether the building blocks for life are formed in space, and possibly delivered to young planets by cometary bodies, or whether life has to start from very simple molecules on a planetary surface.

This thesis utilizes the approach of studying the planet-forming material and focuses on the initial stage of planet formation, the so-called “embedded stage”, in which the planetary building blocks start to form in a disk around the young protostar that is still embedded in its natal cloud. The advent of the Atacama Large Millimeter/submillimeter Array (ALMA) in 2011 has allowed the study of these objects at planetary-system scales, and this thesis uses observations of different molecular species to characterize the physical and chemical conditions at the onset of planet formation.

## 1.1 Formation of low-mass stars and planetary systems

Star formation occurs in dense ( $n \sim 10^4 - 10^5 \text{ cm}^{-3}$ ) and cold ( $T \sim 10 - 20 \text{ K}$ ) regions of giant molecular clouds. After the formation of a prestellar core, the early evolution of low mass stars ( $M \lesssim 2 M_{\odot}$ ) can be divided into four evolutionary *Stages* (Fig. 1.1; Shu et al. 1987). Observationally, the different phases are categorized into *Classes*, as will be described in Sect. 1.4.1. The gravitational collapse of the prestellar core results in a protostar surrounded by an infalling envelope. In this initial stage (*Stage 0*), the envelope mass is much larger than the central protostellar mass. Due to accretion, the protostellar mass increases and exceeds the envelope mass after  $\sim 10^5$  years (*Stage I*). In addition, a disk begins to form during Stage 0 to conserve the angular momentum of the rotating infalling material. Stage 0 and I are referred to as the *protostellar* or *embedded stage*. The envelope dissipates due to accretion onto the disk and mass loss via bipolar outflows such that after  $\sim 10^{5-6}$  years, a gas-rich protoplanetary disk is left surrounding a pre-main sequence star (*Stage II*). Accretion finally ceases (after  $\sim 10^{6-7}$  years) as disk material grows into planets and dissipates due to processes like photoevaporation. In *Stage III*, the pre-main sequence star is surrounded by a gas-poor disk consisting mainly of dust created by collisions of larger bodies. Finally, the star reaches the main sequence and a planetary system is born. A more detailed description is given in the following sections.

<sup>1</sup>see <http://exoplanets.org> and <http://exoplanet.eu>

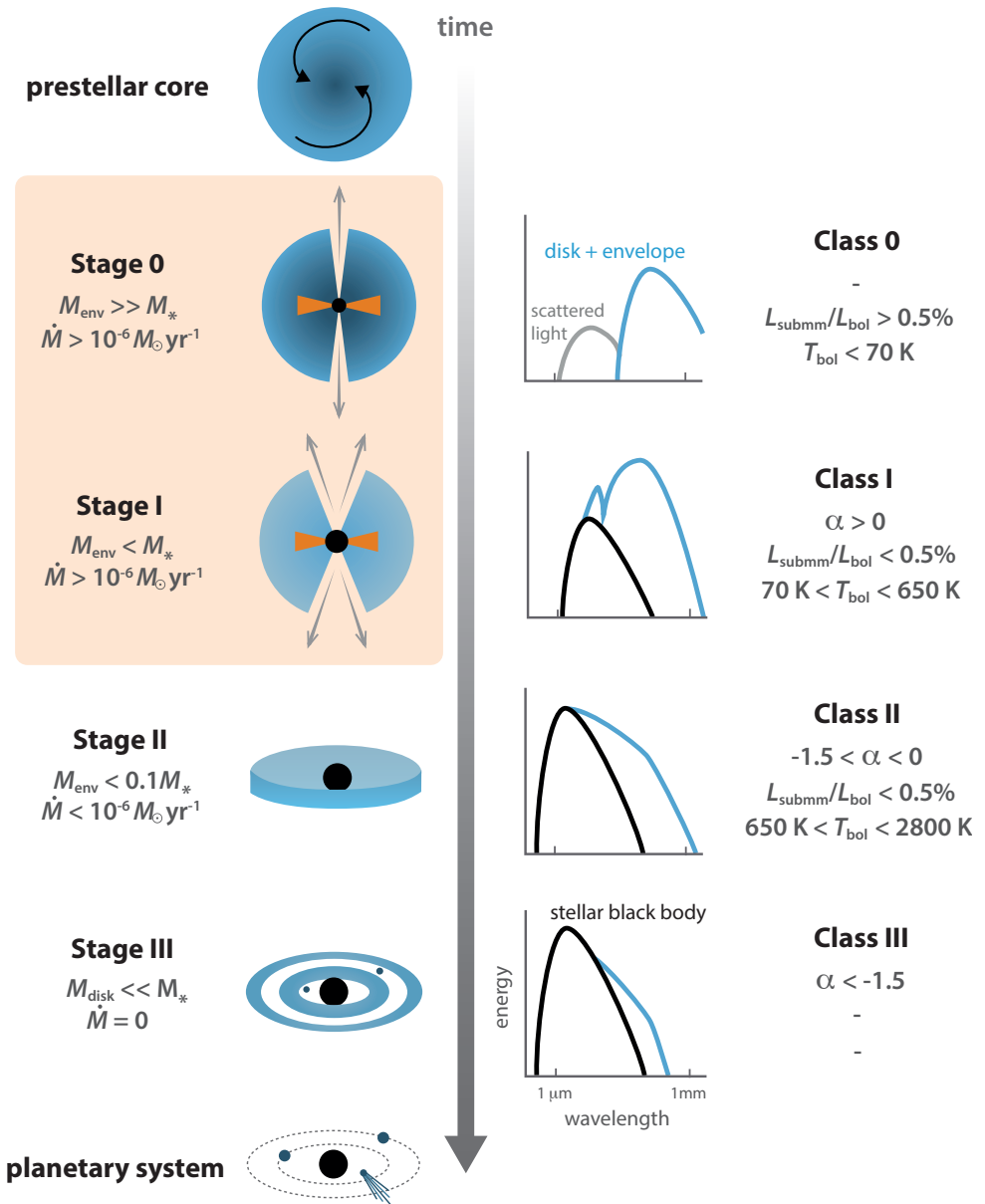


**Figure 1.1:** Schematic overview of the different stages of low-mass star formation (*left panels*) and the observational classification based on the spectral energy distribution (SED; *right panels*). The embedded phase that is the focus of this thesis is marked by the orange box. Stage II disks are also referred to as protoplanetary disks.



### 1.1.1 Protostar formation

The material in giant molecular clouds ( $\sim 10$ – $100$  pc) is not uniformly distributed, but rather concentrated in filamentary structures with typical widths of  $\sim 0.1$  pc (André et al. 2010; Kennicutt & Evans 2012). These filaments fragment into smaller fibers that in turn are the parent structures from which dense cores form (e.g., Hacar & Tafalla 2011). The exact formation mechanism for these cores is still debated, with many scenarios suggested between two extreme paradigms: quasi-static contraction mediated by ambipolar-diffusion and gravo-turbulent fragmentation driven by supersonic motions (see e.g., reviews by Ward-Thompson et al. 2007; André et al. 2014).

The collapse of such a *prestellar core* results in a first hydrostatic core (FHSC) once the inner region becomes opaque to radiation (Larson 1969). The FHSC is a short lived phase (0.5–50 kyr) with a low luminosity ( $< 0.1 L_{\odot}$ ), low mass (0.01–0.1  $M_{\odot}$ ) central object (e.g., Boss & Yorke 1995; Tomida et al. 2010). Several candidate FHSC have been proposed, but none have been unambiguously identified. As the FHSC continues to accrete mass, the central temperature increases until temperatures of  $\sim 2000$  K are reached. Now  $H_2$  starts to dissociate which prevents the temperature from rising and balancing gravity. This leads to a second collapse, forming a protostar deeply embedded in an envelope of infalling material (Larson 1969). Highly collimated bipolar outflows are typically observed during this early phase and aid in mass loss and angular momentum conservation (see e.g., reviews by Frank et al. 2014; Bally 2016).

### 1.1.2 Disk formation

The formation of a circumstellar disk is a natural consequence of angular momentum conservation during the collapse of a rotating core (Cassen & Moosman 1981; Terebey et al. 1984), and hydrodynamical simulations readily form large ( $> 100$  AU) and massive disks early in the embedded phase (e.g., Yorke et al. 1993). Initial observations suggest that, in principle, cores have enough angular momentum to form 100 AU-sized rotationally supported disks (e.g., Goodman et al. 1993; Caselli et al. 2002a), but with higher angular resolution and higher sensitivity observations, organized rotation of cores is found less frequently (e.g., Tobin et al. 2012a). Instead, angular momentum may be the result of residual small-scale turbulent motions or gravitational torques between cloud overdensities (Offner et al. 2016; Kuznetsova et al. 2019).

However, disk formation is far more subtle in the presence of magnetic fields (see e.g., reviews by Li et al. 2014; Lizano & Galli 2015). Ideal magnetohydrodynamic (MHD) simulations show that magnetic braking prevents the formation of a rotationally supported disk: as the material collapses, the magnetic field is dragged inward as well, increasing the field strength toward smaller radii such that the infalling material becomes dominated by the magnetic field in the inner region. Because the magnetic field remains connected to the slower rotating outer part of the envelope, all angular momentum can be removed from the collapsing inner envelope. Instead of a rotationally supported disk, a non-equilibrium flattened structure (a pseudo-disk) is formed, as predicted by Galli & Shu (1993a,b). This “magnetic braking catastrophe” has been confirmed analytically and in multiple numerical simulations (e.g., Galli et al. 2006; Mellon & Li 2008).

Since protoplanetary disks are ubiquitously observed (e.g., Ansdell et al. 2016), several potential solutions are being investigated and remain an active topic of investigation (see e.g., review by Li et al. 2014). Since dense cores are only slightly ionized

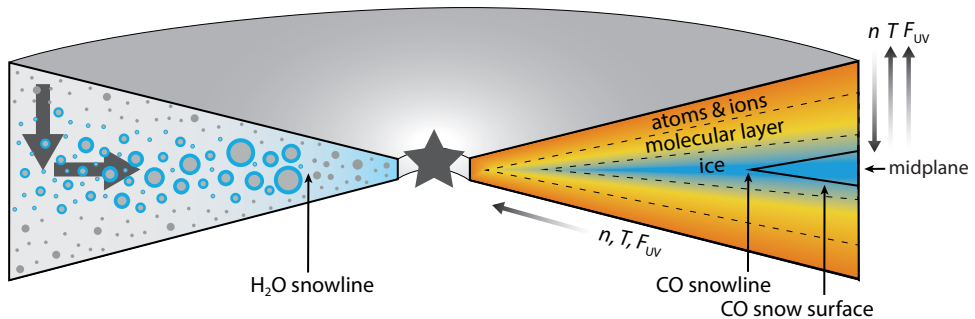


**Figure 1.2:** Physical and chemical structure of a protoplanetary disk. The *left side* shows the growth of ice covered dust grains as they settle toward the midplane and drift inward. Inside the water snowline all ice has evaporated and these bare grains are more prone to fragmentation. The *right side* shows the layered chemical structure due to vertical and radial gradients in density ( $n$ ), temperature ( $T$ ) and UV flux ( $F_{\text{UV}}$ ).

(with a typical electron fractional abundance of  $\sim 10^{-7}$ ; Bergin & Tafalla 2007), the magnetic field is not expected to be perfectly frozen into the material (as is assumed in the ideal MHD case). Multiple groups have therefore developed numerical simulations to study non-ideal MHD effects (ambipolar diffusion, Ohmic dissipation, and the Hall effect). Although the exact conditions for disk formation remain widely debated, the general conclusion so far seems to be that small (10–100 AU) rotationally supported disks can form in the early stage of protostar formation (see e.g., Tsukamoto et al. 2017 and Wurster et al. 2018 for recent results). Other effects that can promote disk formation are misalignment between the magnetic field and the rotation axis, turbulence and rapid depletion of the envelope. A handful of rotationally supported disks has now indeed been observed around deeply embedded objects (see [Sect. 1.4](#)).

Once a disk is formed, most mass is likely accreted onto the protostar through the disk. Two main processes have been proposed for the transport of mass and angular momentum in disks (see e.g., the review by Turner et al. 2014): viscous torques due to turbulence triggered by the magneto-rotational instability (MRI; Balbus & Hawley 1991) and gravitational torques induced by gravitational instability (GI; Lin & Pringle 1987; Laughlin & Bodenheimer 1994). However, simpler numerical models based on the Shakura & Sunyaev (1973)  $\alpha$ -parametrization are often used because they circumvent the complicated physics of MRI and GI by treating both processes as a local viscous transport mechanism. In these models the strength of the turbulent viscosity is described with a dimensionless parameter  $\alpha$ . Angular momentum can also be removed through winds, either launched close to the protostar (X-winds) or from the disk surface (disk winds).

### 1.1.3 Planet formation

Planets form from the dust and gas in disks (for recent reviews, see e.g., Johansen & Lambrechts 2017; Izidoro & Raymond 2018), and the first step in this formation process is the growth of micrometer-sized dust grains into millimeter and centimeter-sized particles (see e.g., the review by Testi et al. 2014). Both laboratory experiments and numerical simulations show that coagulation into mm and cm-sized particles (*pebbles*) occurs quite easily through collisions (e.g., Blum & Wurm 2008). However, further growth faces several obstacles and is the topic of active research. If particles grow be-

yond cm size, their relative velocities become so large that they fragment or bounce, instead of stick, upon impact. These barriers are known as the “bouncing” and “fragmentation barrier”, respectively. Even if particles could grow efficiently, the formation of km-sized bodies is hampered by the “drift barrier”: because the gas orbits at slightly sub-Keplerian speed due to a pressure gradient, larger particles on a Keplerian orbit feel a headwind that creates a drag force (Whipple 1972; Weidenschilling 1977). The subsequent loss of angular momentum then causes them to drift inward (**Fig. 1.2**). This radial drift is important for mm and cm-sized grains, but is especially efficient for decimeter to meter-sized particles; a meter-sized object at 1 AU falls toward the star in  $\sim 100$  years.

A way to overcome the drift barrier is by trapping particles in localized regions of increased pressure, so-called “pressure bumps”. Many mechanisms have been put forward to create pressure bumps and trap particles (see e.g., Pinilla et al. 2017 for a review), such as vortices, spiral arms in self-gravitating disks, magneto-rotational instability and snowlines. In addition, particles can be trapped at the inner edge of the “dead zone” (the region in the disk where the ionisation degree is too low for coupling of the gas to the magnetic field) and at the outer edge of the gap carved by a Jupiter-mass planet. Inside pressure bumps, particles may grow into kilometer-sized bodies (*planetesimals*), because there is more time to grow and the collisional speeds are lower and thus more amenable to growth. If the particle density becomes high enough planetesimals can form by gravitational collapse of cm-sized pebbles.

Friction with the gas may also result in particle concentration by a mechanism called the “streaming instability” if an initial enhancement of solids is present (Youdin & Goodman 2005; Johansen et al. 2007). The region just outside the water snowline seems to be a favorable place to trigger the streaming instability (e.g., Schoonenberg & Ormel 2017; Drażkowska & Alibert 2017), because the solid density will be enhanced by freeze-out of gaseous water that diffuses outward across the snowline (Stevenson & Lunine 1988). Planetesimal formation may also be enhanced outside the water snowline because icy particles are more sticky than silicate grains (e.g., Wada et al. 2011) and can thus grow to larger sizes before they fragment or even grow to highly porous aggregates that can overcome the drift barrier (Okuzumi et al. 2012).

Once km-sized planetesimals have formed, subsequent growth is dominated by gravity. Currently, two main theories exist for planetesimal growth: growth by collisions between planetesimals (“planetesimal accretion”; Kokubo & Ida e.g., 1996; Tanaka & Ida e.g., 1999) and accretion of the remaining cm-sized pebbles (“pebble accretion”, Ormel & Klahr 2010; Lambrechts & Johansen 2012). In the traditional planetesimal accretion scheme, planetary embryos emerge through a phase of runaway growth in which the largest bodies grow the fastest. In order to form a giant planet, a sufficiently large core ( $\sim 10 M_{\text{Earth}}$ ) must form in order to start gas accretion (e.g., Pollack et al. 1996). However, it is very hard to form such cores within the disk lifetime through planetesimal accretion, especially at the distance of Uranus and Neptune (e.g., Thommes et al. 2003). In contrast, growth through the accretion of pebbles can be orders of magnitude faster and thus solve this issue once there are planetesimals to accrete on. Another proposed solution for giant planets at large orbits is formation through gravitational instability (GI) in the gas (Boss 1997; Boley 2009), a scenario most likely to happen in the outer regions of massive ( $M_{\text{disk}} \gtrsim 0.1 M_{\star}$ ) or cold disks ( $T \lesssim 30\text{-}40$  K). However, GI is more likely to form companion stars than planets (e.g., Kratter et al. 2010).

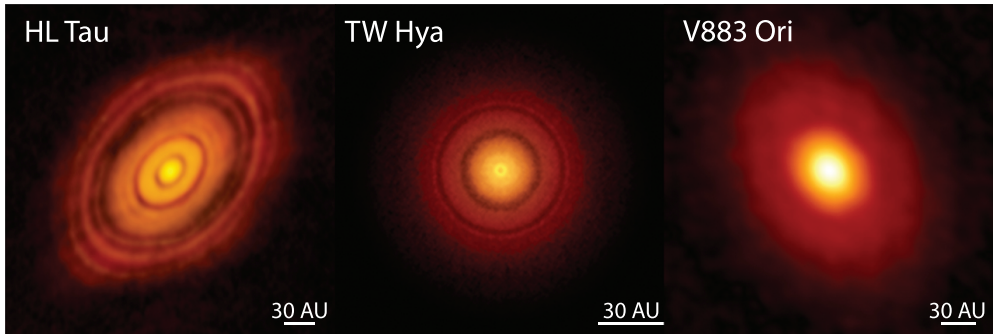


**Figure 1.3:** Rings are ubiquitously observed in ALMA continuum images of disks. If they are caused by forming planets (which is still highly debated), planet formation has to start in the embedded phase, because HL Tau (*left panel*) has not fully emerged from its envelope yet. In contrast, TW Hya (*middle panel*) is an old ( $\sim 10$  Myr) T Tauri star. Other morphologies observed in the dust continuum are bright inner regions with much fainter outer regions. In the young disk V883 Ori (*right panel*) this transition has been suggested to be due to the water snowline. For reference, a 30-AU scale bar (the radius of Neptune’s orbit) is shown in the lower right corner of each panel. Image credits: ALMA(ESO/NAOJ/NRAO); C. Brogan, B. Saxton (NRAO/AUI/NSF) – S. Andrews (Harvard-Smithsonian CfA); B. Saxton (NRAO/AUI/NSF); ALMA (ESO/NAOJ/NRAO) – L. Cieza et al.; ALMA (ESO/NAOJ/NRAO).

### Onset of planet formation

Planet formation was originally thought to start in protoplanetary disks, after the envelope has dissipated. However, more and more studies are providing evidence that the first steps of planet formation already occur much earlier, in young disks that are still embedded. Characteristics of grain growth have been observed in protostellar envelopes (Kwon et al. 2009; Miotello et al. 2014), and recently in the embedded disk TMC1A (Harsono et al. 2018). The ALMA images of the young HL Tau disk suggest that even km-sized bodies may have formed before the envelope has fully dissipated (**Fig. 1.3**; ALMA Partnership et al. 2015), although subsequent studies have shown that rings are not necessarily the result of (young) planets (see e.g., the discussion and references in Huang et al. 2018).

Additional evidence for an early onset of planet formation is given by protoplanetary disk surveys: the majority of protoplanetary disks seem to have too little material to form the planetary systems that we observe (e.g., Ansdell et al. 2016; Manara et al. 2018). In contrast, young disks seem massive enough (Tychoniec et al. 2018, Tobin et al., in prep.). However, the picture of disk mass evolution may be more complicated as not all star forming regions follow the trend of decreasing median disk mass of more-evolved young stars (Cazzoletti et al. 2019; Williams et al. 2019). Furthermore, the dust opacity may be higher than assumed due to neglect of dust scattering (Zhu et al. 2019), which would mean that disk masses are underestimated.

Nonetheless, studies of our own Solar System also point to an early start of planet formation. The observed dichotomy in meteorite composition implies that two dust populations have been spatially separated in the disk for an extended period of time. The most plausible mechanism for this is that a forming Jupiter inhibited the inward drift of material from the outer regions, but this requires that Jupiter had already

grown beyond 20 Earth masses within a million years (Kruijer et al. 2017). Together, these results indicate that planet formation already starts in the embedded phase.

## 1.2 Chemistry during star and planet formation

The material in the local interstellar medium (ISM) consists primarily of hydrogen (H; 90% by number) and helium (He; 8% by number). The heavier elements are predominantly oxygen (O), carbon (C) and nitrogen (N), with solar abundances of  $4.9 \times 10^{-4}$ ,  $2.7 \times 10^{-4}$  and  $0.7 \times 10^{-4}$  with respect to H, respectively (Asplund et al. 2009). Refractory species like magnesium (Mg), silicon (Si) and iron (Fe) are present in even lower amounts (a few times  $10^{-5}$ ), and are almost completely locked up in dust grains. Chemical processes during different stages of star formation convert the former volatile atoms into molecules with increasing complexity, possibly up to building blocks for life (see e.g., Herbst & van Dishoeck 2009; Caselli & Ceccarelli 2012 for a review). A molecule with more than six atoms, that contains carbon and hydrogen, is referred to as a *complex organic molecule (COM)*.

Chemical processes during star formation can roughly be divided into two main types: reactions that occur in the gas phase, and reactions that take place on the surfaces of dust grains (see e.g., reviews by Tielens 2013; van Dishoeck 2014). A third category consists of processes that transfer atoms and molecules between the gas and solid phase. At the low temperatures ( $\lesssim 100$  K) characteristic for most stages of star formation, gas-phase chemistry is dominated by exothermic reactions (that is, reactions releasing energy) and reactions without an activation barrier. Most reactions are therefore either between a neutral molecule and a positively charged atom or molecule (ion-neutral reactions), or between a positively charged (molecular) ion and an electron (recombination reactions).

Dust grains are important to astrochemistry because they provide a surface area on which atoms and molecules can accrete, thereby enhancing the probability that species meet and react. This is, for example, crucial for the formation of the most abundant interstellar molecule,  $\text{H}_2$ . In addition, excess energy created by a reaction can be absorbed by the grain, whereas in the gas phase this has to be stored internally in the newly formed molecule, which may lead to immediate dissociation. Reactions on the grain surface include mainly hydrogen atoms and radicals, that is, atoms or molecules with unpaired electrons. Whether a species is present in the gas phase or on the grain surface (as ice) depends primarily on the temperature. These processes are referred to as *freeze-out* and *thermal desorption*. In addition, some species desorb from the grains upon impact of UV photons (photodesorption) and in other cases the excess energy released in a reaction may be used to transfer the newly formed molecule into the gas phase (chemical desorption).

The following sections give an overview of the main chemical processes during the different stages of star formation.

### 1.2.1 Dark cloud and dense core chemistry

Dark clouds are characterized by temperatures of roughly 10 K and densities in the order of  $10^4$ – $10^5$  hydrogen nuclei  $\text{cm}^{-3}$ . Gas-phase chemistry is initiated by ionization of  $\text{H}_2$  by cosmic rays leading to the formation of  $\text{H}_3^+$ . The reaction between  $\text{H}_3^+$  and C, O and N atoms is followed by a chain of ion-molecule reactions creating a variety

of chemical species, with CO becoming the most abundant gas-phase molecule after  $\text{H}_2$ . A characteristic for molecules formed in the gas phase during this stage is that they tend to be very unsaturated, that is, each atom is not connected to the maximal possible number of other atoms. This is because the transfer of an H atom from  $\text{H}_2$  to molecular ions is often endothermic (requires energy) or possesses an activation barrier and therefore does not occur at low temperatures. In addition, since reactions with C or  $\text{C}^+$  often lead to carbon insertion at low temperatures, dark cloud chemistry produces many long carbon chains. Carbon chains up to  $\text{C}_8\text{H}$ ,  $\text{C}_8\text{H}^-$ ,  $\text{HC}_7\text{O}$  and  $\text{HC}_9\text{N}$  have been observed, for example, in the well-studied core TMC-1 (e.g., Kaifu et al. 2004; Cordiner et al. 2017). Recently, McGuire et al. (2018) reported the detection of the first aromatic molecule, benzonitrile (*c*- $\text{C}_6\text{H}_5\text{CN}$ ), toward this source.

Another characteristic of gas-phase chemistry in cold environments is a high level of deuterium (D) fractionation. Because the reaction between  $\text{H}_3^+$  and HD, which produces  $\text{H}_2\text{D}^+$  and  $\text{H}_2$ , is slightly exothermic, the reverse reaction of  $\text{H}_2\text{D}^+$  and  $\text{H}_2$  does not take place at temperatures below  $\sim 30$  K. This results in a significantly larger  $\text{H}_2\text{D}^+/\text{H}_3^+$  abundance ratio and therefore deuterium fractionation (D/H abundance ratios up to  $\sim 0.1$ ) compared with the elemental D/H ratio (typically  $\sim 2 \times 10^{-5}$ ; Linsky 2007) (Stark et al. 1999). Even doubly- and triply-deuterated molecules such as  $\text{D}_2\text{CO}$  (formaldehyde) and  $\text{ND}_3$  (ammonia) have been detected (see Ceccarelli et al. 2014 for a review).

Freeze-out of atoms onto dust grains, followed by diffusion over the surface leads to efficient hydrogenation reactions producing large amounts of water ice ( $\text{H}_2\text{O}$ ), and smaller amounts of methane ( $\text{CH}_4$ ) and ammonia ( $\text{NH}_3$ ; see e.g., reviews by Tielens & Hagen 1982; van Dishoeck et al. 2013; Linnartz et al. 2015). In addition, freeze-out of CO can result in the formation of  $\text{CO}_2$  ice. In the densest, coldest inner region of dense cores, most of the CO will freeze out, creating a CO ice layer on top of the earlier formed water-dominated layer. Hydrogenation of CO will then result in the formation of formaldehyde ( $\text{H}_2\text{CO}$ ) and methanol ( $\text{CH}_3\text{OH}$ ), and more complex species (Watanabe & Kouchi 2002; Cuppen et al. 2009; Chuang et al. 2016) up to molecules as glycolaldehyde ( $\text{CH}_2(\text{OH})\text{CHO}$ ) and ethylene glycol ( $(\text{CH}_2(\text{OH}))_2$ ) (Fedoseev et al. 2015), even at temperatures as low as 10–15 K (see **Fig. 1.4**).

Ice observations through absorption bands of vibrational transitions in the near-to far-infrared have confirmed the layered ice structure and the formation of methanol on the grain surface, but the presence of more complex species is hard to infer from these observations (see Boogert et al. 2015 for a review). COMs like acetaldehyde ( $\text{CH}_3\text{CHO}$ ), dimethyl ether ( $\text{CH}_3\text{OCH}_3$ ) and methyl formate ( $\text{CH}_3\text{OCHO}$ ) are also detected in the gas phase in cold dense cores (e.g., Bacmann et al. 2012; Cernicharo et al. 2012). This can not be explained by gas-phase chemistry alone, and thus requires non-thermal desorption processes such as photodesorption and chemical desorption to be active (e.g., Öberg et al. 2007; Minissale et al. 2016).

Massive freeze-out of CO in dense cores also influences the gas-phase chemistry, as this means that the main reactant of  $\text{H}_3^+$  and  $\text{H}_2\text{D}^+$  is removed from the gas phase. CO freeze-out therefore results in increased abundances of deuterated species and nitrogen-containing molecules like  $\text{N}_2\text{H}^+$  and  $\text{NH}_3$  (e.g., Caselli et al. 1999; Bergin et al. 2001). Freeze-out of  $\text{H}_2\text{O}$  in dense regions likely increases the abundance of  $\text{HCO}^+$  (e.g., Phillips et al. 1992; Bergin et al. 1998).

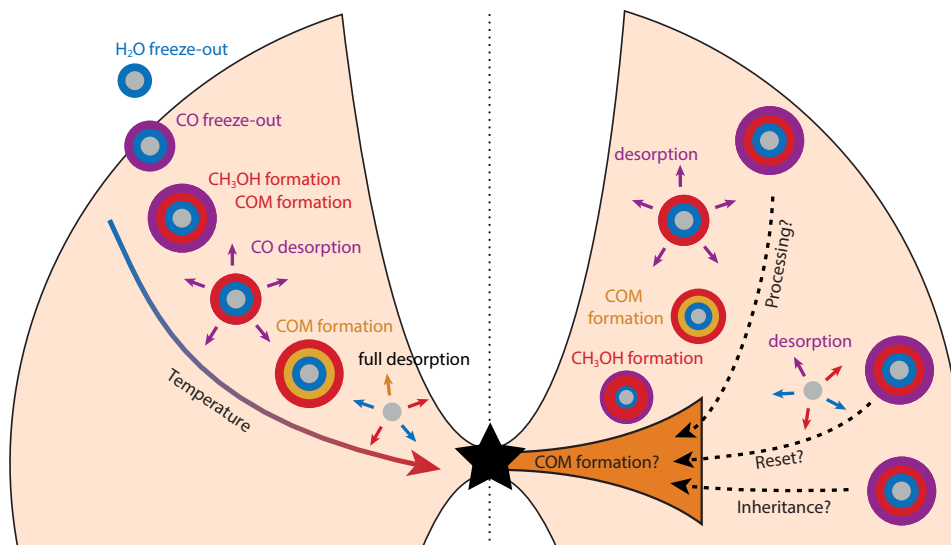


**Figure 1.4:** Schematic overview of some of the chemistry during low-mass star formation. The *left side* shows the build up of ices and the formation of complex organic molecules during core collapse and in the protostellar envelope. The *right side* illustrate three possible scenarios for the disk composition: full inheritance from the core, full reset into atoms, or processing of the core material (freeze-out, redesorption, formation of new species). How much each of these pathways contribute is still unclear, as well as whether COMs can form in the embedded disk.

## 1.2.2 Hot core chemistry

Once the protostar is formed it starts to heat up its surroundings. The first changes occur in the surface chemistry (**Fig. 1.4**). As soon as the grains become warmer than 20 K, H atoms reside for too short a time on the surface to be the dominant reactant and the most volatile species such as  $\text{CH}_4$ , CO and  $\text{N}_2$  start to desorb. Cosmic ray-induced UV photons create radicals that can diffuse along the surface and react to create more complex species such as methyl formate ( $\text{CH}_3\text{OCHO}$ ), dimethyl ether ( $\text{CH}_3\text{OCH}_3$ ) and formic acid ( $\text{HCOOH}$ ) (e.g., Garrod & Herbst 2006). Reactions involving radicals formed in these processes may even lead to formation of the simplest amino acid glycine (Garrod et al. 2008; Garrod 2013).

As the temperature further increases to 100–300 K, the ice mantles will fully sublimate and enrich the chemical complexity of the gas. At these temperatures, endothermic reactions and reactions with a barrier become efficient and the desorbed molecules were therefore thought to drive gas-phase chemistry (e.g., Charnley et al. 1992). However, a re-evaluation of reaction rate coefficients and branching ratios showed that gas-phase chemistry is less important than initially thought (e.g., Geppert et al. 2006) and that most of the complexity is produced in the ice. Meanwhile, the increasing strength of the protostellar radiation field could play an active role in molecular destruction.

Complex molecules are indeed readily detected toward these so-called *hot cores*, but with line surveys (in particular with ALMA) we are now starting to construct the full inventory for both low and high-mass sources (e.g., Jørgensen et al. 2016; Belloche

et al. 2016; Pagani et al. 2017, and see McGuire 2018 for an overview of all species detected so far and corresponding references). The largest number of COMs have been observed (for the first time) toward the high mass hot cores in Sagittarius B2, such as glycolaldehyde ( $\text{CH}_2\text{OHCHO}$ , a sugar-like molecule), acetamide ( $\text{CH}_3\text{CONH}_2$ , the largest interstellar molecule with a peptide bond) and amino acetonitrile ( $\text{NH}_2\text{CH}_2\text{CN}$ , a direct precursor of the amino acid glycine). Glycolaldehyde has now also been detected on the scale of planetary systems toward the low mass protostar IRAS 16293B (Jørgensen et al. 2012). Other detections worth mentioning are the observations of propylene oxide ( $\text{CH}_3\text{CHCH}_2\text{O}$ , the first chiral molecule; chirality is a characteristic of many biomolecules) and iso-propyl cyanide ( $i\text{-C}_3\text{H}_7\text{CN}$ , the first non-linear carbon chain).

However, one of the main surprises of the WISH program (Water In Star-forming Regions with the *Herschel Space Observatory*) was that only very little of the water emission toward protostellar envelopes actually originates in the hot core region (instead, most of the emission traces shocked gas; see e.g., van Dishoeck et al. 2011). Spatially resolved interferometer observations did find warm  $\text{H}_2^{18}\text{O}$  emission towards three hot cores, but with low abundances between  $10^{-8}$  and a few times  $10^{-6}$  (Jørgensen & van Dishoeck 2010; Persson et al. 2012, 2014). In comparison, thermal evaporation of water at  $T \gtrsim 100$  K is expected to produce a gas-phase water abundance of  $10^{-4}$ . A caveat is that the observed abundances are calculated based on a spherical envelope model. Taking into account that a disk can be present in the inner most region increases the derived abundances by  $\sim 1$  order of magnitude, still a few orders of magnitude below what is expected for two of the sources (Persson et al. 2016). Low water abundances could be the result of destruction by X-rays (Stäuber et al. 2006), or maybe the sequestering of water as ice in larger grains that does not desorb.

Another unexpected discovery was the detection of several carbon chains toward the protostar L1527 (see review by Sakai & Yamamoto 2013), as these species are characteristic of dark cloud chemistry. The authors suggest that this may be distinctive for sources where the temperature did not rise above  $\sim 30$  K during the collapse. Such temperatures allow for  $\text{CH}_4$  ice desorption, and the subsequent gas-phase formation of carbon chains, while the more complex species remain frozen out. However, models show that when carbon chains are formed at  $\sim 30$  K, they do not disappear rapidly from the gas as the temperature reaches 200 K. In addition, carbon chains are also abundant in UV-irradiated outflow cavity walls (e.g., Murillo et al. 2018). These observed morphologies could thus also be due to a combination of the source physical structure and the region predominantly probed by the observations.

### 1.2.3 Protoplanetary disk chemistry

After the envelope has dissipated, a protoplanetary disk remains. Radial and vertical gradients in temperature (due to heating by the central star) and density cause a layered chemical structure in these disks (Fig. 1.2; Aikawa et al. 2002, and the review by Dutrey et al. 2014). In the surface layers, molecules are photodissociated and atoms ionized by the UV radiation and in the cold midplane most molecules are frozen out. At intermediate heights (warm molecular layer), the dust grains are warm enough to prevent complete freeze-out and the UV radiation is sufficiently attenuated for molecules to survive, but still strong enough to drive an active ion-molecule chemistry.



Many small molecules and isotopologues (that is, molecules with a less abundant  $^{13}\text{C}$ ,  $^{18}\text{O}$ ,  $^{17}\text{O}$  or  $^{15}\text{N}$  isotope) have been observed in disks, and the resolution and sensitivity provided by ALMA allows to resolve structures (see e.g., a recent overview by Bergin & Cleeves 2018). Small surveys are now being conducted toward the brightest disks, but so far the overall conclusion seems that there is a great diversity between disks (e.g., Thi et al. 2004; Huang et al. 2017).

In contrast to small molecules, only few complex species have been detected in disks. COMs desorb from the dust grains at temperatures  $\gtrsim 100\text{--}150\text{ K}$ , and are thus frozen out except in the inner few AU and possibly the surface layers. Gas-phase formation routes or non-thermal desorption processes are thus required to get observable amounts in the gas phase. The first disk COM to be detected was methyl cyanide ( $\text{CH}_3\text{CN}$ ; Öberg et al. 2015b), which has currently been observed in six disks (Bergner et al. 2018; Loomis et al. 2018). Methanol ( $\text{CH}_3\text{OH}$ ) has only been detected in TW Hya (Walsh et al. 2016) and very deep upper limits were presented for HD163296 (Carney et al. 2019), suggesting that disk chemistry can be strongly influenced by the stellar type. Formic acid (t- $\text{HCOOH}$ ) is the third organic molecule larger than formaldehyde ( $\text{H}_2\text{CO}$ ) that is detected in disks, but again, so far only in TW Hya (Favre et al. 2018). These observations show that it is very challenging to probe the chemical complexity of the protoplanetary disk material.

A current topic of debate is the abundance and fate of CO in protoplanetary disks. Because the most abundant molecule,  $\text{H}_2$ , does not have a dipole moment, it cannot be observed at millimeter wavelengths. Its deuterated counterpart, HD, can be observed in the far-infrared, but not with presently available instruments. The readily observable, second most abundant molecule, CO, is therefore generally used as a tracer of the disk gas mass. However, a comparison between the CO-derived gas mass and the HD-derived gas mass for the three disks with HD detections by the *Herschel Space Observatory* showed that the HD masses are a factor five to two orders of magnitude higher than the CO masses (Favre et al. 2013; McClure et al. 2016). CO seems thus depleted, on top of freeze-out and photodissociation (Kama et al. 2016; Schwarz et al. 2016). Low CO-based gas masses are also observed for the disks in the ALMA survey of the Lupus star forming region (Ansdell et al. 2016; Miotello et al. 2017), suggesting this may be the result of a common process. Independent evidence for CO depletion comes from observations of bright  $\text{C}_2\text{H}$  and c- $\text{C}_3\text{H}_2$  emission, species expected to be especially abundant when both carbon and oxygen are depleted with a gaseous C/O ratio  $>1$  (Kastner et al. 2015; Bergin et al. 2016). A possible explanation can be that gaseous CO is turned into more complex species, that subsequently freeze-out, through reactions with  $\text{He}^+$  (e.g., Aikawa et al. 1999; Bergin et al. 2014; Schwarz et al. 2018). Alternatively, CO can be converted into less volatile species in the ice (e.g., Bosman et al. 2018). A third possibility is that CO is locked up in large icy grains that reside in the midplane and cannot diffuse upward into layers where CO can desorb (e.g., Krijt et al. 2018). These processes are time dependent; young disks are therefore expected to have less CO depletion.

## Snowlines

As described above, protoplanetary disks are characterized by a large cold midplane region where most molecules are frozen out. The midplane radius where a molecule becomes more abundant in the ice than in the gas phase is called a *snowline*. The temperature at which freeze-out occurs depends on a species-specific binding energy

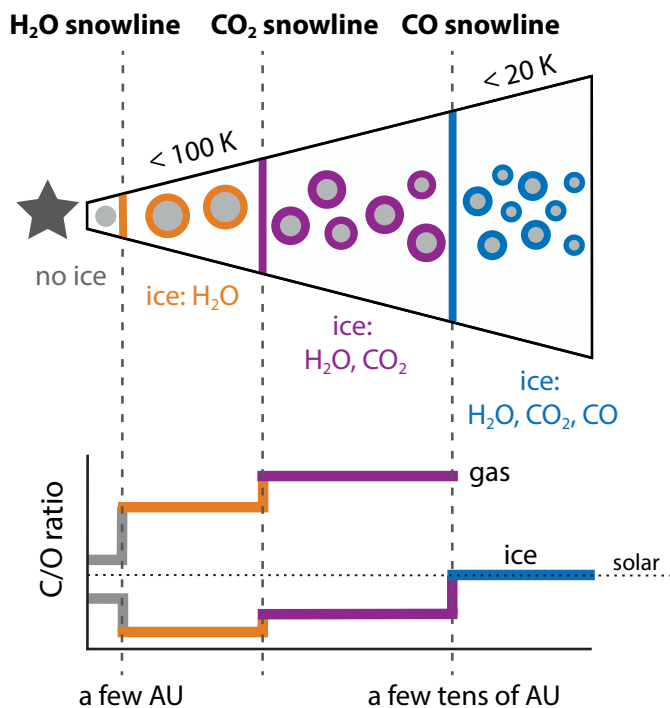


**Figure 1.5:** Schematic overview of the major snowlines and their expected location in protoplanetary disks (*top*). For simplicity, the snowlines are marked as vertical lines instead of snow surfaces (see Fig. 1.2). The sequential freeze-out of these dominant carbon and oxygen carriers results in a radial gradient in the elemental C/O ratio of the planet-forming material (*bottom*; adapted from Öberg et al. 2011).

to the (icy) dust grains. The radial temperature gradient in protoplanetary disks therefore results in sequential freeze-out of volatile molecules (Fig. 1.5). Because of the vertical temperature gradient within disks, the region where a molecule is frozen out is bounded by a *snow surface* (see Fig. 1.2).

Snowlines, and especially the water snowline, play an important role in planet formation (as described in Sect. 1.1.3) as dust growth is enhanced near these freeze-out zones (e.g., Stevenson & Lunine 1988; Schoonenberg & Ormel 2017). Snowlines were therefore postulated as a mechanism to create rings and gaps in protoplanetary disk dust emission (e.g., Zhang et al. 2015; Pinilla et al. 2017). However, high resolution observations with ALMA of a large number of protoplanetary disks show no correlation between the gap locations and the  $\text{CO}_2$ , CO and  $\text{N}_2$  snowlines (van Terwisga et al. 2018; Long et al. 2018; Huang et al. 2018; van der Marel et al. 2019). Effects on grain growth may thus be limited to the water snowline.

In addition to planet formation, snowlines strongly affect the chemical composition of planets. The selective freeze-out of major carbon or oxygen carrying species at different snowlines causes the elemental C/O-ratio of the planet-forming material to vary with radial distance from the star (Fig. 1.5; Öberg et al. 2011; Eistrup et al. 2018). The bulk composition of planets may therefore be regulated by their formation location with respect to the major snowlines (e.g., Madhusudhan et al. 2014; Walsh

et al. 2015; Cridland et al. 2017).

The most important snowline is the water snowline, because of its role in planet formation and because water ice contains the bulk of the ice mass and oxygen budget. Observing the water snowline in protoplanetary disks, however, is very challenging. First, the snowline is located only a few AU from the star due to the high desorption temperature of water of  $\sim 100\text{--}150$  K. This means that an angular resolution of  $\sim 0.01''$  is required to resolve the snowline location in disks around Sun-like stars in the nearest star-forming region Taurus. Second, the only suitable thermal water lines observable from the ground are those from the  $\sim 500$  times less abundant isotopologue  $\text{H}_2^{18}\text{O}$ . High sensitivity is thus required as well, and as such, no detection has yet been made (e.g., Notsu et al. 2019). The only disk for which an indirect measurement of the water snowline location has been reported is V883 Ori (Cieza et al. 2016). This young star is undergoing an accretion burst, which heats the disk and shifts the snowline outward. An abrupt change in the continuum intensity corresponding to a change in the optical depth is observed around  $\sim 40$  AU. Such effect is expected around the water snowline. However, direct molecular line observations are required to confirm the snowline location (see also **Chapter 7**).

Another interesting snowline is the CO snowline, because CO ice is the starting point for the formation of many complex organics (see **Sect. 1.2.1**). Moreover, the low desorption temperature ( $\sim 20\text{--}30$  K) places this snowline far enough from the star (10s–100 AU) to be spatially resolved with ALMA. However, CO line emission is generally optically thick, even for the less abundant isotopologues  $^{13}\text{CO}$  and  $\text{C}^{18}\text{O}$ , and originates in the disk surface layers. The very rare isotopologue  $^{13}\text{C}^{18}\text{O}$  is therefore required to probe the midplane (Zhang et al. 2017), but its low abundance restricts observations to the nearest and brightest disks. An alternative approach is to observe molecules whose abundance is strongly affected by the freeze-out of CO. Examples of such molecules are  $\text{DCO}^+$ ,  $\text{N}_2\text{H}^+$  and  $\text{N}_2\text{D}^+$  (**Fig. 1.6**).

$\text{DCO}^+$  emission is expected to originate in a ring just inside the CO snowline, where the temperature is low enough such that  $\text{H}_2\text{D}^+$  is abundant, but there is still enough gaseous CO left to form  $\text{DCO}^+$  (**Fig. 1.6**). Ring-shaped  $\text{DCO}^+$  emission was indeed observed toward HD163296 and IM Lup (**Fig. 1.6**; Mathews et al. 2013; Öberg et al. 2015a). However, for HD163296, it was later shown that the outer radius does not correspond to the CO snowline (Qi et al. 2015); probably because  $\text{DCO}^+$  can also form in warmer disk layers ( $T \gtrsim 70$  K) through reaction with  $\text{CH}_2\text{D}^+$  (Favre et al. 2015). Although  $\text{DCO}^+$  emission does not seem to have a direct correlation with the CO snowline, detailed modeling including an appropriate physical structure for the target disk can narrow down the snowline location (Carney et al. 2018).

$\text{N}_2\text{H}^+$  (and  $\text{N}_2\text{D}^+$ ) emission is also expected to be ring-shaped, but with the inner edge around the CO snowline because  $\text{N}_2\text{H}^+$  can only be abundant when CO is frozen out (**Fig. 1.6**).  $\text{N}_2\text{H}^+$  has indeed been used to locate the CO snowline in TW Hya and HD163296, at radii of 30 and 90 AU, respectively (**Fig. 1.6**; Qi et al. 2013b, 2015). These studies also highlight the importance of locating the snowline based on molecular emission, as the snowline radius corresponds to a temperature of  $\sim 17$  K in TW Hya and  $\sim 25$  K in HD163296. This difference could be due to different ice compositions in the two disks. However, these snowline radii are likely upper limits (that is, maximum distances from the star), because chemical modeling shows that the  $\text{N}_2\text{H}^+$  abundance and emission peak outside, instead of directly at the snowline (Aikawa et al. 2015 and **Chapter 2**). For TW Hya, this is consistent with the  $^{13}\text{C}^{18}\text{O}$  observations (Zhang et al.

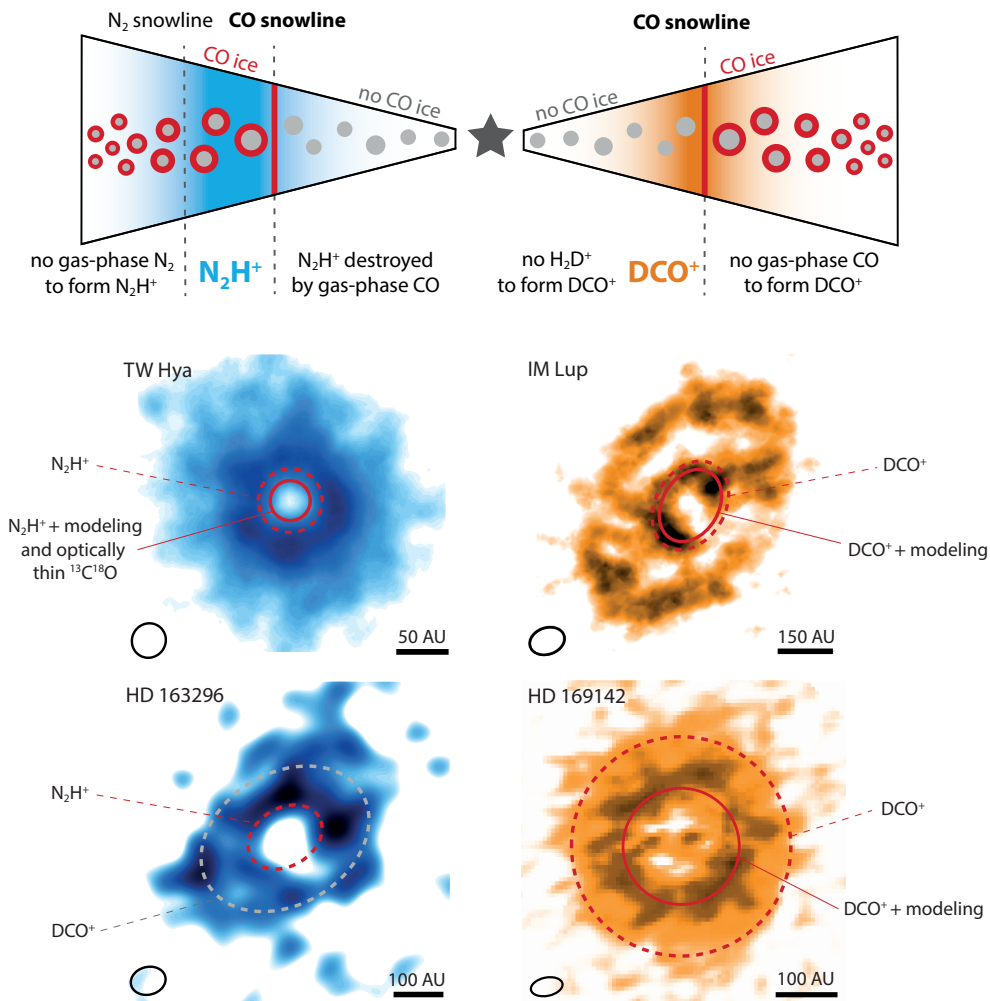


**Figure 1.6:** Schematic overview of the expected relation between the CO snowline and  $N_2H^+$  (blue; *top left panel*) or  $DCO^+$  (orange; *top right panel*) based on simple chemical considerations. ALMA observations of  $N_2H^+$  and  $DCO^+$  in protoplanetary disks are shown in the *middle* and *bottom left panels*, and *middle* and *bottom right panels*, respectively. The corresponding expected CO snowline locations are marked with a red dashed contour. However, based on both chemical modeling (**Chapter 2**) and  $^{13}C^{18}O$  observations, the snowline is located at smaller radii in TW Hya (solid red contour). In HD 163296, a comparison between the snowline location based on  $N_2H^+$  and  $DCO^+$  (dashed gray contour) revealed that the snowline derived from  $N_2H^+$  is in better agreement with the snowline location based on  $C^{18}O$  observations. Modeling of the  $DCO^+$  emission in IM Lup and HD 169142 also places the snowline closer in than the outer edge of the  $DCO^+$  emission due to the contribution of a warm  $DCO^+$  formation route. The outer  $DCO^+$  ring in IM Lup may be due to photodesorption of CO in the outer disk or temperature inversion. Images are adapted from Qi et al. (2013b, 2015), Mathews et al. (2013), Öberg et al. (2015a) and Carney et al. (2018).

2017). In addition, **Chapter 2** predicts that  $\text{N}_2\text{H}^+$  can be abundant as well in a surface region of the disk and this has very recently been confirmed by observations (Schwarz et al. 2019).

### 1.2.4 Chemical composition of comets

Comets are likely formed in the cold outer part of the disk from which the Solar System formed. Assuming that comets have undergone no major processing since their formation, their chemical composition is a direct window to the composition of the outer disk. In addition, comets may have seeded the young Earth with water and prebiotic molecules. Space missions to comets therefore provide valuable information on our origins. A review on cometary abundances is given by Mumma & Charnley (2011) and Bockelée-Morvan et al. (2015), and here a few interesting, more recent results from the *Rosetta* mission to comet 67P/Churyumov-Gerasimenko (67P/C-G) are highlighted (Altwegg et al., in press). An exciting result is the detection of the simplest amino acid, glycine (Altwegg et al. 2016), confirming the earlier detection in comet Wild 2 by the *Stardust* mission (Elsila et al. 2009). Together with the detection of phosphorus and many organic molecules, the *Rosetta* results demonstrate that comets could have played a key role in the emergence of life. A surprise was the detection of a high abundance of molecular oxygen ( $\text{O}_2$ ) in the cometary coma (Bieler et al. 2015), suggesting that the  $\text{O}_2$  is incorporated during the comet's formation. Chemical models show that the  $\text{O}_2$  has to have formed during the dark cloud stage and survived the transport into the disk. This does require slightly warmer cloud conditions ( $\sim 20$  K) than generally assumed for other dark clouds (Taquet et al. 2016a). Re-analysis of the *Giotto* results demonstrate that  $\text{O}_2$  is present in comet 1P/Halley at a similar level as in 67P/C-G ( $\sim 4\%$  with respect to  $\text{H}_2\text{O}$ ; Rubin et al. 2015).

## 1.3 Chemistry as a thermometer

Molecular line observations are indispensable for studying star and planet formation. Not only do they provide information on the chemical composition of the planetary building blocks, they are also excellent tracers of the kinematics and physical conditions in the star- and planet-forming environment. There are several ways in which molecular line emission can be used as a temperature probe:

### Direct observations of freeze-out

The most intuitive way in which molecules react to temperature is that they freeze out from the gas phase onto the dust grains when the temperature falls below their freeze-out temperature. Since this temperature is species specific (**Fig. 1.5**), with only a small density dependence, the absence of a certain molecule can constrain the temperature to below its freeze-out temperature. For example, the region in the disk midplane where CO is absent has a temperature below  $\sim 20$ – $25$  K, and regions with emission from water or complex organics have temperatures  $\gtrsim 100$ – $150$  K. However, this can only be applied when there is a direct line of sight to the region of interest. CO freeze-out is often impossible to see directly in protoplanetary disks because the emission becomes optically thick in the warmer surface layers where CO is not frozen out. Only when the disk is seen edge on can the midplane, and thus CO freeze-out, be observed directly (e.g., Dutrey et al. 2017).

### Chemical effects due to freeze-out

Freeze-out of molecules can also affect other molecules through chemical reactions that can only happen in absence or presence of the frozen out molecule. Examples of such chemical tracers are  $\text{N}_2\text{H}^+$ ,  $\text{N}_2\text{D}^+$ ,  $\text{HCO}^+$  and  $\text{DCO}^+$ . As outlined in **Sect. 1.2.3** (see **Fig. 1.6**),  $\text{N}_2\text{H}^+$  and  $\text{N}_2\text{D}^+$  trace the region where CO is frozen out because these molecules are otherwise destroyed by gaseous CO. Since CO is the main reactant of  $\text{H}_3^+$ , the absence of CO increases the amount of  $\text{H}_2\text{D}^+$  and therefore the amount of  $\text{DCO}^+$ . However, CO is also the parent molecule for  $\text{DCO}^+$ .  $\text{DCO}^+$  therefore traces the region where CO starts to freeze out.  $\text{HCO}^+$  is sensitive to the freeze-out of water, because water is the main destructor of  $\text{HCO}^+$ . Simple chemical models, that is, including only the main reactions for formation and destruction of either  $\text{N}_2\text{H}^+$ ,  $\text{N}_2\text{D}^+$ ,  $\text{HCO}^+$  or  $\text{DCO}^+$ , in combination with radiative transfer (see **Sect. 1.3.2**) can be used to derive the CO and  $\text{H}_2\text{O}$  freeze-out region.

### Rotation diagrams

Rotational energy levels of molecules can be populated (excited) through collisions with other molecules, usually  $\text{H}_2$ , and depopulated (de-excited) through both collisions and the spontaneous emission of a photon. When the density of the collision partner is high enough for the collisional excitation to balance the spontaneous de-excitation (that is, above the so-called critical density), the level populations are thermalized such that they follow a Boltzmann distribution for a given gas kinetic temperature. This is called local thermodynamic equilibrium (LTE). If a molecule is in LTE, and multiple lines are observed, its excitation temperature and column density can be well-constrained through a rotation diagram (e.g., Goldsmith & Langer 1999). For such analysis, the column density of molecules in the upper state,  $N_u$ , is calculated for each transition using the observed integrated flux density  $S_\nu \Delta v$ :

$$N_u = \frac{4\pi S_\nu \Delta v}{A_{ul} \Omega h c}, \quad (1.1)$$

where  $A_{ul}$  is the Einstein A coefficient and  $\Omega$  is the solid angle subtended by the source. The upper state level column density can be related to the total column density,  $N_T$ , by the Boltzmann equation:

$$\frac{N_u}{g_u} = \frac{N_T}{Q(T_{\text{rot}})} e^{-E_u/kT_{\text{rot}}}, \quad (1.2)$$

where  $g_u$  and  $E_u$  are the degeneracy and energy of the upper state level, respectively,  $Q$  is the molecular partition function and  $T_{\text{rot}}$  is the rotational temperature. Taking the logarithm then allows for determining  $T_{\text{rot}}$  and  $N_T$  through a linear least squares regression:

$$\ln \frac{N_u}{g_u} = \ln N_T - \ln Q(T_{\text{rot}}) - \frac{E_u}{kT_{\text{rot}}}. \quad (1.3)$$

If a line is not optically thin, the upper level column density must be multiplied by a correction factor,  $C_\tau$ :

$$C_\tau = \frac{\tau}{1 - e^{-\tau}}, \quad (1.4)$$

where  $\tau$  is the line optical depth. If  $T_{\text{rot}}$  is known, the column density can also be estimated from a single line observation.

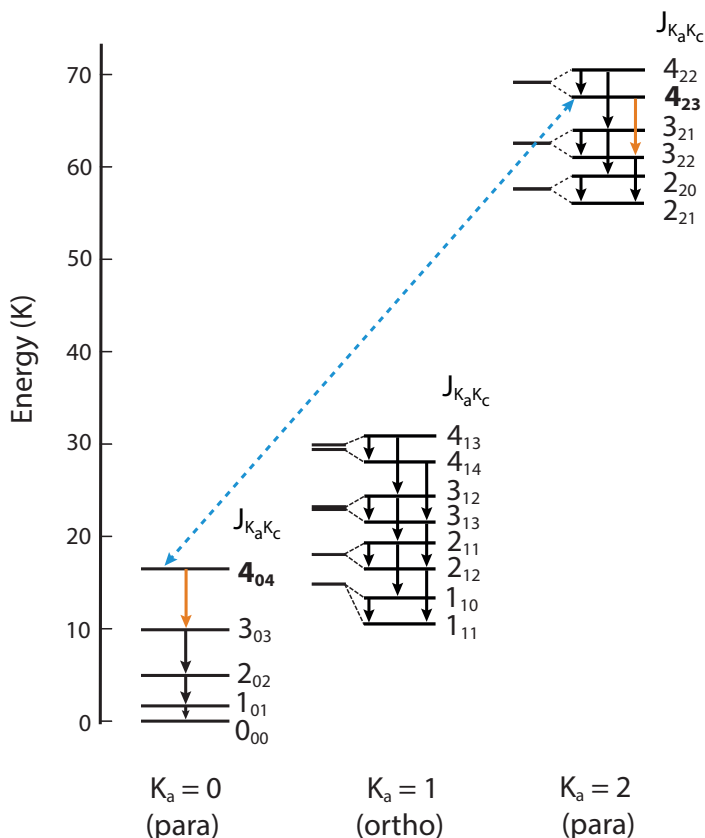


**Figure 1.7:** Energy level diagram for thioformaldehyde (H<sub>2</sub>CS) for levels up to  $J = 4$  and  $K_a = 2$ . Radiative transitions (solid arrows) are only allowed within a  $K_a$  ladder. No transitions are allowed between ortho and para states, but collisional excitation and de-excitation is possible between all ortho states, and all ortho states. Line ratios between two transitions with a different  $K_a$  state (for example the  $4_{23} - 3_{22}/4_{04} - 3_{03}$  ratio; orange arrows) are good temperature tracers because only collisional transitions are possible between the  $4_{04}$  and  $4_{23}$  level (blue dashed arrow). Their ratio is therefore determined by temperature.

### Temperature-dependent line ratios

The relative strength of transitions that can only be populated and depopulated by collisions is a good measure of temperature, since collision rates are determined by temperature. Formaldehyde (H<sub>2</sub>CO) and thioformaldehyde (H<sub>2</sub>CS) have such transitions (e.g., Mangum & Wootten 1993; van Dishoeck et al. 1993, 1995). These slightly asymmetric rotor molecules have their energy levels designated by the quantum numbers  $J$ ,  $K_a$  and  $K_c$  (Fig. 1.7). Line ratios involving different  $K_a$  ladders are good tracers of the kinetic temperature because transitions between energy levels with different  $K_a$  values are radiatively forbidden and thus take place only through collisions. Transitions with the same  $\Delta J$  are closely spaced in frequency, and can therefore often be observed within one frequency tuning. This eliminates calibration uncertainties in the line ratio.

### 1.3.1 Molecular line observations

Both high angular resolution and high sensitivity are required for molecular line observations in (embedded) disks. Therefore, ALMA is the best instrument for such studies. ALMA is a (sub)millimeter wavelength interferometer and consists of 66 antennas located at an altitude of 5000 meters on the Chajnantor plateau in the Atacama desert, Chile. Fifty 12-m antennas make up the main array, that can cover baselines of maximum  $\sim 150$  m in the most compact configuration and up to  $\sim 16$  km in the most extended configuration. This corresponds to angular resolutions between  $1.5''$  and  $0.018''$  at 230 GHz (1.3 mm). In addition, twelve 7-m antennas form the Atacama Compact Array (ACA), with baselines up to 45 meters ( $5.4''$  resolution at 230 GHz), and four 12-m antennas are used for total power observations. Currently, eight of the ten receiver bands are operational, covering frequencies from 84 to 950 GHz (with the exception of a few frequency ranges with strong atmospheric absorption). The maximum spectral resolution is 31 kHz and the total amount of bandwidth covered in one spectral setting depends on the requested spectral resolution with a maximum of 8 GHz at the lowest spectral resolution (0.976 MHz).

Other operational (sub)millimeter interferometers are the Submillimeter Array (SMA) in Hawaiï and the Northern Extended Millimeter Array (NOEMA) in France. The SMA consists of eight 6-m dishes covering baselines of maximum 509 meters and frequencies from 180 to 420 GHz. NOEMA is an extension of the Plateau de Bure Interferometer (PdBI), with currently ten 15-m antennas covering baselines up to 760 meters ( $0.5''$  resolution at 230 GHz) and frequencies between 76 and 274 GHz. With fewer antennas and shorter baselines, these observatories cannot reach the angular resolution and sensitivity of ALMA. However, upgrades of the receivers allow for much larger spectral coverage in one setting. In addition, with their location on the Northern hemisphere, they are more suited for observing high-declination sources, such as Perseus, than ALMA. Most observations in this thesis are done with ALMA, whereas NOEMA observations are used in **Chapter 5**.

Interferometers do not observe the sky brightness of a source directly, but instead measure the interference pattern of each pair of antennas (*visibilities*). The sky brightness distribution can then be retrieved by a Fourier transform of the visibility function. The more baselines with different length and orientation, the more the so-called *uv*-plane gets filled, and the more reliable the image that is reconstructed. The number of baselines equals the number of permutations of pairs of antennas. In addition, due to the Earth's rotation, the orientation of the baselines changes as seen from the source, which helps filling in the *uv*-plane. Calibration, that is, correcting for atmospheric variations, non-uniform response across the receiver bands and total flux measured, and imaging of ALMA data is done with the Common Astronomy Software Applications (CASA; McMullin et al. 2007). For NOEMA data, the software package GILDAS<sup>2</sup> is used.

### 1.3.2 Radiative transfer

To interpret molecular line observations, physical and chemical models with different levels of complexity can be used. Subsequently, a radiative transfer model is employed to produce a synthetic image of the line emission. The three software packages used

---

<sup>2</sup><http://www.iram.fr/IRAMFR/GILDAS>



in this thesis are RADEX, RATRAN and LIME (van der Tak et al. 2007, Brinch & Hogerheijde 2010, and Hogerheijde & van der Tak 2000, respectively). RADEX is a one-dimensional non-LTE code that assumes an isothermal and homogeneous medium. This assumption limits the number of free parameters and reduces the computational time. In the non-LTE situation, the molecular level populations depend on the radiation field, which in turn, depends on the level populations. RADEX uses the “escape probability method” to decouple the radiative transfer calculations from the calculations of the level populations (e.g., Sobolev 1960). This approach considers the probability that a photon will escape the medium, which depends on the optical depth of the transition. The publically available version of RATRAN deals with spherically symmetric geometries of varying temperature and density. In this case the radiation field and level populations have to be solved iteratively as functions of depth into the cloud. Finally, LIME (LIne Modeling Engine) works in arbitrary, three-dimensional geometries using a random grid in which the spacing of the grid cells can be weighted by, for example, density. LIME can be used for both LTE and non-LTE calculations. All codes require molecular collision rates for non-LTE calculations, many of which are collected in the Leiden Atomic and Molecular Database (LAMDA; Schöier et al. 2005).

## 1.4 Studies of embedded disks

Embedded disks are a critical stage, providing the link between the warm inner envelope and cold protoplanetary disk, and the initial conditions for planet formation. However, observational studies of embedded disks have long been hampered by a lack of spatial resolution and sensitivity of existing facilities. The presence of a disk can be derived from unresolved continuum fluxes at different wavelengths, but molecular line observations at high spatial resolution are needed to establish whether such structure is in fact a rotationally supported disk. High spatial and high spectral resolution are also necessary to disentangle emission from the disk and envelope. Line observations, however, require a much longer integration time than continuum observations because the emission covers a very narrow frequency range. ALMA now provides the sensitivity and resolution to study the physical and chemical conditions in embedded disks. The following sections provide a brief overview from early observations to the current ALMA studies.

### 1.4.1 Identification of protostars

Theoretically, the different phases of star formation are divided into four *Stages*, based on age, stellar mass and infall rate (as described in **Sect. 1.1** and **Fig. 1.1**). Since these parameters are not always directly observable, young stellar objects (YSOs) are divided into different *Classes* based on observations. The dust around a YSO heats up by absorbing the high-energy (UV and optical) radiation from the star and accretion, and subsequently re-emits lower-energy radiation at longer wavelengths. YSOs, except for the most deeply embedded protostars, are therefore best identified at infrared to submillimeter wavelengths. The *Spitzer Space Telescope* had the sensitivity to detect YSOs down to the brown dwarf limit, and several large programs have been carried out at 3–160  $\mu\text{m}$  to identify YSOs in several nearby molecular clouds (e.g., Evans et al. 2009; Dunham et al. 2013, 2015). Many of these regions have also been observed

at far-infrared wavelengths (55–670  $\mu\text{m}$ ) with the *Herschel Space Observatory* (e.g., André et al. 2010).

Lada (1987) used the infrared spectral index (the slope of the spectral energy distribution; the SED) between 2 and 10–60  $\mu\text{m}$  to distinguish three groups of YSOs: *Class I*, *II* and *III* (**Fig. 1.1**). Greene et al. (1994) added a fourth class, the “*Flat-spectrum*” sources, and *Class 0* was added for protostars too deeply embedded to detect in the near-infrared (André et al. 1993). Other criteria are the ratio of submillimeter ( $\lambda \geq 350\mu\text{m}$ ) to bolometric luminosity ( $L_{\text{submm}}/L_{\text{bol}}$ ) and the bolometric temperature ( $T_{\text{bol}}$ ). The observed Classes roughly correspond to the theoretical Stages, but the difficulty is that the SED, and thus the parameters used to categorize objects into Classes, is sensitive to the geometry of the protostellar system (e.g., Crapsi et al. 2008). For example,  $T_{\text{bol}}$  can cross at least one Class boundary as the inclination changes from edge-on to face-on. In addition,  $T_{\text{bol}}$  may place an object in a different Class than  $L_{\text{submm}}/L_{\text{bol}}$ . One should thus keep in mind, when studying evolutionary trends, that observed Classes not necessarily correspond to physical Stages.

The large number of YSOs detected with *Spitzer* allowed for a statistical study of the lifetime of different Classes. By assuming a Class II lifetime of 2 Myr, and scaling this to the relative number of YSOs in other Classes, the protostellar lifetime (Class 0 + I) is  $\sim 0.5$  Myr (e.g., Dunham et al. 2014). This method does not take into account that star formation is sequential, that is, the current population of Class II sources comes from an earlier generation of Class 0, I and Flat sources. Kristensen & Dunham (2018) propose a different analysis to overcome this and find that YSOs spend on average  $\sim 10\%$  of their time in the embedded phase (Class 0 + I + Flat) and the remaining 90% of their time as Class II and III objects.

These surveys also confirmed earlier results that the observed protostellar luminosities are generally  $\sim 10$  times lower than expected based on accretion (e.g., Kenyon et al. 1990; Kenyon & Hartmann 1995; Young & Evans 2005; Evans et al. 2009). One solution for this “protostellar luminosity problem” is *episodic accretion*. In the episodic accretion scenario, the accretion process is variable and consists of short bursts of very rapid accretion as those observed for FU Ori objects (see e.g., reviews by Audard et al. 2014; Hartmann et al. 2016). A way to infer the occurrence of such bursts observationally is with the radial extent of CO emission in a protostellar envelope. More extended emission than expected from the current luminosity indicates that the circumstellar material has recently been heated, evaporating the CO ice. Small surveys imply that a protostar undergoes approximately five bursts (e.g., Jørgensen et al. 2015).

## 1.4.2 Embedded disk studies before *ALMA*

Early studies of embedded disks focused on modeling the infrared and (sub)millimeter continuum SEDs of protostars using a theoretical density profile and radiative transfer codes. The first realistic SED models of protostars with an infalling envelope were computed by Adams et al. (1987) based on a one-dimensional rotating collapsing envelope model (Ulrich 1976; Cassen & Moosman 1981; Terebey et al. 1984) with a protostellar disk inside the centrifugal radius (that is, the radius at which the gravitational force is balanced by the centrifugal force). Whitney et al. (2003) improved upon these models by adding a flared accretion disk and bipolar cavities. For many sources a disk was required in order to obtain a reasonable fit (e.g., Kenyon et al. 1993). However, outflow opening angle, inclination, infall rate and centrifugal radius are degenerate in

SED fitting. Some of these parameters can be constrained from images (for example scattered light images; e.g., Eisner et al. 2005), and a more accurate description can be obtained by including the velocity structure as measured through molecular lines (e.g., Hogerheijde & Sandell 2000).

The advent of (sub)millimeter interferometry allowed studies of the colder mm-sized dust in disks at scales down to a few hundred AU. In interferometric observations, the physical scale probed scales inversely with the distance between two telescopes, so-called *baselines*. The longest baselines are most sensitive to disk emission, while shorter baselines probe the inner envelope. Since two telescopes cannot be infinitely close together, emission from the largest physical scales will always be filtered out. (Sub)millimeter interferometry is therefore well suited to distinguish the disk from the envelope. Moreover, at (sub)millimeter wavelengths, the dust is expected to be mostly optically thin and can therefore be used to calculate disk masses.

Small surveys (e.g., Looney et al. 2000; Jørgensen et al. 2009; Maury et al. 2019) and studies of individual sources (e.g., Hogerheijde 2001; Harvey et al. 2003; Enoch et al. 2009a) show that disks with radii of a few hundred AU and masses of a few times  $0.01\text{--}0.1 M_{\odot}$  are present in the embedded phase. But there are also sources where no massive extended disk is observed (e.g., Jørgensen 2004; Maury et al. 2010). Tobin et al. (2016b) performed the first complete survey of all protostars in a single star forming region using the Very Large Array (the VLA Nascent Disk and Multiplicity (VANDAM) survey). From these observations, 33% of the Class 0 protostars and 11% of the Class I protostars show a dust disk at 12 AU diameter resolution (Segura-Cox et al. 2018). Since 8 mm observations trace a population of larger dust grains, which have likely drifted toward the star, these data provide only lower limits to the disk size. Large disks ( $>100$  AU) are thus possible during the embedded phase, although they do not seem to be common.

Although compact, disk-like continuum emission is prevalent in the Class 0 and I phase, molecular line observations are required to determine whether these structures are in fact rotationally supported. Furthermore, disks can be significantly larger in the gas than in the dust. Molecular line observations require much higher sensitivity than continuum observations, and in addition, high angular and spectral resolution are needed to distinguish true Keplerian rotation ( $v_{\text{rot}} \propto r^{-0.5}$ ) from rotation due to infall with angular momentum conservation ( $v_{\text{rot}} \propto r^{-1}$ ) (see e.g., Lee et al. 2009). Pre-ALMA interferometric line observations in combination with detailed radiative transfer modeling made it possible to constrain the radial distribution of molecular abundances and enabled studies of the kinematic structure of protostellar systems (e.g., Jørgensen et al. 2005). Such studies revealed a number of rotationally supported Class I disks based on  $\text{HCO}^+$  emission (e.g., Brinch et al. 2007; Lommen et al. 2008) or emission from CO isotopologues (e.g., Takakuwa et al. 2012; Harsono et al. 2014). A kinematic analysis also allowed the mass of the protostar to be derived. Class 0 disks are harder to study because of the more massive envelope, but Tobin et al. (2012b) detected Keplerian rotation out to  $\sim 150$  AU in the Class 0 disk L1527 (**Fig. 1.8**). Large Keplerian disks ( $R > 100$  AU) are thus clearly present in Class I objects, and there is some evidence for large disks in Class 0 systems.

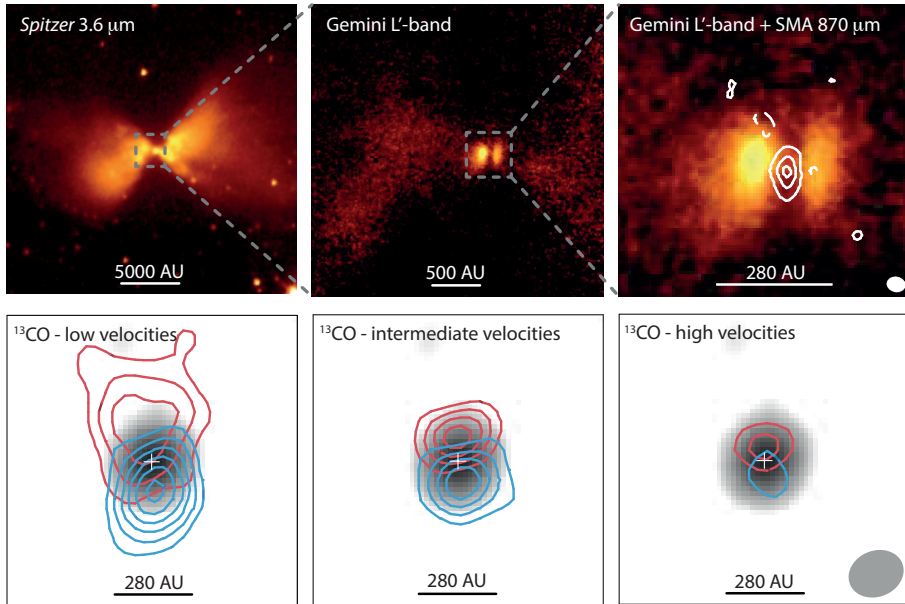


**Figure 1.8:** The first rotationally supported disk around a Class 0 protostar was detected around L1527 IRS in Taurus (Tobin et al. 2012b). The *Spitzer* IRAC 3.6  $\mu\text{m}$  image shows the outflow cavities in scattered light (*top left panel*). The point-like structure in the center of the envelope is resolved into a bipolar scattered light nebula in the Gemini L' image (*top middle and top right panel*). The dark lane is the shadow of the disk, which becomes visible in the 870  $\mu\text{m}$  SMA image (white contours in *top right panel*). Keplerian rotation was established using  $^{13}\text{CO}$  CARMA observations. The *bottom panels* show the integrated blueshifted (blue contours) and redshifted (red contours) emission at different velocity ranges overlaid on the CARMA 1.3 mm image. Images are adapted from Tobin et al. (2010, 2012b, 2013b).

### 1.4.3 Embedded disk studies with ALMA

With the higher sensitivity and spatial resolution of ALMA, continuum observations at wavelengths of  $\sim 1$  mm can be done routinely at subarcsecond resolution ( $\sim$ one minute per source), and disk-like structures in continuum emission are ubiquitously detected in surveys of embedded sources in  $\rho$  Ophiuchus and Orion (Williams et al. 2019; Tobin et al. in prep.). Both studies show that the disk mass decreases from Class 0 to Class II, consistent with the VLA results for Perseus (Tychoniec et al. 2018) and expectations from disk evolution. From the 328 protostars in Orion, 70 objects have disks with dust radii larger than 50 AU. There is a slight decrease in median disk radius for Class 0, Class I and Flat spectrum sources (from 28 to 20 AU; Tobin et al. in prep.), contrary to expectations from viscous disk evolution, which may be an indication of dust radial drift. The distribution of disk radii from the hydrodynamical simulation by Bate (2018) is similar to that observed for Class 0 objects, indicating that the effect of magnetic braking may not be as large as previously suggested.

In addition to these new continuum surveys, ALMA has established Keplerian rotation in four Class 0 disks (Murillo et al. 2013; Lindberg et al. 2014; Codella et al. 2014; Yen et al. 2017). A Keplerian disk was also discovered around a likely Class 0

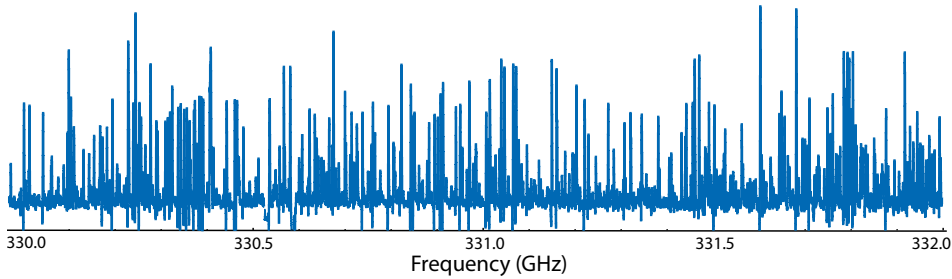


**Figure 1.9:** A small part of the ALMA spectrum (total spectral range of 33.7 GHz) toward the Class 0 protostar IRAS 16293B observed in the Protostellar Interferometric Line Survey (PILS; Jørgensen et al. 2016), illustrating the extreme line-richness of this source (one line every  $\sim 3.4$  MHz). Each vertical line corresponds to a molecular transition; the vertical scale is  $1 \text{ Jy beam}^{-1}$ , whereas the rms is  $\sim 10 \text{ mJy beam}^{-1}$ .

proto-brown dwarf (Hsieh et al. 2019), as well as a disk around a triple Class 0 protostellar system (Tobin et al. 2016a). Moreover, the disk and envelope kinematics have been studied in more detail for the Class 0 source L1527 IRS, and for several Class I sources (e.g., Yen et al. 2014; Aso et al. 2017). Other exciting results include evidence for a disk wind and grain growth in a Class I disk (Bjerkeli et al. 2016b; Harsono et al. 2018), and a possible misalignment between the inner ( $< 40\text{--}60$  AU) and outer disk of L1527 (Sakai et al. 2019).

ALMA also allows for chemical studies on disk-scales. The first of such studies have focussed on the interface between the disk and the envelope, where a possible accretion shock could cause some of the icy grain mantles to sublimate. A change in chemical composition at the disk-envelope interface has been observed for several protostars, although which molecules trace certain spatial scales differs from source to source (Sakai et al. 2014b; Oya et al. 2016). A detailed chemical study has been performed for the the low-mass protostellar binary IRAS 16293. This sources was already known to be chemically rich, but the Protostellar Interferometric Line Survey performed with ALMA (PILS) has started to reveal the full chemical complexity down to 50-AU scales (Fig. 1.9, e.g., Jørgensen et al. 2016). A first chemical survey toward 12 Class I sources in  $\rho$  Ophiuchus, some of which have a Keplerian disk, has recently been presented by Artur de la Villarmois et al. (2019). For these systems,  $\text{C}^{17}\text{O}$  is detected towards the less evolved and less luminous sources, while  $\text{SO}_2$  is detected toward the most evolved sources with a high luminosity. Surprisingly, no methanol is detected, suggesting that maybe only a small portion of the disks have temperatures above  $\sim 100$  K. In contrast, several complex molecules ( $\text{CH}_3\text{OH}$ ,  $\text{CH}_2\text{DOH}$ ,  $\text{CH}_3\text{SH}$ ,  $\text{NH}_2\text{CHO}$ ) have been observed toward the Class 0 source HH212-MM1, but whether their emission originates from the disk surface, a disk wind or an accretion shock at the disk-envelope interface is not yet constrained (Lee et al. 2017; Bianchi et al. 2017).

#### 1.4.4 Modeling of embedded-disk temperature and composition

Temperature is an important parameter in disk evolution and planet formation. It governs, for example, how resistive the gas is to gravitational instabilities (e.g., Offner et al. 2010). Such instabilities could form stellar companions (e.g., Tobin et al. 2016a) and giant planets (e.g., Boss 1997; Boley 2009), or cause luminosity outbursts (e.g.,

Vorobyov 2009). In addition, temperature has a strong effect on the chemical composition of the disk through freeze-out of the major carbon and oxygen carrying species. Models for disks without an envelope have shown that higher mass accretion rates result in warmer disks (e.g., Min et al. 2011). Since accretion rates are expected to be higher during earlier stages, embedded disks may be warmer than evolved protoplanetary disks. The temperature is further influenced by the envelope which acts as an insulating blanket (e.g., D’Alessio et al. 1997; Whitney et al. 2003). In particular, Harsono et al. (2015) showed that the H<sub>2</sub>O, CO<sub>2</sub> and CO snowlines are shifted to larger radii in strongly accreting young embedded disk compared to protoplanetary disks. CO is even expected to be largely present in the gas phase in embedded disks.

The absence of CO ice in embedded disks would mean that the chemical composition of the disk is not fully inherited from the molecular cloud core, where most CO is frozen out. Whether the disk material is inherited from the parental cloud, or whether it is processed, or even completely reset to atoms, on the way to the disk, is still an open question. Physicochemical models of disk formation by Visser et al. (2009b) and Visser et al. (2011) have shown that not all ices are directly incorporated into the disk. Volatile species can have desorbed and even recondensed along the way. These models do not take accretion heating into account, which could mean that ice reprocessing may occur in a larger region of the disk. In addition, Drozdovskaya et al. (2016) show that processing of ices during infall can lead to enhancement of CO<sub>2</sub> ice and organics at the expense of CO and methanol ice, respectively.

## 1.5 This thesis

ALMA has firmly established the presence of rotationally supported disks during the embedded stage of star formation. Although it remains an open question whether most young disks are large or small, and thus what the exact formation mechanism is, it is not impossible to form large  $R \gtrsim 50\text{--}100$  AU disks already in the Class 0 phase. Moreover, there is more and more evidence that the first steps of planet formation already occur in these young disks, instead of in more evolved protoplanetary disks, as was generally assumed. Embedded disks thus provide the true initial conditions for planet formation. Therefore, in order to understand how planets form and what composition they have, we have to know the physical and chemical conditions during this crucial early phase. Such studies are now possible with ALMA. This thesis focusses mainly on the temperature structure of embedded disks, since this is an important parameter for disk evolution and composition, and the consequences for the chemistry. The following questions are addressed:

- Are young embedded disks cold ( $T \lesssim 20\text{--}25$  K), such that there is a large region where CO is frozen out as observed for protoplanetary disks, or too warm for CO ice ( $T \gtrsim 20\text{--}25$  K), as predicted by models?
- Is the temperature profile in young disk-like structures that are not rotationally supported similar to that of embedded Keplerian disks? What are the effects on the chemistry?
- Do disks have a large reservoir of complex organic molecules? And if so, does the chemical composition resembles that of younger protostellar systems?

The first part of the thesis focusses on the temperature regime of CO freeze-out ( $\lesssim 20\text{--}25$  K) and investigates how robust  $\text{N}_2\text{H}^+$  is as a tracer of the CO snowline. Moreover, the question of how to disentangle disk and envelope emission is addressed. The temperature structure is then examined in the edge-on young disks L1527 using  $\text{N}_2\text{D}^+$ ,  $^{13}\text{CO}$  and  $\text{C}^{18}\text{O}$  observations, and in a larger sample of young disks using observations of  $\text{C}^{17}\text{O}$  and  $\text{H}_2\text{CO}$ . The second part of the thesis concentrates on temperatures at which water and complex organics are present in the gas phase ( $\gtrsim 100\text{--}150$  K). First,  $\text{H}^{13}\text{CO}^+$  is demonstrated to be a tracer of the water snowline. Second, the location of the water snowline and the complex molecular reservoir are studied in the young disk around the outbursting star V883 Ori. Finally, multiple  $\text{H}_2\text{CS}$  lines are used to derive the temperature profile of the disk-like structure in the Class 0 protostar IRAS 16293A.

## 1.5.1 Overview of chapters

### The $\lesssim 20\text{--}25$ K regime: freeze-out of CO

#### CHAPTER 2 - Robustness of $\text{N}_2\text{H}^+$ as tracer of the CO snowline

$\text{N}_2\text{H}^+$  has often been used to trace CO freeze-out in dense cores and protoplanetary disks. This Chapter presents a simple network containing the reactions essential for  $\text{N}_2\text{H}^+$  chemistry, applies this to a physical model for the TW Hya protoplanetary disk and studies the correlation between  $\text{N}_2\text{H}^+$  emission and the CO snowline. The main conclusion is that the  $\text{N}_2\text{H}^+$  emission peaks at larger radii than the snowline, as far as  $\sim 50$  AU further out. This is because the 50% reduction in gaseous CO at the snowline is not yet enough to diminish  $\text{N}_2\text{H}^+$  destruction, and because  $\text{N}_2\text{H}^+$  can form in a surface layer where CO is already photodissociated while  $\text{N}_2$  is not. These models place the CO snowline at 19 AU in TW Hya,  $\sim 10$  AU closer in than previously derived from  $\text{N}_2\text{H}^+$  observations without taking the chemistry into account, but in agreement with  $^{13}\text{C}^{18}\text{O}$  observations. Simple chemical modeling and a source-specific physical model are thus required to derive the CO snowline location from  $\text{N}_2\text{H}^+$  observations.

#### CHAPTER 3 - Unveiling the physical conditions of the youngest disk: A warm embedded disk in L1527

Prompted by the non-detection of  $\text{N}_2\text{D}^+$  in archival ALMA observations toward L1527, this Chapter aims to determine whether the young disk is indeed warm enough to prevent CO freeze-out. Since this disk is viewed edge-on, CO freeze-out is expected to be directly observable in the  $^{13}\text{CO}$  and  $\text{C}^{18}\text{O}$  observations. This Chapter shows first how disk emission can be disentangled from the envelope contribution based on kinematics and line optical depth effects. A power law radial temperature profile constructed from the brightness temperature of the optically thick  $^{13}\text{CO}$  and  $\text{C}^{18}\text{O}$  emission shows that the temperature is above 20 K out to at least 75 AU, and possibly throughout the entire 125 AU disk. Radiative transfer modeling for a L1527-specific physical structure shows that a model without CO freeze-out matches the  $\text{C}^{18}\text{O}$  observations better than a model with the CO snowline at  $\sim 70$  AU. The young disk around L1527 is thus likely to be too warm for CO freeze-out, in contrast to more mature protoplanetary disks.

## CHAPTER 4 - Temperature structure of embedded disks: Young disks in Taurus are warm

To address the question whether young embedded disks are generally warmer than protoplanetary disks, this Chapter presents ALMA observations of  $\text{C}^{17}\text{O}$  and  $\text{H}_2\text{CO}$  toward five young disks in Taurus. Signs of CO freeze-out are only observed in the large disk around the borderline Class I – Class II source IRAS 04302 (at radii  $\gtrsim 100$  AU). In addition,  $\text{H}_2\text{CO}$  emission in IRAS 04302 originates from the surface layers. These results suggest that the midplane temperature is  $\gtrsim 20$  K but  $\lesssim 50$  K, such that  $\text{H}_2\text{CO}$  is frozen out while CO can remain in the gas phase. Young embedded disks thus seem indeed to be warmer than their more evolved counterparts.

## The $\gtrsim 100\text{--}150$ K regime: thermal desorption of $\text{H}_2\text{O}$ and COMs

### CHAPTER 5 - Imaging the water snowline in protostellar envelopes with $\text{H}^{13}\text{CO}^+$ : The case of NGC1333 IRAS2A

This Chapter investigates whether  $\text{H}^{13}\text{CO}^+$  can be used as a tracer of the water snowline. Although, ultimately, one wants to locate the water snowline in disks directly, protostellar envelopes are better targets to test the  $\text{HCO}^+$ - $\text{H}_2\text{O}$  anticorrelation. First, the snowline is located at radii of 10s–100 AU instead of a few AU due to the higher accretion rates and lower densities in envelopes as compared to disks. Second,  $\text{H}_2^{18}\text{O}$  has been observed in four protostellar systems, while no warm water images exist for disks. A spatial anticorrelation between  $\text{H}^{13}\text{CO}^+$  and  $\text{H}_2^{18}\text{O}$  emission is indeed observed with NOEMA toward the Class 0 source NGC1333 IRAS2A. Chemical and radiative transfer modeling shows that the  $\text{H}^{13}\text{CO}^+$  abundance should decrease by at least a factor of six to match the observations and that this abundance drop occurs just outside the water snowline (as was shown for  $\text{N}_2\text{H}^+$  and the CO snowline in [Chapter 2](#)). These results thus provide proof of concept that  $\text{H}^{13}\text{CO}^+$  can be used as a tracer of the water snowline.

### CHAPTER 6 - Imaging the water snowline in protostellar envelopes with $\text{H}^{13}\text{CO}^+$ : A small survey of protostars in Perseus

This Chapter establishes  $\text{H}^{13}\text{CO}^+$  as a tracer of the water snowline by observing  $\text{H}^{13}\text{CO}^+$  and COMs toward four Class 0 protostars in Perseus. B1-c provides a textbook example of  $\text{H}^{13}\text{CO}^+$  emission surrounding centrally peaked emission from several COMs. In addition, the compact  $\text{H}^{13}\text{CO}^+$  emission toward HH 211 is consistent with the lower luminosity of this source, or the potential presence of a disk, which would result in a snowline location too close to the star to be resolved at the  $0.5''$  resolution of the observations. The  $\text{H}^{13}\text{CO}^+$  emission displays a more complex morphology for L1448-mm with blueshifted absorption, possibly due to the presence of a wind, and seems associated with larger scales in the overall line-poor source B5-IRS1.  $\text{H}^{13}\text{CO}^+$  is thus a promising tracer of the water snowline, given that the source physical structure is taken into account.

### CHAPTER 7 - Methanol and its relation to the water snowline in the disk around the young outbursting star V883 Ori

A water snowline location has been claimed for one disk, V883 Ori, based only indirectly on continuum observations. However, the relation between snowlines and structures in the dust are still debated. This Chapter presents ALMA observations of



methanol ( $\text{CH}_3\text{OH}$ ), a molecule expected to be released from the ice inside the water snowline. The methanol follows the Keplerian velocity structure observed for  $\text{C}^{18}\text{O}$ , thus the emission originates in the disk and not the envelope or outflow. The derived outer radii of  $\sim 120\text{--}140$  AU (compared to the 360 AU outer radius for  $\text{C}^{18}\text{O}$ ), together with a rotational temperature of  $\sim 100$  K, suggest that the water snowline can be as far out as  $\sim 100$  AU, instead of the previously inferred 42 AU. Detailed modeling with a physical structure for V883 Ori is required to confirm this. In addition, methyl formate ( $\text{CH}_3\text{OCHO}$ ) and acetaldehyde ( $\text{CH}_3\text{CHO}$ ) are tentatively detected. Disks around outbursting young stars are thus good sources to study the chemical complexity of the planet-forming material.

## CHAPTER 8 - Temperature profiles of young disk-like structures: the case of IRAS 16293A

This Chapter uses observations of multiple  $\text{H}_2\text{CS}$  lines from the ALMA Protostellar Interferometric Line Survey (PILS) to study the temperature structure of the Class 0 protostar IRAS 16293A. This source displays rotation on scales  $\lesssim 400$  AU and the presence of a Keplerian disk has been suggested in the inner  $\sim 50$  AU. However, analysis of the same  $\text{H}_2\text{CS}$  line in this Chapter shows that the high velocities attributed to a Keplerian disk are more likely a contamination by weak lines at nearby frequencies. Temperature profiles based on line ratios and rotation diagrams for the  $\text{H}_2\text{CS}$  peak fluxes show that the temperature remains  $\gtrsim 100$  K in the inner 150 AU and drops to  $\sim 75$  K at 200 AU. This is consistent with previously derived temperature profiles assuming an envelope structure. Interestingly, the temperature does not increase above  $\sim 100\text{--}150$  K in the inner 150 AU. High-resolution observations of optically thin lines are needed to establish whether this is the result of effective cooling by water that is released from the grains or due to a putative disk. Over the entire 150 AU, the temperature is  $\sim 100$  K higher than for the L1527 disk, consistent with the higher luminosity (due to a higher accretion rate) of IRAS 16293A.

### 1.5.2 General conclusions and outlook

The main conclusions from this thesis can be summarized as follows (see **Fig. 1.10**):

- Molecules such as  $\text{N}_2\text{H}^+$  and  $\text{H}^{13}\text{CO}^+$  can be used to trace the CO and  $\text{H}_2\text{O}$  snowline, respectively, as long as chemical effects are taken into account and a source-specific physical structure is employed.
- Dust continuum structures are not necessarily related to water snowlines in embedded disks.
- Young embedded disks are warm, with temperatures too high for CO freeze-out ( $T \gtrsim 20\text{--}25$  K). This is in contrast with more evolved protoplanetary disks that have large cold outer regions where CO is frozen out.
- Envelope temperature profiles (typically,  $T \propto r^{-0.7}$  in the optically thick regime) are likely adequate for disk-like structures in Class 0 sources, except in the inner most region ( $\lesssim 100$  AU) that can now be probed by ALMA.
- Young disks around outbursting stars are good sources to study the ice composition of planet-forming material through thermally desorbed complex molecules.

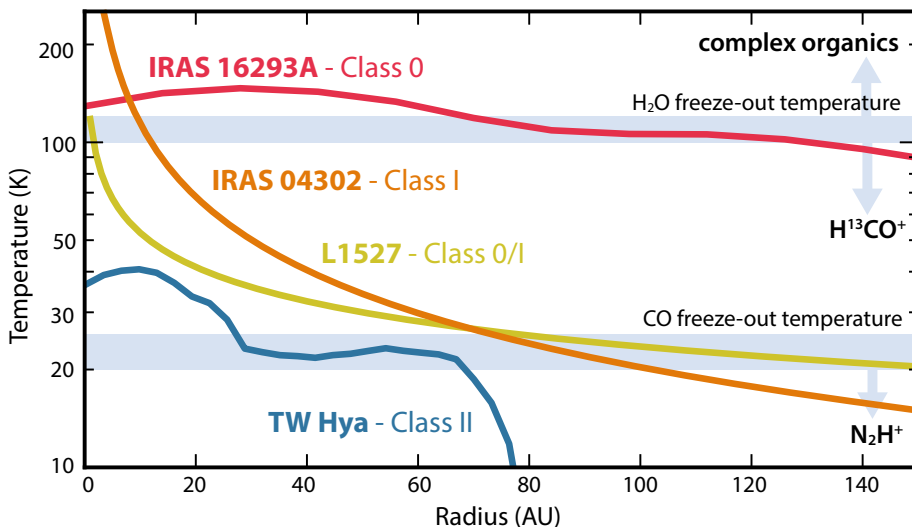


**Figure 1.10:** Summary of the main results in this thesis. The midplane temperature profiles for young disks show a decrease in temperature with evolution. The temperature for the disk-like structure around the Class 0 protostar IRAS 16293A (red line) is determined from  $\text{H}_2\text{CS}$  line ratios (Chapter 8). The midplane temperature for the Class 0/I disk L1527 (yellow line) is constructed based on optically thick  $^{13}\text{CO}$  and  $\text{C}^{18}\text{O}$  emission (Chapter 3), and  $\text{C}^{17}\text{O}$  and  $\text{H}_2\text{CO}$  observations are used for the Class I disk IRAS 04302 (Chapter 4). These young disks are warmer than more evolved protoplanetary disks such as TW Hya (Schwarz et al. 2016). Freeze-out of CO ( $T \lesssim 20 - 25$  K) can be traced with  $\text{N}_2\text{H}^+$  if chemical considerations and the source physical structure are taken into account (Chapter 2) and  $\text{H}^{13}\text{CO}^+$  is a promising tracer for the water snowline (Chapters 5 and 6). Complex organic molecules are released into the gas phase inside the water snowline ( $T \gtrsim 100 - 150$  K) and can therefore be observed in young disk-like structures such as IRAS 16293A and young disks around outbursting protostars such as V883 Ori (Chapter 7). Although embedded disks are warm, they are not warm enough ( $T \lesssim 100$  K) to have a large region where gas-phase methanol is abundant (Chapter 4).

This thesis provides some of the first observational constraints on the temperature structure in young disks and disk-like structures, suggesting that the temperature decreases with decreasing envelope mass and accretion rate, as expected from modeling results. Observations of more sources are now required to confirm this evolutionary trend. In addition, follow-up studies will allow more detailed questions to be answered, such as, when exactly do disks become cold enough for CO freeze-out? Already in the embedded phase, or only after the envelope has fully dissipated? What does the detailed temperature profile look like? Continuum surveys of all protostars in several star-forming regions have paved the way to answer these questions, but an important next step is to establish which sources display Keplerian rotation. Gas radii and masses of a large sample of young disks, and how they compare to values derived from continuum emission, will further our understanding of disk formation and evolution. Whether or not there is a difference in temperature structure between rotationally supported disks and disk-like structures may provide additional constraints. As shown in this thesis, the global temperature structure can be constrained with observations from simple molecules like  $\text{N}_2\text{H}^+$  and  $\text{H}^{13}\text{CO}^+$ . This presents an efficient way for

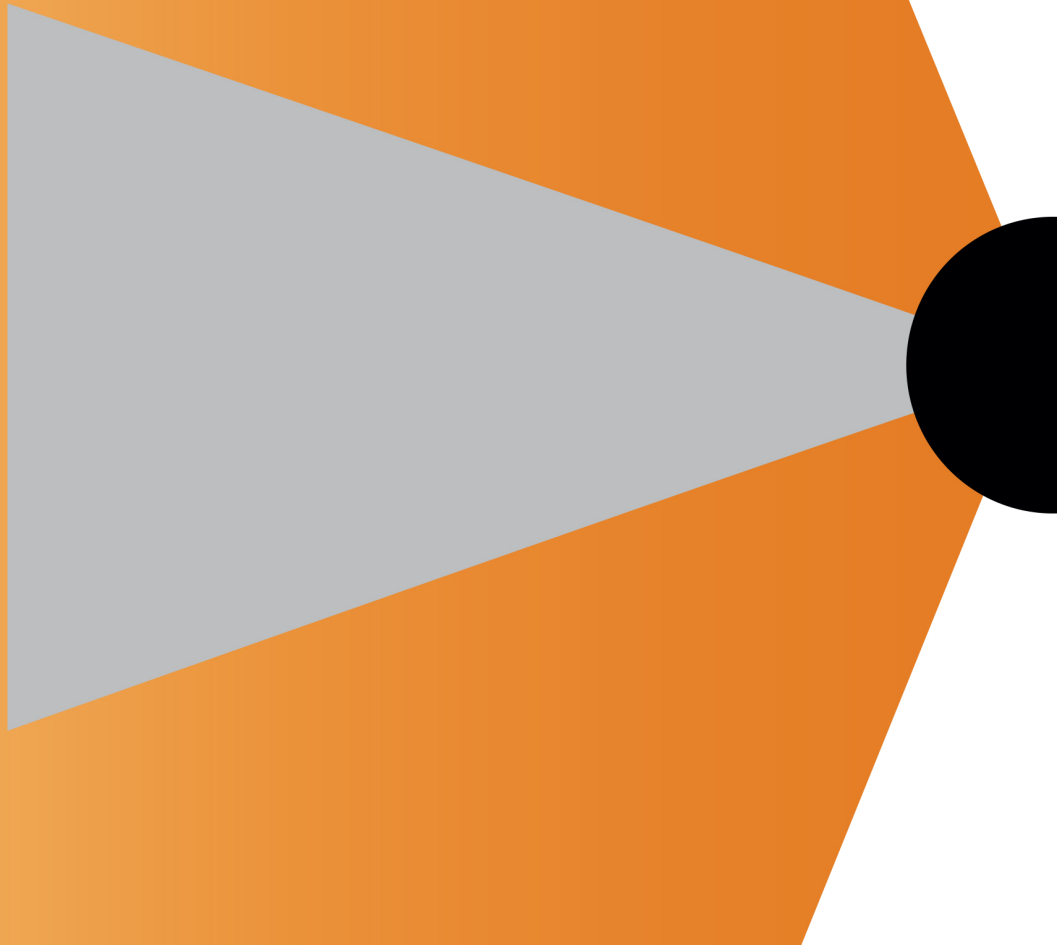
an initial characterization of the large sample of disk (candidates) that can now be studied with ALMA.

Another open question is whether the composition of planet-forming material is inherited from the natal cloud, processed en route to the disk or even completely reset. On the one hand, the absence of CO freeze-out in young disks suggest that no full inheritance takes place. On the other hand, the absence of CO ice will limit the formation of COMs in the embedded disk. The presence of COMs in the V883 Ori disk therefore indicates that no complete reset takes place either. What fraction of the material gets inherited, however, remains an open question. Moreover, how much the material is altered upon entering the disk, for example, through a possible accretion shock at the disk-envelope interface, is still uncertain. Observations of young disks around outbursting protostars can shed light on this matter by providing inventories of complex species that can be compared to protostellar envelopes.

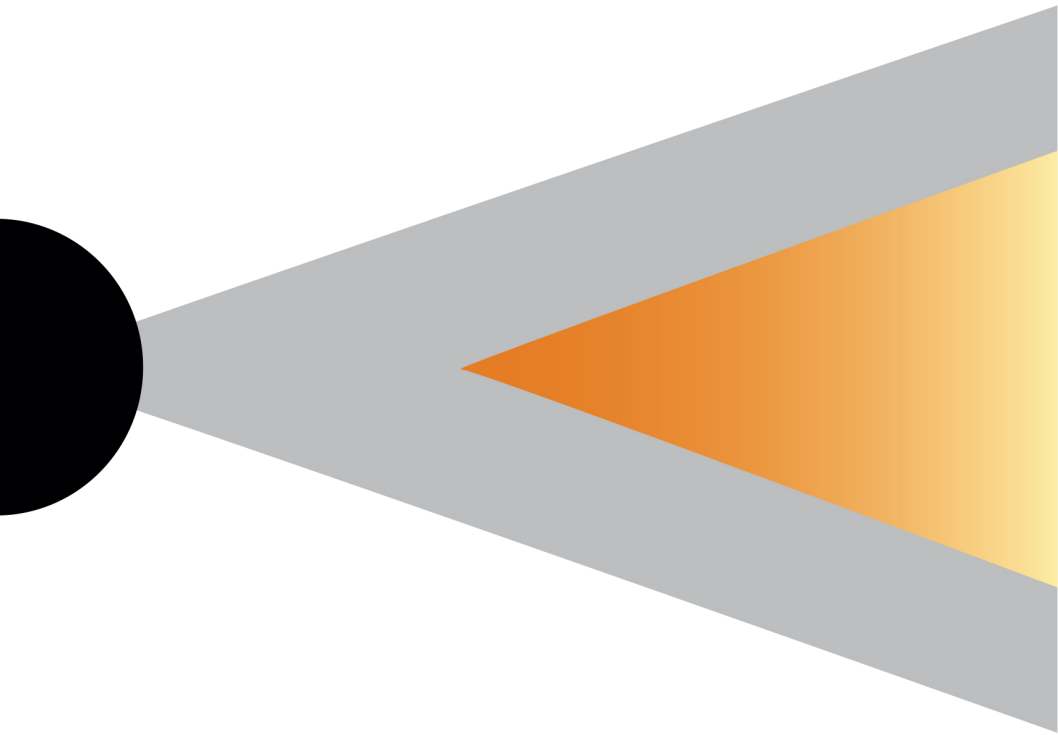
A related problem are the low abundances of CO and H<sub>2</sub>O in protoplanetary disks. Initial results presented in this thesis show no signs of heavy CO depletion in younger disks, and future studies of embedded sources may provide clues to the evolution of planet-forming material in the disk. Another important step in our understanding of planet formation would be the direct observation of the water snowline in a disk using molecular line observations. This thesis shows that H<sup>13</sup>CO<sup>+</sup> is a promising snowline tracer, and the disk around the outbursting star V883 Ori is an obvious candidate for such observations. Finally, a next step would be to incorporate the physical and chemical results for young disks into planet formation models.

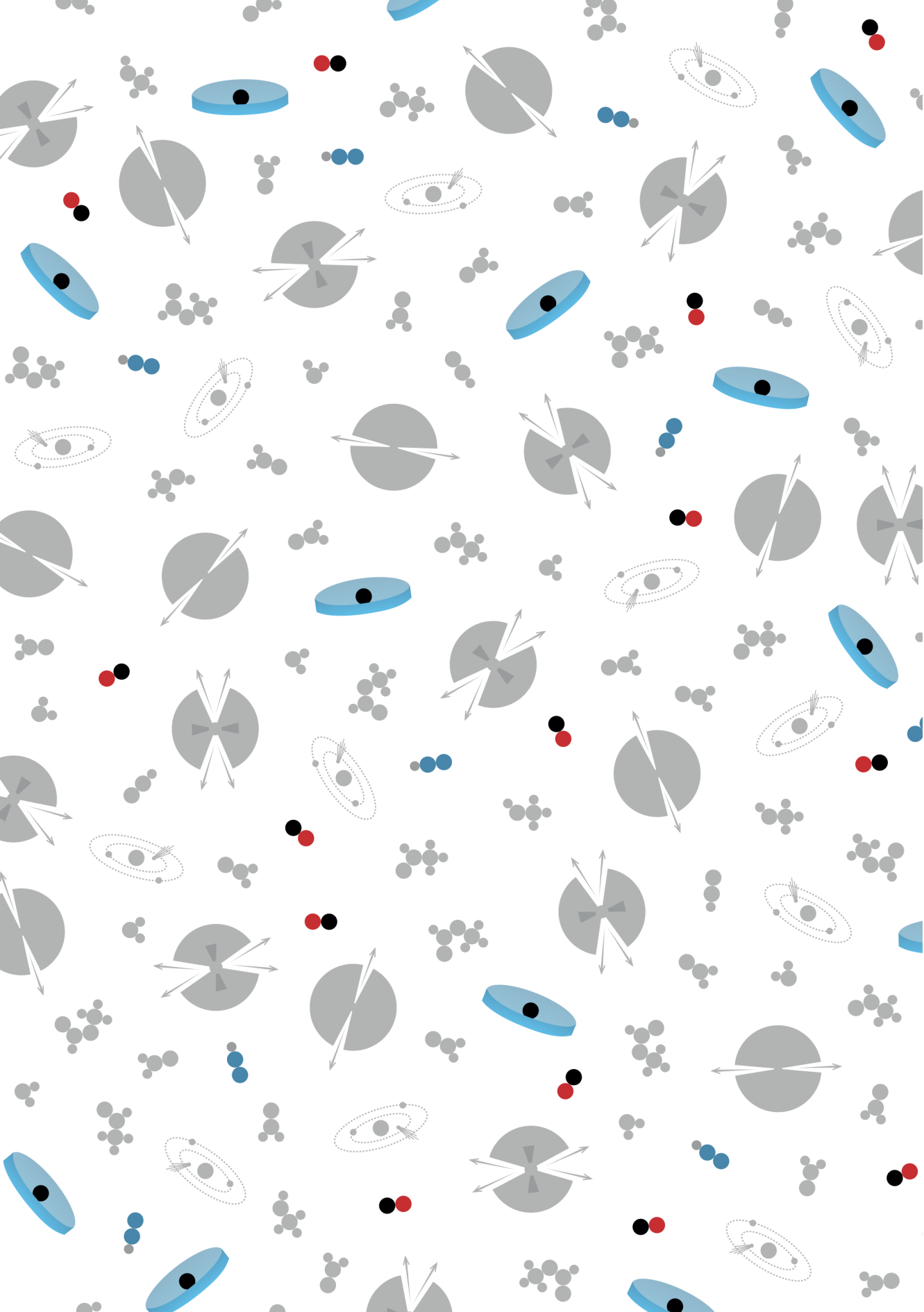


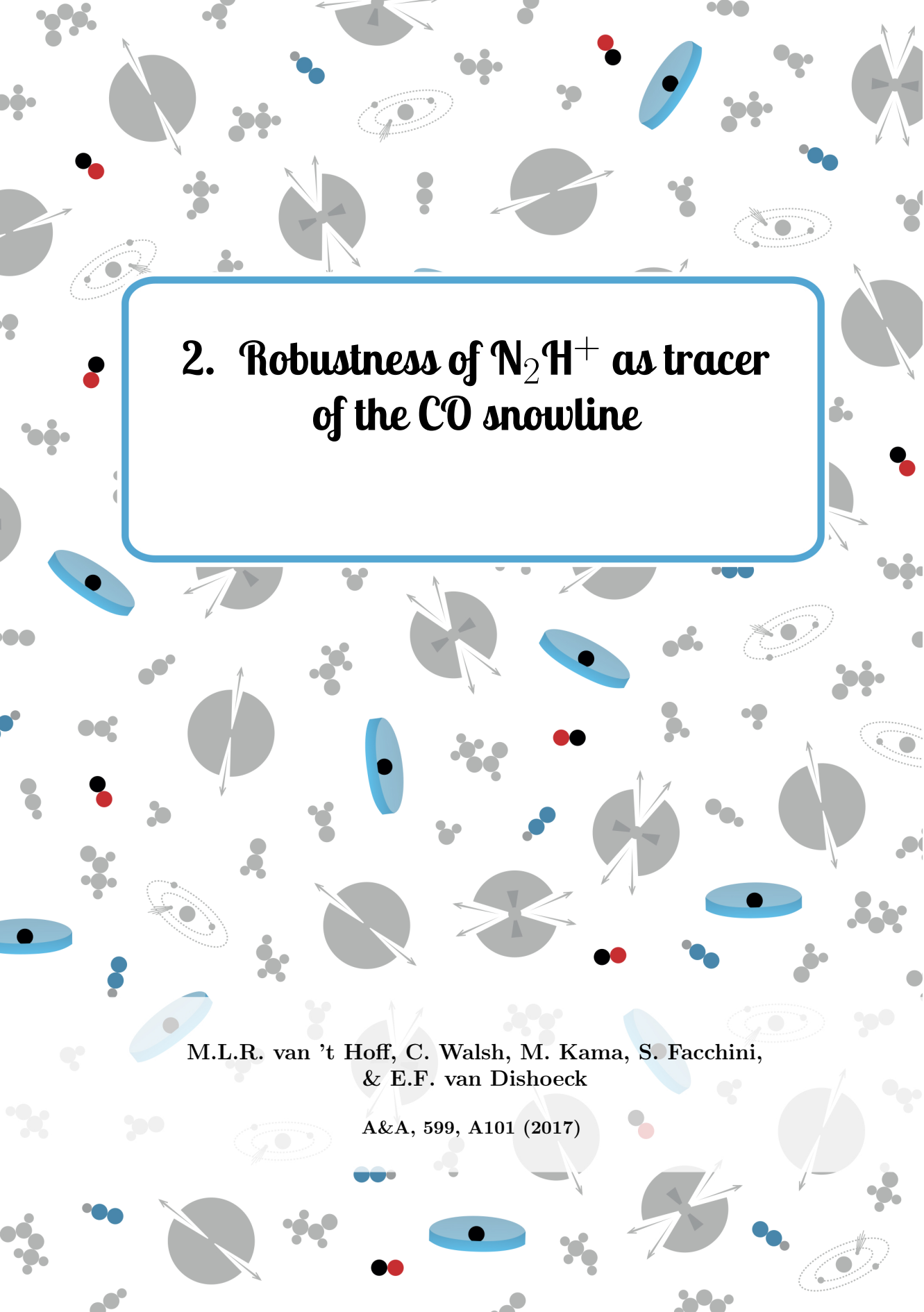
# PART 1



**The < 20-25 K regime:  
Freeze out of CO**







## 2. Robustness of $\text{N}_2\text{H}^+$ as tracer of the CO snowline

M.L.R. van 't Hoff, C. Walsh, M. Kama, S. Facchini,  
& E.F. van Dishoeck

A&A, 599, A101 (2017)





## Abstract

**Context.** Snowlines in protoplanetary disks play an important role in planet formation and composition. Since the CO snowline is difficult to observe directly with CO emission, its location has been inferred in several disks from spatially resolved ALMA observations of  $\text{DCO}^+$  and  $\text{N}_2\text{H}^+$ .

**Aims.**  $\text{N}_2\text{H}^+$  is considered to be a good tracer of the CO snowline based on astrochemical considerations predicting an anti-correlation between  $\text{N}_2\text{H}^+$  and gas-phase CO. In this work, the robustness of  $\text{N}_2\text{H}^+$  as a tracer of the CO snowline is investigated.

**Methods.** A simple chemical network was used in combination with the radiative transfer code LIME to model the  $\text{N}_2\text{H}^+$  distribution and corresponding emission in the disk around TW Hya. The assumed CO and  $\text{N}_2$  abundances, corresponding binding energies, cosmic ray ionization rate, and degree of large-grain settling were varied to determine the effects on the  $\text{N}_2\text{H}^+$  emission and its relation to the CO snowline.

**Results.** For the adopted physical structure of the TW Hya disk and molecular binding energies for pure ices, the balance between freeze-out and thermal desorption predicts a CO snowline at 19 AU, corresponding to a CO midplane freeze-out temperature of 20 K. The  $\text{N}_2\text{H}^+$  column density, however, peaks 5–30 AU outside the snowline for all conditions tested. In addition to the expected  $\text{N}_2\text{H}^+$  layer just below the CO snow surface, models with an  $\text{N}_2/\text{CO}$  ratio  $\gtrsim 0.2$  predict an  $\text{N}_2\text{H}^+$  layer higher up in the disk due to a slightly lower photodissociation rate for  $\text{N}_2$  as compared to CO. The influence of this  $\text{N}_2\text{H}^+$  surface layer on the position of the emission peak depends on the total CO and  $\text{N}_2$  abundances and the disk physical structure, but the emission peak generally does not trace the column density peak. A model with a total (gas plus ice) CO abundance of  $3 \times 10^{-6}$  with respect to  $\text{H}_2$  fits the position of the emission peak previously observed for the TW Hya disk.

**Conclusions.** The relationship between  $\text{N}_2\text{H}^+$  and the CO snowline is more complicated than generally assumed: for the investigated parameters, the  $\text{N}_2\text{H}^+$  column density peaks at least 5 AU outside the CO snowline. Moreover, the  $\text{N}_2\text{H}^+$  emission can peak much further out, as far as  $\sim 50$  AU beyond the snowline. Hence, chemical modeling, as performed here, is necessary to derive a CO snowline location from  $\text{N}_2\text{H}^+$  observations.

## 2.1 Introduction

Protoplanetary disks around young stars contain the gas and dust from which planetary systems will form. In the midplanes of these disks, the temperature becomes so low that molecules freeze out from the gas phase onto dust grains. The radius at which this happens for a certain molecule is defined as its snowline. The position of a snowline depends both on the species-dependent sublimation temperature and disk properties (mass, temperature, pressure and dynamics). Snowlines play an important role in planet formation as increased particle size, surface density of solid material, and grain stickiness at a snowline location may enhance the efficiency of planetesimal formation (Stevenson & Lunine 1988; Ciesla & Cuzzi 2006; Johansen et al. 2007; Chiang & Youdin 2010; Gundlach et al. 2011; Ros & Johansen 2013). Furthermore, the bulk composition of planets may be regulated by the location of planet formation with respect to snowlines, as gas composition and ice reservoirs change across a snowline (Öberg et al. 2011; Madhusudhan et al. 2014; Walsh et al. 2015; Eistrup et al. 2016). Determining snowline locations is thus key to studying planet formation.

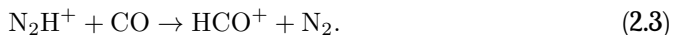
The CO snowline is of particular interest because CO ice is a starting point for prebiotic chemistry (Herbst & van Dishoeck 2009). Assuming a disk around a solar-type star, the CO snowline occurs relatively far (a few tens of AU) from the central star due to the low freeze-out temperature of CO; hence, it is more accessible to direct observations than other snowlines. However, locating it is difficult because CO line emission is generally optically thick, so that the bulk of the emission originates in the warm surface layers. An alternative approach is to observe molecules whose emission is expected to peak around the snowline, or molecules that are abundant only when CO is depleted from the gas phase. Based on the former argument, DCO<sup>+</sup> has been used to constrain the CO snowline location (Mathews et al. 2013; Öberg et al. 2015a), but may be affected by some DCO<sup>+</sup> also formed in warm disk layers (Favre et al. 2015; Qi et al. 2015). A species from the latter category is N<sub>2</sub>H<sup>+</sup> (Qi et al. 2013b, 2015). This molecule forms through proton transfer from H<sub>3</sub><sup>+</sup> to N<sub>2</sub>,



but provided that CO is present in the gas phase, its formation is impeded, because CO competes with N<sub>2</sub> for reaction with H<sub>3</sub><sup>+</sup>,



Furthermore, reactions with CO are the dominant destruction pathway of N<sub>2</sub>H<sup>+</sup>:



N<sub>2</sub>H<sup>+</sup> is therefore expected to be abundant only in regions where CO is depleted from the gas phase, that is, beyond the CO snowline.

Observational evidence for the anti-correlation of N<sub>2</sub>H<sup>+</sup> and gas-phase CO was initially provided for pre-stellar and protostellar environments (e.g., Caselli et al. 1999; Bergin et al. 2001; Jørgensen 2004). However, survival of N<sub>2</sub>H<sup>+</sup> is aided in these systems by the delayed freeze-out of N<sub>2</sub> as compared to CO, because gas-phase N<sub>2</sub> forms more slowly when starting from atomic abundances under diffuse cloud conditions (Aikawa et al. 2001; Maret et al. 2006). In protoplanetary disks, N<sub>2</sub> molecules are

expected to be more abundant than N atoms because of the higher gas density which increases the  $\text{N}_2$  formation rate, and this timescale effect is not important.

So far, the results for protoplanetary disks seem inconclusive. Recent observations of  $\text{C}^{18}\text{O}$  in the disk of HD 163296 suggest a CO snowline location consistent with the observed  $\text{N}_2\text{H}^+$  emission (Qi et al. 2015). On the other hand, several studies indicate a depletion of CO in the disk around TW Hya down to  $\sim 10$  AU (Favre et al. 2013; Nomura et al. 2016; Kama et al. 2016; Schwarz et al. 2016), inconsistent with the prediction that CO is depleted only beyond a snowline at  $\sim 30$  AU, based on modeling of  $\text{N}_2\text{H}^+$  observations (Qi et al. 2013b, hereafter Q13).

In this work, we explore the robustness of the  $\text{N}_2\text{H}^+$  line emission as a tracer of the CO snowline location in the disk midplane, using a physical model (constrained by observations) for the disk around TW Hya. TW Hya is the closest protoplanetary disk system ( $\sim 54$  pc, van Leeuwen 2007) and considered an analog of the Solar Nebula based on disk mass and size. The spatial distribution and emission of  $\text{N}_2\text{H}^+$  are modeled for different CO and  $\text{N}_2$  abundances and binding energies, as well as different cosmic ray ionization rates and degrees of dust settling, using a simple chemical network and full radiative transfer. Aikawa et al. (2015) have shown that analytical formulae for the molecular abundances give a similar  $\text{N}_2\text{H}^+$  distribution as a full chemical network. They also found that the  $\text{N}_2\text{H}^+$  abundance can peak at temperatures slightly below the CO freeze-out temperature in a typical disk around a T Tauri star, but they did not invoke radiative transfer to make a prediction for the resulting  $\text{N}_2\text{H}^+$  emission.

The physical and chemical models used in this work are described in **Sect. 2.2**. **Section 2.3** shows the predicted  $\text{N}_2\text{H}^+$  distributions and emission. The simulated emission is compared with that observed by Q13 and convolved with a smaller beam ( $0.2'' \times 0.2''$ ) to predict results for future higher angular resolution observations. This section also studies the dependence of the model outcome on CO and  $\text{N}_2$  abundances, binding energies, cosmic ray ionization rate, and dust grain settling, and the use of multiple  $\text{N}_2\text{H}^+$  transitions to further constrain the snowline location. Finally, the dependence of the outer edge of the  $\text{N}_2\text{H}^+$  emission on chemical and physical effects is explored. In **Sect. 2.4** the implications of the results will be discussed and in **Sect. 2.5** the conclusions summarized.

## 2.2 Protoplanetary disk model

### 2.2.1 Physical model

For the physical structure we adopt the model for TW Hya from Kama et al. (2016). This model reproduces the dust spectral energy distribution (SED) as well as CO rotational line profiles, from both single-dish and ALMA observations, and spatially resolved CO  $J = 3 - 2$  emission from ALMA. The 2D physical-chemical code DALI (Dust And Lines, Bruderer et al. 2009, 2012; Bruderer 2013) was used to create the model, assuming a stellar mass and radius of  $M_* = 0.74 M_\odot$  and  $R_* = 1.05 R_\odot$ , respectively. The disk is irradiated by UV photons and X-rays from the central star and UV photons from the interstellar radiation field. The stellar UV spectrum from Cleves et al. (2015) is used (based on Herczeg et al. 2002, 2004 and France et al. 2014), which is roughly consistent with a  $\sim 4000$  K blackbody with UV excess due to accretion. The X-ray spectrum is modeled as a thermal spectrum at  $3.2 \times 10^6$  K

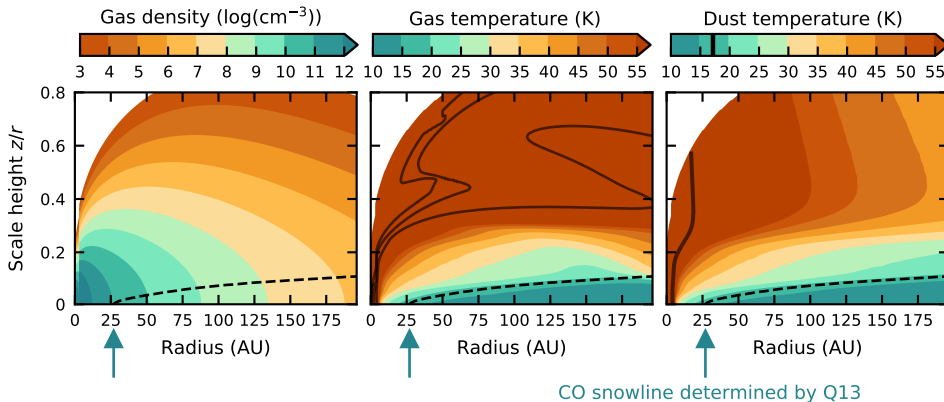


**Figure 2.1:** Gas density, gas temperature, and dust temperature as a function of disk radius,  $r$ , and scale height,  $z/r$ , for the adopted model for the TW Hya disk. The temperature color range is limited to highlight values around the CO snow surface. The solid contours indicate temperatures of 100, 200 and 500 K. The arrow indicates the location of the midplane CO snowline associated with a freeze-out temperature of 17 K, as determined by Q13, and the dashed contour indicates the corresponding snow surface.

with a total X-ray luminosity of  $1.4 \times 10^{30} \text{ erg s}^{-1}$  and the cosmic ray ionization rate is taken to be low,  $5 \times 10^{-19} \text{ s}^{-1}$  (Cleeves et al. 2015).

Starting from an input gas and dust density structure the code uses radiative transfer to determine the dust temperature and local radiation field. The chemical composition is obtained from a chemical network simulation based on a subset of the UMIST 2006 gas-phase network (Woodall et al. 2007) and used in a non-LTE excitation calculation for the heating and cooling rates to derive the gas temperature (see Bruderer et al. 2012 for details). As will be shown in Sect. 2.3 and Fig. 2.1,  $\text{N}_2\text{H}^+$  is predicted in the region where the gas and dust temperatures are coupled ( $z/r \lesssim 0.25$ ). Hence, the temperature in the relevant disk region is not sensitive to changes in molecular abundances.

The input gas density has a radial power law distribution,

$$\Sigma_{\text{gas}} = 30 \text{ g cm}^{-2} \left( \frac{r}{35 \text{ AU}} \right)^{-1} \exp \left( \frac{-r}{35 \text{ AU}} \right), \quad (2.4)$$

and a vertical Gaussian distribution,

$$h = 0.1 \left( \frac{r}{35 \text{ AU}} \right)^{0.3}. \quad (2.5)$$

To match the observations, the gas-to-dust mass ratio is set to 200. Two different dust populations are considered; small grains (0.005 - 1  $\mu\text{m}$ ) represent 1% of the dust surface density, whereas the bulk of the dust surface density is composed of large grains (0.005 - 1000  $\mu\text{m}$ ). The vertical distribution of the dust is such that large grains are settled toward the midplane with a settling parameter  $\chi$  of 0.2, that is, extending to 20% of the scale height of the small grains;

$$\rho_{\text{dust,small}} = \frac{0.01 \Sigma_{\text{dust}}}{\sqrt{2\pi} R h} \exp \left[ -\frac{1}{2} \left( \frac{\pi/2 - \theta}{h} \right)^2 \right] \text{ g cm}^{-3}, \text{ and} \quad (2.6)$$

$$\rho_{\text{dust,large}} = \frac{0.99\Sigma_{\text{dust}}}{\sqrt{2\pi}R\chi h} \exp\left[-\frac{1}{2}\left(\frac{\pi/2 - \theta}{\chi h}\right)^2\right] \text{ g cm}^{-3}, \quad (2.7)$$

where  $\theta$  is the vertical latitude coordinate measured from the pole ( $\theta = 0$ ) to the equator, that is, the midplane ( $\theta = \pi/2$ ; Andrews et al. 2012). In the inner 4 AU, the gas and dust surface density is lowered by a factor of 100 with respect to the outer disk to represent the gap detected in the inner disk (Calvet et al. 2002; Hughes et al. 2007). Recent observations indicate that the dust distribution in this inner region is more complicated (Andrews et al. 2016), but this will not affect the  $\text{N}_2\text{H}^+$  distribution in the outer disk. In **Sect. 2.3.6** we examine the influence of grain settling on the  $\text{N}_2\text{H}^+$  distribution and emission by using a model with  $\chi = 0.8$ , that is, the large grains extending to 80% of the small grain scale height.

The resulting density and thermal structure of the disk are shown in **Fig. 2.1** and used in the chemical modeling described in **Sect. 2.2.2**. A midplane temperature of 17 K corresponds to a radius of 27.5 AU, consistent with the CO snowline properties derived by Q13. In their analysis, Q13 fit ALMA observations using a power law for the radial distribution of the  $\text{N}_2\text{H}^+$  column density, with an inner radius presumed to coincide with the CO snowline.

## 2.2.2 Chemical model

If CO is abundant in the gas phase,  $\text{N}_2\text{H}^+$  formation is slowed down (**Eq. 2.1** and **2.2**) and  $\text{N}_2\text{H}^+$  destruction is enhanced (**Eq. 2.3**). On the other hand, gas-phase  $\text{N}_2$  is required to form  $\text{N}_2\text{H}^+$  (**Eq. 2.1**). Based on these considerations, the simplest method to predict the distribution of  $\text{N}_2\text{H}^+$  is by calculating the balance between freeze-out and desorption for  $\text{N}_2$  and CO at every position in the disk. Assuming a constant total abundance, that is,  $n_{\text{g}}(\text{CO}) + n_{\text{s}}(\text{CO}) = n(\text{CO})$ , the steady state gas phase and ice abundances ( $n_{\text{g}}$  and  $n_{\text{s}}$ , resp.) are then given by,

$$n_{\text{g}}(\text{CO}) = \frac{n(\text{CO})}{k_{\text{f}}/k_{\text{d}} + 1} \text{ cm}^{-3}, \text{ and} \quad (2.8)$$

$$n_{\text{s}}(\text{CO}) = n(\text{CO}) - n_{\text{g}}(\text{CO}) \text{ cm}^{-3}, \quad (2.9)$$

where  $k_{\text{f}}$  and  $k_{\text{d}}$  are the freeze-out and desorption rates, respectively. For  $\text{N}_2$  a similar equation holds. Thermal desorption is considered here as the only desorption process, which is appropriate for volatile molecules such as CO and  $\text{N}_2$ . However, the dust density in the outer disk may be low enough for UV photons to penetrate to the disk midplane, such that photodesorption may become effective. Photodesorption is therefore included when studying the outer edge of the  $\text{N}_2\text{H}^+$  emission in **Sect. 2.3.8**. The thermal desorption rate depends on the specific binding energy for each molecule,  $E_{\text{b}}$ , and for CO and  $\text{N}_2$  values of 855 and 800 K (Bisschop et al. 2006) are adopted, respectively. Expressions for the freeze-out and desorption rates, and a discussion of the adopted parameters can be found in **Appendix 2.A1**. Solving the gas and ice abundances time dependently shows that equilibrium is reached within  $10^5$  years, so steady state is a reasonable assumption for a typical disk lifetime of  $10^6$  years.

The snow surface is defined as the position in the disk where 50% of a species is present in the gas phase and 50% is frozen onto the grains. From **Eq. 2.8** the snow surfaces for CO and  $\text{N}_2$  can thus be predicted. We note that the freeze-out and desorption rates (**Eq. 2.11** and **2.14**), and therefore the fraction of a species that is

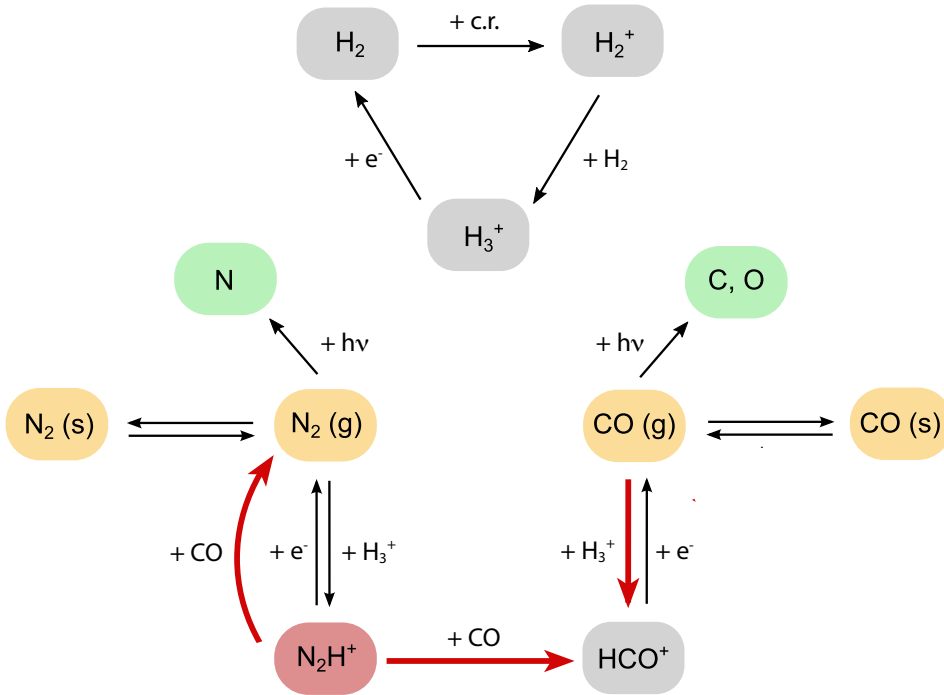


**Figure 2.2:** Schematic representation of the chemical network used to model  $\text{N}_2\text{H}^+$  (red). Freeze-out and desorption products are highlighted in orange and photodissociation products are shown in green. The processes responsible for the anti-correlation between  $\text{N}_2\text{H}^+$  and  $\text{CO}$  are highlighted with red arrows.

present in the gas or ice (e.g.,  $n_g(\text{CO})/n(\text{CO})$ ; see [Eq. 2.8](#)) at a certain temperature, do not depend on abundance. Hence the locations of the midplane snowlines are independent of the total, that is, gas plus ice,  $\text{CO}$  and  $\text{N}_2$  abundances.

As a first approximation,  $\text{N}_2\text{H}^+$  can be considered to be present between the  $\text{CO}$  and  $\text{N}_2$  snow surfaces. Comparison with the result from the chemical model described below shows that the  $\text{N}_2\text{H}^+$  layer extends beyond the  $\text{N}_2$  snow surface, and the outer boundary is better described by the contour where only 0.05% of the  $\text{N}_2$  has desorbed while the bulk remains frozen out. We will refer to the  $\text{N}_2\text{H}^+$  layer bounded by the  $\text{CO}$  snow surface and the contour where 0.05% of the  $\text{N}_2$  has desorbed as model “FD” (freeze-out and desorption).

Prediction of the  $\text{N}_2\text{H}^+$  abundance itself requires solving a chemical model. To avoid uncertainties associated with full chemical network models, a reduced chemical network, incorporating the key processes affecting the  $\text{N}_2\text{H}^+$  abundance, including the freeze-out and thermal desorption of  $\text{CO}$  and  $\text{N}_2$ , is adopted. This network is similar to that used by Jørgensen et al. (2004b) for protostellar envelopes, but with freeze-out, thermal desorption and photodissociation of  $\text{CO}$  and  $\text{N}_2$  included (see [Fig. 2.2](#)). It resembles the analytical approach applied by Aikawa et al. (2015). The most important aspects are described below and a more detailed description can be found in [Appendix 2.A](#).

Incorporation of  $\text{CO}$  and  $\text{N}_2$  destruction by photodissociation in the surface and

**Table 2.1:** Reactions, rate data and related parameters for the  $\text{N}_2\text{H}^+$  chemical network.

Reaction	$\zeta^a$ ( $\text{s}^{-1}$ )	$\alpha^b$ ( $\text{cm}^3 \text{ s}^{-1}$ )	$\beta^b$	$\gamma^b$ (K)	$S^c$	$E_b^d$ (K)	$Y^e$ ( $\text{photon}^{-1}$ )	$k_0(r, z)^f$ ( $\text{s}^{-1}$ )
$\text{H}_2 + \text{C.R.} \rightarrow \text{H}_2^+ + \text{e}^-$	1.20(-17)	...	...	...	...	...	...	...
$\text{H}_2^+ + \text{H}_2 \rightarrow \text{H}_3^+ + \text{H}$	...	2.08(-9)	0	0	...	...	...	...
$\text{H}_3^+ + \text{e}^- \rightarrow \text{H}_2 + \text{H}$	...	2.34(-8)	-0.52	0	...	...	...	...
$\text{N}_2 + \text{H}_3^+ \rightarrow \text{N}_2\text{H}^+ + \text{H}_2$	...	1.80(-9)	0	0	...	...	...	...
$\text{CO} + \text{H}_3^+ \rightarrow \text{HCO}^+ + \text{H}_2$	...	1.36(-9)	-0.14	-3.4	...	...	...	...
$\text{N}_2\text{H}^+ + \text{CO} \rightarrow \text{HCO}^+ + \text{N}_2$	...	8.80(-10)	0	0	...	...	...	...
$\text{HCO}^+ + \text{e}^- \rightarrow \text{CO} + \text{H}$	...	2.40(-7)	-0.69	0	...	...	...	...
$\text{N}_2\text{H}^+ + \text{e}^- \rightarrow \text{N}_2 + \text{H}$	...	2.77(-7)	-0.74	0	...	...	...	...
$\text{CO} \rightarrow \text{CO} \text{ (ice)}$	...	...	...	...	0.90	...	...	...
$\text{N}_2 \rightarrow \text{N}_2 \text{ (ice)}$	...	...	...	...	0.85	...	...	...
$\text{CO} \text{ (ice)} \rightarrow \text{CO}$	...	...	...	...	...	855	...	...
$\text{N}_2 \text{ (ice)} \rightarrow \text{N}_2$	...	...	...	...	...	800	...	...
$\text{CO} \text{ (ice)} + \text{h}\nu \rightarrow \text{CO}$	...	...	...	...	...	...	1.4(-3)	...
$\text{N}_2 \text{ (ice)} + \text{h}\nu \rightarrow \text{N}_2$	...	...	...	...	...	...	2.1(-3)	...
$\text{CO} + \text{h}\nu \rightarrow \text{C} + \text{O}$	...	...	...	...	...	...	...	4.4(-7)
$\text{N}_2 + \text{h}\nu \rightarrow 2 \text{ N}$	...	...	...	...	...	...	...	3.9(-7)

**Notes.** Equations for the reaction rate coefficients or reaction rates can be found in [Appendix 2.1](#). Photodesorption processes are shown in gray and are only considered in model CH-PD. For photodissociation the unshielded rates are listed. The notation a(-b) means  $a \times 10^{-b}$ . <sup>(a)</sup> Cosmic ray ionization rate taken from Cravens & Dalgarno (1978). <sup>(b)</sup> Values taken from the RATE12 release of the UMIST database for Astrochemistry (McElroy et al. 2013). <sup>(c)</sup> Lower limits for the sticking coefficients taken from Bisschop et al. (2006). <sup>(d)</sup> Binding energies for pure ices taken from Bisschop et al. (2006). <sup>(e)</sup> Photodesorption yields. For CO, the yield is taken from Paardekooper et al. (2016) for CO ice at 20 K. For  $\text{N}_2$ , the result from Bertin et al. (2013) for mixed ices with  $\text{CO}:\text{N}_2 = 1:1$  in protoplanetary disks is used. The yield for CO under these conditions is similar to the one reported by Paardekooper et al. (2016). <sup>(f)</sup> Unattenuated photodissociation rates for the adopted radiation field at a disk radius of 25 AU. Unshielded photodissociation rates for CO are taken from Visser et al. (2009a) and for  $\text{N}_2$  from Li et al. (2013) and Heays et al. (2014).

outer layers of the disk is necessary because depletion of the parent molecule, and a possible change in  $\text{N}_2/\text{CO}$  ratio, may affect the  $\text{N}_2\text{H}^+$  abundance. For CO and  $\text{N}_2$ , photodissociation occurs through line absorption, and shielding by  $\text{H}_2$  and self-shielding are important. For CO, photodissociation cross sections and shielding functions were taken from Visser et al. (2009a), and for  $\text{N}_2$  from Li et al. (2013) and Heays et al. (2014). For a given radiation field, both photodissociation rates are accurate to better than 20%, and the difference in unshielded rates ( $2.6 \times 10^{-10}$  versus  $1.7 \times 10^{-10} \text{ s}^{-1}$  in the general interstellar radiation field) turns out to be significant. We note that gas-phase formation of CO and  $\text{N}_2$  are ignored, such that the model predicts a steep cutoff in the gas-phase abundances in the disk atmosphere. However, this should not affect the freeze-out and desorption balance around the snow surfaces, as they are located deeper within in the disk.

The system of ordinary differential equations dictating the reduced chemistry, was solved using the python function `odeint`<sup>1</sup> up to a typical disk lifetime of  $10^6$  yr. As

<sup>1</sup>The function `odeint` is part of the SciPy package (<http://www.scipy.org/>) and uses `lsoda` from the FORTRAN library `odepack`.



**Table 2.2:** Overview of models and adopted parameters.

Model	$\chi^a$	$E_b(\text{CO})^b$ (K)	$E_b(\text{N}_2)^b$ (K)	$\zeta_{\text{CR}}^c$ ( $\text{s}^{-1}$ )	Photo- desorption
CH	0.2	855	800	$1.2 \times 10^{-17}$	-
CH-Eb1	0.2	1150	1000	$1.2 \times 10^{-17}$	-
CH-Eb2	0.2	1150	800	$1.2 \times 10^{-17}$	-
CH-CR1	0.2	855	800	$1.0 \times 10^{-19}$	-
CH-CR2	0.2	855	800	$5.0 \times 10^{-17}$	-
CH-PD	0.2	855	800	$1.2 \times 10^{-17}$	yes
CH- $\chi$ 0.8	0.8	855	800	$1.2 \times 10^{-17}$	-

**Notes.** <sup>(a)</sup> Large grain settling parameter. <sup>(b)</sup> Binding energy. <sup>(c)</sup> Cosmic ray ionization rate.

an initial condition, all CO and  $\text{N}_2$  is considered to be frozen out, while all other abundances (except  $\text{H}_2$ ) are set to zero. In **Sect. 2.3.2** the effect of CO and  $\text{N}_2$  abundances, and the  $\text{N}_2/\text{CO}$  ratio, is studied by varying the total, that is, gas plus ice, abundances between  $10^{-7}$  and  $10^{-4}$  (with respect to  $\text{H}_2$ ) such that the  $\text{N}_2/\text{CO}$  ratio ranges between 0.01 and 100. We will refer to these models as model “CH” (simple CHEMical network). The adopted parameters are listed in **Table 2.1**.

The temperature at which a molecule freezes out depends on the gas density and on the binding energy for each molecule,  $E_b$ . In the fiducial FD and CH models binding energies for pure ices are used. When in contact with water ice, the CO and  $\text{N}_2$  binding energies are higher. Recent results from Fayolle et al. (2016) show that, as long as the ice morphology and composition are equivalent for both CO and  $\text{N}_2$ , the ratio of the binding energies remains the same ( $\sim 0.9$ ). The effect of different binding energies will be studied in **Sect. 2.3.4** by adopting values of 1150 K and 1000 K (model CH-Eb1) and 1150 K and 800 K (model CH-Eb2), for CO and  $\text{N}_2$ , respectively. The former values are for both CO and  $\text{N}_2$  on a water ice surface (Garrod & Herbst 2006), that is, representing a scenario in which all ices evaporate during disk formation and then recondense. The latter model represents a situation in which CO is in contact with water ice, while  $\text{N}_2$  resides in a pure ice layer.

Another important parameter in the simple chemical model is the cosmic ray ionization rate, since it controls the  $\text{H}_3^+$  abundance, important for formation of  $\text{N}_2\text{H}^+$ . Based on modeling of  $\text{HCO}^+$  and  $\text{N}_2\text{H}^+$  line fluxes and spatially resolved emission, Cleeves et al. (2015) have suggested that the cosmic ray ionization rate in TW Hya is very low, of order  $10^{-19} \text{ s}^{-1}$ . The importance of the cosmic ray ionization rate is addressed in **Sect. 2.3.5** by adopting values of  $\zeta = 1 \times 10^{-19} \text{ s}^{-1}$  (CH-CR1) and  $\zeta = 5 \times 10^{-17} \text{ s}^{-1}$  (CH-CR2), as also used by Aikawa et al. (2015) in their study of  $\text{N}_2\text{H}^+$ .

An overview of all CH models is given in **Table 2.2**.

### 2.2.3 Line radiative transfer

Emission from the  $\text{N}_2\text{H}^+$   $J = 4 - 3$  (372 GHz),  $J = 3 - 2$  (279 GHz) and  $J = 1 - 0$  (93 GHz) transitions were simulated with the radiative transfer code LIME (LINE Modeling Engine, Brinch & Hogerheijde 2010) assuming a distance, inclination and position angle appropriate for TW Hya; 54 pc,  $6^\circ$  and  $155^\circ$ , respectively (Hughes et al.

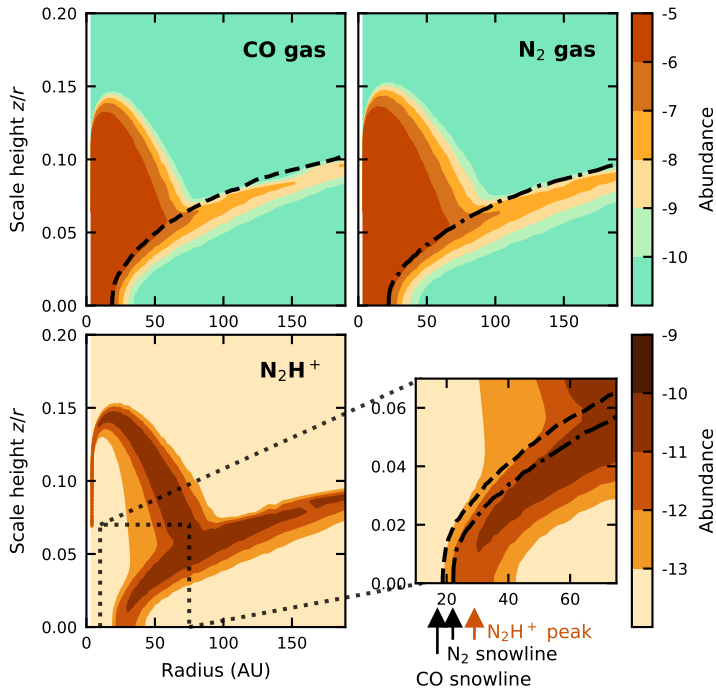


**Figure 2.3:** Distribution of CO gas,  $\text{N}_2$  gas and  $\text{N}_2\text{H}^+$  in the simple chemical model (model CH) with CO and  $\text{N}_2$  abundances of  $3 \times 10^{-6}$ . To focus on the region around the CO snow surface, the vertical scale is limited to a scale height  $z/r \leq 0.2$ . The *bottom right panel* highlights the region where  $\text{N}_2\text{H}^+$  is present near the disk midplane. The dashed and dash-dotted contours represent the CO and  $\text{N}_2$  snow surfaces, respectively, and the corresponding midplane snowlines are indicated by arrows below the horizontal axis of the *bottom right panel*. The midplane radius with the highest  $\text{N}_2\text{H}^+$  abundance is marked with an orange arrow.

2011; Andrews et al. 2012). These are the same values as adopted by Q13. The LIME grid was constructed such that the grid points lie within and just outside the region where the  $\text{N}_2\text{H}^+$  abundance  $> 1 \times 10^{-13}$ . In the disk region where  $\text{N}_2\text{H}^+$  is predicted, the gas density is larger than the  $J = 4 - 3$  critical density of  $\sim 8 \times 10^6 \text{ cm}^{-3}$  (see Fig. 2.1), so to reduce CPU time, models were run in LTE. The simulated images were convolved with a  $0.63'' \times 0.59''$  beam, similar to the reconstructed beam of Q13, and a  $0.2'' \times 0.2''$  beam to anticipate future higher spatial resolution observations. For the  $J = 4 - 3$  transition, the line profiles and the integrated line intensity profiles were compared to the observational data reduced by Q13.

## 2.3 Results

### 2.3.1 Distribution and emission of $\text{N}_2\text{H}^+$

Figure 2.3 shows the distribution of CO gas,  $\text{N}_2$  gas and  $\text{N}_2\text{H}^+$  as predicted by the simple chemical model (model CH). Abundance refers to fractional abundance with respect to  $\text{H}_2$  throughout this work. CO and  $\text{N}_2$  are frozen out in the disk midplane

and destroyed by UV photons higher up in the disk. The snow surface is defined as the position in the disk where the gas-phase and ice abundances become equal (see **Fig. 2.3**, left panels), and the snowline is the radius at which this happens in the midplane. For the physical structure and fiducial binding energies adopted, the CO snowline is then located at 19 AU which corresponds to a temperature for both the gas and dust of  $\sim 20$  K. This is smaller than the snowline location of 30 AU (corresponding to 17 K) as inferred by Q13, but in good agreement with recent results from Zhang et al. (2017) who directly detect the CO snowline around 17 AU using  $^{13}\text{C}^{18}\text{O}$  observations.

Although the  $\text{N}_2\text{H}^+$  abundance starts to increase at the midplane CO snowline, it peaks  $\sim 10$  AU further out (see **Fig. 2.3**, rightmost panel). It thus seems that the reduction in CO gas abundance at the snowline is not sufficient to allow  $\text{N}_2\text{H}^+$  to be abundant, but that an even higher level of depletion is required to favor  $\text{N}_2\text{H}^+$  formation over destruction. On the other hand, very low fractions of  $\text{N}_2$  in the gas phase are sufficient to allow  $\text{N}_2\text{H}^+$  formation, extending the  $\text{N}_2\text{H}^+$  layer beyond the  $\text{N}_2$  snow surface. In addition to the expected  $\text{N}_2\text{H}^+$  layer,  $\text{N}_2\text{H}^+$  is predicted to be abundant in a layer higher up in the disk where the  $\text{N}_2$  abundance in the gas phase exceeds that of CO due to a slightly lower photodissociation rate of  $\text{N}_2$  as compared with CO. The presence of  $\text{N}_2\text{H}^+$  in the surface layers is also seen in full chemical models (Walsh et al. 2010; Cleeves et al. 2014; Aikawa et al. 2015) and its importance is further discussed in **Sect. 2.3.3**.

The results from the simple chemical model thus deviate from the expectation that  $\text{N}_2\text{H}^+$  is most abundant in a layer directly outside the CO snowline, as can also be seen from the radial column density profiles in **Fig. 2.4** (top panel). When considering only freeze-out and desorption (model FD) and assuming a constant  $\text{N}_2\text{H}^+$  abundance of  $3 \times 10^{-10}$  between the CO snow surface and the 0.05% contour for  $\text{N}_2$  gas, the  $\text{N}_2\text{H}^+$  column density peaks only 2 AU outside the snowline. On the contrary, in model CH this peak is located 11 AU further out in the disk, at the snowline location derived by Q13. In addition, the column density profile for model CH is flatter due to the  $\text{N}_2\text{H}^+$  surface layer.

In order to determine whether this difference in  $\text{N}_2\text{H}^+$  distribution is large enough to cause different emission profiles, emission from the  $\text{N}_2\text{H}^+$   $J = 4-3$  (372 GHz) transition was simulated. Model FD fits the observed emission peak reasonably well for an  $\text{N}_2\text{H}^+$  abundance of  $3 \times 10^{-10}$ , although the simulated emission peak is located 7 AU closer to the star than observed. Variations in the assumed  $\text{N}_2\text{H}^+$  abundance only affect the intensity, but not the position of the peak. On the other hand, model CH can reproduce the position of the emission peak for a CO and  $\text{N}_2$  abundance of  $3 \times 10^{-6}$  (**Fig. 2.4**, middle panel). The underprediction of the emission in the outer disk is further discussed in **Sect. 2.3.8**. The difference between the models becomes more prominent at higher spatial resolution (**Fig. 2.4**, bottom panel). In that case, model FD predicts the emission peak 10 AU outside the snowline (instead of 17 AU), while this is 30 AU for model CH (instead of 24 AU) due to the flattened column density profile. An  $\text{N}_2\text{H}^+$  column density peaking at 30 AU, 11 AU outside the snowline, can thus reproduce the observed emission peak, which is in agreement with Q13, unlike a column density profile peaking directly at the CO snowline. However, this is only the case for a low CO and  $\text{N}_2$  abundance of  $3 \times 10^{-6}$ , as discussed further below.

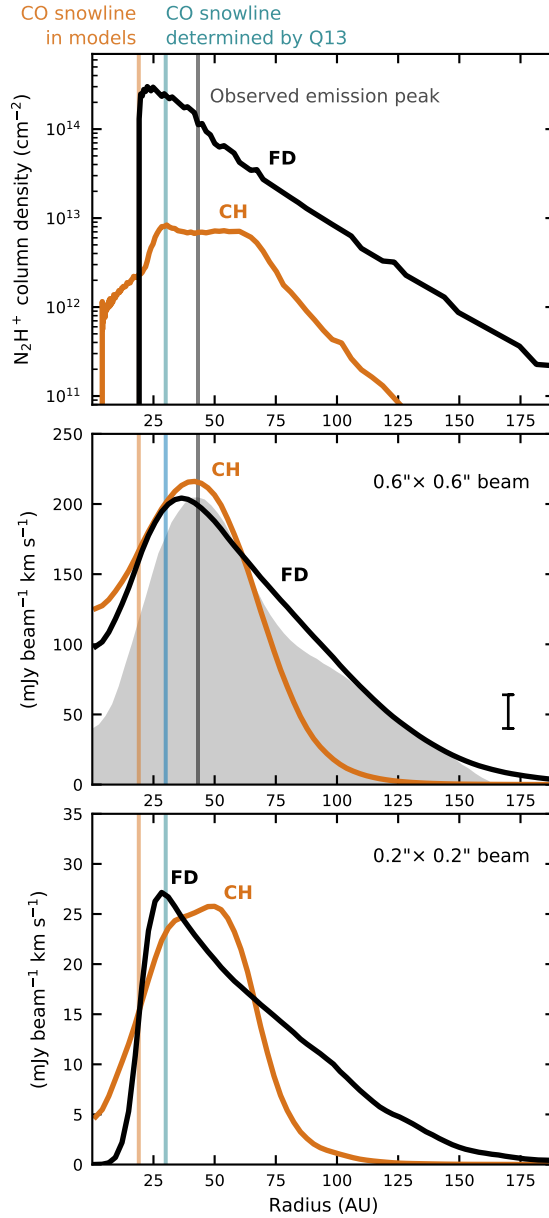


**Figure 2.4:**  $N_2H^+$  column density profile (*top panel*) and simulated  $J = 4-3$  line emission (*middle and bottom panel*) for the  $N_2H^+$  distributions predicted by the simple chemical model with CO and  $N_2$  abundances of  $3 \times 10^{-6}$  (model CH; red lines) and a model incorporating only freeze-out and desorption (model FD; black lines). Integrated line intensity profiles are shown after convolution with a  $0.63'' \times 0.59''$  beam (*middle panel*) or a  $0.2'' \times 0.2''$  beam (*bottom panel*). Observations by Q13 are shown in gray in the middle panel with the  $3\sigma$ -error depicted in the lower right corner. The vertical gray line marks the position of the observed emission peak. The vertical blue line indicates the position of the midplane CO snowline inferred from these observations by Q13, while the orange line indicates the location of the midplane CO snowline in the models.

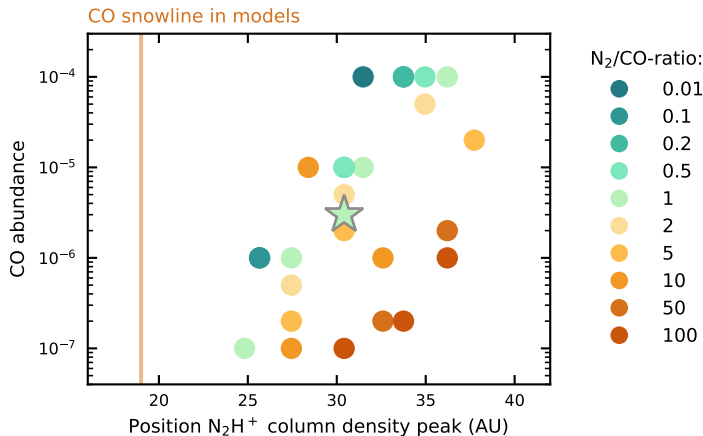


**Figure 2.5:** Position of the  $\text{N}_2\text{H}^+$  column density peak in model CH for different CO and  $\text{N}_2$  abundances. The best-fit model with abundances of  $3 \times 10^{-6}$ , as shown in **Fig. 2.3**, is indicated by a star and the color of the symbols represents the value of the  $\text{N}_2/\text{CO}$  ratio. The vertical orange line marks the location of the CO snowline in the models.

### 2.3.2 Influence of CO and $\text{N}_2$ abundances

To examine whether the exact amount of CO present in the gas phase is more important for the  $\text{N}_2\text{H}^+$  distribution than the location of the CO snowline, as suggested above, the total CO and  $\text{N}_2$  abundances in the simple chemical network were varied. Changing the CO abundance does not influence the  $\text{N}_2\text{H}^+$  distribution via temperature changes since the gas and dust are coupled in the region where  $\text{N}_2\text{H}^+$  is present (see **Sect. 2.2.1** and **Fig. 2.1**). Furthermore, recall that the location of the midplane CO snowline does not depend on abundance and thus remains at 19 AU for all models which adopt the fiducial binding energy. The position of the  $\text{N}_2\text{H}^+$  column density peak, however, turns out to move further away from the snowline with increasing CO abundance (**Fig. 2.5**). This reinforces the idea that the gas-phase CO abundance remains too high for  $\text{N}_2\text{H}^+$  to be abundant after the 50% depletion at the snowline. Instead,  $\text{N}_2\text{H}^+$  peaks once the amount of CO in the gas phase drops below a certain threshold, which is reached further away from the snowline for higher CO abundances. This is in agreement with the conclusions from Aikawa et al. (2015).

Moreover, the position of the column density peak depends also on the  $\text{N}_2$  abundance. For a fixed CO abundance, the position of the maximum  $\text{N}_2\text{H}^+$  column density shifts outward with increasing  $\text{N}_2$  abundance, since the amount of gas-phase  $\text{N}_2$  remains high enough for efficient  $\text{N}_2\text{H}^+$  formation at larger radii. The  $\text{N}_2\text{H}^+$  distribution thus strongly depends on the amount of both CO and  $\text{N}_2$  present in the gas phase, with the column density peaking 6–18 AU outside the CO snowline for different abundances.

### 2.3.3 Importance of the $\text{N}_2\text{H}^+$ surface layer

Besides the expected  $\text{N}_2\text{H}^+$  layer outside the CO snow surface, model CH also predicts a layer higher up in the disk where  $\text{N}_2\text{H}^+$  is abundant as a result of a slightly lower  $\text{N}_2$  photodissociation rate compared with CO. Since both molecules can self-shield, the

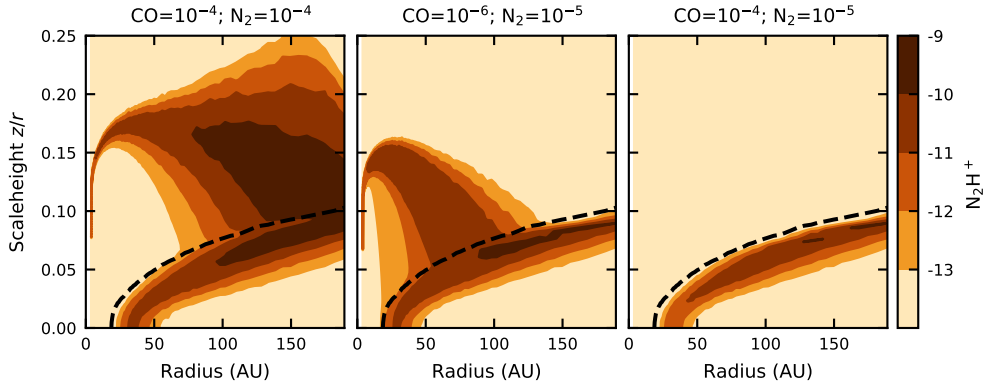


**Figure 2.6:** Distribution of  $\text{N}_2\text{H}^+$  in the simple chemical model (model CH) for different  $\text{N}_2$  and CO abundances as listed above the panels. To focus on the region around the CO snow surface, the vertical scale is limited to a scale height  $z/r \leq 0.25$ . The dashed contour represents the CO snow surface.

photodissociation rates depend on molecular abundances. Therefore, the CO and  $\text{N}_2$  abundances influence the shape of the  $\text{N}_2\text{H}^+$  surface layer as shown in **Fig. 2.6**. When  $\text{N}_2$  is equally or more abundant than CO,  $\text{N}_2\text{H}^+$  can survive in the region where CO is photodissociated but  $\text{N}_2$  is still present. The higher the abundances, the closer to the disk surface a sufficiently high column density is reached for efficient self-shielding and the more extended is the  $\text{N}_2\text{H}^+$  surface layer (**Fig. 2.6**, left panel). The inner boundary of the surface layer is set where CO photodissociation ceases to be effective. For lower CO and  $\text{N}_2$  abundances, photodissociative photons can penetrate deeper into the disk, and the  $\text{N}_2\text{H}^+$  surface layer is located closer to the star (**Fig. 2.6**, middle panel). The layer does not extend to the disk outer radius any longer because most  $\text{N}_2$  is now photodissociated in the outer regions. Finally, when CO is more abundant than  $\text{N}_2$ , the surface layer decreases, until for  $\text{N}_2/\text{CO} \lesssim 0.2$  CO becomes abundant enough everywhere above the snow surface to shift the balance towards  $\text{N}_2\text{H}^+$  destruction (**Fig. 2.6**, right panel).

To address the influence of the  $\text{N}_2\text{H}^+$  surface layer,  $J = 4 - 3$  lines were simulated for model CH with different CO and  $\text{N}_2$  abundances with the CO snow surface set as an upper boundary. In other words, no  $\text{N}_2\text{H}^+$  is present above the CO snow surface in these “snow surface only” models. Removing the  $\text{N}_2\text{H}^+$  surface layer hardly affects the position of the column density peak (**Fig. 2.7**, top left panel), suggesting that the offset between  $\text{N}_2\text{H}^+$  and CO snowline is not caused by the surface layer but rather is a robust chemical effect. The emission, however, is strongly influenced by the surface layer (**Fig. 2.8**, top left panel). In the full CH models, the emission peak is shifted away from the snowline for higher CO abundances by up to  $\sim 50$  AU, while in the snow surface only models, the emission traces the column density peak with an offset related to the beam size. Only for CO abundances  $\sim 10^{-6}$  or  $\text{N}_2/\text{CO}$  ratios  $\lesssim 1$  does the emission trace the column density in the full models, and only for even lower CO abundances ( $\sim 10^{-7}$ ) does the emission peak at the snowline. In addition to the  $\text{N}_2\text{H}^+$  column density offset, the relation between CO snowline and  $\text{N}_2\text{H}^+$  emission is thus weakened even more in models with  $\text{N}_2/\text{CO} \gtrsim 0.2$  due to the presence of an  $\text{N}_2\text{H}^+$  surface layer that causes the emission to shift outward.

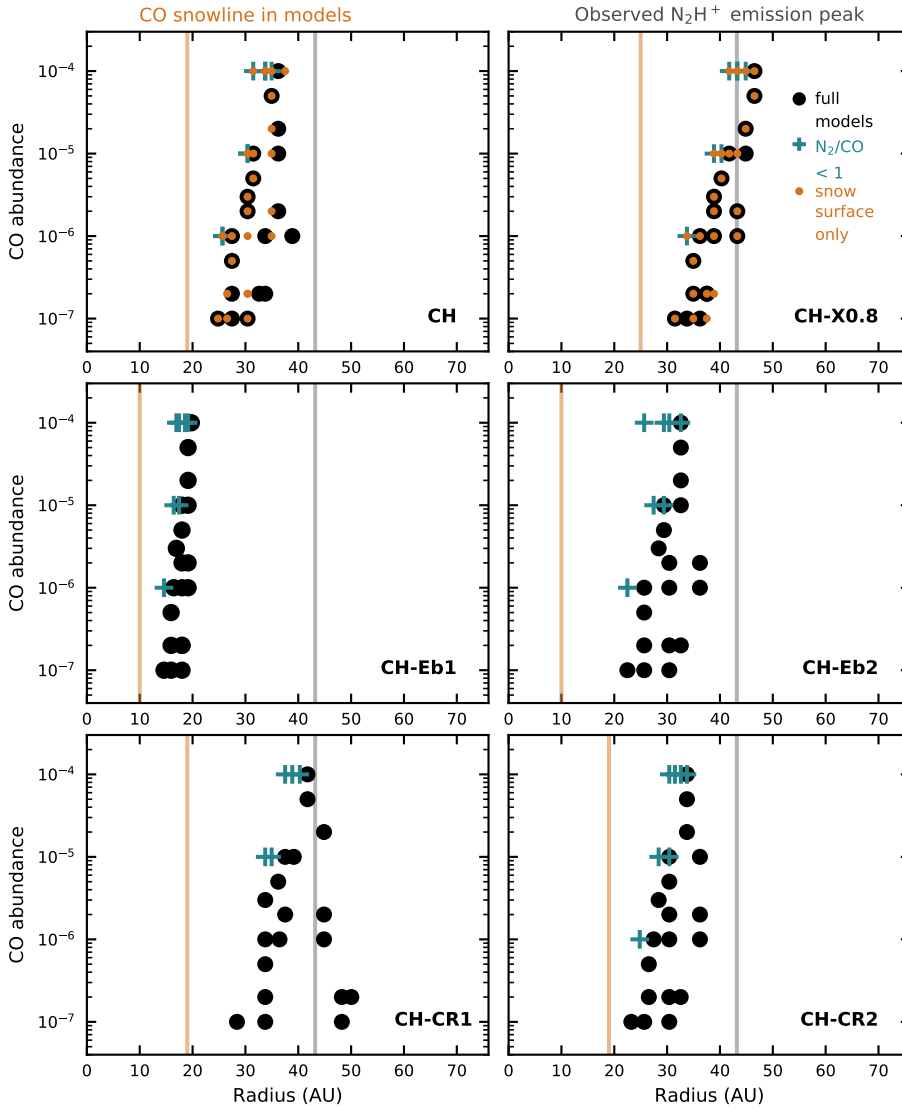


**Figure 2.7:** Position of the  $N_2H^+$  column density peak in the different models (listed in the lower right corner of each panel) for different CO and  $N_2$  abundances. From *left to right* and *top to bottom*: the fiducial models (CH), models with large grains settled to only 80% of small grain scale height (CH- $\chi$ 0.8), models with both CO and  $N_2$  binding energies increased (CH-Eb1), models with only CO binding energy increased (CH-Eb2), models with a lower cosmic ray ionization rate ( $1 \times 10^{-19} \text{ s}^{-1}$ ; CH-CR1) and models with a higher cosmic ray ionization rate ( $5 \times 10^{-17} \text{ s}^{-1}$ ; CH-CR2). Models with  $N_2/CO$  ratios  $< 1$  are highlighted with blue plus signs. Orange circles in the *top panels* represent the snow surface only models, i.e.,  $N_2H^+$  removed above the CO snow surface. The orange lines mark the location of the CO snowline in the models. The gray line indicates the position of the observed emission peak.

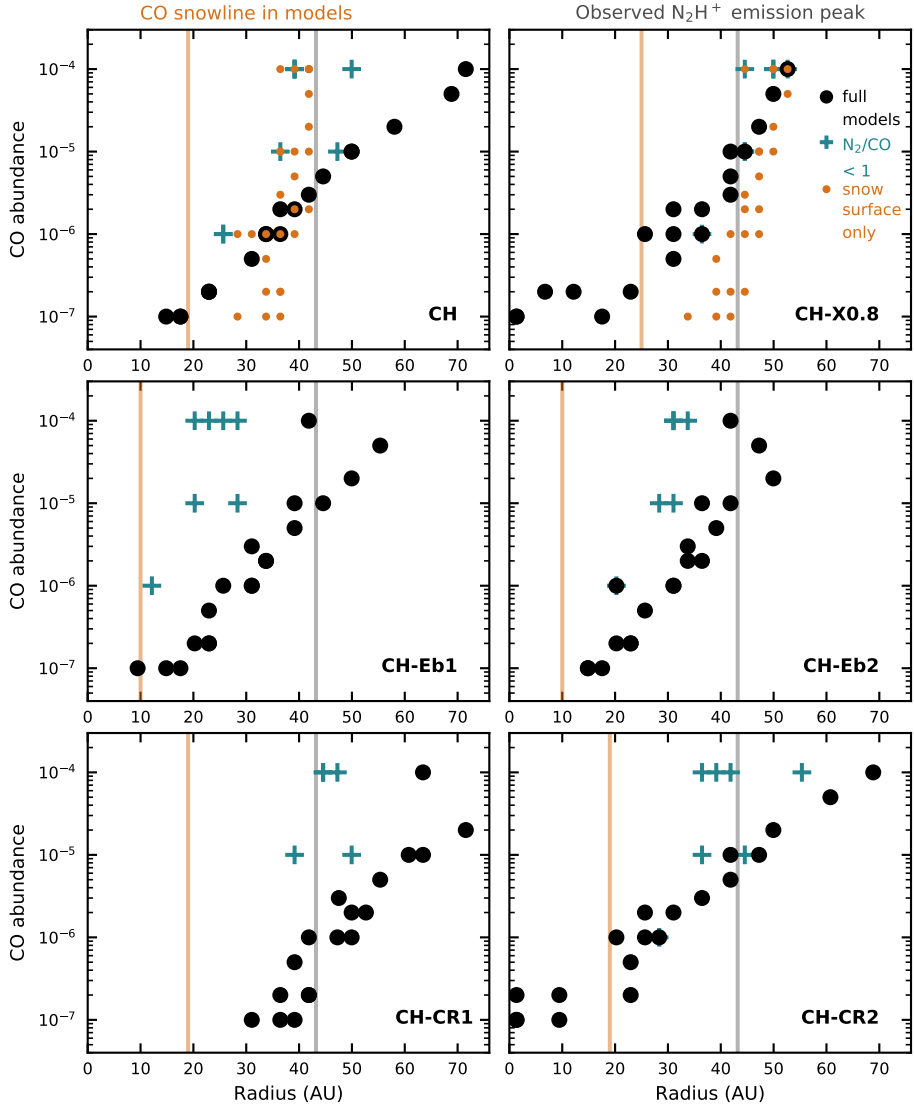


**Figure 2.8:** As Fig. 2.7, but for the position of the simulated  $\text{N}_2\text{H}^+$   $J = 4 - 3$  emission peak after convolution with a  $0.63'' \times 0.59''$  beam.

Furthermore, the  $\text{N}_2\text{H}^+$  surface layer contributes significantly to the peak integrated intensity. This intensity shows a linear correlation with the  $\text{N}_2/\text{CO}$  ratio, but the difference of  $\sim 600 \text{ mJy beam}^{-1} \text{ km s}^{-1}$  (for the  $0.63'' \times 0.59''$  beam) between models with a  $\text{N}_2/\text{CO}$  ratio of 0.01 and 100 reduces to only  $\sim 100 \text{ mJy beam}^{-1} \text{ km s}^{-1}$  in the snow surface only models (see Fig. 2.B.1). For the TW Hya physical model adopted, a surface layer of  $\text{N}_2\text{H}^+$ , in addition to the midplane layer outside the CO snow surface, seems necessary to reproduce the observed integrated peak intensity. This is in agreement with Nomura et al. (2016), who suggest that the  $\text{N}_2\text{H}^+$  emission in TW Hya originates in the disk surface layer based on the brightness temperature.



### 2.3.4 Influence of CO and N<sub>2</sub> binding energies

The location of the CO snowline depends on the CO binding energy. To address whether the offset between N<sub>2</sub>H<sup>+</sup> and CO snowline is a result of the adopted binding energies, models were run with a higher CO binding energy (1150 K), that is, assuming CO on a water ice surface (model CH-Eb2). As the amount of N<sub>2</sub> also influences the N<sub>2</sub>H<sup>+</sup> distribution, models were run with a higher binding energy for both CO and N<sub>2</sub> (1150 and 1100 K, respectively) as well (model CH-Eb1). The position of the N<sub>2</sub>H<sup>+</sup> column density and emission peak for different CO and N<sub>2</sub> abundances are shown in the middle panels of **Figs. 2.7** and **2.8**, respectively. When the binding energy is increased for both species (model CH-Eb1), the results are similar to before. The N<sub>2</sub>H<sup>+</sup> column density peaks 5–9 AU outside the CO snowline, and the emission peak shifts to even larger radii with increasing CO abundance when an N<sub>2</sub>H<sup>+</sup> surface layer is present (black circles in **Fig. 2.8**). Increasing only the CO binding energy, that is, shifting the CO snowline inward but not affecting the N<sub>2</sub> snowline (model CH-Eb2), results in the N<sub>2</sub>H<sup>+</sup> column density to peak 12–26 AU from the CO snowline. The emission peaks, however, stay roughly at the same radii for both models, thus better tracing the column density maximum when the CO and N<sub>2</sub> snowlines are further apart. The peak integrated intensities are similar for all three sets of binding energies.

The N<sub>2</sub>H<sup>+</sup> column density thus peaks outside the CO snowline for all binding energies tested, and the offset is largest when the CO and N<sub>2</sub> snowline are furthest apart. The offset between snowline and emission peak is roughly independent of the binding energies, except for CO abundances of  $\sim 10^{-4}$ . Therefore, a degeneracy exists between the peak position of the emission and the column density.

### 2.3.5 Influence of the cosmic ray ionization rate

The cosmic ray ionization rate controls the H<sub>3</sub><sup>+</sup> abundance, and may therefore have an effect on the N<sub>2</sub>H<sup>+</sup> distribution. To address the importance of the cosmic ray ionization rate, model CH was run with  $\zeta = 5 \times 10^{-17} \text{ s}^{-1}$  (CH-CR2), as also used by Aikawa et al. (2015) in their study of N<sub>2</sub>H<sup>+</sup>, and  $\zeta = 1 \times 10^{-19} \text{ s}^{-1}$  (CH-CR1), as suggested by Cleaves et al. (2015). The results for the N<sub>2</sub>H<sup>+</sup> column density and  $J = 4 - 3$  emission are presented in **Figs. 2.7** and **2.8**, respectively (bottom panels). The trends seen for the position of the column density and emission peak are roughly the same as for the fiducial models with  $\zeta = 1.2 \times 10^{-17} \text{ s}^{-1}$ , although both offsets are  $\sim 10$  AU larger for the lowest cosmic ray ionization rate. The very small radius at which the emission peaks for model CH-CR2 with a CO abundance of  $\sim 10^{-7}$  is due to a combination of a higher N<sub>2</sub>H<sup>+</sup> abundance in the inner few tens of AU as compared to models with higher CO abundance and a 0.6'' ( $\sim 32$  AU) beam. The strongest effect of the cosmic ray ionization rate is on the strength of the peak integrated intensity. Models CH-CR2 predict a higher peak integrated intensity than observed, while N<sub>2</sub> needs to be more than two orders of magnitude more abundant than CO to be consistent with the low cosmic ray ionization rate of  $10^{-19} \text{ s}^{-1}$  in models CH-CR1 (see **Fig. 2.B.2**).

The cosmic ray ionization rate thus influences the distribution of N<sub>2</sub>H<sup>+</sup> with respect to the snowline, with the column density peaking closest to the snowline for the highest values of  $\zeta$  and the lowest CO abundances. However, the smallest offset remains 4 AU.

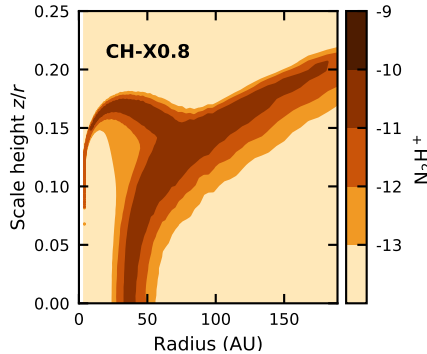


**Figure 2.9:**  $\text{N}_2\text{H}^+$  distribution predicted by the simple chemical model for a physical structure with the large grains settled to only 80% of the small grain scale height (model CH- $\chi$ 0.8). Abundances of  $3 \times 10^{-6}$  are adopted for both CO and  $\text{N}_2$ .

### 2.3.6 Influence of grain settling

In the physical model adopted so far, the large grains have settled toward the disk midplane. The distribution of the dust is important because it affects the UV penetration and the disk thermal structure, which is determined by the processing of UV radiation by the dust particles. Since the location of the CO snow surface is temperature dependent, grain settling may indirectly influence the location of the CO snowline. To examine whether this also influences the relation between  $\text{N}_2\text{H}^+$  and the snowline, a physical model in which the large grains have only settled to 80% of the small grain scale height is used. The  $\text{N}_2\text{H}^+$  distribution predicted by the simple chemical model for CO and  $\text{N}_2$  abundances of  $3 \times 10^{-6}$  is presented in Fig. 2.9. The CO snow surface is now located higher up in the disk as a consequence of the shallower temperature gradient near the midplane. In other words, the temperature stays below the CO freeze-out temperature at larger scale heights. The resulting increase in the  $\text{N}_2\text{H}^+$  column just outside the snowline in combination with the smaller  $\text{N}_2\text{H}^+$  surface layer, reduces the contribution of this layer. This is for instance reflected in the peak integrated intensity; the difference between full models and snow surface only models is now only a factor of approximately two instead approximately five.

Figures 2.7 and 2.8 (top right panels) show what this means for the positions of the  $\text{N}_2\text{H}^+$  column density and emission peaks. Due to the different temperature structure, the CO snowline is located at 25 AU, but the  $\text{N}_2\text{H}^+$  column density still peaks 6–22 AU further out. However, the offset between column density and emission peak is now different. The emission does trace the column density for CO abundances higher than  $\sim 5 \times 10^{-6}$ , while for lower abundances the emission peaks at smaller radii than the column density. Again, when the surface layer is removed, the emission roughly traces the column density for all CO and  $\text{N}_2$  abundances.

Thus, the  $\text{N}_2\text{H}^+$  emission seems not only sensitive to the chemical conditions, but also the physical conditions in the disk and the UV penetration. Depending on the degree of grain settling the emission traces the column density for different CO abundances, although the  $\text{N}_2\text{H}^+$  column density peaks outside the CO snowline in all models.

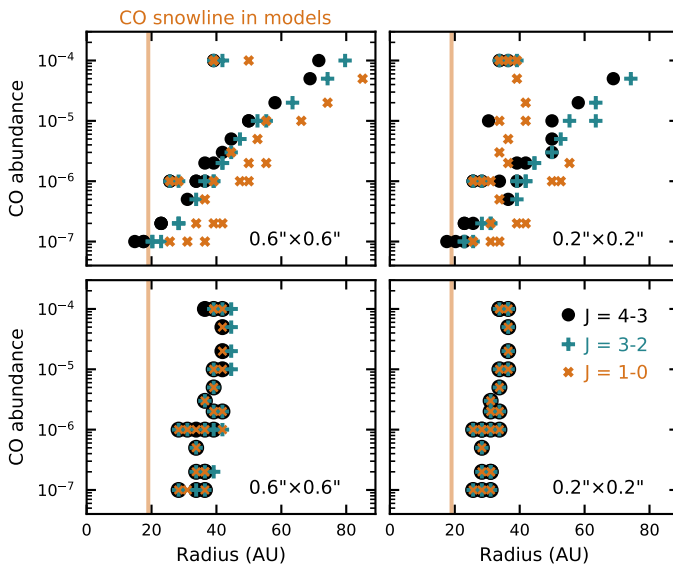


**Figure 2.10:** Position of the  $\text{N}_2\text{H}^+$   $J = 4 - 3$  (black circles),  $J = 3 - 2$  (blue plus signs) and  $J = 1 - 0$  (orange crosses) emission peaks for different CO and  $\text{N}_2$  abundances in the simple chemical model (model CH) (*top panels*) and the corresponding snow surface only models, i.e.,  $\text{N}_2\text{H}^+$  removed above the CO snow surface (*bottom panels*). The emission is convolved with a  $0.63'' \times 0.59''$  beam (*left panels*) or  $0.2'' \times 0.2''$  beam (*right panels*). The orange lines mark the location of the CO snowline in the models.

### 2.3.7 Constraints provided by multiple $\text{N}_2\text{H}^+$ transitions

For  $\text{N}_2/\text{CO}$  ratios larger than  $\sim 0.2$ , the simple chemical network predicts that  $\text{N}_2\text{H}^+$  is also abundant in a surface layer above the CO snow surface. The presence of this surface layer significantly influences the  $\text{N}_2\text{H}^+$   $J = 4 - 3$  emission and complicates the relationship between  $\text{N}_2\text{H}^+$  and the CO snowline. To assess whether a different  $\text{N}_2\text{H}^+$  transition would be better suited to trace the CO snowline, emission was simulated for the  $J = 3 - 2$  (279 GHz) and  $J = 1 - 0$  (93 GHz) transitions for models CH and CH- $\chi 0.8$ . The results for the position of the  $\text{N}_2\text{H}^+$  emission peaks in model CH are shown in **Fig. 2.10**. For the full models with  $\text{N}_2/\text{CO} > 0.2$ , the emission peak shifts outward with decreasing transition frequency (**Fig. 2.10**, top panels), while all transitions peak at a similar radius for the models where the  $\text{N}_2\text{H}^+$  surface layer has been removed (**Fig. 2.10**, bottom panels) or is not present. When the emission is convolved with a  $0.2'' \times 0.2''$  beam, the  $J = 1 - 0$  transition peaks in some models at smaller radii than the other transitions. That is because in these cases the structure caused by the surface layer can be resolved, revealing two components that are smeared into one broad feature by the  $0.63'' \times 0.59''$  beam. Similar results are obtained for model CH- $\chi 0.8$  (not shown). Observing multiple transitions thus seems to provide a good indication whether or not a surface layer of  $\text{N}_2\text{H}^+$  is contributes to the emission, and thus how well the emission traces the column density.

Although comparison of the emission-peak positions for different transitions may indicate the contribution of an  $\text{N}_2\text{H}^+$  surface layer, no information is provided on how far the emission peak is then offset from the column density peak or actual CO

**Table 2.3:** Offset between the CO snowline and the  $\text{N}_2\text{H}^+$  column density and  $J = 4 - 3$  emission peak in the different models.

Model	Offset	Offset $J = 4 - 3$ emission	
	column density (AU)	$0.63'' \times 0.59''$ (AU)	$0.2'' \times 0.2''$ (AU)
CH	6–18	4–53 *	2–50 *
CH-Eb1	5–10	2–45 *	8–43
CH-Eb2	13–26	5–40	8–35
CH-CR1	10–31	12–53	12–55
CH-CR2	4–17	2–50 *	2–53 *
CH- $\chi$ 0.8	6–2	1–28 *	4–22 *

**Notes.** The CO snowline is located at 19 AU in models CH, CH-CR1 and CH-CR2, at 10 AU in models CH-Eb1 and CH-Eb2, and at 25 AU in models CH- $\chi$ 0.8. A value of “0” means coincidence with the CO snowline in the respective model. An asterisk (\*) indicates models for which the emission peaks inside the snowline for CO abundances  $\leq 2 \times 10^{-7}$ .

snowline. To examine whether  $\text{N}_2\text{H}^+$  line ratios may contribute to addressing this problem, the  $J = 4 - 3/J = 3 - 2$  and  $J = 4 - 3/J = 1 - 0$  ratios are calculated. Results for model CH and model CH- $\chi$ 0.8 with three different CO and  $\text{N}_2$  abundances (as shown in Fig. 2.6) are presented in Fig. 2.C.1. When the  $\text{N}_2\text{H}^+$  surface layer is removed or not present at all, both line ratios are nearly constant throughout the disk at  $J = 4 - 3/J = 3 - 2 \approx 1.2$  and  $J = 4 - 3/J = 1 - 0 \approx 20$ . Only at  $0.2''$  resolution does the  $J = 4 - 3/J = 1 - 0$  ratio increase in the inner  $\sim 30$  AU. In the fiducial model with the large grains settled to 20% of the small grain scale height, both line ratios can distinguish between differently shaped  $\text{N}_2\text{H}^+$  surface layers. The line ratios become more steep when the surface layer extends to about half the disk radius and increase in value for a surface layer extending to the disk outer radius. In model CH- $\chi$ 0.8, the surface layer contributes less to the emission and although the line ratios show an increase at around 40 AU when the surface layer is present, distinguishing differently shaped surface layers is not possible.  $\text{N}_2\text{H}^+$  line ratios are thus sensitive to the distribution of  $\text{N}_2\text{H}^+$ , and together with the position of the different emission peaks, can provide modeling constraints and aid in constraining the location of the CO snowline.

### 2.3.8 Outer edge of $\text{N}_2\text{H}^+$ emission

So far, we have focused on the peak of the  $\text{N}_2\text{H}^+$  emission and its relation to the CO snowline. The simple chemical model (model CH) produces a good fit to the emission peak, but underestimates the emission coming from the outer disk (further out than  $\sim 60$  AU). In this region, the density may have become low enough for UV radiation to penetrate the midplane and photodesorption to become effective. To address whether this can account for the observed emission, photodesorption is included in model CH-PD (see Fig. 2.D.1). Although  $\text{N}_2\text{H}^+$  is now present in the midplane at radii larger than  $\sim 60$  AU and this results in an increase in the column density at these radii, the  $\sim 10$  mJy beam $^{-1}$  km s $^{-1}$  gain in emission is not enough to explain the observations. Increasing the photodesorption rates by two orders of magnitude does not yield an higher intensity, so photodesorption alone can not explain the  $\text{N}_2\text{H}^+$  emission

originating in the outer disk.

Interestingly, the radius at which model and observations start to deviate ( $\sim 60$  AU) is equal to the radial extent of the millimeter grains (see e.g., Andrews et al. 2012). The absence of large grains in the outer disk, not accounted for in our model, may influence the temperature structure, such that thermal desorption becomes effective, as shown for CO by Cleeves (2016). An increase in CO and N<sub>2</sub> desorption may then cause an increase in N<sub>2</sub>H<sup>+</sup> in the disk outer region.

Photodissociation turns out to be an important process in N<sub>2</sub>H<sup>+</sup> chemistry, so a logical question to ask is whether N<sub>2</sub> photodissociation is responsible for the outer edge of the N<sub>2</sub>H<sup>+</sup> emission. N<sub>2</sub> self-shielding is not effective until the N<sub>2</sub> column density becomes  $\gtrsim 10^{15}$  cm<sup>-2</sup> (Li et al. 2013), so although the N<sub>2</sub>H<sup>+</sup> layer below the CO snow surface extends over the entire disk in most models (see **Fig. 2.6**), the N<sub>2</sub>H<sup>+</sup> abundance outside  $\sim 100$  AU is two orders of magnitude lower for N<sub>2</sub> abundances  $\lesssim 10^{-6}$ . However, despite an N<sub>2</sub>H<sup>+</sup> layer throughout the entire disk for N<sub>2</sub>  $> 10^{-6}$ , the outer radius of the emission coincides with the outer boundary of the N<sub>2</sub>H<sup>+</sup> surface layer, which is set by N<sub>2</sub> photodissociation. Only for N<sub>2</sub> abundances as high as  $10^{-4}$  does the N<sub>2</sub>H<sup>+</sup> emission extend over the entire disk. For lower abundances is the emission thus truncated due to N<sub>2</sub> photodissociation at the outer edge in this particular model.

## 2.4 Discussion

To study the robustness of N<sub>2</sub>H<sup>+</sup> as tracer of the CO snowline, we model the N<sub>2</sub>H<sup>+</sup> distribution for the disk around TW Hya using a simple chemical model and simulate the resulting emission with the radiative transfer code LIME. The N<sub>2</sub>H<sup>+</sup> column density peaks  $\sim 5$ – $30$  AU outside of the CO snowline, for all physical and chemical conditions tested. Furthermore, the N<sub>2</sub>H<sup>+</sup> emission peaks generally not at the same radius as the column density, and can be up to 53 AU offset from the CO snowline. Only for very low total (gas plus ice) CO abundances ( $\sim 10^{-7}$ ) can the emission peak inside the snowline, although the column density does not. Results for the different models are summarized in **Table 2.3**. Fitting the N<sub>2</sub>H<sup>+</sup> column density using a power law with the inner radius assumed to be at the CO snowline can thus generally only produce an outer boundary to the snowline location.

Triggered by the question on how N<sub>2</sub>H<sup>+</sup> can be abundant in protoplanetary disks in spite of very similar freeze-out temperatures for CO and N<sub>2</sub>, Aikawa et al. (2015) performed a chemical model study of the N<sub>2</sub>H<sup>+</sup> distribution. They attributed its presence to the conversion of CO to less volatile species. However, the models presented in this work predict an N<sub>2</sub>H<sup>+</sup> layer even for canonical CO abundances of  $\sim 10^{-4}$ . Nonetheless, the conclusions that the absolute abundances of CO and N<sub>2</sub> are important and the N<sub>2</sub>H<sup>+</sup> abundance can peak at a temperature below the CO and N<sub>2</sub> freeze-out temperature are reinforced by our models for many different CO and N<sub>2</sub> abundances. Results on the effect of the CO and N<sub>2</sub> binding energies and cosmic ray ionization rate are also in good agreement.

Aikawa et al. (2015) also report the presence of N<sub>2</sub>H<sup>+</sup> in layers higher up in the disk in their full chemical model (in line with Walsh et al. 2010 and Cleeves et al. 2014), but they do not perform a radiative transfer calculation to explore whether this contributes significantly to the resulting emission. Here we show that the discrepancy between column density and emission maxima is caused by such a surface layer that

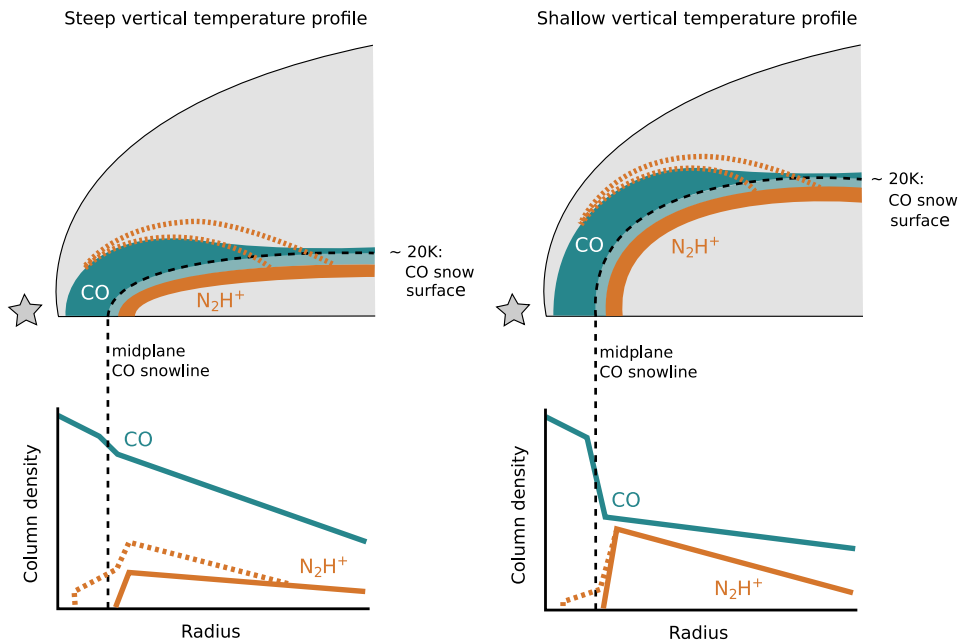


**Figure 2.11:** Schematic representation of the distribution of gas-phase CO (blue) and  $\text{N}_2\text{H}^+$  (orange) in disks with either a steep vertical temperature profile, as for TW Hya (*left panels*), or a shallow vertical temperature profile (*right panels*). These differences can be due to different degrees of grain settling. To highlight the region around the CO snowline, the vertical direction depicts scale height,  $z/r$ . The dashed black contour represents the CO snow surface and the light blue area directly outside this contour shows that, at the snow surface, the gas phase abundance drops by 50%. The  $\text{N}_2\text{H}^+$  surface layer is indicated by dotted orange lines. The predicted column density profiles are shown below. For  $\text{N}_2\text{H}^+$ , the column density profile is shown with (dotted line) and without (solid line) the surface layer. The vertical dashed black line indicates the location of the midplane CO snowline.

is present in models with CO less than approximately five times as abundant as  $\text{N}_2$ , due to a small difference in the CO and  $\text{N}_2$  photodissociation rates. Although CO is more than an order of magnitude more abundant than  $\text{N}_2$  in the ISM, CO can be underabundant in the gas-phase in protoplanetary disks. This underabundance used to be attributed to photodissociation and freeze-out (Dutrey et al. 1997; van Zadelhoff et al. 2001), but recent studies concerning in particular TW Hya, suggest that on top of these well-known processes, CO is also depleted in the warm molecular layer and indeed inside the snowline (Favre et al. 2013; Nomura et al. 2016; Schwarz et al. 2016). Moreover, observations of [C I] lines indicate a general carbon depletion in this disk (Kama et al. 2016). The results presented here show that  $\text{N}_2\text{H}^+$  is very sensitive to the gas-phase CO abundance, and the best fit to the observed emission is acquired for a total CO abundance of  $3 \times 10^{-6}$ , consistent with the CO depletion scenario. To achieve such a low CO gas-phase abundance in the models, a low total CO abundance is required, as the amount of CO present in the gas phase depends on the available ice reservoir. This suggests that CO frozen out in the outer disk may be trapped in the ice or converted to more complex species. Other possibilities are that it has been locked up due to grain growth on the way to the inner disk or locked up in even

larger bodies like planetesimals. The overprediction of  $\text{N}_2\text{H}^+$  emission inside the CO snowline as compared to the observations may indicate that some of the CO is trapped in other ices with higher binding energies, such as  $\text{CO}_2$  and  $\text{H}_2\text{O}$ , since this will allow gradual release of additional CO when these species desorb off the grains at higher temperatures.

The contribution of the surface layer to the total  $\text{N}_2\text{H}^+$  emission seems to depend on the disk physical structure. In the TW Hya model, the high degree of dust settling results in a steep vertical temperature gradient. This confines the CO snow surface, and hence the associated  $\text{N}_2\text{H}^+$  layer, close to the midplane. For a less settled disk, the vertical temperature gradient is shallower and the  $\text{N}_2\text{H}^+$  layer resides higher up in the disk. The  $\text{N}_2\text{H}^+$  column density just outside the CO snowline is much higher in the latter case and therefore the contribution from the  $\text{N}_2\text{H}^+$  surface layer is significantly lower. This is further aided by the lower gas density in the surface layer due to its increased scale height (see **Fig. 2.11**). For CO abundances  $\gtrsim 10^{-6}$  the  $\text{N}_2\text{H}^+$  emission then traces the column density, while the emission is shifted to larger radii in models with substantial grain settling.

Differences in disk vertical structure may also help explain why the CO snowline can be observed directly with CO isotopologues in some disks, but not in others. The higher up in the disk the CO snow surface resides, the larger the CO column density decrease across the snowline, simply because the CO-depleted region extends to larger heights (see **Fig. 2.11**). This may explain why in TW Hya no sharp drop in CO column density is seen around the snowline, on top of the global CO depletion (Nomura et al. 2016; Schwarz et al. 2016). The rise in column density inward of 10 AU may be the result of release of trapped CO at the  $\text{CO}_2$  and  $\text{H}_2\text{O}$  snowlines. On the other hand, in HD 163296, both  $\text{C}^{18}\text{O}$  and  $\text{N}_2\text{H}^+$  emission can be reproduced by a sharp change in column density at roughly the same radius (Qi et al. 2015). The fitted CO freeze-out temperature occurs, for the physical model adopted for HD 163296 by these authors, at a radius of 85–90 AU, while the  $\text{N}_2\text{H}^+$  emission can be reproduced by a column density profile with inner radius between 84 and 98 AU. These results are consistent with the results shown here that the  $\text{N}_2\text{H}^+$  distribution peaks outside the CO snowline. The better agreement between CO and  $\text{N}_2\text{H}^+$  emission could mean that the CO snow surface is located higher up in the disk. As the HD 163296 disk is inclined with respect to the line of sight, (e.g., Dominik et al. 2003), this hypothesis could be tested by deriving the height at which the  $\text{N}_2\text{H}^+$  layer resides from channel maps. Another possibility is that there is no  $\text{N}_2\text{H}^+$  surface layer due to the much stronger UV radiation field of the Herbig Ae star HD 163296 as compared to the T Tauri star TW Hya, so that the  $\text{N}_2\text{H}^+$  emission follows the column density. In addition, a strong drop in CO abundance may be easier to detect in a disk with a low global carbon and CO depletion.

The relationship between  $\text{N}_2\text{H}^+$  and the CO snowline is thus more complicated than direct coincidence and a snowline location can generally not be derived from only a power law fit to the observed  $\text{N}_2\text{H}^+$  emission. For disks with the CO snow surface high above the midplane, for example, due to a low degree of grain settling, the  $\text{N}_2\text{H}^+$  emission seems to generally trace the column density peak quite well. The then obtained outer boundary for the snowline can be improved if a CO column density profile can be derived from  $\text{C}^{18}\text{O}$  observations. On the other hand, when the  $\text{N}_2\text{H}^+$  emission is dominated by a surface layer, for example, in a very settled disk, chemical modeling is required. If the CO snow surface is close to the midplane, the CO column

density change across the snowline will be small and  $\text{C}^{18}\text{O}$  observations will be less helpful (see **Fig. 2.11**). Detailed knowledge about the disk vertical physical structure are thus required to translate  $\text{N}_2\text{H}^+$  emission into a CO snowline location. Comparing emission from multiple  $\text{N}_2\text{H}^+$  transitions can provide information on to what extent the emission is dominated by an  $\text{N}_2\text{H}^+$  surface layer, and thus how well it traces the column density. Higher spatial resolution may also reveal significant contribution from a surface layer, as multiple components may be concealed in a broad emission peak at low resolution.

## 2.5 Conclusions

In this work, we modeled the  $\text{N}_2\text{H}^+$  distribution and resulting emission for the disk around TW Hya using a simple chemical network. Our main conclusions regarding the robustness of  $\text{N}_2\text{H}^+$  as a tracer of the CO snowline are listed below.

- For the adopted physical structure and binding energies, freeze-out and thermal desorption predict a CO snowline at 19 AU, corresponding to a CO midplane freeze-out temperature of 20 K. This is smaller than inferred by Qi et al. (2013b).
- A simple chemical model predicts the  $\text{N}_2\text{H}^+$  column density to peak at least  $\sim 5$  AU outside the CO snowline for all physical and chemical conditions tested. This offset shows an increasing trend with CO abundance, suggesting that the  $\text{N}_2\text{H}^+$  distribution is dictated by the amount of CO present in the gas phase, rather than its snowline location.
- In addition to the  $\text{N}_2\text{H}^+$  layer outside the CO snow surface,  $\text{N}_2\text{H}^+$  is predicted to be abundant in a surface layer where the gas-phase  $\text{N}_2$  abundance exceeds that of CO due to a small difference in the photodissociation rates. Only in models with  $\text{N}_2/\text{CO} \lesssim 0.2$  is no surface layer present.
- The contribution of this surface layer to the total  $\text{N}_2\text{H}^+$  emission depends on the disk vertical structure. For the adopted physical structure for TW Hya, in which the large grains have settled toward the midplane, the simulated  $\text{N}_2\text{H}^+$  emission is dominated by the surface layer. This causes the emission to shift to even larger radii, up to  $\sim 50$  AU beyond the snowline. The influence of the surface layer is much smaller in a less settled disk, and in this case the  $\text{N}_2\text{H}^+$  emission does roughly trace the column density.
- The extent of the  $\text{N}_2\text{H}^+$  surface layer, and therefore the shift of the emission peak, also depends on the CO abundance. Moreover, the peak integrated intensity depends on the  $\text{N}_2/\text{CO}$  ratio. Together, this suggests that  $\text{N}_2\text{H}^+$  may help constrain CO and  $\text{N}_2$  abundances in protoplanetary disks, provided a representative model of the physical structure is derivable from existing observations.
- An  $\text{N}_2\text{H}^+$  distribution based on the freeze-out and desorption balance for CO and  $\text{N}_2$ , and thus peaking directly at the CO snowline, produces an emission peak 7 AU closer to the star than observed. To reproduce the observed emission peak with the simple chemical model, a CO and  $\text{N}_2$  abundance of  $3 \times 10^{-6}$  is required. This is in agreement with a global CO and carbon depletion in TW Hya. The



$\text{N}_2\text{H}^+$  surface layer predicted by the simple chemical model is necessary to fit both the location and the intensity of  $\text{N}_2\text{H}^+$  emission peak.

- The cosmic ray ionization rate influences both the  $\text{N}_2\text{H}^+$  intensity as well as the positions of the column density and emission maxima, while only the peak positions change with different CO and  $\text{N}_2$  binding energies.
- Underprediction of the emission from the region depleted of millimeter grains (radii larger than  $\sim 60$  AU) reinforces the idea that  $\text{N}_2\text{H}^+$  may be very sensitive to the physical structure of the disk.

The relationship between the  $\text{N}_2\text{H}^+$  distribution and the CO snowline location is thus more complicated than initially assumed and simple parametrized column density fits provide only upper boundaries for the snowline radius. Instead, more detailed modeling is needed to derive the CO snowline location from  $\text{N}_2\text{H}^+$  emission, and as shown in this work, a simple chemical model seems to be sufficient. However, detailed knowledge of the disk physical structure is required. On the other hand, the sensitivity to CO and  $\text{N}_2$  abundance and physical structure suggests that  $\text{N}_2\text{H}^+$  may be a more versatile probe, capable of constraining CO and  $\text{N}_2$  abundances, and the thermal structure of protoplanetary disks.

## Acknowledgements

We thank Michiel Hogerheijde for sharing the reduced image cube of the ALMA  $\text{N}_2\text{H}^+$   $J = 4-3$  observations in TW Hya, Ilse Cleeves for fruitful discussions and the anonymous referee for useful comments to improve the manuscript. Astrochemistry in Leiden is supported by the European Union A-ERC grant 291141 CHEMPLAN, by the Netherlands Research School for Astronomy (NOVA) and by a Royal Netherlands Academy of Arts and Sciences (KNAW) professor prize. M.L.R.H acknowledges support from a Huygens fellowship from Leiden University. C.W. acknowledges support from the Netherlands Organisation for Scientific Research (NWO, program number 639.041.335). This paper makes use of the following ALMA data: ADS/JAO.ALMA#2011.0.00340.S. ALMA is a partnership of ESO (representing its member states), NSF (USA) and NINS (Japan), together with NRC (Canada), NSC and ASIAA (Taiwan), and KASI (Republic of Korea), in cooperation with the Republic of Chile. The Joint ALMA Observatory is operated by ESO, AUI/NRAO and NAOJ.

## Appendix

### 2.A Chemical model

#### 2.A.1 Freeze-out and desorption balance

The balance between freeze-out onto dust grains and desorption back into the gas phase can be written as:

$$k_d n_s(\text{CO}) = k_f n_g(\text{CO}), \quad (2.10)$$

where  $n_s(\text{CO})$  is the CO ice abundance,  $n_g(\text{CO})$  the CO gas abundance, and  $k_f$  and  $k_d$  are the freeze-out and desorption rates, respectively. For  $\text{N}_2$  a similar equation holds.

The freeze-out rate depends on the gas temperature  $T_g$  and is given by

$$k_f = \langle v \rangle \sigma_{\text{grain}} n_{\text{grain}} S \text{ s}^{-1}, \quad (2.11)$$

where  $\langle v \rangle = \sqrt{8k_B T_g / \pi m}$  is the mean thermal velocity of molecules with mass  $m$  in the gas phase at a temperature  $T_g$ ,  $k_B$  is Boltzmann's constant,  $\sigma_{\text{grain}} n_{\text{grain}}$  is the average dust-grain cross section per unit volume and  $S$  is the sticking coefficient (Allen & Robinson 1977). The sticking coefficients for CO and  $\text{N}_2$  are taken to be 0.9 and 0.85, respectively, which are the lower limits found by Bisschop et al. (2006). Assuming them to be unity does not significantly affect the results. The average dust-grain cross section per unit volume can be written as

$$\sigma_{\text{grain}} n_{\text{grain}} = C \int_{a_{\text{min}}}^{a_{\text{max}}} a^{-3.5} (\pi a^2) da \text{ cm}^2 \text{ cm}^{-3}, \quad (2.12)$$

where  $a$  is the grain radius, and  $a_{\text{min}}$  and  $a_{\text{max}}$  are the minimum and maximum radius, respectively, for the assumed grain size distribution. The constant of proportionality,  $C$ , can be derived from the total dust mass per unit volume,  $\rho_{\text{dust}}$ :

$$\rho_{\text{dust}} = C \int_{a_{\text{min}}}^{a_{\text{max}}} a^{-3.5} \rho_{\text{bulk}} \left( \frac{4\pi}{3} a^3 \right) da \text{ g cm}^{-3}, \quad (2.13)$$

where  $\rho_{\text{bulk}}$  is the bulk density of the dust grains. For the adopted grain size distributions, this yields results similar to assuming a typical grain size of  $0.1 \mu\text{m}$ , because, although a significant fraction of the grains have grown to larger sizes, the small grains still provide the bulk of the surface area.

Thermal desorption will be considered here as the only desorption process, which is appropriate for volatile molecules such as CO and  $\text{N}_2$ . The desorption rate then depends on the dust temperature  $T_d$  (Allen & Robinson 1977) and can be written as

$$k_d = \nu_0 \exp\left(-\frac{E_b}{T_d}\right) \text{ s}^{-1}, \quad (2.14)$$

where  $E_b$  is the binding energy of a species to the dust grain and  $\nu_0$  is the characteristic vibrational frequency of an adsorbed species in its potential well (Allen & Robinson 1977),

$$\nu_0 = \sqrt{\frac{2n_s E_b}{\pi^2 m}} \text{ s}^{-1}, \quad (2.15)$$

where  $E_b$  is again the binding energy and  $n_s = 1.5 \times 10^{15} \text{ cm}^{-2}$  is the number density of surface sites on each dust grain (Hasegawa et al. 1992). For CO and N<sub>2</sub> a binding energy of 855 K and 800 K (Bisschop et al. 2006) are adopted, respectively, in the fiducial model.

## 2.1.2 Simple chemical network

The rate coefficients for the two-body reactions in the simple chemical network are given by the standard Arrhenius equation:

$$k = \alpha \left( \frac{T_g}{300} \right)^\beta \exp \left( -\frac{\gamma}{T_g} \right) \text{ cm}^3 \text{ s}^{-1}, \quad (2.16)$$

where  $T_g$  is the gas temperature, and  $\alpha$ ,  $\beta$  and  $\gamma$  can be found in the UMIST database for Astrochemistry (McElroy et al. 2013) (see **Table 2.1**), while the cosmic-ray ionization rate of H<sub>2</sub> is taken to be:

$$\zeta = 1.2 \times 10^{-17} \text{ s}^{-1} \quad (2.17)$$

in the fiducial model (Cravens & Dalgarno 1978). The disk surface density is not high enough to shield cosmic rays, that is,  $< 96 \text{ g cm}^{-2}$  everywhere, so no attenuation takes place toward the disk midplane.

The photodissociation rates of CO and N<sub>2</sub> can be written as

$$k(r, z) = k_0(r, z) \exp(-\tau_{UV}) \Theta[N(\text{H}_2), N(\text{X})] \text{ s}^{-1}, \quad (2.18)$$

where  $k_0$  is the unattenuated photodissociation rate,  $\exp(-\tau_{UV})$  is a dust extinction term and  $\Theta[N(\text{H}_2), N(\text{X})]$  is the shielding function for shielding by H<sub>2</sub> and self-shielding (van Dishoeck & Black 1988). For CO and N<sub>2</sub>, photodissociation occurs through line absorption and the unattenuated photodissociation rate are therefore given by

$$k_0(r, z) = \sum_{\lambda} \frac{\pi e^2}{mc^2} \lambda^2 f \eta I(\lambda) \text{ s}^{-1}, \quad (2.19)$$

where  $f$  is the oscillator strength for absorption from the lower to the upper level,  $\eta$  is the dissociation efficiency of the upper level,  $I(\lambda)$  is the mean intensity of the radiation field in photons  $\text{cm}^{-2} \text{ s}^{-1}$  at wavelength  $\lambda$ , and  $\frac{\pi e^2}{mc^2}$  is a numerical factor (van Dishoeck & Black 1988). For the stellar radiation field, the attenuation by dust can be calculated from the attenuated  $F_{\text{att}}^*(r, z)$  and unattenuated radiation field  $F_{\text{unatt}}^*(r, z)$ :

$$\exp(-\tau_{UV}^*) = \frac{F_{\text{att}}^*(r, z)}{F_{\text{unatt}}^*(r, z)} \text{ photons cm}^{-2} \text{ s}^{-1-1}, \quad (2.20)$$

while the attenuation of the interstellar radiation field can be derived from the visual extinction:

$$\tau_{UV}^{ISRF} = \gamma A_V, \quad (2.21)$$

where  $A_V$  is the optical depth in magnitudes and the factor  $\gamma$  depends on the dust properties. The shielding functions depend on the H<sub>2</sub> and CO or N<sub>2</sub> column densities. As photons from the star can reach a molecule either through the inner edge of the disk or from above or below, an effective column density is used assuming  $N_{\text{H}} = 1.59 \times 10^{21} A_V$ . This is translated into effective column densities for CO and N<sub>2</sub> by

scaling with the respective abundances. Interstellar radiation on the other hand can only penetrate from the outside of the disk and for simplicity the radial contribution is ignored as this will provide only a minor contribution to the radiation field in the disk. Therefore, for shielding against the interstellar radiation field vertical column densities are used. For the adopted models, photodissociation is dominated by the stellar radiation field.

### 2.A.3 Photodesorption

Although for volatile species such as CO and N<sub>2</sub>, thermal desorption is the main desorption mechanism, the dust density in the outer disk may be low enough for UV photons to penetrate to the disk midplane, such that photodesorption may become effective. Therefore, photodesorption is included in the chemical model when studying the outer edge of the N<sub>2</sub>H<sup>+</sup> emission (model CH-PD). The photodesorption rate for species X is given by:

$$k_{\text{PD}} = F_{\text{UV}}(r, z) Y \sigma_{\text{grain}} n_{\text{grain}} \frac{n_{\text{s}}(\text{X})}{n_{\text{ice}}} X_{\text{M}}, \quad (2.22)$$

where  $F_{\text{UV}}(r, z)$  is the UV photon flux at position  $(r, z)$ ,  $Y$  is the number of molecules desorbed per incident photon,  $\sigma_{\text{grain}} n_{\text{grain}}$  is again the average dust-grain cross section per unit volume and  $n_{\text{s}}(\text{X})/n_{\text{ice}}$  is the fraction of species X in the ice. The term  $X_{\text{M}}$  accounts for the fact that only molecules in a few monolayers near the ice surface ( $M_{\text{surf}}$ ) can desorb (Andersson & van Dishoeck 2008), and can be written as

$$X_{\text{M}} = \frac{M_{\text{total}}}{M_{\text{surf}}}, \quad (2.23)$$

where  $M_{\text{total}}$  is the total number of monolayers, that is, the number of molecules in the ice divided by the number of available binding sites on the dust grains. Assuming only molecules in the top four monolayers can desorb ( $M_{\text{surf}} = 4$ ),  $X_{\text{M}}$  is set to 1 for  $M_{\text{total}} \geq 4$ . For mixed ices with an equal amount of CO and N<sub>2</sub>, the yield for CO and N<sub>2</sub> is similar and we adopt values of  $1.4 \times 10^{-3}$  and  $2.1 \times 10^{-3}$  molecules photon<sup>-1</sup>, respectively (Bertin et al. 2013; Paardekooper et al. 2016). Since the uncertainty in photodesorption rates is high (see e.g., Paardekooper et al. 2016), also the extreme case with a yield 100 times higher is considered.

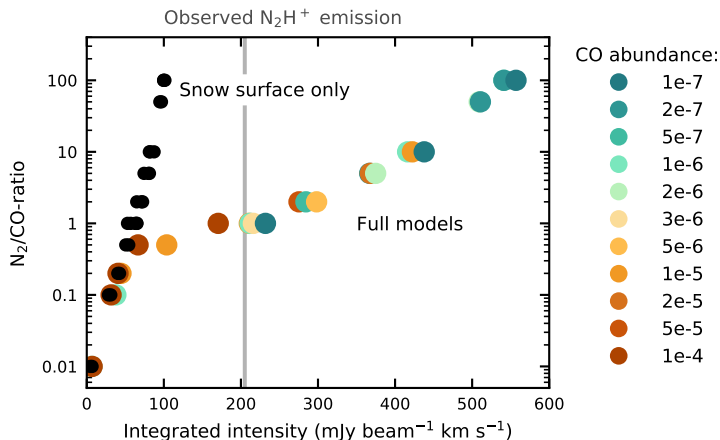


**Figure 2.B.1:**  $\text{N}_2\text{H}^+$   $J = 4 - 3$  peak integrated intensity for models with different CO and  $\text{N}_2$  abundances (models CH). The simulated emission is convolved with a  $0.63'' \times 0.59''$  beam. Black circles represent snow surface only models, i.e.,  $\text{N}_2\text{H}^+$  removed above the CO snow surface. The color of the circles for the full models represent the CO abundance. We note that some points may overlap. The gray line indicates the observed intensity.

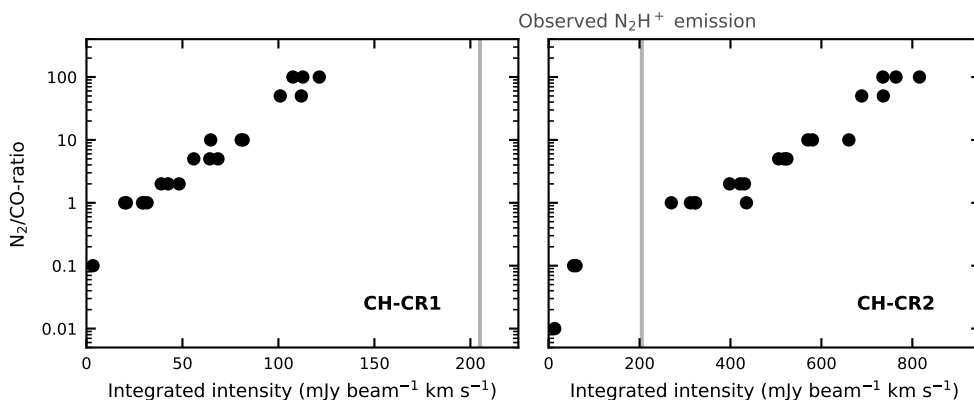


**Figure 2.B.2:**  $\text{N}_2\text{H}^+$   $J = 4 - 3$  peak integrated intensity as function of  $\text{N}_2/\text{CO}$  ratio for models with a cosmic ray ionization rate of  $\zeta = 1 \times 10^{-19} \text{ s}^{-1}$  (model CH-CR1; *left panel*) or  $\zeta = 5 \times 10^{-17} \text{ s}^{-1}$  (model CH-CR2; *right panel*). The simulated emission is convolved with a  $0.63'' \times 0.59''$  beam. The gray line indicates the observed intensity.

## 2.B $\text{N}_2\text{H}^+$ $J=4-3$ peak integrated intensity

In Figs. 2.B.1 and 2.B.2, we show the simulated  $\text{N}_2\text{H}^+$   $J = 4 - 3$  peak integrated intensity for model CH and the models with different cosmic ray ionization rates (models CH-CR1 and CH-CR2), respectively.

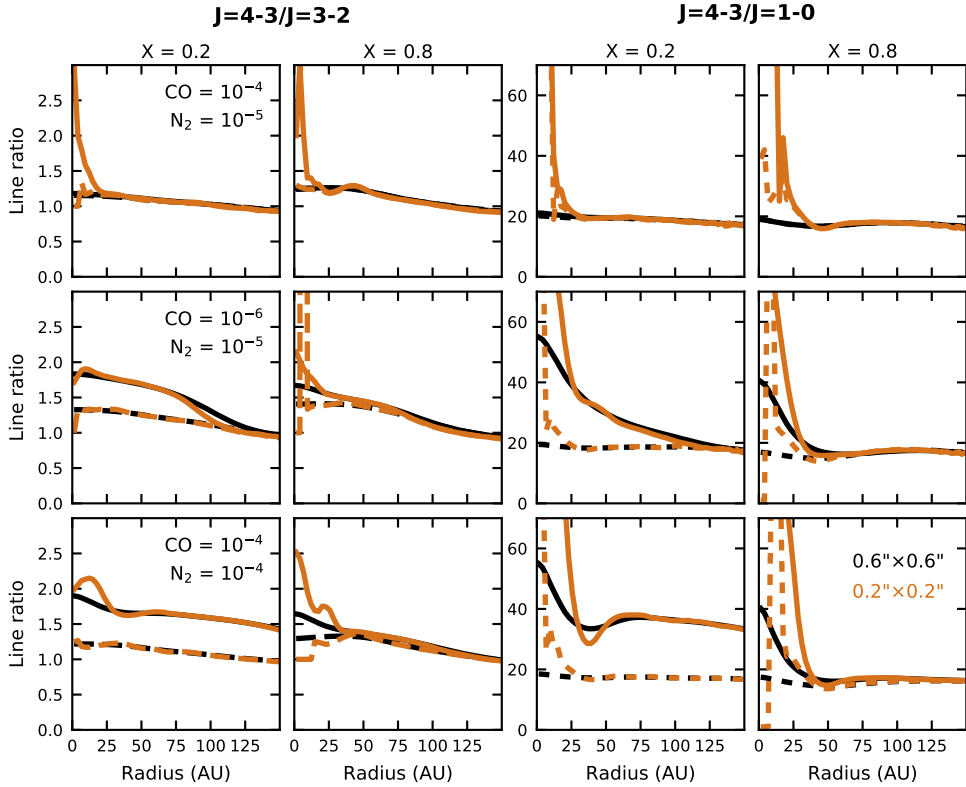


**Figure 2.C.1:**  $\text{N}_2\text{H}^+$   $J = 4 - 3/J = 3 - 2$  (left panels) and  $J = 4 - 3/J = 1 - 0$  line ratios (right panels) for three different CO and  $\text{N}_2$  abundances, as indicated in the leftmost panels, in models with large grains settled to 20% (column one and three) or 80% of the small grain scale height (column two and four). Dashed lines show the snow surface only models, while solid lines represent the full models. The simulated emission is either convolved with a  $0.63'' \times 0.59''$  (black lines) or  $0.2'' \times 0.2''$  beam (orange lines).

## 2.C $\text{N}_2\text{H}^+$ line ratios

$\text{N}_2\text{H}^+$   $J = 4 - 3/J = 3 - 2$  and  $J = 4 - 3/J = 1 - 0$  ratios for model CH and model CH- $\chi 0.8$  are presented in **Fig. 2.C.1**. The three depicted CO and  $\text{N}_2$  abundances represent models with no  $\text{N}_2\text{H}^+$  surface layer ( $\text{CO} = 10^{-4}$ ,  $\text{N}_2 = 10^{-5}$ , top row), a small  $\text{N}_2\text{H}^+$  surface layer ( $\text{CO} = 10^{-6}$ ,  $\text{N}_2 = 10^{-5}$ , middle row) and a large  $\text{N}_2\text{H}^+$  surface layer ( $\text{CO} = 10^{-4}$ ,  $\text{N}_2 = 10^{-4}$ , bottom row), as shown in **Fig. 2.6**.

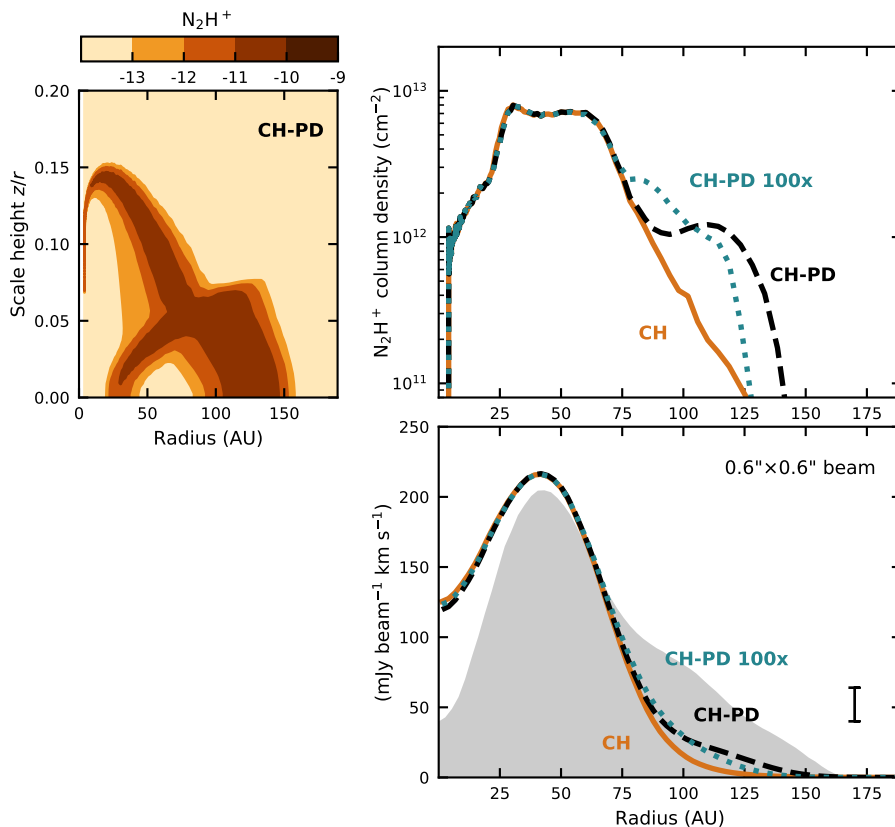


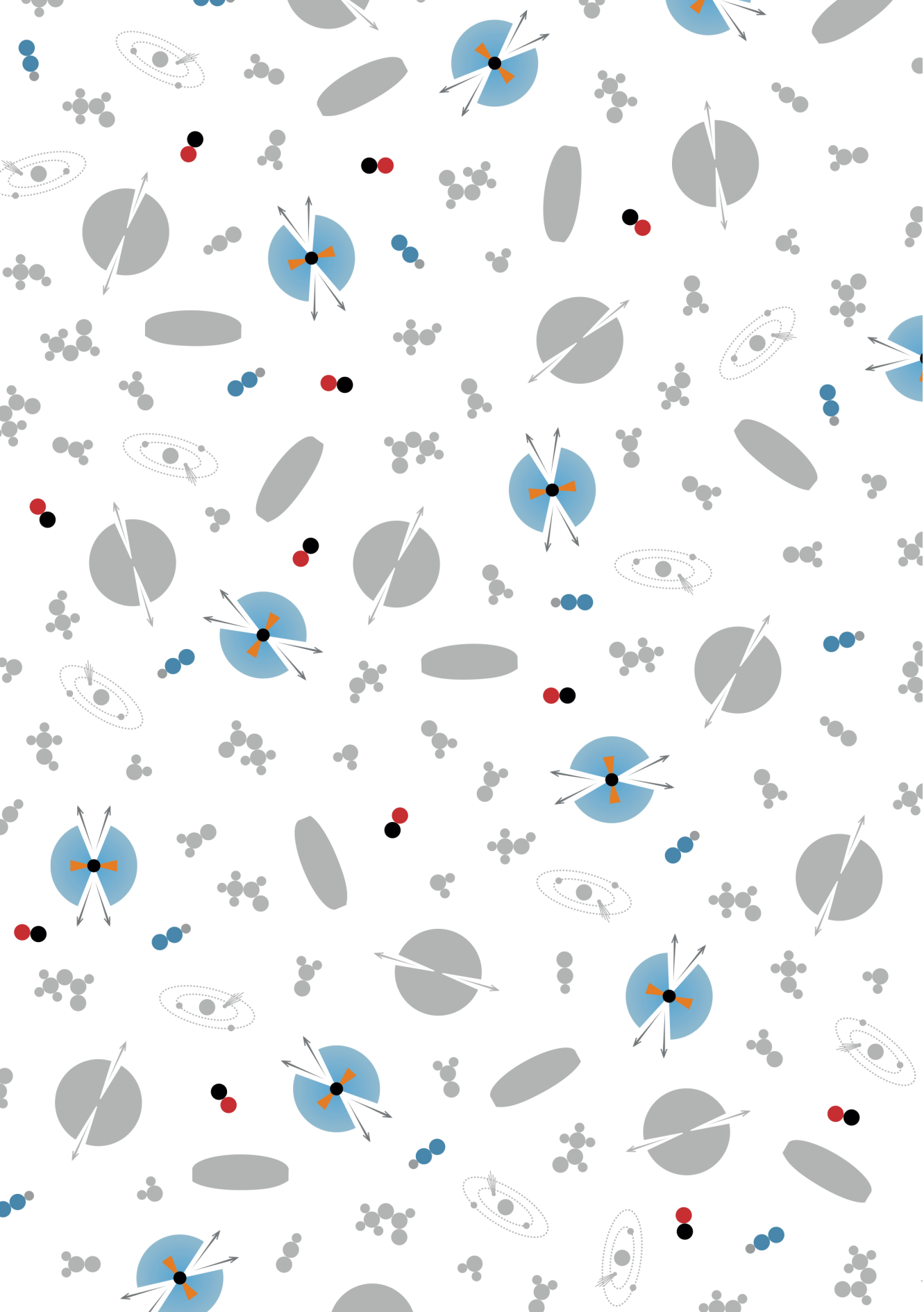
**Figure 2.D.1:**  $N_2H^+$  distribution (*top left panel*), column density (*top right panel*) and radial  $J = 4 - 3$  integrated line intensity profile (*bottom right panel*) when photodesorption is included in the chemistry (model CH-PD with CO and  $N_2$  abundances of  $3 \times 10^{-6}$ ; dashed black lines). The dotted blue lines show a model with photodesorption rates increased by a factor 100 (model CH-PD 100x), and the orange solid lines show the fiducial model without photodesorption (model CH). The simulated emission is convolved with a  $0.63'' \times 0.59''$  beam. Observations by Q13 are shown in gray in the right panel with the  $3\sigma$ -error depicted in the lower right corner.

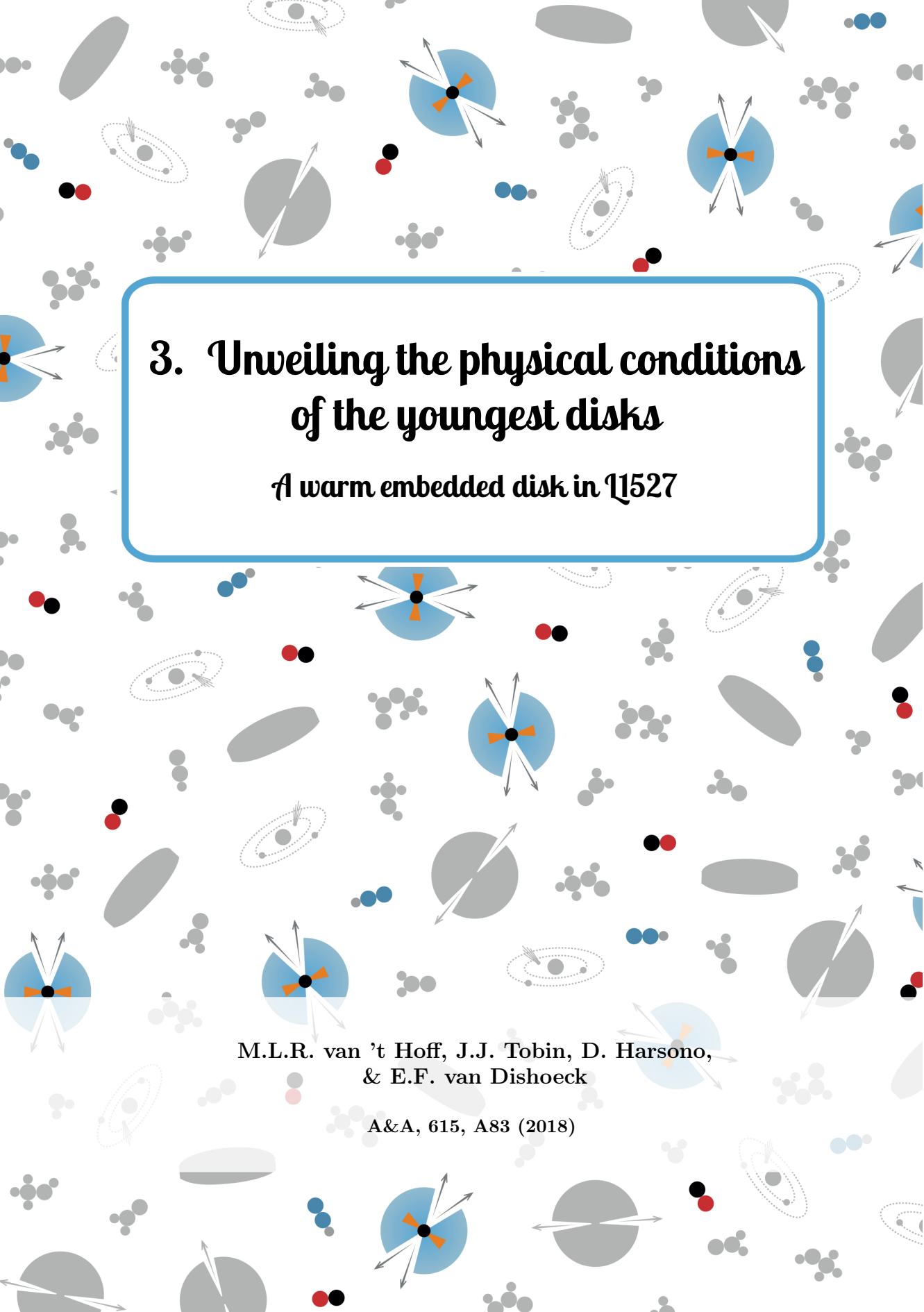
## 2.D Photodesorption

The  $N_2H^+$  distribution, column density profile and  $J = 4 - 3$  integrated line intensity profile for the chemical model with photodesorption included (model CH-PD) are shown in **Fig. 2.D.1**.









### 3. Unveiling the physical conditions of the youngest disks

*A warm embedded disk in  $\tau$ 1527*

M.L.R. van 't Hoff, J.J. Tobin, D. Harsono,  
& E.F. van Dishoeck

A&A, 615, A83 (2018)



## Abstract

**Context.** Protoplanetary disks have been studied extensively, both physically and chemically, to understand the environment in which planets form. However, the first steps of planet formation are likely to occur already when the protostar and disk are still embedded in their natal envelope. The initial conditions for planet formation may thus be provided by these young embedded disks, of which the physical and chemical structure is poorly characterized.

**Aims.** We aim to constrain the midplane temperature structure, one of the critical unknowns, of the embedded disk around L1527. In particular, we set out to determine whether there is an extended cold outer region where CO is frozen out, as is the case for Class II disks. This will show whether young disks are indeed warmer than their more evolved counterparts, as is predicted by physical models.

**Methods.** We used archival ALMA data of  $^{13}\text{CO}$   $J = 2 - 1$ ,  $\text{C}^{18}\text{O}$   $J = 2 - 1$  and  $\text{N}_2\text{D}^+ J = 3 - 2$  to directly observe the midplane of the near edge-on L1527 disk. The optically thick CO isotopologues allowed us to derive a radial temperature profile for the disk midplane, while  $\text{N}_2\text{D}^+$ , which can only be abundant when CO is frozen out, provides an additional constraint on the temperature. Moreover, the effect of CO freeze-out on the  $^{13}\text{CO}$ ,  $\text{C}^{18}\text{O}$  and  $\text{N}_2\text{D}^+$  emission was investigated using 3D radiative transfer modeling.

**Results.** Optically thick  $^{13}\text{CO}$  and  $\text{C}^{18}\text{O}$  emission is observed throughout the disk and inner envelope, while  $\text{N}_2\text{D}^+$  is not detected. Both CO isotopologues have brightness temperatures  $\gtrsim 25$  K along the midplane. Disk and envelope emission can be disentangled kinematically, because the largest velocities are reached in the disk. A power law radial temperature profile constructed using the highest midplane temperature at these velocities suggest that the temperature is above 20 K out to at least 75 AU, and possibly throughout the entire 125 AU disk. The radiative transfer models show that a model without CO freeze-out in the disk matches the  $\text{C}^{18}\text{O}$  observations better than a model with the CO snowline at  $\sim 70$  AU. In addition, there is no evidence for a large (order of magnitude) depletion of CO.

**Conclusions.** The disk around L1527 is likely to be warm enough to have CO present in the gas phase throughout the disk, suggesting that young embedded disks can indeed be warmer than the more evolved Class II disks.

### 3.1 Introduction

Disks around young stars play a fundamental role in the star and planet formation process by regulating mass accretion and providing the mass reservoirs for forming planets. The physical structure of the disk is intimately related to its chemical structure, which in turn determines the initial planet composition. Many studies have therefore focused on the evolved protoplanetary disks around pre-main sequence stars, and these Class II disks are now becoming well characterized both physically (e.g., Andrews et al. 2010; Schwarz et al. 2016; Ansdell et al. 2016) and chemically (e.g., Dutrey et al. 1997; Thi et al. 2004; Öberg et al. 2010; Huang et al. 2017). The thermal and chemical structure that has emerged consists of a cold dense midplane where CO is frozen out, a warm molecular layer where CO and other species are in the gas phase, and a tenuous upper layer where molecules are photodissociated by UV radiation (e.g., Aikawa et al. 2002). In addition, disk masses are typically low; average dust masses range between 5 and 15  $M_{\oplus}$  (depending on the star forming region) and gas masses are generally  $\lesssim 1M_{\text{jup}}$  (Andrews et al. 2013; Ansdell et al. 2016, 2017; Barenfeld et al. 2016; Pascucci et al. 2016; Law et al. 2017).

However, it is now becoming clear that the first steps of planet formation likely occur at an earlier stage, when the disk is still forming within the infalling envelope (Class 0 and I sources). Grain growth begins during this embedded stage (Kwon et al. 2009; Pagani et al. 2010; Foster et al. 2013; Miotello et al. 2014), and the HL Tau images suggest that even the formation of larger bodies may have already started before the envelope has fully dissipated (ALMA Partnership et al. 2015). Thus, young embedded disks may reflect the true initial conditions for planet formation.

Efforts to detect these embedded disks have been made for the past 20 years, but early studies of the dust continuum were hampered by a lack of sensitivity and/or spatial resolution (e.g., Keene & Masson 1990; Looney et al. 2000; Jørgensen et al. 2009). While recent interferometric surveys have resolved disk-like structures in the dust around many protostars (Tobin et al. 2015b; Segura-Cox et al. 2016), molecular line observations are necessary to establish whether these disk structures are in fact rotationally supported. Keplerian rotation has indeed been observed for a handful Class 0 sources (Tobin et al. 2012b; Murillo et al. 2013; Codella et al. 2014; Lindberg et al. 2014; Yen et al. 2017), and more disks have been detected around the less embedded Class I protostars (e.g., Brinch et al. 2007; Lommen et al. 2008; Lee 2010; Takakuwa et al. 2012; Harsono et al. 2014).

So far, studies of these young disk systems have mostly focused on disk size, kinematics and disk formation mechanisms (e.g., Yen et al. 2013; Ohashi et al. 2014; Harsono et al. 2014), or the chemical structure at the disk-envelope interface (Sakai et al. 2014a,b; Murillo et al. 2015). Although a few studies have set out to model the disk radial density profile (e.g., Tobin et al. 2013b; Aso et al. 2017, hereafter T13 and A17, resp.), the physical and chemical structure of embedded disks remains poorly characterized. A simple but crucial question, for example, is whether these young disks are warm ( $T \gtrsim 20$  K, i.e., warmer than the CO freeze-out temperature) or cold (have a large region where  $T \lesssim 20$  K), as this will strongly affect disk evolution as well as the molecular composition.

The effect of temperature on the chemical structure can be readily seen in the snowline locations of the major volatile species. The snowline is the midplane radius where the temperature drops below the freeze-out temperature of a given molecule

and hence this molecule freezes out from the gas phase onto the dust grains. The sequential freeze out of molecules causes molecular abundances and elemental ratios (like the C/O ratio) in both the gas and ice to vary with radius (e.g., Öberg et al. 2011). This in turn affects the composition of planets formed at different orbital distances (e.g., Madhusudhan et al. 2014; Walsh et al. 2015; Eistrup et al. 2016; Ali-Dib 2017). In addition, the solid-state formation of high abundances of complex molecules, which starts from CO ice (e.g., Tielens & Hagen 1982; Garrod & Herbst 2006; Chuang et al. 2016), will be impeded if the disk temperature is higher than the freeze-out temperature of CO ( $\gtrsim 20$  K). Furthermore, the location where grain growth is efficient is related to the water snowline (e.g., Stevenson & Lunine 1988; Schoonenberg & Ormel 2017). The thermal structure of the disk is thus a crucial ingredient in the planet formation process.

Modeling studies of evolved disks without an envelope have shown that the mass accretion rate is an important parameter for the disk temperature; higher accretion rates result in warmer disks (Davis 2005; Garaud & Lin 2007; Min et al. 2011). Since accretion rates are expected to decrease on average as the protostar evolves, disks in the embedded phase may be warmer than their more evolved counterparts. The envelope itself also influences the disk temperature as it serves as an isolating blanket (D’Alessio et al. 1997; Whitney et al. 2003). Specifically, Harsono et al. (2015) showed that both a high accretion rate and the presence of an envelope affects the location of  $T \lesssim 40$  K dust, shifting the CO snowline to larger radii compared to disks without an envelope.

L1527 IRS (IRAS 04368+2557) is a good protostellar source to investigate whether young embedded disks are indeed warm, or have a large cold outer region where CO is frozen out, like the more evolved Class II disks. This protostar located in the Taurus molecular cloud ( $d = 140$  pc, Torres et al. 2007) is a borderline Class 0/I object (see e.g., the discussion in T13), with a bolometric luminosity of  $\sim 1.9 - 2.6 L_{\odot}$  (Tobin et al. 2008; Kristensen et al. 2012). *Spitzer* images revealed bright bipolar outflow cavities in the east-west direction extending  $\sim 10,000$  AU in radius (Tobin et al. 2008). On  $\sim 2000$  AU scales the protostellar envelope has a flattened shape with an infalling rotating velocity profile (Ohashi et al. 1997), and the presence of a rotationally supported disk with a  $\sim 100$  AU radius was derived from the continuum and  $^{13}\text{CO}$  emission (Tobin et al. 2012b). Analysis of  $\text{C}^{18}\text{O}$  emission confirmed the presence of a Keplerian disk with a kinematic estimate of  $\sim 74$  AU for the disk radius (Ohashi et al. 2014, A17). The disk is seen almost edge-on ( $i = 85^{\circ}$ , Tobin et al. 2008; Oya et al. 2015), enabling direct probes of the midplane as shown for the Flying Saucer protoplanetary disk (Dutrey et al. 2017).

T13 modeled the (sub)millimeter continuum emission and visibilities, scattered light  $L'$  image, spectral energy distribution, and mid-infrared spectrum using 3D radiative transfer codes (Whitney et al. 2003; Brinch & Hogerheijde 2010). Their best-fit model has a highly flared disk ( $H \propto R^{1.3}$ , with  $H = 100$  AU at a 48 AU radius) with a radius of 125 AU. The temperature structure has a midplane temperature of 30 K at 100 AU, implying that CO will not freeze out in the disk. Given the edge-on configuration, high resolution CO observations should be able to confirm or refute the presence of gas-phase CO throughout the entire disk midplane. These results can be reinforced by observations of molecular tracers of CO freeze-out like  $\text{N}_2\text{D}^+$ , which will be destroyed as long as CO is present in the gas phase.

In this paper we use archival ALMA observations of CO isotopologues ( $^{13}\text{CO}$  and  $\text{C}^{18}\text{O}$ ) and  $\text{N}_2\text{D}^+$  to determine whether the embedded disk around L1527 resembles a Class II disk with a large cold gas reservoir, or whether this young disk is warm enough to have gaseous CO throughout. The data reduction is described in [Sect. 3.2](#), and the resulting  $^{13}\text{CO}$  and  $\text{C}^{18}\text{O}$  images and non-detection of  $\text{N}_2\text{D}^+$  are presented in [Sect. 3.3](#). In [Sect. 3.4](#), we use the optically thick  $^{13}\text{CO}$  and  $\text{C}^{18}\text{O}$  emission to derive a radial temperature profile for the disk midplane, and discuss the difficulties of disentangling disk and envelope emission. The effect of CO freeze out over different radial extents on the  $^{13}\text{CO}$ ,  $\text{C}^{18}\text{O}$  and  $\text{N}_2\text{D}^+$  emission is examined in [Sect. 3.5](#) using the 3D radiative transfer code LIME (Brinch & Hogerheijde 2010). In addition these models are used to address the CO abundance in the disk. Implications of the absence of CO freeze-out in embedded disks are discussed in [Sect. 3.6](#), and the conclusions are summarized in [Sect. 3.7](#).

## 3.2 Observations

The L1527 data analyzed here were retrieved from the ALMA archive (project code: 2013.1.01086.S, PI: S. Koyamatsu). Observations were carried out during Cycle 2 on 24 May 2015, using 34 antennas sampling baselines between 21 and 539 m, and on 20 September 2015, using 35 antennas sampling baselines between 41 and 2269 m. This corresponds to a maximum angular scale of  $4.2''$  and  $1.3''$ , respectively. The phase center was  $\alpha(\text{J2000}) = 04^{\text{h}}39^{\text{m}}53.91^{\text{s}}$ ;  $\delta(\text{J2000}) = 26^{\circ}03'09.80''$ . During both observations, L1527 was observed with a total on-source integration time of 25 minutes. The correlator setup included a 2 GHz continuum band centered at 233.0 GHz, and spectral windows with a bandwidth of 58.6 MHz targeting the  $^{13}\text{CO}$   $J = 2 - 1$ ,  $\text{C}^{18}\text{O}$   $J = 2 - 1$  and  $\text{N}_2\text{D}^+$   $J = 3 - 2$  transitions. The spectral resolution was 30.5 kHz for  $\text{C}^{18}\text{O}$  and 61.0 kHz for the two other lines, which corresponds to a velocity resolution of 0.04 and 0.08  $\text{km s}^{-1}$ , respectively.

Calibration of the visibilities observed in the compact configuration was done using the ALMA Pipeline and version 4.2.2 of Common Astronomy Software Applications (CASA), while the observations in the more extended configuration were reduced manually by the East Asia ALMA Regional Center staff using CASA version 4.5. Calibrators for the respective observations were J0510+1800 and J0429+2724 (phase), J0423-0120 and J0510+1800 (bandpass and flux). We performed self-calibration on the continuum data and applied the phase and amplitude solutions also to the spectral line bands. The data were imaged using the CASA task CLEAN with natural weighting. For the line images, the continuum was subtracted before imaging. The total 1.3 mm continuum flux density derived from a Gaussian fit to the visibilities is  $184.2 \pm 0.15$  mJy, consistent with the 1.3 mm flux density reported by A17. The natural weighted continuum image has a peak flux density of  $66.0 \pm 0.16$  mJy  $\text{beam}^{-1}$  (for a  $0.30'' \times 0.18''$  beam), and is shown in [Fig. 3.1](#). An overview of the image parameters for the observed molecular lines is provided in [Table 3.1](#). For  $^{13}\text{CO}$  and  $\text{C}^{18}\text{O}$ , only the observations in the extended configuration are used, while the  $\text{N}_2\text{D}^+$  upper limits are derived from the data obtained in the more compact configuration.

**Table 3.1:** Overview of the molecular line observations toward L1527.

Molecule	Transition	Frequency (GHz)	$A_{ul}^a$ ( $s^{-1}$ )	$g_{up}^b$	$E_{up}^c$ (K)	Beam ( $''$ )	$\Delta v^d$ ( $km\ s^{-1}$ )	rms (mJy beam $^{-1}$ channel $^{-1}$ )	rms (K channel $^{-1}$ )
$^{13}CO$	$J = 2 - 1$	220.39868	$6.038 \times 10^{-7}$	5	15.87	$0.32 \times 0.18$ (PA = $39.0^\circ$ )	0.08 <sup>e</sup>	10.2 <sup>f</sup>	4.4 <sup>f</sup>
$C^{18}O$	$J = 2 - 1$	219.56035	$6.011 \times 10^{-7}$	5	15.81	$0.32 \times 0.19$ (PA = $38.7^\circ$ )	0.04 <sup>e</sup>	8.7 <sup>f</sup>	3.6 <sup>f</sup>
$N_2D^+$	$J = 3 - 2$	231.32183	$7.138 \times 10^{-4}$	7	22.20	$0.93 \times 0.71$ (PA = $10.7^\circ$ )	0.08	10.4	0.4

**Notes.** <sup>(a)</sup> Einstein-A coefficient. <sup>(b)</sup> Upper level degeneracy. <sup>(c)</sup> Upper level energy. <sup>(d)</sup> Velocity resolution. <sup>(e)</sup> Velocities were binned to  $0.16\ km\ s^{-1}$ .  
<sup>(f)</sup> In  $0.16\ km\ s^{-1}$  channels.



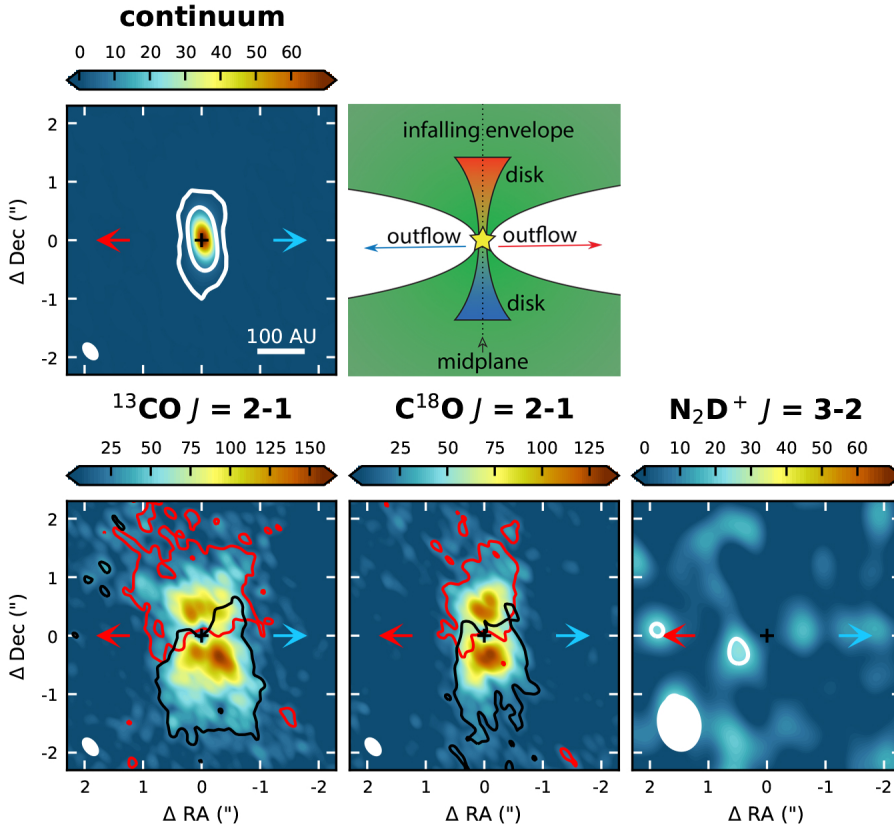


**Figure 3.1:** Continuum image toward L1527 at 1.3 mm (*top left panel*) and integrated intensity maps for the  $^{13}\text{CO}$   $J = 2 - 1$  (*bottom left panel*),  $\text{C}^{18}\text{O}$   $J = 2 - 1$  (*bottom middle panel*) and  $\text{N}_2\text{D}^+$   $J = 3 - 2$  (*bottom right panel*) transitions. For  $^{13}\text{CO}$  and  $\text{C}^{18}\text{O}$ , only channels with a  $>3\sigma$  detection are included. The red and black contours indicate the  $3\sigma$  level of the red- and blueshifted emission, which corresponds to 18 and 21  $\text{mJy beam}^{-1} \text{ km s}^{-1}$  for  $^{13}\text{CO}$ , and 17 and 18  $\text{mJy beam}^{-1} \text{ km s}^{-1}$  for  $\text{C}^{18}\text{O}$ . The white contours denote the  $5\sigma$  and  $50\sigma$  levels ( $1\sigma = 0.13 \text{ mJy beam}^{-1}$ ) for the continuum, and the  $3\sigma$  ( $20 \text{ mJy beam}^{-1} \text{ km s}^{-1}$ ) level for  $\text{N}_2\text{D}^+$ . The position of the continuum peak ( $\alpha(\text{J2000}) = 04^{\text{h}}39^{\text{m}}53.88^{\text{s}}$ ;  $\delta(\text{J2000}) = 26^{\circ}03'09.57''$ ) is marked by a black cross and the blue and red arrows show the direction of the outflow. The beam is shown in the lower left corner of each panel. The *top middle panel* shows a schematic view of the disk and inner envelope. The midplane is indicated by a dotted line.

### 3.3 Results

**Figure 3.1** shows the integrated intensity (zerth moment) maps for  $^{13}\text{CO}$  ( $J = 2 - 1$ ),  $\text{C}^{18}\text{O}$  ( $J = 2 - 1$ ), and  $\text{N}_2\text{D}^+$  ( $J = 3 - 2$ ) toward L1527, as well as a schematic overview of this region with the edge-on disk and inner part of the infalling rotating envelope. Carbon monoxide (CO) emission has been widely used to study the regions in protostellar systems where the material is warm enough ( $\gtrsim 20 \text{ K}$ ) to evaporate CO off the dust grains. Emission lines from the main isotopologue  $^{12}\text{C}^{16}\text{O}$  are optically thick and dominated by the outflow material, while the less abundant isotopologues are relatively more optically thin and expected to probe the disk forming region.

Meanwhile, the cold regions ( $T \lesssim 20$  K) where CO is frozen out are traced by  $\text{N}_2\text{H}^+$  and its deuterated variant  $\text{N}_2\text{D}^+$  (e.g., Jørgensen et al. 2004a; Crapsi et al. 2005; Tobin et al. 2013a).

$^{13}\text{CO}$  emission was detected above the  $3\sigma$  level at relative velocities  $\Delta v$  with respect to the  $v_{\text{LSR}}$  of the source ( $5.9 \text{ km s}^{-1}$ ), between  $-3.2$  and  $-0.3 \text{ km s}^{-1}$ , and between  $0.7$  and  $2.8 \text{ km s}^{-1}$ .  $\text{C}^{18}\text{O}$  emission was detected at similar velocities: between  $-3.0$  and  $-0.3 \text{ km s}^{-1}$ , and between  $0.5$  and  $2.8 \text{ km s}^{-1}$ . Line emission is not detected around the systemic velocity due to large-scale emission being resolved out. The zeroth moment maps presented in **Fig. 3.1** are constructed using only channels with a  $> 3\sigma$  detection. Both CO isotopologues show emission elongated in the direction perpendicular to the outflow, with redshifted emission located north of the continuum peak and blueshifted emission to the south. This is consistent with a Keplerian rotating disk and the inner part of a infalling rotating envelope (Tobin et al. 2012b, T13, Ohashi et al. 2014, A17). Estimates of the Keplerian disk radius vary between  $\sim 74$  and  $\sim 125$  AU (A17, T13, resp.), that is,  $0.5'' - 0.9''$ . The  $^{13}\text{CO}$  isotopologue is more abundant than  $\text{C}^{18}\text{O}$  which results in the  $^{13}\text{CO}$  emission being more extended in the east-west direction while  $\text{C}^{18}\text{O}$  is only detected in the denser regions toward the midplane. The line emission does not peak on source, probably because the continuum becomes optically thick in the innermost region around the protostar ( $R \lesssim 15$  AU, see also the discussion in **Sect. 3.6.1**), lowering the emission peak.

The edge-on orientation of the disk allows for direct observation of the midplane, and thus, theoretically, for a direct determination whether CO is frozen out or present in the gas phase. From these observations, no obvious reduction in  $^{13}\text{CO}$  or  $\text{C}^{18}\text{O}$  emission, corresponding to CO freeze-out, is seen toward the midplane. Some asymmetry is visible, especially for  $^{13}\text{CO}$ , with the southern half of the disk being brightest west of the midplane and the northern half east of the midplane. This asymmetry is, at least partly, the result of the  $uv$ -coverage of the observations. Similar asymmetrical features can be introduced for axisymmetric models simulated with the observed visibilities.

In contrast with the clear CO isotopologue detections, no emission was detected for  $\text{N}_2\text{D}^+$ , which can only be abundant when CO is frozen out (at  $T \lesssim 20$  K and  $n \gtrsim 10^5 \text{ cm}^{-3}$ ). The  $3\sigma$  limit of  $20 \text{ mJy beam km s}^{-1}$  corresponds to an upper level for the beam-averaged  $\text{N}_2\text{D}^+$  column density of  $\sim 2 - 4 \times 10^{12} \text{ cm}^{-2}$  (assuming LTE and excitation temperatures between 10 and 50 K; see e.g., Goldsmith & Langer 1999). Thus, at first inspection there is no evidence in these observations for a large cold outer region in the disk around L1527 where CO is frozen out.

## 3.4 Analysis

To examine the temperature structure of the L1527 disk in more detail we analyse the  $^{13}\text{CO}$  and  $\text{C}^{18}\text{O}$  emission. First, we establish that emission from both molecules is optically thick using the line ratio (**Sect. 3.4.1**). Next, we derive a temperature profile for the disk midplane (**Sect. 3.4.2**). Although the edge-on configuration of the disk allows a direct view of the midplane, deriving a radial temperature profile is not straightforward. The  $^{13}\text{CO}$  and  $\text{C}^{18}\text{O}$  emission trace both the disk and inner envelope, so emission originating from the disk has to be disentangled from envelope emission. In addition, the radius from which the optically thick emission originates has to be determined. Viewing the disk edge-on means that the line of sight goes through

the entire midplane before reaching the inner most part. If the emission becomes optically thick already in the inner envelope or outer disk, the inner disk cannot be observed. Moreover, this means that on-source emission does not necessarily originate at small radii ( $\lesssim 40$  AU). Before addressing these problems in detail using the velocity structure (**Sect. 3.4.3**), we derive a radial temperature profile in a conservative way. That is, we measure the temperature in the disk midplane at the highest possible velocity offsets. Assuming a power law temperature profile we can then estimate the midplane temperature structure for the entire disk (**Sect. 3.4.2**).

### 3.4.1 $^{13}\text{CO}$ optical depth

Given the low critical density of the  $^{13}\text{CO}$   $J = 2 - 1$  transition ( $n_{\text{crit}} \sim 10^4 \text{ cm}^{-3}$ ), the emission is expected to be thermalized throughout the disk and in the inner envelope ( $n > 10^6 \text{ cm}^{-3}$ ). This means that if the emission is optically thick, the brightness temperature is a measure of the excitation temperature, which in turn is a lower limit of the kinetic temperature of the gas. The optical depth of the  $^{13}\text{CO}$  emission can be derived from the  $^{13}\text{CO}/\text{C}^{18}\text{O}$  line ratio. If both lines are optically thin, the line ratio will be equal to the abundance ratio of  $^{13}\text{CO}$  and  $\text{C}^{18}\text{O}$  ( $\sim 7-8$ ), given no isotope-selective photodissociation processes. This is a valid assumption for the disk midplane, since UV radiation will only penetrate into the disk surface layers. As the  $^{13}\text{CO}$  emission becomes optically thick, the line ratio decreases. The line ratio becomes unity when both lines are optically thick.

The  $^{13}\text{CO}$  ( $J = 2 - 1$ ) /  $\text{C}^{18}\text{O}$  ( $J = 2 - 1$ ) line ratio is calculated for each pixel with at least a  $3\sigma$  detection (see **Table 3.1**) for both  $^{13}\text{CO}$  and  $\text{C}^{18}\text{O}$ , and six representative channels are presented in **Fig. 3.2**. The  $^{13}\text{CO}/\text{C}^{18}\text{O}$  ratio is below 3.0 in all regions, and below 2.0 in the pixels with the highest signal-to-noise (along the midplane). The  $3\sigma$  uncertainty on the  $^{13}\text{CO}/\text{C}^{18}\text{O}$  ratio is calculated for each pixel by propagating the rms in the  $0.16 \text{ km s}^{-1}$  channels. Within this uncertainty, the ratio remains below 3.5, except in a few pixels close to the  $3\sigma$  contour of the  $\text{C}^{18}\text{O}$  emission. Theoretically, the ratio cannot be smaller than 1.0, unless  $^{13}\text{CO}$  emission is significantly more resolved out relative to  $\text{C}^{18}\text{O}$ . The lowest values reached are  $\sim 0.5$ , but the  $3\sigma$  uncertainty in these pixels is  $\geq 0.5$ . The values below 1.0 are thus not significant.

Since the optical depth depends on the gas temperature, the quantity we set out to determine, the line ratio is also dependent on the temperature. Therefore, in order to determine whether the emission from either or both CO isotopologues is optically thick, we calculate line ratios for a range of temperatures (20–100 K) and column densities ( $\text{C}^{18}\text{O}$  column densities ranging from  $10^{13} \text{ cm}^{-2}$  to  $10^{18} \text{ cm}^{-2}$ ) using RADEX<sup>1</sup> (van der Tak et al. 2007; van der Tak 2011) with collisional rate coefficients from Yang et al. (2010). The isotope ratios are taken to be  $[^{12}\text{C}]/[^{13}\text{C}] = 77$  and  $[^{16}\text{O}]/[^{18}\text{O}] = 560$  (Wilson & Rood 1994), which gives an abundance ratio of  $\sim 7$  for  $^{13}\text{CO}$  and  $\text{C}^{18}\text{O}$ . For all temperatures considered, a  $^{13}\text{CO}/\text{C}^{18}\text{O}$  ratio below 4.0 can only be reached if the  $^{13}\text{CO}$  emission is optically thick (**Fig. 3.A.1**, left panel). When the  $\text{C}^{18}\text{O}$  emission becomes optically thick as well, the line ratio drops below 1.5 (**Fig. 3.A.1**, right panel). Taking  $[^{12}\text{C}]/[^{13}\text{C}] = 70$ , that is,  $[^{13}\text{CO}]/[\text{C}^{18}\text{O}] = 8$ , does not change these results. This thus means that the observed  $^{13}\text{CO}$  emission is generally optically thick ( $\tau > 1$ ), except maybe in the upper most layers of the disk. In addition,  $\text{C}^{18}\text{O}$  becomes optically thick in the densest regions near the midplane where  $^{13}\text{CO}/\text{C}^{18}\text{O} < 1.5$ .

<sup>1</sup><http://home.strw.leidenuniv.nl/~moldata/radex.html>

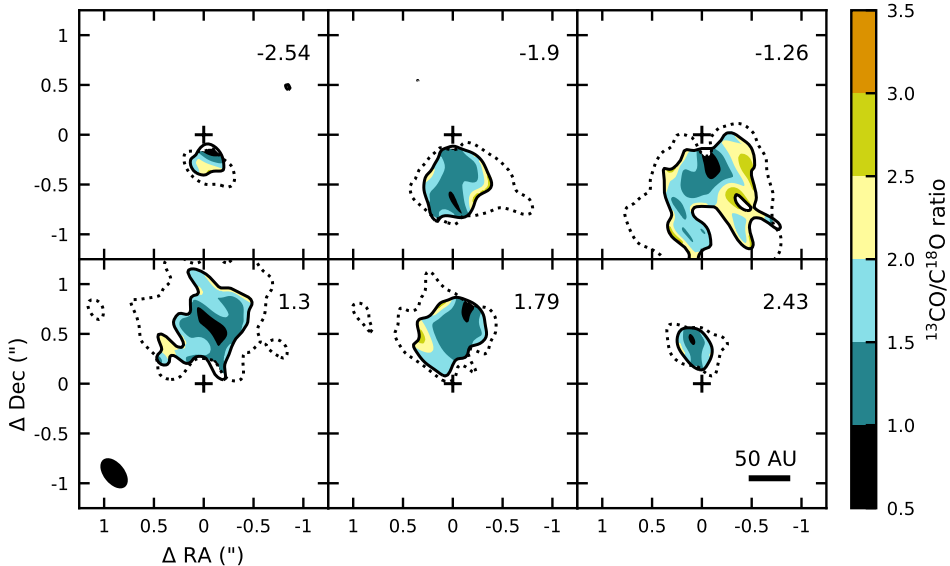


**Figure 3.2:**  $^{13}\text{CO}$  ( $J = 2 - 1$ )/ $\text{C}^{18}\text{O}$  ( $J = 2 - 1$ ) line intensity ratio in six representative velocity channels. The velocity relative to the systemic velocity of  $v_{\text{lsr}} = 5.9 \text{ km s}^{-1}$  is listed in the top right corner of each panel and the channel width is  $0.16 \text{ km s}^{-1}$ . The line ratio is only calculated in pixels with at least a  $3\sigma$  detection for both  $^{13}\text{CO}$  and  $\text{C}^{18}\text{O}$ . The dotted and solid contours mark the respective  $3\sigma$  levels. The plotted spatial scale is such as to highlight the inner  $\sim 1''$  (140 AU), that is, the disk and inner envelope. The continuum peak position is indicated with a cross and the synthesized beam is shown in the lower left corner of the lower left panel.

### 3.4.2 Gas temperature

Since the  $^{13}\text{CO}$  and  $\text{C}^{18}\text{O}$  emission is optically thick ( $\tau > 1$ ), their brightness temperatures can be used as a measure for the kinetic temperature of the gas. The brightness temperature for six representative channels is presented in **Fig. 3.3**. All channels are displayed in **Appendix 3.B**. For  $^{13}\text{CO}$ , the temperature along the midplane is above  $\sim 25 \text{ K}$ , except at  $|\Delta v| \geq 2.7 \text{ km s}^{-1}$ , where the emission is unresolved, and around  $|\Delta v| \sim 1 \text{ km s}^{-1}$ , where there may still be an effect of emission being resolved out. The  $\text{C}^{18}\text{O}$  emission is weaker than the  $^{13}\text{CO}$  emission, but the channels with resolved emission show the same result: the midplane temperature is above  $\sim 25 \text{ K}$ .

Despite the complexity of locating the radial origin of the emission (see **Sect. 3.4.3**), we can make a conservative estimate of the radial temperature profile by determining the maximum temperature in the highest velocity channels and extrapolating this assuming a radial power law dependence,

$$T = T_{\text{obs}}(R/R_{\text{obs}})^{-q}, \quad (3.1)$$

where  $T_{\text{obs}}$  and  $R_{\text{obs}}$  are the temperature and radius derived from the observations. Since the highest velocities are reached closest to the star, these channels are the least likely to be contaminated by envelope emission. Often a power law exponent of  $q = 0.5$  is used, appropriate for a blackbody flared disk with scale height  $h(r) = h_0(r/R_*)^{1.25}$  (Kenyon & Hartmann 1987), but  $q$  can range between 0.33 and 0.75 (see e.g., Adams

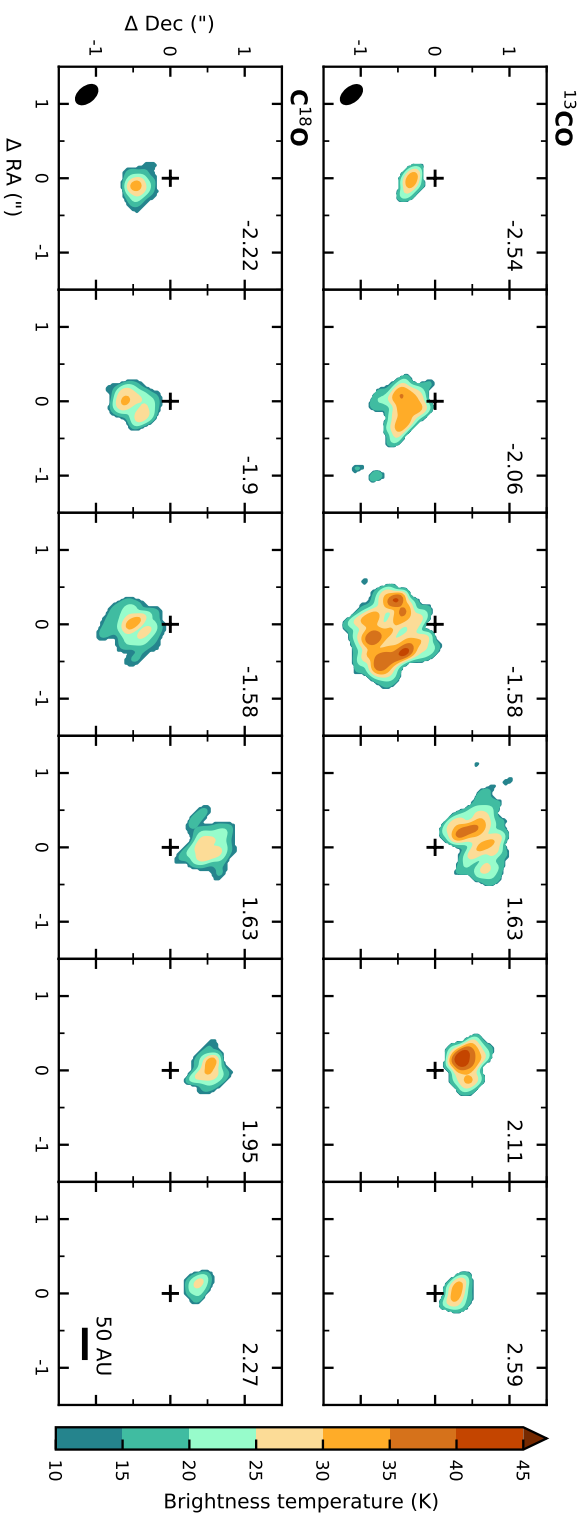


**Figure 3.3:** Brightness temperature for the  $^{13}\text{CO}$   $J = 2 - 1$  (top panels) and  $\text{C}^{18}\text{O}$   $J = 2 - 1$  (bottom panels) transitions in six representative velocity channels. Channel velocities with respect to the systemic velocity of  $v_{\text{sr}} = 5.9 \text{ km s}^{-1}$  are listed in the top right corner of each panel and the channel width is  $0.16 \text{ km s}^{-1}$ . All channels are shown in **Fig. 3.B.1** and **3.B.2**. The continuum peak position is marked with a cross and the beam is shown in the lower left corner of the left panels.

& Shu 1986; Kenyon et al. 1993; Chiang & Goldreich 1997). However, full radiative transfer modeling shows that the temperature can not be characterized by a single power law, and that the midplane temperature profile can be flatter when the disk is embedded in an envelope (e.g., Whitney et al. 2003). We therefore compared a power law with  $q = 0.5$  to the midplane temperature profile from the T13 best fit model (see **Fig. 3.4**, top panel). T13 modeled the disk continuum emission by fitting both the visibilities and images of 870  $\mu\text{m}$  and 3.4 mm observations, the multi-wavelength SED and  $L'$  scattered light images with 3D radiative transfer modeling (see **Appendix 3.C** for a more detailed description). A power law with  $q = 0.5$  appears to be steeper than the T13 profile, while adopting  $q = 0.35$  results in a better match to the T13 model between 40 and 125 AU. Assuming  $q = 0.5$  will thus likely provide a lower limit to the temperature in the outer disk.

For  $^{13}\text{CO}$ , the largest observed velocity offsets containing resolved emission are  $\Delta v = -2.54$  and  $\Delta v = 2.59 \text{ km s}^{-1}$ . The blueshifted channel has a maximum temperature of 34 K along the midplane at 42 AU ( $0.3''$  from the continuum peak position), and in the redshifted channel this is 33 K at 39 AU. Even with the rms of 4 K channel $^{-1}$ , the temperature is thus above 20 K around 40 AU within the  $3\sigma$  uncertainty. The onset of CO freeze-out is therefore expected at radii  $>40$  AU. **Figure 3.4** shows the resulting radial profiles assuming  $q = 0.5$  (middle panel) and  $q = 0.35$  (bottom panel). For  $q = 0.5$ , the temperature drops below 20 K between approximately 100 and 125 AU. Adopting the 125 AU disk radius derived by T13 this would mean that there could be a small cold outer region in the disk where CO is frozen out. A disk radius of 74 AU as determined by A17 would however mean that the entire disk is too warm for CO freeze-out. It is also expected that CO is not frozen out in a 125 AU disk for  $q = 0.35$ .

For  $\text{C}^{18}\text{O}$ , the highest velocity offsets that show resolved emission are  $\Delta v = -2.22$  and  $\Delta v = 2.43 \text{ km s}^{-1}$ . The constructed temperature profiles are very similar to those derived from  $^{13}\text{CO}$  (**Fig. 3.4**). The temperature in the blueshifted channel is probably lower because the emission does not peak along the midplane (see **Fig. 3.3**). Since the  $\text{C}^{18}\text{O}$  emission is more confined to the midplane than  $^{13}\text{CO}$ , which extends to larger heights above the midplane, the similarity in the temperature profiles suggests that the temperature measured in the midplane is not strongly affected by blending with the warmer upper layers. The observed temperatures are lower than expected based on the T13 model. In **Sect. 3.5.1**, we will discuss that the measured brightness temperature, and consequently the corresponding radial temperature profile, underestimates the kinetic gas temperature. In summary, extrapolating the temperature measured for the highest velocity material in the inner disk ( $\lesssim 40$  AU) suggest that the temperature is likely to remain  $\gtrsim 20$  K out to at least  $\sim 75$  AU, and possibly out to  $\sim 150$  AU.

The CO freeze-out temperature is  $\sim 20$  K when CO binds to pure CO ice. When CO binds to a water ice surface the freeze-out temperature is higher ( $\sim 25$  K, see e.g., Burke & Brown 2010, Fayolle et al. 2016). Assuming  $q = 0.5$ , this would mean that the snowline is at radii  $\gtrsim 50$  AU, allowing CO freeze-out in the outer disk also for a radius of 74 AU. With a power law dependence similar to the T13 profile ( $q = 0.35$ ), the disk remains  $\gtrsim 25$  K out to  $\sim 85$  AU. Thus, with measurements of the disk radius varying between 74 and 125 AU, these results indicate that a large fraction of the disk, or even the entire disk, is warm enough to prevent CO freeze-out.

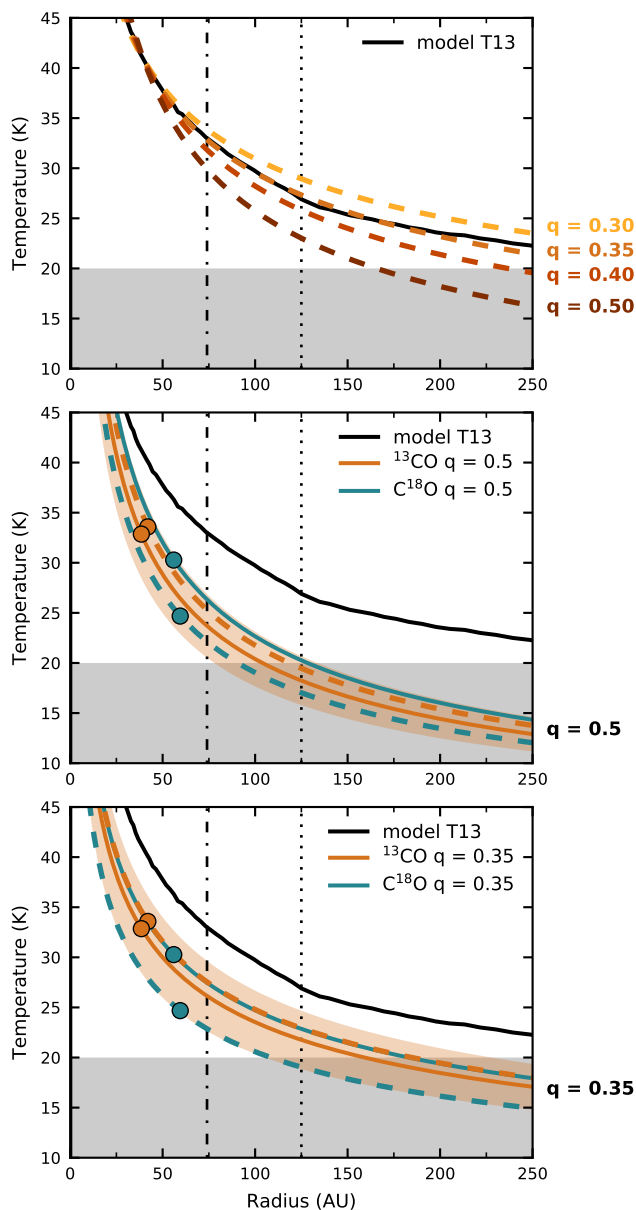


**Figure 3.4:** Radial midplane temperature profiles for the L1527 disk and inner envelope. The *top panel* shows a comparison between the temperature profile from the T13 model and power laws with different exponents ( $q$ ). In the *middle* and *bottom panels*, power law profiles are derived from  $^{13}\text{CO}$  (orange lines) and  $\text{C}^{18}\text{O}$  observations (blue lines) assuming  $q = 0.5$  and  $q = 0.35$ , respectively. Solid lines are derived from a redshifted channel, dashed lines from a blueshifted channel. The measured values are indicated by filled circles. The orange shaded area shows the  $1\sigma$  uncertainty on the solid orange line ( $^{13}\text{CO}$  from redshifted channel). The gray shaded area marks the temperature range for which CO is expected to be frozen out (i.e., below 20 K). The vertical dash-dotted line marks a disk radius of 74 AU as determined by A17, and the dotted line a disk radius of 125 AU derived by T13.

### 3.4.3 Disentangling disk and envelope emission

As mentioned above, determining the radial origin of the optically thick CO isotopologue emission is not trivial as both the disk and inner envelope contain CO. In addition, because the emission originates at the radius at which it becomes optically thick, the observed angular offset does not necessarily correspond to the physical radial offset. These problems, and their effect on the inferred power law temperature profile, can be investigated using the velocity structure of the system. To do so, we calculate the velocity along the line of sight for each position in the midplane. Then, for each  $0.16 \text{ km s}^{-1}$  velocity bin of the observations, we select the material moving at that velocity range and calculate the molecular column density along the line of sight. Finally, we convert this column density  $N$  into optical depth  $\tau$  and locate the  $\tau = 1$  surface:

$$\tau = \frac{c^3}{8\pi\nu^3} \frac{A_{ul}}{\Delta V} \frac{g_{up}N}{Q} \exp\left(\frac{-E_{up}}{kT}\right) \left(\exp\left(\frac{h\nu}{kT}\right) - 1\right), \quad (3.2)$$

where  $\nu$  and  $A_{ul}$  are the frequency and the Einstein-A coefficient of the transition, respectively,  $g_{up}$  and  $E_{up}$  are the degeneracy and energy of the upper level, respectively,  $Q$  is the partition function and  $\Delta V$  is the line width (FWHM).

We adopt the physical structure (dust density and temperature) from T13, who modeled the disk continuum emission by fitting both the visibilities and images of  $870 \mu\text{m}$  and  $3.4 \text{ mm}$  observations, the multi-wavelength SED and  $L'$  scattered light images with 3D radiative transfer modeling. Their best fit model has a disk radius of  $125 \text{ AU}$ . Inside this radius the velocity is Keplerian, while the material in the envelope has a infalling rotating velocity profile (Ulrich 1976; Cassen & Moosman 1981). More details can be found in [Appendix 3.C](#). A critical parameter for the velocity structure is the stellar mass. Tobin et al. (2012b) derived a dynamical mass of  $\sim 0.19 M_{\odot}$ , while recently A17 find a slightly larger value of  $\sim 0.45 M_{\odot}$ . Here we adopt the higher value so our estimate of the channels containing only disk emission is conservative; for lower stellar masses, envelope emission will be confined to smaller velocity offsets. We will refer to this as our fiducial model. To calculate the optical depth we assume a gas-to-dust ratio of 100 and a constant canonical CO/H abundance of  $10^{-4}$  in the region with temperatures larger than  $20 \text{ K}$ . We assume the gas temperature is equal to the dust temperature, which is a valid approximation in the dense midplane.

The resulting midplane velocity profile projected along the line of sight for the fiducial model is shown in [Fig. 3.5](#), and the midplane temperature and density structure from T13 can be found in [Fig. 3.C.3](#). For the above described parameters, velocities larger than  $\sim \pm 2.5 \text{ km s}^{-1}$  can only be reached in the disk, so these velocity channels are expected to contain only disk emission (see [Table 3.2](#)). For a  $0.19 M_{\odot}$  star, disk-only emission would be observed for velocity offsets larger than  $\sim 1.7 \text{ km s}^{-1}$ . Assuming free-fall velocity for the envelope material gives similar results (see [Fig. 3.D.1](#)). A17 use the modified free fall velocity structure from Ohashi et al. (2014), that is, the free fall velocity reduced by a factor of 0.3, and derive a disk radius of  $74 \text{ AU}$ . For these parameters, channels with velocity offsets larger than  $\sim 1.1 \text{ km s}^{-1}$  would contain emission originating only in the disk.

For a  $0.45 M_{\odot}$  star, both the disk and envelope contain material that has line-of-sight velocity offsets smaller than  $\pm 2.5 \text{ km s}^{-1}$ . What material is responsible for the emission thus depends on where the emission becomes optically thick. The  $\tau = 1$  surface for  $^{13}\text{CO}$  in five representative channels ( $\Delta v = -2.70, -2.04, 0, 2.10$  and  $2.74 \text{ km s}^{-1}$ ) is shown in [Fig. 3.6](#) (see [Fig. 3.D.2](#) for the case of a free falling envelope).



**Table 3.2:** Origin of emission at different velocity offsets.

Envelope velocity	$M_*$ ( $M_\odot$ )	Disk only ( $\text{km s}^{-1}$ )	Envelope only <sup>a</sup> ( $\text{km s}^{-1}$ )
UCM <sup>b</sup>	0.19	$v \leq -1.74; v \geq 1.79$	$0.98 \leq v \leq 1.30$
<b>UCM<sup>b</sup></b>	<b>0.45</b>	<b><math>v \leq -2.54; v \geq 2.59</math></b>	<b><math>1.47 \leq v \leq 1.79</math></b>
Free fall	0.19	$v \leq -1.74; v \geq 1.79$	$v = 0.98$
Free fall	0.45	$v \leq -2.54; v \geq 2.59$	$1.47 \leq v \leq 1.63$
Modified free fall <sup>c</sup>	0.45	$v \leq -1.10; v \geq 1.14$	$0.50 \leq v \leq 0.98$

**Notes.** The fiducial model is highlighted in boldface. A disk radius of 125 AU is adopted for all models, except in the modified free fall case where a radius of 74 AU is used (A17). For a 125 AU disk, the disk-only channels would then be  $v \leq -0.94; v \geq 0.98 \text{ km s}^{-1}$  and the envelope-only channels would be  $0.50 \leq v \leq 0.66 \text{ km s}^{-1}$ . <sup>(a)</sup> Only for  $^{13}\text{CO}$  for which the redshifted emission becomes optically thick in the envelope. <sup>(b)</sup> Infalling rotating envelope (Ulrich 1976; Cassen & Moosman 1981). <sup>(c)</sup> Free fall velocity modified by a factor 0.3 and a disk radius of 74 AU (Ohashi et al. 2014, A17).

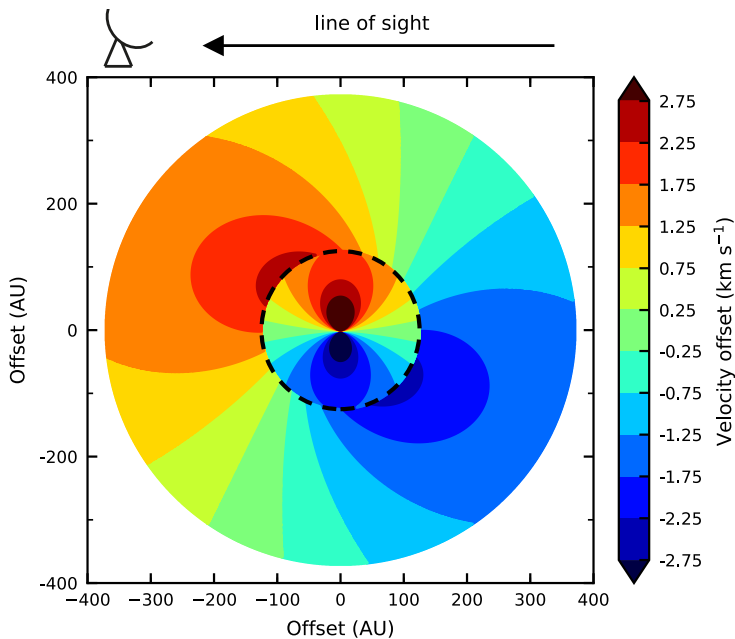


**Figure 3.5:** Face-on view of the midplane in the disk and inner envelope for the fiducial model, showing the velocity component along the line of sight (indicated by the black arrow on top of the panel; the observer is on the left). The envelope material has an infalling rotating velocity profile (Ulrich 1976; Cassen & Moosman 1981), while the disk material is rotating with Keplerian velocity. The adopted disk outer radius of 125 AU is marked by the dashed line. The outer edge of the envelope is set at the radius where the temperature in the best-fit model from T13 drops below 20 K, i.e., the CO freeze-out temperature. The adopted stellar mass is  $0.45 M_\odot$  (A17).

At blueshifted velocities the southern half of the disk is observed, as well as that part of the envelope that is behind the disk for our line of sight (see **Fig. 3.5**). The emission becomes optically thick in the disk, so the envelope is blocked from our view except at velocities where the envelope extends further south than the disk. In this case, at small angular offsets from the source center the emission originates in the disk, while emission at larger offsets traces the envelope (see **Fig. 3.6**, second column). In the redshifted channels the emission becomes optically thick in the envelope between us and the disk. At the highest velocities occurring in the envelope, disk emission will be present very close to the protostar (see **Fig. 3.6**, fourth column), while envelope emission is present at larger angular offsets. However, the angular offset of the envelope emission ( $\sim 30$  AU in this case) is smaller than the radius at which the emission originate ( $\sim 125$  AU). At lower velocities only envelope emission will be observed (see **Table 3.2**), until at velocities close to the systemic velocity the disk can be seen at the source position with envelope emission on both sides (see **Fig. 3.6**, third column). The situation is similar for  $\text{C}^{18}\text{O}$  (see **Fig. 3.6**, bottom row), except that the emission becomes optically thick in the far side of the disk (see **Fig. 3.6**, column one, two and five), instead of the near side. In addition, the emission remains optically thin in most of the envelope at redshifted velocities (for the adopted density structure; see **Fig. 3.6**, fourth column). The disk is thus not hidden from our view.

For clarity, we have neglected the dust opacity in **Fig. 3.6**. Adopting the dust opacity from T13, that is,  $\kappa = 3.1 \text{ cm}^2 \text{ g}^{-1}$  at 220 GHz, the dust would only become optically thick in the inner  $\sim 10$  AU. If the velocity profile in the envelope is free fall (**Fig. 3.D.1**), the highest envelope velocities are found along the line of sight toward the protostellar position, instead of offset to the north (for redshifted emission) or to the south (for blueshifted emission), as in the infalling rotating case. This changes the location of the  $\tau = 1$  contour at velocities that occur in both the disk and envelope (that is, columns two and four in **Fig. 3.6** will look different; see **Fig. 3.D.2** and **Table 3.2**). For blueshifted velocities, the disk will be visible south of the protostar, while envelope emission will be present to the north. For redshifted velocities, emission surrounding the protostar originates from within the envelope, while the emission furthest north is coming from the disk.

In summary, for  $M_* = 0.45 M_\odot$ , channels with velocity offsets larger than  $\sim 2.5 \text{ km s}^{-1}$  are expected to contain only the disk's emission. In contrast, channels with smaller velocity offsets show emission from both the disk and the inner envelope. The most important consequence of this is that the angular offset of optically thick emission with respect to the protostellar position in these channels does not always directly correspond to the radial position of the emitting material.

Determining exactly where the emission originates is non-trivial and requires knowledge of, amongst others, the disk radius, density structure and CO abundance. Nonetheless, a global view of the temperature in the disk and inner envelope can be obtained through the brightness temperature in the different velocity channels. As shown in **Sect. 3.4.2**, for both  $^{13}\text{CO}$  and  $\text{C}^{18}\text{O}$  the temperature along the midplane is above  $\sim 25$  K at all velocities, suggesting a warm disk and inner envelope. The highest velocity channels that contain resolved  $^{13}\text{CO}$  emission, and were used to construct the radial temperature profile, are  $\Delta v = -2.54$  and  $\Delta v = 2.59 \text{ km s}^{-1}$ . For stellar masses  $\leq 0.45 M_\odot$ , these channels are indeed expected to trace only the disk. The velocity offsets used for  $\text{C}^{18}\text{O}$  are slightly smaller ( $\Delta v = -2.22$  and  $\Delta v = 2.43 \text{ km s}^{-1}$ ), and could be contaminated by envelope emission if the stellar mass is  $0.45 M_\odot$ . How-

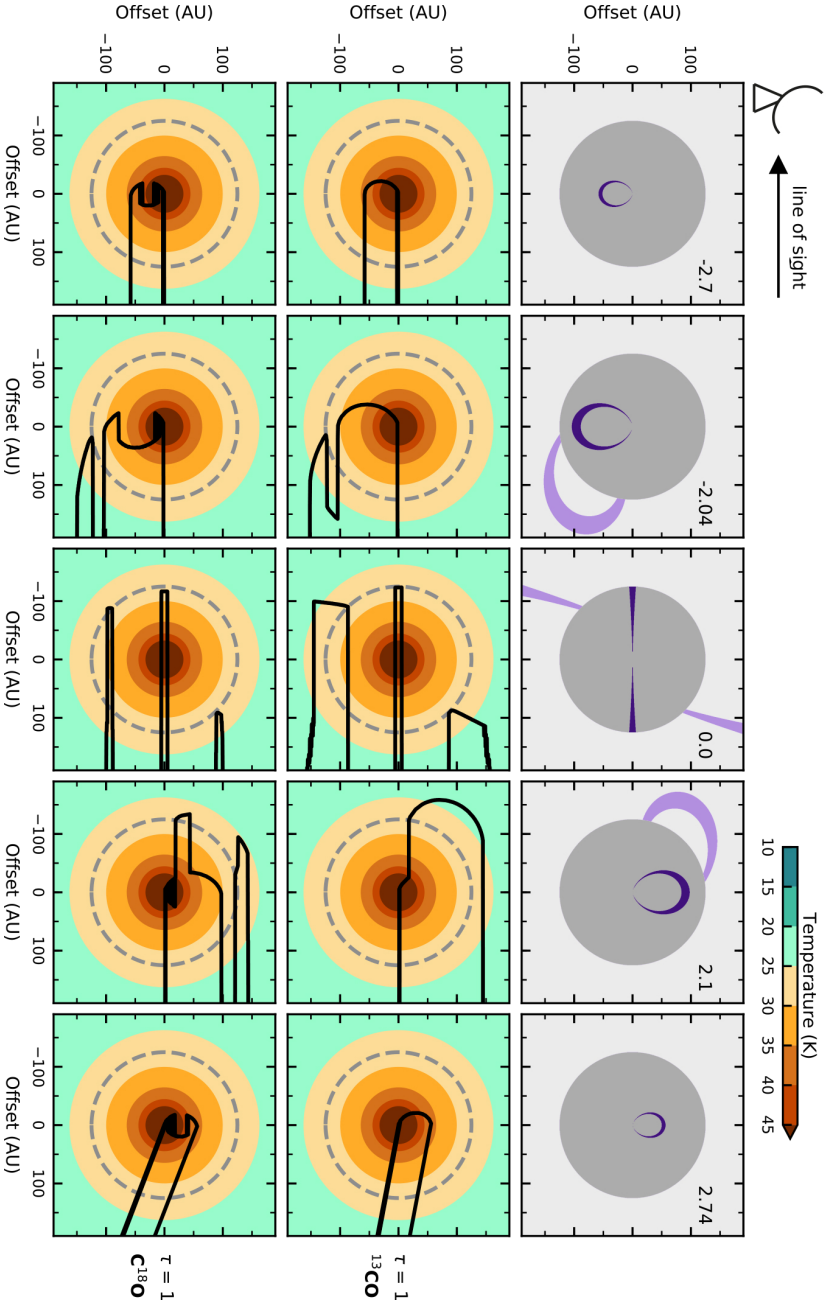


**Figure 3.6:** Five representative velocity channels to illustrate where in the system the  $^{13}\text{CO}$  and  $\text{C}^{18}\text{O}$  emission originates for the fiducial model with a constant  $\text{CO}/\text{H}$  abundance of  $10^{-4}$ . The velocity profile in the disk is Keplerian and the envelope material is rotating and infalling (see Fig. 3.5). The top panels show the material moving at the line-of-sight velocity (with respect to the systemic velocity of  $5.9 \text{ km s}^{-1}$ ) indicated in the top right corner. Material in the disk (dark gray circle) is depicted in dark purple, envelope material in light purple. The solid black line in the middle and bottom panels marks the  $\tau = 1$  surface for an observer located on the left for  $^{13}\text{CO}$  and  $\text{C}^{18}\text{O}$ , respectively. The color scale represents the temperature in the best-fit model from T13 and the dashed line indicates the adopted disk outer radius of 125 AU.

ever, unlike for  $^{13}\text{CO}$ , the redshifted  $\text{C}^{18}\text{O}$  emission is expected to become optically thick mostly in the disk and not already in the envelope. Moreover, the measured temperatures are similar as for  $^{13}\text{CO}$ .

Depending on the stellar mass and the envelope velocity structure, a number of redshifted velocity channels are predicted to contain only  $^{13}\text{CO}$  emission from the inner envelope (see **Table 3.2**). For  $M_* \leq 0.45 M_\odot$ , these channels have velocity offsets smaller than  $1.79 \text{ km s}^{-1}$ . In all these channels the  $^{13}\text{CO}$  brightness temperature remains above  $\sim 25 \text{ K}$  (see **Fig 3.B.1**). So if this emission indeed originates in the inner envelope, the temperature in that region would be higher than  $25 \text{ K}$ . However, the power law temperature profile predicts inner-envelope temperatures of  $\sim 15\text{--}22 \text{ K}$ . This could mean that there is a jump in the temperature between the disk and inner envelope. Such a jump, albeit stronger, has been suggested by Sakai et al. (2014b) based on observations of SO. Or alternatively, the temperature profile is less steep than shown in **Fig. 3.4**, assuming the temperature derived for the inner disk is not underestimated. The inner disk temperature is determined from channels expected to contain only disk emission, and is thus not likely to be underestimated due to envelope contamination (see **Fig. 3.6**). A shallower temperature profile would mean a warmer disk with temperatures  $\gtrsim 25 \text{ K}$  for all radii (125 AU).

## 3.5 Modeling of the line emission

### 3.5.1 $^{13}\text{CO}$ and $\text{C}^{18}\text{O}$

Based on the brightness temperature in the  $^{13}\text{CO}$  and  $\text{C}^{18}\text{O}$  channels, the disk and inner envelope are likely to have midplane temperatures above the CO freeze-out temperature of  $\sim 20 \text{ K}$ . However, a power law temperature profile based on the temperature at the highest velocity offsets suggests that there may still be a cold outer region in the disk. To study in more detail the effect of CO freeze-out on the emission, we simulate  $^{13}\text{CO}$  and  $\text{C}^{18}\text{O}$  emission for three different scenarios (see **Fig. 3.7**). The focus lies on determining whether the observations can show the difference between a completely warm disk and a disk with a cold outer midplane. The first model (“warm” model) consists of a warm disk that has no CO freeze-out. In the second case (“intermediate” model), there is a small region in the outer disk where CO is frozen out, and in the third model (“cold” model) the temperature is only high enough to have gaseous CO in the innermost region of the disk and in the surface layers. In all models CO is present in the gas phase in the inner envelope. Models without CO in the envelope cannot reproduce the angular extent of the observed emission.

The exact distribution of CO in the different models is based on a simple parametrization: for  $T \geq 20 \text{ K}$  CO is present in the gas phase at a constant abundance of  $10^{-4}$  (w.r.t. H), while for  $T < 20 \text{ K}$  CO is frozen out and the abundance is set to zero. For the warm model we adopt the temperature structure of the T13 model, because the temperature is above  $\sim 25 \text{ K}$  in the entire disk (see **Fig. 3.C.1**). For the intermediate and cold models, the T13 temperature is scaled down by a factor to create regions with  $T < 20 \text{ K}$  (schematically shown in **Fig. 3.7**). For the intermediate model the temperature is lowered by 40% and for the cold model by 60%, resulting in a CO snowline at 71 AU and 23 AU, respectively (see **Fig. 3.C.1**). In the intermediate model, 25% of the mass within 125 AU (disk outer radius) has  $T < 20 \text{ K}$ . In the cold model this is 70%, roughly consistent with the result from Kama et al. (2016) that in TW Hya  $\sim 60\%$  of

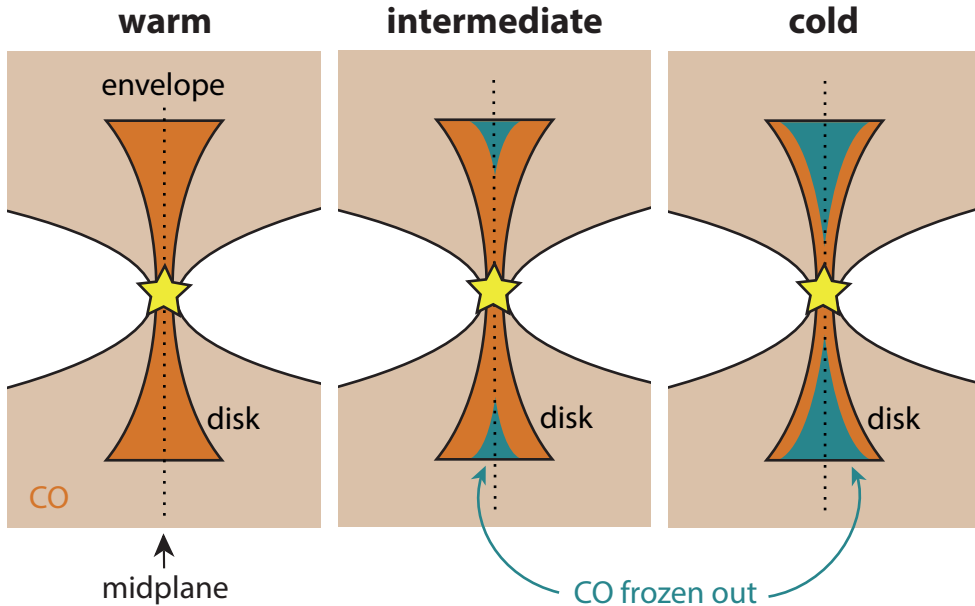


**Figure 3.7:** Three different models for the CO distribution in the L1527 disk. *Left panel:* a warm disk with no CO freeze out. *Middle panel:* a slightly colder disk where CO is frozen out in the outer most region ( $R > 71$  AU) near the midplane. *Right panel:* a cold disk where gaseous CO is only present in the inner most region ( $R < 23$  AU) and in the surface layers. CO is present in the gas phase in the inner envelope in all models.

the dust mass has temperatures below 20 K. The cold model thus resembles a Class II disk. Although for the intermediate and cold model the temperature is lowered to create CO freeze-out regions, the fiducial temperature is used for the excitation calculation. This way the emission from the surface layers is not reduced through an excitation effect. If these regions would in fact also be colder, the difference with the fiducial warm model would increase.

The  $^{13}\text{CO}$  and  $\text{C}^{18}\text{O}$  emission for the three models is simulated with the 3D radiative transfer code LIME (Brinch & Hogerheijde 2010). Again, the velocity inside the disk ( $R < 125$  AU) is Keplerian and the envelope material has an infalling rotating velocity profile. The inclination is set to  $85^\circ$ , that is,  $5^\circ$  offset from edge-on with the disk and envelope west of the protostar tilted toward the observer (see **Fig. 3.C.2**). This is the same orientation as used by Tobin et al. 2008 and T13, but opposite to the results presented by Oya et al. 2015. However, none of our conclusions are sensitive to how the inclination is defined. Synthetic images with the same beam as the observations are then generated in CASA by using a modified version of the task `symobserve` that calculates visibilities for the observed  $uv$ -coverage (`symobs_custom`, Attila Juhász). The continuum subtracted visibilities were then imaged to the noise level of the observations (see **Table 3.1**). In addition, emission was simulated for a five hour integration (compared to 25 minutes for the observations) at an angular resolution similar to that of the observations.

The by eye best matching model and lowest residuals are reached for a stellar mass of  $0.4 M_\odot$ , although the envelope emission in the low and intermediate velocity

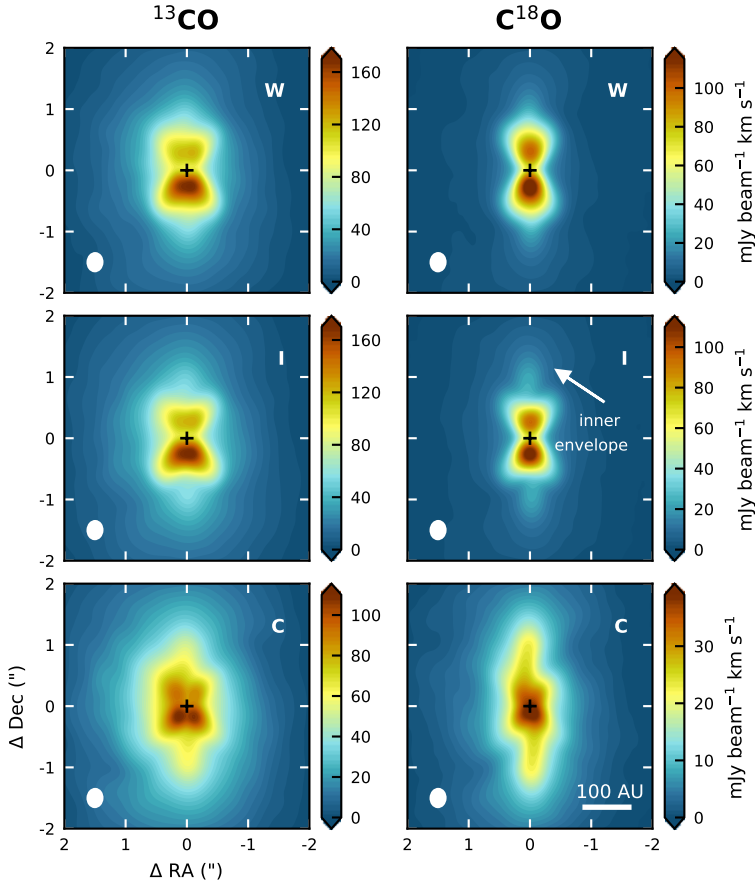


**Figure 3.8:** Integrated intensity (zeroth moment) maps for  $^{13}\text{CO}$  (left panels) and  $\text{C}^{18}\text{O}$  (right panels) in the warm (W; top row), intermediate (I; middle row) and cold (C; bottom row) model. Emission is simulated for a five hour integration using an ALMA configuration resulting in a similar beam size as the observations. The intensity (color) scale is different for each panel. The position of the continuum peak is marked by a black cross and the beam is shown in the lower left corner of the panels.

channels is slightly overproduced for  $^{13}\text{CO}$ . This could be because a canonical CO abundance of  $10^{-4}$  is too high for the more tenuous envelope where photodissociation may play an important role in destroying CO, unlike in the denser disk midplane where UV radiation cannot penetrate (see e.g., Visser et al. 2009a). Another reason could be because the large-scale cloud emission is not taken into account in the model. The effect of emission being resolved out is not as large in the simulated images as it is in the observations, that is, the simulated images still show some emission in the central most channels while the observations do not. We will therefore restrict the comparison between observations and models to velocities  $\Delta v > 1.1 \text{ km s}^{-1}$ . Lower stellar masses give lower residuals in the intermediate velocity channels, but cannot reproduce the disk emission, consistent with the results from Ohashi et al. (2014). Since our goal is not to model the CO isotopologue emission exactly, but to focus on the effect of CO

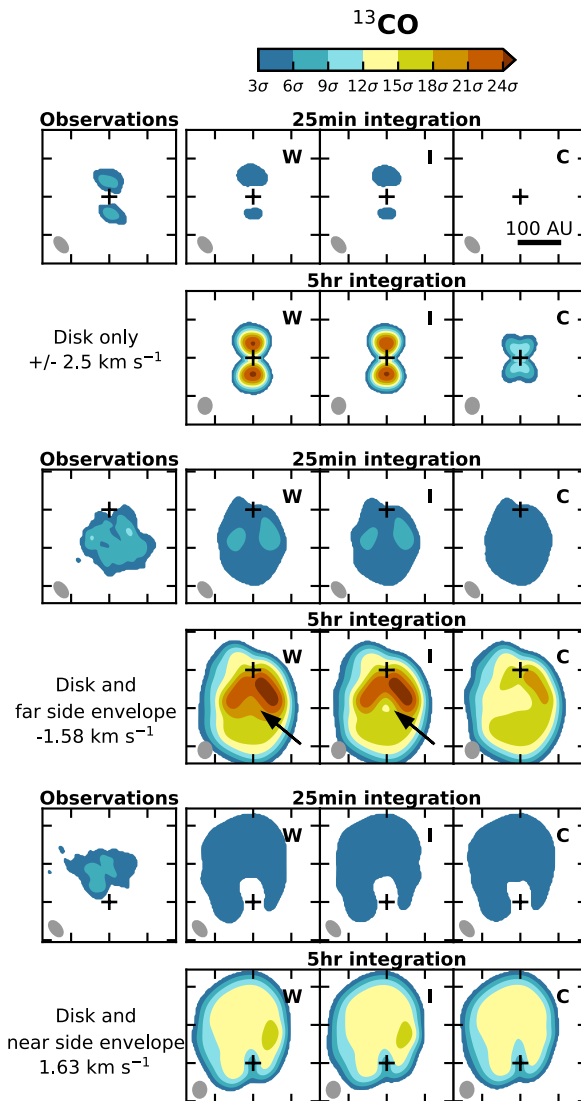


**Figure 3.9:** Comparison between the  $^{13}\text{CO}$  observations (*left column*) and the three different models (see **Fig. 3.7**): warm (W, *second column*), intermediate (I, *third column*), and cold (C, *fourth column*). Emission is simulated with the same visibilities as the observations (25 minutes integration) and for a longer integration time of five hours in a configuration producing a similar beam size. Four representative velocity channels are shown. The *top panels* show emission at  $\pm 2.5 \text{ km s}^{-1}$ , which is expected to originate in the disk. The *middle panels* show blueshifted emission from the disk and far side of the envelope ( $\Delta v = -1.58 \text{ km s}^{-1}$ ), and the *bottom panels* show redshifted emission from the disk and near side of the envelope ( $\Delta v = 1.63 \text{ km s}^{-1}$ ). The color scale is in steps of  $3\sigma$ , which corresponds to  $30.6$  ( $8.8$ )  $\text{mJy beam}^{-1} \text{ channel}^{-1}$  for an integration time of 25 minutes (five hours). The black arrow denotes the difference between the warm and intermediate model, which becomes clear for a five hour integration. The position of the continuum peak is marked by a cross; the vertical scale is the same for all velocities, but slightly shifted. The beam is shown in the lower left corner of each panel.

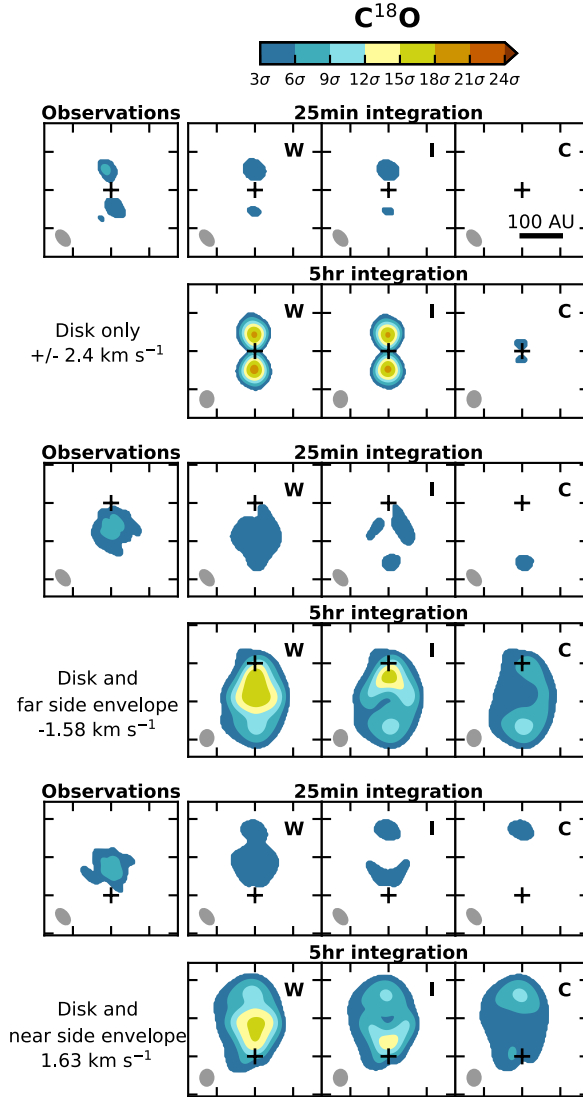


**Figure 3.10:** As Fig. 3.9, but for C<sup>18</sup>O. The 3 $\sigma$  level corresponds to 26.1 (7.5) mJy beam<sup>-1</sup> channel<sup>-1</sup> for an integration time of 25 minutes (five hours).

freeze-out in the disk, we show the results of the 0.4  $M_{\odot}$  models. The only difference between these models and the fiducial model presented in Sect. 3.4.3 is thus the stellar mass (0.4  $M_{\odot}$  instead of 0.45  $M_{\odot}$ ). However, the overall conclusions are valid for stellar masses between 0.19 and 0.5  $M_{\odot}$ .

An overview of the moment zero maps for the models with five hour integrations is presented in Fig. 3.8. Four representative velocity channels are shown in Figs. 3.9 and 3.10 for both integration times, along with the observations. The warm disk model matches the observations for both molecules quite well. The model slightly underpredicts (3–6 $\sigma$  residuals) the compact emission ( $< 0.5''$ ), and overpredicts (3 $\sigma$



residuals) the envelope emission, especially for  $^{13}\text{CO}$ , as discussed above. The cold model is clearly the worst match for both species, as it cannot reproduce the observed intensity. In addition, it predicts similar intensities in the disk and inner envelope (see **Fig. 3.8**), unlike what is observed (see **Fig. 3.1**).

With the current observations, the intermediate disk model with CO frozen out at midplane radii larger than 71 AU would be indistinguishable from the warm disk model using  $^{13}\text{CO}$  emission. A five hour integration would yield high enough signal to noise to distinguish both scenarios using intermediate blueshifted velocities (see **Fig. 3.9**). However, for  $\text{C}^{18}\text{O}$  the warm model is a better match to the data than the intermediate model (see **Fig. 3.10**). This difference can be explained with the  $\text{C}^{18}\text{O}$  isotopologue being less abundant than the  $^{13}\text{CO}$  isotopologue. For the blueshifted velocities (see **Fig. 3.6**, second column), the  $^{13}\text{CO}$  emission becomes optically thick in the inner envelope behind the disk when CO is absent in the outer disk. If the temperature in this region is similar to the temperature in the outer disk, the observed emission will hardly change. The  $\text{C}^{18}\text{O}$  emission on the other is expected to remain optically thin out to larger radii, probing different physical conditions deeper in the envelope. At redshifted velocities (see **Fig. 3.6**, fourth column), the  $^{13}\text{CO}$  emission becomes already optically thick in the inner envelope, blocking the outer disk from our view. Whether CO is present in the outer disk or not thus has no effect on the observations. The  $\text{C}^{18}\text{O}$  emission does not become optically thick in the envelope, so changes in the disk are visible. The effect of CO being frozen out in the outer disk is therefore likely to be stronger for the  $\text{C}^{18}\text{O}$  than the  $^{13}\text{CO}$  emission, and the less abundant  $\text{C}^{18}\text{O}$  seems to be a more sensitive diagnostic of the distribution of gas-phase CO in the disk. Removing CO at disk radii  $> 71$  AU does indeed significantly affect the  $\text{C}^{18}\text{O}$  emission, providing a worse match to the observations than the warm disk model. This is amplified for the cold disk model with CO frozen out at radii  $> 23$  AU, and for five hour integrations. The intermediate and warm model can be distinguished using  $^{13}\text{CO}$  if the reduced temperatures, used to set the CO freeze-out region in the intermediate and cold models, are also used for the excitation calculation. In that case, the blueshifted channels (**Fig. 3.9**, middle panels) for the intermediate model are similar to those of the cold model instead of the warm model. A disk with temperatures reduced by 40% (w.r.t the T13 model) throughout is thus unlikely. In summary, these modeling results thus suggest that gaseous CO is likely present in the entire disk.

The accuracy of the midplane temperature derived from the  $^{13}\text{CO}$  and  $\text{C}^{18}\text{O}$  observations can be assessed by computing a power law temperature profile from the synthetic images for the warm disk model (25 minutes integration) in the same way as done for the observations. The resulting profiles (**Fig. 3.11**, top panel) are much colder than the input midplane temperature of the models, suggesting that the observationally derived temperature is systematically lower than the actual temperature. Moreover, these profiles are also colder than those derived from the observations. This means that the disk midplane may be warmer than the temperature profile derived by T13 from the continuum emission, which has a temperature of  $\sim 26$  K at the disk outer radius, because the underlying temperature profile will be substantially higher than the observationally derived one. This may be because of colder gas along the line of sight. Another effect that plays a role is beam dilution, because concatenating the high resolution data shown here with the data taken in a more compact figuration results in  $\sim 10$  K lower brightness temperatures ( $\sim 0.1''$  larger beam). Higher resolution observations may thus provide more accurate temperatures.

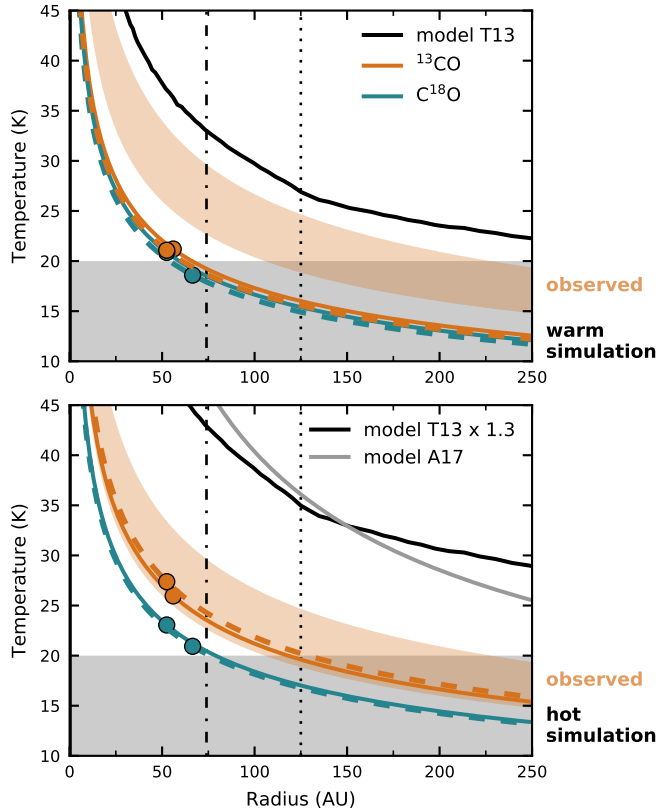


**Figure 3.11:** Power law temperature profiles ( $q = 0.35$ ) as shown in Fig. 3.4, but now derived from images simulated with the observed  $uv$ -coverage (25 minutes integration). The *top panel* shows the results for the warm model, that is, the fiducial T13 temperature structure. The *bottom panel* shows the results for the hot model, that is, the T13 temperature increased by 30%. The black lines show the midplane temperature profile in the corresponding models used to generate the images. The gray line represents the midplane temperature used by A17. The shaded orange area marks the  $1\sigma$  uncertainty on the temperature profile derived from the observations ( $^{13}\text{CO}$ , redshifted channel), as shown in Fig. 3.4.

To examine what temperature would be required to reproduce the observed brightness temperature, models were run with the T13 disk temperature increased by a certain percentage. Increasing the temperature by 30% (hot model) results in a midplane temperature profile similar to that adopted by A17 (see Fig. 3.11, bottom panel). The power law profile derived for this model from  $^{13}\text{CO}$  emission is within the  $1\sigma$  uncertainty for the observations, although the  $\text{C}^{18}\text{O}$  profiles are a few Kelvin colder (Fig. 3.11). These results suggest that the L1527 disk could be warmer than 35 K.

### 3.5.2 CO abundance

The underabundance of gaseous CO in Class II disks, with respect to the ISM abundance of  $10^{-4}$  (w.r.t. H), has been attributed to photodissociation in the upper layers of the disk and freeze-out near the outer disk midplane (Dutrey et al. 1997; van Zadel-

hoff et al. 2001). However, recent detailed studies of in particular TW Hya suggest that on top of this, CO is also depleted in the warm molecular layer and inside its snowline (Favre et al. 2013; Nomura et al. 2016; Schwarz et al. 2016). Moreover, a general carbon depletion was inferred from [C I] lines (Kama et al. 2016). Low CO abundances are also observed for protostellar envelopes (Anderl et al. 2016), and results from large protoplanetary disk surveys with ALMA show that this may be a common feature for Class II disks. For many disks in several star forming regions, CO (isotopologue) emission, and the subsequently derived gas masses and gas-to-dust ratios, are up to two or three orders of magnitude lower than expected (Ansdell et al. 2016, 2017; Barenfeld et al. 2016; Long et al. 2017). The main question now is whether these low CO-derived gas masses are the result of CO depletion or a sign of rapid gas loss (e.g., Miotello et al. 2017). Determining CO abundances during earlier stages of disk evolution may help solve this puzzle.

Given that the  $^{13}\text{CO}$  and  $\text{C}^{18}\text{O}$  emission toward L1527 is optically thick, deriving column densities and abundances is difficult. But we can invert this argument and use radiative transfer modeling to assess the CO abundance required for both molecules to be optically thick. Therefore, we made synthetic  $^{13}\text{CO}$  and  $\text{C}^{18}\text{O}$  ALMA images for the warm disk model with a constant CO abundance of  $10^{-5}$ , instead of  $10^{-4}$  as described in Sect. 3.5.1. The resulting moment zero maps (constructed using velocities  $\Delta v > 1.1 \text{ km s}^{-1}$ ) presented in Fig. 3.12 suggest that reducing the CO abundance by an order of magnitude would give only a  $6\sigma$  detection of  $^{13}\text{CO}$  (peak flux of  $67 \text{ mJy beam}^{-1} \text{ km s}^{-1}$ ), while the observed signal-to-noise ratio is  $15\sigma$  (peak flux of  $125 \text{ mJy beam}^{-1} \text{ km s}^{-1}$  when using the same velocity range as for the simulated images). Moreover,  $\text{C}^{18}\text{O}$  would only be detected at the  $2\sigma$  level (peak flux of  $20 \text{ mJy beam}^{-1} \text{ km s}^{-1}$ ), while it is observed at  $14\sigma$  (peak flux of  $101 \text{ mJy beam}^{-1} \text{ km s}^{-1}$ ). The  $^{13}\text{CO}/\text{C}^{18}\text{O}$  line ratios (not shown) are also higher than observed; generally larger than  $\sim 3.5$ , indicating that the  $\text{C}^{18}\text{O}$  emission is not optically thick and even the  $^{13}\text{CO}$  emission becomes optically thin in some regions. A canonical CO abundance thus produces a better match to the observations than an order of magnitude reduction.

Based on modeling of  $\text{C}^{18}\text{O}$  ALMA observations, A17 suggested a local enhancement of  $\text{C}^{18}\text{O}$  at the disk-envelope interface (that is, an ISM abundance between 80 and 88 AU), and a factor  $\sim 20$  lower abundance in the disk. However, none of the results presented here show an immediate need for a reduced CO abundance in the disk compared to the disk-envelope interface. On the contrary, a constant ISM abundance slightly underpredicts the emission within  $\sim 0.5''$  instead of overpredicting it.

### 3.5.3 $\text{N}_2\text{D}^+$

$\text{N}_2\text{H}^+$  has been shown to trace cold ( $T \lesssim 20 \text{ K}$ ) and dense ( $n > 10^5 \text{ cm}^{-3}$ ) prestellar and protostellar environments where CO is frozen out (e.g., Bergin et al. 2001; Caselli et al. 2002a; Jørgensen et al. 2004a). Another chemical effect of low temperatures and CO freeze-out is the enhancement of deuterated molecules, such as  $\text{N}_2\text{D}^+$  (e.g., Caselli et al. 2002b; Crapsi et al. 2005; Roberts & Millar 2007). With the resolution provided by ALMA,  $\text{N}_2\text{H}^+$  emission has been spatially resolved in a few protoplanetary disks, where it was shown to originate outside the CO snowline (Qi et al. 2013b, 2015). Recently,  $\text{N}_2\text{D}^+$  has also been observed toward one T Tauri and one Herbig disk (Huang & Öberg 2015; Salinas et al. 2017, respectively). In both cases the mea-

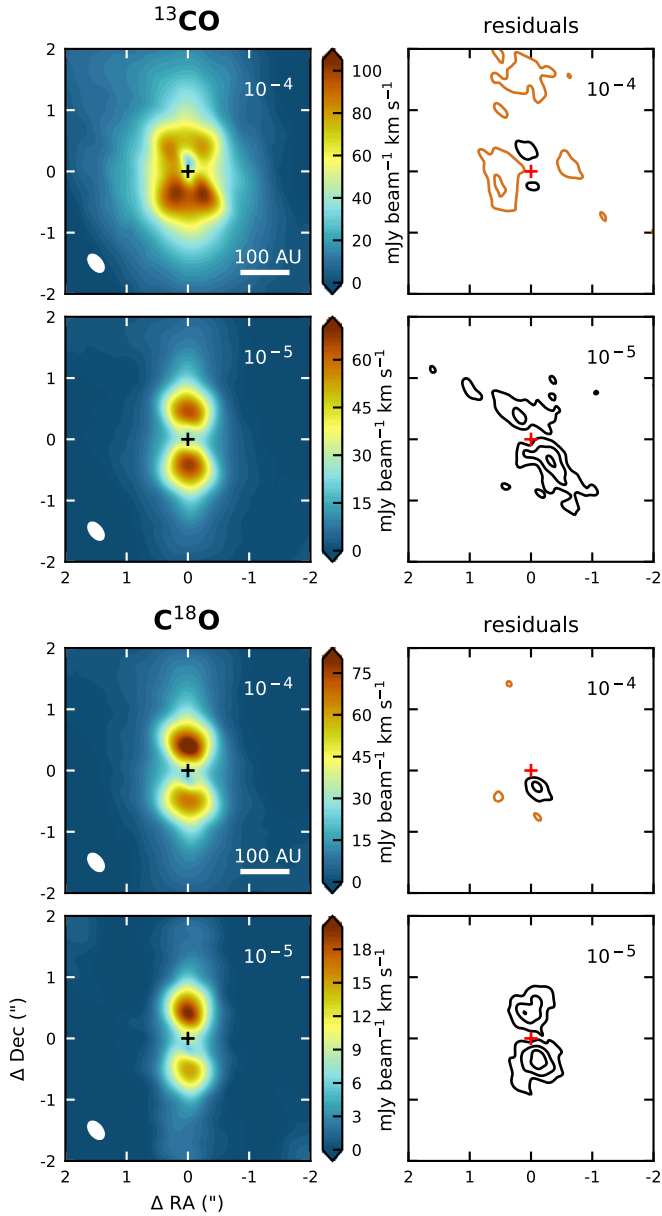


**Figure 3.12:** Integrated intensity (zeroth moment) maps (*left column*) for  $^{13}\text{CO}$  (*top rows*) and  $\text{C}^{18}\text{O}$  (*bottom rows*) in the warm model with a constant CO abundance of  $10^{-4}$  (*first and third row*) and  $10^{-5}$  (*second and fourth row*). The emission is simulated with the observed  $uv$ -coverage (25 minutes integration). The intensity (color) scale is different for each panel. The *right column* shows the residuals obtained by subtracting the models from the observations. Black contours are in steps of  $3\sigma$  starting at  $3\sigma$ , while orange contours are in steps of  $-3\sigma$  and start at  $-3\sigma$ . For  $^{13}\text{CO}$  ( $\text{C}^{18}\text{O}$ ),  $3\sigma$  corresponds to  $25.9$  ( $21.8$ )  $\text{mJy beam}^{-1} \text{ km s}^{-1}$ . The position of the continuum peak is marked by a cross and the beam is shown in the lower left corner of the moment zero maps.

sured  $\text{N}_2\text{D}^+/\text{N}_2\text{H}^+$  ratio of 0.3–0.5 matches the highest values found for protostellar envelopes (Emprechtinger et al. 2009; Tobin et al. 2013a). The latter single dish studies find one of the lowest  $\text{N}_2\text{D}^+/\text{N}_2\text{H}^+$  ratios for L1527 ( $< 0.001$ ) in samples of  $\sim 20$  protostars.

So far, no observations of  $\text{N}_2\text{H}^+$  have been carried out for the L1527 disk. Based on a small chemical network for  $\text{N}_2\text{H}^+$  (van 't Hoff et al. 2017; **Chapter 2**), abundances of  $\sim 10^{-10}$  are expected for the densities in the T13 model if CO freeze-out would occur. This chemical model incorporates the main formation and destruction processes for  $\text{N}_2\text{H}^+$ , as well as freeze-out, thermal desorption and photodissociation of CO and  $\text{N}_2$ . An  $\text{N}_2\text{H}^+$  abundance of  $\sim 10^{-10}$  is consistent with predictions from full chemical models (e.g., Walsh et al. 2012; Aikawa et al. 2015). If the  $\text{N}_2\text{D}^+/\text{N}_2\text{H}^+$  ratio in the disk were similar to the value in the envelope (i.e.,  $< 0.001$ ), an  $\text{N}_2\text{D}^+$  abundance  $\lesssim 10^{-13}$  (w.r.t. H) would be expected in the disk. To assess whether the observations are sensitive enough to have detected  $\text{N}_2\text{D}^+$  abundances  $\lesssim 10^{-13}$ , synthetic images were created for the intermediate and cold disk model. In these models,  $\text{N}_2\text{D}^+$  is present at constant abundance throughout the CO freeze-out region. Based on these simulations, only abundances  $\gtrsim 10^{-11}$  could have been detected with the observations presented here. These findings can also be phrased in terms of column density. For the intermediate model, that is,  $\text{N}_2\text{D}^+$  present outside 71 AU, the  $\text{N}_2\text{D}^+$  column density along the midplane for an abundance of  $10^{-13}$  is  $3 \times 10^{10} \text{ cm}^{-2}$ . This is two orders of magnitude lower than the upper limit derived from the observations ( $\sim 2 - 4 \times 10^{12} \text{ cm}^{-2}$ ). Even for the cold model with  $\text{N}_2\text{D}^+$  at radii  $> 23$  AU, which cannot reproduce the CO observations, the  $\text{N}_2\text{D}^+$  column density would still be an order of magnitude below the observed upper limit. The observations thus seem not sensitive enough to completely rule out the presence of  $\text{N}_2\text{D}^+$  in the outer disk.

However, Emprechtinger et al. (2009) found that the lowest  $\text{N}_2\text{D}^+/\text{N}_2\text{H}^+$  ratios were seen at the highest dust temperatures. In particular, the low ratio for L1527 suggests dust temperatures above  $\sim 25$  K on envelope scale. If the deuterium fractionation in the disk is similar to that in the envelope, this would then be in agreement with a warm disk.

## 3.6 Discussion

Based on analysis and modeling of the optically thick  $^{13}\text{CO}$  and  $\text{C}^{18}\text{O}$  emission observed with ALMA, the young disk around L1527 is likely to be warm enough to prevent CO from freezing out ( $T \gtrsim 20\text{--}25$  K). This is in contrast with observations of more evolved Class II disks which are shown to have relatively large cold outer regions where CO is frozen onto dust grains.

The main difficulty in characterizing the physical properties of young disks is disentangling disk emission from emission originating in the envelope. As shown in **Sect. 3.4.3**, a rough division can be made kinematically, but it becomes more complicated if the emission is optically thick. In the latter case, the angular offset at which emission is observed no longer correlates to the physical radius at which the radiation is emitted. Therefore, careful analysis is required when characterizing disks that are still embedded in their envelope.

Although an accurate determination of the origin of the optically thick  $^{13}\text{CO}$  and  $\text{C}^{18}\text{O}$  emission requires detailed knowledge of the systems physical structure, our inferred power law temperature profile does not depend on these parameters. In the

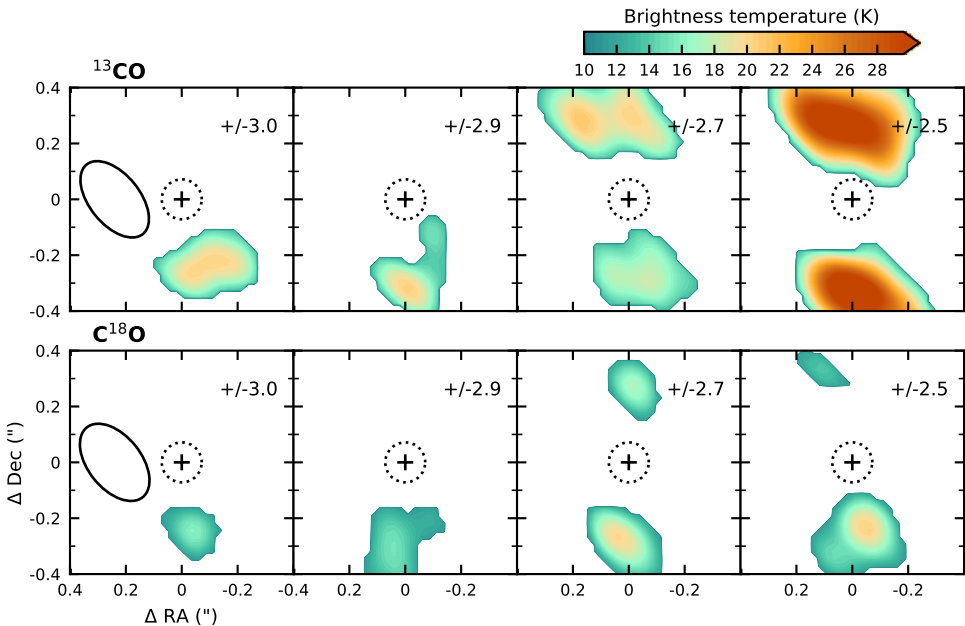


**Figure 3.13:** Magnification of the highest velocity channels for  $^{13}\text{CO}$  (*top panels*) and  $\text{C}^{18}\text{O}$  (*bottom panels*), highlighting that the emission centroid does not move closer to the continuum peak position (marked with a cross) with increasing velocity offset. Only emission above the  $3\sigma$  level is shown. The velocity relative to the systemic velocity of  $v_{\text{lsr}} = 5.9 \text{ km s}^{-1}$  is listed in the top right corner of each panel. For each velocity offset, both blue- (south of source position) and redshifted emission (north of source position) are shown in the same panel. The dotted contour marks the inner 10 AU where the T13 model predicts the continuum to be optically thick. The black contour in the left panels shows the synthesized beam.

analysis, the midplane velocity component along the line of sight is used to predict the velocities that contain only disk emission. This velocity component depends on the stellar mass, disk radius and envelope velocity profile. For both the T13 model ( $M_{\star} = 0.19M_{\odot}$ ,  $R_{\text{disk}} = 125 \text{ AU}$ , and infalling rotating envelope) and the A17 model ( $M_{\star} = 0.45M_{\odot}$ ,  $R_{\text{disk}} = 74$ , and a reduced free fall velocity in the envelope), emission at  $|\Delta v| \geq 2.6 \text{ km s}^{-1}$  is expected to originate only in the disk. The infalling rotating velocity profile predicts higher envelope velocities than the reduced free fall profile, but even for a central mass of  $0.45 M_{\odot}$  no envelope contamination is expected at  $|\Delta v| \geq 2.6 \text{ km s}^{-1}$ . So independent of the assumed model, the brightness temperature at  $|\Delta v| \geq 2.6 \text{ km s}^{-1}$  is likely to probe the temperature in the disk.

### 3.6.1 Dust opacity

To study whether the observations can distinguish between a warm and cold disk, we use the best-fit model from T13, which was obtained by fitting 3D radiative transfer models to sub/millimeter dust emission and infrared scattered light. As pointed out by the authors, the most robust parameters are the disk radius and vertical height. Meanwhile, the disk mass and radial density profile are the most degenerate parameters. Both depend on assumptions made for the dust opacity. Interesting in this

respect is that the observations of the CO isotopologues presented here hint at the 1.3 mm continuum being optically thick close to the protostar. As can be seen in **Fig. 3.13**, the centroids of both the  $^{13}\text{CO}$  and  $\text{C}^{18}\text{O}$  emission remain offset from the stellar position even at the highest velocities. This can be caused by the dust being optically thick in this inner region, obscuring the CO emission. For the T13 density structure and dust opacity ( $\kappa = 3.1 \text{ cm}^2 \text{ g}^{-1}$  at 200 GHz), the continuum becomes optically thick in the inner  $\sim 10$  AU. If the dust is indeed optically thick in the inner disk, the dust mass derived by T13 may be underestimated by a factor of a few. This could lead to our modeled CO isotopologue emission being more optically thin than in the observations, and therefore modeled brightness temperature to be slightly lower than observed. Modeling of higher resolution multi-wavelength observations is needed to better constrain the dust opacity.

### 3.6.2 Comparison with other observations

#### L1527

A good consistency check is to determine whether a warm disk is consistent with the observed luminosity and mass accretion rate. For L1527, mass accretion rates between  $\sim 6.6 \times 10^{-7} M_{\odot} \text{ yr}^{-1}$  (Tobin et al. 2012b, for a  $0.19 M_{\odot}$  star assuming  $L_{\text{acc}} = GM\dot{M}/R_{\star}$ ) and  $\sim 1.8 \times 10^{-6} M_{\odot} \text{ yr}^{-1}$  (Ohashi et al. 1997, for a  $0.1 M_{\odot}$  star) have been estimated. Scaling the value derived by Tobin et al. (2012b) for a  $0.45 M_{\odot}$  star yields a rate of  $\sim 2.9 \times 10^{-7} M_{\odot} \text{ yr}^{-1}$ . According to physical models by Harsono et al. (2015), no CO freeze-out is expected in an embedded disk for accretion rates  $> 10^{-7} M_{\odot} \text{ yr}^{-1}$ . In addition, Frimann et al. (2017) present an expression to predict the size of the  $\text{C}^{18}\text{O}$ -emitting region based on a set of axi-symmetric radiative transfer models for protostellar envelopes:

$$\text{FWHM} = a \left( \frac{d}{235 \text{ pc}} \right)^{-1} \left( \frac{L_{\text{bol}}}{1 L_{\odot}} \right)^{0.41}, \quad (3.3)$$

where  $d$  is the distance to the source, and the angular coefficient  $a$  equals diameters of  $0.89''$  or  $1.64''$  for a CO freeze-out temperature of 28 or 21 K, respectively. For a bolometric luminosity of  $1.9 L_{\odot}$  (Kristensen et al. 2012), the FWHM of the  $\text{C}^{18}\text{O}$ -emitting region is then expected to be  $1.94''$  or  $3.58''$  for the respective freeze-out temperatures. This is larger than the derived disk diameters of  $1.06''$  (A17) or  $1.79''$  (T13). These models thus suggest that a disk warm enough to retain CO in the gas-phase is consistent with the measured accretion rates and luminosity.

Sakai et al. (2014b) assess the physical conditions in L1527 by using a non-LTE large-velocity-gradient (LVG) code. For  $1'' \times 1''$  regions the kinetic temperature of the cyclic- $\text{C}_3\text{H}_2$  emitting region is found to be between 23 and 33 K. This is consistent with the temperature profile from T13. In the SO emitting region around the postulated centrifugal barrier ( $\sim 100$  AU), the gas temperature is suggested to be higher than 60 K. Recent analysis of higher angular resolution SO observations suggest even higher temperatures ( $\sim 200$  K) around the centrifugal barrier (Sakai et al. 2017). Due to a low signal-to-noise ratio within 100 AU, the authors cannot derive a temperature in the disk. The highest velocity offset where SO is present is  $|\Delta v| \sim 1.8 \text{ km s}^{-1}$ . At these blueshifted velocities the outer edge of the disk and inner region of the envelope are expected to be seen. Although the temperature in the outer disk cannot be determined without knowledge of the disk outer radius, a local temperature enhancement

at the disk-envelope interface is expected to be visible. However, the  $^{13}\text{CO}$  and  $\text{C}^{18}\text{O}$  observations presented here show no evidence of such high temperatures, despite being present in the gas phase around the centrifugal barrier. In addition, the beam size for the CO isotopologue observations is comparable to or much smaller than the beams for SO (Sakai et al. 2017, 2014b, resp.), so the lower temperatures based on CO are not likely due to beam dilution.

### **Other Class 0 and Class I disks**

Detailed studies of the gas temperature have not been performed for other young disks. Murillo et al. (2015) show that  $\text{DCO}^+$  emission toward VLA1623 surrounds the disk traced in  $\text{C}^{18}\text{O}$  emission. Since formation of  $\text{DCO}^+$  is enhanced at temperatures  $\lesssim 30$  K, this suggests that the temperature in the disk is too high for CO freeze-out. Attempts to assess whether young disks generally lack CO ice may be based on luminosity or the physical structure derived for the envelope. However, both approaches would yield large uncertainties. In the former case because the temperature structure does not only depend on luminosity, but also on the disk mass. In addition, whether the CO freeze-out temperature will be reached in the disk will depend on disk radius. The latter method is not likely to give reliable disk structures as the temperature and density in the inner envelope not necessarily continue smoothly into the disk (Persson et al. 2016). For example, disk shadowing may lower the temperature in the envelope just outside the disk (Murillo et al. 2015). High resolution (line) observations are thus required to derive the temperature in young disks.

The edge-on configuration of L1527 allows for the midplane temperature to be derived from  $^{13}\text{CO}$  and  $\text{C}^{18}\text{O}$  emission. For less inclined disks, this will be much harder, if not impossible, since the emission is likely to become optically thick in the inner envelope or disk surface layers. Even less abundant isotopologues as  $\text{C}^{17}\text{O}$  or  $^{13}\text{C}^{18}\text{O}$  may be used (Zhang et al. 2017), but likely require long integration times. The easiest way to determine the presence of absence of cold CO-depleted gas may therefore be through observations of cold gas tracers such as  $\text{N}_2\text{H}^+$ ,  $\text{N}_2\text{D}^+$  or  $\text{DCO}^+$ .

### **Class II disks**

Until recently, thermal structures for Class II disks were derived from radiative transfer modeling of continuum emission, analysis of multiple CO lines (e.g., Dartois et al. 2003; Schwarz et al. 2016), or observations of chemical tracers of CO freeze-out (Qi et al. 2013b, 2015; Mathews et al. 2013). These results are generally model-dependent, or limited to the vertical region where the emission originates. With the high spatial and spectral resolution and sensitivity provided by ALMA it is now possible to directly map the 2D temperature structure. Dutrey et al. (2017) present a method to derive the temperature structure (both radially and vertically) of near edge-on disks using position-velocity diagrams. They apply this technique to CO observations of the Flying Saucer disk and find that the overall thermal structure is consistent with a cold ( $< 15 - 12$  K) midplane where CO is frozen out and warmer upper layers. For intermediate inclined disks, emission from different regions can be separated due to the Keplerian rotation, given that the spectral resolution is high enough. Pinte et al. (2018) use this strategy to measure the altitude, velocity and temperature of the CO emitting layers in the disk around IM Lupi. Their results are again consistent with a CO-depleted midplane.



Recent surveys of Class II disks have revealed gas-to-dust ratios up to two or three orders of magnitude below the ISM value of 100 (Ansdell et al. 2016, 2017; Barenfeld et al. 2016; Long et al. 2017). Whether this is the result of general gas loss or a depletion of CO on top of freeze-out and photodissociation remains an open question. Detailed studies of TW Hya, one of the few disks for which the gas mass is derived from HD emission, point to an additional depletion of CO (Favre et al. 2013; Schwarz et al. 2016), and carbon in general (Kama et al. 2016). Possible explanations for these low abundances are chemical evolution into more complex species, either in the gas or in the ice, or the lock up of carbon in large icy bodies. Determination of the CO abundance in younger disks may help shed some light on this problem. For example, low CO abundances in embedded disks would make general gas loss a less likely explanation. However, at least for L1527, we find no evidence for an order of magnitude reduction in CO abundance. This suggests that L1527 has not gone through a long dense pre-stellar core phase in which CO has been turned into other species, and hints that the physical or chemical processes that are responsible for observed low CO abundances occur on timescales longer than the Class 0 lifetime, or start at later stages.

### 3.6.3 Implications of a warm disk in the embedded phase

An important question in planet formation theory is whether the composition of the planet forming material is inherited from the parental cloud, processed on the way to the disk, or completely reset to atoms, as this will influence planet composition (e.g., Aikawa et al. 1999; Hincelin et al. 2013; Pontoppidan et al. 2014; Eistrup et al. 2016). Physicochemical models by Visser et al. (2009b) have shown that not all ices are directly incorporated into the disk, but can instead have desorbed and even recondensed. In addition, Drozdovskaya et al. (2016) show that processing of ices while the material falls onto the disk can lead to enhancement of CO<sub>2</sub> ice and organics, at the expense of CO and methanol ice, respectively. The observed absence of a CO freeze-out region in the L1527 disk thus confirms that the chemical composition of the disk may not be entirely inherited from the dense cloud core, where most CO is frozen out.

In particular, the C/O ratio in the ice will thus not be inherited. The bulk of oxygen is expected to be in H<sub>2</sub>O and CO<sub>2</sub>, while CO is a dominant carbon carrier. Therefore, desorption of CO will relatively deplete the ice of carbon, lowering the C/O ratio (Öberg et al. 2011). The C/O ratio of icy grains in a warm disk will thus be lower than in the parental cloud. Furthermore, if planetesimals are formed during the embedded stage, these planetesimals will have lower bulk C/O ratios than their counterparts formed in the cold outer regions of Class II disks. If young disks in general are found to be warm, an interesting question would be how long this warm phase lasts. That is, do disks remain warm throughout the Class I phase, or have they cooled sufficiently before the envelope is fully dissipated? Answering this question requires detailed studies of young disks during both the Class 0 and Class I phase.

### 3.7 Conclusions

Temperature is an important parameter for the physical and chemical evolution of disks around young stars, and therefore for the outcome of planet formation. Both observations and models point to Class II disks having a large cold gas reservoir where CO is frozen out. In contrast, models suggest that during earlier stages the disk can be warm enough to prevent CO freeze-out. However, so far the temperature structure of embedded disks remained poorly constrained observationally. In this work we have analyzed archival ALMA data of  $^{13}\text{CO}$ ,  $\text{C}^{18}\text{O}$  and  $\text{N}_2\text{D}^+$  to elucidate the midplane temperature structure of the edge-on Class 0/I disk around L1527. Based on the following results we conclude that this young embedded disk is indeed warm enough ( $\gtrsim 20\text{--}25\text{ K}$ ) to have CO in the gas-phase throughout the entire disk:

- $^{13}\text{CO}$  and  $\text{C}^{18}\text{O}$  emission is detected throughout the disk and inner envelope, while  $\text{N}_2\text{D}^+$ , which can only be abundant when CO is frozen out, is not detected.
- Deriving the exact radius at which the  $^{13}\text{CO}$  and  $\text{C}^{18}\text{O}$  emission originates is non-trivial due to CO being present in both the disk and inner envelope, and the emission being optically thick. However, the channel maps provide a global view of the temperature in the disk and inner envelope, and show temperatures above  $\sim 25\text{ K}$  along the midplane.
- A radial power law for the midplane temperature extrapolated from the highest velocity channels suggests that the disk is warm ( $>20\text{ K}$ ) out to at least  $\sim 75\text{ AU}$ . Deriving such power law from synthesized images indicates that these observations underestimate the midplane temperature. More accurate temperature measurements are expected for higher resolution observations. Moreover, the temperature derived from the synthesized images is lower than that from the observations. The disk midplane may thus be warmer than the temperature profile derived by T13 from the continuum emission, which has a temperature of  $\sim 26\text{ K}$  at the disk outer radius (125 AU).
- Radiative transfer modeling for a warm (no CO freeze-out), intermediate (CO snowline at 71 AU) and cold disk (CO snowline at 23 AU) suggest that the less abundant  $\text{C}^{18}\text{O}$  is a more sensitive diagnostic of the CO distribution in the disk than  $^{13}\text{CO}$ . The warm model best reproduces the observations for both molecules, while the intermediate model is a worse match for  $\text{C}^{18}\text{O}$ .

In addition, based on radiative transfer modeling using the best-fit model from T13, there is no evidence for a low gas-phase CO abundance ( $\ll 10^{-4}$ ), as has been suggested for some Class II disks, or an increased abundance at the disk-envelope interface, as suggested by A17. Conclusions about whether young disks in general are warm, and if this is the case, how long this warm phase lasts, will require detailed studies of more disks in both the Class 0 and Class I phase.

## **Acknowledgements**

We would like to thank the referee for constructive and insightful comments. This paper makes use of the following ALMA data: ADS/JAO.ALMA#2013.1.01086.S. ALMA is a partnership of ESO (representing its member states), NSF (USA) and NINS (Japan), together with NRC (Canada), MOST and ASIAA (Taiwan), and KASI (Republic of Korea), in cooperation with the Republic of Chile. The Joint ALMA Observatory is operated by ESO, AUI/NRAO and NAOJ. Astrochemistry in Leiden is supported by the European Union A-ERC grant 291141 CHEMPLAN, by the Netherlands Research School for Astronomy (NOVA) and by a Royal Netherlands Academy of Arts and Sciences (KNAW) professor prize. M.L.R.H acknowledges support from a Huygens fellowship from Leiden University, and J.J.T acknowledges support from grant 639.041.439 from the Netherlands Organisation for Scientific Research (NWO).

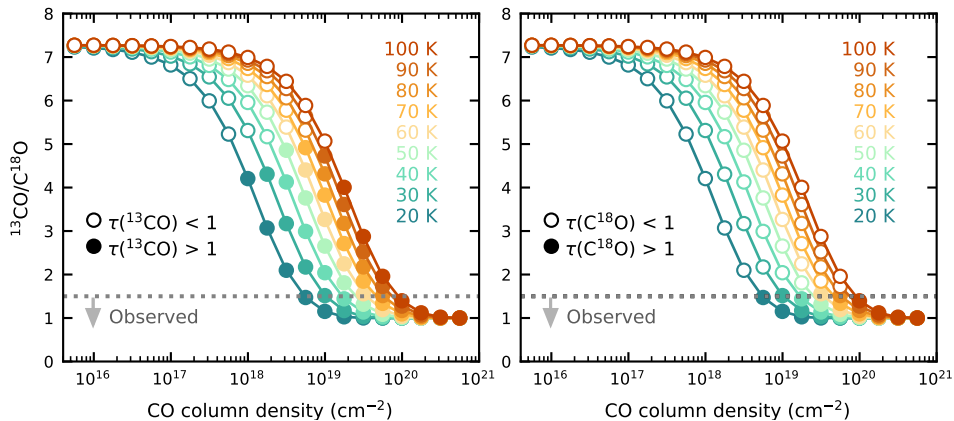


**Figure 3.A.1:**  $^{13}\text{CO}$  ( $J = 2 - 1$ )/ $\text{C}^{18}\text{O}$  ( $J = 2 - 1$ ) line intensity ratio calculated with RADEX for a range of temperatures (different colors) and CO column densities. Isotope ratios of  $^{12}\text{C}/^{13}\text{C} = 77$  and  $^{16}\text{O}/^{18}\text{O} = 560$  are adopted. In the *left panel* (*right panel*), open circles indicate that the  $^{13}\text{CO}$  ( $\text{C}^{18}\text{O}$ ) emission is optically thin (i.e.,  $\tau < 1$ ), whereas filled circles are used when the  $^{13}\text{CO}$  ( $\text{C}^{18}\text{O}$ ) emission is optically thick (i.e.,  $\tau > 1$ ). Values below the dotted line are observed toward the L1527 midplane.

## Appendix

### 3.A $^{13}\text{CO}/\text{C}^{18}\text{O}$ line ratio

Figure 3.A.1 shows the  $^{13}\text{CO}/\text{C}^{18}\text{O}$  line ratios from RADEX calculations for different temperatures and CO column densities.

### 3.B Brightness temperature

The observed brightness temperature for  $^{13}\text{CO}$  and  $\text{C}^{18}\text{O}$  (as shown in Fig. 3.3) for all channels are presented in Figs. 3.B.1 and 3.B.2, respectively. The central channels in which most emission is being resolved out are omitted.

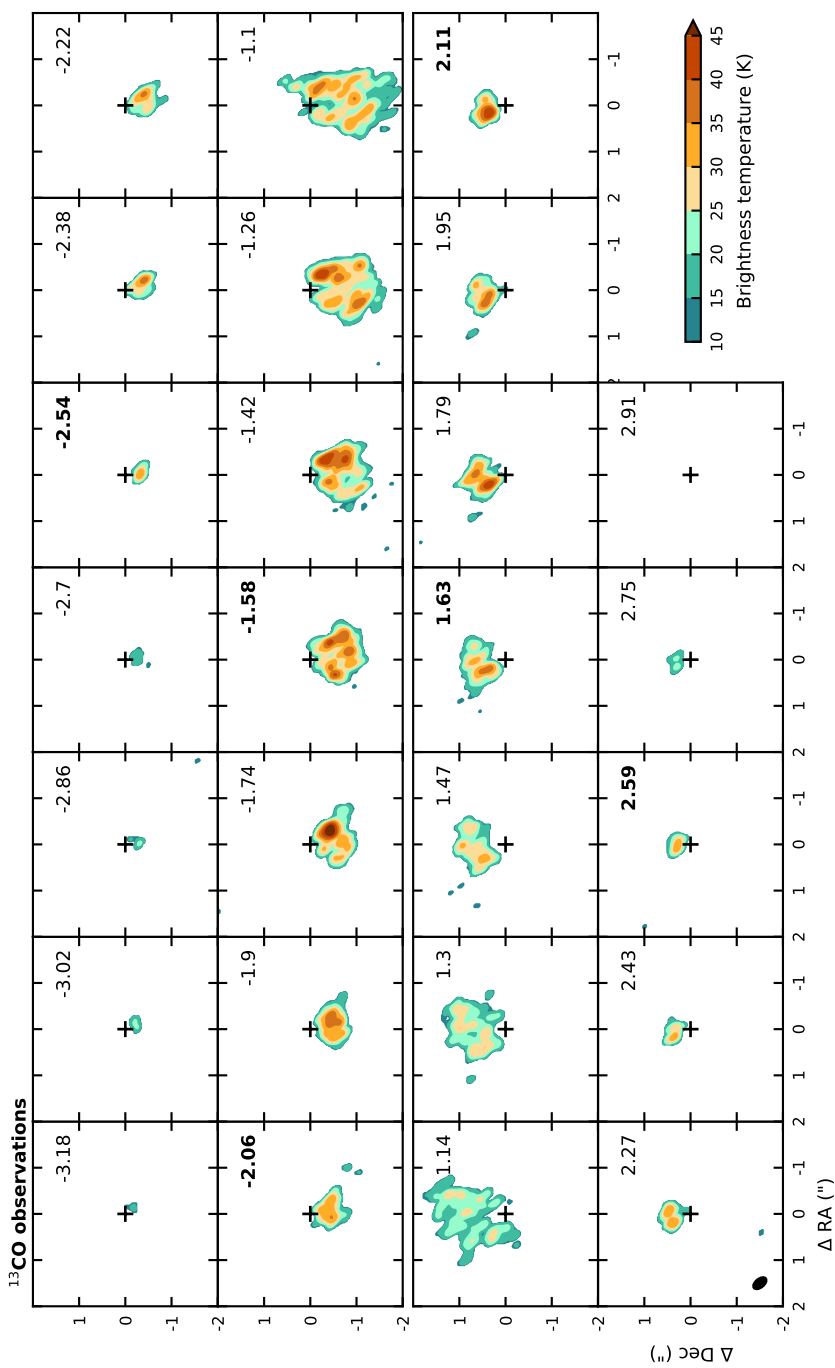


**Figure 3.3.1:** Observed brightness temperature for the  $^{13}\text{CO } J = 2 - 1$  transition, as shown for six channels in **Fig. 3.3**, but now for all channels (expect the central channels,  $\pm \sim 1.0 \text{ km s}^{-1}$ , in which most or all emission is resolved out). Channel velocities with respect to the systemic velocity of  $v_{\text{lsr}} = 5.9 \text{ km s}^{-1}$  are listed in the top right corner of each panel. Velocities presented in **Fig. 3.3** are highlighted in boldface.

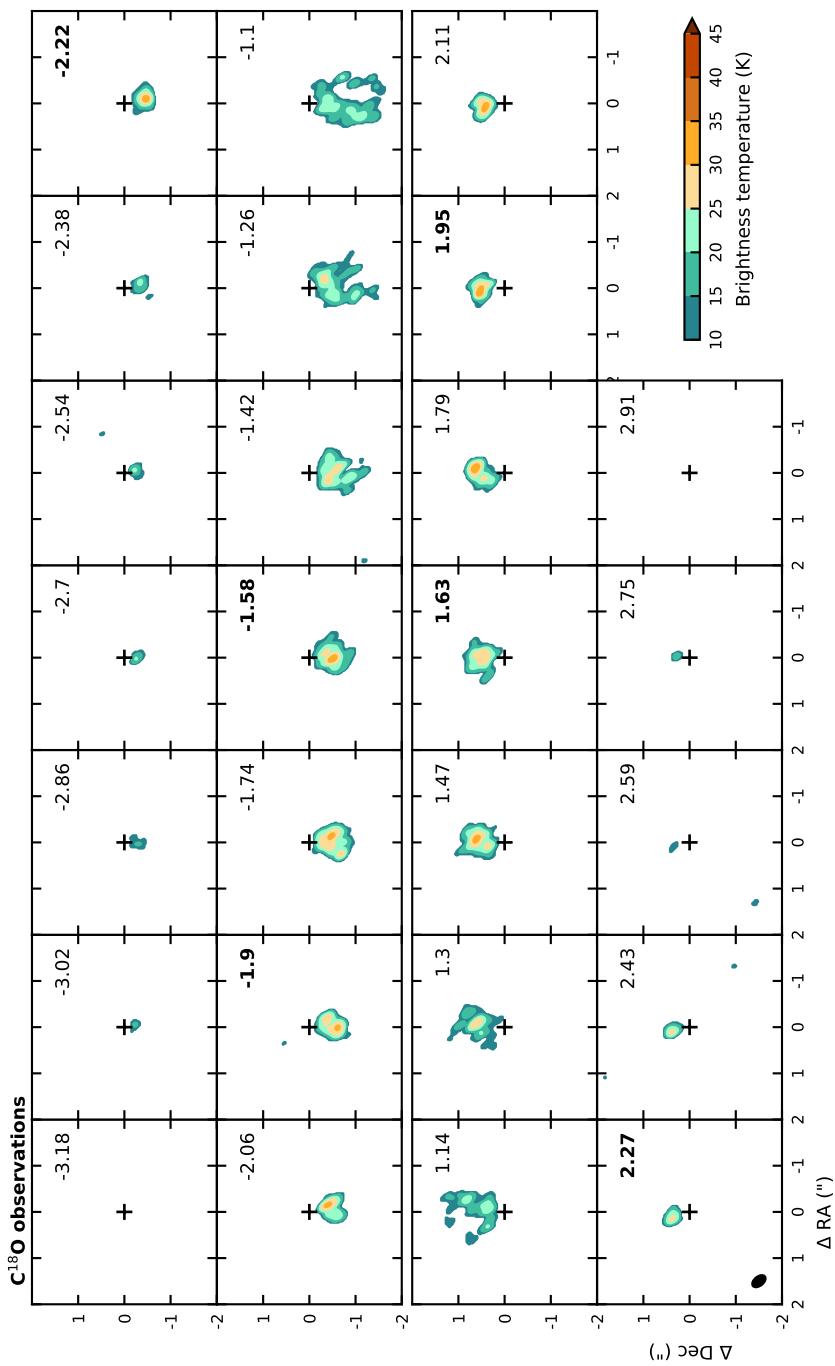


Figure 3.8.2: As Fig. 3.8.1, but for the  $C^{18}O$   $J=2-1$  transition.

### 3.C Physical model for disk and envelope

To analyse the observed CO isotopologue emission and make synthetic images, we adopt for the physical structure the best fit model from T13. This model is the result of fitting a large grid of 3D radiative transfer models to the thermal dust emission in the sub/millimeter, the scattered light  $L'$  image, and the multi-wavelength SED. A full description of the modeling can be found in Whitney et al. (2003), Tobin et al. (2008) and T13, while a brief summary is given below.

The model consists of a Keplerian disk embedded within an infalling rotating envelope. For the envelope, the UCM model is adopted (Ulrich 1976; Cassen & Moosman 1981), which describes the collapse of an isothermal, spherically symmetric, and uniformly rotating cloud. It assumes free fall with each particle conserving angular momentum. As a result, particles move along parabolic paths, with the velocity at point  $(r, \theta)$  given by:

$$v_r(r, \theta) = - \left( \frac{GM_\star}{r} \right)^{1/2} \left( 1 + \frac{\cos \theta}{\cos \theta_0} \right)^{1/2}, \quad (3.4)$$

$$v_\theta(r, \theta) = \left( \frac{GM_\star}{r} \right)^{1/2} (\cos \theta_0 - \cos \theta) \left( \frac{\cos \theta_0 + \cos \theta}{\cos \theta_0 \sin^2 \theta} \right)^{1/2}, \quad (3.5)$$

$$v_\phi(r, \theta) = \left( \frac{GM_\star}{r} \right)^{1/2} \frac{\sin \theta_0}{\sin \theta} \left( 1 - \frac{\cos \theta}{\cos \theta_0} \right)^{1/2}, \quad (3.6)$$

where  $\theta_0$  is the inclination of the particle's orbital plane relative to the rotation axis.  $\theta_0$  can be found analytically by solving the following equation:

$$r = R_c \frac{\cos \theta_0 \sin^2 \theta_0}{\cos \theta_0 - \cos \theta}, \quad (3.7)$$

where  $R_c$  is the centrifugal radius, that is the radius at which the radial velocity is equal to the rotation velocity.

The envelope density structure is spherical at large radii, but becomes flattened near the centrifugal radius due to rotation:

$$\rho_{\text{env}}(r) = \frac{\dot{M}_{\text{env}}}{4\pi(GM_\star r^3)^{1/2}} \left( 1 + \frac{\cos \theta}{\cos \theta_0} \right)^{-1/2} \left( \frac{\cos \theta}{\cos \theta_0} + \frac{2 \cos^2 \theta_0 R_c}{r} \right)^{-1}, \quad (3.8)$$

where  $\dot{M}_{\text{env}}$  is the mass infall rate of the envelope onto the disk. Inside  $R_c$ ,  $\rho_{\text{env}} \propto r^{-1/2}$ , while outside  $R_c$ ,  $\rho_{\text{env}} \propto r^{-3/2}$ . The bipolar outflow cavities extend from the central protostar to the outer radius of the envelope. To reproduce the scattered light morphology, a dual-cavity structure was required, with the cavity being more narrow in the inner  $\sim 100$  AU and wider at larger radii (see **Fig. 3.C.1**, and Tobin et al. 2008 for details). Inside the outflow cavity the density is set to zero.

The disk has a Keplerian velocity profile, that is,

$$v_\phi(r) = \sqrt{\frac{GM_\star}{r}}. \quad (3.9)$$

This means that at radii larger than  $R_c$  the velocity structure is given by **Eq. 3.4-3.6**, while at smaller radii **Eq. 3.9** is adopted. A standard flared accretion density structure

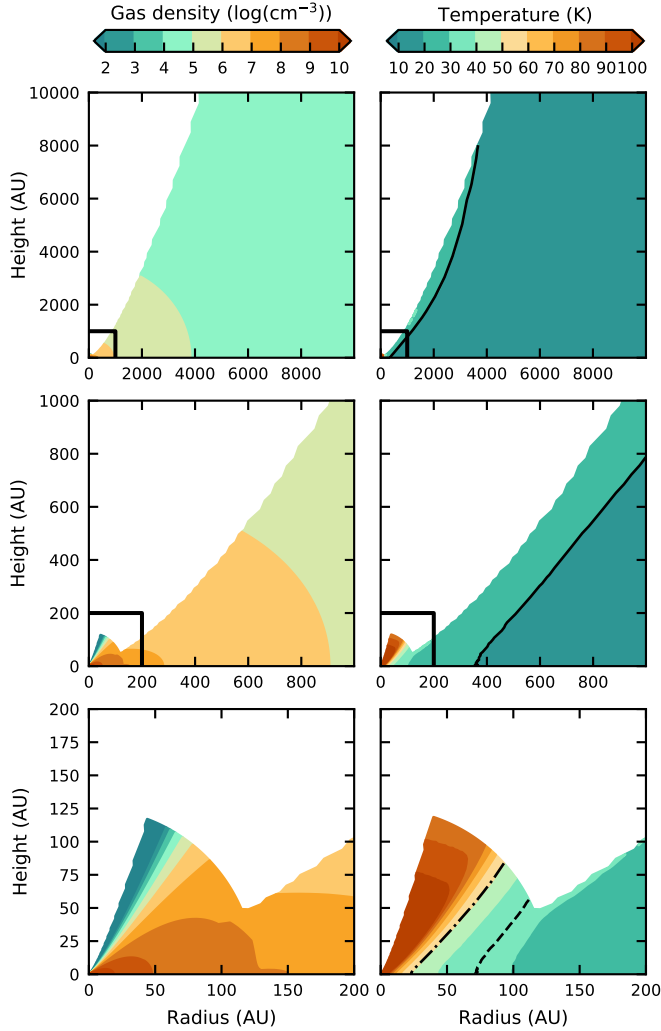


**Figure 3.C.1:** Density (*left panels*) and temperature (*right panels*) structure for the disk and envelope of L1527 from the T13 best fit model on a scale of 10,000 AU (*top panels*), 1000 AU (*middle panels*) and 200 AU (*bottom panels*). The black boxes highlight the area shown in the row below. The solid black contours mark the CO snow surface (20 K). The location of the snow surface in the intermediate and cold models are indicated with dashed and dash-dotted contours, respectively.

was assumed for the disk (Shakura & Sunyaev 1973; Lynden-Bell & Pringle 1974; Hartmann et al. 1998), that is,

$$\rho_{\text{disk}}(r) = \rho_0 \left[ 1 - \left( \frac{R_\star}{r} \right)^{1/2} \right] \left( \frac{R_\star}{r} \right)^\alpha \exp \left\{ -\frac{1}{2} \left[ \frac{z}{h(r)} \right]^2 \right\}, \quad (3.10)$$



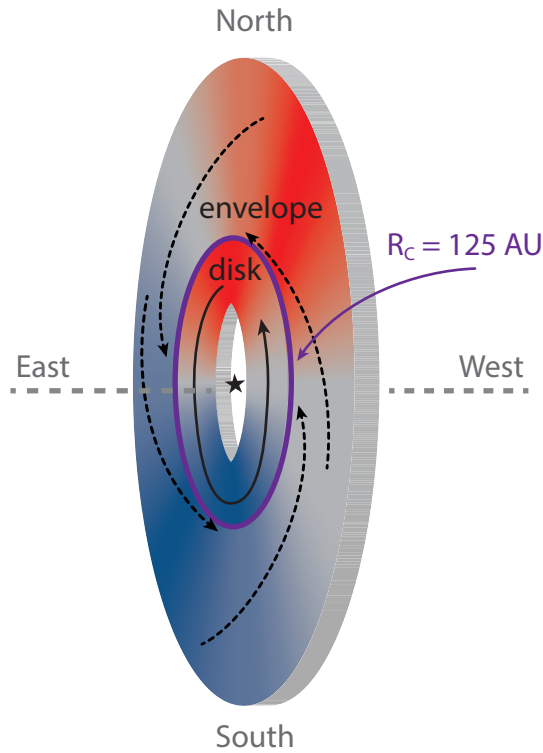


**Figure 3.C.2:** Schematic illustration of the disk-envelope model employed here and by T13. The material inside the centrifugal radius,  $R_C$ , rotates with Keplerian velocity (solid arrow), while the material outside  $R_C$  is rotating and infalling (dashed arrows). The blue- and redshifted material is shown in blue and red, respectively. The system is  $5^\circ$  inclined from edge-on, such that the disk and envelope west of the protostar are nearest to the observer.

where the scaleheight  $h(r)$  is given by

$$h(r) = h_0 \left( \frac{r}{R_\star} \right)^\beta. \quad (3.11)$$

To fit the multi-wavelength continuum observations, a grid of models was created by T13 in which the envelope properties were kept constant, while varying the disk properties (radius, flaring, radial density profile, scale height and mass). In addition, the dust spectral index was varied (see T13 for details on the dust properties). A protostellar mass of  $0.5 M_\odot$  was adopted, but no parameters directly depend on this value. The mass infall rate was taken to be  $1.0 \times 10^{-5} M_\odot \text{ yr}^{-1}$ . The accretion luminosity was set to  $L_{\text{acc}} = 1.75 L_\odot$  and the protostellar luminosity to  $1.0 L_\odot$ . For creating the continuum images, an inclination of  $85^\circ$  was used such that the west side of the disk and envelope is nearest to the observer (see **Fig. 3.C.2**). The best-fitting disk model has a disk radius of  $R_c = 125 \text{ AU}$ . The disk was found to be highly flared ( $h(r) \propto r^{1.3}$ , and  $h(100\text{AU}) = 48 \text{ AU}$ ), and have  $\rho_{\text{disk}} \propto r^{-2.5}$ . The 2D density and temperature (calculated from the dust radiative transfer) structure are presented in **Fig. 3.C.1**, and **Fig. 3.C.3** shows the corresponding radial profiles for the midplane.

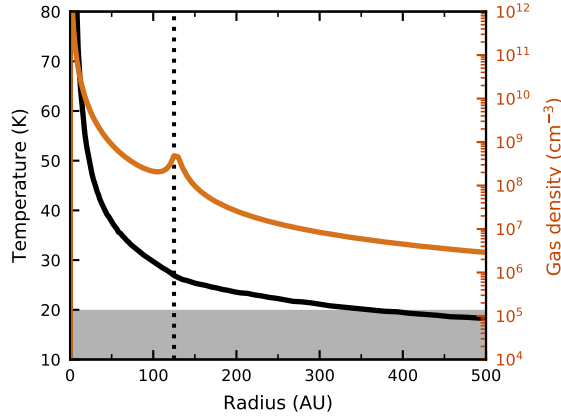


**Figure 3.C.3:** Midplane temperature (black) and density (orange) profile from the best fit model from T13 for the disk and inner envelope of L1527. The vertical dotted line marks the disk outer radius and the gray area shows the temperature range ( $< 20$  K) for which CO is expected to be frozen out.

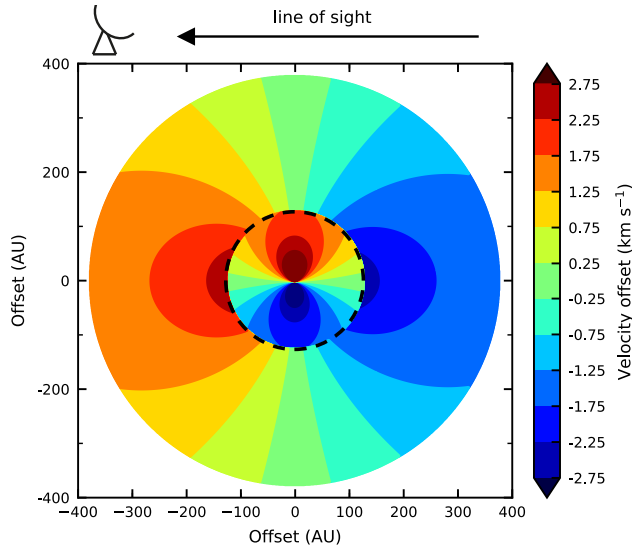


**Figure 3.D.1:** As Fig. 3.5, but for a free fall velocity profile in the envelope.

### 3.D Free fall velocity

Figure 3.D.1 presents the midplane velocity structure along the line of sight as shown in Fig. 3.5, but for a free fall,

$$v_r(r) = \sqrt{\frac{2GM_\star}{r}}, \quad (3.12)$$

rather than a infalling rotating velocity profile (Eq. 3.4-3.6) in the envelope. The  $\tau = 1$  surface for  $^{13}\text{CO}$  and  $\text{C}^{18}\text{O}$  in five representative velocity channels is shown in Fig. 3.D.2.

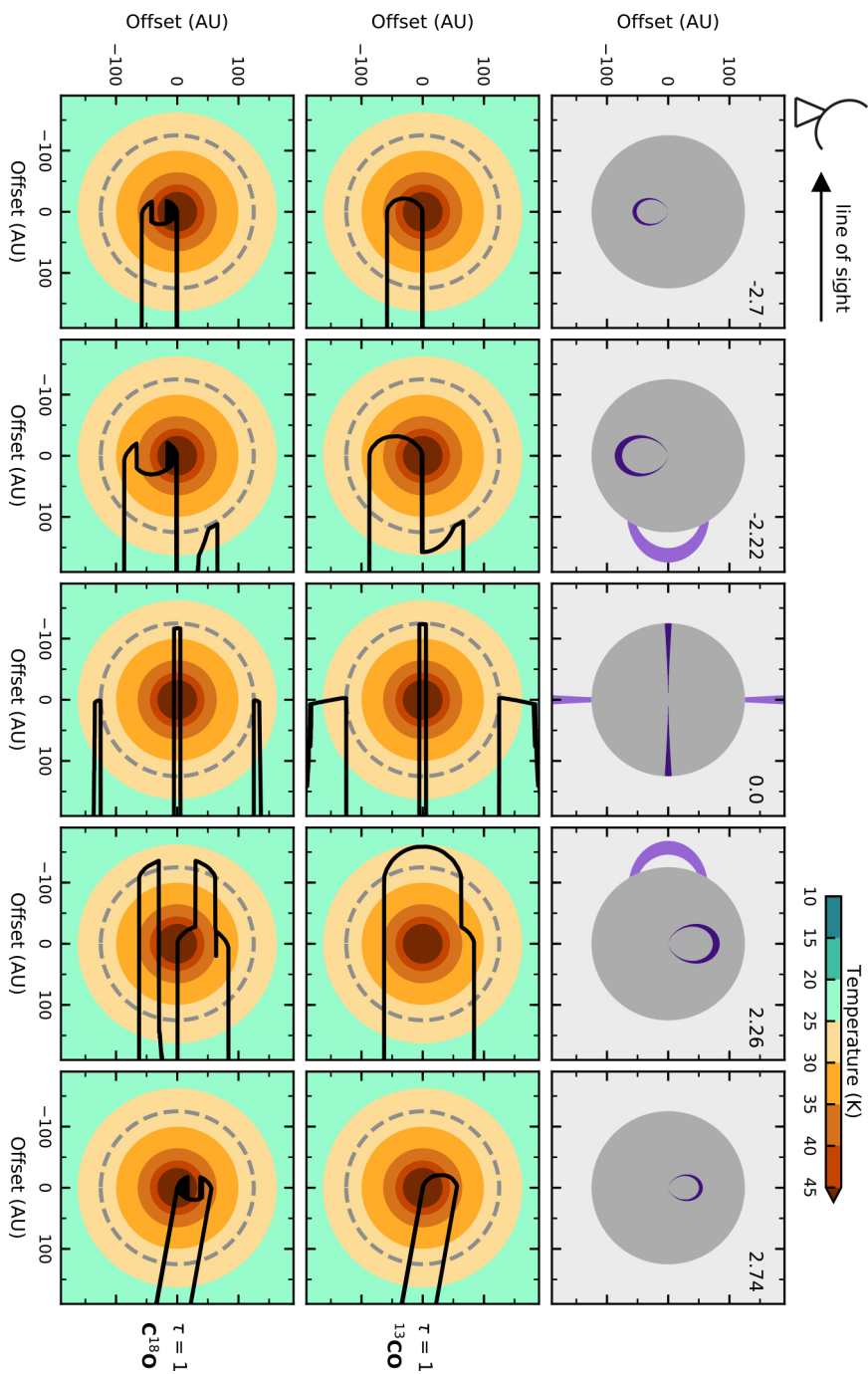
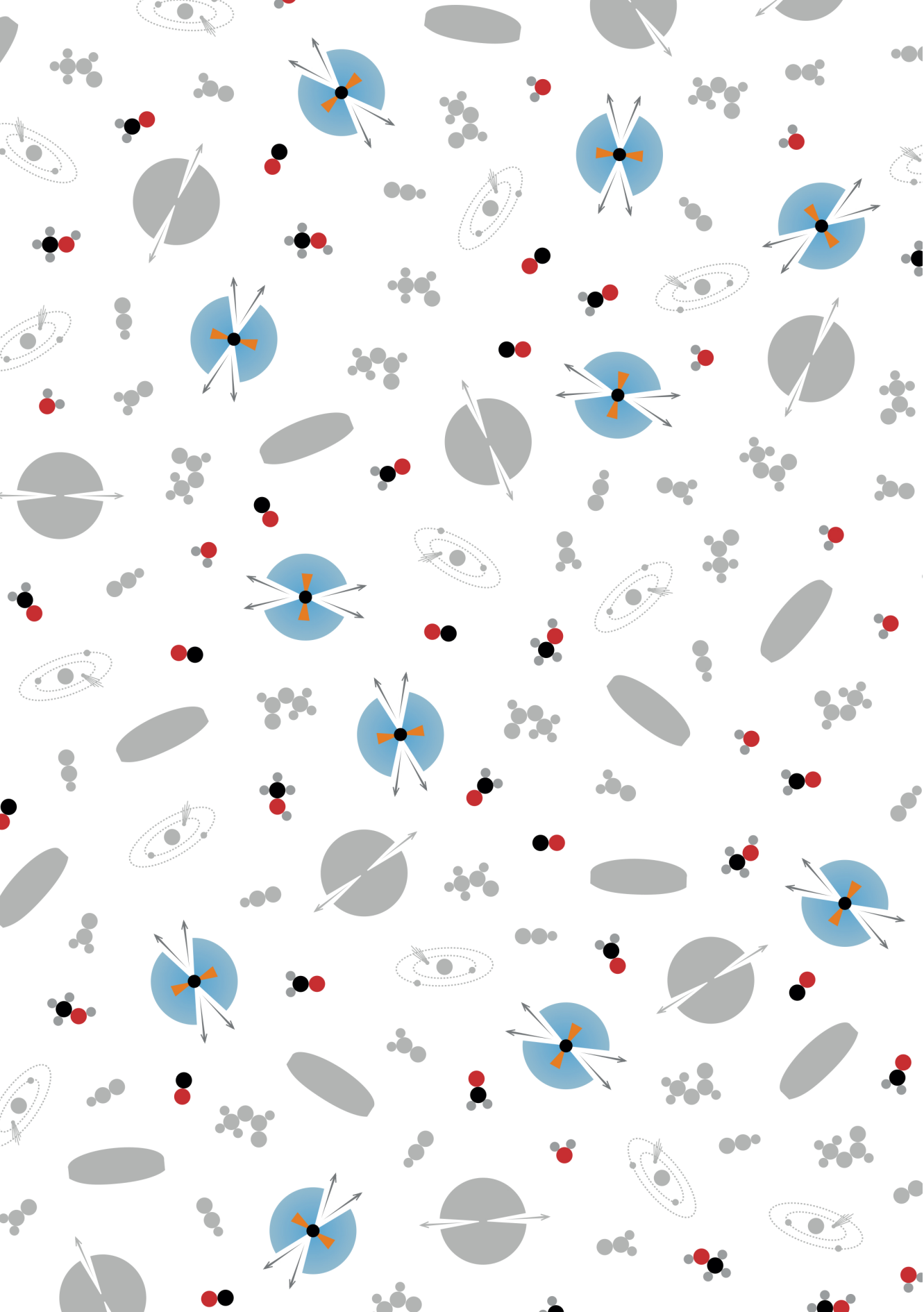


**Figure 3.0.2:** As Fig. 3.6, but for a free fall velocity profile in the envelope, as shown in Fig. 3.0.1.







## 4. Temperature structure of embedded disks

*Young disks in Taurus are warm*

M.L.R. van 't Hoff, D. Harsono, A.D. Bosman, J.J. Tobin,  
& E.F. van Dishoeck

in preparation



## Abstract

**Context.** Protoplanetary disks are observed to have a large cold outer region where CO is frozen out. In contrast, no sign of CO freeze-out was observed toward the young embedded disk L1527.

**Aims.** We aim to constrain the midplane temperature for a sample of five young embedded disks to establish whether young disks are generally warmer than their more evolved counterparts.

**Methods.** We observe five embedded disks in Taurus with the Atacama Large Millimeter/submillimeter Array (ALMA), targeting the  $\text{C}^{17}\text{O } J = 2 - 1$ ,  $\text{H}_2\text{CO } 3_{1,2} - 2_{1,1}$ ,  $\text{HDO } 3_{1,2} - 2_{2,1}$  and several  $\text{CH}_3\text{OH } 5_k - 4_k$  transitions at  $0.5'' \times 0.37''$  ( $\sim 70 \times 52$  AU) resolution. The different freeze-out temperatures of these species allows to derive a global temperature structure.

**Results.**  $\text{C}^{17}\text{O}$  and  $\text{H}_2\text{CO}$  are detected in all disks, with no signs of CO freeze-out in the inner  $\sim 100$  AU.  $\text{H}_2\text{CO}$  is clearly depleted in the midplane of IRAS 04302, with its snowline ( $T \sim 50$  K) around  $\sim 50$  AU.  $\text{HDO}$  and  $\text{CH}_3\text{OH}$  are not detected, with upper limits for the methanol column density ( $\sim 3 \times 10^{14} \text{ cm}^{-2}$ ) and abundance ( $\sim 3\text{--}11 \times 10^{-9}$  w.r.t.  $\text{H}_2$ ) several orders of magnitude lower than for the Class 0 system IRAS 16293 and the young disk around the outbursting star V883 Ori.

**Conclusions.** Young embedded disks are warmer than more evolved protoplanetary disks, with no CO freeze-out, or only in the outermost part of large disks. However, they are not as warm as less evolved Class 0 systems or outbursting sources, and therefore do not have a large gas-phase reservoir of complex molecules. The inferred temperature profiles are consistent with trends found in radiative transfer models of disk-envelope systems with accretion rates decreasing from  $10^{-4}$  to  $10^{-7} M_{\odot} \text{ yr}^{-1}$ .



## 4.1 Introduction

Disks around young stars provide the building material for planets. Knowledge of their physical and chemical structure is therefore crucial for understanding planet formation and composition. Protoplanetary disks have been studied in great detail both physically (e.g., Andrews et al. 2010, 2018; Schwarz et al. 2016; Ansdell et al. 2016) and chemically (e.g., Dutrey et al. 1997; Thi et al. 2004; Öberg et al. 2010; Huang et al. 2017). The emerging picture shows that these Class II disks have a large cold outer region ( $T \lesssim 20$  K) where CO is frozen out (e.g., Aikawa et al. 2002; Qi et al. 2013b, 2015; Mathews et al. 2013). However, it is now becoming clear that planet formation already starts when the disk is still embedded in its natal envelope. Grain growth has been observed in these Class 0 and I sources and even larger bodies may have formed before the envelope has fully dissipated (e.g., Kwon et al. 2009; Jørgensen et al. 2009; Miotello et al. 2014; ALMA Partnership et al. 2015; Harsono et al. 2018). Young embedded disks thus provide the initial conditions for planet formation, but unlike their more evolved counterparts, their structure remains poorly characterized.

A critical parameter is the disk temperature structure because this governs disk evolution and composition. For example, temperature determines how resistive the gas is to gravitational instabilities (see e.g., a review by Kratter & Lodato 2016), a potential mechanism to form giant planets, stellar companions and accretion bursts (e.g., Boss 1997; Boley 2009; Vorobyov 2009; Tobin et al. 2016a). In addition, grain growth is thought to be enhanced in the region where water freezes out from the gas phase onto the dust grains, the water snowline ( $T \sim 100\text{--}150$  K; e.g., Stevenson & Lunine 1988; Schoonenberg & Ormel 2017; Drażkowska & Alibert 2017). Moreover, the freeze out of molecules as the temperature drops below their species-specific freeze-out temperature sets the global chemical composition of the disk. This sequential freeze-out causes radial gradients in molecular abundances and elemental ratios (like the C/O ratio, e.g., Öberg et al. 2011). As a consequence, the composition of a planet then depends on its formation location in the disk (e.g., Madhusudhan et al. 2014; Walsh et al. 2015; Ali-Dib 2017; Cridland et al. 2019). Finally, the formation of high abundances of complex molecules starts from CO ice (e.g., Tielens & Hagen 1982; Garrod & Herbst 2006; Cuppen et al. 2009; Chuang et al. 2016), and will thus be impeded if the temperature is above the CO freeze-out temperature ( $T \gtrsim 20$  K). Whether young disks are warm ( $T \gtrsim 20$  K, i.e., warmer than the CO freeze-out temperature) or cold (i.e., have a large region where  $T \lesssim 20$  K and CO is frozen out) is thus a simple, but crucial question.

Keplerian disks are now detected around several Class 0 and I sources (e.g., Brinch et al. 2007; Tobin et al. 2012b), but most research has focussed on disk formation, size and kinematics (e.g., Yen et al. 2013; Ohashi et al. 2014; Harsono et al. 2014), or the chemical structure at the disk-envelope interface (e.g., Sakai et al. 2014b; Murillo et al. 2015; Oya et al. 2016). Only a few studies have examined the disk structure, and only for one particular disk, L1527. Tobin et al. (2013b) and Aso et al. (2017) modeled the radial density profile and van 't Hoff et al. (2018b) (**Chapter 3**) studied its temperature profile based on optically thick  $^{13}\text{CO}$  and  $\text{C}^{18}\text{O}$  observations. The latter study showed that the entire L1527 disk is likely too warm for CO freeze-out, in agreement with model predictions (e.g., Harsono et al. 2015), but in contrast to protoplanetary disk observations.

In this paper we present ALMA observations of  $\text{C}^{17}\text{O}$  and  $\text{H}_2\text{CO}$  toward five young

**Table 4.1:** Overview of source properties.

Source (IRAS)	Other name	R.A. <sup>a</sup> (J2000)	Decl. <sup>a</sup> (J2000)	Class	$L_{\text{bol}}$ ( $L_{\odot}$ )	$M_*$ ( $M_{\odot}$ )	$M_{\text{env}}$ ( $M_{\odot}$ )	$M_{\text{disk}}$ ( $M_{\odot}$ )	$R_{\text{disk}}$ (AU)	$i$ (deg)	refs <sup>b</sup>
04016+2610	L1489 IRS	04:04:42.8	+26:18:56.3	I	3.7	1.6	0.023	0.004	250–500	66	1,2,3
04302+2247	Butterfly disk	04:33:16.5	+22:53:20.3	I/II	0.34–0.92	0.5	0.02–0.1	0.1	244	>76	1,3,4
04365+2535	TMC1A	04:39:35.2	+25:41:44.2	I	2.2–2.7	0.5–0.7	0.12	0.03	100	55–65	1,5,6,7
04368+2557	L1527 IRS	04:39:53.9	+26:03:09.6	0/I	1.9–2.6	0.2–0.5	1.0	0.0075	75–125	85	7,8,9,10
04381+2540	TMC1	04:41:12.7	+25:46:34.8	I	0.7–0.9	0.54	0.14	0.0039	100	55	1,5,7

**Notes.** <sup>(a)</sup> Phase center of the observations. <sup>(b)</sup> References. (1) Kenyon & Hartmann (1995), (2) Yen et al. (2014), (3) Sheehan & Eisner (2017), (4) Wolf et al. (2003), (5) Harsono et al. (2014) (6) Aso et al. (2015) (7) Kristensen et al. (2012), (8) Tobin et al. (2008) (9) Tobin et al. (2013b) (10) Aso et al. (2017).

disks in Taurus to address the question whether young disks are generally too warm for CO freeze-out. In addition, HDO and CH<sub>3</sub>OH observations are used to determine whether complex molecules can be observed in these young disks, as shown for the V883 Ori disk around an outbursting young star (van 't Hoff et al. 2018c, **Chapter 7**; Lee et al. 2019), but has turned out to be very difficult in mature protoplanetary disks. So far, only CH<sub>3</sub>CN has been detected in a sample of disks, and CH<sub>3</sub>OH and HCOOH have been detected in TW Hya (Öberg et al. 2015b; Walsh et al. 2016; Favre et al. 2018; Bergner et al. 2018; Loomis et al. 2018; Carney et al. 2019).

The observations are described in **Sect. 4.2**, and the resulting C<sup>17</sup>O and H<sub>2</sub>CO images are presented in **Sect. 4.3**. This section also describes the non-detections of HDO and CH<sub>3</sub>OH. The temperature structure of the disks is examined in **Sect. 4.4** based on the C<sup>17</sup>O and H<sub>2</sub>CO observations and radiative transfer modeling. The result that the young disks in this sample seem warm is discussed in **Sect. 4.5** and the conclusions are summarized in **Sect. 4.6**.

## 4.2 Observations

In order to study the temperature structure in young disks, a sample of five Class 0 and I protostars in Taurus was observed with ALMA; IRAS 04302+2247 (also known as the Butterfly disk, hereafter IRAS 04302), L1489, L1527, TMC1 and TMC1A. All sources are known to have a disk and Keplerian rotation has been established for all but IRAS 04302 (Brinch et al. 2007; Tobin et al. 2012b; Harsono et al. 2014). IRAS 04302 and L1527 are seen edge-on, which allows a direct view of the midplane, whereas L1489, TMC1 and TMC1A are moderately inclined  $\sim 50$ – $60^\circ$ . The source properties are listed in **Table 4.1**.

The observations were carried out on 2018 September 10 and 28, for a total on source time of 15 minutes per source (project code 2017.1.01413.S). The observations used 47 antennas sampling baselines between 15 m and 1.4 km. The correlator setup included a 2 GHz continuum band centered at 240.0 GHz, and spectral windows targeting the C<sup>17</sup>O  $J = 2 - 1$ , H<sub>2</sub>CO  $3_{1,2} - 2_{1,1}$ , HDO  $3_{1,2} - 2_{2,1}$  and several CH<sub>3</sub>OH  $5_k - 4_k$  transitions. The spectral resolution was 122.1 kHz for CH<sub>3</sub>OH and 61.0 kHz for the other lines, which corresponds to a velocity resolution of 0.16 and 0.08 km s<sup>-1</sup>, respectively. The properties of the targeted lines can be found in **Table 4.2**.

Calibration and imaging were done using the ALMA Pipeline and version 5.4.0 of the Common Astronomy Software Applications (CASA). The phase calibrator was J0438+3004, and the bandpass and flux calibrator was J0510+1800. The typical restoring beam size is  $0.50'' \times 0.37''$  ( $\sim 70 \times 52$  AU) for the naturally weighted images. The resulting continuum images have a rms of 0.1–0.5 mJy beam<sup>-1</sup>, whereas the rms in the line images is 4–5 mJy beam<sup>-1</sup> channel<sup>-1</sup>. The observed continuum and line flux densities are reported in **Table 4.3**.

## 4.3 Results

### 4.3.1 C<sup>17</sup>O and H<sub>2</sub>CO morphology

**Figure 4.1** shows the 1.3 mm continuum images and integrated intensity (zeroth moment) maps for C<sup>17</sup>O ( $J = 2 - 1$ ) and H<sub>2</sub>CO ( $3_{1,2} - 2_{1,1}$ ) toward the five sources in our

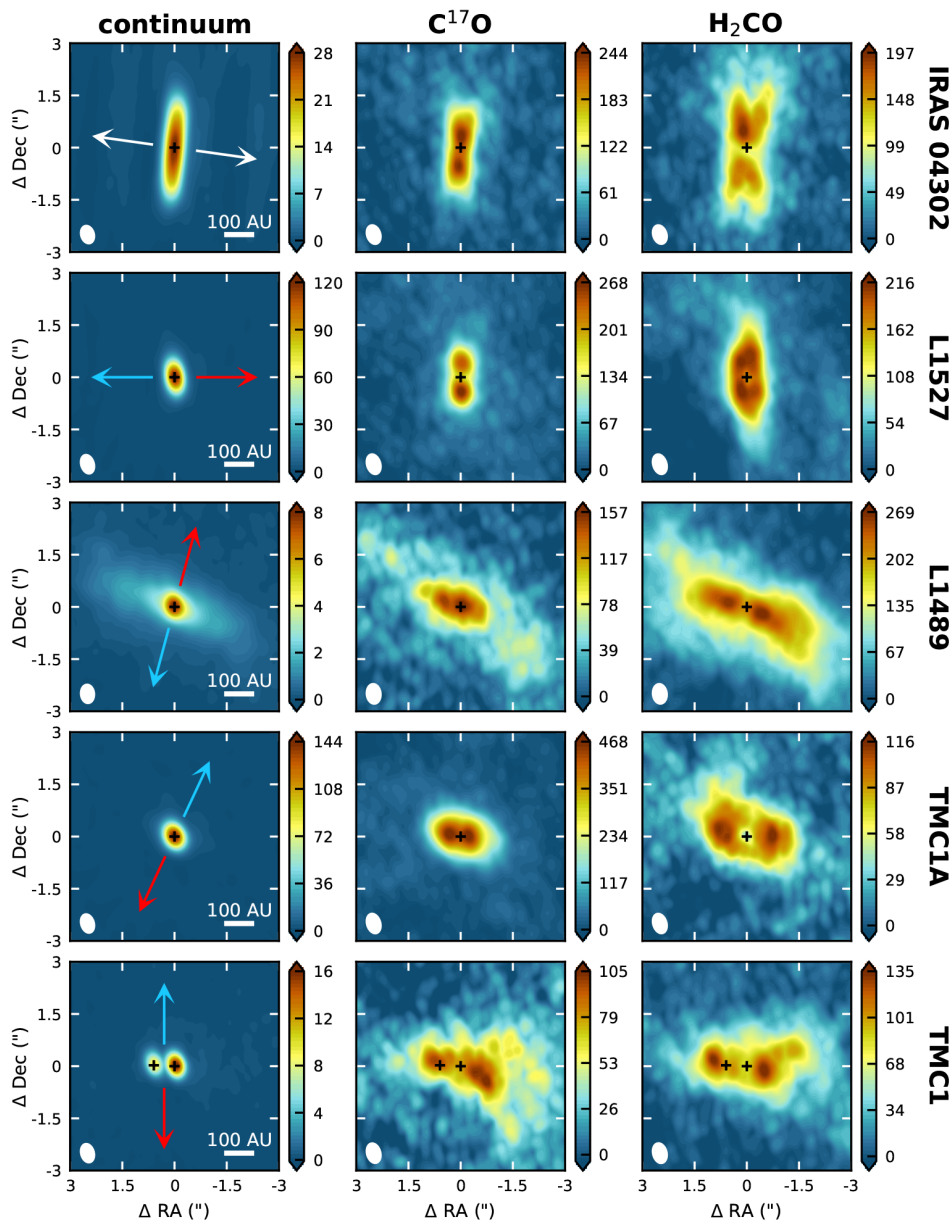


**Figure 4.1:** Continuum images at 1.3 mm (*left column*) and integrated intensity maps for the C<sup>17</sup>O  $J = 2 - 1$  (*middle column*) and H<sub>2</sub>CO  $3_{1,2} - 2_{1,1}$  (*right column*) transitions. The color scale is in mJy beam<sup>-1</sup> for the continuum images and in mJy beam<sup>-1</sup> km s<sup>-1</sup> for the line images. The positions of the continuum peaks are marked with black crosses, and the outflow directions are indicated by arrows in the continuum images. The beam is shown in the lower left corner of each panel.

**Table 4.2:** Overview of the molecular line observations.

Molecule	Transition	Frequency (GHz)	$A_{ul}^a$ ( $s^{-1}$ )	$E_{up}^b$ (K)
C <sup>17</sup> O	2 – 1	224.714385	$6.42 \times 10^{-7}$	16
H <sub>2</sub> CO	3 <sub>1,2</sub> – 2 <sub>1,1</sub>	225.697775	$2.77 \times 10^{-4}$	33
HDO	3 <sub>1,2</sub> – 2 <sub>2,1</sub>	225.896720	$1.32 \times 10^{-5}$	168
CH <sub>3</sub> OH	5 – 4 <sup>c</sup>	241.820762 <sup>d</sup>	$2-6 \times 10^{-5}$	34–131

**Notes.** <sup>(a)</sup> Einstein A coefficient. <sup>(b)</sup> Upper level energy. <sup>(c)</sup> The spectral window covers multiple transitions in the  $5_k - 4_k$  branch for both A- and E-methanol (16 transitions in total). <sup>(d)</sup> Central frequency of the spectral window.

**Table 4.3:** Observed fluxes for the 1.3 mm continuum and molecular lines.

Source	$F_{peak}$ (1.3 mm) (mJy beam <sup>-1</sup> )	$F_{int}$ (1.3 mm) (mJy)	$F_{int}$ (C <sup>17</sup> O) <sup>a</sup> (Jy km s <sup>-1</sup> )	$F_{int}$ (H <sub>2</sub> CO) <sup>a</sup> (Jy km s <sup>-1</sup> )
IRAS 04302	$28.8 \pm 0.2$	$166.4 \pm 1.5$	$3.0 \pm 0.4$	$4.5 \pm 0.5$
L1489	$3.8 \pm 0.1$	$62.5 \pm 1.1$	$3.4 \pm 0.4$	$8.8 \pm 0.4$
L1527	$117.1 \pm 0.4$	$202.7 \pm 1.1$	$2.7 \pm 0.5$	$3.7 \pm 0.8$
TMC1A	$139.5 \pm 0.5$	$219.4 \pm 1.3$	$5.1 \pm 0.5$	$2.9 \pm 0.2$
TMC1	$10.8 \pm 0.1$	$30.6 \pm 0.4$	$2.7 \pm 0.4$	$3.2 \pm 0.3$

**Notes.** <sup>(a)</sup> Integrated flux within a circular aperture with 6.0'' diameter.

sample. The continuum emission is elongated perpendicular to the outflow direction for all sources, consistent with a disk as observed before. TMC1 is resolved into a close binary ( $\sim 70$  AU separation) at this resolution. Both molecular lines are clearly detected in all sources, with a velocity gradient along the continuum structure (see **Fig. 4.1.1**). The peak integrated fluxes are comparable (within  $\sim 25\%$ ) between the two species in IRAS 04302, L1527 and TMC1, with H<sub>2</sub>CO brighter in the latter source. H<sub>2</sub>CO is approximately twice as bright as C<sup>17</sup>O in L1489, but  $\sim$ four times weaker in TMC1A. The integrated fluxes are reported in **Table 4.3**.

The H<sub>2</sub>CO emission is generally more extended both radially and vertically than the C<sup>17</sup>O emission, except in TMC1 and TMC1A where both molecules have the same spatial extent. This is not a signal-to-noise issue, as can be seen from the radial profiles in **Fig. 4.1.2**. The most striking feature is the V-shaped emission pattern of the H<sub>2</sub>CO in IRAS 04302, suggesting that the emission arises from the disk surface layers and not the midplane. In L1489, C<sup>17</sup>O has a bright inner component and a weaker outer component that extends roughly as far as the H<sub>2</sub>CO emission. A similar structure was observed in C<sup>18</sup>O emission by Yen et al. (2014), who showed that the off-axis protrusions pointing to the north and south (here best seen in H<sub>2</sub>CO) are streams of infalling material. Finally, the H<sub>2</sub>CO emission peaks off-source in TMC1A, whereas the C<sup>17</sup>O emission is centrally peaked. The spatial resolution is not high enough to observe the depression in the inner  $\sim 15$  AU that was seen in <sup>13</sup>CO and C<sup>18</sup>O by Harsono et al. (2018) due to the optically thick mm-sized dust.

To get a first impression whether the observed emission originates in the disk or

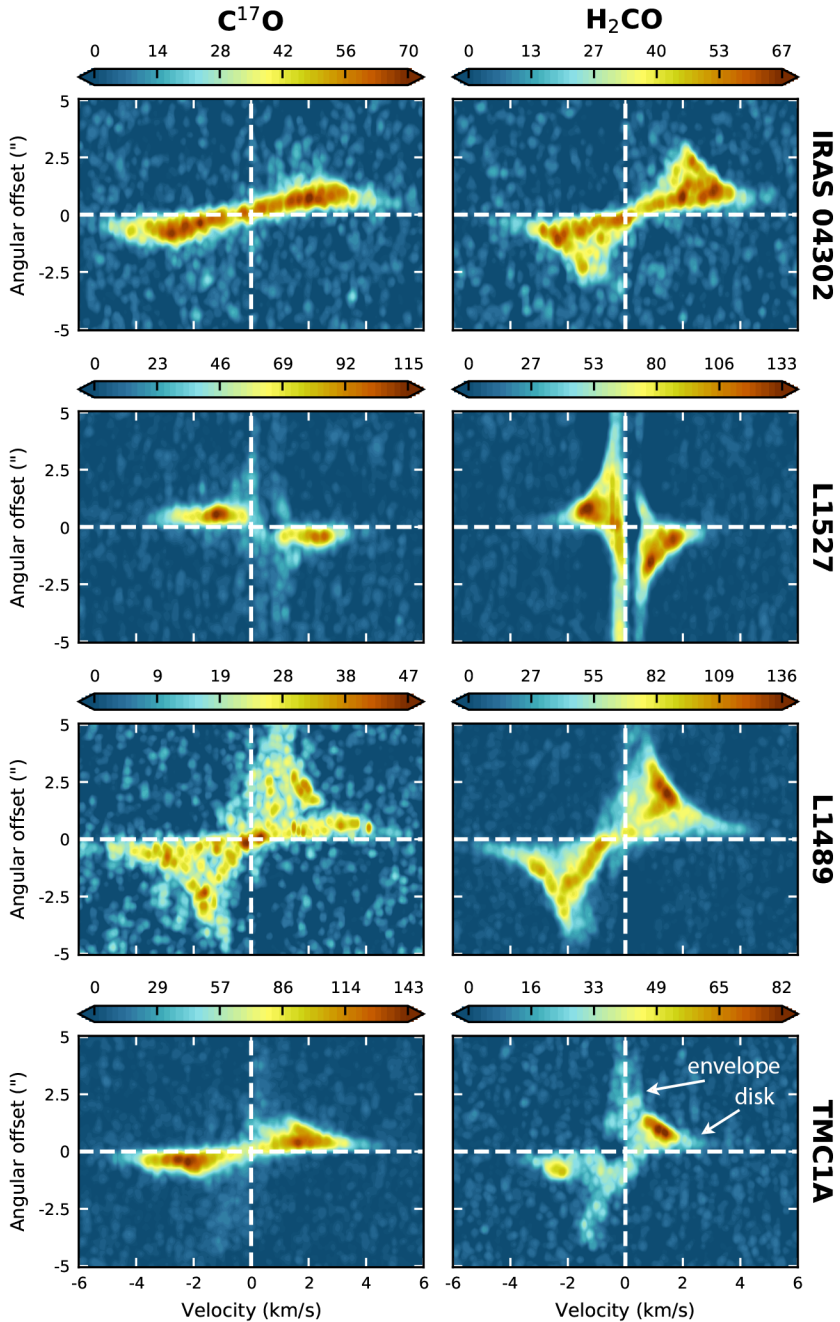


**Figure 4.2:** Position-velocity diagrams for  $\text{C}^{17}\text{O}$  (left panels) and  $\text{H}_2\text{CO}$  (right panels) along the major axis of the disks in the single systems (listed right of the rows).  $\text{C}^{17}\text{O}$  traces predominantly the disk, that is, high velocities at small angular offsets, whereas  $\text{H}_2\text{CO}$  generally has a larger envelope component, that is, low velocities at large angular offsets. The velocity is shifted such that 0  $\text{km s}^{-1}$  corresponds to the systemic velocity. The color scale is in  $\text{mJy beam}^{-1}$ .

in the envelope, position-velocity (pv) diagrams are constructed along the disk major axis for the four single sources (**Fig. 4.2**). A detailed analysis whether TMC1 has two circumstellar disks or one circumbinary disk is beyond the scope of this paper. In these diagrams, disk emission is located at small angular offsets and high velocities, while envelope emission extends to larger offsets but has lower velocities. In all sources, C<sup>17</sup>O traces predominantly the disk, with some envelope contribution in L1527 and L1489. H<sub>2</sub>CO emission also originates in the disk, but has a larger envelope component. This is in agreement with previous observations of L1527 (Sakai et al. 2014a). In L1489, a bright linear feature is present extending from a velocity and angular offset of -2 km s<sup>-1</sup> and -2'', respectively, to offsets of 2 km s<sup>-1</sup> and 2''. This feature matches the shape of the SO pv-diagram (Yen et al. 2014), which was interpreted by the authors as a ring between ~250–390 AU. While a brightness enhancement was also identified by Yen et al. (2014) in the C<sup>18</sup>O emission (similar as seen here for H<sub>2</sub>CO), the C<sup>17</sup>O emission does not display such feature.

Although both C<sup>17</sup>O and H<sub>2</sub>CO have emission originating from the disk, the C<sup>17</sup>O emission extends to higher velocities than the H<sub>2</sub>CO emission in IRAS 04302, L1527 and TMC1A. This is more easily visualized in the spectra presented in **Fig. 4.3**. These spectra are extracted in a 6'' circular aperture and only include pixels with > 3σ emission. While H<sub>2</sub>CO is brighter at intermediate velocities than C<sup>17</sup>O, it is not present at the highest velocities. H<sub>2</sub>CO emission thus seems absent in the inner disk in these sources, which for TMC1A is also visible in the moment zero map (**Fig. 4.1**). In L1489 and TMC1, however, both molecules have similar maximum velocities.

### 4.3.2 C<sup>17</sup>O and H<sub>2</sub>CO column densities

To compare the C<sup>17</sup>O and H<sub>2</sub>CO observations between the different sources more quantitatively, we calculate disk-averaged total column densities,  $N_T$ , using

$$\frac{4\pi S\Delta v}{A_{ul}\Omega h c g_{up}} = \frac{N_T}{Q(T_{rot})} e^{-E_{up}/kT_{rot}}, \quad (4.1)$$

where  $S\Delta v$  is the integrated flux density,  $A_{ul}$  is the Einstein A coefficient,  $\Omega$  is the solid angle subtended by the source,  $E_{up}$  and  $g_{up}$  are the upper level energy and degeneracy, respectively and  $T_{rot}$  is the rotational temperature.

The integrated fluxes are determined within a 0.5'' circular aperture and the central  $|\Delta v| = 1.0$  km s<sup>-1</sup> channels are excluded to limit the contribution from the envelope and resolved-out emission (**Table 4.3**). A temperature of 30 K is adopted for C<sup>17</sup>O and 100 K for H<sub>2</sub>CO. The differences between the sources in our sample are small with column densities varying less than an order of magnitude. The column densities range between ~ 4 – 14 × 10<sup>15</sup> cm<sup>-2</sup> for C<sup>17</sup>O, and between ~ 5 – 12 × 10<sup>13</sup> cm<sup>-2</sup> for H<sub>2</sub>CO. The H<sub>2</sub>CO column density toward L1527 is a factor 2–5 higher than previously derived by Sakai et al. (2014a), possibly because they integrated over different areas and velocity ranges for the envelope, disk and envelope-disk interface. Increasing the aperture size to a 2'' diameter or changing the temperature for H<sub>2</sub>CO to 30 K decreases the column densities by only a factor ≲ 3.

Assuming a C<sup>16</sup>O/C<sup>17</sup>O ratio of 1792 and a CO abundance of 10<sup>-4</sup> with respect to H<sub>2</sub>, an estimate can be made of the H<sub>2</sub> column density (~ 8 – 25 × 10<sup>22</sup> cm<sup>-2</sup>), and hence of the molecular abundances. For H<sub>2</sub>CO, the abundance ranges between ~ 2 × 10<sup>-10</sup> – ~ 2 × 10<sup>-9</sup> in the different sources. This is consistent with chemical models

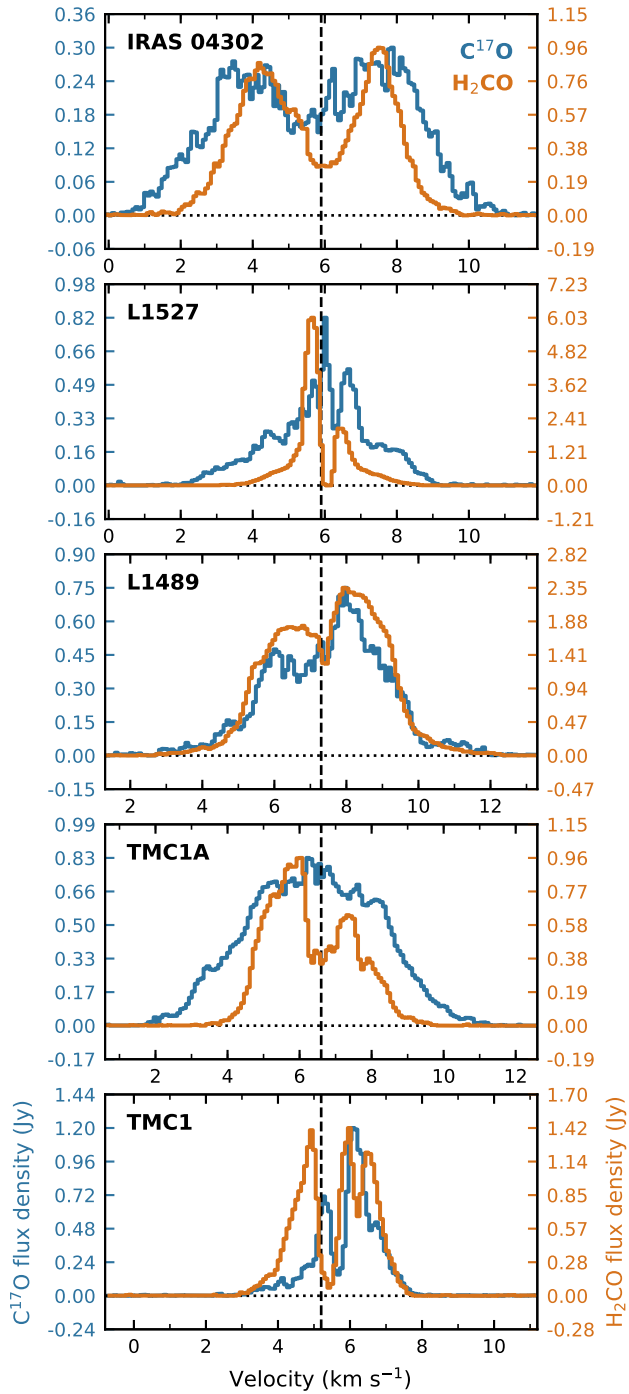


**Figure 4.3:** Spectra for  $C^{17}O$  (blue) and  $H_2CO$  (orange) toward the five sources in our sample. The spectra are extracted in a  $0.6''$  circular aperture centered at the continuum peak and only pixels with  $> 3\sigma$  emission are included. The vertical scale is different for each line. The vertical dashed lines mark the systemic velocities.



for protoplanetary disks (e.g., Willacy & Woods 2009; Walsh et al. 2014; Guzmán et al. 2018). However,  $\text{H}_2\text{CO}$  abundances derived for TW Hya and HD 163296 are 2–3 orders of magnitude lower,  $8.9 \times 10^{-13}$  and  $6.3 \times 10^{-12}$ , respectively (Carney et al. 2019).

### 4.3.3 HDO and $\text{CH}_3\text{OH}$ upper limits

Water and methanol form on ice-covered dust grains and thermally desorb into the gas phase at temperatures  $\sim 100$ – $150$  K. These molecules are thus expected to trace the hot region inside the water snowline. The observations cover one HDO (deuterated water) transition ( $3_{1,2} - 2_{2,1}$ ) with an upper level energy of 168 K, and 16 transitions in the  $\text{CH}_3\text{OH}$   $J = 5_k - 4_k$  branch with upper level energies ranging between 34 and 131 K. None of these lines are detected in any of the sources. To compare these non-detections to observations in other systems, a  $3\sigma$  upper limit is calculated for the disk-averaged total column density by substituting

$$3\sigma = 3 \times 1.1 \sqrt{\delta v \Delta V} \times \text{rms}, \quad (4.2)$$

for the integrated flux density,  $S\Delta v$  in [Eq. 4.2](#). Here  $\delta v$  is the velocity resolution, and  $\Delta V$  is the line width expected based on other line detections. The factor 1.1 takes a 10% calibration uncertainty in account.

Assuming the water and methanol emission arises from the innermost part of the disk, the rms is calculated from the base line of the spectrum integrated over a central  $0.5''$  diameter aperture ( $\sim$  one beam) and amounts to  $\sim 3$  mJy. Adopting a line width of  $4 \text{ km s}^{-1}$  and a rotational temperature of 100 K, this results in a  $3\sigma$  column density upper limit of  $\sim 9 \times 10^{13} \text{ cm}^{-2}$  for HDO. For  $\text{CH}_3\text{OH}$ , the  $5_{0,5} - 4_{0,4}$  (A) transition provides the most stringent upper limit of  $\sim 9 \times 10^{14} \text{ cm}^{-2}$ . This upper limit for methanol is orders of magnitude lower than the column density toward the Class 0 source IRAS 16293 ( $2 \times 10^{19} \text{ cm}^{-2}$  within a 70 AU beam; Jørgensen et al. 2016) and the young disk around the outbursting star V883 Ori (disk-averaged column density of  $\sim 1.0 \times 10^{17} \text{ cm}^{-2}$ ; van 't Hoff et al. 2018c, [Chapter 7](#)). However, it is not stringent enough to constrain the column to the value observed in the TW Hya protoplanetary disk (peak column density of  $3 - 6 \times 10^{12} \text{ cm}^{-2}$ ; Walsh et al. 2016). A more detailed analysis involving, for example, line stacking, Keplerian masking and/or match filtering (see e.g., Carney et al. 2019) or deeper integrations are thus required to determine whether the gas-phase methanol abundance is as low as in Class II disks.

For a better comparison with other sources, column density ratios are calculated with respect to  $\text{C}^{17}\text{O}$  and  $\text{H}_2\text{CO}$ , and are reported in [Table 4.4](#). Using the  $\text{H}_2$  column density derived from  $\text{C}^{17}\text{O}$ , upper limits of  $\sim 4 - 13 \times 10^{-10}$  are found for the HDO abundance.  $\text{CH}_3\text{OH}$  upper limits range between  $3 - 11 \times 10^{-9}$ . This is orders of magnitude lower than what is expected from ice observations ( $10^{-6} - 10^{-5}$ ; Boogert et al. 2015), and thus thermal desorption, as observed in IRAS 16293 ( $\lesssim 3 \times 10^{-6}$ ; e.g., Jørgensen et al. 2016) and V883-Ori ( $\sim 4 \times 10^{-7}$ ; van 't Hoff et al. 2018c, [Chapter 7](#); Lee et al. 2019). Abundances for non-thermally desorbed  $\text{CH}_3\text{OH}$  in TW Hya are estimated to be  $\sim 10^{-12} - 10^{-11}$  (Walsh et al. 2016). Sakai et al. (2014a) detected faint  $\text{CH}_3\text{OH}$  emission (from different transitions than targeted here) toward L1527, with a  $\text{CH}_3\text{OH}/\text{H}_2\text{CO}$  ratio between 0.6 and 5.1. Our upper limit of 6.1 is consistent with these values.  $\text{CH}_3\text{OH}/\text{H}_2\text{CO}$  ratios of 1.3 and  $< 0.2$  were derived for TW Hya and HD 163296, respectively, but our  $\text{CH}_3\text{OH}$  upper limit is not stringent enough to make a meaningful comparison.

**Table 4.4:** Integrated fluxes, column densities and column density ratios.

Source	Molecule	$F_{\text{int}}^a$ (mJy km s <sup>-1</sup> )	$N^b$ (cm <sup>-2</sup> )	$N/N(\text{H}_2)^c$	$N/N(\text{H}_2\text{CO})^d$
IRAS 04302	C <sup>17</sup> O	104 ± 9	6.0 × 10 <sup>15</sup>	-	83
	H <sub>2</sub> CO	55 ± 10	7.2 × 10 <sup>13</sup>	6.7 × 10 <sup>-10</sup>	-
	HDO	< 5.4	< 8.9 × 10 <sup>13</sup>	< 8.3 × 10 <sup>-10</sup>	< 1.24
	CH <sub>3</sub> OH	< 8.2	< 8.6 × 10 <sup>14</sup>	< 8.0 × 10 <sup>-9</sup>	< 11.9
L1489	C <sup>17</sup> O	73 ± 8	4.3 × 10 <sup>15</sup>	-	36
	H <sub>2</sub> CO	90 ± 13	1.2 × 10 <sup>14</sup>	1.6 × 10 <sup>-9</sup>	-
	HDO	< 5.4	< 8.9 × 10 <sup>13</sup>	< 1.2 × 10 <sup>-9</sup>	< 0.74
	CH <sub>3</sub> OH	< 8.2	< 8.6 × 10 <sup>14</sup>	< 1.1 × 10 <sup>-8</sup>	< 7.17
L1527	C <sup>17</sup> O	106 ± 6	6.2 × 10 <sup>15</sup>	-	44
	H <sub>2</sub> CO	94 ± 10	1.2 × 10 <sup>14</sup>	1.3 × 10 <sup>-9</sup>	-
	HDO	< 5.4	< 8.9 × 10 <sup>13</sup>	< 8.0 × 10 <sup>-10</sup>	< 0.64
	CH <sub>3</sub> OH	< 8.2	< 8.6 × 10 <sup>14</sup>	< 7.7 × 10 <sup>-9</sup>	< 6.14
TMC1A	C <sup>17</sup> O	248 ± 11	1.4 × 10 <sup>16</sup>	-	280
	H <sub>2</sub> CO	38 ± 5	5.0 × 10 <sup>13</sup>	2.0 × 10 <sup>-10</sup>	-
	HDO	< 5.4	< 8.9 × 10 <sup>13</sup>	< 3.5 × 10 <sup>-10</sup>	< 1.78
	CH <sub>3</sub> OH	< 8.2	< 8.6 × 10 <sup>14</sup>	< 3.4 × 10 <sup>-9</sup>	< 17.2

**Notes.** <sup>(a)</sup> Integrated flux. For C<sup>17</sup>O and H<sub>2</sub>CO this is extracted within a circular aperture with 0.5'' diameter excluding the central  $|\Delta v| = 1.0$  km s<sup>-1</sup>. For HDO and CH<sub>3</sub>OH this is the 3 $\sigma$  upper limit to the integrated flux. <sup>(b)</sup> Column density. <sup>(c)</sup> Column density with respect to H<sub>2</sub>, where the H<sub>2</sub> column density is derived from C<sup>17</sup>O. <sup>(d)</sup> Column density with respect to H<sub>2</sub>CO.

## 4.4 Analysis

### 4.4.1 Temperature structure in the edge-on disks

For (near) edge-on disks, CO freeze-out should be readily observable as CO emission will be missing from the outer disk midplane (Dutrey et al. 2017; van 't Hoff et al. 2018b). van 't Hoff et al. (2018b) (**Chapter 3**) studied the effect of CO freeze-out on the optically thick <sup>13</sup>CO and C<sup>18</sup>O emission in L1527. The less-abundant C<sup>17</sup>O traces mainly the disk and is expected to be optically thin. The ‘warm’ (no CO freeze-out), ‘intermediate’ (CO freeze-out in the outer disk midplane) and ‘cold’ (CO freeze-out in most of the disk, except the inner part and surface layers) models from van 't Hoff et al. (2018b) are employed to predict the C<sup>17</sup>O emission pattern for varying degrees of CO freeze-out (see **Fig. 4.B.1**). Briefly, in these models gaseous CO is present at a constant abundance of 10<sup>-4</sup> w.r.t. H<sub>2</sub> in the regions where  $T > 20$  K. For the warm model, the L1527 temperature structure from Tobin et al. (2013b) is adopted, and for the intermediate and cold models the temperature is reduced by 40% and 60%, respectively. Synthetic images cubes are generated using the radiative transfer code LIME (Hogerheijde & van der Tak 2000) and convolved with the observed beam size.

**Figure 4.4** shows moment zero maps integrated over the low, intermediate and high velocities for the warm and cold edge-on model. Models with and without an envelope are presented. The difference between the warm and cold model is most clearly distinguishable at intermediate velocities. When an envelope is present the envelope

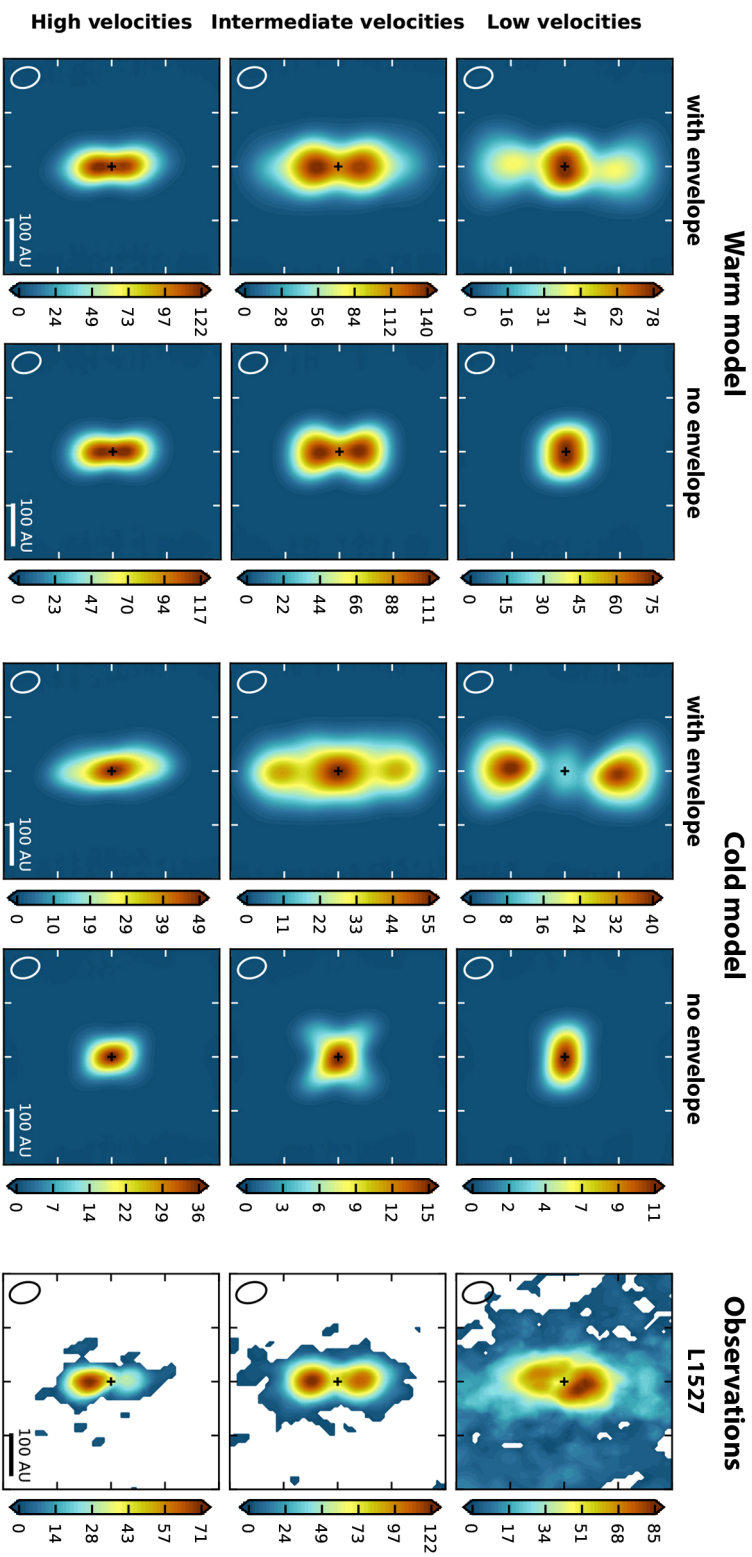


**Figure 4.4:** Integrated intensity (moment zero) maps of the low-velocity (top row), intermediate-velocity (middle row), and high-velocity (bottom row)  $\text{C}^{17}\text{O } J=2-1$  emission in the warm (first and second column) and cold edge-on disk models (third and fourth column) and the L1527 observations (fifth column). The models contain either a disk and envelope (first and third column) or only a disk (second and fourth column). For the observations, only pixels with  $> 3\sigma$  emission are included. Low velocities range from  $-1.11$  to  $1.25 \text{ km s}^{-1}$ , intermediate velocities range from  $-2.42$  to  $-1.19 \text{ km s}^{-1}$  and from  $1.33$  to  $2.39 \text{ km s}^{-1}$ , and high velocities range from  $-3.97$  to  $-2.5 \text{ km s}^{-1}$  and from  $2.48$  to  $3.13 \text{ km s}^{-1}$ . The color scale is in  $\text{mJy beam}^{-1} \text{ km s}^{-1}$ . The source position is marked with a black cross and the beam is shown in the lower left corner of the panels. A 100 AU scalebar is present in the bottom panels.

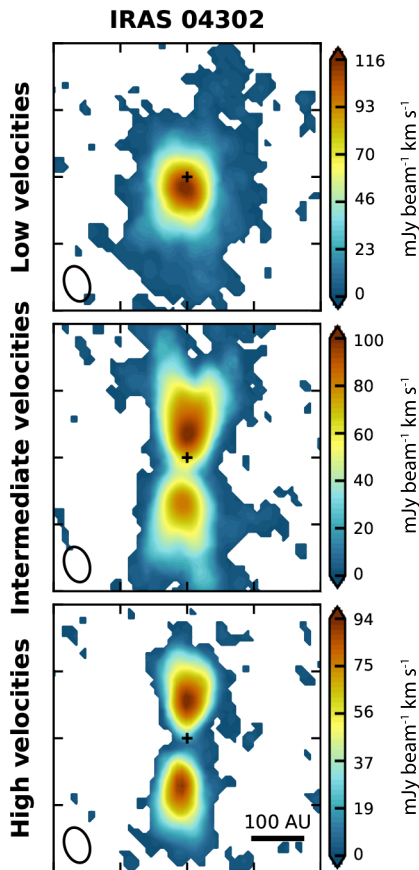


**Figure 4.5:** Integrated intensity (moment zero) maps of the low-velocity (*top row*), intermediate-velocity (*middle row*), and high-velocity (*bottom row*)  $\text{C}^{17}\text{O } J = 2 - 1$  emission toward IRAS 04302. Only pixels with  $> 3\sigma$  emission are included. Low velocities range from  $-1.21$  to  $1.16 \text{ km s}^{-1}$ , intermediate velocities range from  $-2.92$  to  $-1.29 \text{ km s}^{-1}$  and from  $1.24$  to  $2.38 \text{ km s}^{-1}$ , and high velocities range from  $-5.28$  to  $-3.00 \text{ km s}^{-1}$  and from  $2.46$  to  $4.67 \text{ km s}^{-1}$ . The source position is marked with a black cross and the beam is shown in the lower left corner of the panels. A 100 AU scalebar is present in the bottom panel.

emission becomes comparable in strength to the disk emission in the cold model, while the disk emission dominates in the warm model. In the absence of an envelope, the emission becomes V-shaped in the cold model, tracing the warm surface layers where CO is not frozen out. At low velocities, the difference between a warm and cold disk can be distinguished as well when an envelope is present, although in practice this will be much harder due to resolved out emission at these central velocities. Without an envelope, the low velocity emission originates near the source center due to the rotation, and the models are indistinguishable, except for differences in the flux. At the highest velocities, the emission originates in the inner disk, so even if CO is absent in the midplane, very high angular resolution would be required to observe this.

$\text{C}^{17}\text{O}$  moment zero maps integrated over different velocity intervals are presented

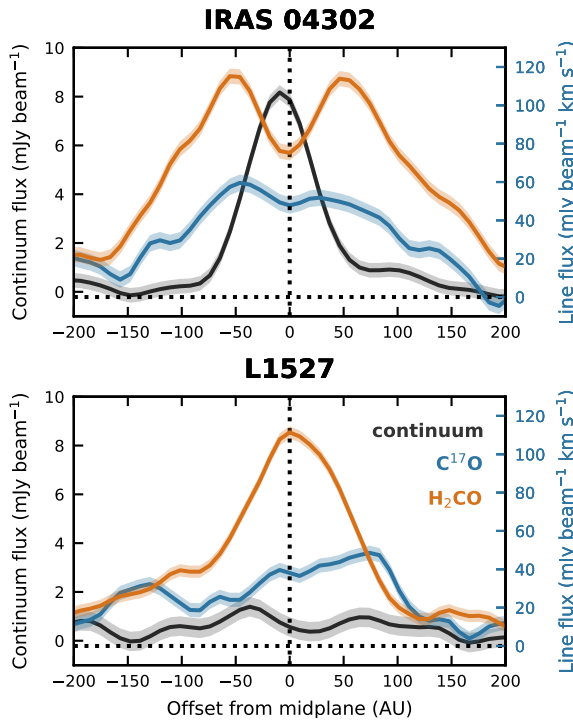


**Figure 4.6:** Vertical cuts through the edge-on disks IRAS 04302 (*top panel*) and L1527 (*bottom panel*) at  $1.5''$  north of the continuum peak. The 1.3 mm continuum is shown in black and the integrated intensity for  $\text{C}^{17}\text{O } J = 2 - 1$  and  $\text{H}_2\text{CO } 3_{1,2}-2_{1,1}$  in blue and orange, resp. The shaded area shows the  $1\sigma$  uncertainty.

in **Fig. 4.4** (right panels) for L1527 and in **Fig. 4.5** for IRAS 04302. The observations show no sign of CO freeze-out in L1527 and resemble the warm model, consistent with previous results for  $\text{C}^{18}\text{O}$  and  $^{13}\text{CO}$ . In contrast, IRAS 04302 displays a distinct V-shaped pattern at intermediate velocities, suggesting that CO is frozen out in the outer part of the disk. A first estimate of the the CO snowline location can be made from the location of the V-shape. In the cold model, the CO snowline is located at 23 AU, but due to the size of the beam, the base of the V-shape is shifted outward by  $\sim 35$  AU. In IRAS 04302, the V-shape begins at a radius of  $\sim 140$  AU, so the CO snowline location is then estimated to be around  $\sim 105$  AU.

A clear V-shaped pattern is also visible in the  $\text{H}_2\text{CO}$  integrated emission map for IRAS 04302 (**Fig. 4.1**). The decrease in emission toward the midplane is highlighted by a vertical cut at  $1.5''$  offset from the source position shown in **Fig. 4.6**. The base of the V-shape is at  $\sim 85$  AU ( $\sim 1.5$  beams offset from the continuum peak). If the reduction of  $\text{H}_2\text{CO}$  in the midplane is fully due to freeze-out, the snowline is then located around  $\sim 50$  AU. Assuming a binding energy of 2050 K (Garrod & Herbst 2006), the freeze-out temperature for  $\text{H}_2\text{CO}$  is  $\sim 50$  K for disk-midplane densities ( $\sim 10^8 - 10^{10} \text{ cm}^{-3}$ ).

A first rough estimate of the midplane temperature profile for IRAS 04302 can be made from these two snowline estimates using a radial power law,  $T \propto R^{-q}$ . For disks, often a power law exponent  $q$  of 0.5 is assumed, but  $q$  can range between 0.33 and 0.75 (see e.g., Adams & Shu 1986; Kenyon et al. 1993; Chiang & Goldreich 1997).

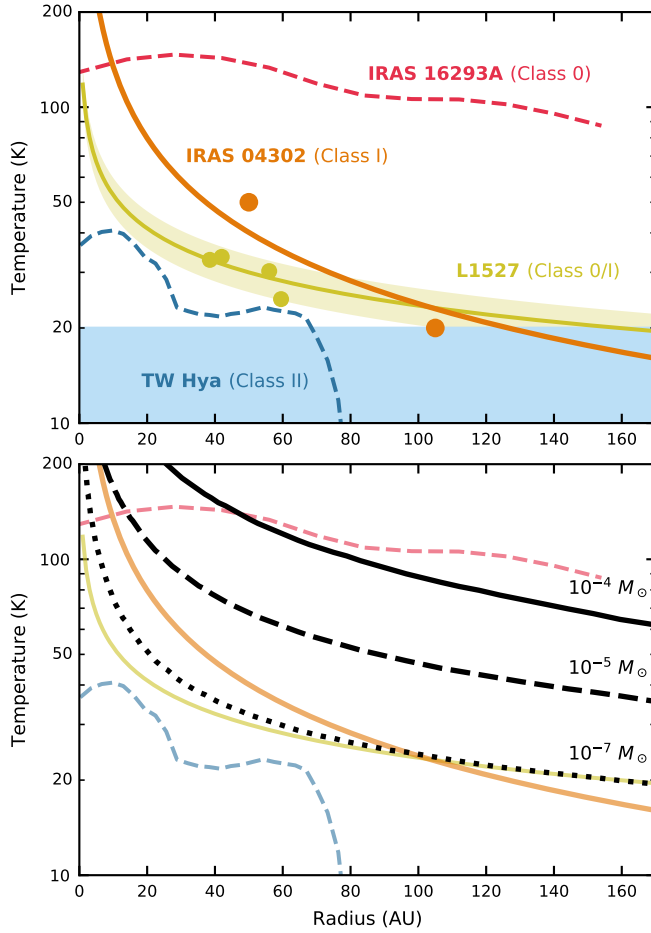


**Figure 4.7:** *Top panel:* Radial midplane temperature profile for IRAS 04302 inferred from the CO and H<sub>2</sub>CO snowline estimates (orange circles). The solid orange line is a power law of the shape  $T \propto R^{-q}$ , where  $q = 0.75$ . For comparison, the temperature measurements for L1527 from <sup>13</sup>CO and C<sup>18</sup>O emission (yellow circles) and a power law temperature profile with  $q = 0.35$  (yellow line) are shown (van 't Hoff et al. 2018b, **Chapter 3**). The yellow shaded area represents the  $1\sigma$  uncertainty on the L1527 temperature profile. The temperature profile derived for the disk-like structure in the Class 0 source IRAS 16293A using H<sub>2</sub>CS line ratios (van 't Hoff et al. in prep., **Chapter 8**) is shown by the dashed red line, and the temperature profile for the Class II disk TW Hya based on observations of multiple CO isotopologue transitions is shown by the dashed blue line (Schwarz et al. 2016). The TW Hya temperature profile does not trace the midplane but slightly higher layers. The midplane CO snowline is located around  $\sim 20$  AU (e.g., van 't Hoff et al. 2017, **Chapter 2**; Zhang et al. 2017). The blue shaded area denotes the temperatures at which CO is frozen out. The *bottom panel* shows the temperature profiles from the *top panel* overlaid with temperature profiles from embedded-disk models from Harsono et al. (2015). All three models have a stellar luminosity of  $1 L_{\odot}$ , an envelope mass of  $1 M_{\odot}$ , a disk mass of  $0.05 M_{\odot}$  and disk radius of 200 AU, but different accretion rates of  $10^{-4} M_{\odot} \text{ yr}^{-1}$  (solid black line),  $10^{-5} M_{\odot} \text{ yr}^{-1}$  (dashed black line) and  $10^{-7} M_{\odot} \text{ yr}^{-1}$  (dotted black line).

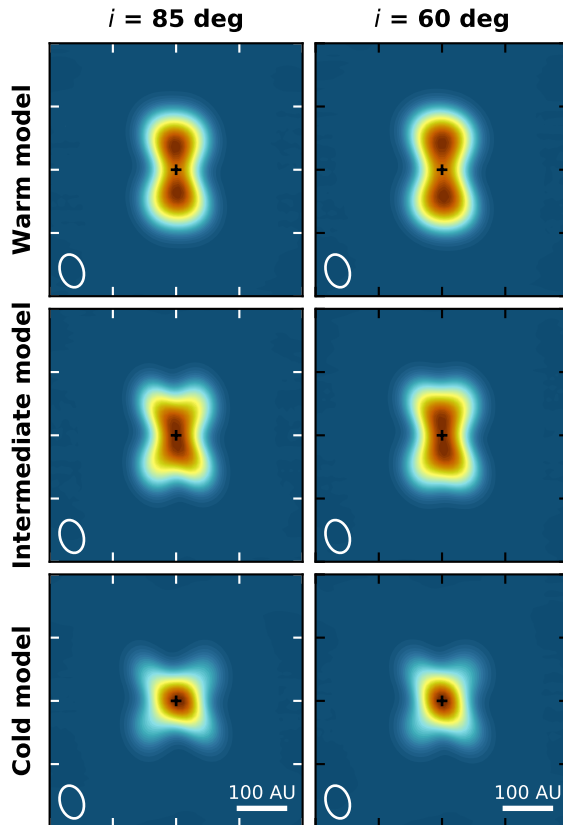


**Figure 4.8:** Integrated intensity (moment zero) maps of the intermediate-velocity  $\text{C}^{17}\text{O}$   $J = 2 - 1$  emission in the warm (*top row*), intermediate (*middle row*) and cold disk model (*bottom row*). The *left column* shows a near edge-on disk ( $i = 85^\circ$ ) as in **Fig. 4.4**, and the *right column* shows a less-inclined disk ( $i = 60^\circ$ ). The velocity range  $\Delta v$  is  $1.0\text{--}1.9 \text{ km s}^{-1}$  for  $i = 85^\circ$  and  $1.3\text{--}1.8 \text{ km s}^{-1}$  for  $i = 60^\circ$ . The source position is marked with a black cross and the beam is shown in the lower left corner of the panels. A 100 AU scalebar is present in the bottom panels.

A power law with  $q = 0.75$  matches the two temperature estimates reasonably well (see **Fig. 4.7**). This temperature profile is quite similar to the profiles constructed for L1527 based on  $^{13}\text{CO}$  and  $\text{C}^{18}\text{O}$  temperature measurements (van 't Hoff et al. 2018b, **Chapter 3**). IRAS 04302 is thus warm like L1527, with freeze-out occurring only in the outermost part of this large disk ( $R_{\text{disk}} \sim 250 \text{ AU}$ , compared to  $R_{\text{disk}} \sim 75\text{--}125 \text{ AU}$  for L1527; Aso et al. 2017; Tobin et al. 2013b; Sheehan & Eisner 2017).

Based on the L1527 temperature profiles, the  $\text{H}_2\text{CO}$  snowline is located at radii  $\lesssim 20 \text{ AU}$ . However, no V-shaped emission pattern is seen for  $\text{H}_2\text{CO}$  toward L1527 (**Fig. 4.1**), also not in the individual velocity channels. Given the strong envelope component for this source, a  $\text{H}_2\text{CO}$  deficit in the midplane could be blocked at intermediate velocities by envelope emission. At high velocities the angular resolution is not high enough to resolve a  $\sim 20 \text{ AU}$  snowline location (see **Fig. 4.4**). Alternatively, this emission morphology could indicate that the temperature is higher than derived from the  $^{13}\text{CO}$  and  $\text{C}^{18}\text{O}$  emission.

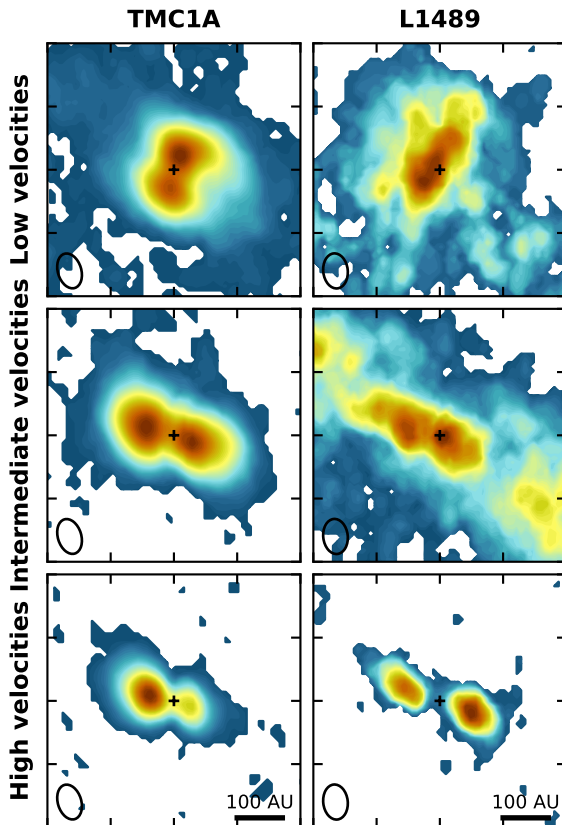


**Figure 4.9:** Integrated intensity (moment zero) maps of the low-velocity (*top row*), intermediate-velocity (*middle row*), and high-velocity (*bottom row*)  $\text{C}^{17}\text{O } J = 2 - 1$  emission toward TMC1A (*left column*) and L1489 (*right column*). Only pixels with  $> 3\sigma$  emission are included. For TMC1A (L1489), low velocities range from  $-1.27$ – $1.26$  ( $-0.47$ – $0.43$ )  $\text{km s}^{-1}$ , the intermediate velocities include  $\Delta v = 1.34$ – $2.49$  ( $0.50$ – $3.00$ )  $\text{km s}^{-1}$ , and the high velocities are  $\Delta v = 2.57$ – $4.94$  ( $3.05$ – $4.65$ )  $\text{km s}^{-1}$ . The source position is marked with a black cross and the beam is shown in the lower left corner of the panels. A 100 AU scalebar is present in the bottom panels.

#### 4.4.2 Temperature structure in less-inclined disks

For less inclined disks, observing freeze-out directly is much harder because now both the near and far side of the disk become visible. Emission from the far side of the disk can then appear to come from the midplane of the near side (see [Fig. 4.B.2](#), and [Pinte et al. 2018](#)). For the L1527 disk model, the intermediate and warm model become almost identical for an inclination of  $60^\circ$  at this angular resolution, and only a cold disk shows a clear V-shaped pattern ([Fig. 4.8](#)). [Figure 4.9](#) shows the  $\text{C}^{17}\text{O}$  moment zero maps for the intermediate inclined disks TMC1A and L1489. The disk size, stellar mass and stellar luminosity of TMC1A are comparable to L1527. At intermediate velocities there is no sign of a V-shaped pattern, so these observations do not suggest heavy freeze out of CO in TMC1A. This is consistent with the results from [Aso et al. \(2015\)](#), who find a temperature of 38 K at 100 AU from fitting a disk model to ALMA



C<sup>18</sup>O observations.

For L1489, the intermediate velocities show a more complex pattern with CO peaking close to the source and at larger offsets ( $\gtrsim 2''$ ). This could be the result of non-thermal desorption of CO ice in the outer disk if the dust-to-gas ratio is low enough for UV photons to penetrate (Cleeves 2016), or due to a radial temperature inversion resulting from radial drift and dust settling (Facchini et al. 2017). Such a double CO snowline has been observed for the protoplanetary disk IM Lup (Öberg et al. 2015a; Cleeves 2016). The structure of the continuum emission, a bright central part and a fainter outer part, make these plausible ideas. If the edge of the compact CO emission is due to freeze-out, the CO snowline is located at roughly 140 AU. However, due to the different velocity patterns in the disk and envelope, a system with gaseous CO throughout the entire disk and inner envelope can also show such a disconnected emission pattern. The temperature structure derived by (Brinch et al. 2007) still has a temperature of 25 K at 500 AU, suggesting that no freeze out would occur in the disk.

## 4.5 Discussion

### 4.5.1 Temperature structure of young disks

No sign of CO freeze-out is detected in the C<sup>17</sup>O observations of L1527, and while freeze-out is much more difficult to see in non-edge on disks, TMC1A does not show hints of large scale freeze-out. A first estimate puts the CO snowline at  $\sim 105$  AU in IRAS 04302, and the CO snowline may be located around  $\sim 140$  AU in L1489. These young disks are thus warmer than T Tauri disks where the snowline is typically at a few tens of AU, as can be seen in **Fig. 4.7**. This figure shows a comparison between the temperature profiles inferred for the embedded disks L1527 (van 't Hoff et al. 2018b; **Chapter 3**) and IRAS 04302, and temperature profiles for the younger Class 0 disk-like structure around IRAS 16293 (van 't Hoff et al. in prep.; **Chapter 8**) and the Class II disk TW Hya (Schwarz et al. 2016). The young disks are warmer than the more evolved Class II disk, but much colder than the Class 0 system.

Such an evolutionary trend is expected because the accretion rate decreases as the envelope and disk dissipate. As a consequence, heating due to viscous accretion diminishes and hence the temperature drops, as shown by two-dimensional physical and radiative transfer models for embedded protostars (D'Alessio et al. 1997; Harsono et al. 2015). As a first comparison between the observations and model predictions, models from Harsono et al. (2015) are overlaid on the observationally inferred temperature profiles in **Fig. 4.7** (bottom panel). In these models the dust temperature is determined based on stellar irradiation and viscous accretion. Models are shown for a stellar luminosity of  $1 L_{\odot}$ , an envelope mass of  $1 M_{\odot}$ , a disk mass of  $0.05 M_{\odot}$ , a disk radius of 200 AU and different accretion rates. The disk mass has a negligible effect on the temperature profiles. For accretion rates  $> 10^{-6} M_{\odot} \text{ yr}^{-1}$ , the temperature decreases for smaller disk radii (see Harsono et al. 2015 for details). IRAS 16293A matches reasonably well with the temperature profile for a heavily accreting system ( $10^{-4} M_{\odot} \text{ yr}^{-1}$ ), consistent with estimates of the accretion rate (e.g.,  $\sim 5 \times 10^{-5} M_{\odot} \text{ yr}^{-1}$ ; Schöier et al. 2002). In contrast, the temperature profile for L1527 is similar to the colder  $10^{-7} M_{\odot} \text{ yr}^{-1}$  model, consistent with an accretion rate of  $\sim 3 \times 10^{-7} M_{\odot} \text{ yr}^{-1}$  (see van 't Hoff et al. 2018b; **Chapter 3**). IRAS 04302 seems to fall

in between the  $10^{-5}$  and  $10^{-7} M_{\odot} \text{ yr}^{-1}$  models. The results presented in this Chapter thus provide observational evidence for cooling of the circumstellar material during evolution. More sources need to be observed to confirm this trend and to answer more detailed questions such as, when has a disk cooled down sufficiently for large-scale CO freeze-out? Does this already happen before the envelope dissipates? IRAS 04302 is a borderline Class I/Class II object embedded in the last remnants of its envelope, but still has a temperature profile more similar to L1527 than TW Hya. This hints that disks may stay warm until the envelope has fully dissipated.

One of the major questions regarding the chemical composition of planetary material, is whether they contain complex organic molecules (COMs). Due to the low temperatures in protoplanetary disks, observations of COMs are very challenging because these molecules thermally desorb at temperatures  $\gtrsim 100\text{--}150$  K, that is, in the inner few AU. In contrast, COMs are readily detected on disk-scales in protostellar envelopes (e.g., IRAS 16293; Jørgensen et al. 2016) and in the young disk V883-Ori, where a luminosity outburst has heated the disk and liberated the COMs from the ice mantles (van 't Hoff et al. 2018c, **Chapter 7**; Lee et al. 2019). Although young disks seem warmer than protoplanetary disks, the  $\text{CH}_3\text{OH}$  and HDO non-detections suggest that they are not warm enough to have a large gas reservoir of COMs. This is consistent with recent findings by Artur de la Villarmois et al. (2019) for a sample of protostars in Ophiuchus. A more detailed analysis of the  $\text{CH}_3\text{OH}$  observations through, for example, line stacking, Keplerian masking or matched filtering may result in more stringent upper limits that can then be compared to TW Hya and HD 163296. A weak detection of  $\text{CH}_3\text{OH}$  has been reported for L1527 (Sakai et al. 2014a), so deep integrations may reveal some of the chemical complexity present in the early stage of planet formation.

A related question to the chemical composition, is whether the disk material is directly inherited from the cloud, processed en route to the disk, or even fully reset upon entering the disk. Young disks like L1527, where no CO freeze-out is observed, suggest that no full inheritance takes place, at least not for the most volatile species like CO. Ice in the outer disk of IRAS 04302 could be inherited. However, the freeze-out timescale for densities  $> 10^6 \text{ cm}^{-3}$  is  $< 10^4$  year, so this CO could have sublimated upon entering the disk and frozen out as the disk cooled (see e.g., Visser et al. 2009b). Without CO ice, no additional formation of COMs is possible in the young disks. So if COMs are present in more evolved disks, as for example shown for V883 Ori, they must have been inherited from a colder pre-collapse phase. Physicochemical models show that prestellar methanol can indeed be incorporated into the disk (Drozdovskaya et al. 2014).

### 4.5.2 Decrease in $\text{H}_2\text{CO}$ in the inner disk

While the  $\text{H}_2\text{CO}$  emission is brighter than the  $\text{C}^{17}\text{O}$  emission at intermediate velocities, no  $\text{H}_2\text{CO}$  emission is detected at the highest velocities in IRAS 04302, L1527 and TMC1A, suggesting a reduction in  $\text{H}_2\text{CO}$  flux in the inner  $\lesssim 20\text{--}30$  AU in these disks. This decrease in emission is unlikely due to the continuum being optically thick because this would affect the  $\text{C}^{17}\text{O}$  emission as well. Formaldehyde rings have also been observed in the protoplanetary disks around TW Hya (Öberg et al. 2017), HD 163296 (Qi et al. 2013a; Carney et al. 2017), DM Tau (Henning & Semenov 2008; Loomis et al. 2015) and DG Tau (Podio et al. 2019). Interestingly, a ring is only

observed for the  $3_{03} - 2_{02}$  and  $3_{12} - 2_{11}$  transitions and not for the  $5_{15} - 4_{14}$  transition. Öberg et al. (2017) argue that the dust opacity cannot be the major contributor in TW Hya, because the dust opacity should be higher at higher frequencies, thus for the  $5_{15} - 4_{14}$  transition. Instead, they suggest a warm inner component that is visible in the  $5_{15} - 4_{14}$  transition ( $E_{\text{up}} = 63$  K) and not in the  $3_{12} - 2_{11}$  transition ( $E_{\text{up}} = 33$  K). However, radiative transfer modeling for the L1527 warm disk model shows that both the  $\text{C}^{17}\text{O}$  ( $E_{\text{up}} = 33$  K) and  $\text{H}_2\text{CO}$  emission goes down by a factor  $\sim 2$  if the temperature is increased by 80%. An excitation effect thus seems unlikely, unless the  $\text{C}^{17}\text{O}$  emission is optically thick. The latter is not expected given that the  $\text{C}^{18}\text{O}$  in L1527 is only marginally optically thick (van 't Hoff et al. 2018b; **Chapter 3**). The absence  $\text{H}_2\text{CO}$  emission in the inner disk thus points to a reduced  $\text{H}_2\text{CO}$  abundance.

The  $\text{H}_2\text{CO}$  abundance can be low if its formation is inefficient.  $\text{H}_2\text{CO}$  can form both in the gas and in the ice (e.g., Willacy & Woods 2009; Walsh et al. 2014; Loomis et al. 2015). On the grain surfaces, the dominant formation route is through hydrogenation of CO (Watanabe & Kouchi 2002; Cuppen et al. 2009; Fuchs et al. 2009). Since there seems to be no CO freeze out in these young disks, or only at radii  $\gtrsim 100$  AU,  $\text{H}_2\text{CO}$  is expected to form predominantly in the gas. Ring-shaped  $\text{H}_2\text{CO}$  emission due to increased ice formation outside the CO snowline, as used to explain the ring observed in HD 163296 (Qi et al. 2013a), is thus not applicable to the disks in this sample. In the gas, the reaction between  $\text{CH}_3$  and O is the most efficient way to form  $\text{H}_2\text{CO}$  (e.g., Loomis et al. 2015). Therefore, a decrease in gas-phase  $\text{H}_2\text{CO}$  formation would require a low abundance of  $\text{CH}_3$  or O.  $\text{CH}_3$  is efficiently produced by photodissociation of  $\text{CH}_4$ . A low  $\text{CH}_3$  abundance thus necessitates a low  $\text{CH}_4$  abundance or a weak UV and X-ray field. However, chemical models generally predict  $\text{CH}_4$  to be abundant. Atomic oxygen is formed through X-ray photodissociation of CO and  $\text{CO}_2$ , or through dissociation of CO via X-ray-generated  $\text{He}^+$ . A low atomic oxygen abundance would thus require a low X-ray flux.

Besides a low formation rate, a high destruction rate would also decrease the amount of  $\text{H}_2\text{CO}$ . However, the destruction products have a limited chemistry and re-creation of  $\text{H}_2\text{CO}$  is the most likely outcome. Willacy & Woods (2009) showed that a third of the ions formed by  $\text{H}_2\text{CO}$  destruction through  $\text{HCO}^+$  and  $\text{DCO}^+$  form CO instead of reforming  $\text{H}_2\text{CO}$ , leading to a depletion between 7 and 20 AU for their disk model. However, this only reduces  $\text{H}_2\text{CO}$  in the midplane, not in the surface layers. In addition, Henning & Semenov (2008) suggested the conversion of CO into  $\text{CO}_2$ -containing molecules and hydrocarbons that freeze out onto dust grains (see also Aikawa et al. 1999). However, the  $\text{C}^{17}\text{O}$  observations do not suggest heavy CO depletion. Observations of higher excitation  $\text{H}_2\text{CO}$  lines and chemical modeling with source-specific structures may provide further insights.

## 4.6 Conclusions

Temperature plays a key role in the physical and chemical evolution of circumstellar disks, and therefore in the outcome of planet formation. However, the temperature structure of young embedded disks, in which the first steps of planet formation take place, is poorly constrained. Our previous analysis of  $^{13}\text{CO}$  and  $\text{C}^{18}\text{O}$  emission in the young disk L1527 suggest that this disk is warm enough ( $T \gtrsim 20\text{-}25$  K) to prevent CO freeze-out (van 't Hoff et al. 2018b; **Chapter 3**) in contrast to protoplanetary disks that show large cold outer regions where CO is frozen out. Here we present ALMA

observations of  $\text{C}^{17}\text{O}$ ,  $\text{H}_2\text{CO}$  and non-detections of  $\text{HDO}$  and  $\text{CH}_3\text{OH}$  for five young disks in Taurus, including L1527. Based on the following results we conclude that young disks are likely warmer than more evolved protoplanetary disks, but not warm enough to have a large gas reservoir of complex molecules, like the young disk around the outbursting star V883-Ori:

- CO freeze-out can be observed directly with  $\text{C}^{17}\text{O}$  observations in edge-on disks. L1527 shows no sign of CO freeze-out, but IRAS 04302 has a large enough disk for the temperature to drop below the CO freeze-out temperature in the outermost part (radii  $\gtrsim 105$  AU).
- $\text{H}_2\text{CO}$  emission originates primarily in the surface layers of IRAS 04302, and the freeze-out radius ( $T \sim 50$  K) is estimated at  $\sim 50$  AU. This is warmer than previously derived for L1527 at these radii, but no sign of  $\text{H}_2\text{CO}$  freeze-out is observed in L1527, possibly due to a large envelope contribution in this more embedded source.
- CO freeze-out is much more difficult to observe in non-edge-on disks, but the  $\text{C}^{17}\text{O}$  emission in TMC1A is not consistent with a snowline at  $\sim 20$  AU. Two spatial components are seen in the  $\text{C}^{17}\text{O}$  emission toward L1489. If the outer edge of the inner component is due to CO freeze-out, the snowline would be around  $\sim 140$  AU.
- The upper limits for the  $\text{CH}_3\text{OH}$  column density ( $\sim 9 \times 10^{14} \text{ cm}^{-2}$ ) and abundance ( $\sim 3 - 11 \times 10^{-9}$ ) are several orders of magnitude lower than observed in IRAS 16293 and V883-Ori, but not stringent enough to determine whether there is more gas-phase methanol than in the protoplanetary disks TW Hya and HD 163296.
- The inferred temperature profiles are consistent with trends found in radiative transfer models of disk-envelope systems with accretion rates decreasing from  $10^{-4}$  to  $10^{-7} M_{\odot} \text{ yr}^{-1}$ .

Without a large CO-ice reservoir, COM formation is restricted in embedded disks. Observations of COMs in more evolved disks therefore suggest that these molecules are inherited from the cold pre-collapse phase.

## Acknowledgements

This paper makes use of the following ALMA data: ADS/JAO.ALMA#2017.1.01413.S. ALMA is a partnership of ESO (representing its member states), NSF (USA) and NINS (Japan), together with NRC (Canada), MOST and ASIAA (Taiwan), and KASI (Republic of Korea), in cooperation with the Republic of Chile. The Joint ALMA Observatory is operated by ESO, AUI/NRAO and NAOJ. Astrochemistry in Leiden is supported by the Netherlands Research School for Astronomy (NOVA). M.L.R.H acknowledges support from a Huygens fellowship from Leiden University.

## Appendix

### 4.A $\text{C}^{17}\text{O}$ and $\text{H}_2\text{CO}$ Observations

Moment one maps for  $\text{C}^{17}\text{O } J = 2 - 1$  and  $\text{H}_2\text{CO } 3_{2,1} - 2_{1,1}$  toward all disks in the sample are shown in **Fig. 4.A.1**. In addition, **Fig. 4.A.2** presents radial cuts of the integrated emission (moment zero) along the disk major axis, that is, perpendicular to the outflow as shown in **Fig. 4.1**.

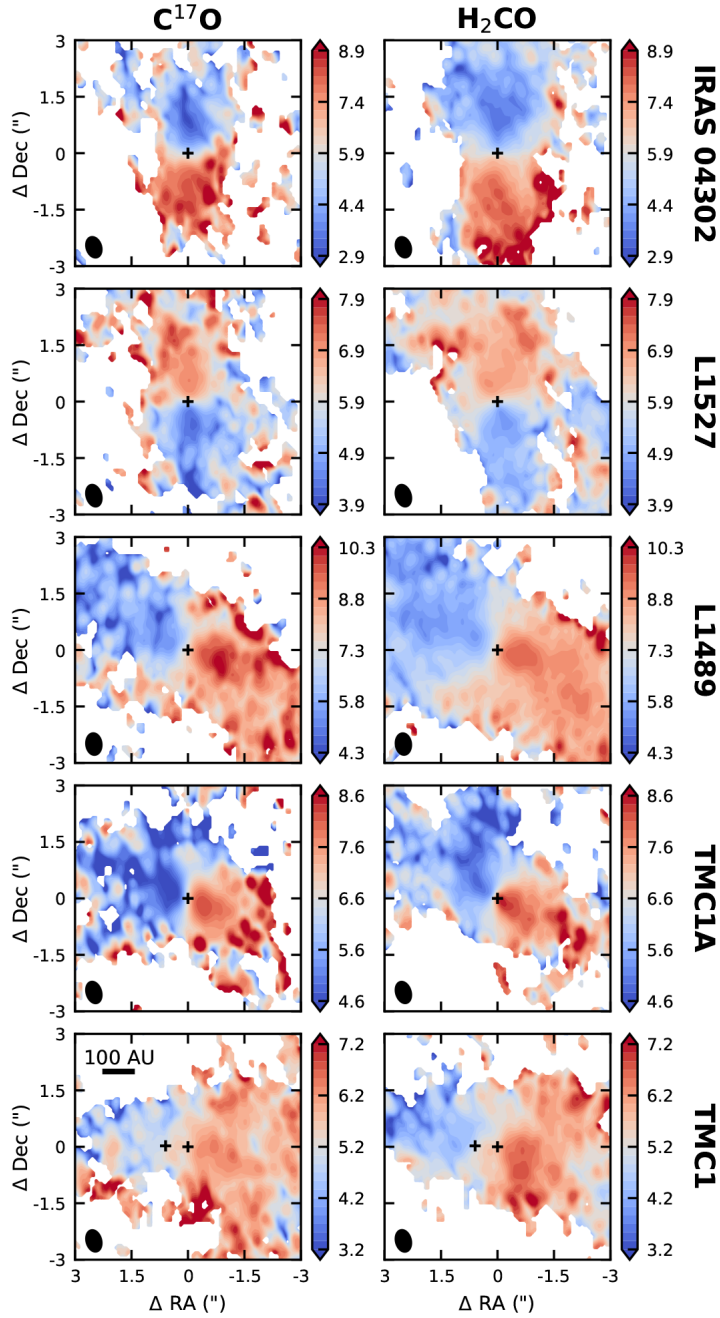


**Figure 4.1.1:** Moment one maps for the C<sup>17</sup>O  $J = 2 - 1$  (left panels) and H<sub>2</sub>CO  $3_{1,2} - 2_{1,1}$  (right panels) transitions. The central velocity of the color scale is the systemic velocity (km s<sup>-1</sup>). The positions of the continuum peaks are marked with black crosses and the beam is shown in the lower left corner of each panel.

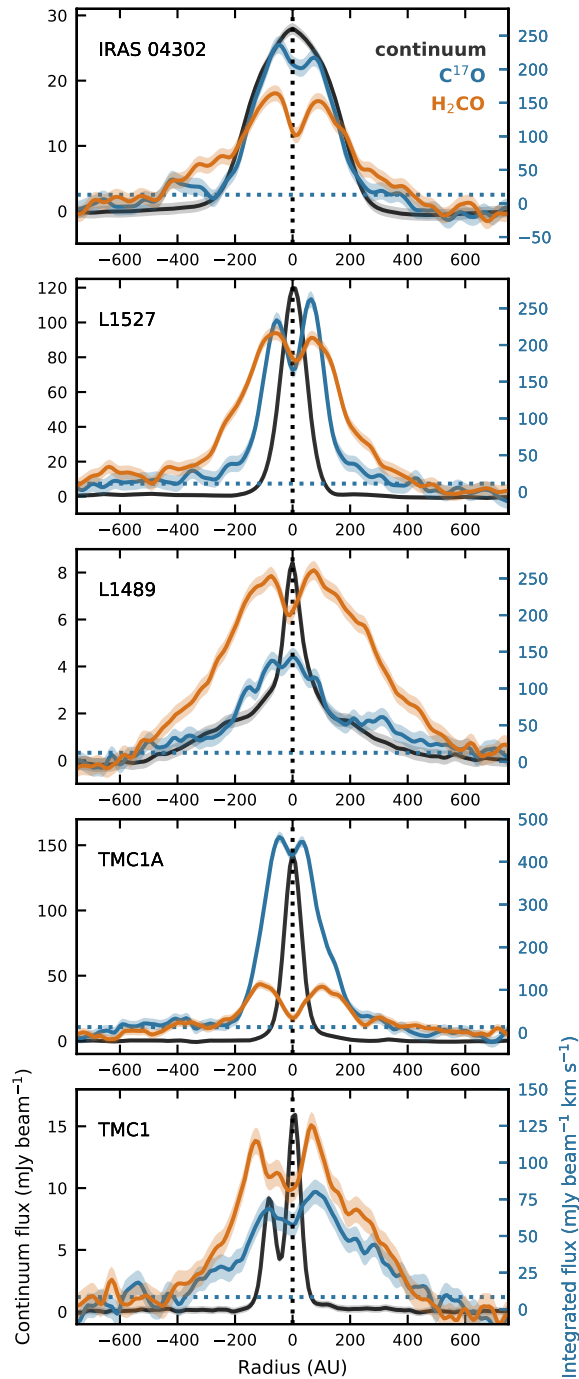


**Figure 4.1.2:** Radial profiles of the 1.3 mm continuum flux (black) and the integrated intensity for C<sup>17</sup>O  $J = 2 - 1$  (blue) and H<sub>2</sub>CO  $3_{1,2} - 2_{1,1}$  (orange) transitions along the disk major axis. The shaded area shows the 3 $\sigma$  uncertainty and the horizontal dotted blue line marks the 3 $\sigma$  level for the line emission.

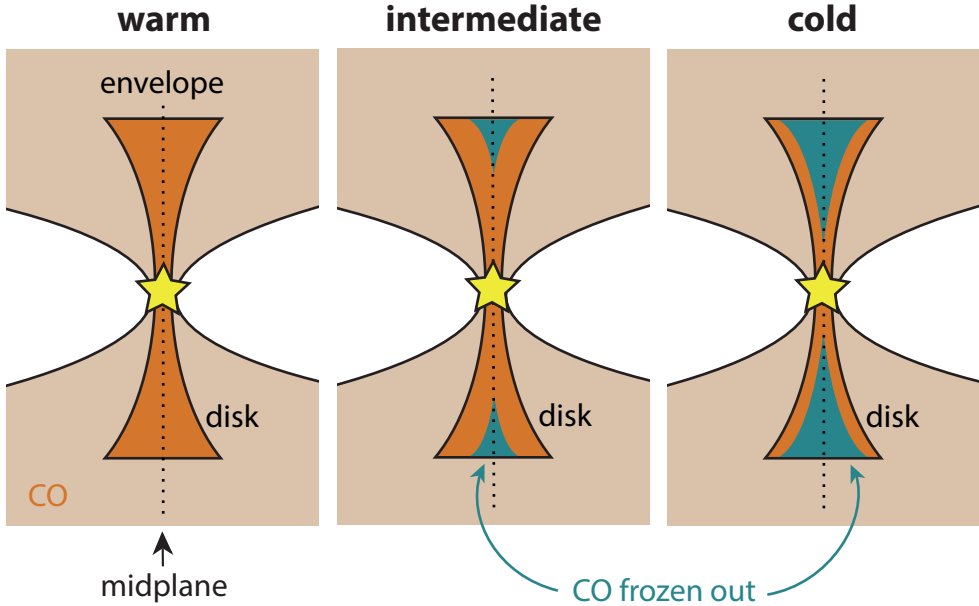


**Figure 4.B.1:** Three different models for the CO distribution in embedded disks. *Left panel:* a warm disk with no CO freeze out. *Middle panel:* a slightly colder disk where CO is frozen out in the outer disk midplane. *Right panel:* a cold disk where gaseous CO is only present in the inner disk and the disk surface layers. Gaseous CO is present in the inner envelope in all models. Figure reproduced from van 't Hoff et al. (2018b).

## 4.B Schematics of the disk models

Figure 4.B.1 shows a schematic overview of the warm, intermediate and cold disk models as presented by van 't Hoff et al. (2018b) (Chapter 3). In the warm model, CO is present in the gas phase in the entire disk, whereas in the cold model CO is frozen out in most of the disk with gas-phase CO only present in the inner disk and disk surface layers. In the intermediate model CO freeze-out occurs in the outer midplane. A constant gas-phase CO abundance of  $10^{-4}$  w.r.t  $\text{H}_2$  is adopted in the regions where  $T > 20$  K. If the envelope is included in the radiative transfer, gas-phase CO is present in the  $T > 20$  K region at an abundance of  $10^{-4}$  as well. For the physical structure (dust density and temperature) we adopt the model for L1527 from Tobin et al. (2013b), who modeled the disk continuum emission by fitting both the visibilities and images of  $870 \mu\text{m}$  and  $3.4 \text{ mm}$  observations, the multi-wavelength SED and  $L'$  scattered light images with 3D radiative transfer modeling.

Figure 4.B.2 illustrates why observing freeze-out directly is very challenging in disks that are not viewed edge-on.



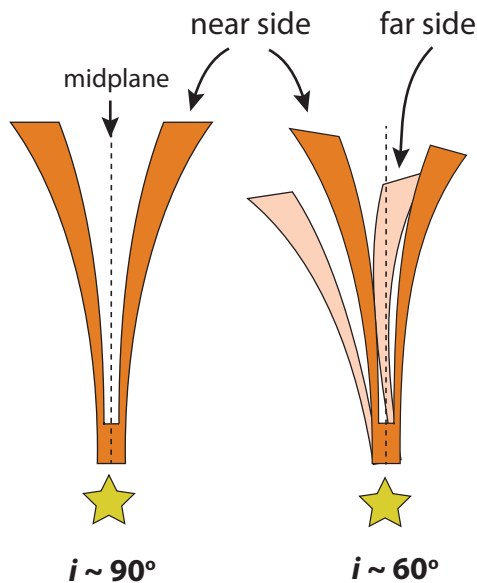
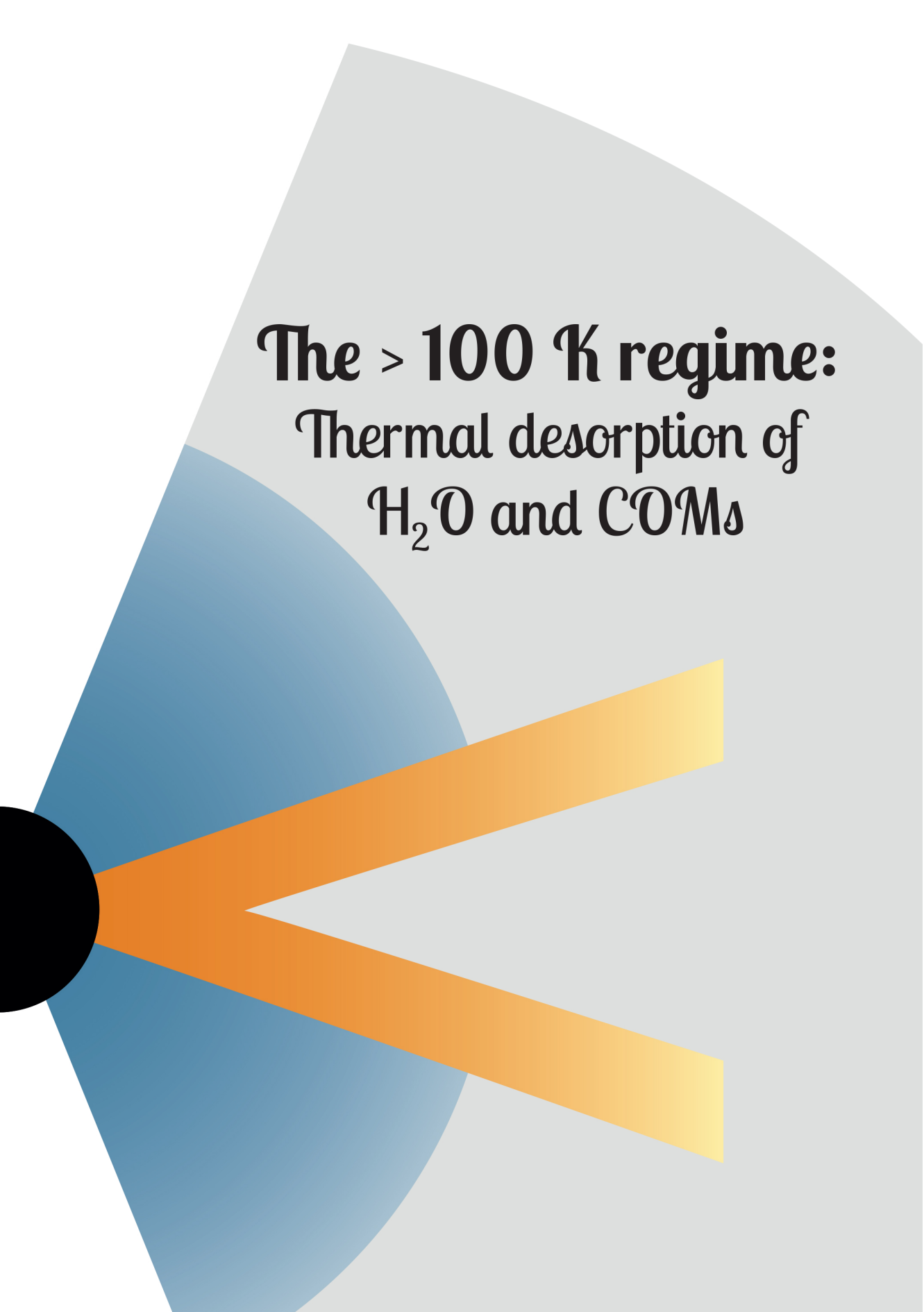


**Figure 4.B.2:** Schematic representation of a disk with emission originating only in the surface layers viewed edge-on ( $\sim 90^\circ$ ; *left panel*) and at an inclination of  $\sim 60^\circ$  (*right panel*). In the edge-on orientation, only the near side of the disk is visible and at sufficient angular resolution a V-shaped emission pattern is observed. In contrast, when the disk is  $\sim 60^\circ$  inclined, the far side of the disk becomes visible and emission from the far side appears to be coming from the midplane.

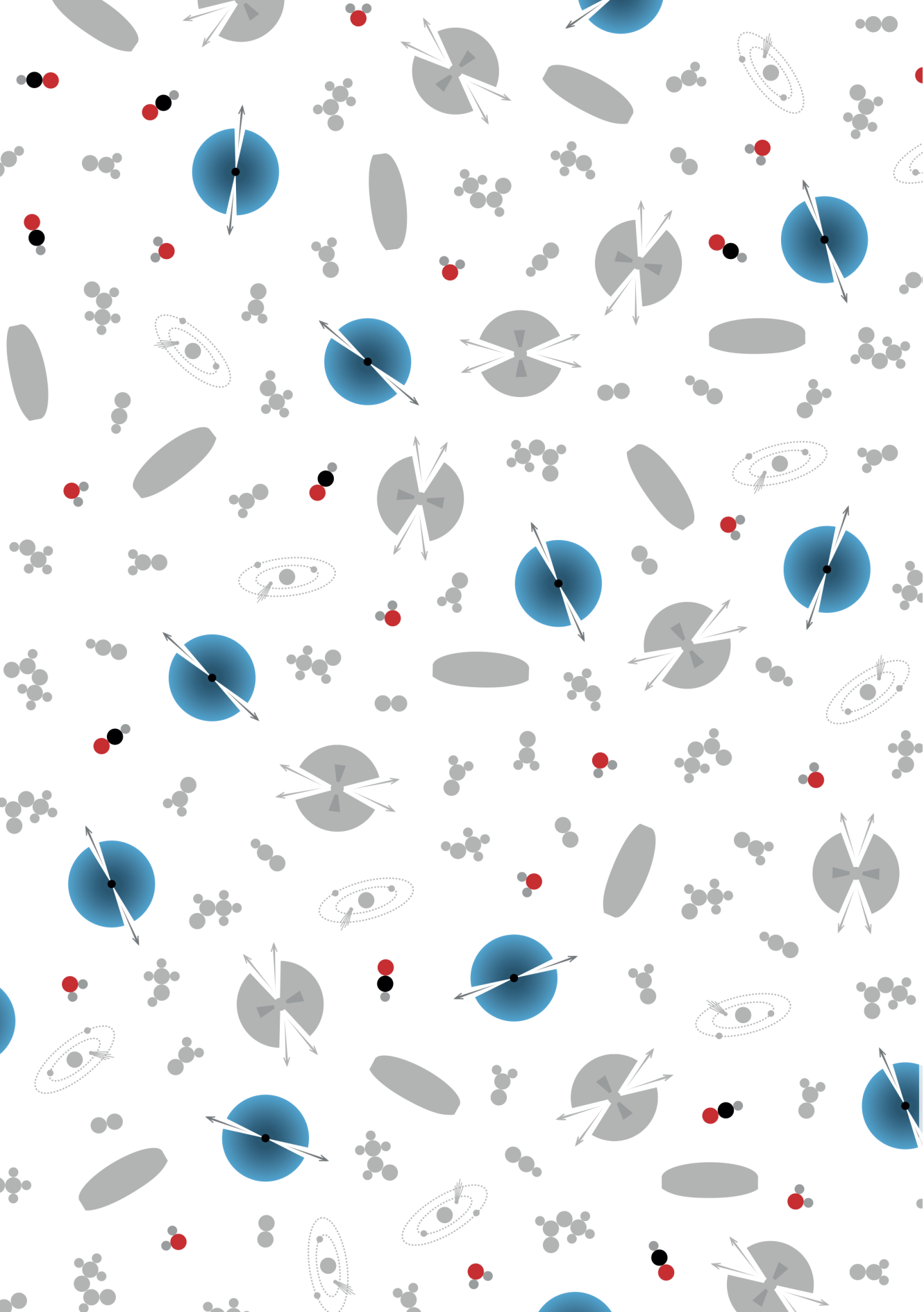


The background features a large, light gray shape on the left side. On the right side, there is a blue shape that overlaps with the gray one. A black semi-circle is positioned on the far right edge, overlapping the blue shape.

# PART 2



**The > 100 K regime:**  
Thermal desorption of  
H<sub>2</sub>O and COMs





# 5. Imaging the water snowline in protostellar envelopes with $\text{H}^{13}\text{CO}^+$

The case of NGC1333 IRAS2A

M.L.R. van 't Hoff, M.V. Persson, D. Harsono, V. Taquet,  
J.K. Jørgensen, R. Visser, E.A. Bergin, & E.F. van Dishoeck

A&A, 613, A29 (2018)



## Abstract

**Context.** Snowlines are key ingredients for planet formation. Providing observational constraints on the locations of the major snowlines is therefore crucial for fully connecting planet compositions to their formation mechanism. Unfortunately, the most important snowline, that of water, is very difficult to observe directly in protoplanetary disks because of the close proximity of this snowline to the central star.

**Aims.** Based on chemical considerations,  $\text{HCO}^+$  is predicted to be a good chemical tracer of the water snowline because it is particularly abundant in dense clouds when water is frozen out. This work aims to map the optically thin isotopolog  $\text{H}^{13}\text{CO}^+$  toward the envelope of the low-mass protostar NGC1333 IRAS2A, where the snowline is at a greater distance from the star than in disks. Comparison with previous observations of  $\text{H}_2^{18}\text{O}$  show whether  $\text{H}^{13}\text{CO}^+$  is indeed a good tracer of the water snowline.

**Methods.** NGC1333 IRAS2A was observed using the NOthern Extended Millimeter Array (NOEMA) at  $\sim 0.9''$  resolution, targeting the  $\text{H}^{13}\text{CO}^+$   $J = 3 - 2$  transition at 260.255 GHz. The integrated emission profile was analyzed using 1D radiative transfer modeling of a spherical envelope with a parametrized abundance profile for  $\text{H}^{13}\text{CO}^+$ . This profile was validated with a full chemical model.

**Results.** The  $\text{H}^{13}\text{CO}^+$  emission peaks  $\sim 2''$  northeast of the continuum peak, whereas  $\text{H}_2^{18}\text{O}$  shows compact emission on source. Quantitative modeling shows that a decrease in  $\text{H}^{13}\text{CO}^+$  abundance by at least a factor of six is needed in the inner  $\sim 360$  AU to reproduce the observed emission profile. Chemical modeling indeed predicts a steep increase in  $\text{HCO}^+$  just outside the water snowline; the 50% decrease in gaseous  $\text{H}_2\text{O}$  at the snowline is not enough to allow  $\text{HCO}^+$  to be abundant. This places the water snowline at 225 AU, further away from the star than expected based on the 1D envelope temperature structure for NGC1333 IRAS2A. In contrast,  $\text{DCO}^+$  observations show that the CO snowline is at the expected location, making an outburst scenario unlikely.

**Conclusions.** The spatial anticorrelation of  $\text{H}^{13}\text{CO}^+$  and  $\text{H}_2^{18}\text{O}$  emission provide proof of concept that  $\text{H}^{13}\text{CO}^+$  can be used as a tracer of the water snowline.



## 5.1 Introduction

Water is probably the molecule that appeals most to our imagination, as it is essential for life as we know it. In star-forming regions, water plays an important role as a coolant of warm gas, a dominant carrier of oxygen, and a major constituent of icy grain mantles deep inside a planet-forming disk (see, e.g., Melnick 2009; Bergin & van Dishoeck 2012; van Dishoeck et al. 2013, for reviews). The transition from water being frozen out onto dust grains to being predominantly present in the gas phase occurs at the water snowline: the midplane radius at which 50% of the water is in the gas phase and 50% is in ice. Since the selective freeze-out of the major oxygen carrier alters the elemental C/O ratio in both gas and ice, the bulk chemical composition of planets depends on their formation location with respect to the freeze-out radius of water (e.g., Öberg et al. 2011; Madhusudhan et al. 2014; Ali-Dib et al. 2014; Ali-Dib 2017; Walsh et al. 2015; Mordasini et al. 2016; Eistrup et al. 2016; Booth et al. 2017). In addition, planetesimal formation is thought to be significantly enhanced in this region (e.g., Stevenson & Lunine 1988; Schoonenberg & Ormel 2017). The exact location and time evolution of the water snowline in protostellar systems is thus a crucial ingredient in planet formation.

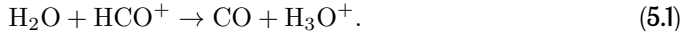
Unfortunately, the water snowline is very hard to observe directly in protoplanetary disks. Because of the large binding energy of  $\text{H}_2\text{O}$ , the transition from ice to gas happens a few AU from the young star where the midplane temperature exceeds  $\sim 100\text{--}200$  K (depending on the vapor pressure). For the nearest star-forming regions, this would already require angular resolutions of  $\lesssim 0.01''$ . Emission originating from cold water ( $E_{\text{up}} < 100$  K) has been detected in the disk around TW Hya with the *Herschel Space Observatory* (Hogerheijde et al. 2011; Zhang et al. 2013), but the large *Herschel* beam ( $10\text{--}45''$ ) could not spatially resolve the snowline. Furthermore, the only thermal water lines that can be observed from the ground (except for the  $\text{H}_2\text{O}$  line at 183 GHz) are lines from the less abundant isotopolog  $\text{H}_2^{18}\text{O}$ . As such, even ALMA will have great difficulty locating the water snowline in protoplanetary disks.

An alternative approach is to use chemical imaging, as has been carried out for the CO snowline. Because CO is highly volatile, its snowline is located tens of AU from the central star (around  $\sim 20$  K; see, e.g., Burke & Brown 2010). Although this is far enough to be spatially resolved with ALMA, locating it directly remains difficult; since CO line emission is generally optically thick, it does not reveal the cold disk midplane. Reactions with gaseous CO are the main destruction route for  $\text{N}_2\text{H}^+$ , therefore  $\text{N}_2\text{H}^+$  is expected to be abundant only when CO is frozen out. Taking simple chemical considerations into account, an upper limit for the CO snowline location can therefore be derived from  $\text{N}_2\text{H}^+$  emission (Aikawa et al. 2015; van 't Hoff et al. 2017, **Chapter 2**), as has been performed for the disks around TW Hya and HD 163296 (Qi et al. 2013b, 2015), and several protostellar envelopes (Jørgensen 2004; Anderl et al. 2016).

For young protostars, the emission of complex organic molecules (COMs) has been used as tracer of the inner region that is warm enough to sublimate water ice, the so-called hot core, because these species are expected to be trapped in water ice. However, the exact binding energy, and thus spatial extent, differs for different molecules. Compact COM emission has been detected toward NGC1333 IRAS2A (hereafter IRAS2A) extending between  $\sim 0.4''$  and  $\sim 1.0''$  (e.g., Jørgensen et al. 2005; Maret et al. 2014; Maury et al. 2014), similar to the size ( $\sim 0.8''$ ) of the  $\text{H}_2^{18}\text{O}$  emission (Persson et al. 2012). The exact relationship between COMs and the water snowline remains unclear,

however. For example, the extent of methanol emission in IRAS2A is half the size of the  $\text{H}_2^{18}\text{O}$  emission (Maret et al. 2014), while it is twice the size in NGC1333-IRAS4A (Anderl et al. 2016). In addition, Persson et al. (2012) concluded that  $\text{C}_2\text{H}_5\text{CN}$  is likely not related to sublimation of water ice. Since the detection of COMs is very difficult in mature protoplanetary disks, where only methyl cyanide and methanol have been observed so far (Öberg et al. 2015b; Walsh et al. 2016), COMs are not suited as tracers of the water snowline in these systems.

The best candidate to chemically trace the water snowline is  $\text{HCO}^+$  because its most abundant destroyer in warm dense gas is gaseous  $\text{H}_2\text{O}$ , that is,



A strong decline in  $\text{HCO}^+$  is thus expected when  $\text{H}_2\text{O}$  desorbs off the dust grains (Phillips et al. 1992; Bergin et al. 1998). Atacama Large Millimeter/submillimeter Array (ALMA) observations of the optically thin isotopolog  $\text{H}^{13}\text{CO}^+$  toward the Class 0 protostar IRAS 15398–3359 indeed revealed ring-shaped emission (Jørgensen et al. 2013). The spatial distribution is consistent with destruction by water in the innermost region, but the inner radius of the  $\text{H}^{13}\text{CO}^+$  emission is further out than expected. This can be explained if the temperature has recently been higher, that is, if the source has undergone a luminosity outburst. Follow-up observations by Bjerkerli et al. (2016a) did not detect the  $\text{H}_2^{18}\text{O}$   $4_{14} - 3_{21}$  high excitation transition ( $E_{up} = 322$  K). However, an HDO transition with lower upper level energy ( $E_{up} = 22$  K) was clearly detected. Although HDO emission is also present in the outflow lobes, the observations are consistent with the  $\text{H}_2\text{O}$ - $\text{HCO}^+$  anticorrelation scenario.

Protostellar envelopes are good targets to test the  $\text{H}^{13}\text{CO}^+$ - $\text{H}_2^{18}\text{O}$  anticorrelation. Because of higher luminosity (due to higher accretion rates) and lower vapor pressure, the snowline is located further away from the star than in protoplanetary disks (10s–100 AU instead of a few AU; Harsono et al. 2015; Cieza et al. 2016). In addition,  $\text{H}_2^{18}\text{O}$  has already been observed toward four of these objects (Jørgensen & van Dishoeck 2010; Persson et al. 2012, 2013). The only thing lacking is thus high-spatial resolution images of  $\text{H}^{13}\text{CO}^+$ . Here, we present NOEMA observations of  $\text{H}^{13}\text{CO}^+$  toward one source, IRAS2A, and compare these to the  $\text{H}_2^{18}\text{O}$  emission presented by Persson et al. (2012). IRAS2A is a deeply embedded Class 0 protostar in the NGC1333 region of the Perseus molecular cloud. The quadruple outflows suggest that it is a close binary (Jørgensen et al. 2004a), which has recently been confirmed (0.6'' separation; Tobin et al. 2015a). Similar to Persson et al. (2012) we adopt a distance of 250 pc (Enoch et al. 2006).

The observations and results are presented in **Sect. 5.2** and **5.3**, and compared with the  $\text{H}_2^{18}\text{O}$  observations from Persson et al. (2012). In **Sect. 5.4**, the integrated  $\text{H}^{13}\text{CO}^+$  emission is analyzed using 1D radiative transfer modeling of a spherical envelope with a parametrized  $\text{H}^{13}\text{CO}^+$  abundance profile. In addition, this abundance profile is validated against the outcome of a full chemical network and low-resolution  $\text{DCO}^+$  observations. The main conclusions, including that we confirm the predicted anticorrelation between  $\text{H}^{13}\text{CO}^+$  and  $\text{H}_2^{18}\text{O}$ , are summarized in **Sect. 5.5**.

**Table 5.1:** Overview of the molecular line observations toward IRAS2A.

Transition	Frequency (GHz)	$E_{up}/k$ (K)	Beam ( $''$ )	$\Delta v^a$ ( $\text{km s}^{-1}$ )
$\text{H}^{13}\text{CO}^+ J = 3 - 2$	260.255	25	$0.93 \times 0.68$	0.09
$\text{H}_2^{18}\text{O } 3_{1,3} - 2_{2,0}$	203.408	204	$0.87 \times 0.72$	0.115
$\text{DCO}^+ J = 2 - 1$	144.068	10	$2.1 \times 1.7$	4.06

**Notes.** <sup>(a)</sup> Velocity resolution.

## 5.2 Observations

IRAS2A ( $\alpha(2000) = 03^{\text{h}}28^{\text{m}}55.58^{\text{s}}$ ;  $\delta(2000) = 31^{\circ}14'37.10''$ ) was observed using the NOthern Extended Millimeter Array (NOEMA) on December 1, 2015 (C configuration), and April 9, 2016 (B configuration) for a total of 2.3 h on source in B configuration and 1.2 h in C configuration. Combining the observations in the different configurations, the data cover baselines from 16.8 to 456.9 m (14.5 to 396.6 k $\lambda$ ). The receivers were tuned to the  $\text{H}^{13}\text{CO}^+ J = 3 - 2$  transition at 260.255 GHz (1.15 mm), and the narrowband correlator was set up with one unit (bandwidth of 40 MHz) centered on this frequency providing a spectral resolution of 0.078 MHz (0.09  $\text{km s}^{-1}$ ). In addition, the WideX correlator was used, covering a 3.6 GHz window (259.2–262.8 GHz) at a resolution of 1.95 MHz (2.2–2.3  $\text{km s}^{-1}$ ).

Calibration and imaging were performed using the CLIC and MAPPING packages of the IRAM GILDAS software<sup>1</sup>. The standard calibration procedure was followed using the quasars 3C454.3 and 3C84 to calibrate the bandpass, 0333+321 to calibrate the complex gains, and the point sources MWC349 and LkH $\alpha$ 101 to calibrate the absolute flux scale. The continuum visibilities were constructed from line-free channels in the WideX spectrum, and the continuum was subtracted from the line data before imaging. Both the line and continuum data were imaged using default robust weighting. For  $\text{H}^{13}\text{CO}^+$  this resulted in a  $0.93'' \times 0.68''$  (PA =  $36^{\circ}$ ) beam, which is comparable to the beam of the  $\text{H}_2^{18}\text{O}$  observations (see below), and a rms of 10 mJy beam $^{-1}$  in 0.09  $\text{km s}^{-1}$  channels. The continuum image has a  $0.95'' \times 0.65''$  (PA =  $27^{\circ}$ ) beam. The continuum flux obtained from a Gaussian fit to the visibilities is 347 mJy. This is consistent with previous observations between 0.8 and 1.47 mm (Jørgensen et al. 2007; Persson et al. 2012; Taquet et al. 2015) within the 20% flux calibration error, assuming a power-law spectrum for thermal dust emission ( $F_{\nu} \propto \nu^{\alpha}$ , with  $\alpha \sim 2.0 - 2.4$ ). The ( $u, v$ )-fitted continuum peak position ( $\alpha(2000) = 03^{\text{h}}28^{\text{m}}55.57^{\text{s}}$ ;  $\delta(2000) = 31^{\circ}14'36.92''$ ) is located  $\sim 0.1''$  south of the bright component of the  $0.6''$  binary identified by (Tobin et al. 2015a).

The  $\text{H}_2^{18}\text{O } 3_{1,3} - 2_{2,0}$  transition at 203.408 GHz (1.47 mm) was observed using the Plateau de Bure Interferometer (PdBI) in December 2009 and March 2010 and was presented by Persson et al. (2012). The data have a spectral resolution of 0.087 MHz (0.115  $\text{km s}^{-1}$ ) and a resulting beam size of  $0.87'' \times 0.72''$  (PA =  $63.5^{\circ}$ ) using natural weighting.

In addition, IRAS2A was observed using the PdBI in July, August, and November

<sup>1</sup><http://www.iram.fr/IRAMFR/GILDAS>

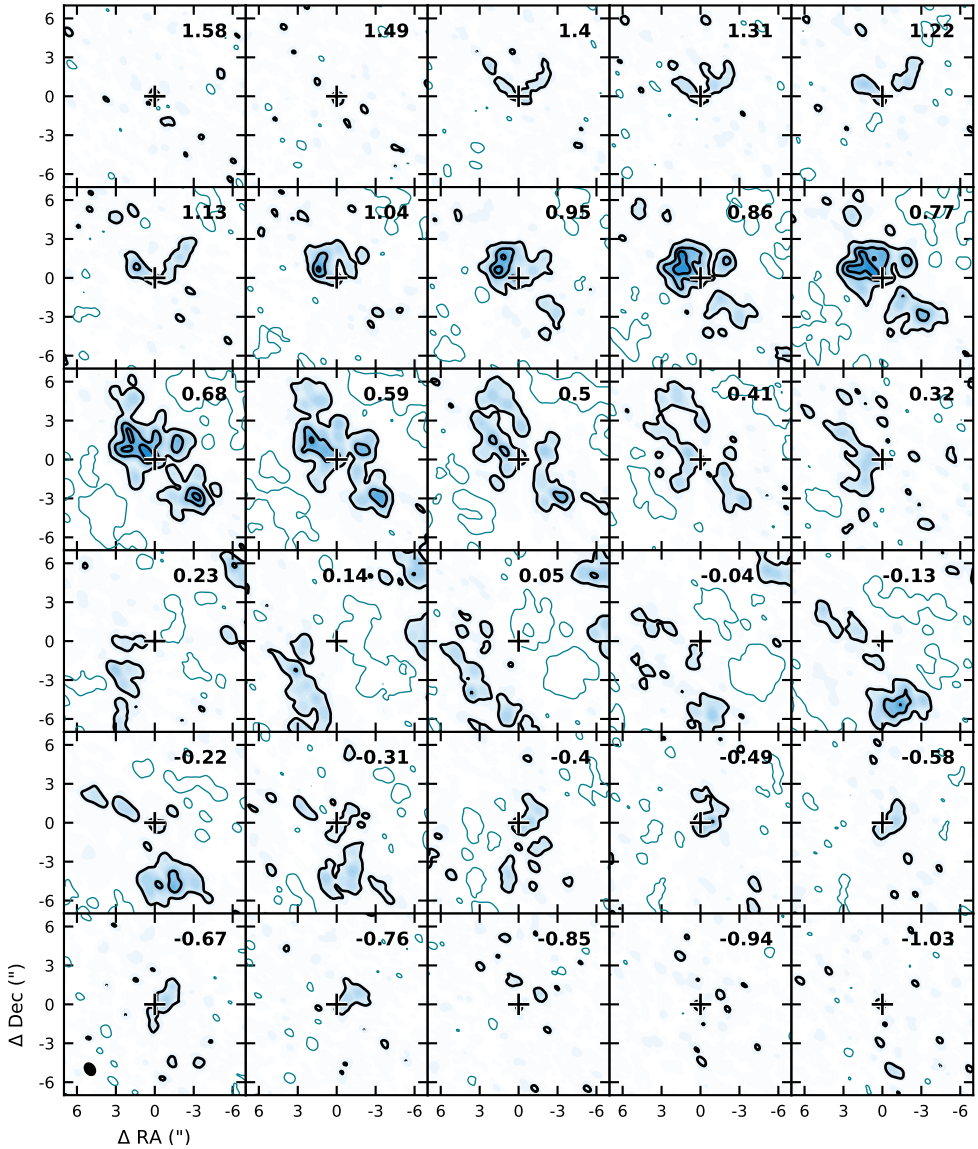


**Figure 5.1:** Channel maps for the  $\text{H}^{13}\text{CO}^+$   $J = 3 - 2$  transition. Black contours are in steps of  $10\sigma$ , starting from a  $3\sigma$  level ( $30 \text{ mJy beam}^{-1}$  in  $0.09 \text{ km s}^{-1}$  channels), and the  $-3\sigma$  contours are shown in blue. The peak intensity is  $324 \text{ mJy beam}^{-1}$  at  $7.68 \text{ km s}^{-1}$  ( $v_{\text{lsr}} + 0.68 \text{ km s}^{-1}$ ). The continuum peak position is indicated with a cross and the beam is shown in the bottom left corner of the bottom left panel. Channel velocities with respect to the systemic velocity of  $v_{\text{lsr}} \approx 7.0 \text{ km s}^{-1}$  are listed in the top right corner of each panel. For the adopted distance to IRAS2A,  $1''$  corresponds to 250 AU.

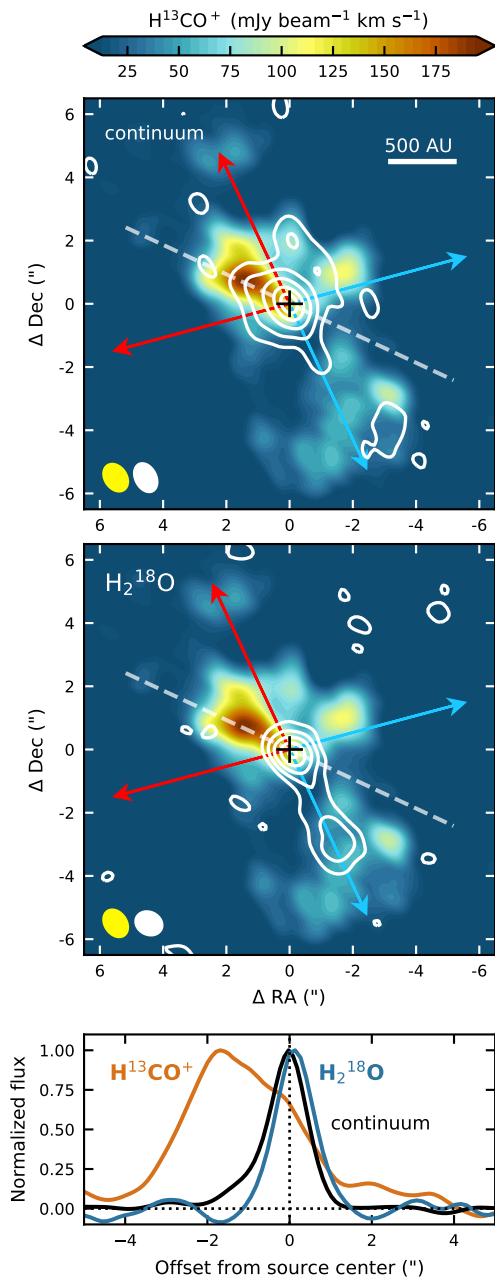


**Figure 5.2:** Integrated intensity map for the  $\text{H}^{13}\text{CO}^+$   $J=3-2$  transition (color scale) toward IRAS2A. The 1.2 mm continuum is overlaid in white contours in the *top panel* and the  $\text{H}_2^{18}\text{O}$   $3_{1,3}-2_{2,0}$  transition is overlaid in the *middle panel*. The continuum contours are  $1.8 (1\sigma) \times [3, 10, 25, 50, 75]$   $\text{mJy beam}^{-1}$ , and the  $\text{H}_2^{18}\text{O}$  contours are  $9.8 (1\sigma) \times [3, 8, 15, 25, 35]$   $\text{mJy beam}^{-1} \text{ km s}^{-1}$ . The beams are depicted in the bottom left corner. The position of the continuum peak is indicated by a black cross (the close binary is unresolved in these data) and the outflow axes by red and blue arrows. The integrated intensities along the dashed white line are shown in the *bottom panel*, normalized to their maximum value. The zero flux level and source position are indicated by dotted lines.

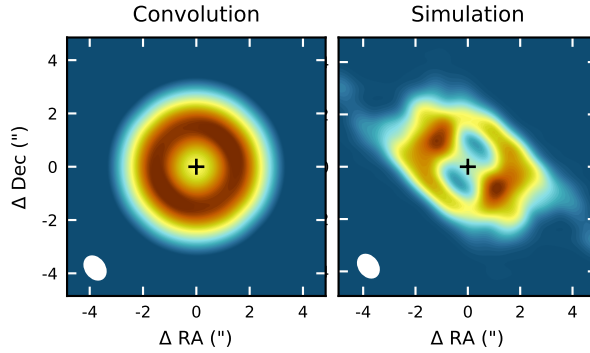


**Figure 5.3:** Integrated intensity maps for a spherically symmetric ring-shaped  $\text{H}^{13}\text{CO}^+$  distribution. Emission simulated with the radiative transfer code Ratran is convolved with the observed beam (*left panel*), and simulated with the  $(u, v)$  coverage of the NOEMA observations (*right panel*). The southern peak in the simulations is probably not observed owing to presence of water in the outflow (see text for details). The continuum peak is denoted with a cross, and the beam is shown in the bottom left corner.

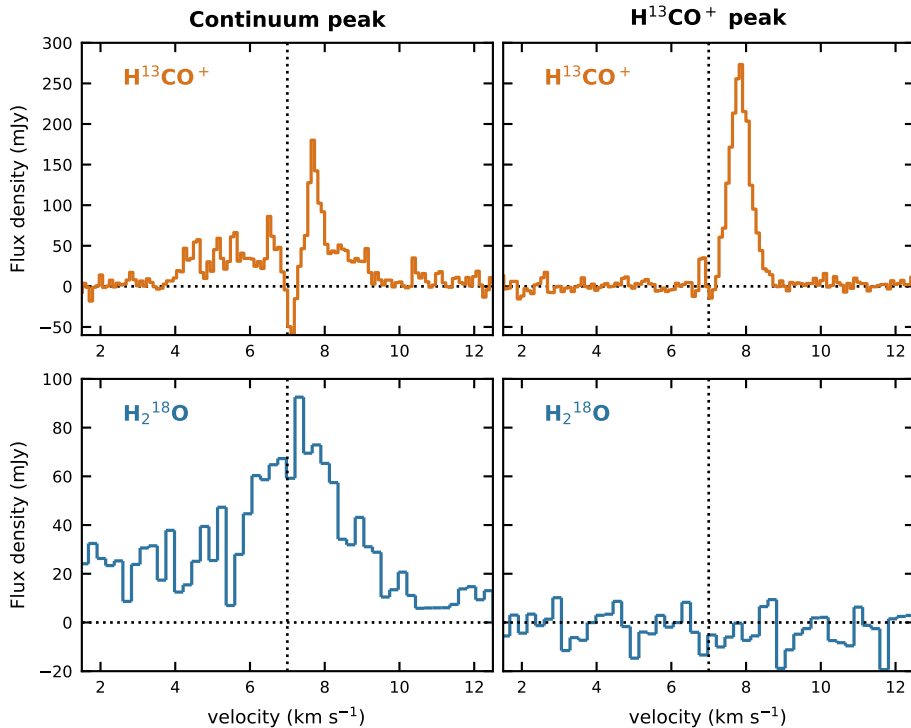


**Figure 5.4:** Spectra extracted in a beam toward the continuum peak position (*left panels*) and the  $\text{H}^{13}\text{CO}^+$  peak position ( $\sim 2''$  NE of the continuum peak, *right panels*). The *top panels* show the  $\text{H}^{13}\text{CO}^+$   $J = 3 - 2$  transition and the *bottom panels* the  $\text{H}_2^{18}\text{O}$   $3_{1,3} - 2_{2,0}$  transition. The two spectra for each species are shown on the same vertical scale. The systemic velocity is indicated by the vertical dotted line at  $v_{\text{lsr}} \approx 7 \text{ km s}^{-1}$ .

2010 and March 2011 in the C and D configurations as part of a study of complex organic molecules toward low-mass protostars (Taquet et al. 2015). The WideX backends were used at  $\sim 145$  GHz providing a bandwidth of 3.6 GHz with a spectral resolution of 1.95 MHz ( $\sim 3.5 - 4$  km s $^{-1}$ ). One of the targeted lines was the DCO $^+$   $J = 2 - 1$  transition at 144.068 GHz. Phase and amplitude were calibrated by performing regular observations of the nearby point sources 3C454.3, 3C84, and 0333+321. Imaging with natural weighting resulted in a  $2.1'' \times 1.7''$  (PA =  $-155^\circ$ ) beam.

An overview of the observed molecular lines and their parameters is provided in Table 5.1.

### 5.3 Results

The H $^{13}$ CO $^+$  channel maps presented in Fig. 5.1 show detection of H $^{13}$ CO $^+$  at velocities between 6.2 and 8.4 km s $^{-1}$  ( $v_{lsr} = 7.0$  km s $^{-1}$ ; Persson et al. 2012), although the emission is brightest for the redshifted velocities. In none of the channels does the H $^{13}$ CO $^+$  emission peak at the source position. Instead, emission peaks are observed at offsets (RA,Dec) of approximately ( $-2'', 1.5''$ ) and ( $3'', -3''$ ) in the redshifted channels, and at ( $1'', -6''$ ) in the blueshifted channels. H $_2^{18}$ O, on the other hand, shows compact emission on source (located by Persson et al. 2012  $\sim 0.1''$  southwest of the continuum peak) and extends along the southern outflow axis. Overlaying the integrated intensity maps for H $^{13}$ CO $^+$  and H $_2^{18}$ O (see Fig. 5.2) shows that the H $^{13}$ CO $^+$  emission surrounds the water emission and peaks  $\sim 2''$  northeast of the continuum peak.

The asymmetry in the spatial distribution of the H $^{13}$ CO $^+$  emission is partly due to the sampling of the ( $u, v$ ) plane; simulating emission from a spherical envelope model with a ring-like H $^{13}$ CO $^+$  abundance distribution using the same ( $u, v$ ) coverage as the observations results in emission peaks in the northeast and southwest rather than a spherically symmetric emission pattern (see Fig. 5.3). The absence of a strong southwestern peak in the data may be attributed to the presence of water in the southern outflow. Alternatively, it could be an effect of the 3D structure of the source, which causes the H $^{13}$ CO $^+$  emission from that part to be blocked. Finally, it could perhaps be the result of asymmetries in the initial filamentary structure at large scales ( $\gg 10,000$  AU).

Spectra for H $^{13}$ CO $^+$  and H $_2^{18}$ O extracted toward the continuum and H $^{13}$ CO $^+$  peak positions are presented in Fig. 5.4. Although there is still H $^{13}$ CO $^+$  emission present on source, it is reduced by  $\sim 40\%$  compared to the region in which water emission is absent. The narrow width (FWHM  $\approx 0.8$  km s $^{-1}$ ) of the H $^{13}$ CO $^+$  line at its peak position indicates that the emission does not originate in the outflow. In comparison, the H $_2^{18}$ O line width is  $\sim 3.5$  km s $^{-1}$ . In addition, it has been shown in Persson et al. (2012) that the outflow component of the H $_2^{18}$ O emission can be distinguished spatially from the compact component. The emission around  $v_{lsr} = 3$  km s $^{-1}$  in the H $_2^{18}$ O spectrum is due to dimethyl ether (CH $_3$ OCH $_3$ ; Persson et al. 2012).

The absorption feature for H $^{13}$ CO $^+$  around the systemic velocity is partly because emission from the large-scale envelope is resolved out, as can be seen from the channel maps in Fig. 5.1 where most of the emission is absent around the systemic velocity. In addition, a comparison with JCMT single dish observations from Jørgensen et al. (2004b) shows that only  $\sim 7\%$  of the peak flux is recovered in the NOEMA observations, demonstrating that the bulk of the H $^{13}$ CO $^+$  is located on larger scales. Imaging the data before continuum subtraction shows that some absorption also occurs against

the continuum in the central channels, which is indicative of cold gas along the line of sight at scales larger than the scale of interest.

## 5.4 Analysis and discussion

### 5.4.1 Parametrized abundance profile for $\text{H}^{13}\text{CO}^+$

To establish the origin of the dip in the  $\text{H}^{13}\text{CO}^+$  emission at the central position, 1D spherically symmetric physical-chemical modeling was performed using the radiative transfer code Ratran (Hogerheijde & van der Tak 2000). For the physical structure we adopted the temperature and density profiles for IRAS2A from Kristensen et al. (2012), derived using the 1D spherically symmetric dust radiative transfer code DUSTY (Ivezić & Elitzur 1997). In this procedure the free model parameters were fitted to the spectral energy distribution (SED) and the spatial extent of the sub-mm continuum emission. Based on the chemical consideration that  $\text{H}^{13}\text{CO}^+$  is particularly abundant when its main destructor  $\text{H}_2\text{O}$  is frozen out, the simplest  $\text{H}^{13}\text{CO}^+$  distribution is an abundance profile with a low abundance inside the 100 K radius (i.e., the water snowline) and a higher abundance at larger radii. Both the inner and outer abundances are varied to get the best match to the observed integrated intensity along the radial cut shown in **Fig 5.2**. The absence of the southwest  $\text{H}^{13}\text{CO}^+$  peak (discussed in **Sect. 5.3**) cannot be modeled with an axisymmetric 1D model. We therefore restrict the comparison to the northeastern part of the radial cut. For a first analysis, we do not adopt a velocity structure. The difference between the blue- and redshifted channels then cannot be reproduced exactly. Since there is almost no emission along the radial cut in the blueshifted channels, only the redshifted channels are used to construct the zeroth moment maps. Including all channels does not significantly change the observed integrated radial profile, but only affects the  $\text{H}^{13}\text{CO}^+$  abundance required to reach the observed intensity (by a factor of  $\sim 3$ ). However, deriving the precise  $\text{H}^{13}\text{CO}^+$  abundance is not the goal of this work. Finally, simulated images representing the observed  $(u, v)$  coverage are produced from the Ratran images in GILDAS by creating a  $(u, v)$  table with the function `uv_fmodel`.

Various  $\text{H}^{13}\text{CO}^+$  abundance profiles with their corresponding integrated emission profiles are presented in **Fig. 5.5**. For the adopted physical structure, the temperature drops below 100 K around 90 AU. An  $\text{H}^{13}\text{CO}^+$  abundance of  $1 \times 10^{-10}$  at radii  $>90$  AU can roughly reproduce the observed integrated intensity (**Fig. 5.5**, second row). However, independent of the inner abundance, the emission always peaks on source, as in the case of a constant  $\text{H}^{13}\text{CO}^+$  abundance at all radii (**Fig. 5.5**, top row). Although a large percentage ( $\sim 90\%$ ) of the emission is already being resolved out with the  $(u, v)$  coverage of the observations, this thus does not result in a dip in the  $\text{H}^{13}\text{CO}^+$  emission toward the source position.

To reproduce the location of the emission peak, the abundance jump has to be shifted outward to a radius of  $\sim 360$  AU. To move the 100 K radius, representing the water snowline, this far out, the temperature profile has to be multiplied by a factor of 2.2 (**Fig. 5.5**, third row). However, the observed integrated intensity cannot be reached with this abundance profile, as the  $\text{H}^{13}\text{CO}^+$  emission becomes optically thick for outer abundances higher than  $3 \times 10^{-10}$ . Varying the abundance does not affect the position of the emission peak.



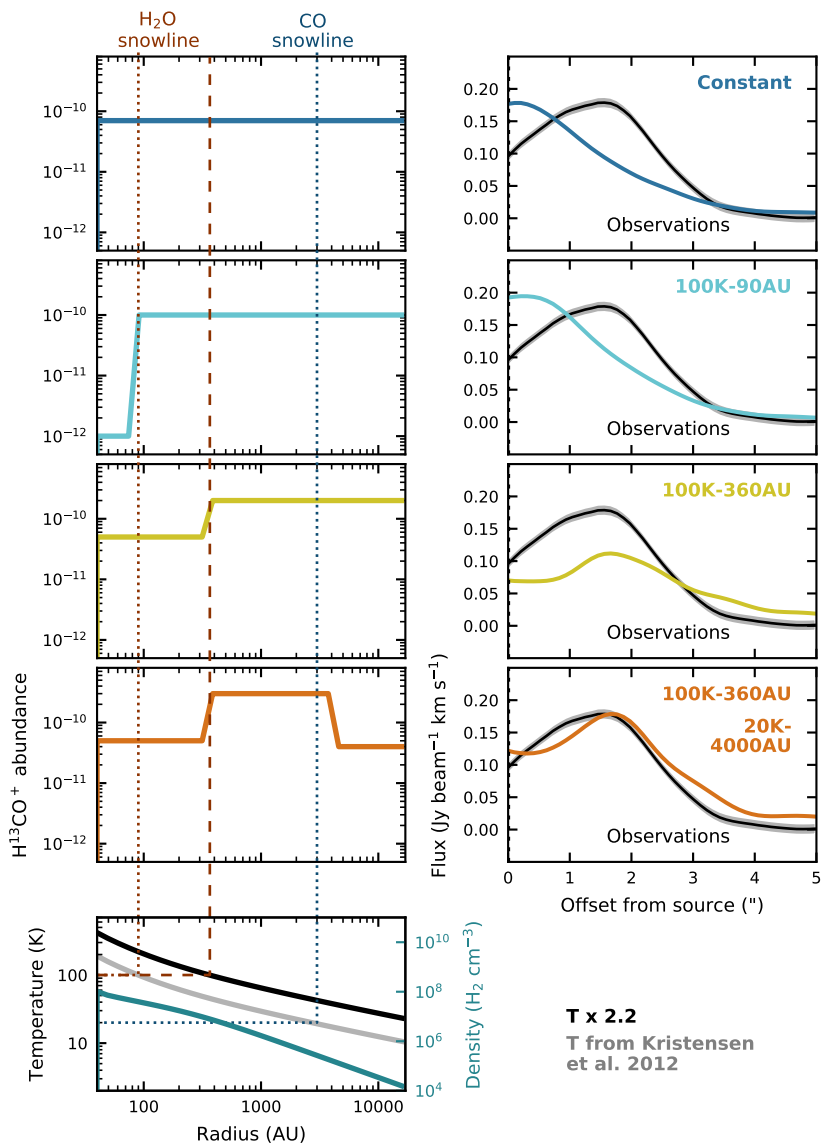


**Figure 5.5:** Various  $\text{H}^{13}\text{CO}^+$  abundance profiles (*left panels*) and the resulting simulated integrated emission along the northeastern part of the radial cut shown in **Fig. 5.2** (*right panels*). The observed emission is shown in black. The location of the abundance jumps (in Kelvin and AU) is indicated in the top right corners. *Bottom panel:* Temperature (gray) and density (blue) profiles for the IRAS2A envelope from Kristensen et al. (2012) used in the top two models. The location of the  $\text{H}_2\text{O}$  and CO snowlines (at 100 K and 20 K, resp.) are indicated by the dotted red and blue lines, respectively. The temperature profile increased by a factor of 2.2, used in the bottom two models, is shown in black. The resulting  $\text{H}_2\text{O}$  snowline is indicated by the dashed red line while the CO snowline now falls outside the adopted radial range. For IRAS2A,  $1''$  corresponds to  $\sim 250$  AU.

The best match to the observed  $\text{H}^{13}\text{CO}^+$  radial profile can be reached by introducing an additional drop in the abundance around  $\sim 4000$  AU (**Fig. 5.5**, fourth row). An increase in abundance of at least a factor of six is required around 360 AU to get the emission peak at the observed location, but the exact radius of the outer drop does not influence the peak position. Such a decrease in the  $\text{H}^{13}\text{CO}^+$  abundance can be expected around the CO snowline because formation of  $\text{HCO}^+$  is limited in this region because of a reduction in the parent gaseous CO molecules. A radius of 4000 AU corresponds to 17 K for the Kristensen et al. (2012) temperature profile, consistent with the CO freeze-out temperature for a pure CO ice binding energy. In contrast, for the increased temperature profile the temperature is 38 K at this radius; temperatures below 20 K are not reached within the 20,000 AU radial extent of the model. An increased temperature is thus required to set the inner radius of the  $\text{H}^{13}\text{CO}^+$  abundance at the water snowline, while the original temperature places the outer radius around the CO snowline. This discrepancy is further discussed in **Sects. 5.4.2** and **5.4.3**. The main result of these models is that the observed position of the  $\text{H}^{13}\text{CO}^+$  emission peak can only be reproduced by a reduction in the abundance of at least a factor 6 in the inner  $\sim 360$  AU.

## 5.4.2 Comparison with a full chemical model

To inspect the legitimacy of the simple abundance profile, we compared it to the outcome of the astrochemical code GRAINOBLE (Taquet et al. 2012a,b, 2013, 2014). In short, GRAINOBLE uses the rate equations approach (Hasegawa et al. 1992) considering three types of reactions (a so-called three-phase model based on Hasegawa & Herbst 1993): reactions for gas-phase species, reactions for species on the ice surface, and reactions for bulk ice species. The gas-phase chemical network is taken from the KIDA database (Wakelam et al. 2015) supplemented by ion-neutral reactions described in Taquet et al. (2016b). A cosmic ray (CR) ionization rate of  $5 \times 10^{-17} \text{ s}^{-1}$  is used. In addition to thermal desorption, UV photodesorption and chemical desorption upon formation of an exothermic surface reaction have been included as desorption processes. The surface chemical network follows the results of recent laboratory experiments to form the main ice species (see Taquet et al. 2013, for references). For CO and  $\text{H}_2\text{O}$  binding energies have been adopted for an amorphous water ice substrate: 1150 K and 5775 K, respectively (Collings et al. 2004; Fraser et al. 2001). The formation of interstellar ices is first followed during the formation of a dense starless core with the method described in Taquet et al. (2014). This ice chemical composition is then used as initial conditions for the gas-grain chemical evolution around IRAS2A, adopting the static 1D physical profile derived by Kristensen et al. (2012). Surface reactions have a negligible impact on the  $\text{HCO}^+$  abundance during the latter protostellar phase. They have a significant importance during the former prestellar phase since they govern the transformation of CO ice into other species, thereby setting the initial ice abundance for the protostellar phase. The initial gas-phase abundances and ice abundances at the start of the protostellar phase are listed in **Appendix 5.1**.

The left panel of **Fig. 5.6** presents the  $\text{H}_2\text{O}$ , CO and  $\text{HCO}^+$  abundances for the IRAS2A envelope structure after  $10^4$  yr of chemical evolution. The abundance profiles do not change significantly for evolution up to  $\sim 10^5$  yr, that is, the duration of the protostellar phase. Going from the outer envelope inward, the temperature rises above 20 K at a radius of  $\sim 2700$  AU, causing CO to desorb from the ice surface into the

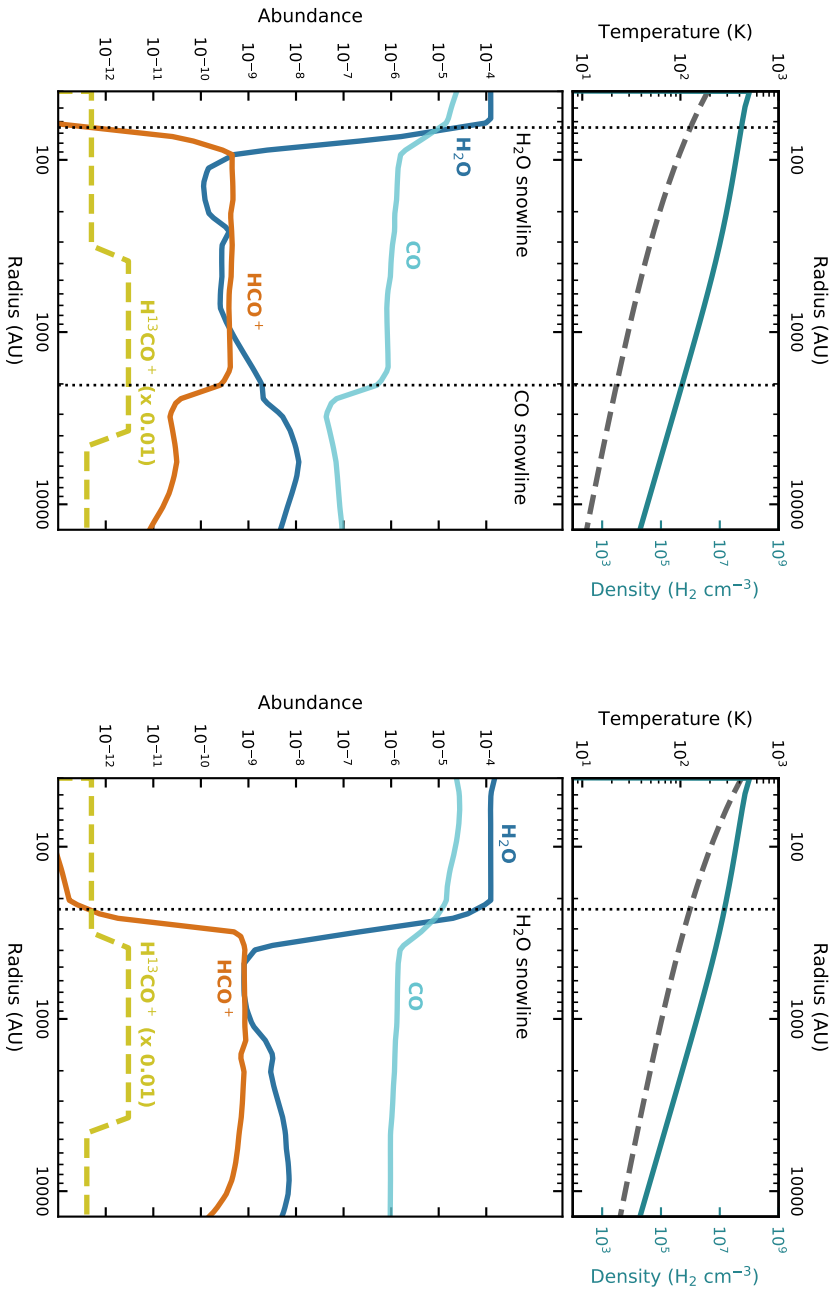


**Figure 5.6:** *Left panels:* Temperature (dashed gray line) and density (solid blue line) profiles for the IRAS2A envelope from Kristensen et al. (2012) (*top*), and the corresponding H<sub>2</sub>O (dark blue), CO (light blue), and HCO<sup>+</sup> (orange) abundances predicted by the GRAINOBLE model (*bottom*). The dashed yellow line shows the empirically inferred abundance profile for H<sup>13</sup>CO<sup>+</sup> (scaled down by a factor 100). *Right panels:* As left panels, but with the temperature increased by a factor 2.2. The vertical dotted lines indicate the H<sub>2</sub>O and CO snowlines.

gas phase. In the three-phase model, a significant part of the icy CO remains trapped in the ice matrix at temperatures higher than the CO desorption temperature. These CO molecules evaporate together with water when the temperature exceeds  $\sim 100$  K, resulting in a double abundance jump profile for CO. The water snowline, that is, the radius where 50% of the water is in the gas phase and 50% is frozen out, is located at a distance of  $\sim 65$  AU from the protostar (corresponding to 127 K). As expected, the  $\text{HCO}^+$  abundance increases sharply at radii beyond the water snowline, where its main destructor is frozen out, and decreases again outside the CO snowline, where the availability of its parent molecule is reduced. Increasing the temperature by a factor of 2.2, as was required to match the observed  $\text{H}^{13}\text{CO}^+$  emission with a drop in the abundance at the 100 K radius, results in a similar chemical profile, only with the snowlines shifted to larger radii (Fig. 5.6, right panel). The water snowline is now located at  $\sim 225$  AU (127 K), while the CO snowline falls outside the modeled radial range. The water snowline location matches the observed radial extent of the  $\text{H}_2^{18}\text{O}$  emission ( $\sim 1'' \approx 250$  AU).

For comparison, the best  $\text{H}^{13}\text{CO}^+$  abundance profile derived from the data is added to Fig. 5.6 (dashed green line). This inferred  $\text{H}^{13}\text{CO}^+$  abundance is higher than expected based on the GRAINOBLE results: similar to the predicted  $\text{HCO}^+$  abundance instead of a factor  $\sim 70$  lower. This can most likely be explained by the relatively low CO abundance between the CO and  $\text{H}_2\text{O}$  snowlines in the chemical model, which directly results in a low  $\text{HCO}^+$  abundance. The CO abundance is low because a large percentage of the CO ice is converted into methanol during the prestellar phase (Table 5.1.2). In addition, in the three-phase model, not all CO evaporates inside its snowline, but remains trapped in water ice (Fig. 5.6). However, it is the overall trend that the  $\text{HCO}^+$  abundance sharply rises at the  $\text{H}_2\text{O}$  snowline and drops at the CO snowline that is important.

The radius where  $\text{H}^{13}\text{CO}^+$  has to increase (360 AU) matches the inner radius of the  $\text{HCO}^+$  distribution in the chemical network with the increased temperature profile (right panel). The water snowline, however, is located  $\sim 135$  AU closer to the star, at 225 AU. Similar behavior is seen in models for  $\text{N}_2\text{H}^+$ ; the 50% reduction in CO, or in this case  $\text{H}_2\text{O}$ , at the snowline is not yet sufficient to diminish the destruction of  $\text{N}_2\text{H}^+$  or  $\text{HCO}^+$ , respectively, moving the emission ring outward (Aikawa et al. 2015; van 't Hoff et al. 2017, Chapter 2). There are thus two effects at play here: first, the  $\text{HCO}^+$  abundance is expected to peak outside rather than directly at the water snowline (360 versus 225 AU). Second, this location for the water snowline is further away from the protostar than expected based on the Kristensen et al. (2012) temperature profile (225 versus 65 AU).

The outer drop in  $\text{H}^{13}\text{CO}^+$  abundance matches less well with the predicted  $\text{HCO}^+$  distributions. The best agreement is for the original temperature profile (for the adopted CO binding energy of 1150 K), although  $\text{HCO}^+$  decreases  $\sim 2000$  AU (2.4 K) further in than the radiative transfer modeling derived from the  $\text{H}^{13}\text{CO}^+$  data. Owing to the shallow gradient of the temperature profile in the outer envelope, the exact location of the CO snowline is very sensitive to small changes in the thermal structure. The mismatch could therefore be due to uncertainties in the derived temperature. Another important parameter for the snowline location is the assumed binding energy for CO, which is related to the assumed ice structure, that is, whether CO ice is mixed with other molecules or pure. Adopting a lower binding energy, corresponding to a CO ice substrate rather than a  $\text{H}_2\text{O}$  ice substrate, would shift the snowline to

larger radii. Anderl et al. (2016) investigated the CO binding energy using NOEMA observations of  $C^{18}O$  and  $N_2H^+$  toward four young protostars and concluded that the extent of the  $C^{18}O$  emission was best reproduced using a CO binding energy of 1200 K, corresponding to a water ice substrate. In addition, these authors showed that the freeze-out temperature is  $\sim 6$  K lower assuming a binding energy of 855 K for pure CO ice instead of 1200 K. Since the temperature difference between the CO snowline and the location of the  $H^{13}CO^+$  drop is only 2.4 K, a high CO binding energy also seems best for IRAS2A. The small discrepancy between the CO snowline location predicted by the chemical model and the location inferred from the  $H^{13}CO^+$  observations may then be the result of asymmetries in IRAS2A, as hinted at by the asymmetric  $C^{18}O$  emission shown by Anderl et al. (2016) for other protostars.

As noted before, the exact location of the drop in  $H^{13}CO^+$  in the outer envelope does not influence the observed position of the emission peak. The main point is that the chemical model indeed predicts a steep rise in  $HCO^+$  abundance just outside the water snowline, and a drop outside the CO snowline. This justifies the abundance profile used in the radiative transfer modeling, and corroborates that the depression in  $H^{13}CO^+$  in the center is due to the presence of gas-phase water.

### 5.4.3 Tracing the CO snowline: signs of an accretion burst?

Having the snowlines located further out than expected based on the adopted temperature profile derived from SED models, such as found here for the water snowline, could be a sign that the protostar has recently undergone a luminosity outburst. Such an outburst heats up the envelope, causing ices to sublimate off the grains. After the burst, the envelope cools rapidly (Johnstone et al. 2013), while it takes much longer for the molecules to freeze back onto the dust grains (Rodgers & Charnley 2003). As a result, snowlines are shifted away from the star (Visser et al. 2015; Jørgensen et al. 2015; Cieza et al. 2016; Frimann et al. 2017). An increased temperature structure is required to fit the  $H^{13}CO^+$  emission, suggesting that the water snowline is further out than expected. In case of an outburst, the CO snowline would also be shifted outward. Observational constraints for the CO snowline can thus help to establish whether IRAS2A has indeed recently undergone an accretion burst.

The deuterated form of  $HCO^+$ ,  $DCO^+$ , can be used to trace the freeze-out of CO (e.g., Mathews et al. 2013).  $DCO^+$  forms via reaction of  $H_2D^+$  and CO. Formation of  $H_2D^+$  is enhanced at low temperatures ( $< 30$  K), but below  $\sim 20$  K CO starts to freeze-out. This balance results in  $DCO^+$  peaking around the CO snowline (Murillo et al. 2015). Contamination of the emission by  $DCO^+$  formed in warmer layers from  $CH_2D^+$  is not likely to be important in protostellar envelopes, unlike in protoplanetary disks (Favre et al. 2015). The  $DCO^+$  abundance profile for the IRAS2A envelope structure is predicted with GRAINOBLE by extending the chemical network with a small network that includes reactions between CO and  $H_2D^+$ ,  $HD_2^+$  and  $D_3^+$ . The  $DCO^+$  abundance indeed peaks around the CO snowline (see Fig. 5.7), which is located at  $\sim 2000$  AU for the fiducial temperature structure. As such,  $DCO^+$  emission can be used to estimate the CO snowline location and constrain the temperature profile in the envelope.

The observed integrated intensity map for  $DCO^+$  toward IRAS2A is presented in Fig. 5.8. Emission is observed south of the continuum peak and peaks  $\sim 10''$  off source. Such an asymmetric emission pattern is observed for more protostars (e.g., Murillo

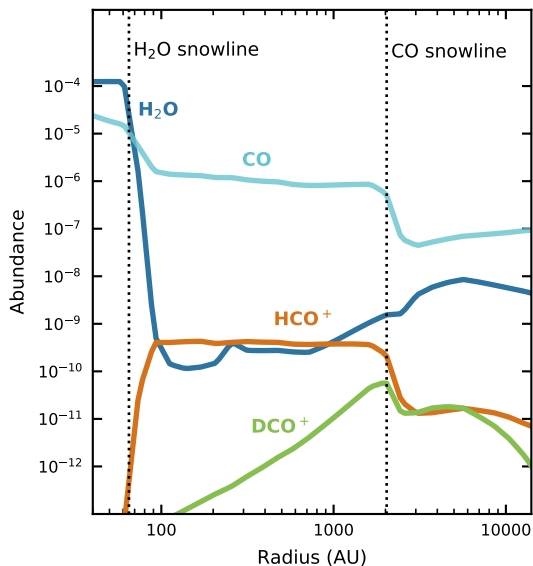


**Figure 5.7:**  $\text{H}_2\text{O}$  (dark blue),  $\text{CO}$  (light blue),  $\text{HCO}^+$  (orange), and  $\text{DCO}^+$  (green) abundances predicted by the GRAINOBLE model for the IRAS2A temperature and density profile from Kristensen et al. (2012). The vertical dotted lines indicate the  $\text{H}_2\text{O}$  and  $\text{CO}$  snowlines.

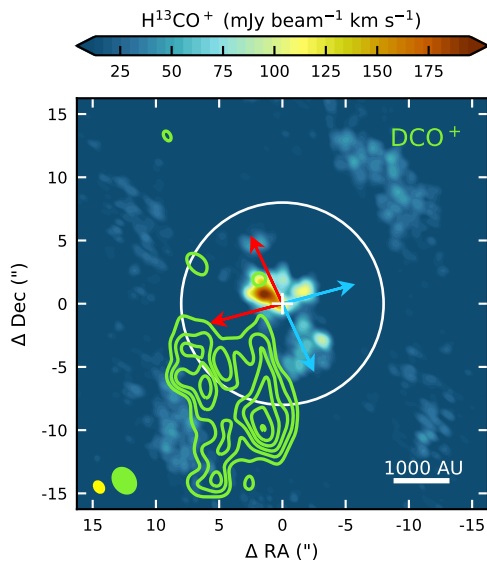


**Figure 5.8:** Integrated intensity map for the  $\text{H}^{13}\text{CO}^+$   $J = 3 - 2$  transition (color scale) toward IRAS2A. The  $\text{DCO}^+$   $J = 2 - 1$  transition is overlaid in green contours. Contours are shown in steps of  $1\sigma$  starting from a  $3\sigma$  level ( $15 \text{ mJy beam}^{-1} \text{ km s}^{-1}$ ). The beams are depicted in the bottom left corner. The position of the continuum peak is indicated by a white cross and the outflow axes by red and blue arrows. The length of the arrows is the same as in Fig. 5.2 to compare the scales. The solid white contour represents the  $\text{CO}$  snowline radius predicted by the chemical model for the Kristensen et al. (2012) temperature profile ( $\sim 2000 \text{ AU}$ ).

et al. 2015). A CO snowline around  $\sim 2000$  AU, as predicted by the chemical model for the Kristensen et al. (2012) temperature profile, is in agreement with the DCO<sup>+</sup> emission. Thus, although the H<sub>2</sub>O snowline is located at larger radii than predicted based on the IRAS2A temperature profile (225 vs. 65 AU), the location of the CO snowline is as expected. Since the chemical reset after an outburst is faster at high densities, it is unlikely that the CO snowline has already shifted back while the H<sub>2</sub>O snowline has not. In addition, Jørgensen et al. (2015) presented C<sup>18</sup>O images obtained with the Submillimeter Array (SMA) for which the spatial extent matches well with the current luminosity. It is thus unlikely that IRAS2A has recently undergone an accretion burst. Why the temperature profile matches the snowline location for CO but not for H<sub>2</sub>O is further discussed in  **Sect. 5.4.5**.

#### 5.4.4 Attenuation of the cosmic ray ionization rate

The chemistry leading to the formation of HCO<sup>+</sup> is initiated by the ionization of H<sub>2</sub> molecules by cosmic rays (CRs). A reduction in the CR ionization rate therefore results in a lower HCO<sup>+</sup> abundance. Numerical simulations performed by Padovani et al. (2013) showed that the CR ionization rate can be reduced by an order of magnitude in the inner region of a collapsing cloud core owing to twisting of the magnetic field lines. However, the exact value of the CR ionization rate in the inner regions of protostellar envelopes is unknown, and more recent work by Padovani et al. (2015, 2016) has shown that jet shocks and protostellar surface shocks can drive particle acceleration, leading to increased CR ionization rates.

Nonetheless, to assess if the effect of CR attenuation is large enough to cause the drop in H<sup>13</sup>CO<sup>+</sup> emission that we observe, we performed an order of magnitude calculation. As such, we approximate the reactions producing H<sub>3</sub><sup>+</sup> upon CR ionization by



where  $\zeta_{\text{CR}}$  is the CR ionization rate. In this formalism we ignore H<sub>2</sub><sup>+</sup>, as the ionization is the rate limiting step for H<sub>3</sub><sup>+</sup>. Formation of HCO<sup>+</sup> is dominated by the reaction between H<sub>3</sub><sup>+</sup> and CO,



and to estimate the importance of CRs, only recombination is considered as destruction reaction for HCO<sup>+</sup>, that is,



Assuming steady state and  $n(\text{e}^-) \approx n(\text{HCO}^+)$ , the following relation can then be derived between the HCO<sup>+</sup> density,  $n(\text{HCO}^+)$ , and the CR ionization rate,  $\zeta_{\text{CR}}$  (see  **Appendix 5.B** for more details):

$$n(\text{HCO}^+) = \sqrt{\frac{\zeta_{\text{CR}} n(\text{H}_2)}{k}}, \quad (5.5)$$

where  $n(\text{H}_2)$  is the molecular density of H<sub>2</sub> and  $k$  is the reaction rate coefficient for the HCO<sup>+</sup> destruction reaction ( **Eq. 5.4**). From this it can be seen that an order of magnitude reduction in the CR ionization rate gives a factor of three reduction in HCO<sup>+</sup> abundance. Based on our radiative transfer modeling, at least a factor of six

is required to fit the observations. Attenuation of the CR ionization rate alone is thus not likely to be the cause of the observed reduced  $\text{H}^{13}\text{CO}^+$  emission toward the center of IRAS2A.

### 5.4.5 Physical structure

Finally, a more likely explanation for the discrepancy between the temperatures needed for the CO and  $\text{H}_2\text{O}$  snowlines may be that the physical structure of IRAS2A is more complicated than assumed with the 1D model. For several young protostars, it has been shown that a spherical envelope model cannot reproduce all of the continuum emission on small scales (e.g., Hogerheijde et al. 1999; Looney et al. 2003). This is also the case for IRAS2A (Brown et al. 2000; Jørgensen et al. 2005) and Persson et al. (2016) have derived the presence a compact disk-like structure with a  $167_{-21}^{+63}$  AU radius. The density may therefore change significantly on these scales of disk-envelope transition, that is, the scale at which we observe the  $\text{H}_2^{18}\text{O}$ - $\text{H}^{13}\text{CO}^+$  anticorrelation. Since the envelope around IRAS2A is relatively optically thick to its own infrared radiation on  $\sim 100$  AU scales, the exact temperature distribution becomes very dependent on the assumption about the density structure. In addition, the presence of an outflow cavity can shift the 100 K radius outward in specific directions (Bjerkeli et al. 2016a), as the temperature along the cavity wall is higher at certain radii than in the envelope midplane (Visser et al. 2012). However, these considerations do not affect the main conclusion that the observations show a clear anticorrelation between  $\text{H}_2^{18}\text{O}$  and  $\text{H}^{13}\text{CO}^+$  emission.

## 5.5 Summary and outlook

We have presented subarcsecond resolution observations of the  $\text{H}^{13}\text{CO}^+$   $J = 3 - 2$  transition at 260.255 GHz toward the Class 0 protostar IRAS2A, and for the first time, compared these directly to observations of  $\text{H}_2^{18}\text{O}$ , which were presented by Persson et al. (2012). While the  $\text{H}_2^{18}\text{O}$   $3_{1,3} - 2_{2,0}$  emission is centered at the continuum peak within a  $\sim 1''$  radius, the  $\text{H}^{13}\text{CO}^+$  emission peaks  $\sim 2''$  to the northeast.

Using a 1D envelope model for IRAS2A, this offset in  $\text{H}^{13}\text{CO}^+$  emission can be explained by an abundance decrease of at least a factor of six in the inner  $\sim 360$  AU, but not by a constant  $\text{H}^{13}\text{CO}^+$  abundance. An increase in  $\text{H}^{13}\text{CO}^+$  abundance just outside the water snowline is consistent with chemical model predictions; the water snowline is then located around 225 AU, whereas the  $\text{H}^{13}\text{CO}^+$  abundance peaks  $\sim 135$  AU further out at 360 AU. This snowline radius is larger than expected if the 1D spherically symmetric temperature profile from Kristensen et al. (2012) is adopted.  $\text{DCO}^+$  observations place the CO snowline at the expected location, making an outburst scenario unlikely.

The combined observations of  $\text{H}^{13}\text{CO}^+$  and  $\text{H}_2^{18}\text{O}$ , together with radiative transfer and chemical modeling, thus provide proof of concept for the  $\text{HCO}^+$ - $\text{H}_2\text{O}$  anticorrelation. The next step would be to corroborate this for more protostellar systems. Establishing  $\text{H}^{13}\text{CO}^+$  as a good tracer of the water snowline may allow localization of the snowline in protoplanetary disks for which direct detection is very difficult.



**Table 5.A.1:** Initial gas-phase elemental abundances.

Species	Abundance <sup>a</sup>
H <sub>2</sub>	0.5
HD	$1.5 \times 10^{-5}$
H	$1.6 \times 10^{-4}$
He	$9.0 \times 10^{-2}$
C+	$7.3 \times 10^{-5}$
N	$2.1 \times 10^{-5}$
O	$1.8 \times 10^{-4}$
Si	$8.0 \times 10^{-9}$
S	$8.0 \times 10^{-8}$
Fe	$3.0 \times 10^{-9}$
Na	$2.0 \times 10^{-9}$
Mg	$7.0 \times 10^{-9}$
Cl	$1.0 \times 10^{-9}$

**Notes.** <sup>(a)</sup> Abundances with respect to the total number of hydrogen nuclei.

## Acknowledgements

We would like to thank the referee for useful comments, and Nadia Murillo and Arthur Bosman for fruitful discussions. The observations are carried out with the IRAM NOEMA interferometer. IRAM is supported by INSU/CNRS (France), MPG (Germany), and IGN (Spain). We are grateful to the IRAM staff, in particular Miguel Montargès, for his help with the observations and reduction of the data. Astrochemistry in Leiden is supported by the European Union A-ERC grant 291141 CHEMPLAN, by the Netherlands Research School for Astronomy (NOVA) and by a Royal Netherlands Academy of Arts and Sciences (KNAW) professor prize. M.L.R.H acknowledges support from a Huygens fellowship from Leiden University. M.V.P. postdoctoral position is funded by the ERC consolidator grant 614264. V.T. has received funding from the European Union’s Horizon 2020 research and innovation programme under the Marie Skłodowska-Curie grant agreement n. 664931. The research of J.K.J. is supported by European Union ERC Consolidator Grant “S4F” (grant agreement No 646908) and Centre for Star and Planet Formation funded by the Danish National Research Foundation.

## Appendix

### 5.A Initial abundances in the GRAINOBLE model

Table 5.A.1 lists the initial elemental abundances in the gas phase for the prestellar phase of the GRAINOBLE model, based on the low-metal model from Wakelam & Herbst (2008). The ice composition at the end of this phase (after 1.7 Myr) is listed in Table 5.A.2. These are the initial conditions for the chemical evolution around IRAS2A.

**Table 5.1.2:** Ice chemical composition at the end of the prestellar phase.

Species	Abundance <sup>a</sup>
H <sub>2</sub> O	$1.1 \times 10^{-4}$
CO	$1.3 \times 10^{-5}$
CO <sub>2</sub>	$1.7 \times 10^{-7}$
N <sub>2</sub>	$9.8 \times 10^{-6}$
H <sub>2</sub> CO	$6.7 \times 10^{-5}$
CH <sub>3</sub> OH	$5.5 \times 10^{-5}$
NH <sub>3</sub>	$1.3 \times 10^{-6}$
CH <sub>4</sub>	$4.4 \times 10^{-6}$

**Notes.** <sup>(a)</sup> Abundances with respect to the total number of hydrogen nuclei.

## 5.B Effect of an attenuated cosmic ray ionization rate

A first order approximation of the effect of CR ionization rate on the HCO<sup>+</sup> abundance can be made by considering the main formation and destruction reactions of HCO<sup>+</sup>. Assuming steady state, that is, assuming that the HCO<sup>+</sup> abundance does not change over time, we can write

$$\frac{dn(\text{HCO}^+)}{dt} = \text{formation rate} - \text{destruction rate} = 0. \quad (5.6)$$

The main formation pathway of HCO<sup>+</sup> is through reaction between CO and H<sub>3</sub><sup>+</sup>,



and recombination with electrons is the main destruction route,



The reaction of HCO<sup>+</sup> with H<sub>2</sub>O is ignored in this calculation to assess the importance of the CR ionization rate.

The rate of these reactions can be written as

$$\text{rate} = kn(\text{A})n(\text{B}), \quad (5.9)$$

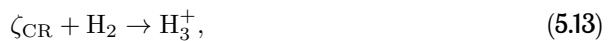
where  $k$  is the rate coefficient, and  $n(\text{A})$  and  $n(\text{B})$  are the molecular densities of the reacting species. Eq. 5.6 then becomes

$$k_1n(\text{H}_3^+)n(\text{CO}) - k_2n(\text{HCO}^+)n(\text{e}^-) = 0. \quad (5.10)$$

The H<sub>3</sub><sup>+</sup> density,  $n(\text{H}_3^+)$ , can be calculated by following the same procedure. The formation reactions are



In order to solve Eq. 5.10 analytically, we summarize the formation of H<sub>3</sub><sup>+</sup> as follows:



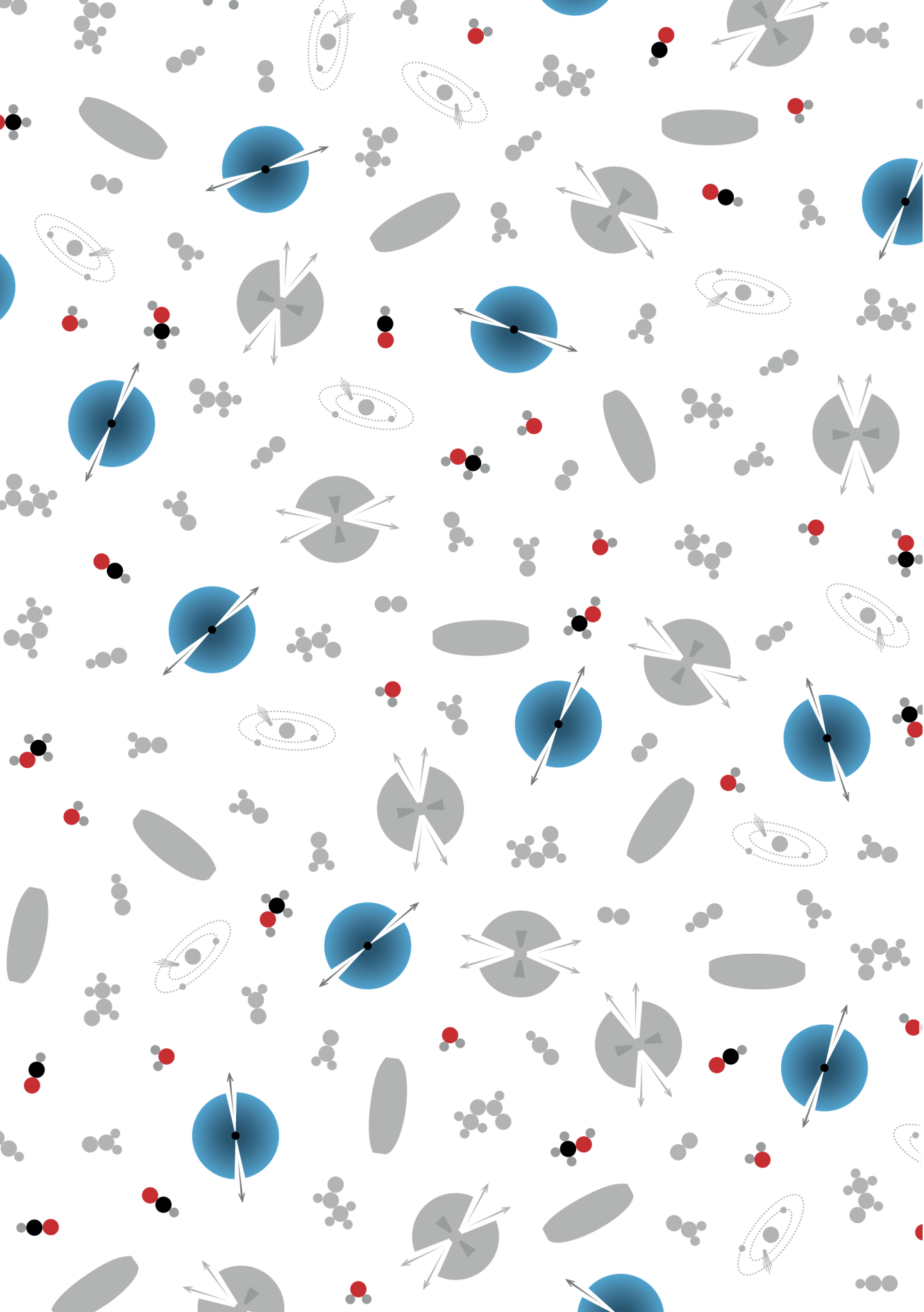
because the ionization reaction is the rate limiting step. In addition, only the reaction with CO (**Eq. 5.8**) is considered as destruction mechanism. We can then write an equation similar to **Eq. 5.10**, that is,

$$\zeta_{\text{CR}}n(\text{H}_2) - k_1n(\text{H}_3^+)n(\text{CO}) = 0. \quad (5.14)$$

Substituting **Eq. 5.14** into **Eq. 5.10**, and assuming  $n(e^-) \approx n(\text{HCO}^+)$ , we can solve **Eq. 5.10** to get the following expression for the  $\text{HCO}^+$  density:

$$n(\text{HCO}^+) = \sqrt{\frac{\zeta_{\text{CR}}n(\text{H}_2)}{k_2}}. \quad (5.15)$$







## 6. Imaging the water snowline in protostellar envelopes with $\text{H}^{13}\text{CO}^+$

*A small survey of protostars in Perseus*

M.L.R. van 't Hoff, E.F. van Dishoeck, E.A. Bergin, D.  
Harsono, J.K. Jørgensen, M.V. Persson, V. Taquet,  
& J.J. Tobin

in preparation



## Abstract

**Context.** The midplane radius in circumstellar disks at which water freezes out from the gas phase onto the dust grains ( $T \lesssim 100 - 150$  K), the water snowline, plays a key role in the formation and composition of planets. However, it is very challenging to locate this snowline through direct observations of water.

**Aims.**  $\text{HCO}^+$  is predicted to be a good tracer based on the chemical consideration that its main destructor is gaseous water.  $\text{H}^{13}\text{CO}^+$  emission is therefore expected only outside of the water snowline. The spatial anti-correlation of  $\text{H}^{13}\text{CO}^+$  and  $\text{H}_2^{18}\text{O}$  emission has been observed toward one source: the Class 0 protostar NGC1333 IRAS2A. We set out to firmly establish  $\text{H}^{13}\text{CO}^+$  as a tracer of the water snowline.

**Methods.** We observed  $\text{H}^{13}\text{CO}^+$  ( $J = 2 - 1$ ) with the Atacama Large Millimeter/sub-millimeter Array (ALMA) toward four protostellar envelopes in Perseus. These sources are ideal targets to test  $\text{H}^{13}\text{CO}^+$  as a snowline tracer because the snowline is located at larger distances from the star than in disks. In addition, emission from complex organic molecules (COMs) can be observed from regions where  $T \gtrsim 100 - 150$  K in these systems, and thus serve as a proxy for the region where water should be present in the gas phase. The spatial extent of the  $\text{H}^{13}\text{CO}^+$  emission can therefore be compared to that of COMs to determine whether  $\text{H}^{13}\text{CO}^+$  emission originates outside the water snowline.

**Results.** The  $\text{H}^{13}\text{CO}^+$  emission indeed peaks off source in B1-c, and surrounds the compact emission displayed by many COM lines, providing a textbook example. In HH 211, the  $\text{H}^{13}\text{CO}^+$  emission peaks on source and no COMs are detected, consistent with the lower luminosity of this source.  $\text{H}^{13}\text{CO}^+$  shows a more complex morphology toward L1448-mm, with blueshifted absorption, and seems associated with larger scales in the line-poor source B5-IRS1.

**Conclusions.** These observations confirm that  $\text{H}^{13}\text{CO}^+$  is a promising tracer for the water snowline, as long as the source structure is taken into consideration.



## 6.1 Introduction

Young stars are surrounded by disks of dust, gas and ice. The location in the disk where the transition between gas and ice occurs is molecule dependent, and is set by the species-specific binding energy to the grains and the temperature structure in the disk. The midplane radius at which 50% of a molecule is frozen out is called a snowline. The sequential freeze out of molecules creates a chemical gradient in the gas and ice, and the composition of forming planets is thus related to the location where they accrete most of their solids and gas (e.g., Öberg et al. 2011; Madhusudhan et al. 2014; Walsh et al. 2015; Mordasini et al. 2016; Eistrup et al. 2016; Booth et al. 2017; Cridland et al. 2019). In addition, the growth of dust grains, and thus the planet formation efficiency, is thought to be significantly enhanced at the water snowline (e.g., Stevenson & Lunine 1988; Schoonenberg & Ormel 2017; Drażkowska & Alibert 2017; Pinilla et al. 2017).

Unfortunately, it is very challenging to observe the water snowline in protoplanetary disks. Because of the large binding energy of water, freeze-out already occurs at temperatures  $\lesssim 100\text{--}150$  K, that is, at radii of a few AU in disks around most Sun-like stars without an accretion burst. Moreover, only lines from the less abundant isotopologue  $\text{H}_2^{18}\text{O}$  can be observed from the ground (except for the  $\text{H}_2\text{O}$  line at 183 GHz that is often masing). Another complication is that gas-phase water may not be as abundant in disks as expected from the measured ice abundances (e.g., Hogerheijde et al. 2011; Zhang et al. 2013). Observations of warm water therefore require both high angular resolution and high sensitivity, and as such, no detection has yet been made (e.g., Notsu et al. 2019). The only disk for which a water snowline location has been claimed, is V883 Ori where a recent accretion burst has heated the disk shifting the snowline outward (Cieza et al. 2016). However, the snowline location was inferred from a change in the dust opacity as is predicted for dust evolution around the snowline (e.g., Banzatti et al. 2015; Schoonenberg et al. 2017). Recent observations of multiple protoplanetary disks have shown that rings in continuum emission are likely not caused by the  $\text{CO}_2$ , CO or  $\text{N}_2$  snowline (Zhang et al. 2017; van Terwisga et al. 2018; Huang et al. 2018; Long et al. 2018; van der Marel et al. 2019). Molecular line observations are thus required to locate the water snowline and establish whether there is a relation with structures in the dust. In fact, observations of methanol and other complex organic molecules (COMs) suggest that the snowline in V883 Ori may be further out than reported (van 't Hoff et al. 2018c, **Chapter 7**; Lee et al. 2019).

COM emission can be used as a proxy for the region inside the water snowline, because many COMs have desorption temperatures similar to water. However, COMs are very difficult to detect in protoplanetary disks, with currently only detections of  $\text{CH}_3\text{CN}$  and  $\text{CH}_3\text{OH}$  (Öberg et al. 2015b; Walsh et al. 2016; Bergner et al. 2018; Loomis et al. 2018). A simpler molecule with strong sub-mm lines, such as  $\text{HCO}^+$ , is therefore a better candidate to trace the water snowline. Gaseous  $\text{H}_2\text{O}$  is the most abundant destroyer of  $\text{HCO}^+$  in warm dense gas.  $\text{HCO}^+$  is therefore expected to be abundant only when water is frozen out (Phillips et al. 1992; Bergin et al. 1998). This principle of a chemical tracer has been successfully applied to locate the CO snowline in protoplanetary disks with molecules like  $\text{N}_2\text{H}^+$  and  $\text{DCO}^+$ , although both chemical effects and the physical structure of the source have to be taken into account (e.g., Qi et al. 2013b, 2015; Mathews et al. 2013; Öberg et al. 2015a; van 't Hoff et al. 2017, **Chapter 2**; Favre et al. 2015; Carney et al. 2018).

**Table 6.1:** Overview of source properties.

Source <sup>e</sup>	Other name	R.A. <sup>b</sup> (hh:mm:ss.s)	Decl. <sup>b</sup> (dd:mm:ss.s)	$L_{\text{bol}}^c$ ( $L_{\odot}$ )	Disk <sup>d</sup> candidate	$F_{\text{peak}}$ 1.7 mm (mJy beam <sup>-1</sup> )	$F_{\text{int}}$ 1.7 mm (mJy)	$F_{\text{int}}^e$ H <sup>13</sup> CO <sup>+</sup> (Jy km s <sup>-1</sup> )
Per-emb-1	HH 211-mms	03:43:56.8	+32:00:50.2	1.8	Yes	17.4 ± 0.2	53.8 ± 0.8	4.2 ± 0.02
Per-emb-26	L1448-mm, L1448C	03:25:38.9	+30:44:05.3	9.2	Yes	59.6 ± 0.2	86.3 ± 0.5	4.8 ± 0.03
Per-emb-29	B1-c	03:33:17.9	+31:09:31.8	3.7	Unknown	27.8 ± 0.2	68.2 ± 0.7	5.3 ± 0.02
Per-emb-53	B5-IRS1	03:47:41.6	+32:51:43.7	4.7	No	5.2 ± 0.1	10.3 ± 0.3	2.3 ± 0.02

**Notes.** <sup>(a)</sup> Naming scheme of Enoch et al. 2009b. <sup>(b)</sup> Phase center of observations. <sup>(c)</sup> Luminosities from Sadavoy et al. 2014 <sup>(d)</sup> Tobin et al. 2015b; Segura-Cox et al. 2018; Lee et al. 2018; Maury et al. 2019 <sup>(e)</sup> Flux integrated within a circular aperture with 10'' diameter over channels with  $> 3\sigma$  emission.

The first observational hint that  $\text{HCO}^+$  can trace the water snowline came from observations of the Class 0 protostar IRAS 15398–335. The optically thin isotopologue  $\text{H}^{13}\text{CO}^+$  displays ring-shaped emission in this source while the methanol emission is centrally peaked (Jørgensen et al. 2013). In addition, recent observations of the spatial anticorrelation between  $\text{H}_2^{18}\text{O}$  and  $\text{H}^{13}\text{CO}^+$  in the Class 0 protostar NGC1333 IRAS2A provided a proof of concept that  $\text{H}^{13}\text{CO}^+$  can be used to trace the water snowline (van 't Hoff et al. 2018a, **Chapter 5**).

In this work, we confirm that  $\text{HCO}^+$  is a promising tracer of the water snowline using observations of  $\text{H}^{13}\text{CO}^+$  toward four protostellar envelopes in Perseus ( $d \sim 300$  AU; Ortiz-León et al. 2018). Although, ultimately, we want to locate the snowline in protoplanetary disks, protostellar envelopes are better targets to establish  $\text{H}^{13}\text{CO}^+$  as a snowline tracer. Due to the higher luminosity, the snowline is located further away from the star in these younger systems. In addition, COMs like methanol can be used in these systems as a proxy for the region where water is expected to be in the gas phase. Moreover, locating the water snowline in envelopes is interesting by itself, because such observations can be used to trace the mass accretion evolution such as episodic accretion;  $\text{H}^{13}\text{CO}^+$  emission at larger radii than expected from the source luminosity indicates that the protostar has recently undergone an accretion burst that shifted the snowline outward (e.g., Jørgensen et al. 2015; Frimann et al. 2017; Hsieh et al. *subm.*) The observations are described in **Sect. 6.2** and presented in **Sect. 6.3**. The results are discussed in **Sect. 6.4**.

## 6.2 Observations

Because of their high luminosities and dense envelopes, deeply embedded Class 0 sources are the best targets to trace the water snowline. The Perseus molecular cloud hosts a large number of Class 0 protostars, including NGC1333 IRAS2A in which we previously observed the spatial anticorrelation between  $\text{H}_2^{18}\text{O}$  and  $\text{H}^{13}\text{CO}^+$  (van 't Hoff et al. 2018a, **Chapter 5**). Here we target four of the more luminous protostars in this region that are not a close ( $< 4''$ ) binary (Tobin et al. 2016b): L1448-mm, B5-IRS1, B1-c and HH 211 (see **Table 6.1** for an overview of the source properties). L1448-mm is in an  $8.1''$  binary. The latter three targets also exhibit signs of a recent accretion burst based on  $\text{C}^{18}\text{O}$  emission, which would have shifted the snowline to larger radii (Frimann et al. 2017).

The observations were carried out with ALMA on 2018 September 16 and 25 (project code 2017.1.01371.S), for a total on source time of 23 minutes per source. For both executions, 43 antennas were used, sampling baselines between 15 m and 1.4 km. The correlator was setup to include two continuum windows with 977 kHz ( $1.6\text{--}1.7$  km  $\text{s}^{-1}$ ) resolution centered at 174.106 and 187.493 GHz. In addition three spectral windows with 61 kHz ( $\sim 0.1$  km  $\text{s}^{-1}$ ) resolution were included with central frequencies of 172.671, 173.500 (targeting  $\text{H}^{13}\text{CO}^+$   $J = 2 - 1$ ), and 186.338 GHz.

Calibration and imaging were done using the ALMA Pipeline and version 5.1.1 of the Common Astronomy Software Applications (CASA). The phase calibrator was J0336+3218, and the bandpass and flux calibrator was J0237+2848. The typical restoring beam size is  $0.6'' \times 0.4''$  ( $\sim 180 \times 120$  AU) for the naturally weighted images. The resulting continuum images have a rms of  $\sim 0.2$  mJy  $\text{beam}^{-1}$ , whereas the rms in the line images is 2–10 mJy  $\text{beam}^{-1}$  channel $^{-1}$ . The observed continuum and  $\text{H}^{13}\text{CO}^+$  line flux densities are reported in **Table 6.1**.

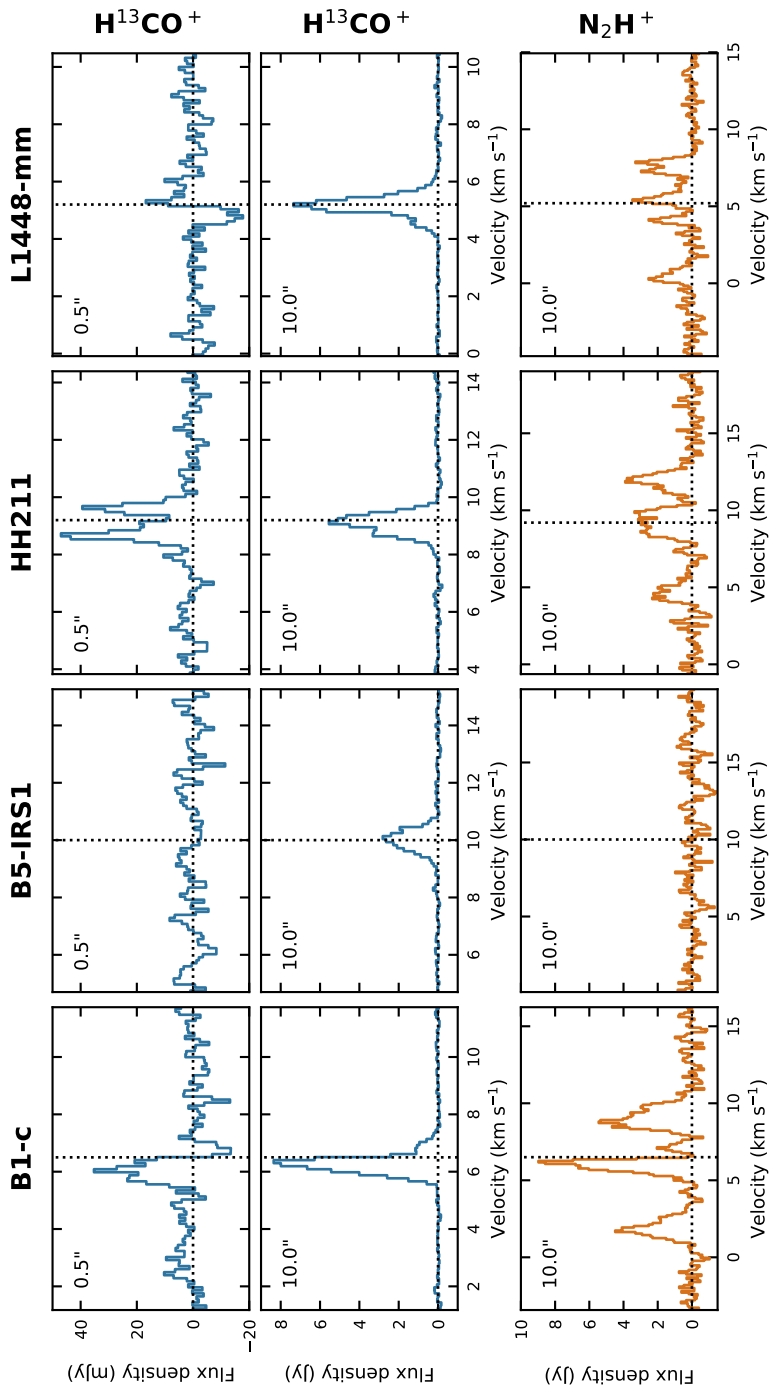


**Figure 6.1:** Spectra of the  $\text{H}^{13}\text{CO}^+$   $J = 2 - 1$  (blue lines; *top and middle panels*) and  $\text{N}_2\text{H}^+$   $J = 2 - 1$  transitions (orange lines; *bottom panels*). The multiple peaks in the  $\text{N}_2\text{H}^+$  spectra are due to hyperfine splitting. The  $\text{H}^{13}\text{CO}^+$  spectra in the *top panels* are extracted within a circular  $0.5''$  diameter aperture ( $\sim$ one beam) centered on source. The other spectra are extracted in a  $10''$  aperture. The horizontal dotted line marks the zero flux level, and the vertical dotted line represents the source velocity.

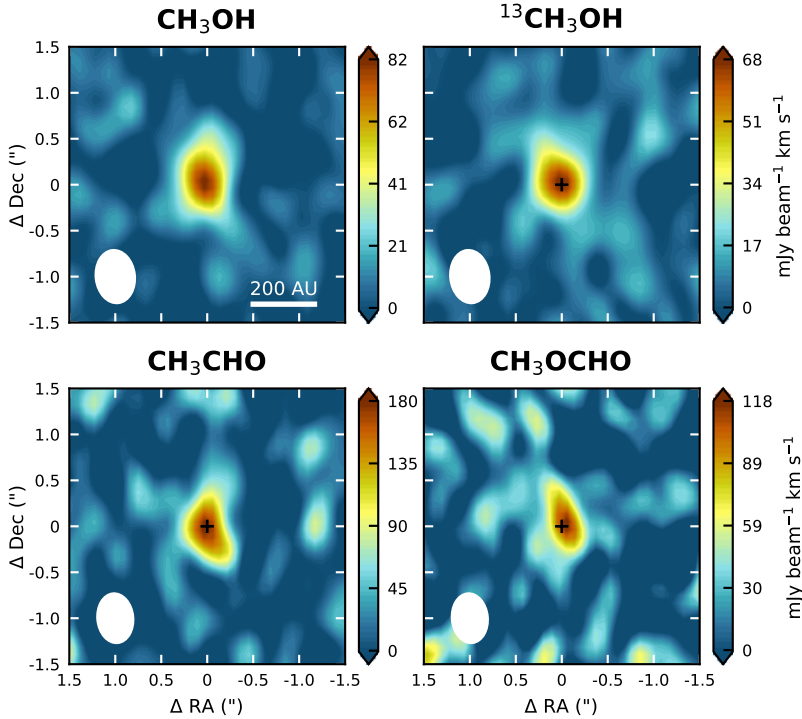


**Figure 6.2:** Integrated intensity maps for  $\text{CH}_3\text{OH}$   $15_{2,14} - 14_{1,14}$  (methanol; *top left panel*),  $^{13}\text{CH}_3\text{OH}$   $7_{-1,7} - 6_{0,6}$  (methanol; *top right panel*),  $\text{CH}_3\text{CHO}$   $17_{3,14} - 18_{0,18}$  (acetaldehyde; *bottom left panel*) and  $\text{CH}_3\text{OCHO}$   $15_{5,10} - 14_{5,9}$  (methyl formate; *bottom right panel*) in the inner  $1.5''$  of B1-c. The positions of the continuum peak is marked with a black cross, and the beam is shown in the lower left corner of each panel.

## 6.3 Results

### 6.3.1 Line detections

$\text{H}^{13}\text{CO}^+$  emission is detected toward all four sources in our sample. The narrow lines ( $\sim 1 \text{ km s}^{-1}$ ; see **Fig. 6.1**), indicate that the emission arises from the inner envelope and not the outflow. Some redshifted absorption toward the continuum peak is observed for B1-c, indicative of infalling material, whereas blueshifted absorption is visible toward L1448-mm. Several other small molecules are detected toward B1-c, HH 211 and L1448-mm, such as  $\text{N}_2\text{H}^+$ ,  $\text{H}^{13}\text{CN}$ ,  $\text{D}_2\text{CO}$ ,  $\text{H}_2\text{CS}$  and  $\text{SiO}$ . Besides  $\text{SiO}$ , which is present in a collimated jet, these molecules generally display compact, barely resolved emission. Other than  $\text{H}^{13}\text{CO}^+$ , and possibly  $\text{D}_2\text{CO}$  and  $\text{H}_2\text{CS}$ , no molecular lines are detected toward B5-IRS1. In contrast, B1-c is very line rich and multiple complex organics are visible, for example, methanol ( $\text{CH}_3\text{OH}$ ,  $^{13}\text{CH}_3\text{OH}$ ), acetaldehyde ( $\text{CH}_3\text{CHO}$ ) and methyl formate ( $\text{CH}_3\text{OCHO}$ ) (see **Fig. 6.2**). A few of these strongest lines are also detected in L1448-mm, but not toward HH 211. A full chemical inventory and characterization will be presented in future work. Here, we focus on  $\text{H}^{13}\text{CO}^+$  and use  $^{13}\text{CH}_3\text{OH}$  as a proxy for the warm ( $T \gtrsim 100 \text{ K}$ ) region inside the water snowline.

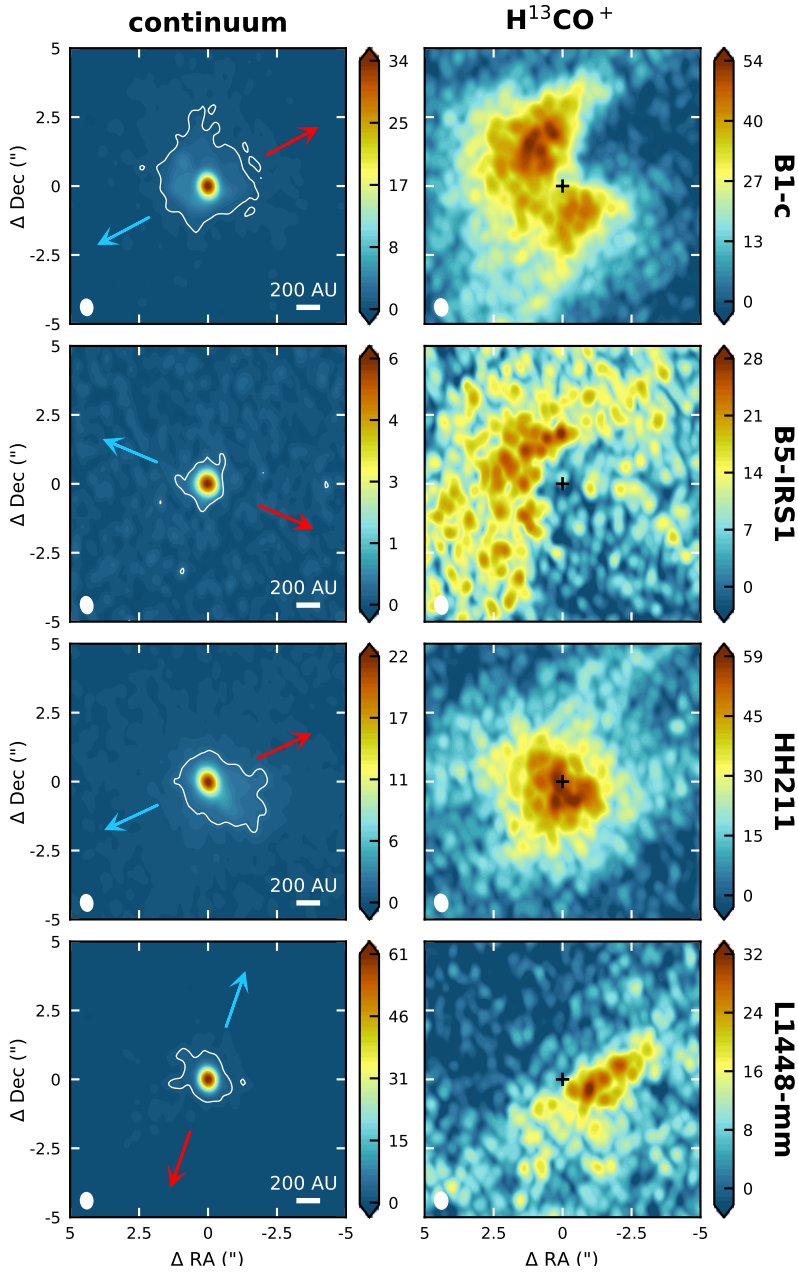


**Figure 6.3:** Continuum images at 1.7 mm (*left panels*) and integrated intensity maps for the  $\text{H}^{13}\text{CO}^+$   $J = 2 - 1$  transition (*right panels*). The  $\text{H}^{13}\text{CO}^+$  emission is integrated only over blueshifted velocities for B1-c and only over redshifted velocities for L1448-mm to avoid channels with absorption. The color scale is in  $\text{mJy beam}^{-1}$  for the continuum images and in  $\text{mJy beam}^{-1} \text{ km s}^{-1}$  for the line images. The white contour in the continuum images marks the  $3\sigma$  level. The positions of the continuum peaks are marked with black crosses, and the outflow directions are indicated by arrows in the continuum images. The beam is shown in the lower left corner of each panel.

### 6.3.2 $\text{H}^{13}\text{CO}^+$ emission morphology

The main destructor of  $\text{HCO}^+$  in warm dense gas is water. The optically thin isotope  $\text{H}^{13}\text{CO}^+$  is therefore expected to have ring-shaped emission just outside the water snowline. **Figure 6.3** shows the integrated intensity (zerth moment) maps together with the 1.7 mm continuum images. Channels that display absorption toward the continuum peak (see **Fig. 6.1**) are excluded in the moment zero map because this can create ring-shaped  $\text{H}^{13}\text{CO}^+$  emission unrelated to the water snowline. All channels are presented in **Appendix 6.A**.

The continuum emission is compact on scales of  $\sim 300$  AU, whereas the  $\text{H}^{13}\text{CO}^+$  emission is more extended.  $\text{H}^{13}\text{CO}^+$  peaks  $\sim 1.5''$  (450 AU) off source in B1-c, with the ring shape disrupted along the direction of the outflow axes. The central depression is not due to optically thick continuum because several other lines with various upper level energies are peaking on source. Compact  $\text{H}^{13}\text{CO}^+$  emission is observed toward HH 211, whereas B5-IRS1 and L1448-mm display asymmetric morphologies. In B5-IRS1 the emission seems to originate predominantly in a ridge-like structure northeast of the source that extends out to larger scales than displayed in **Fig. 6.3**. The emission toward this target is also 3–4 times weaker compared to the other sources. In L1448-mm,  $\text{H}^{13}\text{CO}^+$  is mainly present in the southwest at redshifted velocities. Some blueshifted emission is present in the northeast (see **Fig. 6.A.2**), but these channels display absorption features (see **Fig. 6.1**) and resolved out emission. No strong velocity gradient is observed for any of the sources, as can be seen in the moment one maps in **Fig. 6.B.1**.

The outer radius of the  $\text{H}^{13}\text{CO}^+$  emission is likely set by the onset of CO freeze-out, because CO is the parent molecule for  $\text{H}^{13}\text{CO}^+$ . The CO snowline can be traced by  $\text{N}_2\text{H}^+$ , a molecule that can only be abundant when CO is frozen out. No  $\text{N}_2\text{H}^+$   $J = 2 - 1$  emission is detected in the individual channels, but the lines become clearly visible in spectra extracted in apertures with diameters  $\gtrsim 2''$  (**Fig. 6.1**), except for B5-IRS1. Cold ( $T \lesssim 20\text{K}$ ) gas is thus present on 1000 AU scales, but higher sensitivity is required to locate the CO snowline with this  $\text{N}_2\text{H}^+$  transition ( $E_{\text{up}} = 13$  K).

### 6.3.3 $\text{H}^{13}\text{CO}^+$ and the water snowline

B1-c displays most clearly the expected ring-shaped  $\text{H}^{13}\text{CO}^+$  emission profile. To assess whether this is indeed related to  $\text{H}^{13}\text{CO}^+$  destruction inside the water snowline, we compare the spatial extent to that of  $^{13}\text{CH}_3\text{OH}$ . **Figure 6.4** shows a radial cut along a position angle of  $45^\circ$ . The central depression is clearly visible for  $\text{H}^{13}\text{CO}^+$ . There is still residual emission left on source, similar as what was observed for NGC1333 IRAS2A (van 't Hoff et al. 2018a, **Chapter 5**). Most importantly,  $^{13}\text{CH}_3\text{OH}$  peaks on source and the emission drops rapidly at radii  $\gtrsim 100$  AU.  $\text{H}^{13}\text{CO}^+$  emission starts to rise at this point and peaks around 300–400 AU. This suggests that the water snowline is located between  $\sim 100$  and  $\sim 400$  AU.

A rotation diagram is constructed with six  $^{13}\text{CH}_3\text{OH}$  transitions that are clearly detected and do not seem to be blended with other lines (**Fig. 6.5**). Fluxes are extracted in a  $1''$  diameter aperture, where most of the methanol emission originates. Fitting a linear function results in a rotational temperature of  $\sim 173$  K, consistent with methanol that is thermally desorbed inside the water snowline ( $T \gtrsim 100$ – $150$  K) and observations toward other protostars (e.g., Taquet et al. 2015).

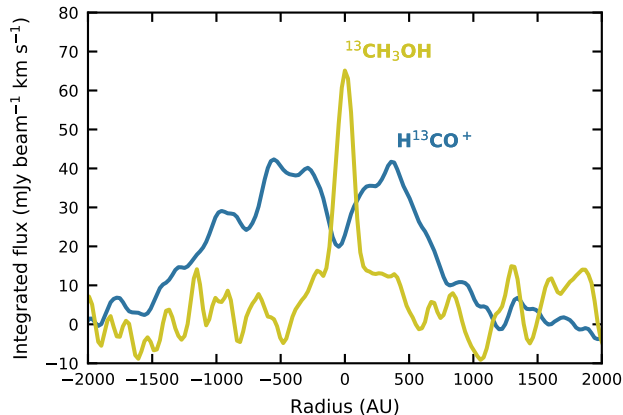


**Figure 6.4:** Radial intensity profiles for  $\text{H}^{13}\text{CO}^+$   $J = 2-1$  (blue line) and  $^{13}\text{CH}_3\text{OH}$   $7_{-1,7}-6_{0,6}$  (yellow line) toward B1-c along a position angle of  $45^\circ$ , showing the spatial anticorrelation between the two species.

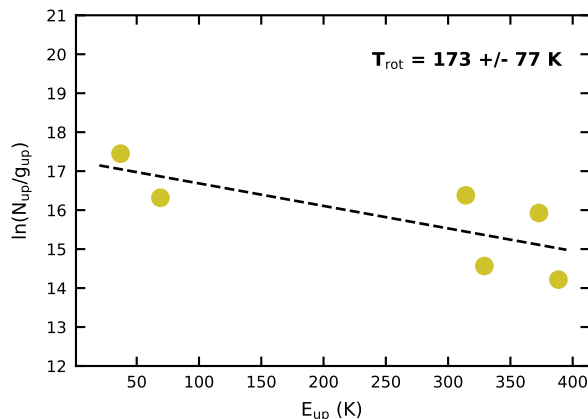


**Figure 6.5:** Rotation diagram for  $^{13}\text{CH}_3\text{OH}$  toward B1-c. The fluxes are extracted in a circular  $1.0''$  aperture centered on the continuum peak.

## 6.4 Discussion and Conclusions

Ring-shaped  $\text{H}^{13}\text{CO}^+$  emission surrounding compact emission from warm methanol (and other complex organics) is observed toward B1-c, suggesting that  $\text{H}^{13}\text{CO}^+$  traces the water snowline. Based on the extent of the methanol emission and the concurrent rise in  $\text{H}^{13}\text{CO}^+$ , the water snowline is located between  $\sim 100$  AU and  $\sim 400$  AU. Because chemical models show that  $\text{H}^{13}\text{CO}^+$  does not peak directly at the snowline, but instead at slightly larger radii, chemical modeling with a source specific physical structure is required to derive a more precise snowline location (see van 't Hoff et al. 2018a, Chapter 5).

A good consistency check is to determine whether this snowline location is in agreement with the luminosity. In IRAS2A, which has a luminosity of  $\sim 19 L_\odot$ , the snowline was located around 225 AU by above mentioned analysis. The temperature,



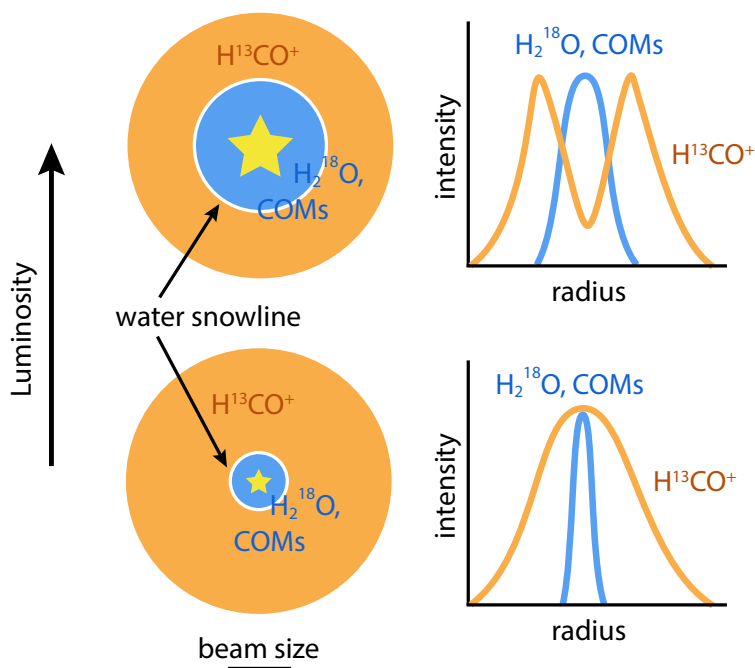


**Figure 6.6:** Schematic representation of the distribution of  $\text{H}^{13}\text{CO}^+$  and the water snowline for different luminosities (*left panels*) and the effect of the angular resolution on the observed emission profiles (*right panels*). In a low-luminosity source (*bottom panels*), the water snowline is located close to the protostar. If the angular resolution is not high enough to resolve the snowline location,  $\text{H}^{13}\text{CO}^+$  will have broad centrally peaked emission. Emission from water and complex organics is expected to be unresolved and possibly weak. In a high-luminosity source (*top panel*), the snowline is located far enough from the star to be spatially resolved. This will result in ring-shaped  $\text{H}^{13}\text{CO}^+$  emission around compact emission from water and complex organics. B1-c is likely an example of the high-luminosity case, while HH 211 may represent the low-luminosity case.

and thus to first order the snowline location, scales radially with the square root of the luminosity. The luminosity of  $3.7 L_{\odot}$  for B1-c then predicts a snowline location of  $\sim 100$  AU. Frimann et al. (2017) found that the spatial extent of the  $\text{C}^{18}\text{O}$  emission in B1-c required a luminosity 2–11 times higher than the current luminosity, indicating that the star had recently undergone an accretion burst. Due to the higher densities in the inner envelope, the water snowline is expected to return to its previous location faster than the CO snowline after an accretion burst. Nonetheless, if the water snowline has not returned yet, it would be expected at radii between 140 and 329 AU for luminosities of 2–11 times higher than the current luminosity. This is still located within the emission peaks of  $\text{H}^{13}\text{CO}^+$ . The  $\text{H}^{13}\text{CO}^+$  emission toward B1-c is thus consistent with the expected snowline location.

Luminosity may also explain why the  $\text{H}^{13}\text{CO}^+$  emission is centrally peaked in HH 211; for the bolometric luminosity of  $1.8 L_{\odot}$ , the snowline is expected at 70 AU. Alternatively, the snowline is located closer to the star due to the presence of a putative disk as this would increase the amount of dense and cold material on small scales (see

e.g., Persson et al. 2016 for the effect of a disk on the water abundance). In either case, this means that there is only one beam inside the snowline at our  $\sim 0.5''$  (150 AU) resolution. The  $\text{H}^{13}\text{CO}^+$  emission is consistent with an unresolved snowline (see Fig. 6.6). Higher angular resolution observations, preferably from  $\text{H}_2^{18}\text{O}$ , are needed to confirm this.

Based on luminosity, the snowline is expected at the largest radius in L1448-mm. However, the structure of this source appears complex with blueshifted absorption, possibly due to the presence of a wide-opening angle wind (e.g., Hirano et al. 2010). B5-IRS1 also has a higher luminosity than B1-c, but this source turned out to be very poor in molecular emission in general.

The results presented here thus confirm that  $\text{H}^{13}\text{CO}^+$  is a promising tracer for the water snowline, as long as the structure of the source is taken into account. Observations of  $\text{H}_2^{18}\text{O}$  emission are required to firmly establish  $\text{H}^{13}\text{CO}^+$  as a snowline tracer. B1-c and HH 211 are good candidates because at  $0.5''$  resolution,  $\text{H}_2^{18}\text{O}$  emission is expected to be spatially extended in B1-c and unresolved in HH 211. Such studies would pave the way for observations of the water snowline in protoplanetary disks.

## Acknowledgements

This paper makes use of the following ALMA data: ADS/JAO.ALMA#2017.1.01371.S. ALMA is a partnership of ESO (representing its member states), NSF (USA) and NINS (Japan), together with NRC (Canada), MOST and ASIAA (Taiwan), and KASI (Republic of Korea), in cooperation with the Republic of Chile. The Joint ALMA Observatory is operated by ESO, AUI/NRAO and NAOJ. Astrochemistry in Leiden is supported by the Netherlands Research School for Astronomy (NOVA). M.L.R.H acknowledges support from a Huygens fellowship from Leiden University.

## Appendix

### 6.A $\text{H}^{13}\text{CO}^+$ channelmaps

Channelmaps for the  $\text{H}^{13}\text{CO}^+$   $J = 2 - 1$  transition are presented in Figs 6.A.1-6.A.2 for the four sources in our sample.

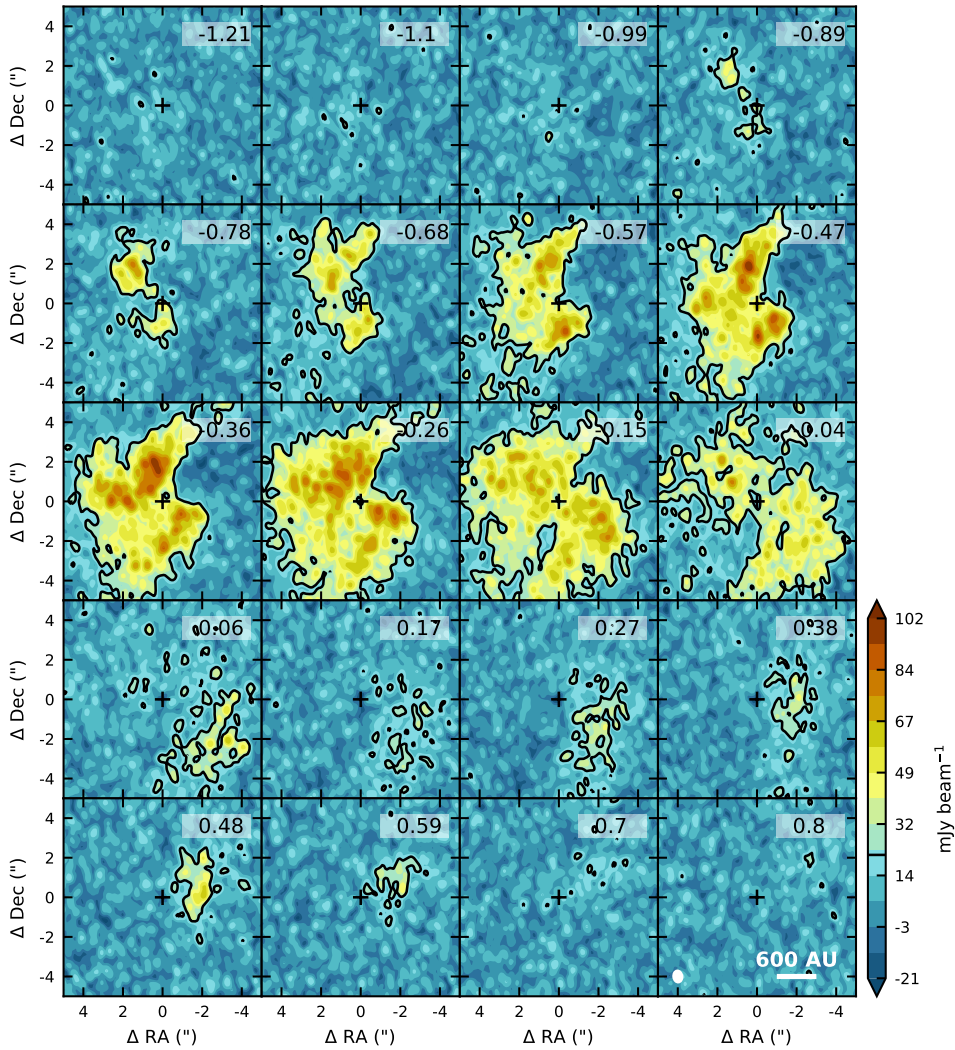


**Figure 6.1.1:** Channelmaps of  $\text{H}^{13}\text{CO}^+ J=2-1$  toward B1-c. The black contour denotes the  $3\sigma$  level. The velocity is listed in the top right corner of each panel. The continuum peak position is marked with a black cross and the beam is shown in the top left corner of the bottom right panel.

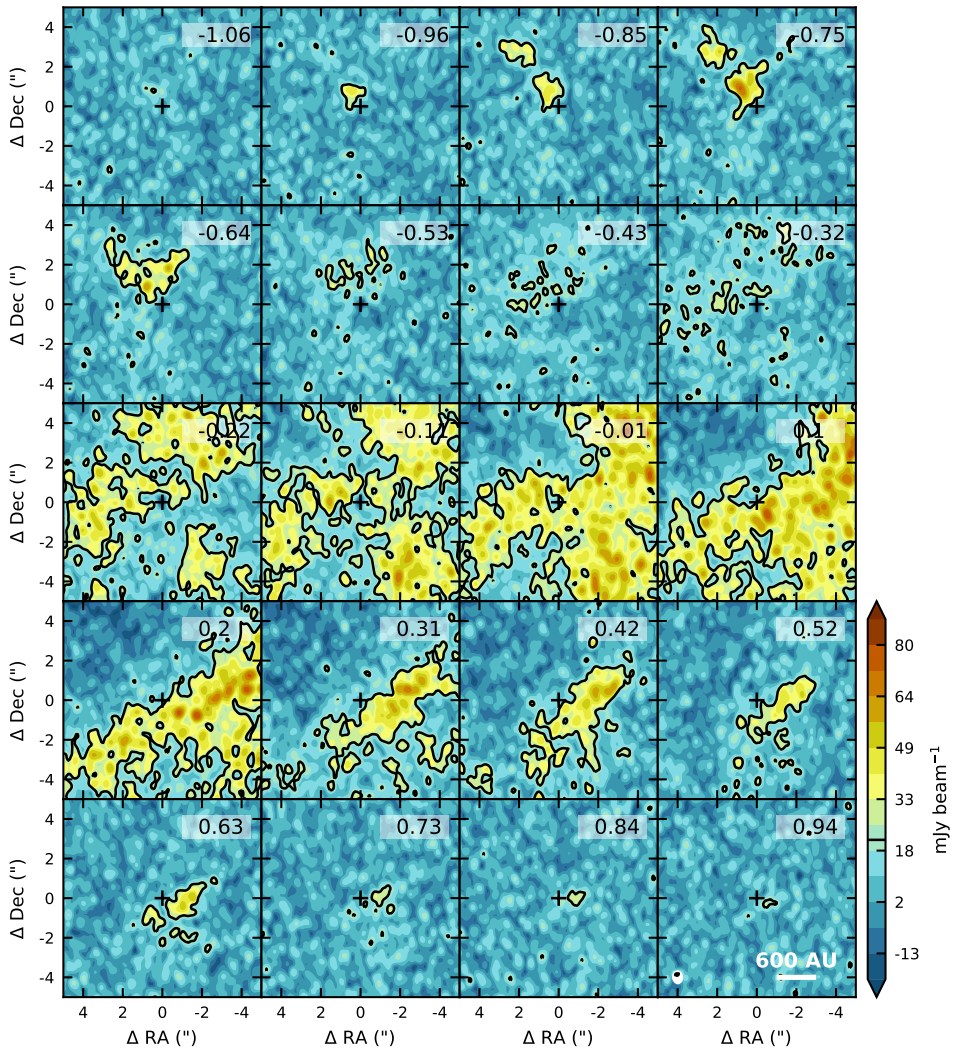


Figure 6.A.2: As Fig. 6.A.1, but for L1448-mm.

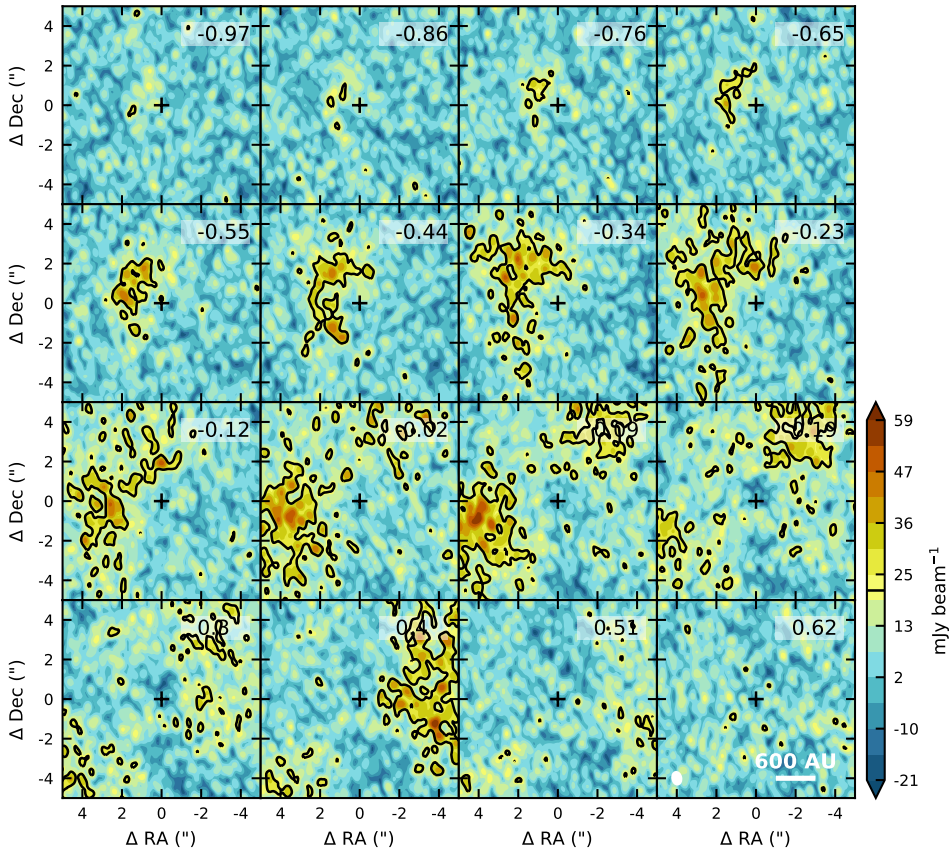


Figure 6.1.3: As Fig. 6.1.1, but for B5-IRS1.

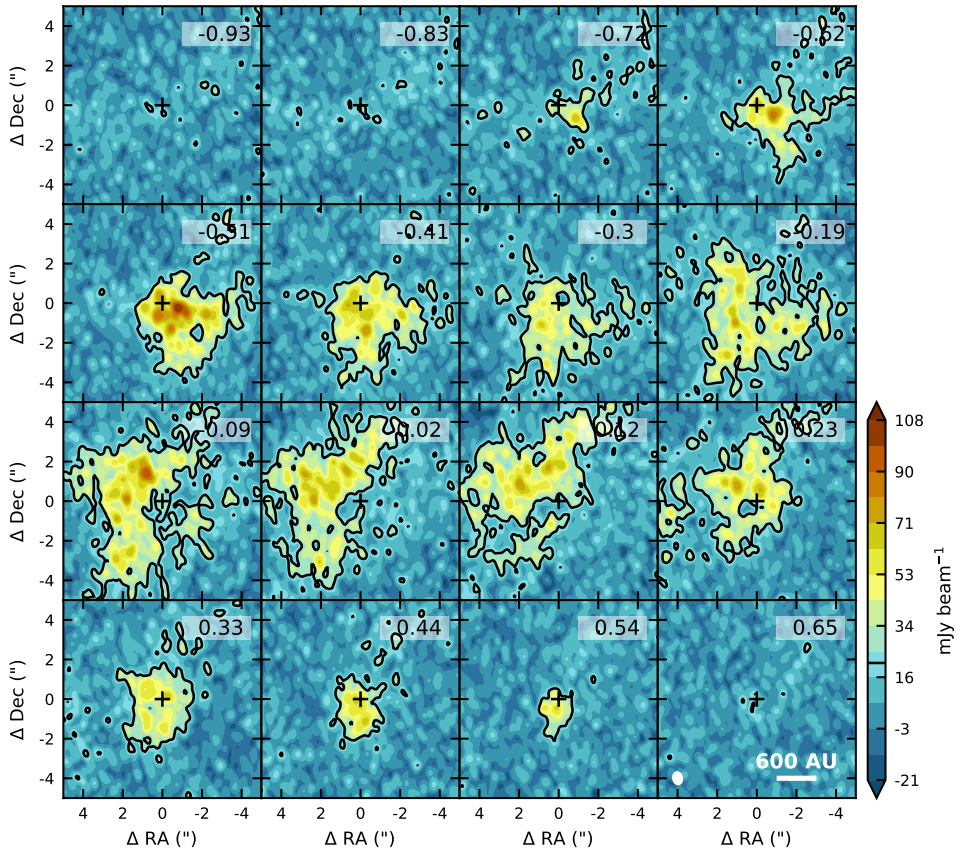
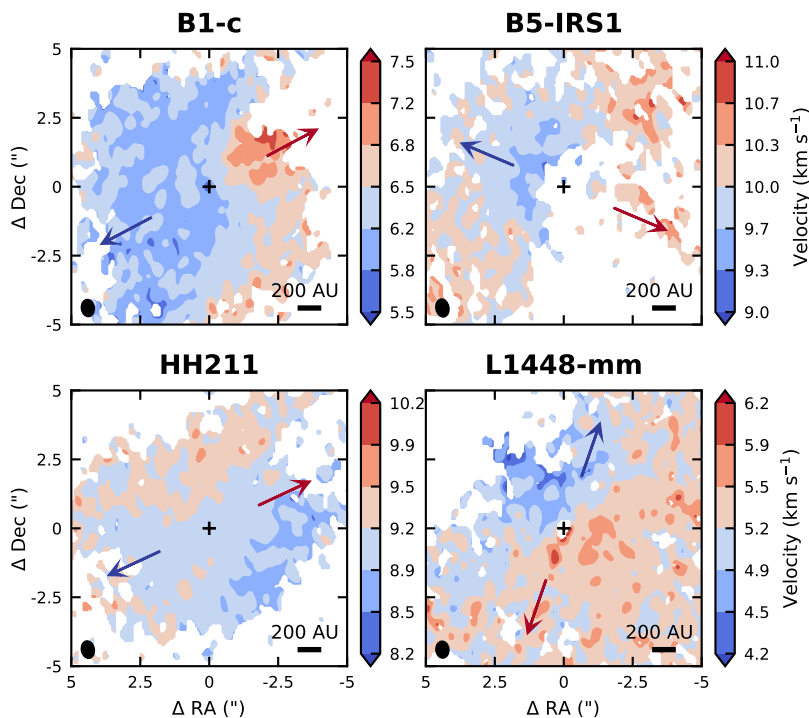


Figure 6.14: As Fig. 6.11, but for HH 211.



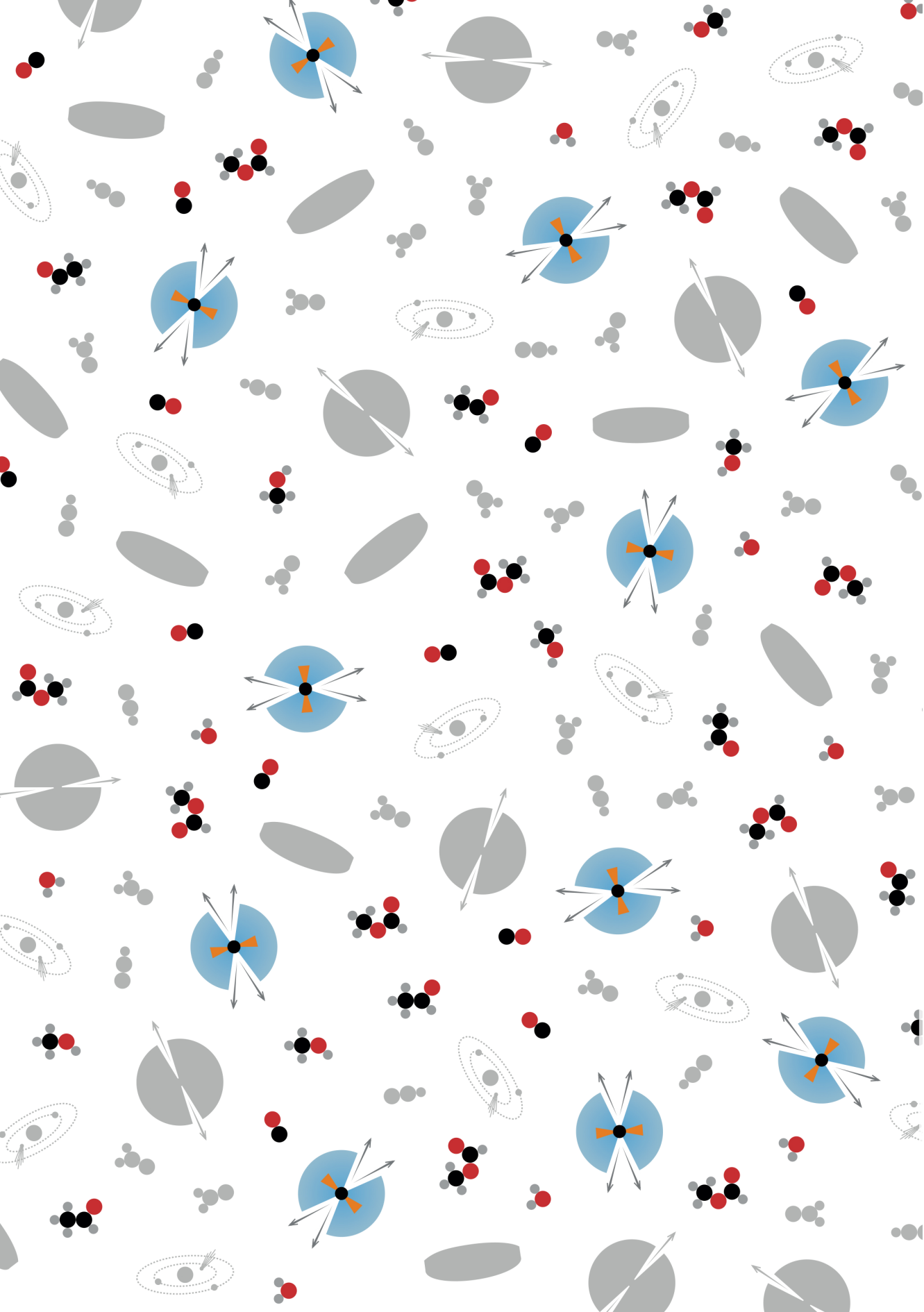
**Figure 6.B.1:** Moment one maps for  $\text{H}^{13}\text{CO}^+$   $J = 2 - 1$ . Pixels with  $< 3\sigma$  emission are masked out. The velocity listed in the scale bars between blue and red is the systemic velocity. The outflow directions are indicated by arrows and the continuum peak position is marked with a black cross. The beam is shown in the lower left corner of each panel.

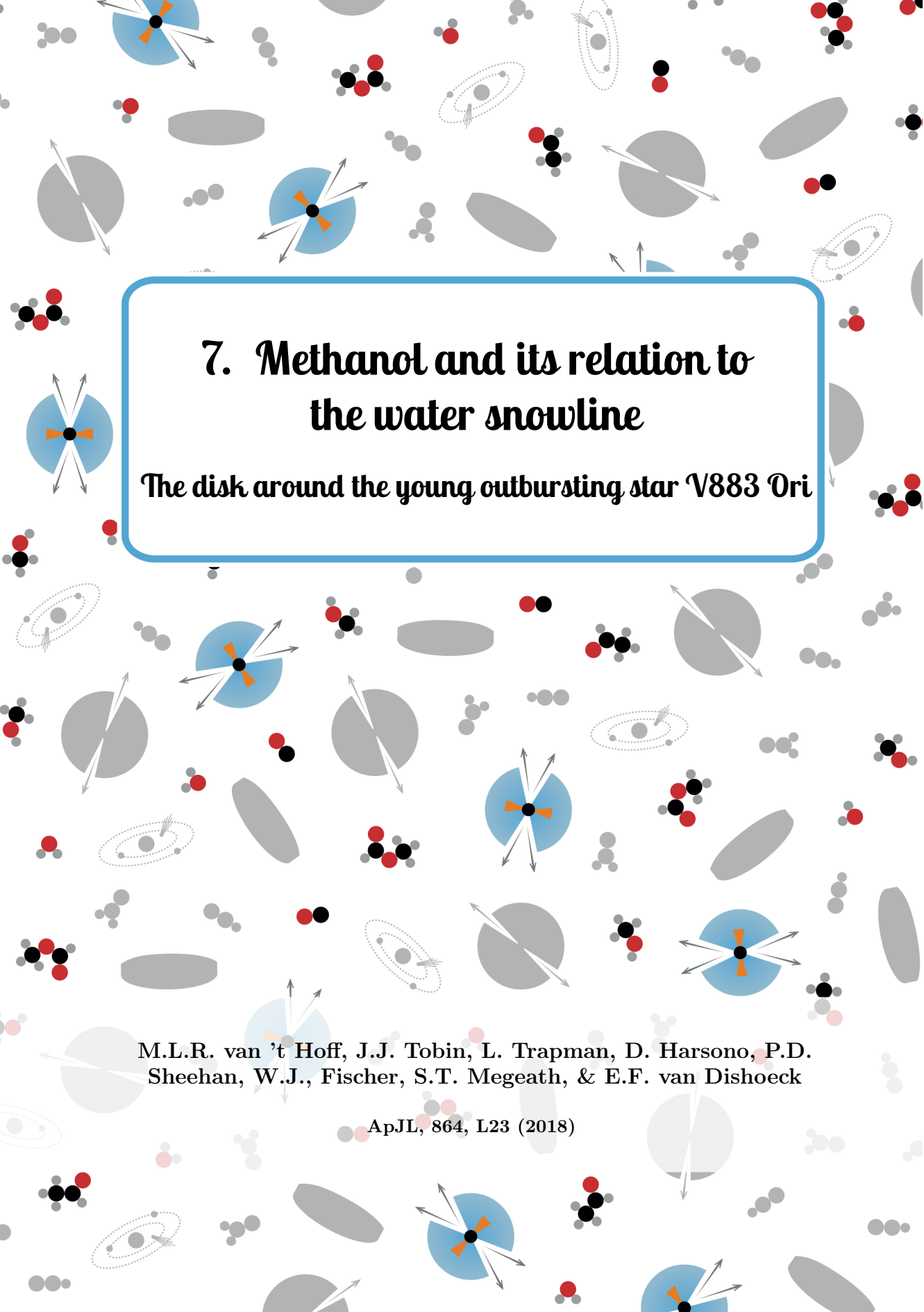
## 6.B $\text{H}^{13}\text{CO}^+$ moment one maps

$\text{H}^{13}\text{CO}^+$   $J = 2 - 1$  moment one maps for all targets are shown in [Fig. 6.B.1](#).









## 7. Methanol and its relation to the water snowline

The disk around the young outbursting star V883 Ori

M.L.R. van 't Hoff, J.J. Tobin, L. Trapman, D. Harsono, P.D. Sheehan, W.J., Fischer, S.T. Megeath, & E.F. van Dishoeck

ApJL, 864, L23 (2018)



---

## Abstract

We report the detection of methanol in the disk around the young outbursting star V883 Ori with the Atacama Large Millimeter/submillimeter Array (ALMA). Four transitions are observed with upper level energies ranging between 115 and 459 K. The emission is spatially resolved with the  $0.14''$  beam and follows the Keplerian rotation previously observed for  $\text{C}^{18}\text{O}$ . Using a rotational diagram analysis, we find a disk-averaged column density of  $\sim 10^{17} \text{ cm}^{-2}$  and a rotational temperature of  $\sim 90 - 100 \text{ K}$ , suggesting that the methanol has thermally desorbed from the dust grains. We derive outer radii between 120 and 140 AU for the different transitions, compared to the 360 AU outer radius for  $\text{C}^{18}\text{O}$ . Depending on the exact physical structure of the disk, the methanol emission could originate in the surface layers beyond the water snowline. Alternatively, the bulk of the methanol emission originates inside the water snowline, which can then be as far out as  $\sim 100 \text{ AU}$ , instead of 42 AU as was previously inferred from the continuum opacity.

In addition, these results show that outbursting young stars like V883 Ori are good sources to study the ice composition of planet forming material through thermally desorbed complex molecules, which have proven to be hard to observe in more evolved protoplanetary disks.

## 7.1 Introduction

Snowlines in disks around young stars mark the midplane locations where molecular species freeze out from the gas phase onto dust grains. The most important snowline for planet formation is the water snowline. Planetesimal formation is expected to be significantly enhanced at this snowline because the bulk of the ice mass is in water ice (e.g., Stevenson & Lunine 1988; Ros & Johansen 2013; Schoonenberg & Ormel 2017). In addition, the elemental composition of both the gas and ice changes across this snowline since water is a major carrier of oxygen. The bulk composition of planets therefore depends on their formation location with respect to the water snowline (e.g., Öberg et al. 2011; Madhusudhan et al. 2014; Eistrup et al. 2018).

For water, the transition from ice to gas occurs when the temperature exceeds roughly 100 K (Fraser et al. 2001). This places the snowline at a few AU from the star in protoplanetary disks, making it hard to observe. However, heating is temporarily enhanced during protostellar accretion bursts, which causes ices to sublimate out to larger radii. After such a burst, the circumstellar dust cools rapidly (Johnstone et al. 2013), while for the molecules it takes much longer to freeze back onto the grains (Rodgers & Charnley 2003). As a result snowlines are shifted away from the star (Lee 2007; Visser & Bergin 2012; Vorobyov et al. 2013; Visser et al. 2015). This has been observed for CO toward a sample of protostars (Jørgensen et al. 2015; Frimann et al. 2017).

V883 Ori is a FU Orionis object in the Orion A L1641 molecular cloud ( $d \sim 400$  pc; Kounkel et al. 2017) with a bolometric luminosity of  $\sim 218L_{\odot}$  (Strom & Strom 1993; Furlan et al. 2016). Although the onset of the V883 Ori outburst was not directly observed, evidence for an ongoing outburst that began before 1888 comes from its associated reflection nebula (Pickering 1890) and the similarity of its near-IR spectrum to that of FU Ori (Connelley & Reipurth 2018). The  $1.3 M_{\odot}$  star is surrounded by a  $\gtrsim 0.3 M_{\odot}$  rotationally supported disk (Cieza et al. 2016, 2018) still embedded in its envelope.

The location of the water snowline in V883 Ori was inferred from a change in the continuum opacity at 42 AU (Cieza et al. 2016), which may be due to a pileup of dust interior to the snowline (Birnstiel et al. 2010; Banzatti et al. 2015; Pinilla et al. 2016), or water evaporation and re-coagulation of silicates (Schoonenberg et al. 2017). However, the origin of various structures seen in continuum emission of disks is still heavily debated and radial discontinuities in the spectral index are not necessarily related to snowlines (van Terwisga et al. 2018). Molecular observations are thus needed to confirm or refute the snowline location. Unfortunately, water is hard to observe from the ground and warm water ( $T \gtrsim 100$  K) has not yet been observed in young disks (Harsono et al., in prep.), so observing the snowline directly is difficult. A complementary approach is to observe other molecules whose distribution can be related to the snowline. Methanol ( $\text{CH}_3\text{OH}$ ) is generally used to probe the  $\gtrsim 100$  K region in hot cores (Herbst & van Dishoeck 2009), because its volatility is similar to that of water (e.g., Brown & Bolina 2007).

We serendipitously detected spatially resolved methanol emission in the V883 Ori disk with the VLA/ALMA Nascent Disk And Multiplicity (VANDAM) Orion survey that aims to characterize the embedded disks in Orion (PI: Tobin, Tobin et al., in prep.). Analysis of the methanol observations and comparison with earlier  $\text{C}^{18}\text{O}$  observations shows that the methanol is thermally desorbed and suggests that the water snowline can be as far out as  $\sim 100$  AU.

**Table 7.1:** Overview of the molecular line observations toward V883 Ori.

Species	Transition	Frequency (GHz)	$A_{ul}$ ( $s^{-1}$ )	$E_{up}/k$ (K)	$g_{up}$	$F_{peak}$ (mJy beam $^{-1}$ )	$F_{int}^a$ (Jy km s $^{-1}$ )	$R_{out}$ (AU)
C $^{18}$ O	2 – 1	219.560354	$6.03 \times 10^{-7}$	16	3	$117 \pm 6$	$1.1 \pm 0.08$	$361 \pm 23$
CH $_3$ OH (A $^-$ )	5 $_4$ – 6 $_3$	346.202719	$2.12 \times 10^{-5}$	115	11	$105 \pm 21^b$	$1.6 \pm 0.18^b$	$142 \pm 27^b$
CH $_3$ OH (A $^+$ )	5 $_4$ – 6 $_3$	346.204271	$2.12 \times 10^{-5}$	115	11	$105 \pm 21^b$	$1.6 \pm 0.18^b$	$142 \pm 27^b$
CH $_3$ OH (A $^-$ )	16 $_1$ – 15 $_2$	345.903916	$8.78 \times 10^{-5}$	333	33	$108 \pm 21$	$1.1 \pm 0.18$	$136 \pm 18$
CH $_3$ OH (E2)	18 $_3$ – 17 $_4$	345.919260	$7.10 \times 10^{-5}$	459	37	$77 \pm 21$	$0.5 \pm 0.18$	$117 \pm 26$

**Notes.** <sup>(a)</sup> Within a 1.0'' aperture for C $^{18}$ O and within a 0.6'' aperture for CH $_3$ OH. <sup>(b)</sup> Between 0.5 and 7.0 km s $^{-1}$ , that is, for both lines combined.

## 7.2 Observations

V883 Ori was observed on 2016 September 6 and 2017 July 19 in Band 7 as part of ALMA Cycle 4 project 2015.1.00041.S. The total on-source integration time was 54 seconds, and baselines between 16.7 m and 3697 m were covered. The correlator setup consisted of two low spectral resolution (31.25 MHz) 1.875 GHz continuum windows centered at 333 GHz and 344 GHz, a 234.375 MHz spectral window (122 kHz resolution) centered at 330.6 GHz, and a 937.5 MHz spectral window (488 kHz  $\approx$  0.42 km s<sup>-1</sup> resolution) centered at 345.8 GHz. The latter spectral window contained the methanol transitions.

The bandpass calibrator was J0510+1800 for the 2016 observations and J0522-3627 for the 2017 observations. The absolute flux calibrators were J0510+1800, J0522-3627 and J0750+1231 for the respective executions, and J0541-0541 was used as complex gain calibrator for all executions. The data were reduced manually by the Dutch Allegro ARC Node to properly account for variation of quasar J0510+1800. Following the standard calibration, phase-only self-calibration was performed on the continuum data using version 4.7.2 of the Common Astronomy Software Application (CASA, McMullin et al. 2007). The self-calibration solutions were also applied to the spectral line data. The line data was imaged after continuum subtraction, using the CASA task *clean* with natural weighting and a velocity resolution of 0.5 km s<sup>-1</sup>. This resulted in a synthesized beam size of 0.13''  $\times$  0.14'' and a rms of 21 mJy beam<sup>-1</sup> per channel.

V883 Ori was also observed in Band 6 (project 2013.1.00710.S). In these observations the correlator was configured to have one baseband centered on the C<sup>18</sup>O  $J = 2 - 1$  transition at 219.560 GHz. The C<sup>18</sup>O data reduction is described by Cieza et al. (2016). The resulting image has a synthesized beam of 0.23''  $\times$  0.30'' and a rms of 9 mJy beam<sup>-1</sup> in 0.5 km s<sup>-1</sup> channels.

## 7.3 Results

### 7.3.1 Detection of warm methanol in the disk

The spectral setting of the ALMA Band 7 observations covers four CH<sub>3</sub>OH lines with upper level energies ranging from 115 to 459 K (see **Table 7.1**). Spectra centered at the corresponding rest frequencies are presented in **Fig. 7.1**. All four lines are detected between  $\sim$ 0.5 and  $\sim$ 7.0 km s<sup>-1</sup>, but the two nearby  $5_4 - 6_3$  transitions from A<sup>+</sup> and A<sup>-</sup> CH<sub>3</sub>OH are blended. The peak signal-to-noise in the 0.5 km s<sup>-1</sup> channels is  $\sim$ 4 for the highest energy transition ( $18_3 - 17_4$ ) and  $\sim$ 5 for the other lines.

In addition to the CH<sub>3</sub>OH transitions, several other lines are marginally detected (**Fig. 7.1**, top panels). Using the Jet Propulsion Laboratory (JPL, Pickett et al. 1998) and the Cologne Database for Molecular Spectroscopy (CDMS, Müller et al. 2001) databases through Splatalogue<sup>1</sup> we can assign transitions of <sup>13</sup>CH<sub>3</sub>OH, the formaldehyde isotopologues H<sub>2</sub>C<sup>18</sup>O and D<sub>2</sub>CO, methyl formate (CH<sub>3</sub>OCHO) and acetaldehyde (CH<sub>3</sub>CHO). The peak signal-to-noise of these transitions are  $\sim$  4–5 $\sigma$  in 1.0 km s<sup>-1</sup> channels, but unambiguous identification requires detection of more lines.

<sup>1</sup>www.splatalogue.net

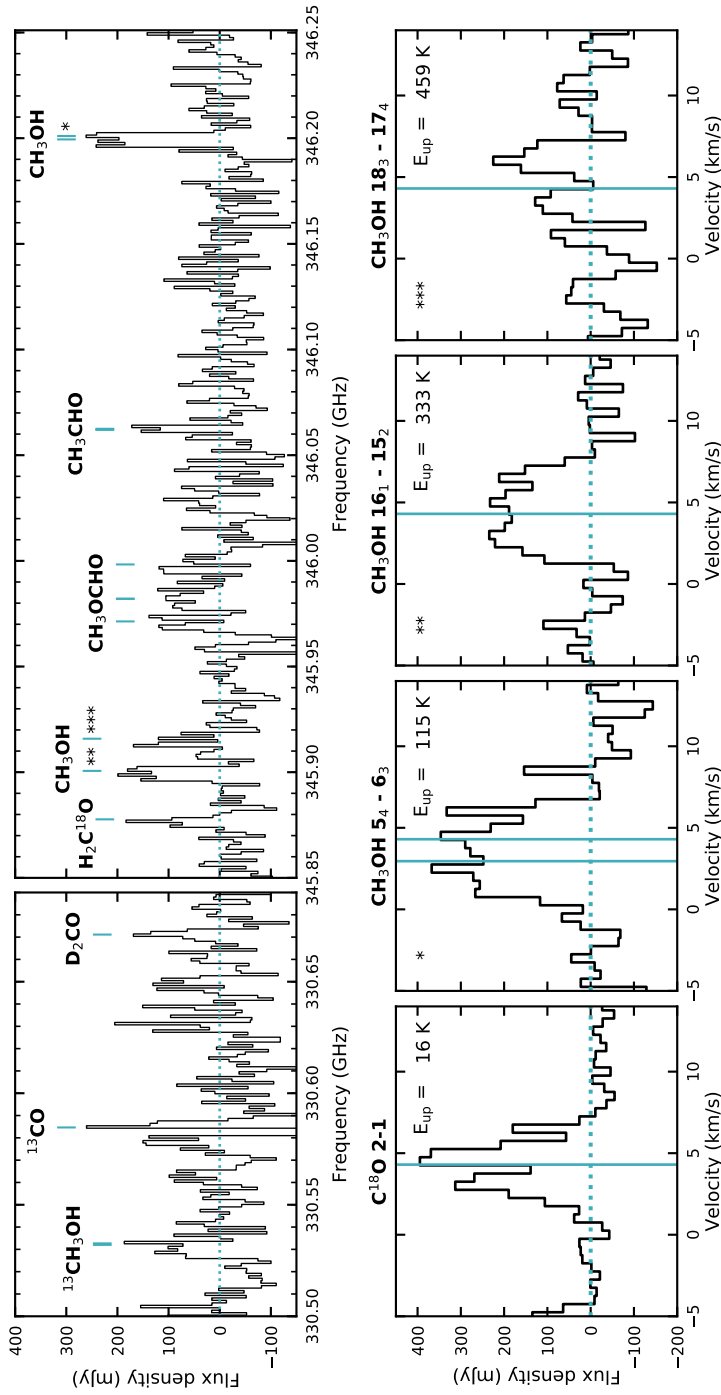


**Figure 7.1:** Spectra extracted within a  $0.6''$  circular aperture ( $1.0''$  for  $\text{C}^{18}\text{O}$ ) toward V883 Ori. The *top panels* display part of the spectral windows centered at 330.6 GHz and 345.8 GHz binned to a resolution of 1.10 and 1.16 MHz, respectively ( $1.0 \text{ km s}^{-1}$ ). In addition, an outer taper of 2000 k $\lambda$  was applied before imaging. The transitions for  $\text{CH}_3\text{OH}$  and a few other key species are labeled and marked with a vertical blue line. The rms from a line-free region is  $\sim 50$  mJy. The *bottom panels* show the  $\text{C}^{18}\text{O}$  and  $\text{CH}_3\text{OH}$  spectra at  $0.5 \text{ km s}^{-1}$  resolution. The asterisks in the top left corner of the  $\text{CH}_3\text{OH}$  panels correspond to the asterisks in the *top right panel*. The vertical blue lines indicate the line centers ( $v_{\text{sys}} = 4.3 \text{ km s}^{-1}$ ).



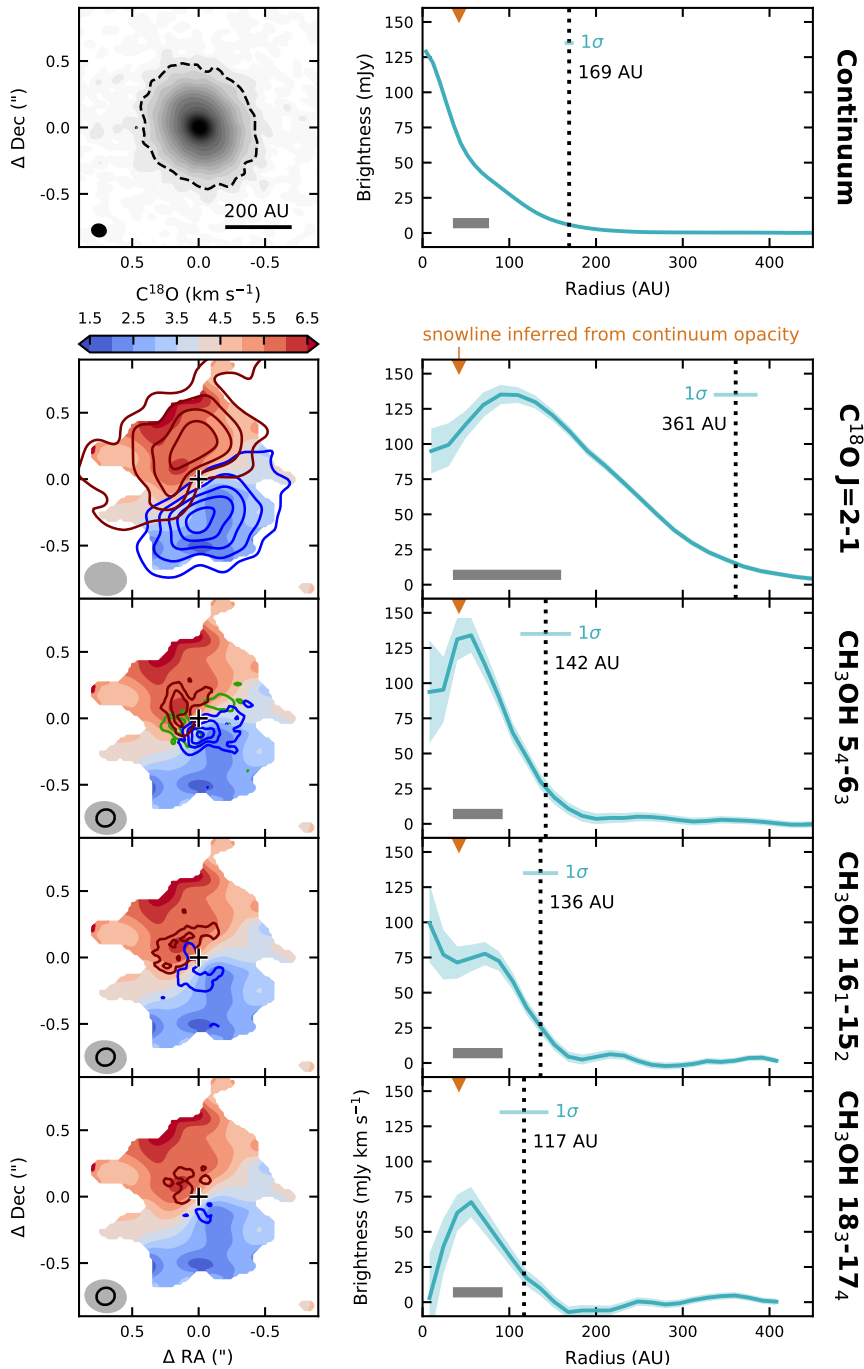


**Figure 7.2:** Continuum image toward V883 Ori at  $870\ \mu\text{m}$  (top left panel), and integrated intensity (moment zero) maps for  $\text{C}^{18}\text{O}$  and  $\text{CH}_3\text{OH}$  (solid contours) overlaid on the  $\text{C}^{18}\text{O}$  intensity-weighted mean velocity (moment one) map (color scale in km s $^{-1}$ , bottom left panels). *Caption continues on next page.*

**Figure 7.2 continued:** The dashed black contour marks the  $5\sigma$  ( $2.6 \text{ mJy beam}^{-1}$ ) level for the continuum. The red (blue) solid contours show the emission integrated over redshifted (blueshifted) velocity channels containing  $> 3\sigma$  emission. The green contours for the  $\text{CH}_3\text{OH } 5_4 - 6_3$  transitions show emission integrated over velocities between the line centers of the  $A^-$  and  $A^+$  transitions. For  $\text{C}^{18}\text{O}$ , contours are in steps of  $3\sigma$  starting at  $3\sigma$  ( $11 \text{ mJy beam}^{-1} \text{ km s}^{-1}$ ). For  $\text{CH}_3\text{OH}$ , a Keplerian mask is used, so each moment zero pixel represents the sum of a different number of channels. A signal-to-noise map is therefore calculated using the channel rms and the number of channels used per pixel. Contours are shown in steps of  $2\sigma$  starting at  $3\sigma$ . The continuum peak position ( $\text{RA} = 05^{\text{h}}38^{\text{m}}18.10^{\text{s}}$ ;  $\text{Dec} = -7^{\circ}02'25.96''$ ) is marked with a cross. The synthesized beams are shown in the lower left corner of the panels, with the continuum beam in black, the  $\text{C}^{18}\text{O}$  beam in gray and the  $\text{CH}_3\text{OH}$  beams in black contours. The *right panels* show the corresponding deprojected and azimuthally averaged radial profiles. Shaded regions denote the  $1\sigma$  uncertainty levels. The dotted line indicates the emission outer radius, that is, the radius containing 90% of the total integrated flux. The corresponding  $1\sigma$  uncertainty is calculated from the  $1\sigma$  uncertainty on the 90% flux measurement (horizontal blue line). The gray bars (lower left corners) represent the major axis of the restoring beam and the orange triangles (top left corners) mark the snowline location (42 AU) inferred by Cieza et al. (2016) from the continuum opacity.

The  $\text{CH}_3\text{OH}$  channel maps (not shown) display the the same butterfly pattern as  $\text{C}^{18}\text{O}$ , typical for a Keplerian rotating disk (Cieza et al. 2016). The kinematics can be more clearly visualized using moment maps. **Figure 7.2** (left panels) shows the moment zero (integrated intensity) maps for blue- and redshifted emission of the different  $\text{CH}_3\text{OH}$  transitions overlaid on the 1st moment (intensity-weighted mean velocity) map of  $\text{C}^{18}\text{O}$ . These moment maps are constructed using a Keplerian mask to enhance the signal-to-noise, that is, only those pixels that are expected to emit for a Keplerian rotating disk are included (see e.g., Salinas et al. 2017; Loomis et al. 2018). The  $\text{C}^{18}\text{O}$  1st moment map shows a clear velocity gradient as expected for a Keplerian rotating disk. The  $\text{CH}_3\text{OH}$  emission is more compact than the  $\text{C}^{18}\text{O}$  emission, but for all  $\text{CH}_3\text{OH}$  transitions a similar velocity gradient is observed with the blueshifted emission spatially coinciding with the blueshifted part of the  $\text{C}^{18}\text{O}$  disk and the redshifted emission with the redshifted part. The  $\text{CH}_3\text{OH}$  emission thus originates in the disk and not in the surrounding envelope or outflow.

### 7.3.2 Column density and excitation temperature

A rotational diagram for  $\text{CH}_3\text{OH}$  is presented in **Fig. 8.7**. The total flux for the two  $5_4 - 6_3$  transitions is divided by two, because the two lines have the same upper level energy and Einstein A coefficient. Fitting a linear function results in a rotation temperature of  $104 \pm 8 \text{ K}$  when the flux is extracted within a  $0.6''$  aperture, and  $T_{\text{rot}} = 92 \pm 6 \text{ K}$  for the Keplerian mask with an outer radius of 225 AU ( $0.54''$ ). The resulting disk-averaged column densities are  $8.9 \pm 1.6 \times 10^{16} \text{ cm}^{-2}$  and  $1.4 \pm 0.2 \times 10^{17} \text{ cm}^{-2}$ , respectively.

If the emission is optically thin and in LTE, the rotational temperature equals the kinetic temperature of the gas. For densities higher than  $\sim 10^8 - 10^9 \text{ cm}^{-3}$  the  $\text{CH}_3\text{OH}$  excitation temperature is similar to the kinetic temperature (see e.g., Johnstone et al. 2003; Jørgensen et al. 2016), so LTE is a valid assumption in the bulk of the disk where the density is of order  $10^9 - 10^{13} \text{ cm}^{-3}$ . The observed ratios of the integrated fluxes are consistent with optically thin emission based on a LTE calculation, although optically thick emission cannot be completely ruled out with the signal-to-noise of the

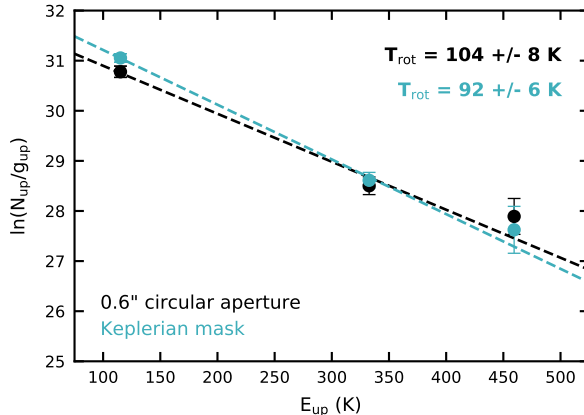


**Figure 7.3:**  $\text{CH}_3\text{OH}$  rotational diagram, constructed from the total integrated flux within a  $0.6''$  circular aperture (black) or within a Keplerian mask (blue). The dashed lines represent the best fit to the data points and the corresponding rotational temperatures are presented in the top right corner.

observations. However, upper levels with an energy of 459 K are hardly populated at temperatures  $\lesssim 30$  K, and temperatures  $\gtrsim 75$  K are required for the  $18_3 - 17_4$  flux ( $E_{\text{up}} = 459$  K) to be more than 30% of the  $16_1 - 15_2$  flux ( $E_{\text{up}} = 333$  K). These results thus suggest that we observe methanol that has desorbed thermally.

A first estimate of the  $\text{CH}_3\text{OH}$  abundance can be made by comparing the  $\text{CH}_3\text{OH}$  and  $\text{C}^{18}\text{O}$  column densities. Using the total flux within a  $0.6''$  aperture, the  $\text{C}^{18}\text{O}$  column density is  $\sim 4 \times 10^{16} \text{ cm}^{-2}$ . Assuming a standard interstellar medium (ISM)  $^{16}\text{O}/^{18}\text{O}$  ratio of 560 (Wilson & Rood 1994) and a CO abundance of  $10^{-4}$  with respect to  $\text{H}_2$ , we then derive a  $\text{CH}_3\text{OH}$  abundance of  $\sim 4 \times 10^{-7}$  with respect to  $\text{H}_2$ . This is consistent with observed  $\text{CH}_3\text{OH}$  ice abundances of  $\sim 10^{-6} - 10^{-5}$  (Boogert et al. 2015), but not with the gas-phase abundance of  $\sim 10^{-12} - 10^{-11}$  required to explain the TW Hya observations of non-thermally desorbed  $\text{CH}_3\text{OH}$  (Walsh et al. 2016).

### 7.3.3 Methanol outer radius

The radial intensity profiles for  $\text{C}^{18}\text{O}$  and  $\text{CH}_3\text{OH}$  are calculated from the moment zero maps and shown in **Figure 7.2**. An inclination of  $38^\circ$  and a position angle of  $32^\circ$  east of north (Cieza et al. 2016) are used for deprojection and azimuthally averaging. All transitions, except the  $16_1 - 15_2$   $\text{CH}_3\text{OH}$  transition, peak off source. This is likely due to the dust being optically thick in the inner  $\sim 40$  AU (Cieza et al. 2016). The  $\text{C}^{18}\text{O}$  peak is shifted further outward compared to the  $\text{CH}_3\text{OH}$  peaks due to the larger beam for  $\text{C}^{18}\text{O}$  and possibly optical depth effects.

We derive outer radii for the emission using a curve-of-growth method (e.g., Tripathi et al. 2017; Ansdell et al. 2018), in which the flux is measured within successively larger photometric apertures until the measured flux is 90% of the total flux. The same elliptical apertures are used as for the radial intensity profiles. The resulting outer radii ( $R_{\text{out}}$ ) are listed in **Table 7.1** and indicated in **Fig. 7.2** (right panels). The  $\text{CH}_3\text{OH}$  outer radii range between  $\sim 117$  and  $\sim 142$  AU for the different transitions, with the outer radius decreasing with upper level energy. The  $\text{CH}_3\text{OH}$  outer radii are  $\sim 2.5 - 3.0 \times$

smaller than the  $\text{C}^{18}\text{O}$  outer radius of  $\sim 361$  AU. The largest angular scale (LAS) is  $\sim 4''$  ( $\sim 1650$  AU) for the  $\text{C}^{18}\text{O}$  observations and  $\sim 1.5''$  ( $\sim 600$  AU) for the  $\text{CH}_3\text{OH}$  observations.

## 7.4 Discussion

### 7.4.1 Location of the water snowline

The distribution of  $\text{CH}_3\text{OH}$ , and hence the relationship between its emission and the water snowline, depends on the physical structure of the disk, as illustrated in **Fig. 7.4**.  $\text{CH}_3\text{OH}$  is present in the gas phase where the temperature exceeds the thermal desorption temperature of  $\sim 100$  K, and where there is a sufficiently large column of material to shield the UV radiation and prevent photodissociation ( $A_V \geq 3$ ). In the surface layers, the photodissociation timescale is tens of years (Heays et al. 2017), comparable to the outburst duration (10-100 years). This means that the radial extent of the methanol layer higher up in the disk beyond the midplane water snowline is set by the intercept of the snow surface and the  $A_V = 3$  contour. In addition, the magnitude of the  $\text{CH}_3\text{OH}$  column density drop across the water snowline depends on the height of the snow surface; the higher up in the disk the larger the drop. Whether the emission then traces this column density profile depends on the optical depth of both the  $\text{CH}_3\text{OH}$  as well as the dust.

Due to this interplay of several parameters, a detailed physical model of the disk is required to derive the water snowline location from methanol emission. It may thus be possible to see  $\text{CH}_3\text{OH}$  emission out to  $\sim 120 - 140$  AU while the snowline is around 40 AU. This would require for example a water snow surface close to the midplane, and/or optically thick methanol emission (**Fig. 7.4**, left panel). The vertical temperature structure is strongly dependent on the dust distribution and settling of the large grains can result in a steep vertical temperature profile with the snow surface closer to the midplane than in the case of less grain settling (e.g., Facchini et al. 2017). However, especially if the emission is optically thin, the bulk of the methanol emission is more likely to originate inside the water snowline (**Fig. 7.4**, right panel), since the  $\text{CH}_3\text{OH}$  column density can drop  $\sim 3$  orders of magnitude crossing the snowline assuming a constant abundance for the gas-phase  $\text{CH}_3\text{OH}$  (see e.g., the simple model for the CO snowline in Qi et al. 2013b). Assuming a step function for the column density, this would mean that the snowline in V883 Ori can be as far out as  $\sim 100 - 125$  AU, taking into account the 40 AU beam by deconvolving the radial profiles.

Non-thermal desorption processes are not expected to influence the relationship between  $\text{CH}_3\text{OH}$  and the water snowline. Such processes have been invoked to explain the  $\text{CH}_3\text{OH}$  emission in TW Hya (Walsh et al. 2016), but this required gas-phase  $\text{CH}_3\text{OH}$  outside the CO snowline ( $T \lesssim 20$  K) at an abundance of  $\sim 10^{-12} - 10^{-11}$ , several orders of magnitude lower than observed here and expected from ice abundances (Sect. 7.3.2).

Besides detailed modeling, observations of other molecular tracers could put better constraints on the water snowline location.  $\text{H}^{13}\text{CO}^+$  has shown to be a promising tracer in protostellar envelopes (van 't Hoff et al. 2018a, **Chapter 5**; van 't Hoff et al. in prep., **Chapter 6**), because the main destroyer of  $\text{HCO}^+$  is gas-phase water.

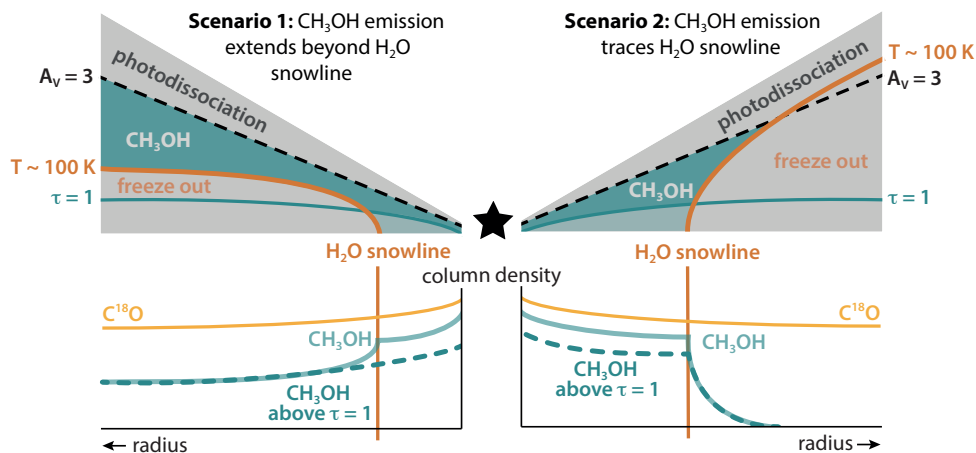


**Figure 7.4:** Illustration showing two possible scenarios for the distribution of  $\text{CH}_3\text{OH}$  with respect to the water snowline (*top*), and the corresponding column density profiles (*bottom*). Distinguishing between the scenarios requires a detailed physical model of the V883 Ori disk. The region where  $\text{CH}_3\text{OH}$  is present in the gas phase is highlighted in blue. If the  $\text{CH}_3\text{OH}$  emission is optically thick, only molecules above the  $\tau = 1$  surface (blue curve) are observed. The location of the  $\tau = 1$  surface depends on both the disk structure and the  $\text{CH}_3\text{OH}$  transition. The corresponding column density traced in the optically thick case is shown with a dashed line, while the solid line represents the total  $\text{CH}_3\text{OH}$  column. The orange curve indicates the water snow surface at  $\sim 100$  K, and the vertical orange line the corresponding midplane water snowline.  $\text{CH}_3\text{OH}$  desorbs at a similar temperature as water. The dashed black line marks the  $A_V = 3$  contour above which  $\text{CH}_3\text{OH}$  is photodissociated. The  $\text{C}^{18}\text{O}$  column density profile is shown in yellow.

## 7.4.2 Ice composition of planet forming material

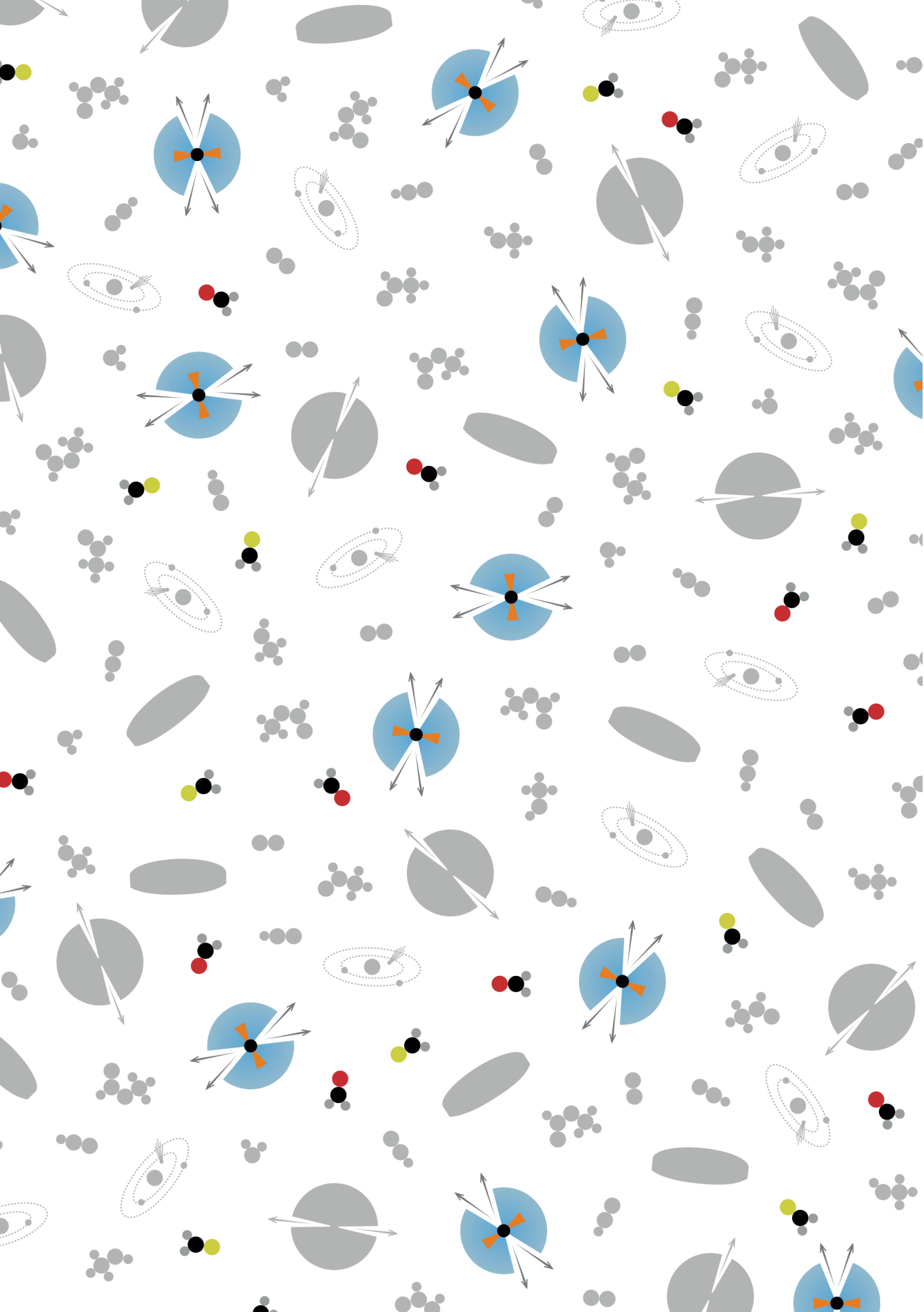
One of the key questions in planet formation is whether planetary systems inherit their chemical composition from the natal cloud or whether the material is significantly processed en route to the disk. Observations of many complex molecules, including methanol, around young protostars at solar system scales (e.g., Jørgensen et al. 2016) and in comets (e.g., Mumma & Charnley 2011; Le Roy et al. 2015) show that a large complexity is present during both the early as well as the final stages of planet formation. The chemical complexity in protoplanetary disks, however, is hard to probe. Due to the low temperatures ( $< 100$  K), complex molecules are frozen out onto dust grains at radii larger than a few AU, and ices can only be observed through infrared absorption in edge-on systems. Although alternative desorption processes may get these molecules into the gas phase, as has been shown for water (Hogerheijde et al. 2011), so far only  $\text{CH}_3\text{OH}$  and  $\text{CH}_3\text{CN}$  have been observed in disks (Öberg et al. 2015a; Walsh et al. 2016; Bergner et al. 2018; Loomis et al. 2018). Moreover, as it is unclear which processes operate for which species and what the efficiencies are, the observed gas composition cannot directly be linked to the ice composition of planet forming bodies.

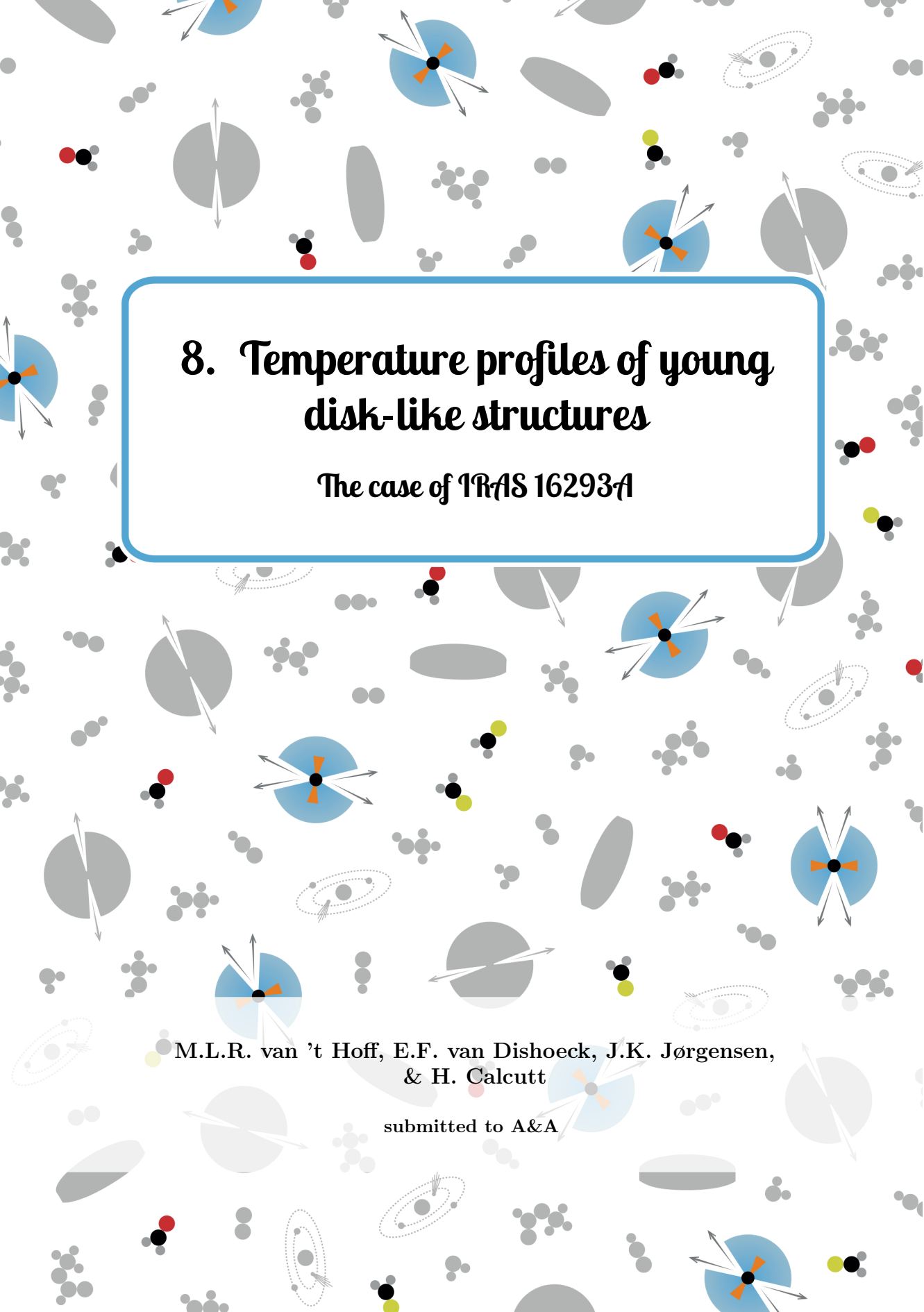
The results presented here show that complex molecules can thermally desorb in disks around young stars that have recently undergone an accretion burst. Moreover,

their emission extends out to more than 100 AU around V883 Ori and is readily detected and spatially resolved with only one minute of integration with ALMA. V883 Ori is the longest-lasting known outburst and one of, if not the, most luminous. This makes it an archetype for understanding disk chemistry in fainter outbursts. It also provides a look at how younger outbursts may evolve over the century following their outbursts. Young disks like V883 Ori thus provide the unique opportunity to study the chemical complexity at the onset of planet formation.

### **Acknowledgements**

We thank the referee for helpful comments. Astrochemistry in Leiden is supported by NOVA, KNAW and EU A-ERC grant 291141 CHEMPLAN. M.L.R.H. acknowledges support from a Huygens fellowship from Leiden University. J.J.T. acknowledges support from the Homer L. Dodge Endowed Chair at the University of Oklahoma and NWO grant 639.041.439. This paper makes use of the following ALMA data: ADS/JAO.ALMA#2013.1.00710.S, and ADS/JAO.ALMA#2015.1.00041.S. ALMA is a partnership of ESO (representing its member states), NSF (USA) and NINS (Japan), together with NRC (Canada), MOST and ASIAA (Taiwan), and KASI (Republic of Korea), in cooperation with the Republic of Chile. The Joint ALMA Observatory is operated by ESO, AUI/NRAO and NAOJ.





# 8. Temperature profiles of young disk-like structures

The case of IRAS 16293A

M.L.R. van 't Hoff, E.F. van Dishoeck, J.K. Jørgensen,  
& H. Calcutt

submitted to A&A





## Abstract

**Context.** Temperature is a crucial parameter in circumstellar disk evolution and planet formation, because it governs the resistivity of the gas to gravitational instability and sets the chemical composition of the planet-forming material.

**Aims.** We set out to determine the gas temperature of the young disk-like structure around the Class 0 protostar IRAS 16293–2422A.

**Methods.** We use Atacama Large Millimeter/submillimeter Array (ALMA) observations of multiple  $\text{H}_2\text{CS}$   $J = 7 - 6$  and  $J = 10 - 9$  lines from the Protostellar Interferometric Line Survey (PILS) to create a temperature map for the inner  $\sim 200$  AU of the disk-like structure. This molecule is a particularly useful temperature probe because transitions between energy levels with different  $K_a$  quantum numbers operate only through collisions.

**Results.** Based on the  $\text{H}_2\text{CS}$  line ratios, the temperature is between  $\sim 100$ – $175$  K in the inner  $\sim 150$  AU, and drops to  $\sim 75$  K at  $\sim 200$  AU. At the current resolution ( $0.5'' \sim 70$  AU), no jump is seen in the temperature at the disk-envelope interface.

**Conclusions.** The temperature structure derived from  $\text{H}_2\text{CS}$  is consistent with envelope temperature profiles that constrain the temperature from 1000 AU scales down to  $\sim 100$  AU, but does not follow the temperature rise seen in these profiles at smaller radii. Higher angular resolution observations of optically thin temperature tracers are needed to establish whether cooling by gas-phase water and/or the presence of a putative disk influences the gas temperature at  $\lesssim 100$  AU scales. The temperature in IRAS 16293A is higher than in the embedded Class 0/I disk L1527, providing observational evidence for cooling of circumstellar material in the embedded phase.

## 8.1 Introduction

Disks form around young stars due to conservation of angular momentum during the gravitational collapse of a dense core (Cassen & Moosman 1981) and many disks have been reported around T Tauri and Herbig stars (Class II objects, e.g., Andrews & Williams 2005; Ansdell et al. 2016). Disk-like structures are also observed in continuum emission toward embedded protostars (Class 0 and II, e.g., Jørgensen et al. 2009; Tobin et al. 2016b), but Keplerian rotation has been established for only a handful of the youngest Class 0 sources (Tobin et al. 2012b; Murillo et al. 2013; Lindberg et al. 2014; Codella et al. 2014; Yen et al. 2017). The formation of rotationally supported disks thus remain poorly constrained (see e.g., Li et al. 2014, for a review), as well as their physical and chemical structure. However, it is now becoming clear that planet formation already starts in these young disks. The mass of mature protoplanetary disks seems too low to form the planetary systems that we observe (e.g., Ansdell et al. 2016; Manara et al. 2018), while younger disks are more massive (Tychoniec et al. 2018; Williams et al. 2019). This suggests that by the Class II stage, material has grown to larger bodies that can not be observed at (sub-)mm wavelengths. The first steps of grain growth have indeed been observed in disks that have not yet fully emerged from their envelope (Kwon et al. 2009; Jørgensen et al. 2009; Pagani et al. 2010; Foster et al. 2013; Miotello et al. 2014; Harsono et al. 2018). Young embedded disks thus provide the initial conditions for planet formation.

An important unknown for young disks is the temperature structure because this governs whether they are gravitationally unstable and thus capable of forming planets through gravitational instabilities (e.g., Boss 1997; Boley 2009) or prone to luminosity outbursts (Vorobyov 2009). In addition, knowledge of temperature is required to derive disk masses, and thus the amount of material available for planet formation, from continuum observations. Finally, the temperature sets the chemical composition of the planet-forming material, for example, through the sequential freeze-out of volatiles as the temperature decreases at larger distances from the central star (e.g., Öberg et al. 2011).

The radial onset of CO freeze-out, the CO snowline, has been located in several protoplanetary disks, revealing that these disks have a large reservoir of cold ( $\lesssim 25$  K) gas with CO freeze-out starting at a few tens to  $\sim 100$  AU from the star (Qi et al. 2013b, 2015; Öberg et al. 2015a; Dutrey et al. 2017). In contrast to these mature disks, the young embedded disk in L1527 shows no signs of CO freeze-out (van 't Hoff et al. 2018b) in agreement with model predictions (Harsono et al. 2015). But whether all young disks are warm and if so, when they start to cool, remain open questions. Moreover, while mature disks can be described with a power law midplane temperature profile, this is not necessarily the case for embedded disks as material may be heated in shocks at the disk-envelope interface (centrifugal barrier; e.g., Sakai et al. 2014b). Here, we study the gas temperature of the young disk-like structure around one component of the Class 0 protostellar system IRAS 16293–2422.

IRAS 16293–2422 (hereafter IRAS 16293) is a well-studied deeply embedded protostellar binary in the L1689 region in  $\rho$  Ophiuchus ( $d \sim 140$  pc; Dzib et al. 2018). The separation between the two components, often referred to as IRAS 16293A and IRAS 16293B, is  $\sim 5.1''$  ( $\sim 715$  AU; Wootten 1989; Mundy et al. 1992; Looney et al. 2000; Chandler et al. 2005; Pech et al. 2010; Hernández-Gómez et al. 2019) and both protostars show compact millimeter continuum emission on 100 AU scales (Looney

et al. 2000; Schöier et al. 2004). IRAS 16293A has a velocity gradient in the NE-SW direction that could be attributed to a rotating disk viewed edge-on, while rotating motion is hardly detected toward source B, suggesting a near face-on orientation (Pineda et al. 2012; Favre et al. 2014; Oya et al. 2016). The protostellar masses are estimated to be  $M_A \sim 1M_\odot$  and  $M_B \sim 0.1M_\odot$  (Bottinelli et al. 2004; Caux et al. 2011), but two continuum sources ( $\sim 50$  AU separation) have been detected toward IRAS 16293A at cm and mm wavelengths, suggesting that IRAS 16293A itself may be a binary as well (Wootten 1989; Chandler et al. 2005; Pech et al. 2010).

Existing temperature structures for IRAS 16293 are based on modeling of continuum emission (e.g., Schöier et al. 2002) and spatially unresolved observations of water and oxygen lines with the Infrared Space Observatory (ISO), assuming an infalling envelope around a single protostar (e.g., Ceccarelli et al. 2000; Crimier et al. 2010). The first detailed 3D modeling of the continuum,  $^{13}\text{CO}$  and  $\text{C}^{18}\text{O}$  emission, including two radiation sources ( $\sim 18 L_\odot$  for source A and  $\sim 3 L_\odot$  for source B), was presented by Jacobsen et al. (2018). All these temperature profiles are consistent with water ice desorption ( $\sim 100$  K) at  $\sim 100$ – $150$  AU.

IRAS 16293 was the first low-mass protostar for which complex organics were detected (van Dishoeck et al. 1995; Cazaux et al. 2003). The ALMA Protostellar Interferometric Line Survey (PILS; an unbiased spectral survey between 329 and 363 GHz at  $0.5''$  resolution presented by Jørgensen et al. 2016) fully revealed the chemical richness of this source with approximately one line detected per  $3 \text{ km s}^{-1}$ . The large frequency range covered makes the PILS data also very well-suited to study the temperature structure through ratios of line emission from different transitions within one molecule. Particularly good tracers of temperature are  $\text{H}_2\text{CO}$  and  $\text{H}_2\text{CS}$  (e.g., Mangum & Wootten 1993; van Dishoeck et al. 1993, 1995) for which multiple lines are covered by the PILS survey (Persson et al. 2018).

$\text{H}_2\text{CO}$  and  $\text{H}_2\text{CS}$  are slightly asymmetric rotor molecules and have their energy levels designated by the quantum numbers  $J$ ,  $K_a$  and  $K_c$ . Since transitions between energy levels with different  $K_a$  values operate only through collisional excitation, line ratios involving different  $K_a$  ladders are good tracers of the kinetic temperature (e.g., Mangum & Wootten 1993; van Dishoeck et al. 1993, 1995). Moreover, transitions from different  $K_a$  levels connecting the same  $J$  levels are closely spaced in frequency such that they can be observed simultaneously. Therefore, line ratios from  $K_a$  transitions within the same  $\Delta J$  transition can provide a measure of the kinetic temperature unaffected by relative pointing uncertainties, beam-size differences and absolute calibration uncertainties.

In this paper we focus on  $\text{H}_2\text{CS}$  to derive a temperature profile for the disk-like structure around IRAS 16293A, because too few unblended lines were available for  $\text{H}_2\text{CO}$  and  $\text{H}_2^{13}\text{CO}$ , and the  $\text{H}_2\text{CO}$  and  $\text{D}_2\text{CO}$  lines are optically thick. The observations are briefly described in **Sect. 8.2**. In **Sect. 8.3**, we present temperature maps based on  $\text{H}_2\text{CS}$  line ratios and rotation diagrams, showing that the temperature remains between  $\sim 100$  and  $\sim 175$  K out to  $\sim 150$  AU, consistent with envelope temperature profiles, but flattens in the inner  $\sim 100$  AU. At the current spatial resolution of the data, no jump in temperature is seen at the disk-envelope interface. This temperature profile is further discussed in **Sect. 8.4** and the conclusions are summarized in **Sect. 8.5**.

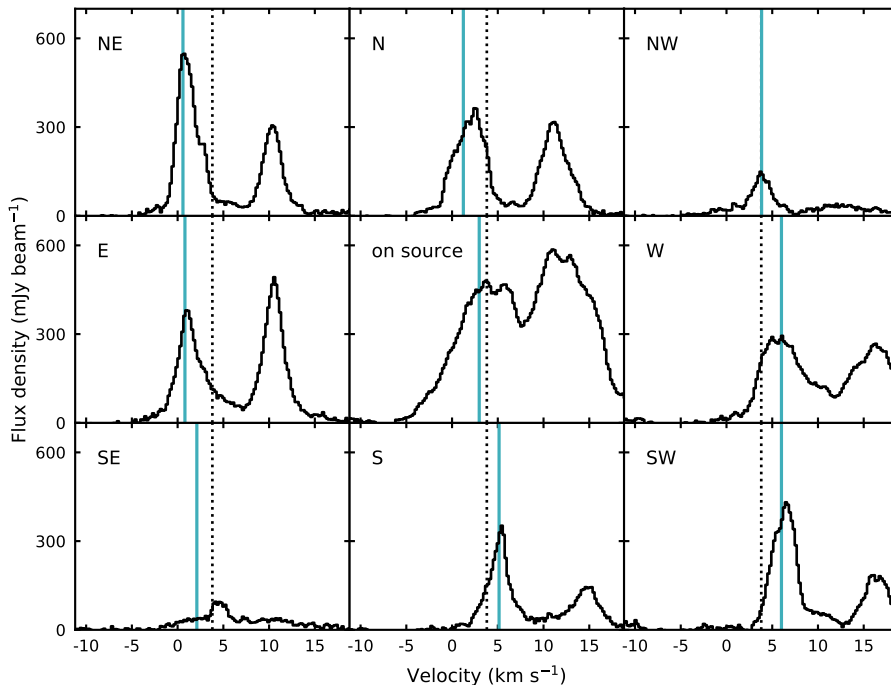


**Figure 8.1:** Spectra of the  $\text{H}_2\text{CS } 10_{0,10} - 9_{0,9}$  line at nine positions toward IRAS 16293A illustrating the variation in line blending across the source. The *central panel* shows the spectrum in the central pixel (continuum peak), the other spectra are taken at a beam offset ( $0.5''$ ) in the different directions as denoted in the top left corner of each panel. The vertical dotted line marks the system velocity of  $3.8 \text{ km s}^{-1}$ , and the vertical blue solid line indicates the peak velocity from the  $\text{CH}_3\text{OH}$  line used to isolate the target lines (in this case  $\text{H}_2\text{CS } 10_{0,10} - 9_{0,9}$ ).

## 8.2 Observations

The Protostellar Interferometric Line Survey (PILS) is an unbiased spectral survey of the low-mass protobinary IRAS 16293 with the Atacama Large Millimeter/submillimeter Array (ALMA) covering frequencies between 329.147 and 362.896 GHz in Band 7 (project-id: 2013.1.00278.S). Multiple lines from  $\text{H}_2\text{CO}$ ,  $\text{H}_2\text{CO}$  isotopologues and  $\text{H}_2\text{CS}$  fall within this spectral range.  $\Delta J$  transitions with multiple  $K_a$  transitions available are listed in **Table 8.1.1**. The transition frequencies and other line data were taken from the CDMS database (Müller et al. 2001, 2005). The  $\text{H}_2\text{CO}$  and entries are based on Bocquet et al. (1996), Cornet & Winnewisser (1980), Brünken et al. (2003), and Müller & Lewen (2017), and the  $\text{H}_2^{13}\text{CO}$  entries are taken from Müller et al. (2000). Entries of the deuterated isotopologues are based on Dangoisse et al. (1978), Bocquet et al. (1999), and Zakharenko et al. (2015).  $\text{H}_2\text{CS}$  data are provided by Fabricant et al. (1977), Maeda et al. (2008), and Müller et al. (2019).

The data have a spectral resolution of  $0.2 \text{ km s}^{-1}$  (244 kHz), a restoring beam of  $0.5''$  ( $\sim 70 \text{ AU}$ ), and a sensitivity of  $7\text{--}10 \text{ mJy beam}^{-1} \text{ channel}^{-1}$ , or  $\sim 5 \text{ mJy beam}^{-1} \text{ km s}^{-1}$  across the entire frequency range. The phase center is located between the two continuum sources at  $\alpha(\text{J2000}) = 16^{\text{h}}32^{\text{m}}22.72^{\text{s}}$ ;  $\delta(\text{J2000}) = -24^{\circ}28'34.3''$ . In this

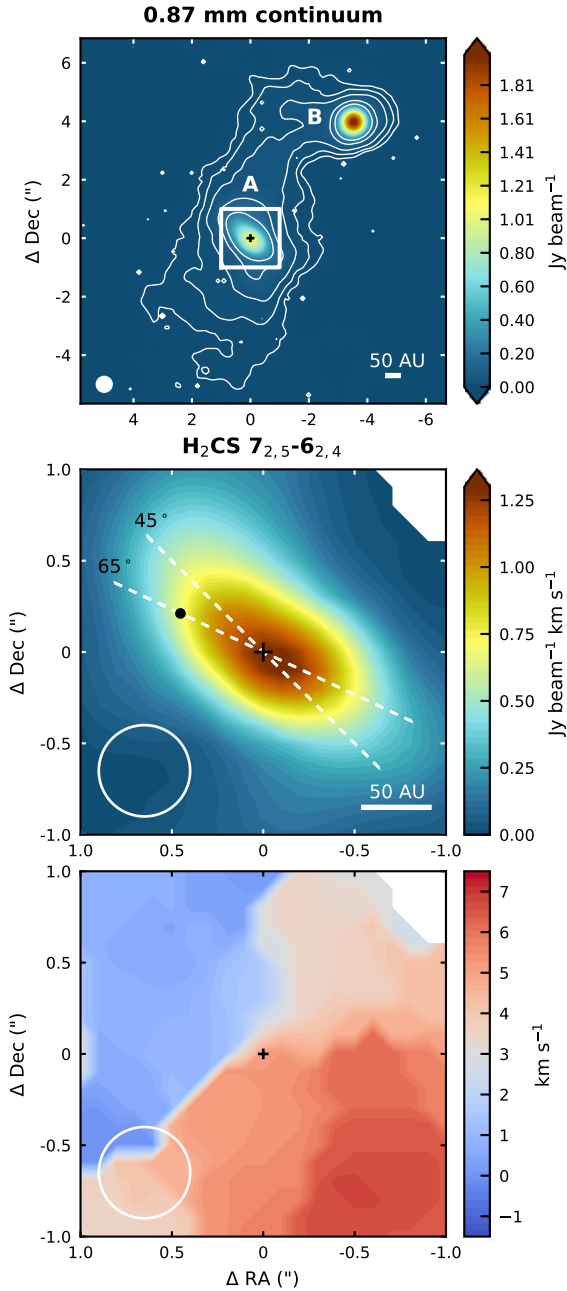


**Figure 8.2:** Continuum image of IRAS 16293 at 0.87 mm (*top panel*) with contour levels at 0.5%, 1%, 2%, 5% and 10% of the peak flux. The white box marks the region around the A source for which the velocity-corrected integrated emission (VINE) map of the H<sub>2</sub>CS 7<sub>2,5</sub> – 6<sub>2,4</sub> line at 240.549 GHz ( $E_{\text{up}} = 99$  K) is shown in the *middle panel* and the peak velocity at each position in the *bottom panel*. The continuum peak position of IRAS 16293A is marked with a cross in all panels and the beam is depicted in the lower left corners. The white lines in the *middle panel* indicate the position angle of the major axis of the disk-like structure found by Oya et al. (2016) (65°) and our by-eye best matching position angle of 45°. The black circle marks the position where the spectra in **Fig. 8.3** are extracted.

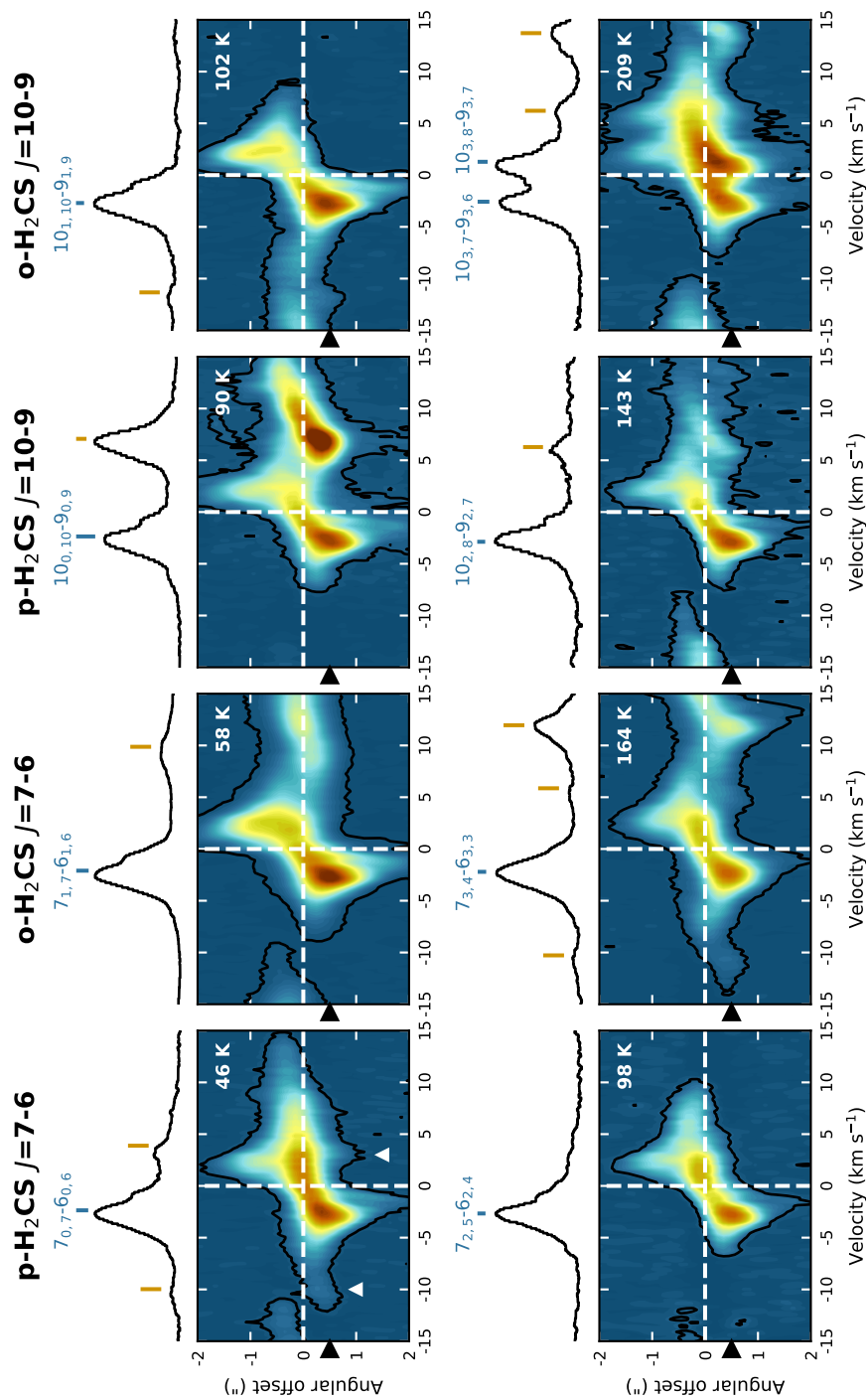


**Figure 8.3:** Position-velocity diagrams of the H<sub>2</sub>CS lines along the major axis (PA = 65°) of the disk-like structure (positive angular offsets denote the northeast direction, i.e., blueshifted emission, negative offsets denote the southwest direction, i.e., redshifted emission). The intensity (color) scale is normalized to the brightest line in each panel. The black contour denotes the 3σ emission. The dashed white lines mark the source position and systemic velocity of 3.8 km s<sup>-1</sup> (shifted to 0 km s<sup>-1</sup>). **Figure and caption continue on next page.**

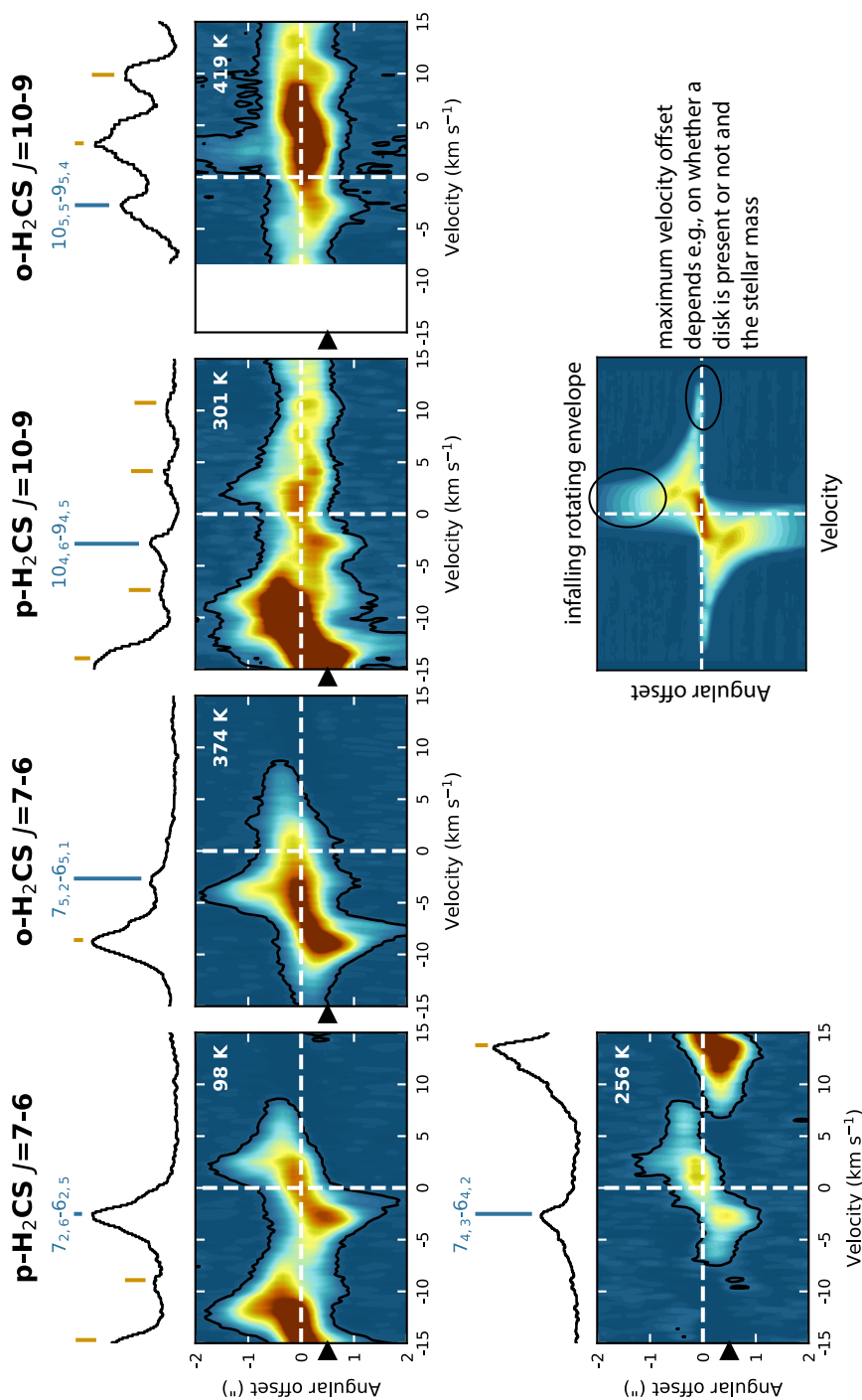


**Figure 8.3 continued:** The upper level energy is denoted in the top right corner of each panel. The spectra at  $\sim 0.5''$  northeast of the source (indicated by black triangles left of the vertical axes) are shown on top of the pv-diagram panels. The H<sub>2</sub>CS lines are identified by a vertical blue line, other lines by vertical orange lines. The white triangles in the top left panel highlight blending of the 7<sub>0,7</sub> – 6<sub>0,6</sub> line. For reference, the bottom right panel shows the pv-diagram for a thin disk model with keplerian disk and infalling rotating envelope.



work we focus on the A source ( $\alpha(\text{J2000}) = 16^{\text{h}}32^{\text{m}}22.873^{\text{s}}$ ;  $\delta(\text{J2000}) = -24^{\circ}28'36.54''$ ). A detailed description of the data reduction and continuum subtraction can be found in Jørgensen et al. (2016).

The PILS program also contains eight selected windows in Band 6 ( $\sim 230$  GHz) at the same angular resolution as the Band 7 data ( $0.5''$ ; project-id: 2012.1.00712.S). These data have a spectral resolution of  $0.15 \text{ km s}^{-1}$  (122 kHz) and a sensitivity of  $\sim 4 \text{ mJy beam}^{-1} \text{ channel}^{-1}$ , or  $\sim 1.5 \text{ mJy beam}^{-1} \text{ km s}^{-1}$ . The data reduction proceeded in the same manner as the Band 7 data (Jørgensen et al. 2016). Several  $\text{H}_2\text{CS } J_{K_a K_c} = 7_{xx} - 6_{xx}$  transitions are covered by this spectral setup (see **Table 8.1.1**).

IRAS 16293 was also observed at  $0.5''$  resolution by program 2016.1.01150.S (PI: Taquet). This dataset has a spectral resolution of  $0.15 \text{ km s}^{-1}$  (122 kHz) and a sensitivity of  $\sim 1.3 \text{ mJy beam}^{-1} \text{ channel}^{-1}$ , or  $\sim 0.5 \text{ mJy beam}^{-1} \text{ km s}^{-1}$  and covers the  $\text{H}_2\text{CS } 7_{1,7} - 6_{1,6}$  transition (**Table 8.1.1**). The data reduction is described in Taquet et al. (2018).

## 8.3 Results

### 8.3.1 Kinematics

The incredible line-richness of IRAS 16293 (on average one line per 3.4 MHz) means that many lines are blended (e.g., Jørgensen et al. 2016). In addition, the large velocity gradient due to the near edge-on rotating structure around the A source ( $\sim 6 \text{ km s}^{-1}$ ; Pineda et al. 2012; Favre et al. 2014) results in varying line widths and hence varying degrees of blending at different positions (see **Fig. 8.1**). Therefore, we make use of the method outlined in Calcutt et al. (2018) to isolate the formaldehyde and thioformaldehyde lines: the peak velocity in each pixel is determined using a bright methanol transition ( $7_{3,5} - 6_{4,4}$  at 337.519 GHz) and this velocity map is then used to identify the target lines listed in **Appendix 8.A**.

Of the 18 formaldehyde and 15 thioformaldehyde lines, only the  $\text{H}_2\text{CO } 5_{1,5} - 4_{1,4}$ ,  $\text{H}_2^{13}\text{CO } 5_{2,4} - 4_{2,3}$ ,  $\text{H}_2^{13}\text{CO } 5_{4,1} - 4_{4,0}$ ,  $\text{D}_2\text{CO } 6_{3,4} - 5_{3,3}$  and  $\text{H}_2\text{CS } 7_{2,5} - 6_{2,4}$  lines can be fully isolated. **Figure 8.2** shows the Velocity-corrected INtegrated emission (VINE) map for  $\text{H}_2\text{CS } 7_{2,5} - 6_{2,4}$ , that is, the moment zero map but integrated over different velocities in each pixel (Calcutt et al. 2018), as well as a map of the corresponding peak velocities. The emission shows an elongated structure in the northeast-southwest direction along the velocity gradient. The  $\text{H}_2^{13}\text{CO } 5_{1,5} - 4_{1,4}$ ,  $\text{H}_2^{13}\text{CO } 5_{2,3} - 4_{2,2}$ ,  $\text{D}_2\text{CO } 6_{2,5} - 5_{2,4}$  and  $\text{H}_2\text{CS } 10_{2,9} - 9_{2,8}$  lines are severely blended ( $< 4$  MHz to another line) and excluded from the analysis (see **Table 8.1.1** for details). All other lines are blended to some degree. In most cases this means that one or both of the line wings in the central pixels ( $\sim 0.5''$  radius) overlap with the wing of another line.

An overview of the 14  $\text{H}_2\text{CS}$  lines is shown in **Fig. 8.3** in the form of position-velocity (pv) diagrams along the major axis of the disk-like structure ( $\text{PA} = 65^\circ$ ; Oya et al. 2016) and spectra extracted  $\sim 0.5''$  to the northeast of the source center (see **Fig. 8.2**). Similar pv-diagrams for  $\text{H}_2\text{CO}$ ,  $\text{H}_2^{13}\text{CO}$  and  $\text{D}_2\text{CO}$  are presented in **Appendix 8.B**. All lines show signs of rotation, that is, low velocities at large angular offsets and high velocities closer to the source center.  $\text{H}_2\text{CO}$  and  $\text{H}_2\text{CS}$  emission extends out to  $\gtrsim 2''$ , while emission from the less abundant isotopologues  $\text{H}_2^{13}\text{CO}$  and  $\text{D}_2\text{CO}$  is more compact ( $\lesssim 1''$ ), probably due to sensitivity. The emission also becomes more compact for transitions with higher upper level energies, which are expected

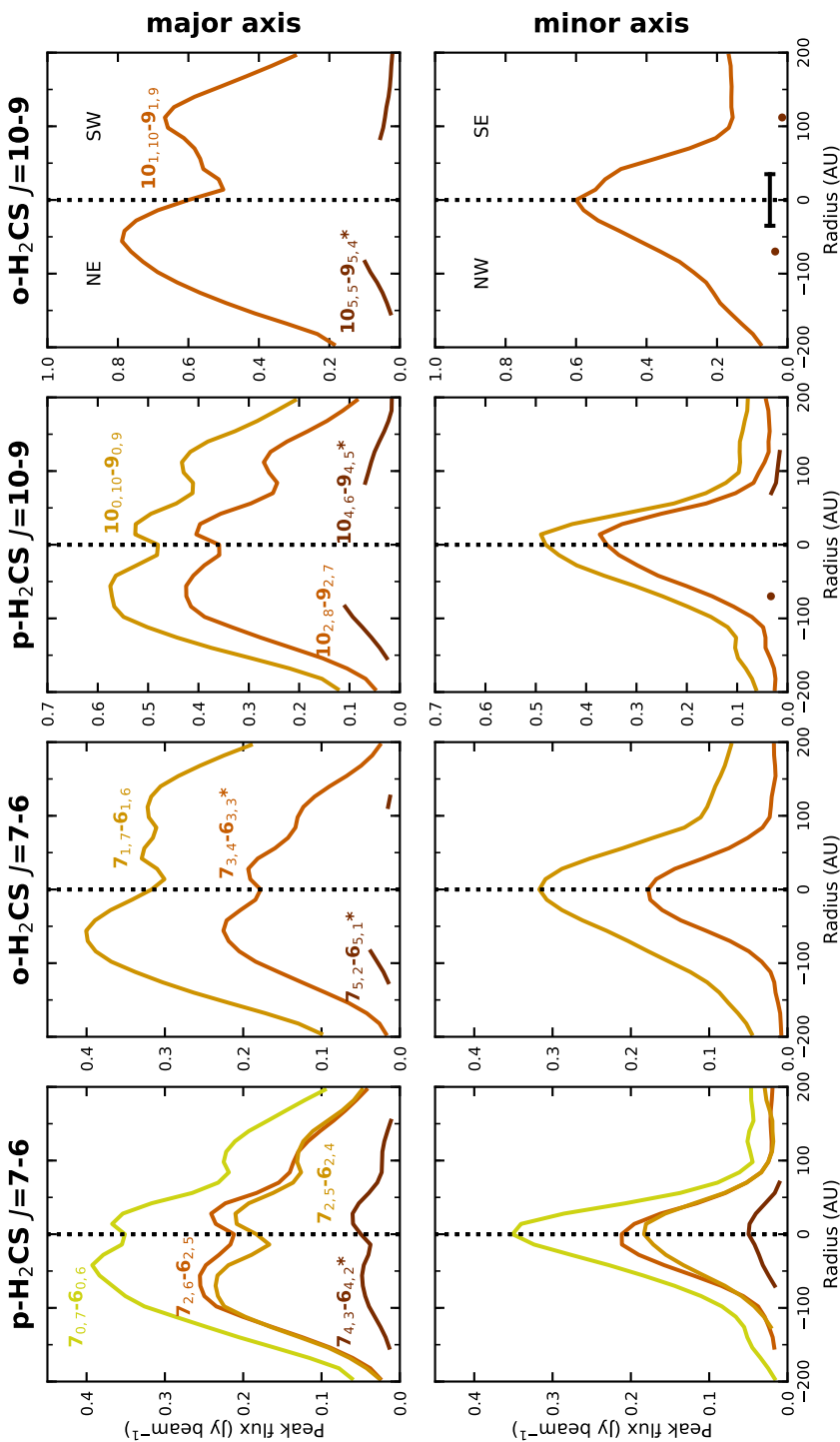


**Figure 8.4:** Radial profiles of the  $\text{H}_2\text{CS}$  peak fluxes along the major axis ( $\text{PA} = 45^\circ$ ; *top panels*) and minor axis ( $\text{PA} = 135^\circ$ ; *bottom panels*) of the disk-like structure. In each panel, transitions with higher upper level energy are plotted in darker colors. Fluxes for transitions labeled with an asterisk (\*) have been divided by 2 to account for two transitions with the same upper level energy and Einstein A coefficient at the same frequency (see Table 8.A.1). The horizontal bar in the *lower right panel* marks the beam size. The rms ranges between 2 and 8 mJy beam<sup>-1</sup>.

to trace the warmest inner region. The  $\text{H}_2\text{CO}$  lines show red-shifted absorption for velocities slightly above the systemic velocity of  $3.8 \text{ km s}^{-1}$ .

Based on large shifts in velocity from the systemic velocity (up to  $14 \text{ km s}^{-1}$ ) for the  $\text{H}_2\text{CS } 7_{0,7} - 6_{0,6}$  line, Oya et al. (2016) suggested that a Keplerian disk may be present inside the centrifugal barrier (at  $\sim 50 \text{ AU}$ ). However, careful analysis of the data shows that a weak line is present on both the blue and red side of this  $\text{H}_2\text{CS}$  line (see **Fig. 8.3**, top left panel). The large velocity gradient thus seems the result of line blending and not Keplerian rotation. This conclusion is reinforced by the velocity structure of the other  $\text{H}_2\text{CS}$  lines. The unblended  $7_{2,5} - 6_{2,4}$  line shows a maximum velocity offset of  $\sim 6 \text{ km s}^{-1}$  on the blue side, and  $\sim 10 \text{ km s}^{-1}$  on the red side. Unblended wings from the other lines show similar offsets. This is comparable to the velocity offsets presented for the  $\text{OCS}$ ,  $\text{CH}_3\text{OH}$  and  $\text{HCOOCH}_3$  lines by Oya et al. (2016), which were attributed to the infalling rotating envelope.

### 8.3.2 Peak fluxes

Most lines show some degree of blending, such that generally, in the central pixels ( $\sim 0.5''$  radius), one or both of the line wings overlap with the wing of another line. As this does not significantly influence the peak flux, we extract the peak flux per pixel in order to make spatial maps of the line ratios and hence temperature structure. Pixels with too much line blending to extract a reliable peak flux are excluded. Since the data cover only one ortho- $\text{H}_2\text{CO}$  and one para- $\text{H}_2\text{CO}$  line, the main isotopologue lines cannot be used for a temperature measurement and we exclude  $\text{H}_2\text{CO}$  from further analysis. The  $\text{D}_2\text{CO } 6_{4,2} - 5_{4,1}$  and  $6_{4,3} - 5_{4,2}$  lines, as well as the  $\text{H}_2\text{CS } 10_{3,7} - 9_{3,6}$  and  $10_{3,8} - 9_{3,7}$  lines, are located within 4 MHz of each other and are too blended to obtain individual peak fluxes (see also **Fig. 8.3** and **8.B.3**). Maps of the peak fluxes (moment 8 maps) of the remaining  $\text{H}_2^{13}\text{CO}$ ,  $\text{D}_2\text{CO}$  and  $\text{H}_2\text{CS}$  lines without severe blending are presented in **Appendix 8.C** and radial profiles for the  $\text{H}_2\text{CS}$  lines are shown in **Fig. 8.4**.

All  $\text{H}_2\text{CS}$  lines show an elongated structure with the major axis at  $\sim 45^\circ$  (**Figs. 8.2** and **8.C.1**). This is slightly different from the  $65^\circ \pm 10^\circ$  derived by Oya et al. (2016), but radial profiles along a position angle of  $45^\circ$  or  $65^\circ$  are very similar. For all lines, the emission peaks on either side of the continuum peak, as has been seen for most other species toward IRAS 16293A (see e.g., Calcutt et al. 2018; Manigand et al. 2019). This could correspond to the double peaks seen in cm continuum emission (Wootten 1989; Chandler et al. 2005; Pech et al. 2010), although those positions are slightly off (see discussion in Calcutt et al. 2018). Alternatively, they can be due to an edge-on rotating toroidal structure, as, for example, seen in synthetic CO images (Jacobsen et al. 2018). The NE peak is  $\sim 60 \text{ AU}$  offset from the continuum peak, except for the  $7_{0,7} - 6_{0,6}$  transition that peaks around  $\sim 40 \text{ AU}$  (see **Fig. 8.4**). The SW peak is around  $\sim 25 \text{ AU}$ , and is weaker than the NE peak, except for the  $7_{4,3} - 6_{4,2}$  transition. Most  $\text{H}_2\text{CS}$  lines seem to have a weaker third peak  $\sim 120 \text{ AU}$  SW off the source center. The  $\text{H}_2^{13}\text{CO}$  and  $\text{D}_2\text{CO}$  lines also show an elongated double-peaked structure, albeit more compact and without the third peak seen for  $\text{H}_2\text{CS}$  (**Fig. 8.C.2**). In addition, the northern part is more elongated perpendicular to the major axis than for the  $\text{H}_2\text{CS}$  lines.

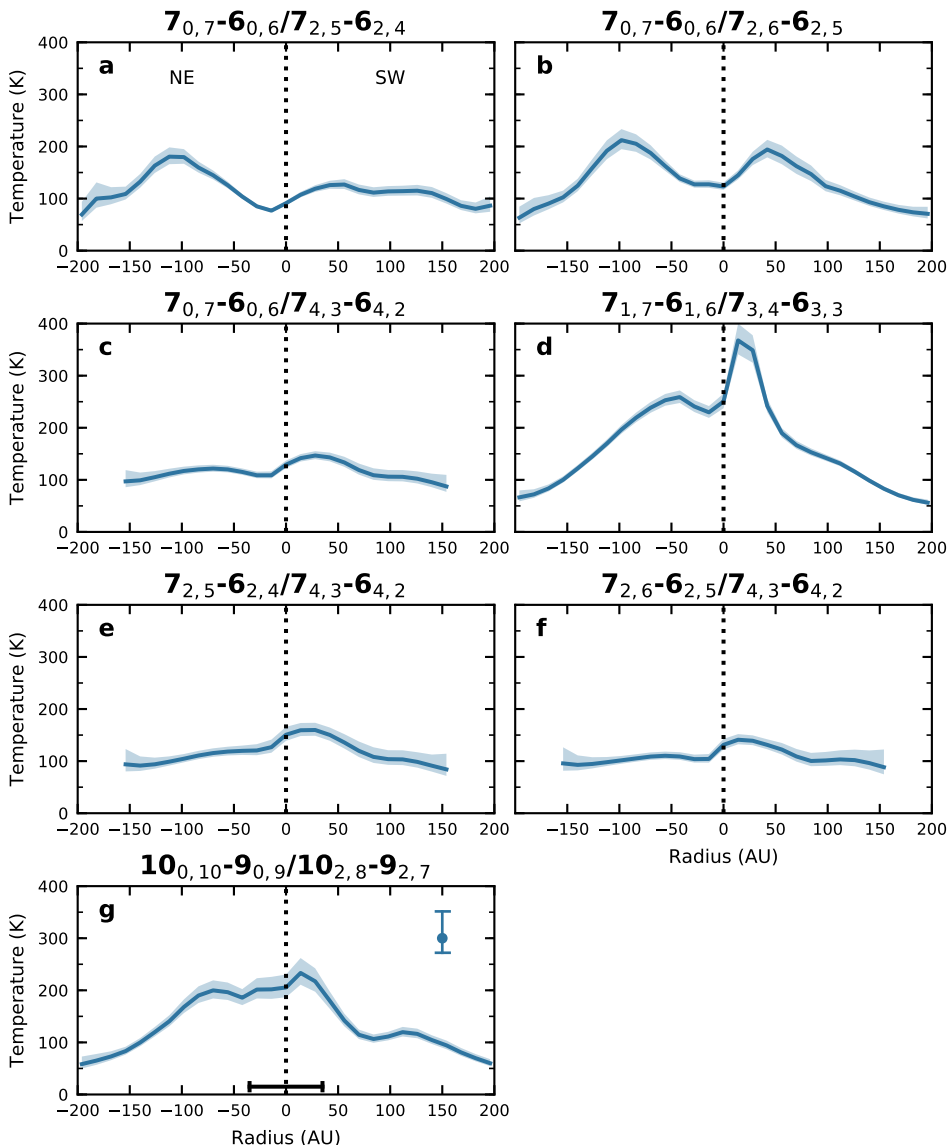


**Figure 8.5:** Radial temperature profiles derived from  $\text{H}_2\text{CS}$  line ratios (listed above the panels) along the major axis of the disk-like structure (PA =  $45^\circ$ ) using the RADEX results. The shaded area represents the  $1\sigma$  uncertainty based on the noise level of the observations. The vertical bar in the *bottom left panel* shows a  $3\sigma$  error bar representative for the inner 100 AU and the horizontal bar marks the beam size.

### 8.3.3 Temperature

Only  $\text{H}_2\text{CS}$  lines are used in the temperature analysis, for the reasons outlined below. For  $\text{H}_2^{13}\text{CO}$  there are three line ratios that probe temperature ( $5_{0,5} - 4_{0,4}/5_{2,4} - 4_{2,3}$ ,  $5_{0,5} - 4_{0,4}/5_{4,1} - 4_{4,0}$  and  $5_{2,4} - 4_{2,3}/5_{4,1} - 4_{4,0}$ ), but for the two highest energy lines, the continuum seems to be oversubtracted to varying degrees in different pixels.

Reliable peak fluxes can therefore not be obtained for these two lines and  $\text{H}_2^{13}\text{CO}$  is not used to derive the temperature structure. For  $\text{D}_2\text{CO}$  there are six suitable line ratios. However, all these ratios are near unity, suggesting that the emission is optically thick (see [Appendix 8.C](#)). Their brightness temperature is  $\sim 30$  K, much lower than expected for the inner region of an envelope, as also shown for other optically thick lines in the PILS data (e.g.,  $\text{CH}_2\text{DOH}$ ; Jørgensen et al. 2018), indicating that those lines probe colder foreground material.

The maps of the  $\text{H}_2\text{CS}$  peak fluxes are used to calculate line ratios, and these are converted into temperature maps using a grid of RADEX non-LTE radiative transfer models (van der Tak et al. 2007). The molecular data are obtained from the Leiden Atomic and Molecular Database (LAMDA; Schöier et al. 2005, which contains collisional rate coefficients for  $\text{H}_2\text{CS}$  from Wiesenfeld & Faure 2013). The line ratios as a function of temperature for different  $\text{H}_2$  densities and  $\text{H}_2\text{CS}$  column densities are shown in [Fig. 8.D.1](#). For densities  $\gtrsim 10^6\text{--}10^7\text{ cm}^{-3}$  and column densities  $\lesssim 10^{15}\text{ cm}^{-2}$  the line ratios are independent of density and column density, respectively, and thus good tracers of the temperature. For a disk-like structure, densities are expected to be  $> 10^7\text{ cm}^{-3}$ , so the exact value adopted for the density does not influence the derived temperatures and we use a value of  $10^{10}\text{ cm}^{-3}$ . Toward IRAS 16293B, a  $\text{H}_2\text{CS}$  column density of  $1.3 \times 10^{15}\text{ cm}^{-2}$  was found (Drozdovskaya et al. 2018). As will be discussed later in this section, based on the line ratios, the  $\text{H}_2\text{CS}$  column density toward IRAS 16293A cannot exceed more than a few times  $10^{15}\text{ cm}^{-2}$ . A column density of  $10^{14}\text{ cm}^{-2}$  is adopted in the temperature calculations. For only a few line ratios, using  $10^{15}\text{ cm}^{-2}$  would result in temperatures lower by less than  $\sim 10$  K. In addition to a density and column density, a line width of  $2\text{ km s}^{-1}$  is adopted to convert the observed line ratios to temperature. Error bars on the line ratios are calculated from the image rms, and converted into error bars on the temperature using the RADEX calculations (see [Fig. 8.D.1](#)). The error bars therefore depend on the sensitivity of the line ratio to the temperature and the relative uncertainty on the peak flux. Since collisional rate coefficients are not available for all observed transitions, we also performed LTE calculations.

Radial temperature profiles along the major axis of the disk-like structure ( $\text{PA} = 45^\circ$ ) are presented in [Fig. 8.5](#) for ratios with collisional rate coefficients and in [Fig. 8.E.1](#) for the remaining ratios. [Figure 8.E.2](#) shows radial temperature profiles for different position angles. For clarity, we will refer to the panels in [Fig. 8.5](#) instead of to the quantum numbers of the line ratios in the following discussion. Along the major axis, all line ratios result in temperatures between  $\sim 100$  and  $\sim 175$  K out to  $\sim 150$  AU, with temperatures dropping to  $\sim 75$  K at  $\sim 200$  AU. The non-LTE RADEX results give temperatures higher by  $\sim 20\text{--}50$  K than the LTE results (see [Fig. 8.E.1](#)), suggesting that the lines are not completely thermalized. Panels **d** and **g** show temperatures  $\gtrsim 150$  K in the inner  $\sim 100$  AU. On the other hand, panels **a** and **b** display a decrease in temperature in the inner  $\sim 100$  AU (down to  $\sim 100$  K). The other three p- $\text{H}_2\text{CS}$  ratios (panels **c**, **e** and **f**) show a rather flat temperature profile, with temperatures of  $\sim 100\text{--}150$  K throughout the inner 150 AU. The five line ratios in [Fig. 8.E.1](#) cannot be used to constrain the temperature in the inner 100 AU due to severe line blending, but the temperature between  $\sim 100\text{--}150$  AU is  $> 100$  K. Another constraint can be provided by the ratio between the different  $\Delta J$  transitions. The  $10 - 9$  lines are brighter than the  $7 - 6$  lines over the 200 AU radius studied, which means temperatures  $\gtrsim 60$  K (see [Fig. 8.D.1](#)).

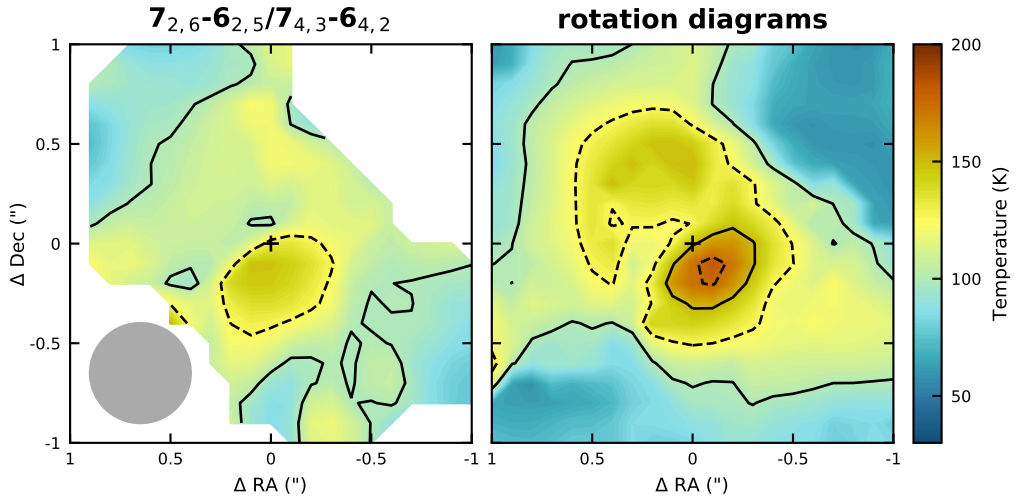


**Figure 8.6:** Temperature in a  $2'' \times 2''$  ( $280 \times 280$  AU) region around IRAS 16293A derived from the  $\text{H}_2\text{CS}$   $7_{2,6} - 6_{2,5}/7_{4,3} - 6_{4,2}$  line ratio (*left panel*), and from the rotation diagrams in each pixel (*right panel*). Solid contours indicate temperatures of 100 and 150 K and dashed contours are at 125 and 175 K. The continuum peak position is marked with a black cross and the beam is depicted in the lower left corner of the *left panel*.

The central decrease in panels **a** and **b** is not likely to be due to the continuum becoming optically thick as this is expected to effect all lines equally. Instead, it could be due to the fact that the  $7_{0,7} - 6_{0,6}$  line (which has the lowest upper level energy) peaks closer to the continuum position than the other lines, causing a central increase in the line ratio and hence decrease in the derived temperature. In addition, the temperature derived from these ratios is very sensitive to small changes in the fluxes, because the energy levels involved range from only 46 to 98 K (see **Fig. 8.D.1**). The ratio changes from 1.4 to 1.5 if the temperature drops from 200 K to 150 K, and to 1.8 at 100 K. This means that a variation of  $<10\%$  in one of the peak fluxes can change the derived temperature from 200 K to 150 K, and a 20% variation can change the temperature from 150 K to 100 K. Such variations can occur even though the transitions are present in the same dataset as can be seen from the difference between panels **a** and **b**. The  $7_{2,6} - 6_{2,5}$  and  $7_{2,5} - 6_{2,4}$  transitions have the same upper level energy and Einstein A coefficient, and should thus be equally strong. However, in the SW there is a 100 K difference in the derived temperature using either of the two lines. This variation is slightly larger than the  $3\sigma$  uncertainty based on the rms noise, and may be due to blending with a weak line.

The  $7_{4,3} - 6_{4,2}$  has a relatively high upper level energy (257 K) and therefore temperatures derived using this transition are less sensitive to flux changes. For example, as the temperature increases from 100 K to 200 K, the  $7_{0,7} - 6_{0,6}/7_{4,3} - 6_{4,2}$  ratio decreases from 11 to 4.1, and the  $7_{2,6} - 6_{2,5}/7_{4,3} - 6_{4,2}$  ratio decreases from 6.1 to 2.9. A temperature map for the  $2'' \times 2''$  region around IRAS 16293A derived from the  $7_{2,6} - 6_{2,5}/7_{4,3} - 6_{4,2}$  ratio (panel **f**) is presented in **Fig. 8.6**. This shows that the radial temperature profiles are not strongly affected by the chosen position angle.

The higher temperatures in panels **d** and **g** are likely due to optical depth effects. As can be seen from **Fig. 8.D.2**, the  $7_{1,7} - 6_{1,6}$  and  $10_{0,10} - 9_{0,9}$  transitions are among

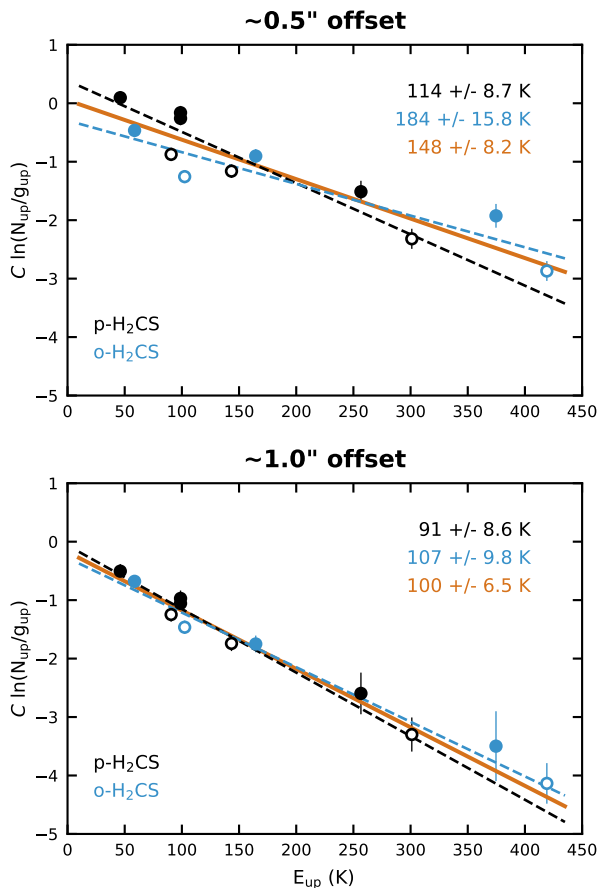


**Figure 8.7:** Rotation diagrams for the H<sub>2</sub>CS peak fluxes along the major axis (PA = 45°) of the disk like structure at 0.5'' (*top panel*) and 1.0'' (*bottom panel*) from the source center. Para transitions are shown in black and ortho transitions in blue. An ortho-to-para ratio of 2 is assumed.  $J = 7 - 6$  transitions are displayed by filled symbols and  $J = 10 - 9$  transitions by open symbols. The error bars include a 10% uncertainty. The best fit to all transitions is presented by the orange line, whereas the dashed lines show fits to only the ortho (blue) and only the para transitions (black). The corresponding rotation temperatures are listed in the top right corners.

the first transitions to become optically thick. If these transitions are optically thick while the higher energy transitions remain optically thin, the flux of the lower energy transition is relatively too low and hence the derived temperature is too high. In turn, an estimate of the H<sub>2</sub>CS column density can be made based on these results; for the  $7_{0,7} - 6_{0,6}$  transition to remain optically thin, the column density of para H<sub>2</sub>CS cannot exceed more than a few times  $10^{15}$  cm<sup>-2</sup>.

To assess whether one of the H<sub>2</sub>CS lines is affected by blending with a weak line at a similar frequency and therefore has its peak flux overestimated, rotation diagrams are made for every pixel in a 2'' × 2'' region surrounding the continuum position. Representative diagrams at 0.5'' and 1.0'' offsets are presented in **Fig. 8.7**. An ortho-to-para ratio of 2 is assumed, but varying this between 1 and 3 does not change the

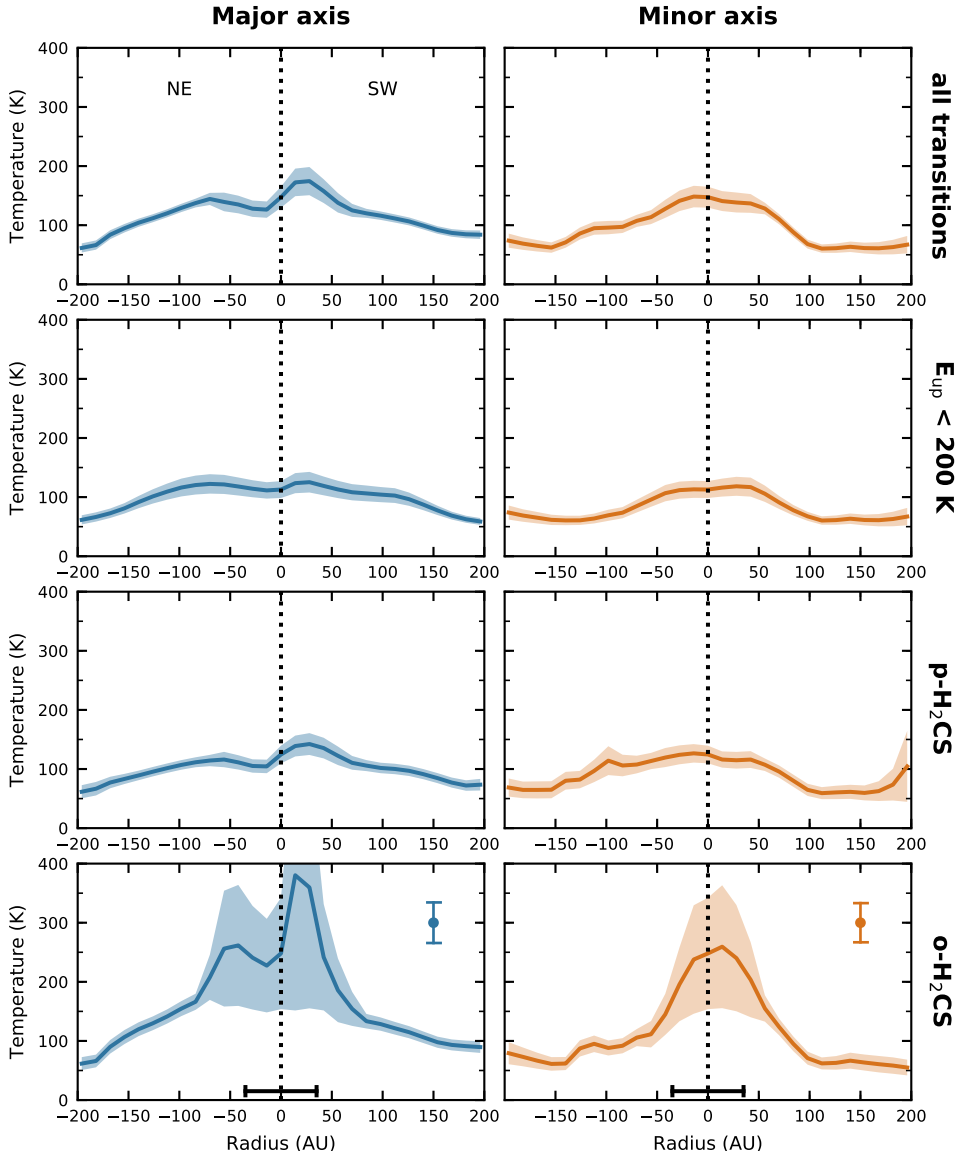


**Figure 8.8:** Radial temperature profiles derived from the rotation diagrams including all transitions (*first row*), only transitions with  $E_{\text{up}} < 200 \text{ K}$  (*second row*), only para transitions (*third row*) or only ortho transitions (*fourth row*). The *left column* shows radial profiles along the major axis of the disk-like structure ( $\text{PA} = 45^\circ$ ) and the *right column* shows profiles along the minor axis. The shaded area represents the  $1\sigma$  uncertainty. The vertical bar in the *bottom panels* shows a typical  $3\sigma$  error for the inner 100 AU and the horizontal bar marks the beam size.

derived temperature significantly ( $\lesssim 30 \text{ K}$ ). At offsets  $\gtrsim 0.8''$  all transitions follow a straight line and similar temperatures are found when using all transitions, only ortho transitions or only para transitions in the fit. At smaller angular offsets the scatter becomes larger, but no transition is found to strongly deviate from the general trend.



For the lower energy transitions ( $E_{\text{up}} < 200$  K) this scatter is at least partly because some of the transitions become optically thick.

Radial profiles based on the temperatures derived from the rotation diagrams are shown in **Fig. 8.8**. These profiles are constructed from fitting either all transitions, only transitions with  $E_{\text{up}} < 200$  K, only para transitions or only ortho transitions. The first three cases result in temperatures of  $\sim 60$  K at 200 AU rising up to  $\sim 150$  at source center. Using only the ortho transitions results in temperatures  $> 200$  K in the inner 100 AU, likely because the lower energy transitions become optically thick. The central decrease in temperature seen for the  $7_{0,7} - 6_{0,6}/7_{2,5} - 6_{2,4}$  and  $7_{0,7} - 6_{0,6}/7_{2,6} - 6_{2,5}$  ratios (panels **a** and **b** in **Fig. 8.5**) is not seen in these profiles, and may be due to the  $7_{0,7} - 6_{0,6}$  transition peaking closer in and these ratios being not sensitive to temperature, as discussed above.

## 8.4 Discussion

Based on line ratios of several  $J = 7 - 6$  and  $J = 10 - 9$   $\text{H}_2\text{CS}$  transitions, the temperature in the inner  $\sim 150$  AU of IRAS 16293A is  $\sim 100$ – $175$  K, and drops to  $\sim 75$  K at  $\sim 200$  AU. In **Fig. 8.9**, the  $\text{H}_2\text{CS}$  temperature profiles are compared to temperature profiles obtained from continuum radiative transfer modeling and from spatially unresolved  $\text{H}_2\text{O}$  observations with the ISO satellite (Ceccarelli et al. 2000; Schöier et al. 2002; Crimier et al. 2010). These latter profiles were derived assuming a spherically symmetric collapsing envelope structure around a single protostar. Recently, Jacobsen et al. (2018) performed detailed 3D radiative transfer modeling including two protostars. All previously derived temperatures show a very similar structure with a radial power law dependence of approximately  $T \propto r^{-0.7}$  in the inner few hundred AU and a temperature of 100 K around  $\sim 100$  AU. The  $\text{H}_2\text{CS}$  temperature is consistent with the envelope temperature profiles down to radii of  $\sim 100$  AU, but lacks the temperature rise at smaller radii.

Such a flattening of the temperature could be the result of efficient cooling by water molecules that are released into the gas phase at  $\sim 100$  K. However, water can also heat the gas through absorption of NIR photons from warm dust. Ceccarelli et al. (1996) studied the gas and dust temperature profile of an infalling envelope with a model that includes dynamics, chemistry, heating and cooling, and concluded that the gas and dust temperatures are generally well-coupled. For different model parameters (e.g., luminosity, mass accretion rate, stellar mass), the difference between the gas and dust temperature ranges from  $\sim 10$  K to more than a 100 K, but applying this model to IRAS 16293 (assuming a collapsing envelope around a single central source of  $27 L_{\odot}$ ) results in differences of only a few Kelvin between the gas and dust (Ceccarelli et al. 2000; Crimier et al. 2010). However, this model does not include a disk or disk-like structure. The presence of a disk may result in a lower temperatures than in the case of only an envelope, as for example shown by the models from e.g., Whitney et al. (2003), observations toward VLA 1623 (Murillo et al. 2015) and analysis of  $\text{H}_2^{18}\text{O}$  observations toward four protostars in Perseus (Persson et al. 2016). **Figure 8.9** also shows the gas temperature profile for the embedded Class 0/I disk L1527 based on optically thick  $^{13}\text{CO}$  and  $\text{C}^{18}\text{O}$  observations (van 't Hoff et al. 2018b), illustrating that the temperature in the disk is  $\sim 75$  K lower than in the IRAS 16293A disk-like structure. This is consistent with the higher accretion rate, and hence higher luminosity of IRAS 16293A ( $\sim 4 \times 10^{-6} - 5 \times 10^{-5} M_{\odot} \text{ yr}^{-1}$  and  $18 L_{\odot}$ ; Schöier et al. 2002; Jacobsen et al.

2018) compared to L1527 ( $3 \times 10^{-7} M_{\odot} \text{ yr}^{-1}$  and  $1.9\text{-}2.6 L_{\odot}$ ; Kristensen et al. 2012; Tobin et al. 2012b, 2013b).

Oya et al. (2016) also used the  $7_{0,7} - 6_{0,6}/7_{2,5} - 6_{2,4}$  and  $7_{0,7} - 6_{0,6}/7_{4,3} - 6_{4,2}$  ratios (Fig. 8.5, panels a and c) to measure the gas temperature in the envelope, disk and envelope-disk interface (centrifugal barrier). Using the flux within a  $0.5''$  region at  $0''$ ,  $0.5''$  (70 AU) and  $1.0''$  (140 AU) offsets from the continuum peak position along the disk major axis (PA =  $65^{\circ}$ ) integrated over different velocity ranges at each position, they derive temperatures between 70 and 190 K. In addition, they find the highest temperatures at the  $0.5''$  offset position and attribute these temperature increases to weak accretion shocks at the centrifugal barrier ( $\sim 50$  AU) or to directly heating of a more extended envelope in front of the centrifugal barrier. Although we find a similar temperature range for the inner  $\sim 150$  AU, we do not see temperature peaks in the  $7_{0,7} - 6_{0,6}/7_{4,3} - 6_{4,2}$  (Fig. 8.5, panel c). Peaks are visible for the  $7_{0,7} - 6_{0,6}/7_{2,5} - 6_{2,4}$  and  $7_{0,7} - 6_{0,6}/7_{2,6} - 6_{2,5}$  (Fig. 8.5, panels a and b), but this is likely due to the  $7_{0,7} - 6_{0,6}$  transition peaking slightly closer to the protostar than the other transitions in combination with the high sensitivity of these ratios to small changes in flux, as discussed in Sect. 8.3.3. Moreover, no temperature peaks are found either from the  $7_{2,5} - 6_{2,4}/7_{4,3} - 6_{4,2}$  and  $7_{2,6} - 6_{2,5}/7_{4,3} - 6_{4,2}$  ratios (Fig. 8.5, panels e and f) nor from the rotational diagrams. Additional, higher resolution observations thus seem necessary to substantiate local temperature enhancements at the centrifugal barrier.

## 8.5 Conclusions

We used  $\text{H}_2\text{CS}$  line ratios observed in the ALMA-PILS survey to study the gas temperature in the disk-like structure around the Class 0 protostar IRAS 16293A. Because of the line-richness of this source, almost all  $\text{H}_2\text{CS}$  lines are blended in their line wings. Therefore, peak fluxes extracted per pixel are used in the analysis instead of integrated fluxes. Formaldehyde is not used because the optically thick  $\text{H}_2\text{CO}$  and  $\text{D}_2\text{CO}$  lines also trace colder foreground material, and not enough unblended  $\text{H}_2^{13}\text{CO}$  transitions were available. Our conclusions can be summarized as follows:

- Strong evidence for a rotationally supported disk is still lacking: the high velocity wings of the  $\text{H}_2\text{CS}$   $7_{0,7} - 6_{0,6}$  transition are the result of blending with nearby weak lines instead of a Keplerian disk.
- The temperature is between  $\sim 100\text{--}175$  K in the inner  $\sim 150$  AU, and drops to  $\sim 75$  K at  $\sim 200$  AU. This profile is consistent with envelope temperature profiles constrained on 1000 AU scales down to scales of  $\sim 100$  AU ( $T \propto r^{-0.7}$  in the region where the dust becomes optically thick). However, the envelope profile breaks down in the inner most region that can now be probed by ALMA, because the observed temperature does not show a steep rise at radii  $\lesssim 100$  AU.
- The temperature in the disk-like structure around IRAS 16293A is  $\sim 75$  K higher than in the young Class 0/I disk L1527, on similar scales.

The flattening of the temperature profile at radii  $\lesssim 100$  AU may be the result of efficient cooling by water that has sublimated from the grains in this region. Alternatively, the presence of a disk could affect the temperature structure, by having a larger fraction

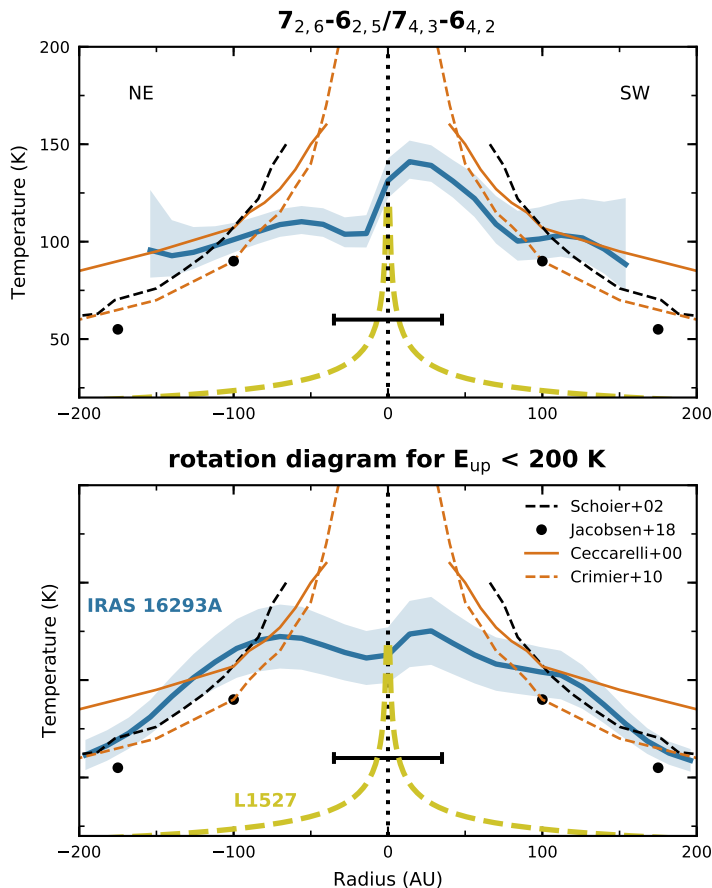


**Figure 8.9:** Radial temperature profiles for IRAS 16293A derived in this work from  $\text{H}_2\text{CS}$  transitions (blue lines) compared to dust (black lines and circles) and gas (orange lines) temperature profiles from the literature. The  $\text{H}_2\text{CS}$  temperature profile in the *top panel* is derived from the  $7_{2,6} - 6_{2,5} / 7_{4,3} - 6_{4,2}$  line ratio and the profile in the *bottom panel* is based on fits to the peak flux rotation diagrams including only transitions with  $E_{\text{up}} < 200$  K. The blue shaded area represents the  $1\sigma$  uncertainty. The dashed black line shows the IRAS 16293 dust temperature assuming an envelope around a central source of  $27 L_{\odot}$  (Schöier et al. 2002), and the black dots represent dust temperature contours for IRAS 16293A from detailed modeling including both protostars and the bridge structure (Jacobsen et al. 2018). The gas temperatures are based on  $\text{H}_2\text{O}$  observations with the ISO satellite using a model that computes the gas temperature through an envelope by solving a chemical network and equating the heating and cooling rates (Ceccarelli et al. 1996). The solid orange line shows the initial results assuming a single  $27 L_{\odot}$  protostar at 160 pc (Ceccarelli et al. 2000), the dashed orange line presents the revised results for a  $22 L_{\odot}$  protostar at 120 pc (Crimier et al. 2010). The dashed yellow line shows the midplane gas temperature for the Class 0/I disk L1527 based on optically thick  $^{13}\text{CO}$  and  $\text{C}^{18}\text{O}$  emission (van 't Hoff et al. 2018b, [Chapter 3](#)). The horizontal bar marks the beam size of the  $\text{H}_2\text{CS}$  observations.

of the mass at higher density and lower temperatures. High resolution observations of optically thin lines are required to establish the details of the temperature profile in the inner  $\sim 100$  AU.

### **Acknowledgements**

This paper makes use of the following ALMA data: ADS/JAO.ALMA#2012.1.00712.S, ADS/JAO.ALMA#2013.1.00278.S and ADS/JAO.ALMA#2016.1.01150.S. ALMA is a partnership of ESO (representing its member states), NSF (USA) and NINS (Japan), together with NRC (Canada), MOST and ASIAA (Taiwan), and KASI (Republic of Korea), in cooperation with the Republic of Chile. The Joint ALMA Observatory is operated by ESO, AUI/NRAO and NAOJ. Astrochemistry in Leiden is supported by the Netherlands Research School for Astronomy (NOVA). M.L.R.H acknowledges support from a Huygens fellowship from Leiden University. The research of J.K.J. is supported by the European Union through the ERC Consolidator Grant “S4F” (grant agreement No 646908).

## **Appendix**

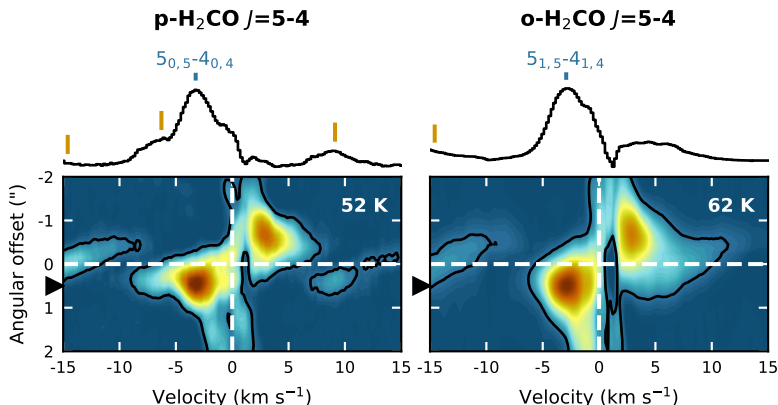
### **8.1 Formaldehyde and thioformaldehyde lines**

Table 8.1.1 provides an overview of the  $\text{H}_2\text{CO}$ ,  $\text{H}_2^{13}\text{CO}$ ,  $\text{D}_2\text{CO}$  and  $\text{H}_2\text{CS}$  lines that have  $\Delta J$  transitions with multiple  $K_a$  transitions in the spectral coverage of the ALMA-PILS survey.

**Table 8.1.1:** Line list of formaldehyde and thioformaldehyde lines.

Species	Transition	Frequency (GHz)	$\log(A_{ul})$ ( $s^{-1}$ )	$E_u$ (K)	Used in analysis	Data- set <sup>a</sup>	Notes
H <sub>2</sub> CO	5 <sub>0,5</sub> – 4 <sub>0,4</sub>	362.736	-2.863	52	-	(2)	
	5 <sub>1,5</sub> – 4 <sub>1,4</sub>	351.769	-2.920	62	-	(2)	
H <sub>2</sub> <sup>13</sup> CO	5 <sub>0,5</sub> – 4 <sub>0,4</sub>	353.812	-2.895	51	-	(2)	
	5 <sub>1,5</sub> – 4 <sub>1,4</sub>	343.326	-2.952	61	-	(2)	Blended with H <sub>2</sub> CS 10 <sub>2,9</sub> – 9 <sub>2,8</sub>
	5 <sub>2,3</sub> – 4 <sub>2,2</sub>	356.176	-2.962	99	-	(2)	CH <sub>2</sub> DOH line at 356.176 GHz
	5 <sub>2,4</sub> – 4 <sub>2,3</sub>	354.899	-2.966	98	-	(2)	
	5 <sub>3,2</sub> – 4 <sub>3,1</sub>	355.203	-3.083	158	-	(2)	
	5 <sub>3,3</sub> – 4 <sub>3,2</sub>	355.191	-3.083	158	-	(2)	
	5 <sub>4,1</sub> – 4 <sub>4,0</sub>	355.029	-3.334	240	-	(2)	At same frequency as 5 <sub>4,2</sub> – 4 <sub>4,1</sub>
	5 <sub>4,2</sub> – 4 <sub>4,1</sub>	355.029	-3.334	240	-	(2)	At same frequency as 5 <sub>4,1</sub> – 4 <sub>4,0</sub>
D <sub>2</sub> CO	6 <sub>0,6</sub> – 5 <sub>0,5</sub>	342.522	-2.933	58	-	(2)	CH <sub>2</sub> DOH line at 342.522 GHz
	6 <sub>1,6</sub> – 5 <sub>1,5</sub>	330.674	-2.989	61	-	(2)	
	6 <sub>2,4</sub> – 5 <sub>2,3</sub>	357.871	-2.925	81	-	(2)	
	6 <sub>2,5</sub> – 5 <sub>2,4</sub>	349.631	-2.955	80	-	(2)	CH <sub>2</sub> DOH line at 349.635 GHz
	6 <sub>3,3</sub> – 5 <sub>3,2</sub>	352.244	-3.019	108	-	(2)	
	6 <sub>3,4</sub> – 5 <sub>3,3</sub>	351.894	-3.020	108	-	(2)	
	6 <sub>4,2</sub> – 5 <sub>4,1</sub>	351.492	-3.152	145	-	(2)	
	6 <sub>4,3</sub> – 5 <sub>4,2</sub>	351.487	-3.152	145	-	(2)	
	6 <sub>5,1</sub> – 5 <sub>5,0</sub>	351.196	-3.413	194	-	(2)	At same frequency as 6 <sub>5,2</sub> – 5 <sub>5,1</sub>
	6 <sub>5,2</sub> – 5 <sub>5,1</sub>	351.196	-3.413	194	-	(2)	At same frequency as 6 <sub>5,1</sub> – 5 <sub>5,0</sub>
H <sub>2</sub> CS	7 <sub>0,7</sub> – 6 <sub>0,6</sub>	240.267	-3.688	46	yes	(1)	
	7 <sub>1,7</sub> – 6 <sub>1,6</sub>	236.727	-3.717	59	yes	(3)	
	7 <sub>2,5</sub> – 6 <sub>2,4</sub>	240.549	-3.724	99	yes	(1)	
	7 <sub>2,6</sub> – 6 <sub>2,5</sub>	240.382	-3.725	99	yes	(1)	
	7 <sub>3,4</sub> – 6 <sub>3,3</sub>	240.394	-3.776	165	yes	(1)	At same frequency as 7 <sub>3,5</sub> – 6 <sub>3,4</sub>
	7 <sub>3,5</sub> – 6 <sub>3,4</sub>	240.393	-3.776	165	-	(1)	At same frequency as 7 <sub>3,4</sub> – 6 <sub>3,3</sub>
	7 <sub>4,3</sub> – 6 <sub>4,2</sub>	240.332	-3.860	257	yes	(1)	At same frequency as 7 <sub>4,4</sub> – 6 <sub>4,3</sub>
	7 <sub>4,4</sub> – 6 <sub>4,3</sub>	240.332	-3.860	257	-	(1)	At same frequency as 7 <sub>4,3</sub> – 6 <sub>4,2</sub>
	7 <sub>5,2</sub> – 6 <sub>5,1</sub>	240.262	-3.998	375	yes	(1)	At same frequency as 7 <sub>5,3</sub> – 6 <sub>5,2</sub>
	7 <sub>5,3</sub> – 6 <sub>5,2</sub>	240.262	-3.998	375	-	(1)	At same frequency as 7 <sub>5,2</sub> – 6 <sub>5,1</sub>
	10 <sub>0,10</sub> – 9 <sub>0,9</sub>	342.946	-3.216	91	yes	(2)	
	10 <sub>1,9</sub> – 9 <sub>1,8</sub>	348.534	-3.199	105	-	(2)	Several lines at similar frequency
	10 <sub>1,10</sub> – 9 <sub>1,9</sub>	338.083	-3.239	102	yes	(2)	
	10 <sub>2,8</sub> – 9 <sub>2,7</sub>	343.813	-3.231	143	yes	(2)	
	10 <sub>2,9</sub> – 9 <sub>2,8</sub>	343.322	-3.232	143	-	(2)	Blended with H <sub>2</sub> <sup>13</sup> CO 5 <sub>1,5</sub> – 4 <sub>1,4</sub>
	10 <sub>3,7</sub> – 9 <sub>3,6</sub>	343.414	-3.255	209	-	(2)	Blended with H <sub>2</sub> CS 10 <sub>3,8</sub> – 9 <sub>3,7</sub>
	10 <sub>3,8</sub> – 9 <sub>3,7</sub>	343.410	-3.255	209	-	(2)	Blended with H <sub>2</sub> CS 10 <sub>3,7</sub> – 9 <sub>3,6</sub>
	10 <sub>4,6</sub> – 9 <sub>4,5</sub>	343.310	-3.290	301	yes	(2)	At same frequency as 10 <sub>4,7</sub> – 9 <sub>4,6</sub>
	10 <sub>4,7</sub> – 9 <sub>4,6</sub>	343.310	-3.290	301	-	(2)	At same frequency as 10 <sub>4,6</sub> – 9 <sub>4,5</sub>
10 <sub>5,5</sub> – 9 <sub>5,4</sub>	343.203	-3.340	419	-	(2)	Not detected	
10 <sub>5,6</sub> – 9 <sub>5,5</sub>	343.203	-3.340	419	-	(2)	Not detected	

**Notes.** Transitions are denoted with the quantum numbers  $J_{K_a, K_b}$ . Ortho transitions have an odd value for  $K_a$ , while para transitions have an even value. <sup>(a)</sup> ALMA project-id: (1) 2012.1.00712.S; (2) 2013.1.00278.S; (3) 2016.1.01150.S



**Figure 8.B.1:** Position-velocity diagrams of the  $\text{H}_2\text{CO}$  lines along the major axis of the disk-like structure (positive angular offsets denote the northeast direction, i.e., blueshifted emission, and negative offsets denote the southwest direction, i.e., redshifted emission). The intensity (color) scale is normalized to the brightest line in each panel. The black contour denotes the  $3\sigma$  contour. The dashed white lines mark the source position and systemic velocity of  $3.8 \text{ km s}^{-1}$  (shifted to  $0 \text{ km s}^{-1}$ ). The upper level energy is denoted in the top right corner of each panel. The spectra at  $\sim 0.5''$  northeast of the source (indicated by black triangles left of the vertical axes) are shown on top of the pv-diagram panels. The  $\text{H}_2\text{CO}$  lines are identified by a vertical blue line, other lines by vertical orange lines.

## 8.B Position-velocity diagrams

Position-velocity diagrams for  $\text{H}_2\text{CO}$ ,  $\text{H}_2^{13}\text{CO}$  and  $\text{D}_2\text{CO}$  are presented in **Figs. 8.B.1**, **8.B.2** and **8.B.3**, respectively.

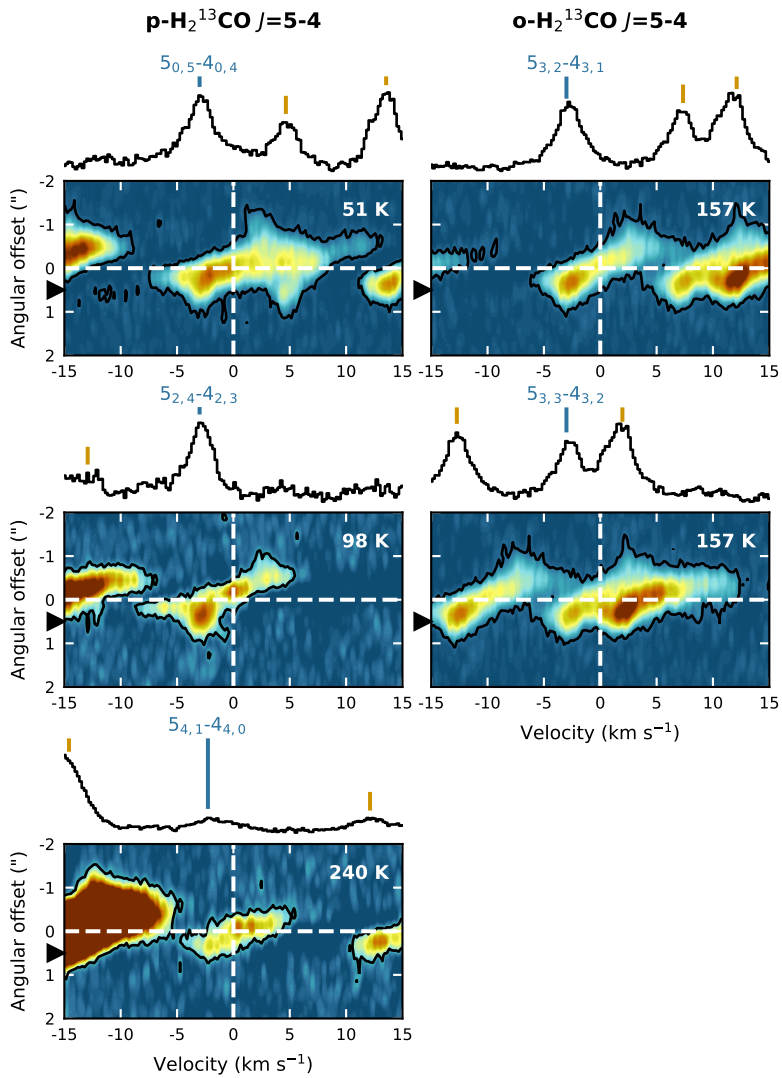


**Figure 8.B.2:** As Fig. 8.B.1, but for H<sub>2</sub><sup>13</sup>CO.

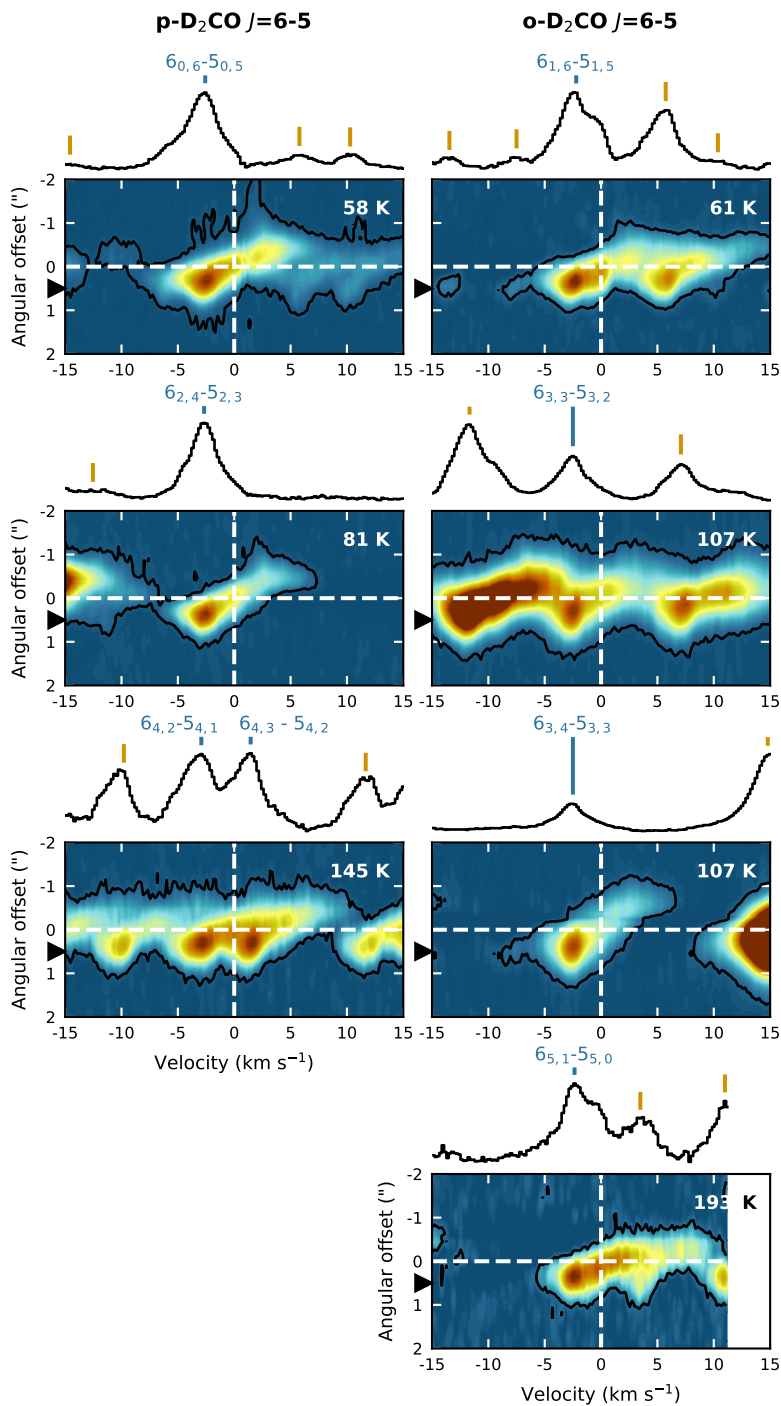
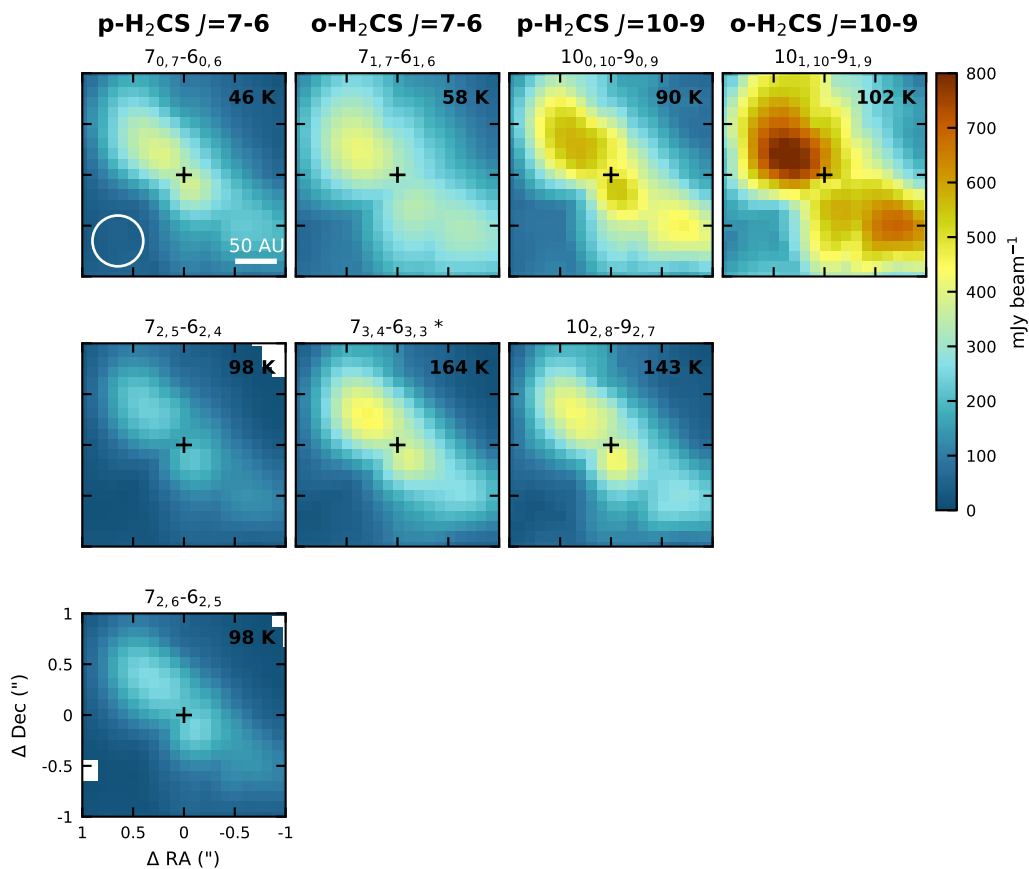


Figure 8.B.3: As Fig. 8.B.1, but for  $\text{D}_2\text{CO}$ .





**Figure 8.C.1:** Maps of the peak fluxes (moment 8) of the H<sub>2</sub>CS lines. Only lines for which reliable peak fluxes could be extracted in the center, i.e., that are not too blended, are shown. The transitions are denoted above the panels and the corresponding upper level energies are listed in the top right corner of each panel. Asterisks (\*) behind the transition indicate that the flux is coming from two lines with the same  $J$  and  $K_a$ -level located at the same frequency (see [Table 8.71.1](#) for details). All panels are shown at the same intensity (color) scale for comparison. Pixels with no emission  $>3\sigma$  are masked out. The continuum peak position is marked with a black cross and the beam is depicted in the lower left corner of the *top left panel*.

## 8.C Peak fluxes

Maps of the peak fluxes (moment 8 maps) are shown in [Fig. 8.C.1](#) for H<sub>2</sub>CS and in [Fig. 8.C.2](#) for H<sub>2</sub><sup>13</sup>CO and D<sub>2</sub>CO. Lines that are too blended in the central region to extract reliable peak fluxes are excluded.

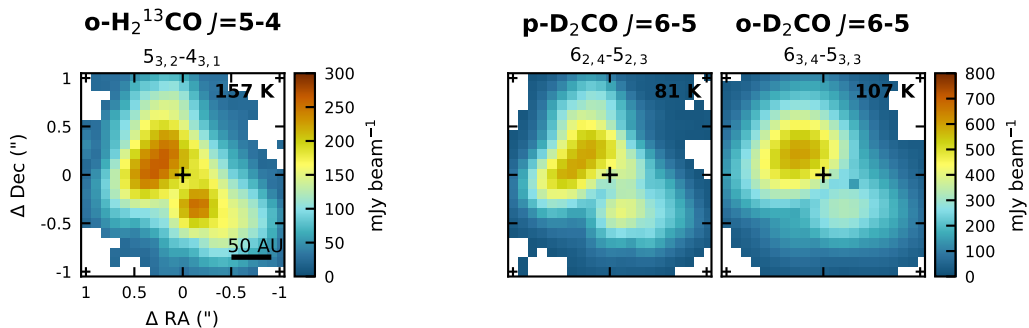


**Figure 8.C.2:** As Fig. 8.C.1, but for H<sub>2</sub><sup>13</sup>CO (left panel) and D<sub>2</sub>CO (middle and right panel).

## 8.D RADEX results for H<sub>2</sub>CS

H<sub>2</sub>CS line ratios as function of temperature and density or temperature and column density derived from a grid of non-LTE radiative transfer calculations with RADEX are presented in Fig. 8.D.1. Figure 8.D.2 shows the column densities at which the different H<sub>2</sub>CS lines become optically thick based on the same radiative transfer models.

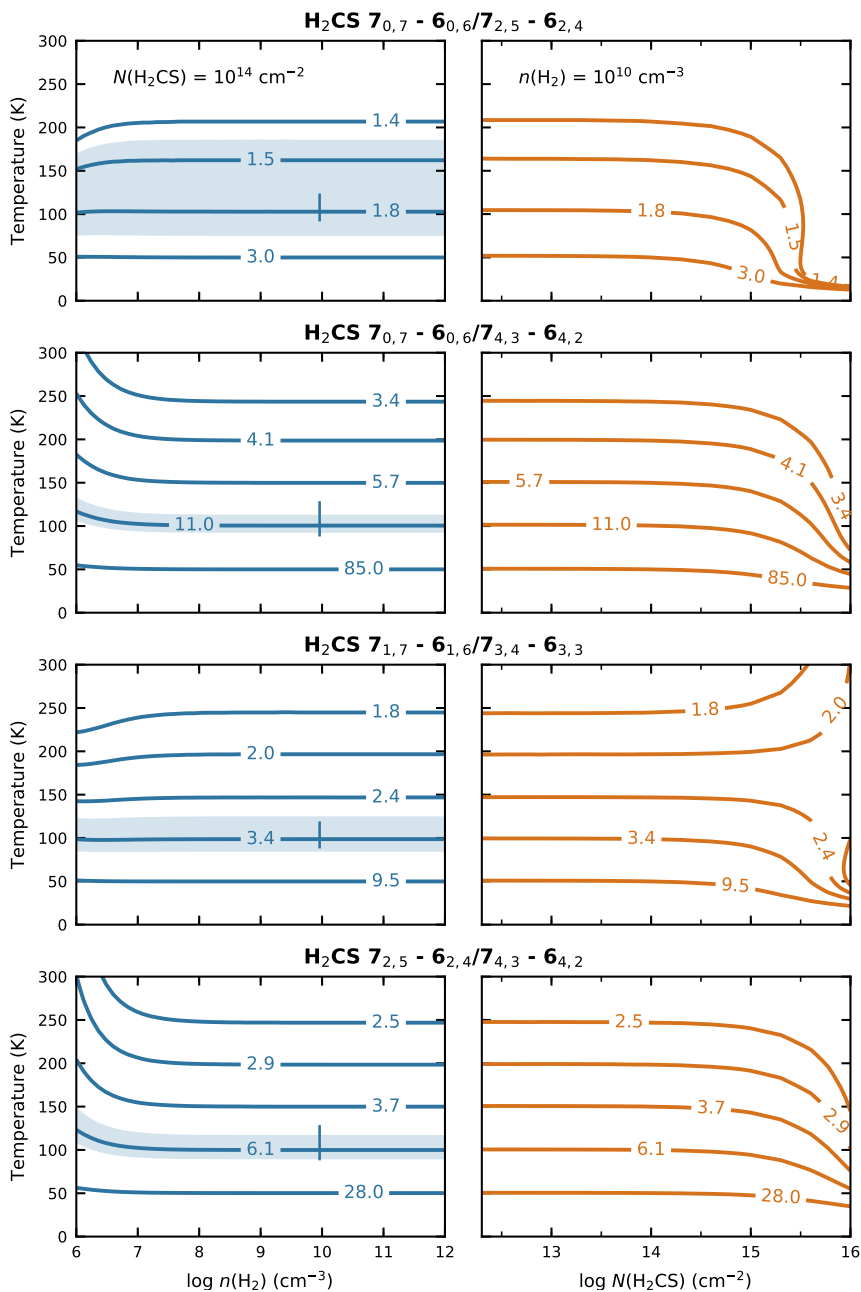


**Figure 8.D.1:** Temperature sensitivity of the H<sub>2</sub>CS line ratios as a function of H<sub>2</sub> density (blue lines) and H<sub>2</sub>CS column density (orange lines). **Figure and caption continue on next page.**

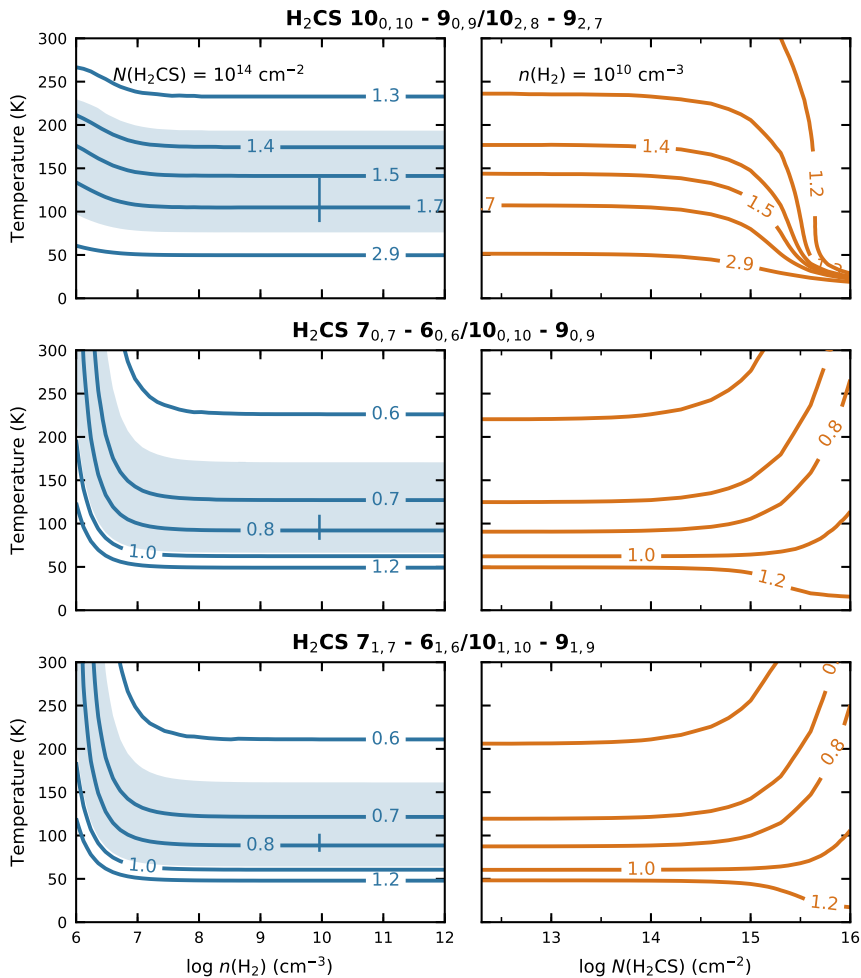


**Figure 8.D.1 continued:** For the density plots, a H<sub>2</sub>CS column density of  $10^{14}$  cm<sup>-2</sup> is adopted for both o-H<sub>2</sub>CS and p-H<sub>2</sub>CS, and a H<sub>2</sub> density of  $10^{10}$  cm<sup>-3</sup> is used for the column density plots. The line ratio is listed above the panels and contours are chosen such to mark the ratios at temperatures of 50, 100, 150, 200 and 250 K. The blue shaded area shows the change in derived temperature if the 100 K ratio changes by 20%. The blue vertical line represents the typical  $3\sigma$  error on the temperature based on the observed uncertainty in the line ratio solely due to the rms in the images. The  $7_{0,7} - 6_{0,6} / 7_{2,5} - 6_{2,4}$  ratio is equal to the  $7_{0,7} - 6_{0,6} / 7_{2,6} - 6_{2,5}$  ratio (not shown) and the  $7_{2,5} - 6_{2,4} / 7_{4,3} - 6_{4,2}$  ratio is equal to the  $7_{2,6} - 6_{2,5} / 7_{4,3} - 6_{4,2}$  ratio (not shown).

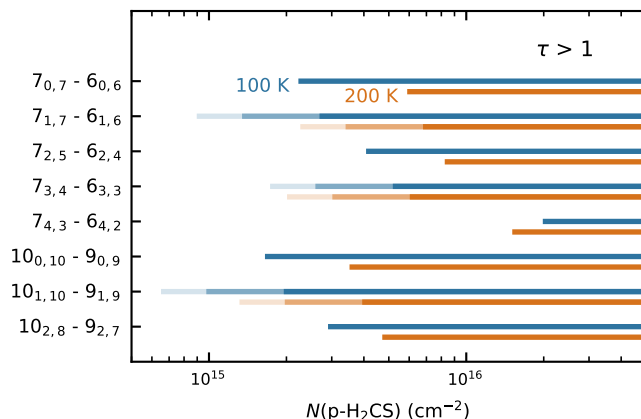


**Figure 8.D.2:** Column densities (expressed in p-H<sub>2</sub>CS column density) at which the H<sub>2</sub>CS lines are optically thick at 100 K (blue) and 200 K (orange) based on the non-LTE RADEX calculation. For the ortho transitions, solid dark lines assume an ortho-to-para ratio of 1, and the shaded lines assume ortho-to-para ratios of 2 and 3 (lightest shade).

## 8.ℰ Radial temperature profiles

**Figure 8.ℰ.1** shows radial temperature profiles derived from H<sub>2</sub>CS line ratios including transitions for which no collisional rate coefficients are available. These temperatures therefore result from an LTE calculation. **Figure 8.ℰ.2** presents the radial temperature profiles based on the  $7_{0,7} - 6_{0,6}/7_{2,5} - 6_{2,4}$  and  $7_{0,7} - 6_{0,6}/7_{4,3} - 6_{4,2}$  ratios (**Fig. 8.5** panels **a** and **c**) for different position angles.

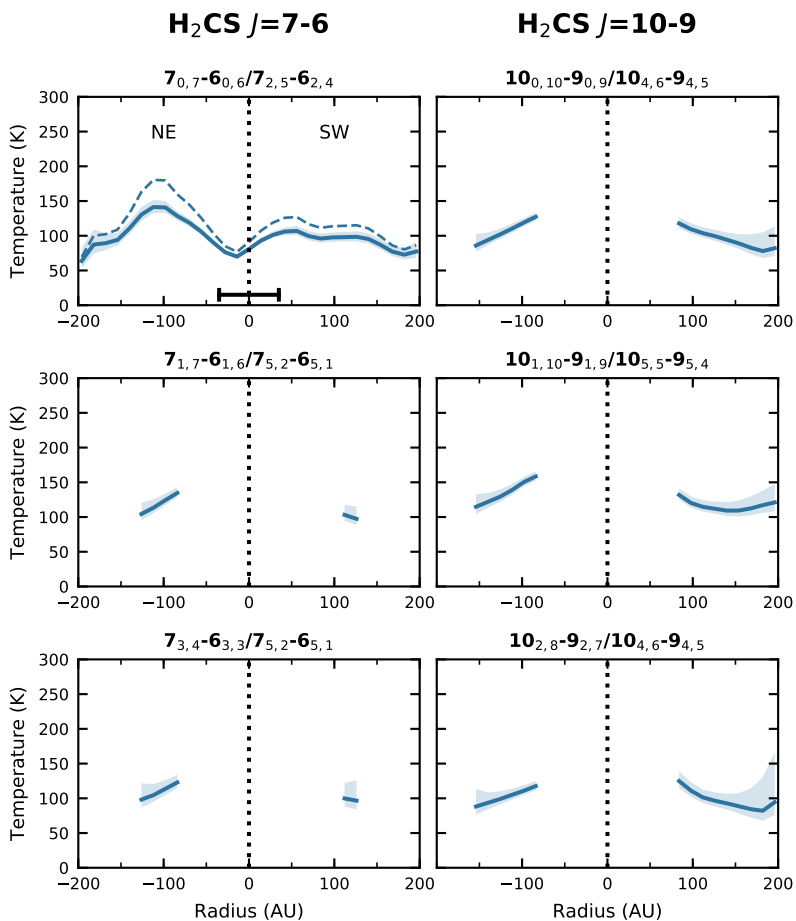


**Figure 8.8.1:** Radial temperature profiles derived from  $\text{H}_2\text{CS}$  line ratios (listed above the panels) for which no collisional rate coefficients are available. The temperature profiles are taken along the major axis of the disk-like structure ( $\text{PA} = 45^\circ$ ) and calculated assuming LTE. As a reference, the non-LTE result is shown as well as for the  $7_{0,7} - 6_{0,6}/7_{2,5} - 6_{2,4}$  transition (dashed line in *top left panel*). The shaded area represents the  $1\sigma$  uncertainty based on statistical errors. The horizontal bar in the *top left panel* marks the beam size.

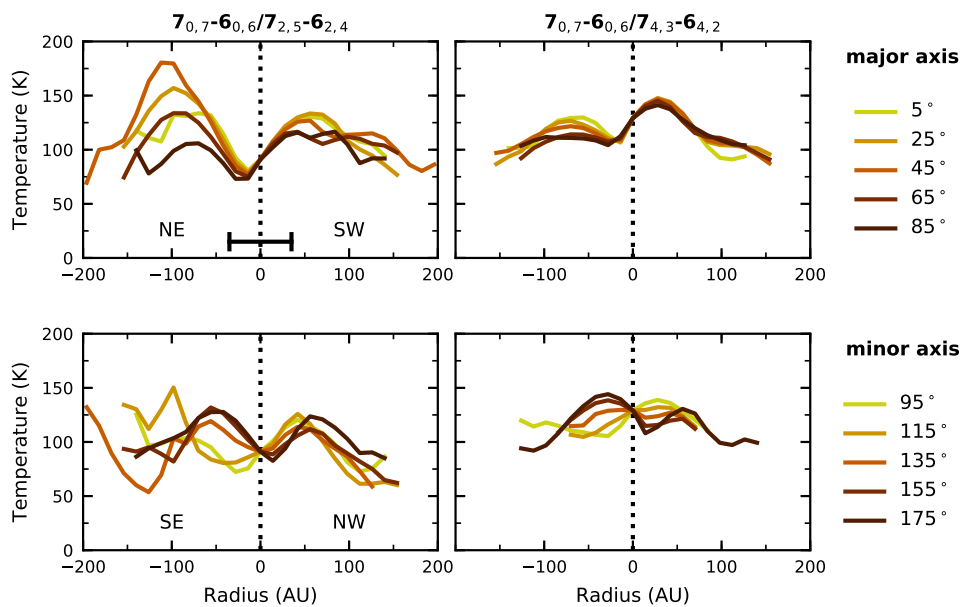


**Figure 8.8.2:** Radial temperature profiles derived from two  $\text{H}_2\text{CS}$  line ratios (listed above the panels) along different position angles (different colors) using the non-LTE RADEX results. A PA of  $45^\circ$  corresponds to the major axis of the disk-like structure as presented in **Fig 8.5**. The horizontal bar in the *top left panel* marks the beam size.







# Bibliography

- Adams, F. C., Lada, C. J., & Shu, F. H. 1987, *ApJ*, 312, 788
- Adams, F. C. & Shu, F. H. 1986, *ApJ*, 308, 836
- Aikawa, Y., Furuya, K., Nomura, H., & Qi, C. 2015, *ApJ*, 807, 120
- Aikawa, Y., Ohashi, N., Inutsuka, S.-i., Herbst, E., & Takakuwa, S. 2001, *ApJ*, 552, 639
- Aikawa, Y., Umebayashi, T., Nakano, T., & Miyama, S. M. 1999, *ApJ*, 519, 705
- Aikawa, Y., van Zadelhoff, G. J., van Dishoeck, E. F., & Herbst, E. 2002, *A&A*, 386, 622
- Ali-Dib, M. 2017, *MNRAS*, 467, 2845
- Ali-Dib, M., Mousis, O., Petit, J.-M., & Lunine, J. I. 2014, *ApJ*, 785, 125
- Allen, M. & Robinson, G. W. 1977, *ApJ*, 212, 396
- ALMA Partnership, Brogan, C. L., Pérez, L. M., et al. 2015, *ApJ*, 808, L3
- Altwegg, K., Balsiger, H., Bar-Nun, A., et al. 2016, *Science Advances*, 2, e1600285
- Anderl, S., Maret, S., Cabrit, S., et al. 2016, *A&A*, 591, A3
- Andersson, S. & van Dishoeck, E. F. 2008, *A&A*, 491, 907
- André, P., Di Francesco, J., Ward-Thompson, D., et al. 2014, *Protostars and Planets VI*, 27
- André, P., Men'shchikov, A., Bontemps, S., et al. 2010, *A&A*, 518, L102
- André, P., Ward-Thompson, D., & Barsony, M. 1993, *ApJ*, 406, 122
- Andrews, S. M., Huang, J., Pérez, L. M., et al. 2018, *ApJ*, 869, L41
- Andrews, S. M., Rosenfeld, K. A., Kraus, A. L., & Wilner, D. J. 2013, *ApJ*, 771, 129
- Andrews, S. M. & Williams, J. P. 2005, *ApJ*, 631, 1134
- Andrews, S. M., Wilner, D. J., Hughes, A. M., Qi, C., & Dullemond, C. P. 2010, *ApJ*, 723, 1241
- Andrews, S. M., Wilner, D. J., Hughes, A. M., et al. 2012, *ApJ*, 744, 162
- Andrews, S. M., Wilner, D. J., Zhu, Z., et al. 2016, *ApJ*, 820, L40
- Ansdell, M., Williams, J. P., Manara, C. F., et al. 2017, *AJ*, 153, 240
- Ansdell, M., Williams, J. P., Trapman, L., et al. 2018, *ApJ*, 859, 21
- Ansdell, M., Williams, J. P., van der Marel, N., et al. 2016, *ApJ*, 828, 46
- Artur de la Villarmois, E., Jørgensen, J. K., Kristensen, L. E., et al. 2019, *A&A*, 626, A71
- Aso, Y., Ohashi, N., Aikawa, Y., et al. 2017, *ApJ*, 849, 56
- Aso, Y., Ohashi, N., Saigo, K., et al. 2015, *ApJ*, 812, 27

- Asplund, M., Grevesse, N., Sauval, A. J., & Scott, P. 2009, *ARA&A*, 47, 481
- Audard, M., Ábrahám, P., Dunham, M. M., et al. 2014, *Protostars and Planets VI*, 387
- Bacmann, A., Taquet, V., Faure, A., Kahane, C., & Ceccarelli, C. 2012, *A&A*, 541, L12
- Balbus, S. A. & Hawley, J. F. 1991, *ApJ*, 376, 214
- Bally, J. 2016, *ARA&A*, 54, 491
- Banzatti, A., Pinilla, P., Ricci, L., et al. 2015, *ApJ*, 815, L15
- Barenfeld, S. A., Carpenter, J. M., Ricci, L., & Isella, A. 2016, *ApJ*, 827, 142
- Bate, M. R. 2018, *MNRAS*, 475, 5618
- Belloche, A., Müller, H. S. P., Garrod, R. T., & Menten, K. M. 2016, *A&A*, 587, A91
- Bergin, E. A., Ciardi, D. R., Lada, C. J., Alves, J., & Lada, E. A. 2001, *ApJ*, 557, 209
- Bergin, E. A. & Cleeves, L. I. 2018, *Chemistry During the Gas-Rich Stage of Planet Formation*, 137
- Bergin, E. A., Cleeves, L. I., Crockett, N., & Blake, G. A. 2014, *Faraday Discussions*, 168 [arXiv:1405.7394]
- Bergin, E. A., Du, F., Cleeves, L. I., et al. 2016, *ApJ*, 831, 101
- Bergin, E. A., Melnick, G. J., & Neufeld, D. A. 1998, *ApJ*, 499, 777
- Bergin, E. A. & Tafalla, M. 2007, *ARA&A*, 45, 339
- Bergin, E. A. & van Dishoeck, E. F. 2012, *Philosophical Transactions of the Royal Society of London Series A*, 370, 2778
- Bergner, J. B., Guzmán, V. G., Öberg, K. I., Loomis, R. A., & Pegues, J. 2018, *ApJ*, 857, 69
- Bertin, M., Fayolle, E. C., Romanzin, C., et al. 2013, *ApJ*, 779, 120
- Bianchi, E., Codella, C., Ceccarelli, C., et al. 2017, *A&A*, 606, L7
- Bieler, A., Altwegg, K., Balsiger, H., et al. 2015, *Nature*, 526, 678
- Birnstiel, T., Dullemond, C. P., & Brauer, F. 2010, *A&A*, 513, A79
- Bisschop, S. E., Fraser, H. J., Öberg, K. I., van Dishoeck, E. F., & Schlemmer, S. 2006, *A&A*, 449, 1297
- Bjerkeli, P., Jørgensen, J. K., Bergin, E. A., et al. 2016a, *A&A*, 595, A39
- Bjerkeli, P., van der Wiel, M. H. D., Harsono, D., Ramsey, J. P., & Jørgensen, J. K. 2016b, *Nature*, 540, 406
- Blum, J. & Wurm, G. 2008, *ARA&A*, 46, 21
- Bockelée-Morvan, D., Calmonte, U., Charnley, S., et al. 2015, *Space Sci. Rev.*, 197, 47
- Bocquet, R., Demaison, J., Cosléou, J., et al. 1999, *Journal of Molecular Spectroscopy*, 195, 345
- Bocquet, R., Demaison, J., Poteau, L., et al. 1996, *Journal of Molecular Spectroscopy*, 177, 154
- Boley, A. C. 2009, *ApJ*, 695, L53
- Boogert, A. C. A., Gerakines, P. A., & Whittet, D. C. B. 2015, *ARA&A*, 53, 541
- Booth, R. A., Clarke, C. J., Madhusudhan, N., & Ilee, J. D. 2017, *MNRAS*, 469, 3994
- Bosman, A. D., Walsh, C., & van Dishoeck, E. F. 2018, *A&A*, 618, A182
- Boss, A. P. 1997, *Science*, 276, 1836
- Boss, A. P. & Yorke, H. W. 1995, *ApJ*, 439, L55
- Bottinelli, S., Ceccarelli, C., Neri, R., et al. 2004, *ApJ*, 617, L69

- Brinch, C., Crapsi, A., Jørgensen, J. K., Hogerheijde, M. R., & Hill, T. 2007, *A&A*, 475, 915
- Brinch, C. & Hogerheijde, M. R. 2010, *A&A*, 523, A25
- Brown, D. W., Chandler, C. J., Carlstrom, J. E., et al. 2000, *MNRAS*, 319, 154
- Brown, W. A. & Bolina, A. S. 2007, *MNRAS*, 374, 1006
- Bruderer, S. 2013, *A&A*, 559, A46
- Bruderer, S., Doty, S. D., & Benz, A. O. 2009, *ApJS*, 183, 179
- Bruderer, S., van Dishoeck, E. F., Doty, S. D., & Herczeg, G. J. 2012, *A&A*, 541, A91
- Brünken, S., Müller, H. S. P., Lewen, F., & Winnewisser, G. 2003, *Physical Chemistry Chemical Physics (Incorporating Faraday Transactions)*, 5
- Burke, D. J. & Brown, W. A. 2010, *Physical Chemistry Chemical Physics (Incorporating Faraday Transactions)*, 12, 5947
- Calcutt, H., Jørgensen, J. K., Müller, H. S. P., et al. 2018, *A&A*, 616, A90
- Calvet, N., D'Alessio, P., Hartmann, L., et al. 2002, *ApJ*, 568, 1008
- Carney, M. T., Fedele, D., Hogerheijde, M. R., et al. 2018, *A&A*, 614, A106
- Carney, M. T., Hogerheijde, M. R., Guzmán, V. V., et al. 2019, *A&A*, 623, A124
- Carney, M. T., Hogerheijde, M. R., Loomis, R. A., et al. 2017, *A&A*, 605, A21
- Caselli, P., Benson, P. J., Myers, P. C., & Tafalla, M. 2002a, *ApJ*, 572, 238
- Caselli, P. & Ceccarelli, C. 2012, *A&A Rev.*, 20, 56
- Caselli, P., Walmsley, C. M., Tafalla, M., Dore, L., & Myers, P. C. 1999, *ApJ*, 523, L165
- Caselli, P., Walmsley, C. M., Zucconi, A., et al. 2002b, *ApJ*, 565, 344
- Cassen, P. & Moosman, A. 1981, *Icarus*, 48, 353
- Caux, E., Kahane, C., Castets, A., et al. 2011, *A&A*, 532, A23
- Cazaux, S., Tielens, A. G. G. M., Ceccarelli, C., et al. 2003, *ApJ*, 593, L51
- Cazzoletti, P., Manara, C. F., Baobab Liu, H., et al. 2019, *A&A*, 626, A11
- Ceccarelli, C., Caselli, P., Bockelée-Morvan, D., et al. 2014, *Protostars and Planets VI*, 859
- Ceccarelli, C., Castets, A., Caux, E., et al. 2000, *A&A*, 355, 1129
- Ceccarelli, C., Hollenbach, D. J., & Tielens, A. G. G. M. 1996, *ApJ*, 471, 400
- Cernicharo, J., Marcelino, N., Roueff, E., et al. 2012, *ApJ*, 759, L43
- Chandler, C. J., Brogan, C. L., Shirley, Y. L., & Loinard, L. 2005, *ApJ*, 632, 371
- Charnley, S. B., Tielens, A. G. G. M., & Millar, T. J. 1992, *ApJ*, 399, L71
- Chiang, E. & Youdin, A. N. 2010, *Annu. Rev. Earth Planet. Sci.*, 38, 493
- Chiang, E. I. & Goldreich, P. 1997, *ApJ*, 490, 368
- Chuang, K.-J., Fedoseev, G., Ioppolo, S., van Dishoeck, E. F., & Linnartz, H. 2016, *MNRAS*, 455, 1702
- Ciesla, F. J. & Cuzzi, J. N. 2006, *Icarus*, 181, 178
- Cieza, L. A., Casassus, S., Tobin, J., et al. 2016, *Nature*, 535, 258
- Cieza, L. A., Ruíz-Rodríguez, D., Perez, S., et al. 2018, *MNRAS*, 474, 4347
- Cleeves, L. I. 2016, *ApJ*, 816, L21
- Cleeves, L. I., Bergin, E. A., & Adams, F. C. 2014, *ApJ*, 794, 123
- Cleeves, L. I., Bergin, E. A., Qi, C., Adams, F. C., & Öberg, K. I. 2015, *ApJ*, 799, 204
- Codella, C., Cabrit, S., Gueth, F., et al. 2014, *A&A*, 568, L5
- Collings, M. P., Anderson, M. A., Chen, R., et al. 2004, *MNRAS*, 354, 1133

- Connelley, M. & Reipurth, B. 2018, ArXiv e-prints [arXiv:1806.08880]
- Cordiner, M. A., Charnley, S. B., Kisiel, Z., McGuire, B. A., & Kuan, Y.-J. 2017, *ApJ*, 850, 187
- Cornet, R. A. & Winnewisser, G. 1980, *Journal of Molecular Spectroscopy*, 80, 438
- Crapsi, A., Caselli, P., Walmsley, C. M., et al. 2005, *ApJ*, 619, 379
- Crapsi, A., van Dishoeck, E. F., Hogerheijde, M. R., Pontoppidan, K. M., & Dullemond, C. P. 2008, *A&A*, 486, 245
- Cravens, T. E. & Dalgarno, A. 1978, *ApJ*, 219, 750
- Cridland, A. J., Eistrup, C., & van Dishoeck, E. F. 2019, *A&A*, 627, A127
- Cridland, A. J., Pudritz, R. E., Birnstiel, T., Cleeves, L. I., & Bergin, E. A. 2017, *MNRAS*, 469, 3910
- Crimier, N., Ceccarelli, C., Maret, S., et al. 2010, *A&A*, 519, A65
- Cuppen, H. M., van Dishoeck, E. F., Herbst, E., & Tielens, A. G. G. M. 2009, *A&A*, 508, 275
- D'Alessio, P., Calvet, N., & Hartmann, L. 1997, *ApJ*, 474, 397
- Dangoisse, D., Willemot, E., & Bellet, J. 1978, *Journal of Molecular Spectroscopy*, 71, 414
- Dartois, E., Dutrey, A., & Guilloteau, S. 2003, *A&A*, 399, 773
- Davis, S. S. 2005, *ApJ*, 620, 994
- Dominik, C., Dullemond, C. P., Waters, L. B. F. M., & Walch, S. 2003, *A&A*, 398, 607
- Drążkowska, J. & Alibert, Y. 2017, *A&A*, 608, A92
- Drozdovskaya, M. N., van Dishoeck, E. F., Jørgensen, J. K., et al. 2018, *MNRAS*, 476, 4949
- Drozdovskaya, M. N., Walsh, C., van Dishoeck, E. F., et al. 2016, *MNRAS*, 462, 977
- Drozdovskaya, M. N., Walsh, C., Visser, R., Harsono, D., & van Dishoeck, E. F. 2014, *MNRAS*, 445, 913
- Dunham, M. M., Allen, L. E., Evans, II, N. J., et al. 2015, *ApJS*, 220, 11
- Dunham, M. M., Arce, H. G., Allen, L. E., et al. 2013, *AJ*, 145, 94
- Dunham, M. M., Stutz, A. M., Allen, L. E., et al. 2014, *Protostars and Planets VI*, 195
- Dutrey, A., Guilloteau, S., & Guelin, M. 1997, *A&A*, 317, L55
- Dutrey, A., Guilloteau, S., Piétu, V., et al. 2017, *A&A*, 607, A130
- Dutrey, A., Semenov, D., Chapillon, E., et al. 2014, *Protostars and Planets VI*, 317
- Dzib, S. A., Ortiz-León, G. N., Hernández-Gómez, A., et al. 2018, *A&A*, 614, A20
- Eisner, J. A., Hillenbrand, L. A., Carpenter, J. M., & Wolf, S. 2005, *ApJ*, 635, 396
- Eistrup, C., Walsh, C., & van Dishoeck, E. F. 2016, *A&A*, 595, A83
- Eistrup, C., Walsh, C., & van Dishoeck, E. F. 2018, *A&A*, 613, A14
- Elsila, J. E., Glavin, D. P., & Dworkin, J. P. 2009, *Meteoritics and Planetary Science*, 44, 1323
- Emprechtinger, M., Caselli, P., Volgenau, N. H., Stutzki, J., & Wiedner, M. C. 2009, *A&A*, 493, 89
- Enoch, M. L., Corder, S., Dunham, M. M., & Duchêne, G. 2009a, *ApJ*, 707, 103
- Enoch, M. L., Evans, II, N. J., Sargent, A. I., & Glenn, J. 2009b, *ApJ*, 692, 973
- Enoch, M. L., Young, K. E., Glenn, J., et al. 2006, *ApJ*, 638, 293

- Evans, II, N. J., Dunham, M. M., Jørgensen, J. K., et al. 2009, *ApJS*, 181, 321
- Fabricant, B., Krieger, D., & Muentner, J. S. 1977, *J. Chem. Phys.*, 67, 1576
- Facchini, S., Birnstiel, T., Bruderer, S., & van Dishoeck, E. F. 2017, *A&A*, 605, A16
- Favre, C., Bergin, E. A., Cleeves, L. I., et al. 2015, *ApJ*, 802, L23
- Favre, C., Cleeves, L. I., Bergin, E. A., Qi, C., & Blake, G. A. 2013, *ApJ*, 776, L38
- Favre, C., Fedele, D., Semenov, D., et al. 2018, *ApJ*, 862, L2
- Favre, C., Jørgensen, J. K., Field, D., et al. 2014, *ApJ*, 790, 55
- Fayolle, E. C., Balfe, J., Loomis, R., et al. 2016, *ApJ*, 816, L28
- Fedoseev, G., Cuppen, H. M., Ioppolo, S., Lamberts, T., & Linnartz, H. 2015, *MNRAS*, 448, 1288
- Foster, J. B., Mandel, K. S., Pineda, J. E., et al. 2013, *MNRAS*, 428, 1606
- France, K., Schindhelm, E., Bergin, E. A., Roueff, E., & Abgrall, H. 2014, *ApJ*, 784, 127
- Frank, A., Ray, T. P., Cabrit, S., et al. 2014, *Protostars and Planets VI*, 451
- Fraser, H. J., Collings, M. P., McCoustra, M. R. S., & Williams, D. A. 2001, *MNRAS*, 327, 1165
- Frimann, S., Jørgensen, J. K., Dunham, M. M., et al. 2017, *A&A*, 602, A120
- Fuchs, G. W., Cuppen, H. M., Ioppolo, S., et al. 2009, *A&A*, 505, 629
- Furlan, E., Fischer, W. J., Ali, B., et al. 2016, *ApJS*, 224, 5
- Galli, D., Lizano, S., Shu, F. H., & Allen, A. 2006, *ApJ*, 647, 374
- Galli, D. & Shu, F. H. 1993a, *ApJ*, 417, 220
- Galli, D. & Shu, F. H. 1993b, *ApJ*, 417, 243
- Garaud, P. & Lin, D. N. C. 2007, *ApJ*, 654, 606
- Garrod, R. T. 2013, *ApJ*, 765, 60
- Garrod, R. T. & Herbst, E. 2006, *A&A*, 457, 927
- Garrod, R. T., Widicus Weaver, S. L., & Herbst, E. 2008, *ApJ*, 682, 283
- Geppert, W. D., Hamberg, M., Thomas, R. D., et al. 2006, *Faraday Discussions*, 133, 177
- Goldsmith, P. F. & Langer, W. D. 1999, *ApJ*, 517, 209
- Goodman, A. A., Benson, P. J., Fuller, G. A., & Myers, P. C. 1993, *ApJ*, 406, 528
- Greene, T. P., Wilking, B. A., Andre, P., Young, E. T., & Lada, C. J. 1994, *ApJ*, 434, 614
- Gundlach, B., Kiliyas, S., Beitz, E., & Blum, J. 2011, *Icarus*, 214, 717
- Guzmán, V. V., Öberg, K. I., Carpenter, J., et al. 2018, *ApJ*, 864, 170
- Hacar, A. & Tafalla, M. 2011, *A&A*, 533, A34
- Harsono, D., Bjerkerli, P., van der Wiel, M. H. D., et al. 2018, *Nature Astronomy*, 2, 646
- Harsono, D., Bruderer, S., & van Dishoeck, E. F. 2015, *A&A*, 582, A41
- Harsono, D., Jørgensen, J. K., van Dishoeck, E. F., et al. 2014, *A&A*, 562, A77
- Hartmann, L., Calvet, N., Gullbring, E., & D'Alessio, P. 1998, *ApJ*, 495, 385
- Hartmann, L., Herczeg, G., & Calvet, N. 2016, *ARA&A*, 54, 135
- Harvey, D. W. A., Wilner, D. J., Myers, P. C., & Tafalla, M. 2003, *ApJ*, 596, 383
- Hasegawa, T. I. & Herbst, E. 1993, *MNRAS*, 263, 589
- Hasegawa, T. I., Herbst, E., & Leung, C. M. 1992, *ApJS*, 82, 167
- Heays, A. N., Bosman, A. D., & van Dishoeck, E. F. 2017, *A&A*, 602, A105

- Heays, A. N., Visser, R., Gredel, R., et al. 2014, *A&A*, 562, A61
- Henning, T. & Semenov, D. 2008, in *IAU Symposium*, Vol. 251, *Organic Matter in Space*, ed. S. Kwok & S. Sanford, 89–98
- Herbst, E. & van Dishoeck, E. F. 2009, *ARA&A*, 47, 427
- Herczeg, G. J., Linsky, J. L., Valenti, J. A., Johns-Krull, C. M., & Wood, B. E. 2002, *ApJ*, 572, 310
- Herczeg, G. J., Wood, B. E., Linsky, J. L., Valenti, J. A., & Johns-Krull, C. M. 2004, *ApJ*, 607, 369
- Hernández-Gómez, A., Loinard, L., Chandler, C. J., et al. 2019, *ApJ*, 875, 94
- Hincelin, U., Wakelam, V., Commerçon, B., Hersant, F., & Guilloteau, S. 2013, *ApJ*, 775, 44
- Hirano, N., Ho, P. P. T., Liu, S.-Y., et al. 2010, *ApJ*, 717, 58
- Hogerheijde, M. R. 2001, *ApJ*, 553, 618
- Hogerheijde, M. R., Bergin, E. A., Brinch, C., et al. 2011, *Science*, 334, 338
- Hogerheijde, M. R. & Sandell, G. 2000, *ApJ*, 534, 880
- Hogerheijde, M. R. & van der Tak, F. F. S. 2000, *A&A*, 362, 697
- Hogerheijde, M. R., van Dishoeck, E. F., Salverda, J. M., & Blake, G. A. 1999, *ApJ*, 513, 350
- Hsieh, T.-H., Hirano, N., Belloche, A., et al. 2019, *ApJ*, 871, 100
- Huang, J., Andrews, S. M., Dullemond, C. P., et al. 2018, *ApJ*, 869, L42
- Huang, J. & Öberg, K. I. 2015, *ApJ*, 809, L26
- Huang, J., Öberg, K. I., Qi, C., et al. 2017, *ApJ*, 835, 231
- Hughes, A. M., Wilner, D. J., Andrews, S. M., Qi, C., & Hogerheijde, M. R. 2011, *ApJ*, 727, 85
- Hughes, A. M., Wilner, D. J., Calvet, N., et al. 2007, *ApJ*, 664, 536
- Ivezić, Z. & Elitzur, M. 1997, *MNRAS*, 287, 799
- Izidoro, A. & Raymond, S. N. 2018, *Formation of Terrestrial Planets*, 142
- Jacobsen, S. K., Jørgensen, J. K., van der Wiel, M. H. D., et al. 2018, *A&A*, 612, A72
- Johansen, A. & Lambrechts, M. 2017, *Annual Review of Earth and Planetary Sciences*, 45, 359
- Johansen, A., Oishi, J. S., Mac Low, M.-M., et al. 2007, *Nature*, 448, 1022
- Johnstone, D., Boonman, A. M. S., & van Dishoeck, E. F. 2003, *A&A*, 412, 157
- Johnstone, D., Hendricks, B., Herczeg, G. J., & Bruderer, S. 2013, *ApJ*, 765, 133
- Jørgensen, J. K. 2004, *A&A*, 424, 589
- Jørgensen, J. K., Bourke, T. L., Myers, P. C., et al. 2007, *ApJ*, 659, 479
- Jørgensen, J. K., Bourke, T. L., Myers, P. C., et al. 2005, *ApJ*, 632, 973
- Jørgensen, J. K., Favre, C., Bisschop, S. E., et al. 2012, *ApJ*, 757, L4
- Jørgensen, J. K., Hogerheijde, M. R., van Dishoeck, E. F., Blake, G. A., & Schöier, F. L. 2004a, *A&A*, 413, 993
- Jørgensen, J. K., Müller, H. S. P., Calcutt, H., et al. 2018, *A&A*, 620, A170
- Jørgensen, J. K., Schöier, F. L., & van Dishoeck, E. F. 2004b, *A&A*, 416, 603
- Jørgensen, J. K., van der Wiel, M. H. D., Coutens, A., et al. 2016, *A&A*, 595, A117
- Jørgensen, J. K. & van Dishoeck, E. F. 2010, *ApJ*, 710, L72
- Jørgensen, J. K., van Dishoeck, E. F., Visser, R., et al. 2009, *A&A*, 507, 861
- Jørgensen, J. K., Visser, R., Sakai, N., et al. 2013, *ApJ*, 779, L22

- Jørgensen, J. K., Visser, R., Williams, J. P., & Bergin, E. A. 2015, *A&A*, 579, A23
- Kaifu, N., Ohishi, M., Kawaguchi, K., et al. 2004, *PASJ*, 56, 69
- Kama, M., Bruderer, S., van Dishoeck, E. F., et al. 2016, *A&A*, 592, A83
- Kastner, J. H., Qi, C., Gorti, U., et al. 2015, *ApJ*, 806, 75
- Keene, J. & Masson, C. R. 1990, *ApJ*, 355, 635
- Kennicutt, R. C. & Evans, N. J. 2012, *ARA&A*, 50, 531
- Kenyon, S. J., Calvet, N., & Hartmann, L. 1993, *ApJ*, 414, 676
- Kenyon, S. J. & Hartmann, L. 1987, *ApJ*, 323, 714
- Kenyon, S. J. & Hartmann, L. 1995, *ApJS*, 101, 117
- Kenyon, S. J., Hartmann, L. W., Strom, K. M., & Strom, S. E. 1990, *AJ*, 99, 869
- Kokubo, E. & Ida, S. 1996, *Icarus*, 123, 180
- Kounkel, M., Hartmann, L., Loinard, L., et al. 2017, *ApJ*, 834, 142
- Kratter, K. & Lodato, G. 2016, *ARA&A*, 54, 271
- Kratter, K. M., Murray-Clay, R. A., & Youdin, A. N. 2010, *ApJ*, 710, 1375
- Krijt, S., Schwarz, K. R., Bergin, E. A., & Ciesla, F. J. 2018, *ApJ*, 864, 78
- Kristensen, L. E. & Dunham, M. M. 2018, *A&A*, 618, A158
- Kristensen, L. E., van Dishoeck, E. F., Bergin, E. A., et al. 2012, *A&A*, 542, A8
- Kruijer, T. S., Burkhardt, C., Budde, G., & Kleine, T. 2017, *Proceedings of the National Academy of Science*, 114, 6712
- Kuznetsova, A., Hartmann, L., & Heitsch, F. 2019, *ApJ*, 876, 33
- Kwon, W., Looney, L. W., Mundy, L. G., Chiang, H.-F., & Kemball, A. J. 2009, *ApJ*, 696, 841
- Lada, C. J. 1987, in *IAU Symposium, Vol. 115, Star Forming Regions*, ed. M. Peimbert & J. Jugaku, 1–17
- Lambrechts, M. & Johansen, A. 2012, *A&A*, 544, A32
- Larson, R. B. 1969, *MNRAS*, 145, 271
- Laughlin, G. & Bodenheimer, P. 1994, *ApJ*, 436, 335
- Law, C. J., Ricci, L., Andrews, S. M., Wilner, D. J., & Qi, C. 2017, *AJ*, 154, 255
- Le Roy, L., Altwegg, K., Balsiger, H., et al. 2015, *A&A*, 583, A1
- Lee, C.-F. 2010, *ApJ*, 725, 712
- Lee, C.-F., Hirano, N., Palau, A., et al. 2009, *ApJ*, 699, 1584
- Lee, C.-F., Li, Z.-Y., Hirano, N., et al. 2018, *ApJ*, 863, 94
- Lee, C.-F., Li, Z.-Y., Ho, P. T. P., et al. 2017, *ApJ*, 843, 27
- Lee, J.-E. 2007, *Journal of Korean Astronomical Society*, 40, 83
- Lee, J.-E., Lee, S., Baek, G., et al. 2019, *Nature Astronomy*, 3, 314
- Li, X., Heays, A. N., Visser, R., et al. 2013, *A&A*, 555, A14
- Li, Z. Y., Banerjee, R., Pudritz, R. E., et al. 2014, in *Protostars and Planets VI*, ed. H. Beuther, R. S. Klessen, C. P. Dullemond, & T. Henning, 173
- Lin, D. N. C. & Pringle, J. E. 1987, *MNRAS*, 225, 607
- Lindberg, J. E., Jørgensen, J. K., Brinch, C., et al. 2014, *A&A*, 566, A74
- Linnartz, H., Ioppolo, S., & Fedoseev, G. 2015, *arXiv e-prints* [[arXiv:1507.02729](https://arxiv.org/abs/1507.02729)]
- Linsky, J. L. 2007, *Space Sci. Rev.*, 130, 367
- Lizano, S. & Galli, D. 2015, in *Astrophysics and Space Science Library, Vol. 407, Magnetic Fields in Diffuse Media*, ed. A. Lazarian, E. M. de Gouveia Dal Pino, & C. Melioli, 459



- Lommen, D., Jørgensen, J. K., van Dishoeck, E. F., & Crapsi, A. 2008, *A&A*, 481, 141
- Long, F., Herczeg, G. J., Pascucci, I., et al. 2017, *ApJ*, 844, 99
- Long, F., Pinilla, P., Herczeg, G. J., et al. 2018, *ApJ*, 869, 17
- Loomis, R. A., Cleeves, L. I., Öberg, K. I., et al. 2018, *ApJ*, 859, 131
- Loomis, R. A., Cleeves, L. I., Öberg, K. I., Guzman, V. V., & Andrews, S. M. 2015, *ApJ*, 809, L25
- Looney, L. W., Mundy, L. G., & Welch, W. J. 2000, *ApJ*, 529, 477
- Looney, L. W., Mundy, L. G., & Welch, W. J. 2003, *ApJ*, 592, 255
- Lynden-Bell, D. & Pringle, J. E. 1974, *MNRAS*, 168, 603
- Madhusudhan, N., Amin, M. A., & Kennedy, G. M. 2014, *ApJ*, 794, L12
- Maeda, A., Medvedev, I. R., Winnemisser, M., et al. 2008, *ApJS*, 176, 543
- Manara, C. F., Morbidelli, A., & Guillot, T. 2018, *A&A*, 618, L3
- Mangum, J. G. & Wootten, A. 1993, *ApJS*, 89, 123
- Manigand, S., Calcutt, H., Jørgensen, J. K., et al. 2019, *A&A*, 623, A69
- Maret, S., Belloche, A., Maury, A. J., et al. 2014, *A&A*, 563, L1
- Maret, S., Bergin, E. A., & Lada, C. J. 2006, *Nature*, 442, 425
- Mathews, G. S., Klaassen, P. D., Juhász, A., et al. 2013, *A&A*, 557, A132
- Maury, A. J., André, P., Hennebelle, P., et al. 2010, *A&A*, 512, A40
- Maury, A. J., André, P., Testi, L., et al. 2019, *A&A*, 621, A76
- Maury, A. J., Belloche, A., André, P., et al. 2014, *A&A*, 563, L2
- van 't Hoff, M. L. R., Walsh, C., Kama, M., Facchini, S., & van Dishoeck, E. F. 2017, *A&A*, 599, A101
- McClure, M. K., Bergin, E. A., Cleeves, L. I., et al. 2016, *ApJ*, 831, 167
- McElroy, D., Walsh, C., Markwick, A. J., et al. 2013, *A&A*, 550, A36
- McGuire, B. A. 2018, *ApJS*, 239, 17
- McGuire, B. A., Burkhardt, A. M., Kalenskii, S., et al. 2018, *Science*, 359, 202
- McMullin, J. P., Waters, B., Schiebel, D., Young, W., & Golap, K. 2007, in *Astronomical Society of the Pacific Conference Series*, Vol. 376, *Astronomical Data Analysis Software and Systems XVI*, ed. R. A. Shaw, F. Hill, & D. J. Bell, 127
- Mellon, R. R. & Li, Z.-Y. 2008, *ApJ*, 681, 1356
- Melnick, G. J. 2009, in *Astronomical Society of the Pacific Conference Series*, Vol. 417, *Submillimeter Astrophysics and Technology: a Symposium Honoring Thomas G. Phillips*, ed. D. C. Lis, J. E. Vaillancourt, P. F. Goldsmith, T. A. Bell, N. Z. Scoville, & J. Zmuidzinas, 59
- Min, M., Dullemond, C. P., Kama, M., & Dominik, C. 2011, *Icarus*, 212, 416
- Minissale, M., Dulieu, F., Cazaux, S., & Hocuk, S. 2016, *A&A*, 585, A24
- Miotello, A., Testi, L., Lodato, G., et al. 2014, *A&A*, 567, A32
- Miotello, A., van Dishoeck, E. F., Williams, J. P., et al. 2017, *A&A*, 599, A113
- Mordasini, C., van Boekel, R., Mollière, P., Henning, T., & Benneke, B. 2016, *ApJ*, 832, 41
- Müller, H. S. P., Gendriesch, R., Margulès, L., et al. 2000, *Physical Chemistry Chemical Physics (Incorporating Faraday Transactions)*, 2
- Müller, H. S. P. & Lewen, F. 2017, *Journal of Molecular Spectroscopy*, 331, 28
- Müller, H. S. P., Maeda, A., Thorwirth, S., et al. 2019, *A&A*, 621, A143

- Müller, H. S. P., Schlöder, F., Stutzki, J., & Winnewisser, G. 2005, *Journal of Molecular Structure*, 742, 215
- Müller, H. S. P., Thorwirth, S., Roth, D. A., & Winnewisser, G. 2001, *A&A*, 370, L49
- Mumma, M. J. & Charnley, S. B. 2011, *ARA&A*, 49, 471
- Mundy, L. G., Wootten, A., Wilking, B. A., Blake, G. A., & Sargent, A. I. 1992, *ApJ*, 385, 306
- Murillo, N. M., Bruderer, S., van Dishoeck, E. F., et al. 2015, *A&A*, 579, A114
- Murillo, N. M., Lai, S.-P., Bruderer, S., Harsono, D., & van Dishoeck, E. F. 2013, *A&A*, 560, A103
- Murillo, N. M., van Dishoeck, E. F., van der Wiel, M. H. D., et al. 2018, *A&A*, 617, A120
- Nomura, H., Tsukagoshi, T., Kawabe, R., et al. 2016, *ApJ*, 819, L7
- Notsu, S., Akiyama, E., Booth, A., et al. 2019, *ApJ*, 875, 96
- Öberg, K. I., Fuchs, G. W., Awad, Z., et al. 2007, *ApJ*, 662, L23
- Öberg, K. I., Furuya, K., Loomis, R., et al. 2015a, *ApJ*, 810, 112
- Öberg, K. I., Guzmán, V. V., Furuya, K., et al. 2015b, *Nature*, 520, 198
- Öberg, K. I., Guzmán, V. V., Merchantz, C. J., et al. 2017, *ApJ*, 839, 43
- Öberg, K. I., Murray-Clay, R., & Bergin, E. A. 2011, *ApJ*, 743, L16
- Öberg, K. I., Qi, C., Fogel, J. K. J., et al. 2010, *ApJ*, 720, 480
- Offner, S. S. R., Dunham, M. M., Lee, K. I., Arce, H. G., & Fielding, D. B. 2016, *ApJ*, 827, L11
- Offner, S. S. R., Kratter, K. M., Matzner, C. D., Krumholz, M. R., & Klein, R. I. 2010, *ApJ*, 725, 1485
- Ohashi, N., Hayashi, M., Ho, P. T. P., & Momose, M. 1997, *ApJ*, 475, 211
- Ohashi, N., Saigo, K., Aso, Y., et al. 2014, *ApJ*, 796, 131
- Okuzumi, S., Tanaka, H., Kobayashi, H., & Wada, K. 2012, *ApJ*, 752, 106
- Ormel, C. W. & Klahr, H. H. 2010, *A&A*, 520, A43
- Ortiz-León, G. N., Loinard, L., Dzib, S. A., et al. 2018, *ApJ*, 865, 73
- Oya, Y., Sakai, N., Lefloch, B., et al. 2015, *ApJ*, 812, 59
- Oya, Y., Sakai, N., López-Sepulcre, A., et al. 2016, *ApJ*, 824, 88
- Paardekooper, D. M., Fedoseev, G., Riedo, A., & Linnartz, H. 2016, *A&A*, 596, A72
- Padovani, M., Hennebelle, P., & Galli, D. 2013, *A&A*, 560, A114
- Padovani, M., Hennebelle, P., Marcowith, A., & Ferrière, K. 2015, *A&A*, 582, L13
- Padovani, M., Marcowith, A., Hennebelle, P., & Ferrière, K. 2016, *A&A*, 590, A8
- Pagani, L., Favre, C., Goldsmith, P. F., et al. 2017, *A&A*, 604, A32
- Pagani, L., Steinacker, J., Bacmann, A., Stutz, A., & Henning, T. 2010, *Science*, 329, 1622
- Pascucci, I., Testi, L., Herczeg, G. J., et al. 2016, *ApJ*, 831, 125
- Pech, G., Loinard, L., Chandler, C. J., et al. 2010, *ApJ*, 712, 1403
- Persson, M. V., Harsono, D., Tobin, J. J., et al. 2016, *A&A*, 590, A33
- Persson, M. V., Jørgensen, J. K., Müller, H. S. P., et al. 2018, *A&A*, 610, A54
- Persson, M. V., Jørgensen, J. K., & van Dishoeck, E. F. 2012, *A&A*, 541, A39
- Persson, M. V., Jørgensen, J. K., & van Dishoeck, E. F. 2013, *A&A*, 549, L3
- Persson, M. V., Jørgensen, J. K., van Dishoeck, E. F., & Harsono, D. 2014, *A&A*, 563, A74

- Phillips, T. G., van Dishoeck, E. F., & Keene, J. 1992, *ApJ*, 399, 533
- Pickering, E. C. 1890, *Annals of Harvard College Observatory*, 18, 113
- Pickett, H. M., Poynter, R. L., Cohen, E. A., et al. 1998, *JQSRT*, 60, 883
- Pineda, J. E., Maury, A. J., Fuller, G. A., et al. 2012, *A&A*, 544, L7
- Pinilla, P., Klarmann, L., Birnstiel, T., et al. 2016, *A&A*, 585, A35
- Pinilla, P., Pohl, A., Stammer, S. M., & Birnstiel, T. 2017, *ApJ*, 845, 68
- Pinte, C., Ménard, F., Duchêne, G., et al. 2018, *A&A*, 609, A47
- Podio, L., Bacciotti, F., Fedele, D., et al. 2019, *A&A*, 623, L6
- Pollack, J. B., Hubickyj, O., Bodenheimer, P., et al. 1996, *Icarus*, 124, 62
- Pontoppidan, K. M., Salyk, C., Bergin, E. A., et al. 2014, *Protostars and Planets VI*, 363
- Qi, C., Öberg, K. I., Andrews, S. M., et al. 2015, *ApJ*, 813, 128
- Qi, C., Öberg, K. I., & Wilner, D. J. 2013a, *ApJ*, 765, 34
- Qi, C., Öberg, K. I., Wilner, D. J., et al. 2013b, *Science*, 341, 630
- Raymond, S. N., Izidoro, A., & Morbidelli, A. 2019, Chapter in *Planetary Astrobiology*, ed. Victoria Meadows, Giada Arney, David Des Marais, and Britney Schmidt (The University of Arizona Press)
- Roberts, H. & Millar, T. J. 2007, *A&A*, 471, 849
- Rodgers, S. D. & Charnley, S. B. 2003, *ApJ*, 585, 355
- Ros, K. & Johansen, A. 2013, *A&A*, 552, A137
- Rubin, M., Altwegg, K., van Dishoeck, E. F., & Schwehm, G. 2015, *ApJ*, 815, L11
- Sadavoy, S. I., Di Francesco, J., André, P., et al. 2014, *ApJ*, 787, L18
- Sakai, N., Hanawa, T., Zhang, Y., et al. 2019, *Nature*, 565, 206
- Sakai, N., Oya, Y., Higuchi, A. E., et al. 2017, *MNRAS*, 467, L76
- Sakai, N., Oya, Y., Sakai, T., et al. 2014a, *ApJ*, 791, L38
- Sakai, N., Sakai, T., Hirota, T., et al. 2014b, *Nature*, 507, 78
- Sakai, N. & Yamamoto, S. 2013, *Chemical Reviews*, 113, 8981
- Salinas, V. N., Hogerheijde, M. R., Mathews, G. S., et al. 2017, *A&A*, 606, A125
- Schöier, F. L., Jørgensen, J. K., van Dishoeck, E. F., & Blake, G. A. 2002, *A&A*, 390, 1001
- Schöier, F. L., Jørgensen, J. K., van Dishoeck, E. F., & Blake, G. A. 2004, *A&A*, 418, 185
- Schöier, F. L., van der Tak, F. F. S., van Dishoeck, E. F., & Black, J. H. 2005, *A&A*, 432, 369
- Schoonenberg, D., Okuzumi, S., & Ormel, C. W. 2017, *A&A*, 605, L2
- Schoonenberg, D. & Ormel, C. W. 2017, *A&A*, 602, A21
- Schwarz, K. R., Bergin, E. A., Cleeves, L. I., et al. 2016, *ApJ*, 823, 91
- Schwarz, K. R., Bergin, E. A., Cleeves, L. I., et al. 2018, *ApJ*, 856, 85
- Schwarz, K. R., Teague, R., & Bergin, E. A. 2019, *ApJ*, 876, L13
- Segura-Cox, D. M., Harris, R. J., Tobin, J. J., et al. 2016, *ApJ*, 817, L14
- Segura-Cox, D. M., Looney, L. W., Tobin, J. J., et al. 2018, *ApJ*, 866, 161
- Shakura, N. I. & Sunyaev, R. A. 1973, *A&A*, 24, 337
- Sheehan, P. D. & Eisner, J. A. 2017, *ApJ*, 851, 45
- Shu, F. H., Adams, F. C., & Lizano, S. 1987, *ARA&A*, 25, 23
- Sobolev, V. V. 1960, *Moving envelopes of stars*

- Stark, R., van der Tak, F. F. S., & van Dishoeck, E. F. 1999, *ApJ*, 521, L67
- Stäuber, P., Jørgensen, J. K., van Dishoeck, E. F., Doty, S. D., & Benz, A. O. 2006, *A&A*, 453, 555
- Stevenson, D. J. & Lunine, J. I. 1988, *Icarus*, 75, 146
- Strom, K. M. & Strom, S. E. 1993, *ApJ*, 412, L63
- Takakuwa, S., Saito, M., Lim, J., et al. 2012, *ApJ*, 754, 52
- Tanaka, H. & Ida, S. 1999, *Icarus*, 139, 350
- Taquet, V., Ceccarelli, C., & Kahane, C. 2012a, *ApJ*, 748, L3
- Taquet, V., Ceccarelli, C., & Kahane, C. 2012b, *A&A*, 538, A42
- Taquet, V., Charnley, S. B., & Sipilä, O. 2014, *ApJ*, 791, 1
- Taquet, V., Furuya, K., Walsh, C., & van Dishoeck, E. F. 2016a, *MNRAS*, 462, S99
- Taquet, V., López-Sepulcre, A., Ceccarelli, C., et al. 2015, *ApJ*, 804, 81
- Taquet, V., Peters, P. S., Kahane, C., et al. 2013, *A&A*, 550, A127
- Taquet, V., van Dishoeck, E. F., Swayne, M., et al. 2018, *A&A*, 618, A11
- Taquet, V., Wirström, E. S., & Charnley, S. B. 2016b, *ApJ*, 821, 46
- Terebey, S., Shu, F. H., & Cassen, P. 1984, *ApJ*, 286, 529
- Testi, L., Birnstiel, T., Ricci, L., et al. 2014, *Protostars and Planets VI*, 339
- Thi, W.-F., van Zadelhoff, G.-J., & van Dishoeck, E. F. 2004, *A&A*, 425, 955
- Thommes, E. W., Duncan, M. J., & Levison, H. F. 2003, *Icarus*, 161, 431
- Tielens, A. G. G. M. 2013, *Reviews of Modern Physics*, 85, 1021
- Tielens, A. G. G. M. & Hagen, W. 1982, *A&A*, 114, 245
- Tobin, J. J., Bergin, E. A., Hartmann, L., et al. 2013a, *ApJ*, 765, 18
- Tobin, J. J., Dunham, M. M., Looney, L. W., et al. 2015a, *ApJ*, 798, 61
- Tobin, J. J., Hartmann, L., Bergin, E., et al. 2012a, *ApJ*, 748, 16
- Tobin, J. J., Hartmann, L., Calvet, N., & D'Alessio, P. 2008, *ApJ*, 679, 1364
- Tobin, J. J., Hartmann, L., Chiang, H.-F., et al. 2012b, *Nature*, 492, 83
- Tobin, J. J., Hartmann, L., Chiang, H.-F., et al. 2013b, *ApJ*, 771, 48
- Tobin, J. J., Hartmann, L., & Loinard, L. 2010, *ApJ*, 722, L12
- Tobin, J. J., Kratter, K. M., Persson, M. V., et al. 2016a, *Nature*, 538, 483
- Tobin, J. J., Looney, L. W., Li, Z.-Y., et al. 2016b, *ApJ*, 818, 73
- Tobin, J. J., Looney, L. W., Wilner, D. J., et al. 2015b, *ApJ*, 805, 125
- Tomida, K., Tomisaka, K., Matsumoto, T., et al. 2010, *ApJ*, 714, L58
- Torres, R. M., Loinard, L., Mioduszewski, A. J., & Rodríguez, L. F. 2007, *ApJ*, 671, 1813
- Tripathi, A., Andrews, S. M., Birnstiel, T., & Wilner, D. J. 2017, *ApJ*, 845, 44
- Tsukamoto, Y., Okuzumi, S., Iwasaki, K., Machida, M. N., & Inutsuka, S.-i. 2017, *PASJ*, 69, 95
- Turner, N. J., Fromang, S., Gammie, C., et al. 2014, *Protostars and Planets VI*, 411
- Tychoniec, Ł., Tobin, J. J., Karska, A., et al. 2018, *ApJS*, 238, 19
- Ulrich, R. K. 1976, *ApJ*, 210, 377
- van der Marel, N., Dong, R., di Francesco, J., Williams, J. P., & Tobin, J. 2019, *ApJ*, 872, 112
- van der Tak, F. 2011, in *IAU Symposium*, Vol. 280, *The Molecular Universe*, ed. J. Cernicharo & R. Bachiller, 449–460

- van der Tak, F. F. S., Black, J. H., Schöier, F. L., Jansen, D. J., & van Dishoeck, E. F. 2007, *A&A*, 468, 627
- van Dishoeck, E. F. 2014, *Faraday Discussions*, 168, 9
- van Dishoeck, E. F. & Black, J. H. 1988, *ApJ*, 334, 771
- van Dishoeck, E. F., Blake, G. A., Jansen, D. J., & Groesbeck, T. D. 1995, *ApJ*, 447, 760
- van Dishoeck, E. F., Herbst, E., & Neufeld, D. A. 2013, *Chemical Reviews*, 113, 9043
- van Dishoeck, E. F., Jansen, D. J., & Phillips, T. G. 1993, *A&A*, 279, 541
- van Dishoeck, E. F., Kristensen, L. E., Benz, A. O., et al. 2011, *PASP*, 123, 138
- van Leeuwen, F. 2007, *A&A*, 474, 653
- van 't Hoff, M. L. R., Persson, M. V., Harsono, D., et al. 2018a, *A&A*, 613, A29
- van 't Hoff, M. L. R., Tobin, J. J., Harsono, D., & van Dishoeck, E. F. 2018b, *A&A*, 615, A83
- van 't Hoff, M. L. R., Tobin, J. J., Trapman, L., et al. 2018c, *ApJ*, 864, L23
- van Terwisga, S. E., van Dishoeck, E. F., Ansdell, M., et al. 2018, *A&A*, 616, A88
- van Zadelhoff, G.-J., van Dishoeck, E. F., Thi, W.-F., & Blake, G. A. 2001, *A&A*, 377, 566
- Visser, R. & Bergin, E. A. 2012, *ApJ*, 754, L18
- Visser, R., Bergin, E. A., & Jørgensen, J. K. 2015, *A&A*, 577, A102
- Visser, R., Doty, S. D., & van Dishoeck, E. F. 2011, *A&A*, 534, A132
- Visser, R., Kristensen, L. E., Bruderer, S., et al. 2012, *A&A*, 537, A55
- Visser, R., van Dishoeck, E. F., & Black, J. H. 2009a, *A&A*, 503, 323
- Visser, R., van Dishoeck, E. F., Doty, S. D., & Dullemond, C. P. 2009b, *A&A*, 495, 881
- Vorobyov, E. I. 2009, *ApJ*, 704, 715
- Vorobyov, E. I., Baraffe, I., Harries, T., & Chabrier, G. 2013, *A&A*, 557, A35
- Wada, K., Tanaka, H., Suyama, T., Kimura, H., & Yamamoto, T. 2011, *ApJ*, 737, 36
- Wakelam, V. & Herbst, E. 2008, *ApJ*, 680, 371
- Wakelam, V., Loison, J.-C., Herbst, E., et al. 2015, *ApJS*, 217, 20
- Walsh, C., Loomis, R. A., Öberg, K. I., et al. 2016, *ApJ*, 823, L10
- Walsh, C., Millar, T. J., & Nomura, H. 2010, *ApJ*, 722, 1607
- Walsh, C., Millar, T. J., Nomura, H., et al. 2014, *A&A*, 563, A33
- Walsh, C., Nomura, H., Millar, T. J., & Aikawa, Y. 2012, *ApJ*, 747, 114
- Walsh, C., Nomura, H., & van Dishoeck, E. 2015, *A&A*, 582, A88
- Ward-Thompson, D., André, P., Crutcher, R., et al. 2007, *Protostars and Planets V*, 33
- Watanabe, N. & Kouchi, A. 2002, *ApJ*, 571, L173
- Weidenschilling, S. J. 1977, *MNRAS*, 180, 57
- Whipple, F. L. 1972, in *From Plasma to Planet*, ed. A. Elvius, 211
- Whitney, B. A., Wood, K., Bjorkman, J. E., & Wolff, M. J. 2003, *ApJ*, 591, 1049
- Wiesenfeld, L. & Faure, A. 2013, *MNRAS*, 432, 2573
- Willacy, K. & Woods, P. M. 2009, *ApJ*, 703, 479
- Williams, J. P., Cieza, L., Hales, A., et al. 2019, *ApJ*, 875, L9
- Wilson, T. L. & Rood, R. 1994, *ARA&A*, 32, 191
- Wolf, S., Padgett, D. L., & Stapelfeldt, K. R. 2003, *ApJ*, 588, 373

- Woodall, J., Agúndez, M., Markwick-Kemper, A. J., & Millar, T. J. 2007, *A&A*, 466, 1197
- Wootten, A. 1989, *ApJ*, 337, 858
- Wurster, J., Bate, M. R., & Price, D. J. 2018, *MNRAS*, 480, 4434
- Yang, B., Stancil, P. C., Balakrishnan, N., & Forrey, R. C. 2010, *ApJ*, 718, 1062
- Yen, H.-W., Koch, P. M., Takakuwa, S., et al. 2017, *ApJ*, 834, 178
- Yen, H.-W., Takakuwa, S., Ohashi, N., et al. 2014, *ApJ*, 793, 1
- Yen, H.-W., Takakuwa, S., Ohashi, N., & Ho, P. T. P. 2013, *ApJ*, 772, 22
- Yorke, H. W., Bodenheimer, P., & Laughlin, G. 1993, *ApJ*, 411, 274
- Youdin, A. N. & Goodman, J. 2005, *ApJ*, 620, 459
- Young, C. H. & Evans, II, N. J. 2005, *ApJ*, 627, 293
- Zakharenko, O., Motiyenko, R. A., Margulès, L., & Huet, T. R. 2015, *Journal of Molecular Spectroscopy*, 317, 41
- Zhang, K., Bergin, E. A., Blake, G. A., Cleeves, L. I., & Schwarz, K. R. 2017, *Nature Astronomy*, 1, 0130
- Zhang, K., Blake, G. A., & Bergin, E. A. 2015, *ApJ*, 806, L7
- Zhang, K., Pontoppidan, K. M., Salyk, C., & Blake, G. A. 2013, *ApJ*, 766, 82
- Zhu, Z., Zhang, S., Jiang, Y.-F., et al. 2019, *ApJ*, 877, L18



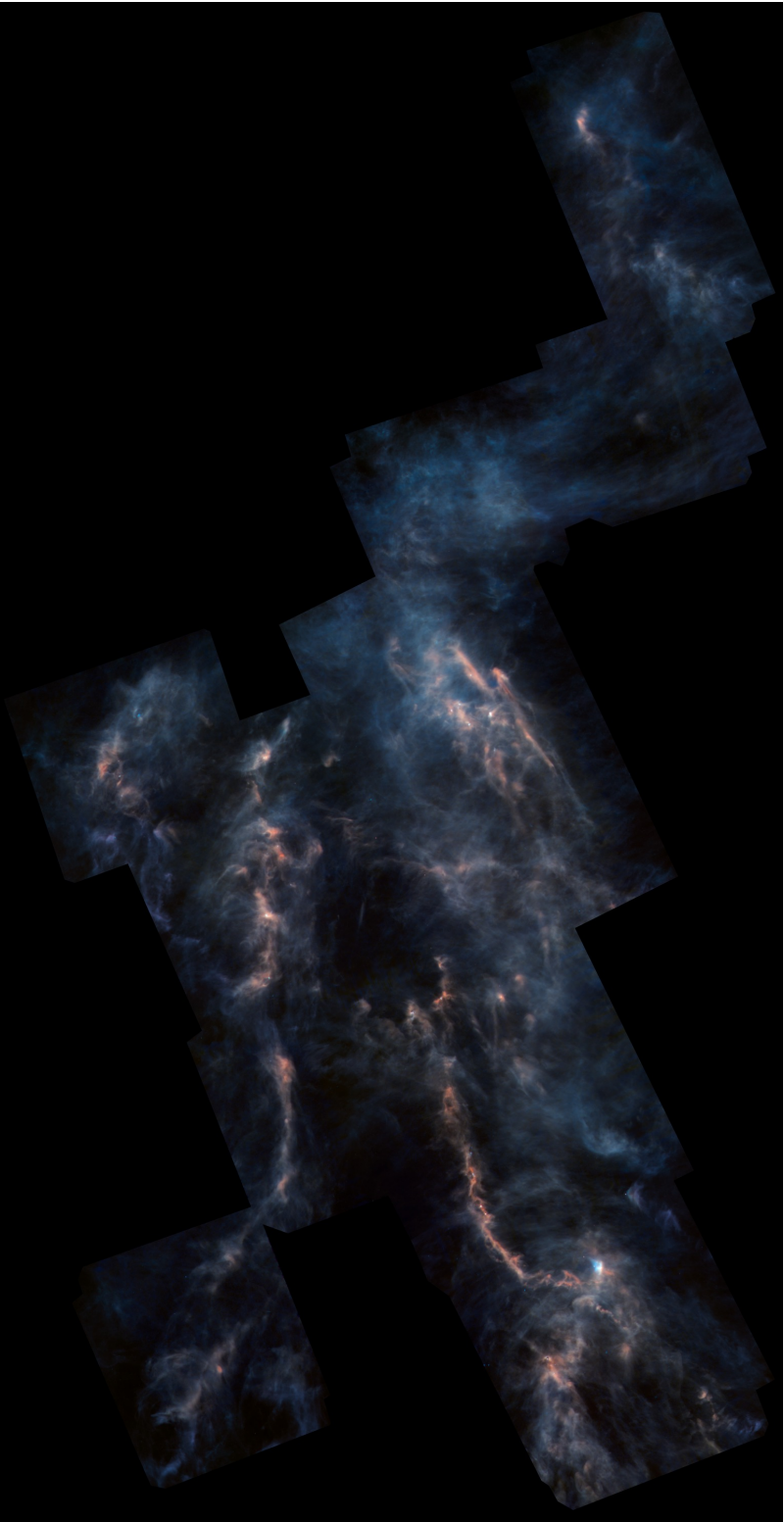
# Nederlandse samenvatting

Al eeuwenlang staren mensen naar de sterren en planeten aan de nachtelijke hemel en verwonderen zich over onze plaats in het universum. Waar komen we vandaan? En zijn we alleen? In de afgelopen decennia zijn er meer dan 3000 planeten ontdekt rond andere sterren dan onze zon. Hiermee is het bestaan van leven op andere plaatsen in het heelal een reële mogelijkheid geworden. De waargenomen planetenstelsels vertonen een grote diversiteit in onder andere het aantal en type planeten dat aanwezig is en de afstand van deze planeten tot de ster. Ondanks deze verscheidenheid lijken de andere planetenstelsels niet op ons zonnestelsel. Dit roept dan de vraag op of de aanwezigheid van leven ook zeldzaam is. Een manier om antwoord te vinden op deze vraag is het nauwkeurig bestuderen van de ontdekte planeten. Door bijvoorbeeld te achterhalen wat de samenstelling is van hun atmosfeer en die te vergelijken met wat we denken dat de vereisten zijn voor leven, kunnen we inschatten op hoeveel van de ontdekte planeten mogelijk leven kan bestaan. Een tweede manier is om juist te kijken naar het materiaal waaruit planeten nog gevormd zullen worden. De samenstelling van deze bouwstenen kan vergeleken worden met de compositie van kometen. Omdat kometen overblijfselen zijn uit de tijd waarin de planeten in ons zonnestelsel gevormd zijn, kan deze vergelijking laten zien of de condities in het jonge zonnestelsel uniek waren of veelvuldig voorkomen. De opgedane kennis over het planetaire bouw materiaal kan ook gebruikt worden in modellen om te voorspellen hoe groot de kans is dat onder bepaalde omstandigheden een aardachtige planeet gevormd wordt. Ten slotte kunnen we te weten komen of de complexe ingrediënten voor leven al gevormd worden in de ruimte, en vervolgens op planeten terechtkomen waar dan leven kan ontstaan, of dat leven moet ontspringen uit hele simpele moleculen die aanwezig zijn op het planeetoppervlak. Dit proefschrift past de tweede benadering toe en bestudeert het materiaal dat aanwezig is als planeetvorming begint.

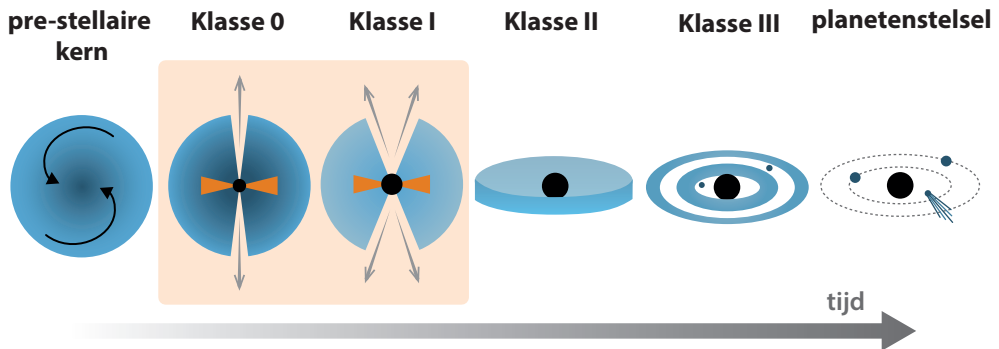
## Vorming van sterren en planeten

De vorming van sterren en planeten begint in gigantische moleculaire wolken. Een voorbeeld hiervan is zichtbaar in **Fig. 1**. Zulke wolken bestaan uit gas en minuscule stofdeeltjes. De meest voorkomende gassen zijn waterstof ( $H_2$ ) en helium (He), maar er zijn ook kleine hoeveelheden koolstof (C), zuurstof (O) en stikstof (N) aanwezig. De evolutie van wolk tot planetenstelsel kan opgedeeld worden in verschillende stadia, zoals afgebeeld in **Fig. 2**. Gebieden in de wolk waar de dichtheid hoog is (rood in **Fig. 1**) kunnen onder invloed van de zwaartekracht ineenstorten. In het binnenste gedeelte van zo'n instortende *pre-stellaire kern* wordt dan een jonge ster, een zogenaamde *protoster*,





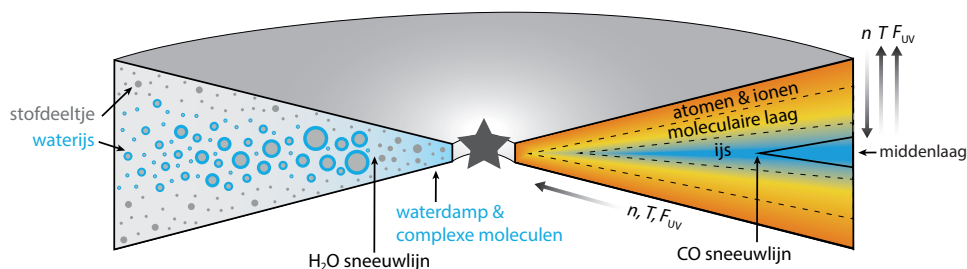
**Figuur 1:** Foto van de Taurus Moleculaire wolk genomen met de ruimtetelescoop *Herschel*. Deze uitgestrekte interstellaire wolken bevinden zich op 450 lichtjaar afstand en vormen de kraankamers waarin sterren geboren worden. De meeste sterren worden gevormd in gebieden met een grote hoeveelheid gas en stof (weergegeven in rood). De ijlere gedeelten van de wolk zijn blauw gekleurd. De jonge schijven die in **Hoofstuk 3** en **4** worden bestudeerd, bevinden zich in dit ster vormingsgebied. De afbeelding bestaat een doorsnede van 110 lichtjaar. Afbeelding van: ESA/Herschel/NASA/JPL-Caltech CC BY-SA 3.0 IGO; R. Hurt (JPL-Caltech).



**Figuur 2:** Schematische weergave van de verschillende fasen gedurende de vorming van een ster en planeten, zoals beschreven in de tekst. Het onderwerp van dit proefschrift is het vroege stadium waarin de jonge ster (zwarte cirkel) en schijf (oranje) nog omhuld zijn met materiaal van de instortende wolk (aangegeven met een oranje vak).

geboren. Er blijft materiaal vanuit de wolk neerregenen, maar omdat het hoekmoment van de langzaam roterende wolk behouden moet blijven valt deze materie niet direct op de protoster. In plaats daarvan wordt er een ronddraaiende schijf gevormd. In eerste instantie worden de jonge ster en schijf omhuld door gas en stof (Klasse 0 en Klasse I objecten). Gaandeweg verdwijnt dit omhulsel, doordat een deel van het materiaal via de schijf in de ster terecht komt en een ander deel door de ster wordt weggeblazen via krachtige straalstromen. De schijf wordt nu een *protoplanetaire schijf* genoemd. De stofdeeltjes in de schijf groeien door onderlinge botsingen uit tot rotsblokken en worden uiteindelijk rotsachtige planeten. Er wordt een gasplaneet gevormd als een lichaam genoeg massa heeft om een grote hoeveelheid gas aan te trekken en vast te houden. De vorming van planeten, het neerregenen van schijfmateriaal op de jonge ster en het wegblazen van gas door de ster zorgt ervoor dat de schijf verdwijnt (Klasse III objecten), zodat uiteindelijk een ster overblijft die omringd wordt door planeten.

Omdat protoplanetaire schijven het materiaal bevatten waaruit planeten ontstaan, zijn deze systemen uitgebreid bestudeerd, zowel aan de hand van waarnemingen als met behulp van fysische en chemische modellen. Daardoor hebben we nu een goed beeld van de globale structuur van deze schijven (zie **Fig. 3**). Het binnenste gedeelte en het oppervlak van de schijf vangen het meeste sterlicht op en zijn daardoor het warmst. De UV-straling van de ster zorgt er ook voor dat de meeste moleculen in deze gebieden afgebroken worden tot losse atomen en ionen. Dieper in de schijf waar de UV-straling niet kan doordringen, kunnen wel moleculen bestaan. Een heel scala aan simpele moleculen (minder dan zes atomen) is hier waargenomen, zoals koolstofmonoxide (CO), water (H<sub>2</sub>O) en formaldehyde (H<sub>2</sub>CO). In het binnenste gedeelte van de schijf wordt de temperatuur zo laag dat de meeste moleculen vastvriezen aan de stofdeeltjes. De specifieke temperatuur waarbij dit gebeurt, verschilt per molecuul. Water bevriest bijvoorbeeld bij temperaturen van ongeveer 100 K (dichtbij de ster), terwijl vluchtige moleculen, zoals CO, pas in het buitenste gedeelte van de schijf bevriezen waar de temperatuur onder de 20 K zakt. De plaats waar de overgang van gas naar ijs plaatsvindt heet een *sneeuwlijn*. Weten waar de verschillende sneeuwlijnen zich precies bevinden, is cruciaal om te begrijpen wat voor soort planeten gevormd kunnen worden, omdat de samenstelling van het gas en ijs - de bouwstenen voor planeten - op deze plaatsen sterk verandert.



**Figuur 3:** Schematische weergave van de fysieke en chemische structuur van een schijf. De *linkerkant* laat zien dat stofdeeltjes (grijs) in het grootste gedeelte van de schijf bedekt zijn met waterijs (blauw). Waterdamp is alleen aanwezig in het binnenste van de schijf, binnen de watersneeuwlijn, en aan het oppervlak. De groei van minuscule stofdeeltjes tot rotsblokken is het meest efficiënt net buiten de watersneeuwlijn. De *rechterkant* laat de chemische structuur zien die het gevolg is van verticale en radiale gradiënten in de dichtheid ( $n$ ), temperatuur ( $T$ ) en sterkte van de UV-straling ( $F_{UV}$ ), zoals beschreven in de tekst. Water bevriest bij redelijk hoge temperaturen (100 K) en dus dicht bij de ster (zoals *links* te zien is), terwijl CO pas bevriest bij 20 K in het buitenste gedeelte van de schijf (*rechts*).

## Dit proefschrift

Lange tijd werd gedacht dat planeetvorming zich afspeelt in protoplanetaire schijven. De laatste jaren is er echter steeds meer bewijs gekomen dat de eerste stappen al eerder plaatsvinden, als de schijf nog omhuld is door gas en stof. Om te begrijpen hoe planeten gevormd worden en wanneer er een aardachtige planeet kan ontstaan, moeten we dus de omstandigheden in deze jonge schijven kennen. Vanwege hun omhulsel zijn jonge schijven moeilijker te bestuderen dan oudere protoplanetaire schijven, maar met de Atacama Large Millimeter/submillimeter Array (ALMA; zie **Fig. 4**) is het nu mogelijk om de schijf van het omhulsel te onderscheiden. ALMA is een telescoop in Chili bestaand uit 66 schotels die samenwerken om heel gevoelige waarnemingen te doen van submillimeterstraling: het licht dat wordt uitgezonden door het stof en de moleculen in de schijf. Dit proefschrift richt zich hoofdzakelijk op de temperatuur in jonge schijven, omdat dit een cruciale rol speelt in de verdere evolutie van de schijf en de chemische samenstelling van de planetaire bouwstenen. De volgende twee hoofdvragen worden behandeld:

- Zijn jonge schijven, net als protoplanetaire schijven, koud ( $\lesssim 20\text{--}25$  K), zodat er een groot gebied is waar koolstofmonoxide (CO) is uitgevoren? Of zijn jonge schijven te warm voor CO-ijs ( $\gtrsim 20\text{--}25$  K), zoals voorspeld door modellen?
- Bevatten jonge schijven grote hoeveelheden complexe organische moleculen? En zo ja, is de chemische samenstelling van deze schijven dan gelijk aan dat van jongere objecten waarin nog geen schijf gevormd is?



**Figuur 4:** Luchtfoto van de Atacama Large Millimeter/submillimeter Array (ALMA) op het Chajnantor-plateau in de Chileense Andes (5000 m hoogte). Een deel van de in totaal 66 schotels is zichtbaar. In **Hoofdstuk 3, 4, 6, 7 en 8** wordt gebruik gemaakt van waarnemingen die gedaan zijn met deze telescoop. Afbeelding van: Clem & Adri Bacri-Normier (wingsfor-science.com)/ESO.

## De CO-sneeuwlijn

Het eerste gedeelte van dit proefschrift richt zich op de temperatuur waarbij koolstofmonoxide (CO) bevriest (20–25 K). Het is belangrijk om te weten waar in een schijf CO aan de stofdeeltjes vastgevroren zit, omdat CO één van de voornaamste bronnen van koolstof en zuurstof is. Bovendien is CO-ijs nodig om complexere moleculen te kunnen vormen. Zulke waarnemingen zijn echter niet triviaal omdat ijsmoleculen heel lastig waargenomen kunnen worden. Dit betekent dat de aanwezigheid van CO-ijs afgeleid moet worden uit de afwezigheid van CO-gas. Maar omdat CO-gas altijd aanwezig is in het oppervlak van de schijf, is het in de meeste gevallen niet mogelijk om de afwezigheid van gas in de middenlaag van de schijf te zien. Dit is vergelijkbaar met de rand van het poolijs willen waarnemen vanuit een vliegtuig op een bewolkte dag. Om dit probleem te omzeilen worden moleculen gebruikt die alleen in het gas kunnen voorkomen als CO is uitgevroren. Een voorbeeld van zo'n molecuul is  $\text{N}_2\text{H}^+$ ; dit wordt namelijk vernietigd door CO. In **Hoofdstuk 2** wordt een eenvoudig chemisch model gepresenteerd waarmee gekeken wordt hoe goed de CO-sneeuwlijn gevonden kan worden met  $\text{N}_2\text{H}^+$ . Uit deze studie blijkt dat  $\text{N}_2\text{H}^+$  inderdaad gebruikt kan worden om te bepalen waar de CO-sneeuwlijn is, maar hiervoor moeten wel een aantal chemische effecten en de fysische structuur van de schijf in beschouwing genomen worden.

Het feit dat er geen  $\text{N}_2\text{D}^+$  ( $\text{N}_2\text{H}^+$  met een deuteriumatoom in plaats van een waterstofatoom) is waargenomen in de jonge schijf L1527, suggereert daarom dat er geen

CO-ijs aanwezig is. In **Hoofdstuk 3** wordt gekeken of de temperatuur inderdaad te hoog is om CO-ijs te vormen in deze jonge schijf. Hiervoor wordt eerst gedemonstreerd dat de schijf van het omhulsel kan worden onderscheiden aan de hand van verschillen in de beweging tussen materiaal in de schijf en in het omhulsel. Vervolgens wordt aangetoond dat het direct geobserveerd kan worden als CO uitgevroren is in de middenlaag, omdat L1527 precies vanaf de zijkant wordt waargenomen. Het hierboven beschreven probleem, waarbij het niet mogelijk is om de afwezigheid van gas in de middenlaag van de schijf te zien, speelt in dit geval geen rol. De analyse van CO-waarnemingen laat zien dat deze jonge schijf te warm is voor CO-ijs, in tegenstelling tot oudere protoplanetaire schijven. Om de vraag te beantwoorden of dit in het algemeen het geval is, worden in **Hoofdstuk 4** vijf jonge schijven bestudeerd. In geen van deze schijven zijn duidelijke signalen zichtbaar dat CO uitgevroren is. In één van de schijven die van de zijkant waargenomen wordt, is formaldehyde ( $\text{H}_2\text{CO}$ ) alleen aanwezig in het schijfoppervlak. Omdat formaldehyde al bevriest bij ongeveer 50 K, wekken deze waarnemingen de suggestie dat de temperatuur in de middenlaag van deze schijf dus tussen de 20 en 50 K ligt: te warm voor CO-ijs maar koud genoeg om formaldehyde te laten bevriezen. Deze resultaten laten zien dat jonge schijven inderdaad warmer zijn dan oudere schijven.

## De watersneeuwlijn

Het tweede gedeelte van dit proefschrift richt zich op het binnenste gedeelte van de schijf waar het te warm is voor waterijs. Het is belangrijk om te weten waar water bevriest, omdat de groei van stofdeeltjes het meest efficiënt is net buiten de watersneeuwlijn (zie **Fig. 3**). Daarnaast wordt verondersteld dat aardachtige planeten binnen de watersneeuwlijn gevormd worden. Dit warme gebied is ook interessant omdat complexe organische moleculen (moleculen die opgebouwd zijn uit zes of meer atomen, waaronder koolstof), hier in de gasfase aanwezig zijn en dus waargenomen kunnen worden. Deze stoffen zijn mogelijk de voorlopers van prebiotische moleculen. Vanwege de grote hoeveelheid water in de atmosfeer is het heel lastig om water in astronomische objecten vanaf de grond te observeren en kunnen deze waarnemingen alleen gedaan worden via het veel minder voorkomende isotopoloog  $\text{H}_2^{18}\text{O}$ . De beste manier om de watersneeuwlijn te vinden is daarom door, net als voor CO, een ander molecuul te gebruiken.  $\text{H}^{13}\text{CO}^+$  wordt verwacht een geschikt molecuul te zijn, omdat het vernietigd wordt door waterdamp en dus vooral aanwezig is in gebieden waar water bevroren is. **Hoofdstuk 5** en **6** laten zien dat  $\text{H}^{13}\text{CO}^+$  inderdaad geschikt is om de watersneeuwlijn te vinden. Een *proof of concept* wordt geleverd in **Hoofdstuk 5**, waar de anticorrelatie tussen  $\text{H}_2^{18}\text{O}$  en  $\text{H}^{13}\text{CO}^+$  aangetoond wordt rond de protoster IRAS2A. Protosterren die nog geen schijf hebben zijn ideale kandidaten, omdat het gas en stof rond deze objecten veel warmer is. Hierdoor bevindt de watersneeuwlijn zich op grotere afstand van de ster. **Hoofdstuk 6** bevestigt deze conclusie met waarnemingen van  $\text{H}^{13}\text{CO}^+$  rond vier andere protosterren, maar dit hoofdstuk laat ook zien dat de fysische structuur rond de protosterren in acht genomen moet worden bij de interpretatie.

Omdat de watersneeuwlijn in schijven erg dicht bij de ster ligt, is er pas in één schijf een sneeuwlijnlocatie geopperd. Deze schijf (V883 Ori) bevindt zich rond een jonge ster die recentelijk een uitbarsting heeft ondergaan en daardoor tijdelijk een stuk helderder is. De schijf is hierdoor opgewarmd, waardoor de sneeuwlijn zich op grotere afstand bevindt. Deze claim is echter gedaan aan de hand van waarnemingen van het

stof, en de correlatie tussen structuren in het stof en sneeuwlijnen staat nog ter discussie. Methanol ( $\text{CH}_3\text{OH}$ ) is een molecuul dat voornamelijk binnen de watersneeuwlijn in het gas voorkomt. Waarnemingen van methanol in V883 Ori die in **Hoofdstuk 7** gepresenteerd worden, suggereren inderdaad dat de watersneeuwlijn veel verder van de protoster verwijderd kan zijn dan was afgeleid van de stofwaarnemingen. In deze observaties zijn ook zwakke signalen van methylformiaat en acetaldehyde zichtbaar. Zulke complexe moleculen blijken heel moeilijk waar te nemen in protoplanetaire schijven. Jonge schijven rond uitbarstende sterren zijn dus de meest geschikte objecten om de chemische complexiteit van planetaire bouwstenen te meten.

In **Hoofdstuk 8** wordt ten slotte de temperatuur bestudeerd van de schijfachtige structuur rond de protoster IRAS 16293A. Waarnemingen van thioformaldehyde ( $\text{H}_2\text{CS}$ ) spreken een eerdere analyse tegen die suggereerde dat er daadwerkelijk een schijf aanwezig is. Een temperatuurprofiel dat is afgeleid van de  $\text{H}_2\text{CS}$ -observaties laat zien dat de temperatuur overeenkomt met wat verwacht wordt voor het materiaal rond een protoster zonder schijf, behalve in het binnenste gedeelte dat nu met ALMA waargenomen kan worden. In dit gedeelte lijkt de temperatuur niet hoger te worden dan 150 K. Desalniettemin is het overal ongeveer 100 K warmer dan in de jonge schijf L1527. Dit is geheel in overeenstemming met de grotere helderheid van IRAS 16293A die zich in een vroeger evolutionair stadium bevindt dan L1527.

## Conclusies en toekomstperspectief

Dit proefschrift presenteert een aantal van de eerste observationele metingen van de temperatuur in jonge schijven en schijfachtige structuren. Deze waarnemingen suggereren dat de temperatuur afneemt in objecten die minder ingekapseld zijn in gas en stof, en minder heftige accretie hebben, zoals theoretisch voorspeld was. Er zijn nu waarnemingen van meer schijven nodig om deze evolutionaire trend te bevestigen en om gedetailleerdere vragen te beantwoorden, zoals wanneer zijn schijven ver genoeg afgekoeld om CO te laten bevriezen? Gebeurt dit al voordat het omhulsel van de schijf volledig verdwenen is? Dit proefschrift heeft laten zien dat de globale temperatuurstructuur bepaald kan worden met  $\text{N}_2\text{H}^+$  en  $\text{H}^{13}\text{CO}^+$ . Met zulke waarnemingen kan dus een grote populatie schijven globaal bestudeerd worden. Een gedetailleerder temperatuurprofiel kan vervolgens achterhaald worden aan de hand van moleculen zoals formaldehyde ( $\text{H}_2\text{CO}$ ) en thioformaldehyde ( $\text{H}_2\text{CS}$ ). Deze resultaten kunnen vervolgens gebruikt worden in modellen voor planeetvorming.

Een andere belangrijke stap in ons begrip van planeetvorming is de directe waarneming van de watersneeuwlijn in een schijf. Dit proefschrift laat zien dat  $\text{H}^{13}\text{CO}^+$  een veelbelovend molecuul is om de watersneeuwlijn te traceren. V883 Ori is de meest voor de hand liggende doelwit voor dergelijke waarnemingen, omdat de uitbarsting van de ster de sneeuwlijn in de schijf naar buiten heeft geschoven.

Verder levert dit proefschrift een stukje van de puzzel omtrent de oorsprong van de chemische samenstelling van het planetaire bouw materiaal. Een belangrijke open vraag is of deze compositie hetzelfde is als in de wolk waaruit de schijf gevormd is of dat er veranderingen optreden als het materiaal de schijf binnenkomt. Als het laatste het geval is, hoe groot zijn die veranderingen dan? Aan de ene kant laat de afwezigheid van CO-ijs in jonge schijven zien dat de samenstelling niet geheel gelijk is aan die voordat de ster geboren was, want in die fase was CO nagenoeg volledig uitgevroren. Aan de andere kant zorgt de afwezigheid van CO-ijs er voor dat er bijna

geen complexe moleculen gevormd kunnen worden in jonge schijven. De aanwezigheid van zulke moleculen in de V883 Ori schijf suggereert daarom dat in ieder geval een deel van de oorspronkelijke samenstelling behouden blijft. Andere open vragen blijven bijvoorbeeld hoe veel van het materiaal verandert en hoe groot deze veranderingen zijn. Toekomstige waarnemingen van jonge schijven rond uitbarstende sterren kunnen helpen deze vragen te beantwoorden. Ten slotte kunnen de hier behaalde resultaten gebruikt worden in modellen voor planeetvorming om de samenstelling van planeten te voorspellen.

# List of publications

## Refereed publications

*Methanol and its relation to the water snowline in the disk around the young outbursting star V883 Ori.*

van 't Hoff, M.L.R., Tobin, J.J., Trapman, L., Harsono, D., Sheehan, P.D., Fischer, W.J., Megeath, S.T., & van Dishoeck, E.F. 2018, *Astrophysical Journal Letters*, 864, L23.

*Linking interstellar and cometary O<sub>2</sub>: a deep search for <sup>16</sup>O<sup>18</sup>O in the solar-type protostar IRAS 16293-2422.*

Taquet, V., van Dishoeck, E.F., Swayne, M., Harsono, D., Jørgensen, J.K., Maud, L., Ligterink, N.F.W., Müller, H.S.P., Codella, C., Altwegg, K., Bieler, A., Coutens, A., Drozdovskaya, M.N., Furuya, K., Persson, M.V., van 't Hoff, M.L.R., Walsh, C., & Wampfler, S.F. 2018, *Astronomy & Astrophysics*, 618, A11.

*Unveiling the physical conditions of the youngest disk. A warm embedded disk in L1527.*

van 't Hoff, M.L.R., Tobin, J.J., Harsono, D., & van Dishoeck, E.F. 2018, *Astronomy & Astrophysics*, 615, A83.

*Imaging the water snowline in a protostellar envelope with H<sup>13</sup>CO<sup>+</sup>.*

van 't Hoff, M.L.R., Persson, M.V., Harsono, D., Taquet, V., Jørgensen, J.K., Visser, R., Bergin, E.A., & van Dishoeck, E.F. 2018, *Astronomy & Astrophysics*, 613, A29.

*Robustness of N<sub>2</sub>H<sup>+</sup> as tracer of the CO snowline.*

van 't Hoff, M.L.R., Walsh, C., Kama, M., Facchini, S., & van Dishoeck, E.F. 2017, *Astronomy & Astrophysics*, 599, A101.

*First detection of methanol in a protoplanetary disk.*

Walsh, C., Loomis, R.A., Öberg, K.I., Kama, M., van 't Hoff, M.L.R., Millar, T.J., Aikawa, Y., Herbst, E., Widicus Weaver, S.L., & Nomura, H. 2016, *Astrophysical Journal Letters*, 823, L10.



## Submitted publications

*Temperature profiles of young disk-like structures: The case of IRAS 16293A.*

van 't Hoff, M.L.R., van Dishoeck, E.F., Jørgensen, J.K., & Calcutt, H. 2019, submitted to *Astronomy & Astrophysics*.

*The VLA/ALMA Nascent Disk and Multiplicity (VANDAM) survey of Orion protostars I. Identifying and characterizing the protostellar content of the OMC2-FIR4 and OMC2-FIR3 regions.*

Tobin, J.J., Megeath, S.T., van 't Hoff, M.L.R., Díaz-Rodríguez, A.K., Reynolds, N., *et al.*, submitted to the *Astrophysical Journal*.

## Conference proceedings

*Imaging the water snowline in protostellar envelopes.*

van 't Hoff, M.L.R. 2018, in *Astrochemistry VII: Through the cosmos from galaxies to planets*, IAU Symposium 332, ed. M. Cunningham, T. Millar & Y. Aikawa (Cambridge Univ. Press, Cambridge), p. 88.

*Unveiling the physical and chemical conditions in the young disk around L1527.*

van 't Hoff, M.L.R., Tobin, J.J., Harsono, D., & van Dishoeck, E.F. 2018, in *Astrochemistry VII: Through the cosmos from galaxies to planets*, IAU Symposium 332, ed. M. Cunningham, T. Millar & Y. Aikawa (Cambridge Univ. Press, Cambridge), p. 121.

# Curriculum Vitae

I was born in Groningen, but within a year we moved to a small nearby village, Garrelsweer. For as long as I can remember, I have been interested in science and nature and spent many weekend days (and nights) joining my father to go bird watching. The advantage of a rural village in the north of the Netherlands is a relatively dark night sky, so our small telescope proved useful not only for birds but also for celestial bodies. During my final year of primary school I followed an extracurricular course on the planets in our Solar System, and my mind was set on becoming an astronaut. However, in high school, the 'Praedinius Gymnasium' in Groningen, I discovered that chemistry and biology (and Greek, Latin, Russian and geography) were just as interesting as physics, leaving me clueless as to what to do after graduation. Until I visited the open day of the Technical University in Delft. Being there mainly for the morning program of Aerospace Engineering, I had an empty schedule for the afternoon and decided to listen to the presentation for Life Science & Technology. This program on biotechnology, cell biology and genetics turned out to combine physics, chemistry and biology, and thus looked like my dream program.

Well, almost, because during my first year I kept wondering "what if I had chosen Astronomy instead?" And with the idea of better having to find out that studying two topics is impossible than always wondering "what if", I enrolled in the Astronomy program in Leiden. The observing trip to La Palma was an amazing experience, where, for once, having difficulty sleeping was an advantage: while my fellow students fell asleep, I helped the PhD student who was observing. In hindsight this experience painted a much too rosy picture - if only all observing runs had beautiful weather and science cases that could be observed in two minutes - but I knew I had made the right decision to start studying Astronomy. For my Bachelor project I went to MPA in Garching, Germany, to work with Henk Spruit and make movies to accompany his manuscript on MHD. This was a great opportunity that drove me further in the direction of Astronomy. However, after finishing both Bachelors I still couldn't choose between looking at cells through a microscope or at stars through a telescope. And, because if you do something, do it right, I decided to continue with both Master programs. For Astronomy, I followed the general research track and I did a minor research project on the false positive rate of *Kepler* planet candidates with Ignas Snellen and Matteo Brogi. My major research project was on  $\text{N}_2\text{H}^+$  as a chemical tracer of CO freeze-out in protoplanetary disks with Ewine van Dishoeck, Catherine Walsh and Mihkel Kama. This was for me an ideal way to do astronomy without losing the chemistry completely.

During my studies I served as a teaching assistant for several Life Science & Technology (lab) courses. An invaluable experience that taught me more than following the course myself. In addition, I was an active member of the Life Science & Technology study society LIFE, where I participated in several committees. An especially fun and memorable highlight was the organization of a symposium with national and international speakers from both academia and industry that was attended by almost 350 students. In my first year, I also joined the student rowing association Asopos de Vliet. For many years, I was involved every day with either rowing or coaching and I was active in numerous committees, both as member and as chairman.

After I finished most of the Astronomy Master program, Ewine van Dishoeck encouraged me to apply for a Leiden Huygens PhD Fellowship, that I ended up being awarded, to study the chemical conditions in young circumstellar disks. Even though I finally made the decision to continue in Astronomy, I immensely enjoyed the Life Science & Technology research project to make 3D images of zebrafish using Optical Projection Tomography that I carried out with Fons Verbeek and Gerda Lamers in the year before starting my PhD. As a PhD student I finished the modeling work that I started during my major research project, and proceeded working on observations of young embedded disks. I have had the privilege to present this work at conferences in Exeter, Madrid, Puerto Varas, Leiden, Zurich, Tucson, Pasadena, Baltimore and Gothenburg and summer schools in Bad Honnef and Grenoble. I also greatly enjoyed an observing run at the IRAM 30m telescope, and visits to the University of Oklahoma, IRAM, Harvard CfA and SAO, the University of Virginia, NRAO Charlottesville, Carnegie DTM and the University of Michigan.

In addition to my own research, I was the teaching assistant for Ewine van Dishoeck's astrochemistry course and I had the pleasure to co-supervise the major research project of Margot Leemker. It was a great experience to organise the Astronomy Olympiad for high school students. I also enjoyed hosting twice the PhD candidates during the Leiden interview days and being involved in the organization of the first year PhD weekend. Moreover, it was an honor to give presentations at several Leiden University open days and to help with various activities. Furthermore, recording a one-minute movie as part of the Eye Openers project of the KNCV<sup>1</sup> was an exciting and instructive opportunity. Finally, I had a lot of fun with the Astronomy on Tap team and I loved giving talks during the main event and many of our "on tour" events. Seeing the enthusiasm of the general public for astronomy is sometimes a welcome reminder that being an astronomer is the best job in the world. I will continue my research as a member of the Michigan Society of Fellows in Ann Arbor.

---

<sup>1</sup><https://www.eye-openers.nl/nl/meetthecrew/merel-van-t-hoff/>

# Acknowledgements

Although, ultimately, you have to write your PhD thesis yourself, there are many people who have contributed in a direct or indirect way. In the 12 years that I spent at the observatory, I have come across many wonderful and inspiring people, many more than I can thank on these few pages, and I am grateful that I had the opportunity to study and work here. Thank you all for making me feel at home, and thank you to all the support staff for making everything run smoothly. I would like to mention some of the people without whom these last four years would have been much more difficult and definitely a lot less fun.

First of all I would like to thank everyone who supervised me during my studies and PhD. Henk, Ignas, Matteo, without your enthusiasm and guidance this thesis would have had a completely different topic. Ignas, I really appreciate the support you gave me as study advisor. Catherine, thank you for being such an inspiring person and mentor, and for teaching me astrochemical modeling. Mihkel, your positivity is very contagious and I enjoyed our conversations on science, life, wine and rowing. John, unfortunately our time in Leiden did not overlap very long, but on the bright side, that did result in a couple very instructive and productive trips. And it made me one of the probably few people who spent their first two stays in the US in Norman, Oklahoma... I greatly enjoyed these trips from both a scientific and personal point of view. I would like to thank you, Alice and Sean, for your hospitality and for showing me around. It were those visits that opened my mind to applying for jobs in the US. Daniel, thank you for always answering all my questions, and for our random chats and rants. I will miss your "what the ...". I would also like to thank everyone I collaborated with. Jes, thank you for including me in the PILS team. But above all, I am grateful, Ewine, for your encouragement to apply for the Huygens Fellowship, for all the invaluable things you have thought me, and for helping me become who I am today.

I am very grateful to have been part of such an amazing and diverse research group. Thank you all for the science, the intense but fun group retreats, the weird discussions during lunch, and the many dinners and after-work drinks. Arthur, Łukasz, it was a great pleasure to share this experience with you and I could fill a book with our travel adventures and inside jokes. Thank you for being there for me when I needed it. Arthur, thank you for getting me to take coffee breaks, for the sarcasm, and for the soul searching. Łukasz, it was always comforting to not be alone in the office at weird hours and I am very happy that we invented rocket shots. Alex, thanks for your cheerfulness and many hilarious conversations. I will miss our civilized Saturday afternoons, guys. Anna, thank you for helping me out with everything when I started my PhD and for being the ideal conference room mate. I am especially grateful that

you shared your story at a for me very crucial time. Andrew, Benoît, Christian, Martijn, Vianney, you were great office mates. Benoît and Martijn, I really enjoyed our protostellar task force discussions, although, was that really the reason we got to share an office? Nadia, thanks for the delicious cakes and the always practical and down-to-earth advice. Maria, chats that we had when I was a Master student made me really feel welcome in the group, and catching up with you at conferences is always fun. Sierk, your trivia knowledge never ceases to amaze and I am very glad you did join for borrel sometimes. Niels, never a dull moment when you are around. Alvaro, thank you for your hospitality and awesome barbecues. Margot, I could not have wished for a better student and I really enjoyed working with you. Paolo, Stefano, unfortunately most of our interactions were via a screen. Paolo, I am looking forward to our rendezvous with Anna, Arthur and Łukasz at the ELT. Stefano, you were the best student in the astrochemistry course; your reaction is what makes teaching fun. Thank you for letting me teach you, and in turn, for teaching me about disk modeling.

There are many other people that made life at the observatory and conferences so enjoyable. Danna, Kirstin, Michał, Alex, Arthur, Łukasz, I have fond memories of our morning coffees. Leon, thank you for all the  $N_2H^+$  discussions and for what turned out to be a much discussed bike ride. Jeroen, vriendelijk afgewezen! Liz, I am very happy that you started with Astronomy on Tap. Thank you and the rest of the team for many wonderful events. Richard, it was largely due to you that I felt so at home at my first conference. Djoeke, you are a wonderful travel companion. Ilse, I am grateful for all the advice you gave me over the years.

Finally, Eric, Eveline, Florianne, Janneke, Lisa, Lotte, Marjolein, Thijs, although our get-togethers were too infrequent, they were always very gezellig and a welcome distraction. Papa, mama, thank you for always supporting me, whatever crazy I decided to do. This means the world to me. Michel, Vera, Lotte, your interest and questions about what I am doing have been a great encouragement. Wat betreft de Nederlandse samenvatting; bedankt voor de tip, Marjan! Daniël, thank you for having been there every step of the way and for believing in me, especially at all those moments that I did not.